istituto nazionale di fisica nucleare
laboratori nazionali di frascati

2009
ANNUAL REPORT

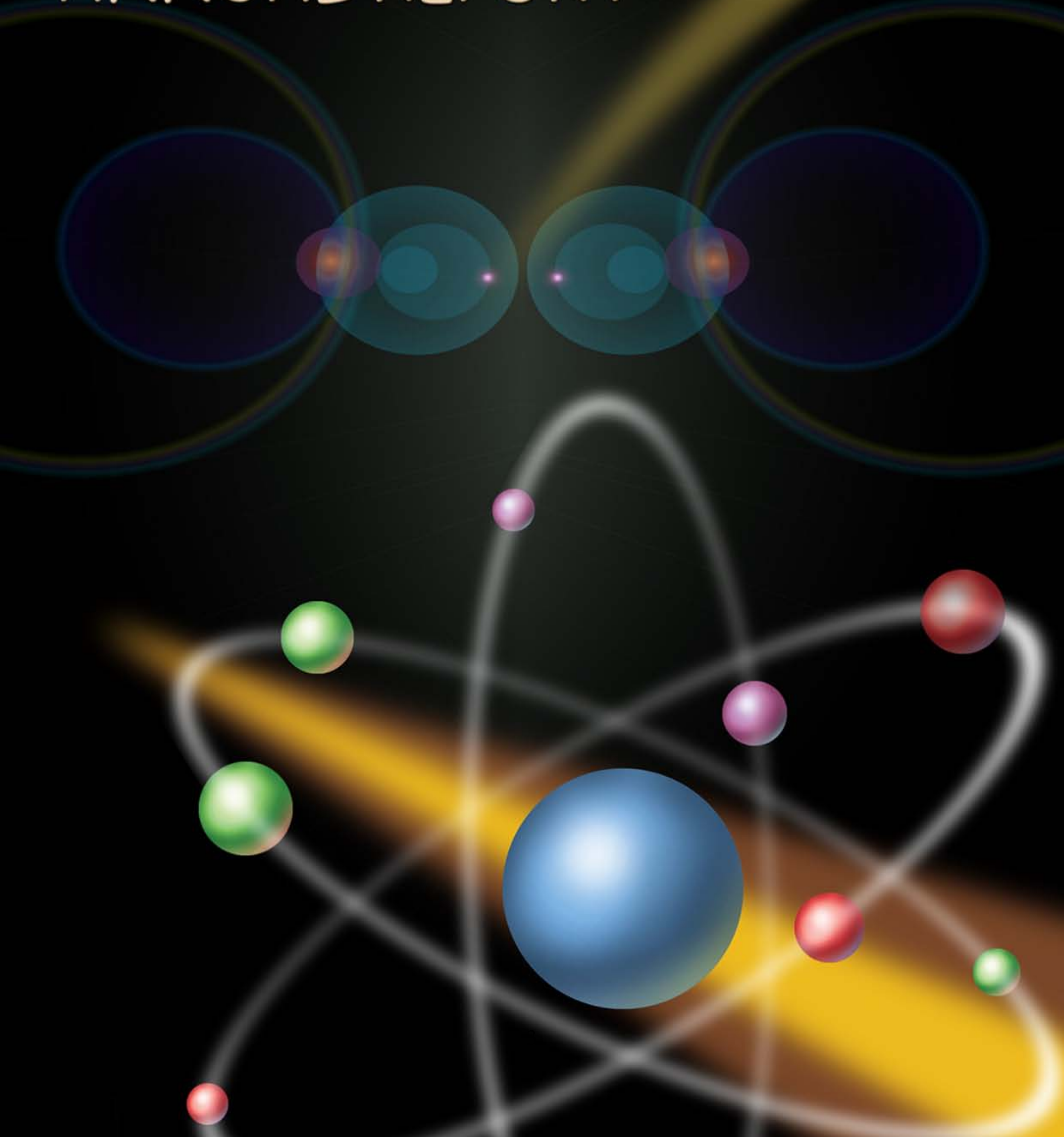

Scientific Editor
D. Babusci

Technical Editor
L. Invidia

Editorial Office
D. Bifaretti
A. Cupellini

Cover: “Collision”
Cover artwork: Claudio Federici

istituto nazionale di fisica nucleare

laboratori nazionali di frascati

2009

ANNUAL REPORT

LNF-10/15 (IR)
May, 2010

Published by
SIDS-Publications & Library
P.O. Box 13 – I–00044 Frascati (Italia)

Available at www.lnf.infn.it/rapatt

Mario Calvetti
LNF Director

Vitaliano Chiarella
Head, Research Division

Pantaleo Raimondi
Head, Accelerator Division

Claudio Sanelli
Head, Technical Division

LNF Scientific Coordinators

Riccardo de Sangro
Particle Physics

Francesco Terranova
Astroparticle Physics

Pasquale Di Nezza
Nuclear Physics

Gino Isidori
Theory and Phenomenology

Roberto Cimino
Technological and Interdisciplinary Research

2009 ANNUAL REPORT
CONTENTS

1 – Particle Physics

2 – Astroparticle Physics

3 – Nuclear Physics

4 – Theory and Phenomenology

5 – Technological and Interdisciplinary Research

6 – Accelerator Physics

General Informations

1 – Particle Physics

ATLAS

A. Annovi, M. Antonelli, M.M. Beretta (Art. 23), H. Bilokon, E. Capitolo (Tecn.), F. Cerutti,
V. Chiarella, M. Curatolo, B. Esposito (Resp.), M.L. Ferrer, C. Gatti,
P.F. Laurelli, G. Maccarrone, A. Martini, G. Nicoletti, G. Pileggi (Tecn.),
B. Ponzio (Tecn.), V. Russo (Tecn.), A. Salvucci (Laur.), A. Sansoni,
M. Testa (Ass. Ric.), T. Vassilieva (Tecn.), E. Vilucchi (Art. 23), V. Zambrano (Bors.).

In collaboration with:
Centro di Calcolo:
M. Pistoni, C. Soprano

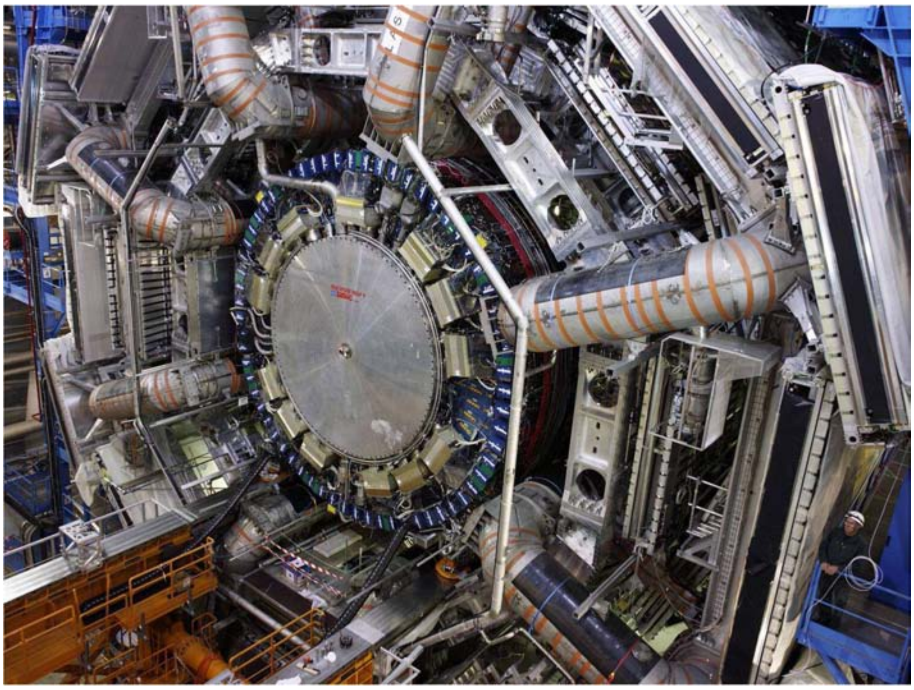

1 Introduction

In the year 2009, after a long shut-down to make the necessary repairs on the LHC machine following the September 2008 accident, there has been a LHC run in November and December. The ATLAS experiment has used the long shut-down to consolidate the status of the detector. All the monitoring and analysis tools have been finalized and tested. The analysis chain has been exercised as much as possible. ATLAS has collected hundreds of millions of cosmic muons in several detector configurations. The data, together with the cosmics data taken in 2008, have been used to deeply understand the detector performance. As a consequence of the very accurate preparation, at the start of the data taking with collisions (November 23, 2009), the percentage of working channels in all the ATLAS sub-detectors was larger than 98%.

In the November-December run, ATLAS has collected an integrated luminosity of $\sim 20\ \mu\mathrm{b}^{-1}$ (any beam condition) and $12\ \mu\mathrm{b}^{-1}$ (stable beam condition) at 900 GeV, and of $\sim 0.7\mu\mathrm{b}^{-1}$ (any beam condition) at 2.36 TeV. The events have been collected using mainly a minimum bias trigger. The number of minimum bias events collected is $\sim$ 1 Million.

The analysis of these events has allowed a detailed commissioning of the inner part of ATLAS while limited studies were possible for the muon spectrometer because of the limited number of muons (<200), dominated by low momentum π/K decays. ATLAS has proven to master track reconstruction and momentum scale within expectations (K^0, Λ invariant mass peaks agree with the PDG values and with simulation), has reconstructed photon conversions inside the tracker and verified the transition radiation onset with electrons from conversions. First indication of proper operation of the calorimeters has been obtained with the reconstruction of the π^0 invariant mass peak and with the measurement of the $\not{E}_T$ resolution (both measurements have been found to match the simulation expectations).

The muon reconstruction and trigger commissioning remain still to be finalized when the luminosity and the energy of the accelerator will increase.

The activity of the Frascati group has been mostly focused on the study of the performances of the muon detector, the preparation of the analysis in the channels Z$\rightarrow \mu\mu$, W$\rightarrow \mu\nu$, Z$' \rightarrow \mu\mu$, the operation of the computing resources of the Frascati Proto-Tier2 and the development of the Fast Track (FTK) proposal for the upgrade of the trigger system.

In the following sections more is reported about these activities.

2 MDT Detector status

The Monitored Drift Tube (MDT) chambers provide the precision tracking in the muon spectrometer. During the year 2009, with the cavern open, activities have been carried on to repair, where possible, the very last not working channels and to install some of the staged EE chambers. Several hundred millions of cosmic tracks have been recorded in the period May-August 2009 allowing the commissioning of the DCS (Detector Control System), the online/offline Data Quality and the calibration. The analysis of these data complemented the results of the 2008 run and allowed additional systematic studies on MDT performance and alignment. All this information is now summarized in an Atlas note.

2.1 Single Tube Resolution

The cosmic ray muons cross the tubes with an arbitrary phase with respect to the front-end electronics clock. This implies a time jitter corresponding to a 25 ns uniform distribution. Two methods have been studied to correct for this effect. In the first method the MDT timing is corrected by using the RPC trigger time reference. This is feasible for the Medium Chambers, but difficult for Inner and Outer Chambers. The second method consists in refitting the overall track using a further parameter called global T_0, which takes care of the time position of the track in the 25 ns clock interval. Both methods improve the value of the intrinsic spatial resolution (as compared to 2008 data) approaching the MDT single tube resolution value as measured in the test beam (Fig. 1).

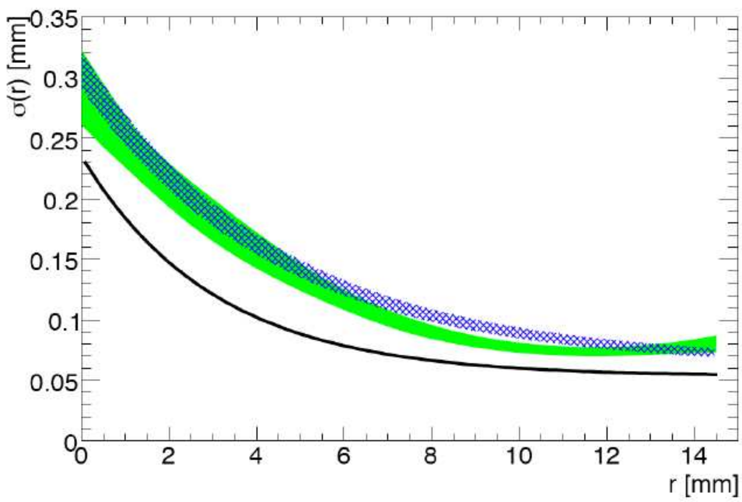

Figure 1: (color online). Drift tube resolution as a function of the radius. The green shadowed and the blue hatched bands represent the resolution function measured with cosmic rays with the two different methods described in the text. The solid line represents the resolution measured with a high momentum muon beam.

2.2 Single Tube Efficiency

The single tube efficiency was studied excluding one MDT layer at the time in a track segment reconstruction. Two different causes of inefficiencies can happen; one due to really missing hits, the other due to non association of an existing hit because of a too large residual . This second kind of inefficiency is mostly due to delta-rays produced by the muon itself. The measured efficiency runs from 99,8% for the hardware efficiency, to 96,3% for hits at 5σ distance from the segment. In Fig. 2 the single tube efficiency for a BML, the chambers built in Frascati, is shown.

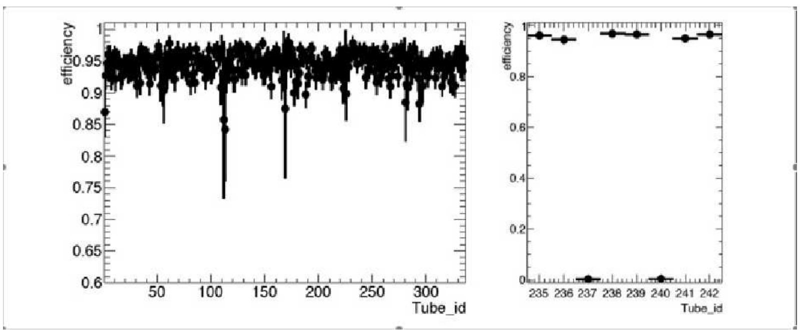

Figure 2: Single tube tracking efficiencies with a 5σ association cut, as explained in the text, for a BML chamber. The plot on the right shows an expanded view in the region where two tubes with the wire disconnected were found.

2.3 Alignment

The chamber alignment in the Endcap region achieved already the expected performance ($\sim 40\mu$m) using only the optical alignment sensors. The chamber alignment in the Barrel region could not reach the same performance without a final tuning with reconstructed tracks. This has been done in 2009 with cosmic tracks which were straight in the muon spectrometer (toroidal field off), with momentum selected using the solenoid and the Inner Detector (ID). The results agree with expectations, but are limited to those sectors well covered by the cosmic ray flux.

2.4 Sagitta Resolution

The sagitta resolution for runs with B-field = 0 in the Muon Spectrometer (MS) can be studied as a function of the muon momentum measured in the ATLAS inner detector when the solenoidal field is on. The sagitta resolution as a function of the muon momentum can be parametrized as:

$$\sigma_{sag(p)} = \frac{K_0}{p} \oplus K_1 \tag{1}$$

The first contribution, the K_0 term, comes from the multiple scattering due to the material in the MS and the second contribution, the K_1 term, takes into account the intrinsic single tube resolution and the chamber alignment. These two terms have been already measured at the test beam at CERN and found to be K_0 = 9 mm·GeV and K_1 = 50 μm. A similar measurement has been performed on cosmics data by selecting segment triplets (Inner, Middle and Outer station) of MS projective towers. The rms of the sagitta of the Middle station segment with respect to the Outer-Inner straight line has been fitted in six momentum bins. The result shown in Fig. 3 is for the upper large sector. The RPC-time corrections, as described before have been applied in the calibration procedure. The fitted value for the two terms are $K_0 = (12.2 \pm 0.7)$ mm·GeV and $K_1 = (107 \pm 21)$ μm. In the ATLAS detector the multiple scattering term is expected to be worse than the one measured at the test beam setup. Moreover this term is expected to be much larger for Small sectors due to the presence of the toroid coils in between the Inner and Outer chambers. Concernign the intrinsic term the value for this specific sector is about a factor two worse than the test beam one. Several effects are contributing to that including alignment, chamber deformations, calibration and single-tube resolution.

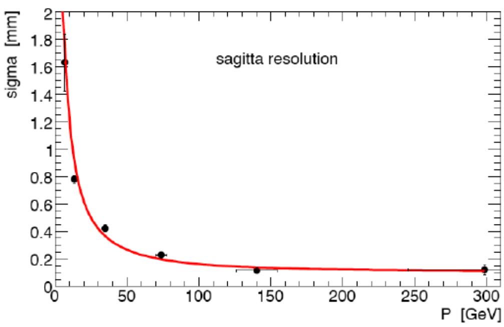

Figure 3: Mean value of the sagitta rms for sector 5 as a function of the Muon momentum as measured by the Inner Detector. The fit to the function described in the text is superimposed.

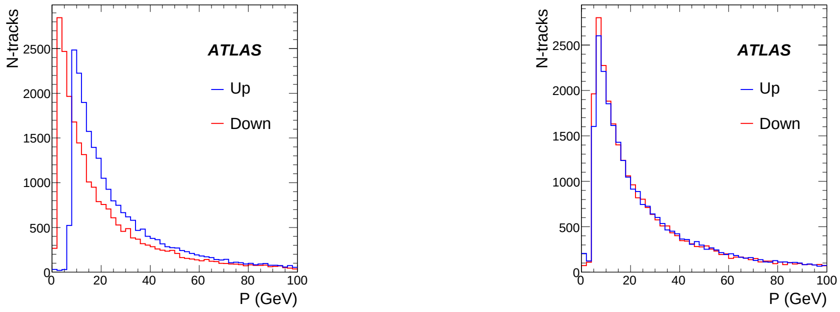

Figure 4: Left: Distribution of momentum of cosmic muons as measured at the MS entrance for the upper and lower hemispheres. The difference between the two distributions is due to the ID track momentum cut of 5 GeV. Right: same distributions extrapolated at the IP.

2.5 Cosmic Muon Spectrum

The distribution of cosmic muons momentum was measured when the magnetic field was on. The momentum measurement can be referred at the MS entrance or at the point of closest approach to the ATLAS Intersection Point(IP). In the second case, for tracks crossing the ID, the energy loss in the calorimeters was corrected for. The distribution of momentum at the MS entrance is shown on the left of Fig. 4 for the top and bottom hemispheres separately. The difference between the two distributions is due to the ID track momentum cut of 5 GeV that translates in different momentum cut-offs in the two MS hemispheres since cosmic muons are directed downwards. In the same figure on the right the same distribution extrapolated at the IP is shown. In this case the correction for the energy loss in the calorimeter removes the offset.

2.6 Momentum Resolution

For each track the value of transverse momentum was evaluated at the IP in the two hemispheres. The difference between the two values divided by their average was considered for eleven bins of p_T.

$$\frac{\Delta p_T}{p_T} = 2\,\frac{p_{Tup} - p_{Tdw}}{p_{Tup} + p_{Tdw}} \tag{2}$$

The distribution was fitted in each bin with a double-Gaussian function with the narrow Gaussian convoluted with a Landau function. The p_T relative resolution as a function of the transverse momentum is shown in Fig. 5. The resolution function can be fitted with the sum in quadrature of three terms, the term due to the energy loss corrections P_0, the multiple scattering term P_1, and the intrinsic resolution P_2.

$$\frac{\sigma_{p_T}}{p_T} = \frac{P_0}{p_T} \oplus P_1 \oplus P_2 \star p_T \tag{3}$$

The result of the fit is shown in the same figure. The values of the parameters are: P_0 = 0.29±0.03±0.01 GeV, P_1 = 0.043±0.002±0.002, P_2 = (4.1±0.4±0.6)$\star 10^{-4}$ GeV^{-1}. The values of the three parameters were also computed with a Monte Carlo simulation of the MS, using single muons from collision samples, obtainig: P_0 = 0.35 GeV, P_1 = 0.035 and P_2 = 1.2$\star 10^{-4}$ GeV^{-1}. The result is in fair agreement with the expected values for the first two terms, while the intrinsic term is worse. The difference has been investigated to trace the effects that contribute to worsen the resolution with cosmics, mostly due to time jitter not completely corrected and chamber misalignment.

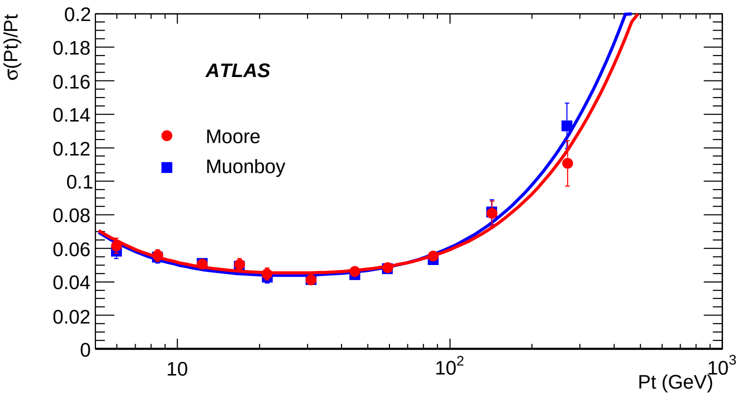

Figure 5: (color online). Transverse momentum resolution evaluated with the top bottom method explained in the text as a function of p_T. The fit to the three resoluton parameters as described in the text is superimposed.

2.7 Collision Data

From late November 2009 some collision events (mostly with beams at 450 GeV) have been recorded and analyzed. Due to the low energy and low integrated luminosity only few muons have been recorded and mostly in the forward spectrometer. These muons have been reconstructed (in the muon spectrometer and the inner tracker) and allowed to perform all the checks which are possible with such low statistics.

3 Analysis Activity

During the year 2009 the preparatory analysis on the measurement of Z and W cross sections has been completed. This work, carried out together with INFN sections of Pavia, Cosenza, Roma 2 and Roma 3, is briefly described in the next section. In section 5, the status of the preparatory analysis for the search of an extra gauge boson at the TeV scale (Z') is described.

4 Measurement of the cross section for the processes $pp \to Z/\gamma^* \to \mu\mu$ and $pp \to W \to \mu\nu$

The measurement of W and Z cross sections in the muonic channels, and in particular their ratio, can be done with high accuracy already with an integrated luminosity equal to 10 pb^{-1} that will be collected in the coming months. The uncertainty on the luminosity cancels out in the ratio, and so does part of the theoretical error, allowing to measure this quantity to about 3%. Infact, with this integrated luminosity the expectation is to obtain order of 50,000 W's and 5,000 Z's, corresponding to a statistical error on the ratio of about 1.5%.

In order to reach this accuracy, the analysis of the events cannot rely completely on the Monte Carlo simulation for extracting the selection efficiencies. Moreover, there are large theoretical uncertainties on the cross sections for the production of $b\bar{b}$ and $c\bar{c}$ final states. These events give infact the largest contribution to the muon rate and are the main contribution to the background. Therefore, in the preparatory work all the experimental methods needed to extract from the data efficiencies, background shapes and normalizations, momentum scale and resolution have been implemented.

Pre-selection and filtering of the signal and control samples is performed on the Grid. The initial dataset occupancy is reduced from about 100 kB per event to few kB per event for the final steps of the analysis, that consists of event counting, efficiency determination, and determination of the systematic errors. This approach allows for a fast access to data and Monte Carlo samples (in particular after any re-reconstruction), and a reduced output size that facilitates the final stage of the analysis. The code has been prepared and successfully tested on Monte Carlo samples and is presently being tested running it on the first data.

The outline of the analysis is the following: selection of $Z \to \mu\mu$ events and signal counting, selection of $W \to \mu\nu$ events and signal counting, measurement of single particle efficiencies and determination of the event selection efficiency, study of the impact of momentum and missing energy mis-calibrations.

4.1 Selection of $Z \to \mu\mu$ events

$Z \to \mu\mu$ events are selected by requiring two reconstructed muon tracks in the detector. These tracks must be reconstructed both in the inner detector (ID) and in the muon spectrometer (MS). At least one of the two tracks must fire a muon trigger sector. The lower p_T of the muons must be 15 GeV. This cut is varied up to 25 GeV to study the stability of the measurement.

The main background contribution comes from the decays into muons of $b\bar{b}$ and $c\bar{c}$ pairs. By cutting on the muon isolation their contribution under the Z invariant mass peak can be reduced to few per mil. Since there is a large uncertainty on the cross sections for these processes, methods for determining it from data have been used. The isolation can be defined in such a way to reduce the correlations with the other selection requirements. In this way, the events rejected by the isolation cut reproduce with good accuracy the invariant mass shape of the selected background events. This shape is then used to fit the background under the signal. A procedure to determine the background has also been developed with same sign dimuons.

The correctness of the analysis procedure has been verified with the analysis of a pseudo-data sample showing that the correct number of signal events is obtained.

The other main sources of background are $Z \to \tau\tau$ and $t\bar{t}$ events. For these events the theoretical uncertainties are much smaller (12% for $t\bar{t}$ cross section). As a first approximation, their contribution is fixed by the Monte Carlo simulation relatively to the Z yield. Moreover, a method based on the selection of muon-electron pairs has been developed to constrain the background from the data.

4.2 Selection of $W \rightarrow \mu\nu$ events

The largest uncertainty to the contamination to W events is again due to $b\bar{b}$ and $c\bar{c}$ processes. Once more, two methods to constrain this contribution from data have been developed. In a first approach, a signal and a sideband region is defined according to the value of the impact parameter of the muon. The sideband region is enriched by heavy-Q decays. These events are used for determining the transverse mass shape of the QCD background in the signal region. It is also possible to determine the relative amount of $b\bar{b}$ and $c\bar{c}$ decays from the distribution of the p_T of the muon relative to the jet direction. This variable is infact related to the mass of the parent hadron.

In the second approach, the events rejected by the isolation cut are used to reproduce the transverse mass shape of the QCD background.

4.3 Impact of momentum and missing energy miscalibrations

In order to determine the impact of miscalibration on the event counting, several Monte Carlo samples have been reconstructed with a different geometry with respect to the one used in the simulation. The new geometries were obtained by shifting and rotating muon chambers and ID elements, ending up in misalignments from few tens of microns to a few hundreds. Moreover, a less refined calibration of the missing energy for the pseudo-data sample has been used, while using the most refined reconstruction for the Monte Carlo samples. The induced miscalibration effects are of the order or higher than those measured from studies with cosmic rays and minimum bias data.

First, the maximal impact of the miscalibrations on the measurement has been estimated, then a parametrization of these effects has been included in the Monte Carlo and the relevant parameters have been determined: the global scale and resolution for the muon momentum and for the missing energy. In this way the systematic error reduction and the simultaneous determination of important performance parameters, also useful for other measurements, for instance for the discovery of a Z', can be achieved.

4.4 Determination of the event selection efficiency

The event selection efficiency is determined by factorizing it into the product of single-particle efficiencies: ID tracking; MS tracking; Isolation; Trigger. Each single particle efficiency is measured from $Z \rightarrow \mu\mu$ control samples. For each efficiency determination, $Z \rightarrow \mu\mu$ events are selected without making use of the sub-detector information under test. For instance, MS track efficiency is measured selecting events with one full reconstructed muon track (MS+ID) and an ID track that is associated to an energy release in the calorimeters that is compatible with the passage of a muon. Further cuts on the track impact parameters and on the pair invariant mass are done to reject the background. The efficiencies are measured as a function of kinematic variables and convoluted in a second step with the Monte Carlo signal kinematic to determine the final efficiency. Finally, a correction to the Monte Carlo efficiency is determined. In the Monte Carlo based analysis, the final correction is expected to be equal to one within the statistical error. The impact of miscalibration have been seen to be negligible. The deviation from one has been taken as an estimate of the systematic error.

One of the main sources of systematic error arises from the estimate of the background in the efficiency control sample. Methods similar to those used for the Z counting have been developed to constrain this background with the data.

The analysis on a pseudo-data sample corresponding to 15 pb^{-1} at 10 TeV center of mass energy has been completely performed. The main systematic effects introduced and taken into account, and the experimental techniques implemented to correct them, will be a very useful exercise to be able to fast perform a complete analysis of the data as soon as they will be available. In the coming months several aspects such as the comparison of data and Monte Carlo shapes for several quantities used in the analysis will be deeply investigated, the impact of cosmic-ray background will be studied in particular at low luminosity, and technical details will be considered, such as inserting in the output files data-quality information regarding the detector status.

5 Search for $Z' \to \mu\mu$

The discovery or exclusion of a heavy gauge boson at LHC is possible already with an integrated luminosity of few tens of pb^{-1}. In the past year the impact of misalignments on the potential discovery has been investigated. Misalignments have been considered both in the MS and in the ID. Misalignments that are negligible at the Z scale, where the sagitta is on the order of 1 cm, may lead to large errors and/or inefficiencies in the track reconstruction at the TeV scale. As for the Z and W analysis, the Monte Carlo samples have been reconstructed with geometries different from those used in the simulation. These geometries were obtained by shifting and rotating both the MS chambers and ID elements. Typical misalignments were of the order of tens to hundreds of microns. The impact of the so called "weak-modes" in the inner detector has also been investigated. Such "weak-modes" correspond to geometry distortions that leave the χ^2 of the track unchanged, and therefore are not corrected by a χ^2-based calibration. Such impact has been studied both on selection efficiencies and on resolutions . This work provided a useful feedback to the ATLAS tracking community. Alerted by the effects observed in this study, the ATLAS algorithms taking into account the possible presence of misalignments have been strengthened. It must be stressed that the same tracking algorithms are used in the high level trigger, and a loss of efficiency would lead to an unrecoverable loss of events.

6 Reconstruction of the missing transverse energy

The reconstruction of the missing transverse energy, $\not{E}_T$, is fundamental for the W analysis, in particular for the precise measurement of its mass, as well as for many other studies, including searches for SUSY particles.
A study about the $\not{E}_T$ on $Z(\mu\mu) + X$ events has been performed. Being free from neutrinos, this channel is a good candidate to study the performances of the $\not{E}_T$ reconstruction. In particular the $\not{E}_T$ component along the Z direction, MET_L, which is sensitive to the inter-calibration between the measurement of high-p_T muons from the spectrometer and the energy of the hadronic recoil measured by the calorimeter has been studied .

Fig. 6 shows the average value of MET_L as a function of the transverse momentum of the Z boson for events in which no jets are reconstructed. A miscalibration proportional to the Z boson transverse momentum is visible. In such events the is dominated by soft particles, with average energy below 1 GeV. At such low energies the calorimeter performances are not optimal: the efficiency is low and the E/P distribution is very broad with an average value of ∼0.5. In addition, charged particles with transverse momentum smaller than 500 MeV have a low probability to reach the calorimeter. These effects induce the observed $\not{E}_T$ miscalibration which is not restricted to $Z + X$ events, but is present in all channels where few high-p_T objects are balanced by many soft particles.

For this study, an energy-flow algorithm that adds low-p_T tracks not reaching the calorimeter in the $\not{E}_T$ calculation and substitutes the measurement of the cluster energy with that of the momentum of the associated track, extrapolated to the calorimeter has been developed. The algorithm reduces significantly the miscalibration and improves the resolution of the $\not{E}_T$ (see Figs. 6 and 7).

The algorithm has been checked on a sample of minimum bias data collected at 900 GeV center of mass energy. The resolution of the $\not{E}_T$ x-axis component is shown in Fig. 7 as a function of the sum of transverse energy, ΣE_T, both for the standard and the energy-flow $\not{E}_T$ reconstruction.

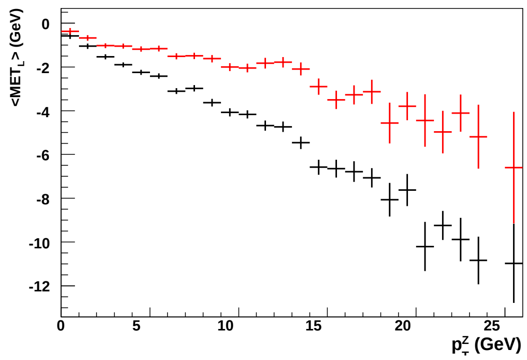

Figure 6: (color online). Average value of MET_L vs the transverse momentum of the Z for $N_{jet} = 0$ for the standard (black line) and the energy-flow (red line) $\not{E}_T$ reconstruction.

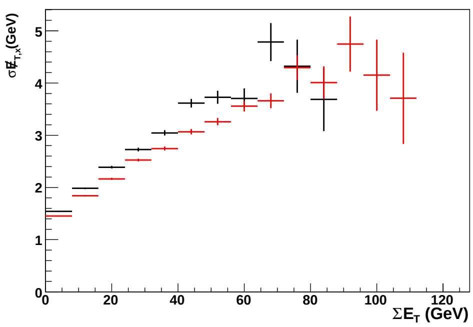

Figure 7: (color online). Resolution of the $\not{E}_T$ x-axis component vs ΣE_T for the standard (black line) and the energy-flow (red line) $\not{E}_T$ reconstruction.

7 LNF Tier-2 activity

The LNF proto-Tier2 is one of the ATLAS computing sites and is part of the ATLAS Italian Tier2 Cloud. In the year 2009 ATLAS has performed the final commissioning of the computing system and has managed and analysed cosmic ray data and the LHC collision data. The final and most important validation has been the Scale Testing for Experiment Program (STEP09) in June, a combined test of all the LHC experiments to verify that the computing system deployed by WLCG (Worldwide LHC Computing Grid) is able to sustain the activities of all the LHC experiments together. The Italian Cloud has been deeply involved in this test and the results obtained were satisfactory. Functional tests of data distribution, production and analysis jobs submissions run continuously in order to check the status of the sites on a daily basis. The readiness of the Tier2 sites to host efficiently all the analysis activities has been tested over the whole year with dedicated periodical stress tests called Hammer Cloud. Moreover in October a User Analysis Test (UAT09) has been set up with a concurrent and chaotic submission of a large number of real analysis jobs in order to verify the behaviour of the sites in conditions similar to those expected during the data taking. Particular attention has been dedicated to the distributed analysis tools, the network systems and the data access protocols which are crucial for an efficient exploitation of the limited computing resources available in the sites. In the last months of 2009 the data collected at LHC has been processed trough the ATLAS computing system.

During 2009 the LNF Tier-2 computing farm has worked at full efficiency providing computing power and data storage for official and private ATLAS simulation and production campaigns. Fig. 8 shows in red the available KSI2k per day and in bordeaux the CPU used by the experiment.

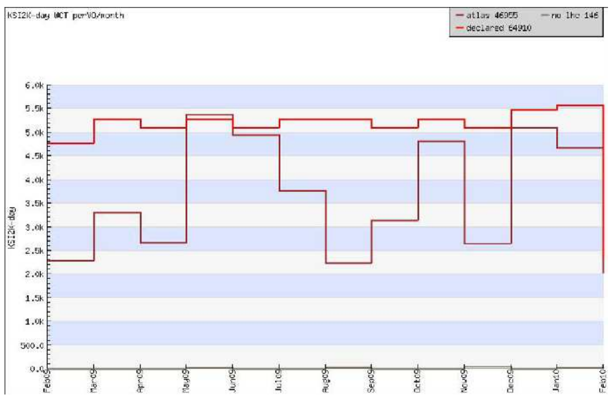

Figure 8: (color online). Available KSI2k per day (red) and CPU used by the experiment (bordeaux).

In 2009 new resources were acquired for the LNF Tier-2 by means of common orders together with the other three Italian ATLAS Tier-2s.

The current configuration of the Tier-2 and local farm are:

- The Tier-2 computing power increased by 3 twin worker nodes (48 cores in addition to the present 80);

- Two new servers replaced the old Computing Element and Storage Element;
- The Tier-2 storage capability of 46 TB usable increased with 48TB raw;
- The local computing power is still of 4 dual-quad core server (i.e. 80 KSI2k);
- The new local storage capability is 30 TB raw.

The LNF Tier-2 personnel has partecipated to all the computing acitivities carried on by the Federation of ATLAS Italian Tier-2s and has contributed to improve the efficiency of Tier-2s, to be ready for the next data tacking.

8 Fast Track

The trigger is a fundamental part of any experiment at hadron colliders. It is needed to select on-line the low cross-section physics from the huge QCD background.

Experience at high luminosity hadron collider experiments shows that controlling trigger rates at high instantaneous luminosity can be extremely challenging. As the luminosity increases, physics goals change in response to new discoveries, and detector aging. It is thus essential that the trigger system be flexible and robust, and have redundancy and significant operating margin. Providing high quality track reconstruction over the full ATLAS Inner Detector by the start of processing in the level-2 computer farm can be an important element in achieving these goals.

With the goal to improve and make more robust the ATLAS trigger, during summer 2007 the group joined the Fast-Track proposal for "A hardware track finder for the ATLAS trigger". This is a proposal to build a hardware track finder (FTK) as an upgrade to the ATLAS trigger. It will provide global reconstruction of tracks above 1 GeV/c in the silicon detectors, with high quality helix parameters, by the beginning of level-2 trigger processing. FTK can be particularly important for the selection of 3rd-generation fermions (b and τ). These have enormous background from QCD jets, which can be quickly rejected in level-2 if reconstructed tracks are available early. This R&D proposal is aimed at producing a full technical design report for FTK. The Frascati group studied a hardware-implementable clustering algorithm for the pixel detector. Clustering in the pixel detector is a non trivial computational problem because of the 2D nature of the pixel detectors and of the huge amount of data involved. The pixel detector's RODs deliver data over 132 S-Link fibers each with a 1.2 Gbs bandwidth. The clustering algorithm must identify and cluster hits as well as calculate the center of the cluster.

These ideas have been studied and resulted in a first implementation of the algorithm that solves the clustering problem with a sensible amount of hardware that is one FPGA (xc5vlx155) for each S-Link fiber. We have a FPGA implementation of the algorithm core. It is a proof of feasibility in the FPGA simulation framework. The outcome of this work was presented at international conferences and published in 3 proceedings:

During the remainder of 2009 we worked on the simulation studies of a possible FTK architecture and of its performances. The goal was to design the FTK architecture for online tracking at the LHC design luminosity of 10^{34} cm^{-2} s^{-1}. During the year, this goal was further increased to SLHC Phase I luminosity of 3*10^{34} cm^{-2} s^{-1}. In 2009, the FTK group managed to prepare the first ATLAS MC samples with pile-up corresponding to 1 and 3 times 10^{34} cm^{-2} s^{-1} luminosity.

These samples were a big surprise because the combinatorial due to high occupancy was larger than expected.

The FTK processor performs pattern recognition with a custom device called the Associative Memory (AM). It is an array of VLSI chips that stores pre-calculated trajectories for a ultra-fast comparison with data. The first way to reduce the combinatorial at high luminosity is to work with better resolution in the AM. In order to do that, we will need a new AM chip with a high density of patterns, so that all possible tracks with a thinner resolution can be stored in the AM. Even with better resolution the number of candidate tracks that the AM will find at these high instantaneous luminosities will be very large. For this reason we redesigned the FTK architecture to increase the internal parallelism and data-flow to accommodate a larger flux of data. Besides increasing the computing power and parallelism, 3 different pattern matching strategies have been designed and simulated. The 11 layer architecture that uses the AM to find tracks segment in all 11 layers (3 pixel layer and 4 double SCT layers). The 8 layer architecture that uses the AM to find tracks segment in the 4 double SCT layers and then extends the found track in the pixels using a second AM system. The 7 layer architecture that uses the AM to find tracks segment in the 3 pixel layers and the 4 r-phi SCT layers. The 7 layer segments are then extended extrapolating and searching for the 4 extra hits in the 4 SCT stereo layers. For all architectures the final fit is a 11 layer fit with full resolution. This work was a joint effort between Frascati, Pisa, Chicago and Illinois to prepare the FTK Technical Proposal. The architecture for running up to LHC design luminosity has been presented to the 11th ICATPP Conference, held in Como in October 2009. In late 2009, Frascati, in collaboration with Pisa and Ferrara, started the R&D work for the new AM chip. This is a very challenging task because its goal is to increase the pattern density with respect to the current AM chip designed for the SVT upgrade at CDF. In order to achieve this goal several separate improvements will be needed: better technology, 90nm instead of 180nm, design full custom cell that implements the core AM logic and possibly implement a 3D silicon device to increase the available area. Frascati is working on the design of the full custom AM cell. An AM chip prototype is expected to be submitted for a mini-asic run by mid 2010.

9 Conference Talks

1. F. Cerutti, *Search for the SM Higgs boson at the LHC*, XXth Hadron Collider Physics Symposium, Evian, France.

2. B. Esposito, *Early physics with ATLAS at LHC*, 14th Lomonosov Conference on Elementary Particle Physics, Moscow, Russia.

3. C. Gatti, *Early new physics searches with leptons at LHC*, Europhysics Conference on High Energy Physics, Krakow, Poland.

4. A. Annovi, *A fast general-purpose clustering algorithm based on FPGAs for high-throughput data processing*, 11th Pisa Meeting on Advanced Detectors, Pisa, Italy.

5. A. Annovi, *The evolution of FTK, a real-time tracker for hadron collider experiments*, 11th ICATPP Conference, Como, Italy.

References

1. A. Doria et al., *Deployment of Job Priority mechanisms in the Italian cloud of the ATLAS experiment*, Proc. 17th International Conference on Computing in High Energy and Nuclear Physics (CHEP09).

2. E. Vilucchi et al., *Activities and Performance Optimization of the Italian Computing Centers Supporting the ATLAS Experiment*, Nuclear Science Symposium Record, IEEE, 516, (2009).

3. A. Baroncelli et al., *$pp \to \gamma/Z \to \mu^+\mu^-$ and $pp \to W \to \mu\nu$ inclusive cross-section measurement in early data with the ATLAS detector*, ATL-COM-PHYS-2010-124.

4. C. Gatti, *Early new physics searches with leptons at LHC*, PoS(EPS-HEP 2009)240.

5. E. Bouhova-Thacker et al., *Impact of Inner Detector and Muon Spectrometer Misalignments on Physics*, ATL-PHYS-INT-2009-067.

6. A. Annovi, M. Beretta, *A fast general-purpose clustering algorithm based on FPGAs for high-throughput data processing*, Proc. 11th Pisa Meeting on Advanced Detectors, 2009

7. A. Annovi et al., *A Fast FPGA-Based Clustering Algorithm for Real Time Image Processin*, book of abstract ITBS 2009 Milos, Greece.

BABAR

R. Baldini Ferroli, A. Calcaterra, L. Daniello (Tecn.), R. de Sangro, G. Finocchiaro, S. Pacetti (Bors.), P. Patteri, I. Peruzzi (Resp.), M. Piccolo, M. Rama, A. Zallo

1 Introduction

The *BaBar* experiment has been running at the PEP-II asymmetric B factory of the SLAC National Laboratory (Stanford, USA) from 2001 to 2008, collecting a data sample corresponding to approximately $0.5\,\mathrm{ab}^{-1}$. The data were collected mostly at the CM energy corresponding to the $\Upsilon(4S)$ mass; large data sample were also obtained at the CM energy corresponding to the $\Upsilon(2S)$ and $\Upsilon(3S)$ resonances. The experiment has produced a wealth of important physics results, ranging from measurements of all three angles of the Unitarity triangle, to the discovery of the $D-\bar{D}$ mixing, the discovery of the η_b, the discovery of several interesting charm and charmonium states. The study of the ISR events, also pursued at *BaBar* has produced many important results in the energy range down hadron threshold production. To date the *BaBar* analysis effort has resulted in more than 400 publications. The *BaBar* contribution to the test of the Standard Model predictions for the CP violation in the B system was recognized in the 2008 Nobel Prize motivation. After the end of data taking the complete data set was reprocessed, and large amount of Montecarlo events were generated and fully reconstructed; 2009 was part of the "intense analysis" period which will be completed at the end of 2010, and will be followed by a "steady analysis" period. In collaboration with the BELLE group, the preparation of a "Physics of the B-factories" book to illustrate the analysis strategies and the physics results of the B-factories has started. The *BaBar* collaboration is still over 400 people strong, belonging to 76 Institutions in 12 countries. A schematic view of the *BaBar* detector is presented in Fig. 1.

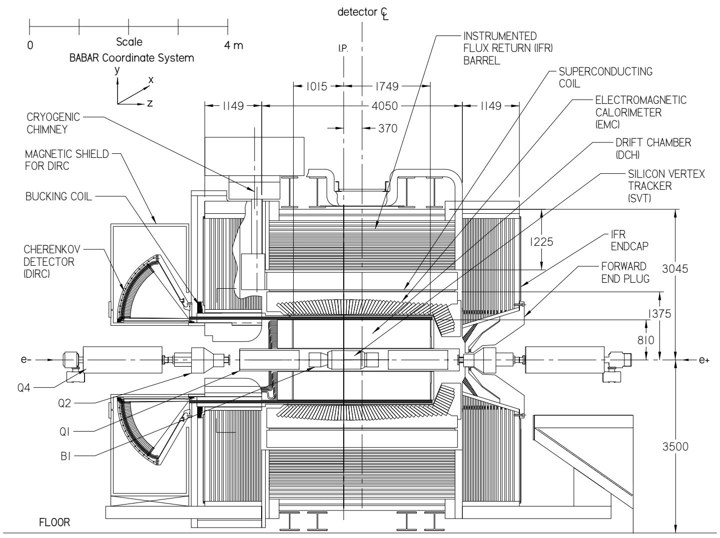

Figure 1: Elevation view of the *BaBar* Detector.

2 Activity

Initial state radiation (ISR) events can be used to measure e^+e^- annihilation at a high luminosity storage ring, such as the B-factory PEP-II. A wide mass range is accessible, contrary to the case of energy scan experiments, which are optimized only in a limited energy region. In addition, the broad-band coverage may result also in greater control of systematic effects because only one experimental setup is involved. Measurements of the main hadronic final states in the energy range between thresholds and 7 GeV have been carried out at BABAR. Besides the study of the $KK\pi$ and $KK\eta$ final states, we are now finalizing the analysis of various $K_SK_L\pi + n\pi^0$ channels, with one, two and three additional π^0's and a study for measuring $e^+e^- \to \pi^0\gamma$ cross section is on going.

2.1 The $K_SK^\pm\pi^\mp$ channel

The previous measurement of the $e^+e^- \to K_SK^\pm\pi^\mp$ cross section [1], obtained with an integrated luminosity of 232 fb^{-1}, has been upgraded including the full available statistics, i.e. 454 fb^{-1}. The new data are shown in Fig. 2, red points, in comparison with the old ones, black points. Besides the dominant isoscalar component, characterized by a main contribution due to the $\phi(1680)$, these new data confirm the presence of significant signal around 2.1 GeV, already observed in $\phi f(980)$ [2] and $\phi\eta$ [1] channels.

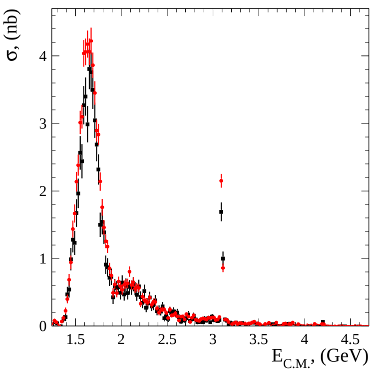

Figure 2: Comparison between previous (black) and new (red) cross section for $e^+e^- \to K_SK^\pm\pi^\mp$.

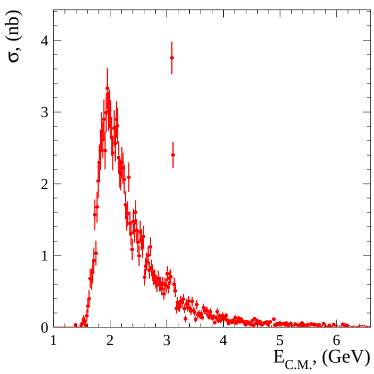

Figure 3: *Cross section for the process* $e^+e^- \to K_SK^\pm\pi^\mp\pi^0$.

2.2 The $K_SK^\pm\pi^\mp\pi^0$ and $K_SK^\pm\pi^\mp\eta$ channels

Figs. 3 and 4 show the $e^+e^- \to K_SK^\pm\pi^\mp\pi^0$ and $e^+e^- \to K_SK^\pm\pi^\mp\eta$ cross sections respectively. In the first case we obtained a cross section very similar the $K_SK\pi$, we have similar structures even though shifted forward by about 300 MeV.
Meanwhile the $K_SK^\pm\pi^\mp\eta$ cross section is lower than the $K_SK^\pm\pi^\mp$ one and shows as a prominent structure only the J/ψ.

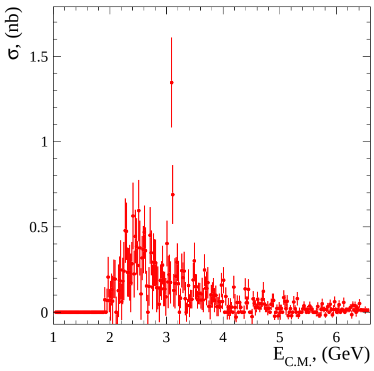

Figure 4: Cross section for the process $e^+e^- \to K_S K^\pm \pi^\mp \eta$.

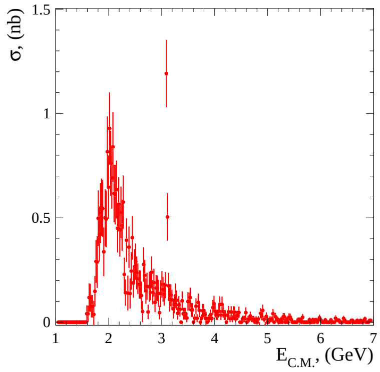

Figure 5: *Cross section for the process* $e^+e^- \to K_S K_S \pi^\pm \pi^\mp$.

2.3 The $K_S K_S \pi^\pm \pi^\mp$ channel

Fig. 5 shows the $e^+e^- \to K_S K_S \pi^\pm \pi^\mp$, this cross section mimics the shape of the $K_S K^\pm \pi^\mp \pi^0$ being a factor of three lower. Such a behavior has also been observed for $K_S K^\pm \pi^\mp$ and $K^\pm K^\mp \pi^0$ final states. This suggests that, as the production of the $KK\pi$ states proceeds via a $K^*(892)\pi$ intermediate state, with the subsequent decay $K^*(892) \to K\pi$, the production of $KK\pi\pi$ passes through two $K^*(892)$ states. In this scenario the dominance of the $K_S K^\pm \pi^\mp \pi^0$ channel over the $K_S K_S \pi^\pm \pi^\mp$ one is a consequence of the fact that in the first case both, neutral and charged $K^*(892)$ can contribute, while in the second case only charged channels are allowed.

2.4 The $K_S K^\pm \pi^\mp \pi^0 \pi^0$ channel

The $e^+e^- \to K_S K^\pm \pi^\mp \pi^0 \pi^0$ cross section, reported in Fig. 6, shows a shape similar to that of the $K_S K^\pm \pi^\mp \eta$, reported in Fig. 4. However in this case two ψ resonances are well visible, the dominant J/ψ and also the $\psi(2S)$, which is not observed in the $K_S K^\pm \pi^\mp \eta$ final state, maybe because of the lower statistics.

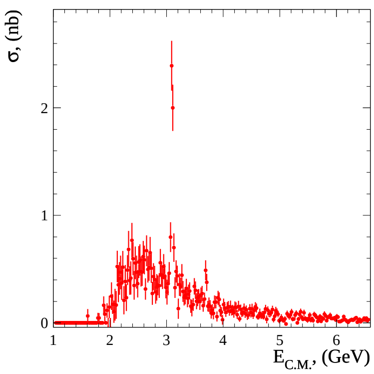

Figure 6: Cross section for the process $e^+e^- \to K_S K^\pm \pi^\mp \pi^0 \pi^0$.

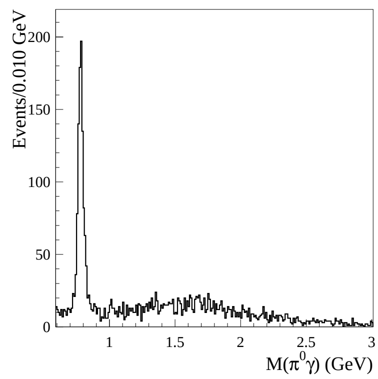

Figure 7: Mass distribution of $e^+e^- \to \pi^0\gamma$ events.

2.5 The $\pi^0\gamma$ channel

The study of the process $e^+e^- \to \pi^0\gamma$ is crucial to gain a better understanding of the dynamics underlying the $\pi^0\gamma^*\gamma$ coupling. In particular we investigate the case where one of the photons is real and the other is virtual with time-like momenta. Furthermore, studying the process $e^+e^- \to \pi^0\gamma^* \to \pi^0 e^+e^-$, where the final photon couples with a pair e^+e^-, we can also gain information on the $\pi^0\gamma^*\gamma^*$ vertex, i.e. π^0 decaying into two virtual and time-like photons. This analysis is still in progress. Fig. 7 shows the preliminary $\pi^0\gamma$ mass distribution. As expected the main contribution is due to the $\omega(782)$ resonance, while only a tiny signal of $\phi(1020)$ is visible.

3 List of Conference Talks

1. R. Baldini Ferroli, *Nucleon form factors via ISR*, 6$^{\text{th}}$ International Workshop on e^+e^- Collisions From Phi to Psi (PHIPSI09), Beijing, China.
2. R. de Sangro, *CKM Physics,* XXXVII International Meeting on Fundamental Physics, Benasque, Spain.
3. R. de Sangro, *New Physics Searches at the B-Factories*, 17$^{\text{th}}$ International Conference on Supersymmetry and the Unification of Fundamental Interactions (SUSY09), Boston, USA.
4. M. Rama, *Measurement of the CKM angle γ,* Flavor Physics and *CP* Violation (FPCP09), Lake Placid, NY, USA.
5. S. Pacetti, *Exotic $c\bar{c}$ Spectroscopy via ISR*, Charmed Exotics 447$^{\text{th}}$ Wilhelm and Else Heraeus Seminar, Bad Honnef, Germany.

4 List of Publications

1. The BaBar Coll., Phys. Rev. D **80**, 092001 (2009).
2. The BaBar Coll., Phys. Rev. D **80**, 092005 (2009).
3. The BaBar Coll.,Phys. Rev. Lett. **103**, 231801 (2009).
4. The BaBar Coll., Phys. Rev. D **80**, 092003 (2009).
5. The BaBar Coll.,Phys. Rev. D **80**, 071103 (2009).
6. The BaBar Coll., Phys. Rev. D **80**, 051105 (2009).
7. The BaBar Coll.,Phys. Rev. D **80**, 051101 (2009).
8. The BaBar Coll.,Phys. Rev. D **80**, 092007 (2009).
9. The BaBar Coll., Phys. Rev. D **80**, 112002 (2009).
10. The BaBar Coll., Phys. Rev. D **80**, 111105 (2009).
11. The BaBar Coll., Phys. Rev. Lett. **103**, 181801 (2009).
12. The BaBar Coll., Phys. Rev. Lett. **103**, 211802 (2009).

13. The BaBaR Coll., Phys. Rev. D **80**, 052002 (2009).
14. The BaBar Coll., Phys. Rev. Lett. **103**, 081803 (2009).
15. The BaBar Coll., Phys. Rev. D **80**, 112001 (2009).
16. The BaBar Coll., Phys. Rev. D **80**, 011101 (2009).
17. The BaBar Coll., Phys. Rev. D **79**, 112009 (2009).
18. The BaBar Coll., Phys. Rev. Lett. **103**, 041802 (2009).
19. The BaBar Coll., Phys. Rev. D **80**, 031102 (2009).
20. The BaBar Coll., Phys. Rev. Lett. **103**, 021801 (2009).
21. The BaBar Coll., Phys. Rev. D **79**, 092001 (2009).
22. The BaBar Coll., Phys. Rev. D **79**, 091101 (2009).
23. The BaBar Coll., Phys. Rev. Lett. **103**, 161801 (2009).
24. The BaBar Coll., Phys. Rev. D **79**, 092002 (2009).
25. The BaBar Coll., Phys. Rev. D **79**, 072006 (2009).
26. The BaBar Coll., Phys. Rev. D **79**, 072009 (2009).
27. The BaBar Coll., Phys. Rev. D **79**, 052005 (2009).
28. The BaBar Coll., Phys. Rev. Lett. **102**, 141802 (2009).
29. The BaBar Coll., Phys. Rev. D **79**, 112004 (2009).
30. The BaBar Coll., Phys. Rev. D **79**, 051102 (2009).
31. The BaBar Coll., Phys. Rev. D **79**, 012004 (2009).

References

1. The BaBar Coll., Phys. Rev. D **77**, 092002 (2008).
2. The BaBar Coll., Phys. Rev. D **74**, 091103 (2006);
   The BaBar Coll., Phys. Rev. D **76**, 012008 (2007).

CDF-2

A. Annovi, M. Cordelli (Resp.), P. Giromini, F. Happacher

1 Introduction

The Tevatron, with a $p\bar{p}$ collision energy of 1.96 TeV in the center of mass system, is running with a record instantaneous luminosity, L, delivered to the experiments of 350×10^{30} cm^{-2}s^{-1} ($vs. \sim 10^{31}$ of Run I). At the end of year 2009, the Tevatron has delivered to the experiments $\sim$ 8400 pb^{-1}; CDF experiment has collected on tape $\sim$ 7000 pb^{-1} (see Figure 1); during the whole Run I we collected $\sim$ 109 pb^{-1}. The CDF data taking is expected to continue through all of year 2010 and likely also through 2011.

The CDF group of Frascati has built the central hadronic calorimeter (the iron-scintillator based calorimeter in the central and end-wall region, CHA and WHA) and is responsible for the hardware maintenance and for the energy scale calibration.

Since year 2005 we are also responsible of the Silicon Vertex Trigger operations.

The analysis interest of the Frascati group focuses on the measurements of b quark production cross sections and vetor Bosons production.

Indeed, the bottom quark production at the Fermilab Tevatron has been called one of the few instances in which experimental results appear to challenge the ability of perturbative QCD to accurately predict absolute rates in hadronic collisions. We are repeating the most significant b quark cross section measurements from Run I in order to clarify the current situation.

Analysis searching for SM pair production of heavy boson pair in the lepton neutrino jet jet channel, that is sensitive to the WW and WZ processes together, is interesting since these events have the same signature of low mass SM Higgs events.

2 Calibration of the central hadron calorimeter

The Frascati group plays a leading role in the calibration of the central hadron calorimeters, CHA/WHA.

For the WHA calorimeter the original Run I ^{137}Cs Sources system is fully working and therefore it can be used to set the absolute energy scale for all the towers; we have taken two ^{137}Cs Source runs during 2007 and we have accordingly computed a set of Linear Energy Response:

$$LER = \frac{^{137}Cs(test - beam)e^{-\Delta t/\tau}}{^{137}Cs(today)}$$

that have been downloaded in the front end electronics to correct the raw ADMEM counts. This system effectively probes the behavior of the calorimeter since the source runs in front of the inner scintillator plane of the wedges thus irradiating few of the scintillator/absorber layers of the calorimeter. In this way we monitor aging phenomena of the scintillator together with PM gain variations.

We calibrate the CHA calorimeter looking at the energy deposition of Minimum Ionizing Particles (i.e. muons from J/Ψ decays).

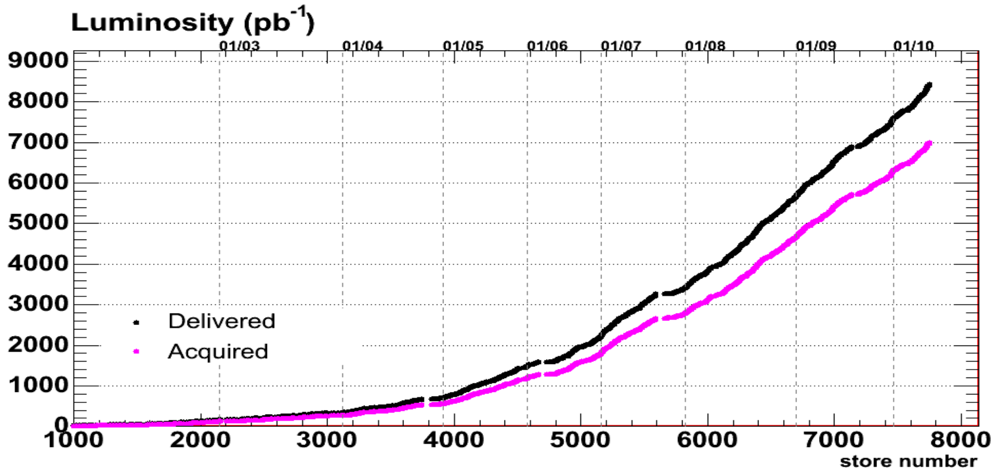

Figure 1: Integrated Luminosity vs time.

We briefly recall the procedure to set the absolute calorimeter energy scale using Mip's. Looking at μ's from the $\sim$ 81 pb^{-1} dimuon trigger sample collected in Run Ib, we determined the necessary statistics to determine the peaks of μ's hadronic energy, HadE, distributions with enough precision per every CHA tower. With a statistics of $\sim$ 40 pb^{-1} we find that the tower by tower peak is determined with a precision of $\sim$ 1.5%. The LER's correction factors are derived comparing tower by tower the HadE deposition for Run I and Run II mips every 30-40 pb^{-1} of data; the LER at a given time time t are defined as the previous set of LER (t-1) multiplied by the observed ratio of the Mip's at a time t and in Run I:

$$LER(t) = LER^{t-1} \times \frac{MIP(RunI)}{MIP(t)}$$

We look at Mip's peaks response every $\sim$ 100 pb^{-1} and the typical response shows a tiny 1.5% gain variations on average and few channels that drift more than 5%.

The laser system represents a quick tool to follow the trend of the PM's gains. We have continuously acquired laser runs since year 2003 to monitor the gain variations of each photomultiplier; the CHA is stable within $\sim$ 2%.

2.1 ONLINE-OFFLINE energy scale calibration

At CDF with the current luminosity the data are being processed through the OFFLINE reconstruction every couple of months. Before producing the fully reconstructed events from the raw information of the detector we first produce small dedicated calibration samples to derive the calibrations constants for all the sub detectors. Every 6-8 weeks we run an executable called CalibExe which produces all the data ntuples for different data sets, including the dimuon trigger data sample where we reconstruct J/Ψ events; then the various calibrators use these samples to derive the calibrations. We made all this procedure automatic during the year 2006.

Usually for the Hadron calorimeters we produce two set of calibrations: ONLINE calibrations are directly downloaded in the ADMEM electronics and are intended to correct the energy response for data that have to be acquired afterward; the OFFLINE calibrations attempts to propagate back to the data already acquired the needed corrections. The calibration constants are then filled in appropriate ORACLE data base tables called CHALINERESPONSE and CHAOFFLER. To validate the OFFLINE calibrations, the same data sets are reconstructed again picking the right calibration tables for every run range they have been produced for and the calibrators have to repeat their analysis to check that the calibrations are correct.

With this procedure the calorimeter response is kept constant at $\sim 2\%$ level over the running period.

3 SVT

The Silicon Vertex Trigger (SVT) is part of the L2 trigger of CDF II. The SVT reconstructs tracks by associating Silicon hits to Central Tracker (COT) tracks reconstructed by the L1 trigger. By using the hits in the silicon, SVT is able to measure the impact parameter of the tracks so that this information can be used by the L2 to select data enriched of heavy flavor decays. Data collected using the SVT processor made possible the first measurement of the B_s mixing.

An upgrade of the track fitting boards of the SVT was developed in Pisa. It is called Giga fitter for its ability to perform one fit per nanosecond. We offer consultancy for development, tests and commissioning.

4 Studies of b quark cross section

4.1 Status of the Tevatron measurements

The bottom quark production at the Fermilab Tevatron has been called one of the few instances in which experimental results appear to challenge the ability of perturbative QCD to accurately predict absolute rates in hadronic collisions. In general, the data are underestimated by the exact next-to-leading-order (NLO) QCD prediction. The most recent measurement from the Tevatron is however in very good agreement with an improved QCD calculation (FONLL), and has prompted a number of studies suggesting that the apparent discrepancy has been resolved with incremental improvements of the measurements and predictions. The increase of the cross-section predicted by FONLL with respect to original NLO calculations, which results into a better agreement with data, is mostly coming from new structure functions and fragmentation functions that have been computed at next-to-leading-order, in order to match the perturbative order of the FONLL calculation. The measured single b-quark cross-section is also in agreement with the prediction of LL shower MC, with an *ad hoc* tuning.

Because of the experimental difficulty inherent to each result, we reviewed all measurements of the single b cross section performed at the Tevatron, and then compared their average to the standard and to the improved QCD predictions. We have also compared the cross sections for producing both b and $\bar{b}$ quarks - centrally and above a given transverse momentum cut - to theoretical predictions. The single b-quark cross section is inferred from the measurement of the production rate as a function of the transverse momentum, p_T, of: B hadrons; or some of their decay products (leptons or ψ mesons); or jets produced by the hadronization of b quarks. Most of the Tevatron measurements correspond to b quarks produced centrally (rapidity $|y^b| \leq 1$) and with $p_T \geq 6$ GeV/c (up to $p_T \simeq 100$ GeV/c). We have performed a consistency check of all available

Table 1: Ratio R of measured single b cross sections to a prediction based on the exact NLO calculation.

channel	R for $p_T^{\min}$ (GeV/c) =					
	6	$8-10$	$12-15$	$19-21$	$\simeq 29$	$\simeq 40$
$J/\psi K^+$		$4.0 \pm 15\%$	(3.4)			
$J/\psi K^+$		$2.9 \pm 23\%$	(1.9)			
$\mu\ X$				$2.5 \pm 26\%$	(1.9)	
$e\ X$			$2.4 \pm 27\%$			
eD^0				$2.1 \pm 34\%$		
$J/\psi\ X$		$4.0 \pm 10\%$	(3.4)			
$J/\psi\ X$		$3.1 \pm 9\%$	(2.7)			
$\mu\ X$	$2.1 \pm 27\%$		(1.7)			
$\mu\ X$	$2.5 \pm 25\%$		(3.5)			
b jets (μ)				$2.4 \pm 20\%$		(2.0)

data. For that purpose, we use the value of the single b-quark cross section extracted from the data and integrated from the p_T threshold of each experiment. We determined the ratio R of each measurement to the same theoretical prediction. We have then evaluated the average R and its dispersion. As benchmark prediction of the b-quark parton-level cross section we choose the exact NLO calculation implemented with old but consistent sets of parton distribution functions (PDF), since it has been used in most published works, convoluted with the Peterson fragmentation function; B-hadron decay are modeled with the QQ Monte Carlo generator program.

There are 10 measurements of the single b cross section performed by the CDF and DØ collaborations at the Tevatron. The ratios of these measurements to the standard theory are summarized in Table 1.

Using the measurements listed in Table 1, we derive an average ratio of the data to the standard theory that is $< R >= 2.8$; the RMS deviation of the 10 measurements in Table 1 is 0.7 It has to be noticed that all the measurement involving the J/Ψ reconstruction, experimentally the cleanest, are consistently much higher than the ones based on the detection of a semileptonic decay.

The new measurement of the $B^+ \to J/\Psi(\to \mu^+\mu^-)K^+$ differential cross section (see next paragraph) carried on by the Frascati group finds a ratio R with the theory of 2.80 ± 0.24, somehow closer to the average of all measurements.

Leading-order (LO) and higher-than-LO terms are sources of b and $\bar{b}$ quarks with quite different topological structure. The production of events with both a b and $\bar{b}$ quark with $p_T \geq$ 6 GeV/c and $|y| \leq 1$ is dominated by LO diagrams and the parton-level cross sections predicted by the exact NLO calculation is comparable to that predicted by LL Monte Carlo generators.

R_{2b}, the ratio of $\sigma_{b\bar{b}}$ measured at the Tevatron to the exact NLO prediction, $\simeq 1$ would imply that the parton-level cross section predicted by LL generators (NLO) is correct and that the contribution of higher-than-LO terms has to be a factor of two larger than in the present NLO or FONLL prediction. If the ratio R_{2b} is much larger than one, then the agreement between the

Table 2: Ratio R_{2b} of $\sigma_{b\bar{b}}$, the observed cross section for producing both b and $\bar{b}$ quarks, centrally and above a given $p_T^{\rm min}$ threshold, to the exact NLO prediction.

channel	R_{2b} for $p_T^{\rm min}$ (GeV/c) =			
	$6-7$	10	15	$\simeq 20$
$b+b$ jets			$1.2 \pm 25\%$	
$b+\bar{b}$ jets				$1.0 \pm 32\%$
$\mu + b$ jet		$1.5 \pm 10\%$		
$\mu^+ + \mu^-$	$3.0 \pm 20\%$			
$\mu^+ + \mu^-$	$2.3 \pm 33\%$			

observed single b cross section and the prediction of LL Monte Carlo generators is fortuitous and agreement with the data may be found by using harder fragmentation functions as in the FONLL calculation.

We review five measurements, listed in Table 2, and derive a value of $< R_{2b} >= 1.8$ with a 0.8 RMS deviation. Such a large RMS deviation indicates that the experimental results are inconsistent among themselves. Additional measurements are certainly needed to clarify the experimental situation.

4.2 $b\bar{b}$ correlation

This study is a new measurement of $\sigma_{b\bar{b}}$ that uses dimuons arising from from $b\bar{b}$ production. At the Tevatron, dimuon events result from decays of heavy quark pairs ($b\bar{b}$ and $c\bar{c}$), the Drell-Yan process, charmonium and bottomonium decays, and decays of π and K mesons. Background to dilepton events also comes from the misidentification of π or K mesons. We make use of the precision tracking provided by the CDF silicon microvertex detector to evaluate the fractions of leptons due to long-lived b- and c-hadron decays, and to the other background contributions.

The method used to determine the $b\bar{b}$ and $c\bar{c}$ content of the data is to fit the observed impact parameter distribution of the muon pairs with the expected impact parameter distributions of leptons from various sources. After data selection, the main sources of reconstructed muons are semileptonic decays of bottom and charmed hadrons, and prompt decays of onia and Drell-Yan production.

Herwig Monte Carlo simulations are used to model the impact parameter distributions for leptons from b- and c-hadron decays. The impact parameter distribution of leptons from prompt sources such as quarkonia decays and Drell-Yan production is derived using muons from $\Upsilon(1S)$ decays. Fig. 2 shows the breakdown of the result of the fit to the data with the various sources of dimuon events.

For muons with $p_T \geq 3$ GeV/c and $|\eta| \leq 0.7$, that are produced by b and $\bar{b}$ quarks with $p_T \geq 2$ GeV/c and $|y| \leq 1.3$, we measure $\sigma_{b\to\mu,\bar{b}\to\mu} = 1549 \pm 133$ pb. The NLO prediction is $\sigma_{b\to\mu,\bar{b}\to\mu} = 1293 \pm 201$ pb. The ratio of the data to the NLO prediction is 1.20 ± 0.21.

This analysis has been published on Phys. Rev. D **77**, 072004 (2008).

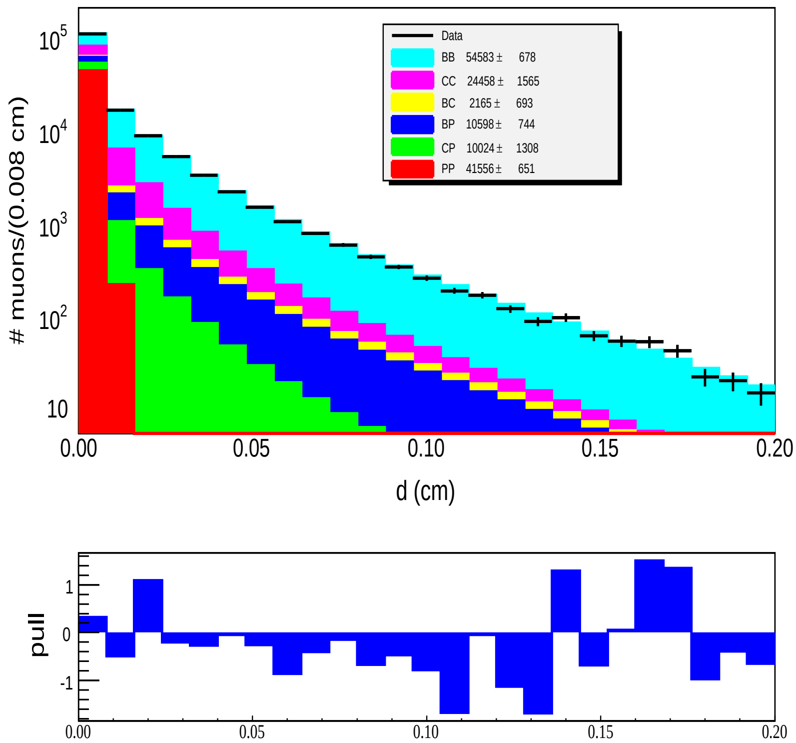

Figure 2: (color online). For each contribution the impact parameter distribution of muon pairs is compared to the fit result (histogram).

5 Study of Multi-Muons events

This study reports the observation of an anomalous muon production in $p\bar{p}$ interactions at $\sqrt{s} =$ 1.96 TeV. The analysis was motivated by the presence of several inconsistencies that affect or affected the $b\bar{b}$ production at the Tevatron: (a) the ratio of the observed $b\bar{b}$ correlated production cross section to the exact next-to-leading-order (NLO) QCD prediction is 1.15 ± 0.21 when b quarks are selected via secondary vertex identification, whereas this ratio is found to be significantly larger than two when b quarks are identified through their semileptonic decays; (b) sequential semileptonic decays of single b quarks are considered to be the main source of dilepton events with invariant mass smaller than that of a b quark. However, the observed invariant mass spectrum is not well modeled by the standard model (SM) simulation of this process; and (c) the value of $\bar{\chi}$, the average time integrated mixing probability of b flavored hadrons derived from the ratio of muon pairs from b and $\bar{b}$ quarks semileptonic decays with opposite and same sign charge, is measured at hadron colliders to be larger than that measured by the LEP experiments. This analysis extends a recent study by the CDF collaboration which has used a dimuon data sample to measure the correlated $\sigma_{b\to\mu,\bar{b}\to\mu}$ cross section. After briefly describing that study, it is shown that varying the dimuon selection criteria isolates a sizable, but unexpected background that contains muons with an anomalous impact parameter distribution. Further investigation shows that a smaller fraction of these events also has anomalously large track and muon multiplicities. We are unable to account for the size and properties of these events in terms of known SM processes, even in conjunction with possible detector mismeasurement effects.

The study presented here uses the same data and Monte Carlo simulated samples, and the same analysis methods used in the $\sigma_{b\to\mu,\bar{b}\to\mu}$ measurement. We use events containing two central ($|\eta| < 0.7$) muons, each with transverse momentum $p_T \geq 3$ GeV/c, and with invariant mass larger than 5 GeV/c^2. The value of $\sigma_{b\to\mu,\bar{b}\to\mu}$ is determined by fitting the impact parameter distribution of these primary muons with the expected shapes from all known sources. To ensure an accurate impact parameter determination, it is used a subset of dimuon events in which each muon track is reconstructed in the SVX with hits in the two inner layers and in at least four of the inner six layers. The data are nicely described by a fit with contributions from the following QCD processes: semileptonic heavy flavor decays, prompt quarkonia decays, Drell-Yan production, and instrumental backgrounds from hadrons mimicking the muon signal. Using the fit result, shown in Fig. 2, we measure $\sigma_{b\to\mu,\bar{b}\to\mu} = 1549 \pm 133$ pb for muons with $p_T \geq 3$ GeV/c and $|\eta| \leq 0.7$.

This result is in good agreement with theoretical expectations as well as with analogous measurements that identify b quarks via secondary vertex identification. However, it is also substantially smaller than previous measurements of this cross section, and raises some concern about the composition of the initial dimuon sample prior to the SVX requirements. The tight SVX requirements used in the $\sigma_{b\to\mu,\bar{b}\to\mu}$ measurement select events in which both muons arise from parent particles that have decayed within a distance of $\simeq 1.5$ cm from the $p\bar{p}$ interaction primary vertex in the plane transverse to the beam line. Using Monte Carlo simulations, we estimate that approximately 96% of the dimuon events contributed by known QCD processes satisfy this latter condition. Since the events selected in the $b\bar{b}$ correlation measurement are well described by known QCD processes, we can independently estimate the efficiency of the tight SVX requirements. Using control samples of data from various sources and the sample composition determined by the fit to the muon impact parameter distribution, we estimate that (24.4 ± 0.2)% of the initial sample should survive the tight SVX requirements, whereas only (19.30 ± 0.04)% actually do.

This suggests the presence of an additional background that has been suppressed when making the tight SVX requirements. The size of this unexpected dimuon source is estimated as the difference of the total number of dimuon events, prior to any SVX requirements, and the expected contribution from the known QCD sources. This latter contribution is estimated as the number of events surviving the tight SVX requirements divided by the efficiency of that selection. In a data set corresponding to an integrated luminosity of 742 pb^{-1}, 143743 dimuon events survive the tight SVX cuts. Dividing this number by the 24.4% efficiency of the tight SVX selection criteria we expect 589111 ± 4829 QCD events to contribute to the initial sample whereas 743006 are observed. The difference, 153895 ± 4829 events, is comparable in magnitude to the expected dimuon contribution from $b\bar{b}$ production, 221564 ± 11615. This estimate assumes the unexpected source of dimuon events is completely rejected by the tight SVX requirements. Most CDF analyses use a set of SVX criteria, referred in the following as standard SVX, in which tracks are required to have hits in at least three of the eight SVX layers. This standard SVX selection accepts muons from parent particles with decay lengths as long as 10.6 cm. Applying the standard SVX selection reduces the estimated size of the unknown dimuon source by a factor of two, whereas 88% of the known QCD contribution is expected to survive.

A summary of the estimates of the size of this unexpected source of dimuon events, whimsically called ghost events, for various sets of SVX criteria is shown in Table 3. In this table and throughout this report the expected contribution from known QCD sources, referred to as QCD contribution, will be estimated from the sample of dimuons surviving the tight SVX requirements

Table 3: Number of events that pass different SVX requirements. Dimuons are also split into pairs with opposite (OS) and same (SS) sign charge.

Type	No SVX	Tight SVX	Standard SVX
Total	743006	143743	590970
Total OS		98218	392020
Total SS		45525	198950
QCD	589111 ± 4829	143743	518417 ± 7264
QCD OS		98218	354228 ± 4963
QCD SS		45525	164188 ± 2301
Ghost	153895 ± 4829	0	72553 ± 7264
Ghost OS		0	37792 ± 4963
Ghost SS		0	34762 ± 2301

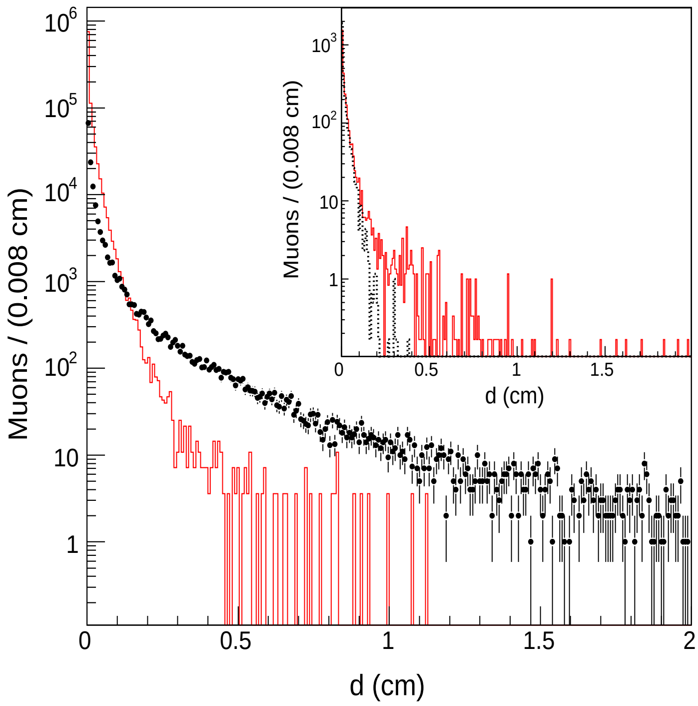

Figure 3: Impact parameter distribution of muons contributed by ghost (•) and QCD (histogram) events. Muon tracks are selected with the standard SVX requirements. The detector resolution is $\simeq 30\ \mu$m. The insert shows the distribution of simulated muons (histogram) that pass the same analysis selection as the data and arise from in-flight-decays of pions and kaons produced in a QCD heavy flavor simulation. The dashed histogram shows the impact parameter of the parent hadrons.

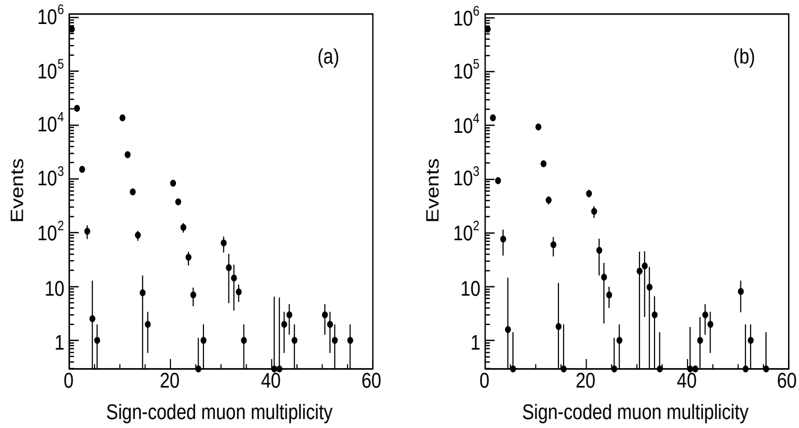

Figure 4: Multiplicity distribution of additional muons found in a $\cos\theta \geq 0.8$ cone around the direction of a primary muon before (a) and after (b) correcting for the fake muon contribution. An additional muon increases the multiplicity by 1 when it has opposite and by 10 when it has same sign charge as the initial muon.

and properly accounting for the relevant SVX efficiencies using the sample composition from the fits. We elect to follow this approach since the tight SVX sample provides a well understood sample. The ghost contribution will always be estimated from the total number of events observed in the data after subtracting the expected QCD contribution. Table 3 shows also the event yields separately for the subset of events in which the dimuons have opposite-sign (OS) and same-sign (SS) charge. The ratio of OS to SS dimuons is approximately 2:1 for QCD processes but is approximately 1:1 for the ghost contribution. At this stage it is worth commenting further on the set of inconsistencies related to $b\bar{b}$ production and decay mentioned above. The general observation is that the measured $\sigma_{b\to\mu,\bar{b}\to\mu}$ increases as the SVX requirements are made looser and is almost a factor of two larger than that measured in $\sigma_{b\bar{b}}$ when no SVX requirements are made. As mentioned above, the magnitude of the ghost contribution is comparable to the $b\bar{b}$ contribution when no SVX selection is made. Similarly, for the standard SVX criteria, the magnitude of the ghost contribution, when added to the expected $b\bar{b}$ contribution of 194976 ± 10221 events, coincides with the cross section measurement reported in previous measurements that use similar sets of silicon criteria. Moreover, when applying the tight SVX criteria to initial muons, the invariant mass spectrum of combinations of an initial muon with an additional accompanying muon is well described by known QCD sources and is dominated by sequential semileptonic heavy flavor decays. In contrast, without any SVX requirement the invariant mass spectrum cannot be modeled with the SM simulation and the inconsistencies at low invariant mass are reproduced. Thus, this unknown source of dimuon events seems to offer a plausible resolution to these long-standing inconsistencies related to $b\bar{b}$ production and decay. The remainder of this paper is dedicated to a further exploration of these events. The nature of the anomalous events can be characterized by four main features. The impact parameter distribution of the initial muon pair cannot be readily understood in terms of known SM processes. In small angular cones around the initial muons the rate of additional muons is significantly higher than that expected from SM processes. The invariant mass of the initial and additional muons looks different from that expected from sequential semileptonic decays of heavy flavor hadrons. The impact parameter distribution of the additional muons has the same anomalous behavior as the initial muons. We will discuss these features in turn. As shown in Fig. 3, muons due to ghost events have an impact parameter distribution that is completely different from that of muons due to QCD events.

5.1 Events with additional muons

We search QCD and ghost events that contain a pair of initial muons that pass our analysis selection (without any SVX requirement) for additional muons with $p_T \geq 2$ GeV/c and $|\eta| \leq 1.1$. We have the following motivations: (a) events acquired because of in-flight decays or secondary interactions are not expected to contain an appreciable number of additional muons; (b) QCD events that might appear in the ghost sample because of not-yet-understood detector malfunctions should not contain more additional leptons than QCD events with well reconstructed initial dimuons; and (c) we want to investigate if the anomaly of the low dimuon invariant mass excess reported in the past is also related to the presence of the unexpected background. According to the simulation, additional muons arise from sequential decays of single b hadrons. In addition, one expects a contribution due to hadrons mimicking the muon signal. In the data, 9.7% of the dimuon events contain an additional muon (71835 out of 743006 events). The contribution of events without heavy flavor, such as all conventional sources of ghost events mentioned above, is depressed by the request of an additional muon. For example, in events containing a $\Upsilon(1S)$ or K^0_S candidate and are included in the dimuon sample, the probability of finding an additional muon is (0.90 ± 0.01)% and (1.7 ± 0.8)%, respectively. However, the efficiency of the tight SVX selection in dimuon events that contain additional muons drops from 0.1930 ± 0.0004 to 0.166 ± 0.001. This observation anticipates that a fraction of ghost events contains more additional muons than QCD data.

Therefore, the study of ghost events is further restricted to muons and tracks contained in a cone of angle $\theta \leq 36.8^\circ$ ($\cos\theta \geq 0.8$) around the direction of each initial muon. Less than half of the OS and SS muon combinations in ghost events can be accounted for by fake muons, and ghost events are shown to contain a fraction of additional real muons (9.4%) that is four times larger than that of QCD events (2.1%). We have investigated at length the possibility that the predicted rate of fake muons is underestimated. The fraction of additional real muons in QCD and ghost events is verified by selecting additional muons with $p_T \geq 3$ GeV/c and $|\eta| \leq 0.7$. In this case, because of the larger number of interaction lengths traversed by hadronic tracks, the fake rate is negligible. In this study the muon detector acceptance is reduced by a factor of five but the rate of such additional muons is (0.40 ± 0.01)% in QCD and (1.64 ± 0.08)% in ghost events.

The impact parameter distribution of the additional muons is found to be as anomalous as that of primary muons. However, the impact parameter of the additional and initial muons are weakly correlated (the correlation factor is $\rho_{d_{0p}d_{0s}} = 0.03$). The impact parameter distribution of additional muons in QCD events is not anomalous at all. It is difficult to reconcile the rate and characteristics of these anomalous events with expectations from known SM sources. Although one can never rule out the possibility that these data could be at least partially explained by detector effects not presently understood, we will present some additional properties of the ghost sample. Figure 4 (a) shows the distribution of the number of muons found in a $\cos\theta \geq 0.8$ cone around a primary muon in ghost events. In the plot, an additional muon increases the multiplicity by 1 when of opposite and by 10 when of same sign charge as the initial muon. Leaving aside the case in which no additional muons are found, it is interesting to note that an increase of one unit in the muon multiplicity corresponds in average to a population decrease of approximately a factor of seven. This factor is very close to the inverse of the $\tau \to \mu$ branching fraction (0.174) multiplied by the 83% efficiency of the muon detector, and makes it hard to resist the interpretation that these muons arise from τ decays with a kinematic acceptance close to unity. The multiplicity distribution corrected for the fake muon contribution is shown in Fig. 4 (b). The fake contribution is evaluated on a track-by-track basis using the probability that pions from D^0 mesons from B hadron decays mimic a muon signal. Unfortunately, the multiplicity distribution of muons and tracks contained in a 36.8° cone around the direction of such D^0 mesons does not have the high multiplicity tail of ghost events. In the D^0 control sample, we do not observe any dependence of the fake rate on the track and muon multiplicity, but we also cannot rule out a drastic increase of the fake probability per track in events with multiplicities much larger than those of QCD standard processes. A study based on higher quality muons does not show any evidence of that being the case.

6 Measurement of Heavy Boson pair production

As CDF is collected more data the search for the Higgs is becoming more and more intersing with limits getting close to SM expectations. We started an analysis searching for SM pair production of heavy boson pair in the lepton neutrino jet jet channel, that is sensitive to the WW and WZ processes together. This work was done in collaboration with Viviana Cavaliere (University of Siena) and Pierluigi Catastini (University of Siena).

The road to the Higgs is paved with di-bosons. Indeed, a di-boson signal must be well established before the SM Higgs signal can be observed. This channel is very interesting because it is very similar to the most sensitive final state (WH $\rightarrow$ lνb$\bar{\text{b}}$) for Higgs searches at low mass (around 120 GeV). This is true not only for this channel, but for all di-boson channels that correspond to either the associated $p\bar{p} \rightarrow W/Z+H$ production or the $p\bar{p} \rightarrow H \rightarrow WW$ process. The measurement of di-boson production is also interesting because they are sensitive to triple gauge coupling and are a probe into the electroweak symmetry breaking part of the SM. For these reasons, now we have the integrated luminosity to observe these signals in semileptonic final states with two jets, di-boson physics is a hot topic at CDF. Here we report a brief summary of the analysis and the main results.

The analysis selects a leptonic W decaying into electrons or muons. The main kinematical cuts are $E_T > 20$ GeV and $|\eta| <1.1$ for the lepton and missing $E_T > 25$ GeV. From this inclusive sample, we select events with at least 2 jets with $E_T > 20$ GeV (corrected for out-of-cone and underlying event). In the W + 2 jets sample we search of our di-boson signal. Our analysis strategy is conceptually simple. We want to separate the signal from background using a direct fit to the di-jet invariant mass. On one hand, the di-jet invariant mass contains most of the information available to separate signal from background, on the other using a direct di-jet mass fit the result is of strait forward interpretation. We also want the background di-jet invariant mass shape to be different from the signal shape. Specifically we want the background distribution to turn on at mass well below the signal peak. For these reason our di-jet candidate is made only from the 2 highest E_T jets[1] and the p_T of the di-jet candidate is required to be greater than 40 GeV. The motivation for this last cut, which is the key feature of the analysis, will be explained below.

First we have to explain how we model our backgrounds. We consider the following background processes: W+jets, Z/γ+jets, t$\bar{\text{t}}$ and single top. These processes are modeled with ALPGEN+Pythia MC (W+jets and Z/γ+jets), while t$\bar{\text{t}}$, single top and the di-boson signals are modeled with Pythia. For these background we use the MC to model both the kinematics and the absolute normalization. The most difficult background to model is the non-W background (also called QCD

[1]This cut is used to avoid multiple di-jet combinations

or fake-W). We model QCD using data. For electron we select fake-W using electrons that fails electron quality cuts. For muons we use non isolated muons.

Using our QCD model for the electron and muon channels we first estimate the QCD normalization. To do that we fit the missing E_T distribution for our sample releasing the missing E_T cut to 0. From this fit we get a first estimate of the number of W+jets and QCD events above the MET > 25 GeV cut. All other backgrounds normalizations are taken from MC. The fit projections are show in Fig. 5. The expected event yield for all samples are reported in table 4.

Table 4: MC estimate of the expected number of events for signal and each background component for $M_{jj} \in [28,200]$ GeV/c^2.

Sample	**CEM**	**CMUP + CMX**
MC W +jets	18010 ± 531	16673 ± 482
MC Z+jets	353 ± 42	966 ± 115
di-boson	750 ± 68	651 ± 59
top	1324 ± 134	1149 ± 115
QCD (from data)	2314 ± 462	639 ± 159
Total MC + QCD	22751	20078
data	22204 ± 149	19738 ± 141

It is well know that it is difficult to reconstruct jets at low E_T because jets are better measured and have better correlation with the original partons if they have high E_T. Experimentally an E_T threshold is always applied to jets. Unfortunately this results into a sculpting of the di-jet invariant mass distribution, that is usually a major troubles when looking for resonances such as W and Z whose mass is not much larger than the E_T threshold.[2] This effect can be observed in Fig. 6. The di-boson signal in red is close to the background turn-on. We also notice that the invariant mass shape has peculiar features. For this analysis we investigated the reasons for this background shape. We consider di-jet candidates with a given jet-jet p_T. As illustrated in Fig. 7, if the jet-jet candidate has $p_T > 40$ GeV any $\Delta\phi_{jj}$ is allowed by our $E_T > 20$ GeV threshold. Instead if the di-jet candidate has low p_T e.g. 10 GeV, the jet $E_T > 20$ GeV threshold puts a lower limit on the accessible $\Delta\phi_{jj}$. This is the source of the di-jet invariant mass sculpting.

Di-jet candidates above and below p_T of 40 GeV correspond to two different kinematical regimes: non-sculpted and $\Delta\phi_{jj}$ sculpted. This is clearly illustrated in Fig. 8. For di-jet candidates of $p_T > 40$ GeV all $\Delta\phi_{jj}$ are accessible. In this case the backgrounds peak at low $\Delta\phi_{jj}$, this is due to the increase in gluon-splitting cross-section at low angle. The W/Z jet pairs coming from the decay of a heavy particle peak at large angle because of the decay kinematic and can be easily separated from background. On the contrary for di-jet candidates of $p_T < 40$ GeV the $\Delta\phi_{jj}$ acceptance is sculpted as function of p_T. We notice that the background peaks at large angles, where the signal also peaks. It will be harder to disentangle signal from background for low p_T candidates. One important outcome of these considerations is that is it better to treat separately the data above and below p_T of 40 GeV because they correspond to two different kinematically

[2] Even if the W mass is 4 times the $E_T > 20$ GeV threshold this is not enough to have a good separation between the W di-jet peak and the background turn-on.

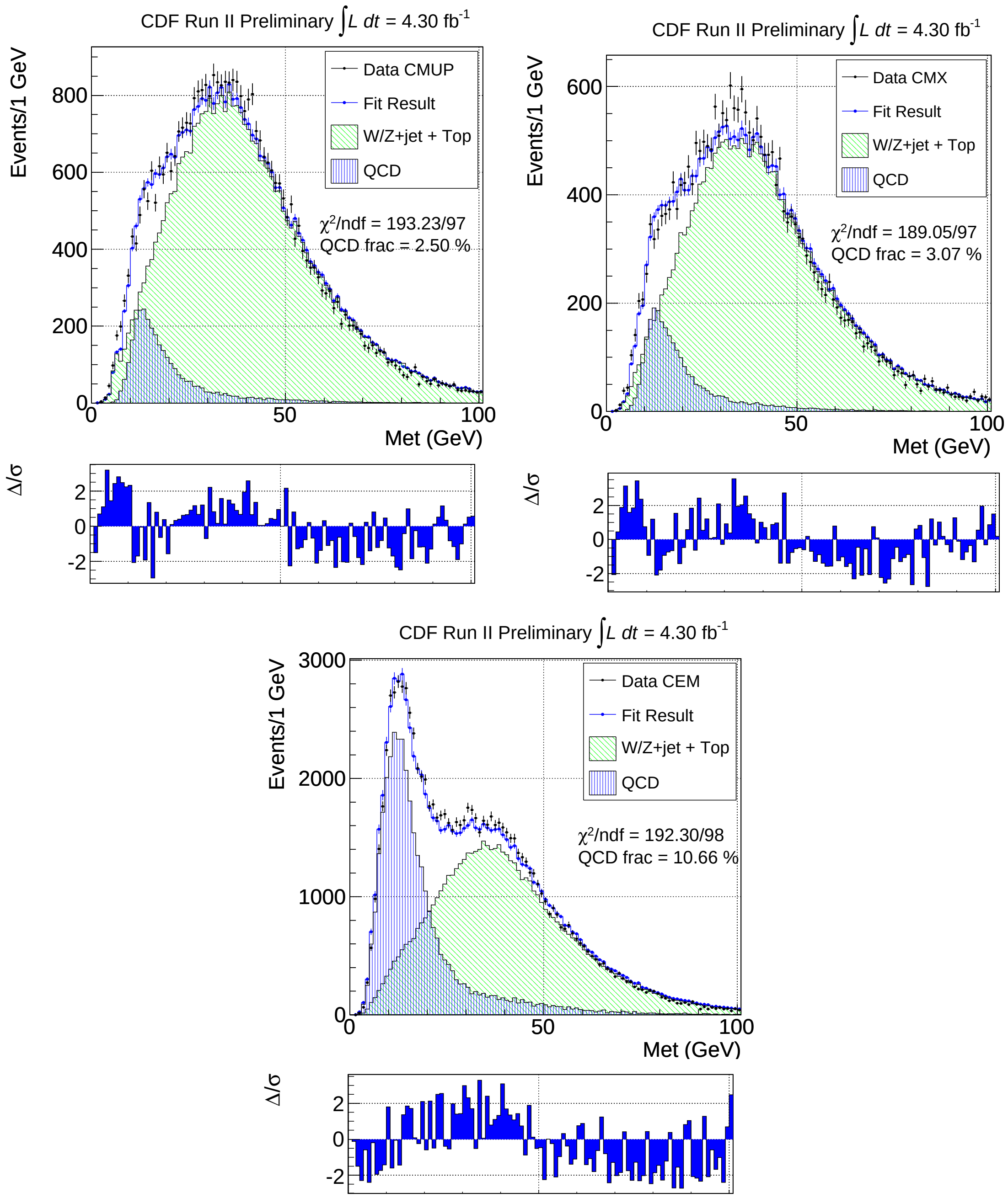

Figure 5: (color online). Upper left: $\not{E}_T$ fit of the QCD background for CMUP. Upper right: $\not{E}_T$ fit of the QCD background for CMX. Bottom: $\not{E}_T$ fit of the QCD background for CEM. These fits refer to the di-jet selection.

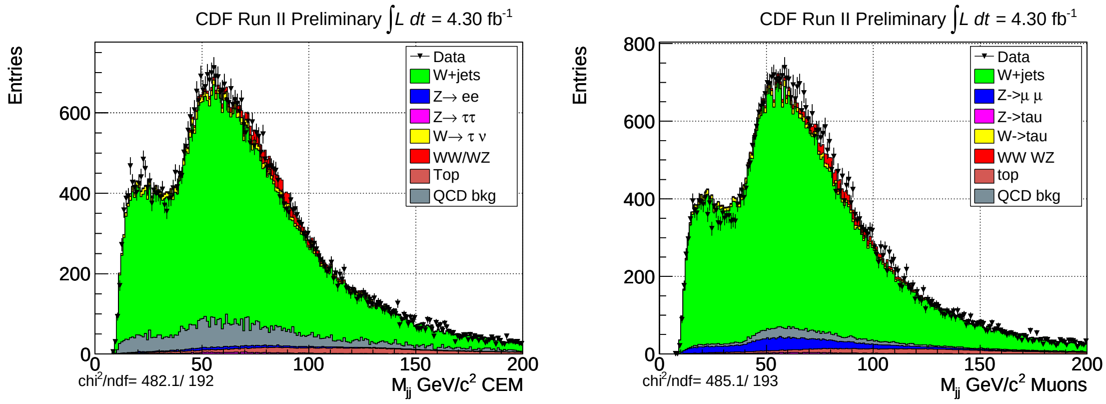

Figure 6: (color online). M_{jj} distribution without the $p_T(jj) > 40\,\mathrm{GeV/c}$ cut; left: CEM; right: CMUP + CMX.

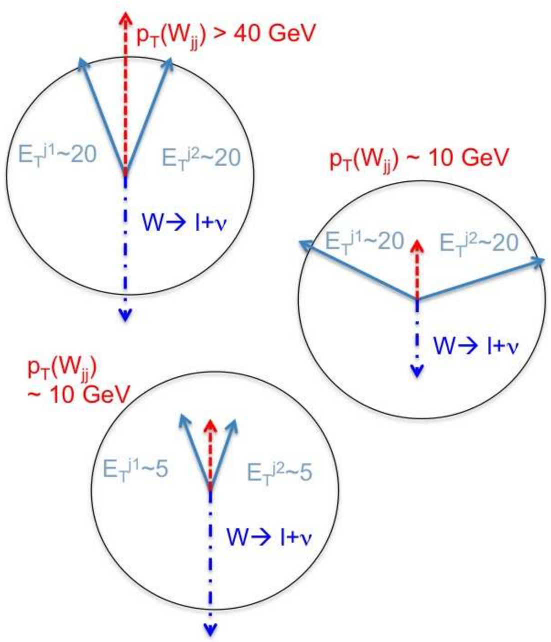

Figure 7: (color online). Different configurations for the di-jet candidate. If the di-jet p_T is low (below 40 GeV) only large $\Delta\phi_{jj}$ decays correspond to jets above the 20 GeV threshold.

regimes[3]. The di-jet invariant mass for the two regions separately are shown in Fig. 9 and 10. Fig. 10 shows a smooth background shape with the background turning on at about 20 GeV. The

[3]Here the value of 40 GeV is set by the jet E_T threshold. For generic jet threshold the di-jet p_T that separates the two regimes will be $p_T = (min\,E_T^{j1}) + (min\,E_T^{j2})$

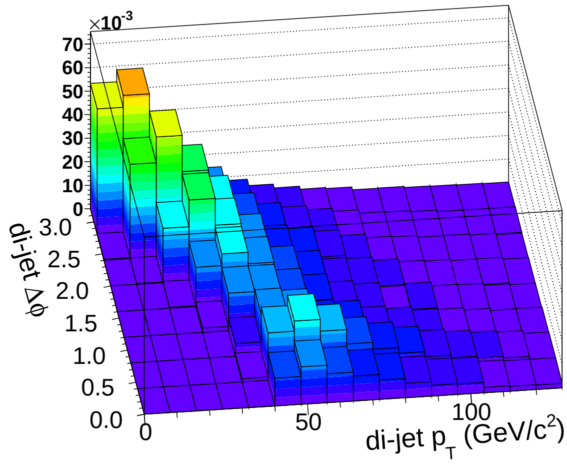

Figure 8: (color online). Di-jet p_T versus $\Delta\phi_{jj}$ for expected backgrounds. The figure shows the $\Delta\phi$ as function of p_T.

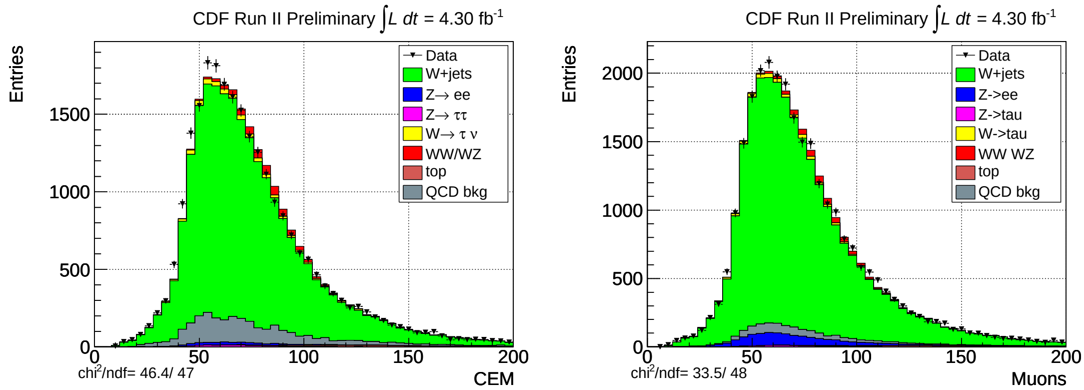

Figure 9: (color online). M_{jj} distribution with $p_T(jj) < 40\,\mathrm{GeV/c}$ for electrons (left) and muons (right).

residual mismodeling between data and MC at about 20 GeV is connected to mismodeling issues for jets with ΔR separation close to the clustering cone limit.

If the two samples (above and below p_T of 40 GeV) are combined the background with $p_T < 40$ that peaks that large $\Delta\phi_{jj}$ will be folded into the $p_T > 40$ region spoiling the smooth unsculpted features of the $p_T > 40$ data. The resulting di-jet invariant mass distribution is shown in Fig. 6. This analysis doesn't use at all the $p_T < 40$ GeV data. It can be recovered and used treating it separately from the $p_T > 40$ GeV data.

Using our expectation for the di-jet invariant mass templates for MC background and QCD,

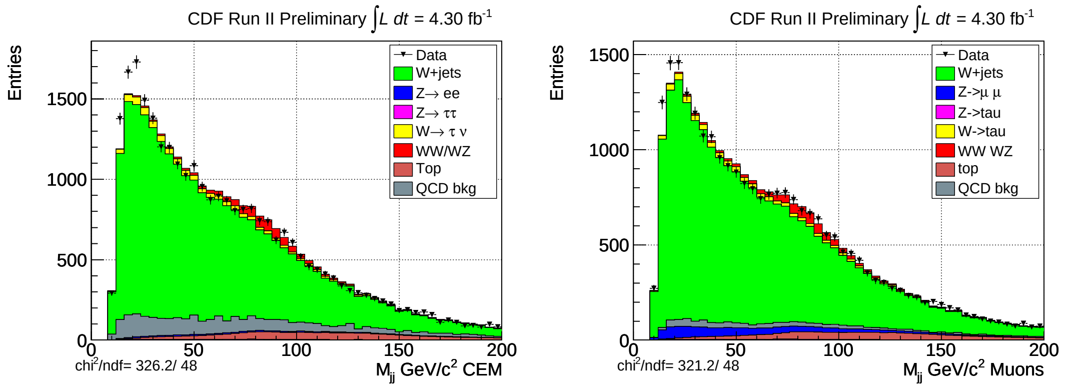

Figure 10: (color online). M_{jj} distribution with $p_T(jj) > 40$ GeV/c for electrons (left) and muons (right).

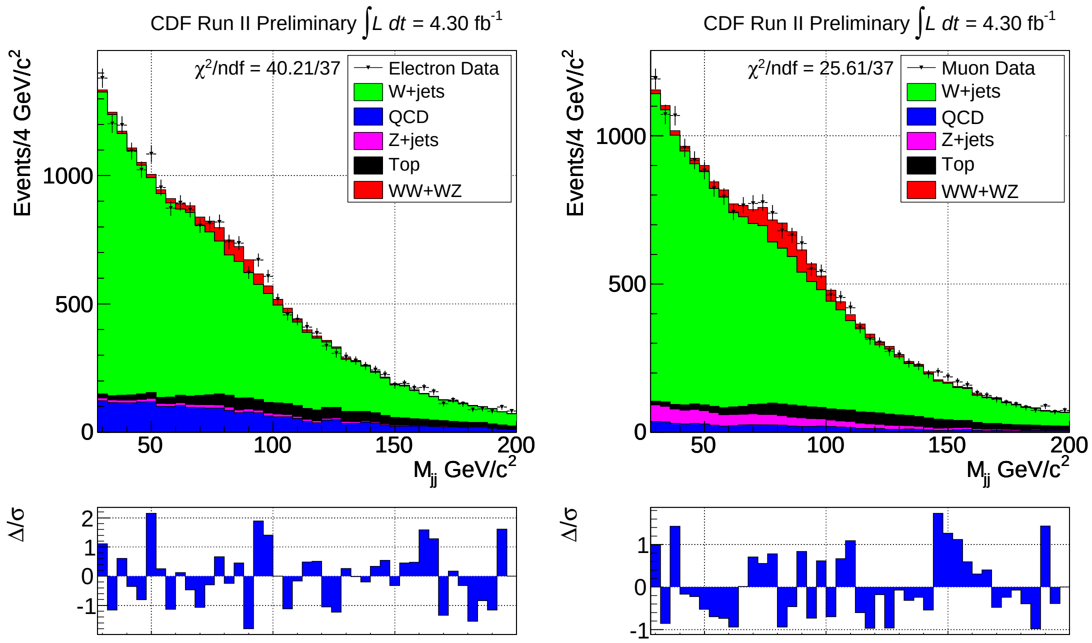

Figure 11: (color online). Fit on data for electrons (left) and muons (right).

we fit the di-jet mass of muons and electrons separately. The signal and W+jets normalizations are free in the fit, while the other background normalizations are constrained to the expected yield and uncertainty (10% for top and 12% for Z+jets). For the QCD background that is more uncertain only a loose constraint of 25% is applied. The results of the fit are shown in Fig. 11.

We skip the details of systematics and significance estimation. In summary, using a fit to the invariant mass distribution M_{jj} we estimate 630 $\pm$ 203 (stat.) $\pm$ 67 (syst.) events in the $WW/WZ \to e\nu jj$ sample and 952 $\pm$ 188 (stat.) $\pm$ 85 (syst) events in the $WW/WZ \to \mu\nu jj$

sample that leads to a cross section of 13.5 ± 4.4 (stat.) ± 1.9 (syst.) pb for electrons and 23.5 ± 4.9 (stat.) ± 3.2 (syst.) pb for muons, respectively. The sum of the electron and muon fits is show in Fig. 12.

Combining the two decays, we estimate a total of 1582 ± 275 (stat.) ± 107 (syst.) $WW/WZ \rightarrow l\nu jj$ events, corresponding to a significance of approximately 5.24 σ. Finally, we measure $\sigma_{WW/WZ}$ = 18.1 ± 3.3 (stat.) ± 2.5 (syst.) pb.

This analysis has been initially blessed on June 25th, 2009 and then published in PRL [1] that is the first observation of WW+WZ di-boson signal in the semi-leptonic channel. The results reported here correspond to the update blessed on November 25th, 2009.

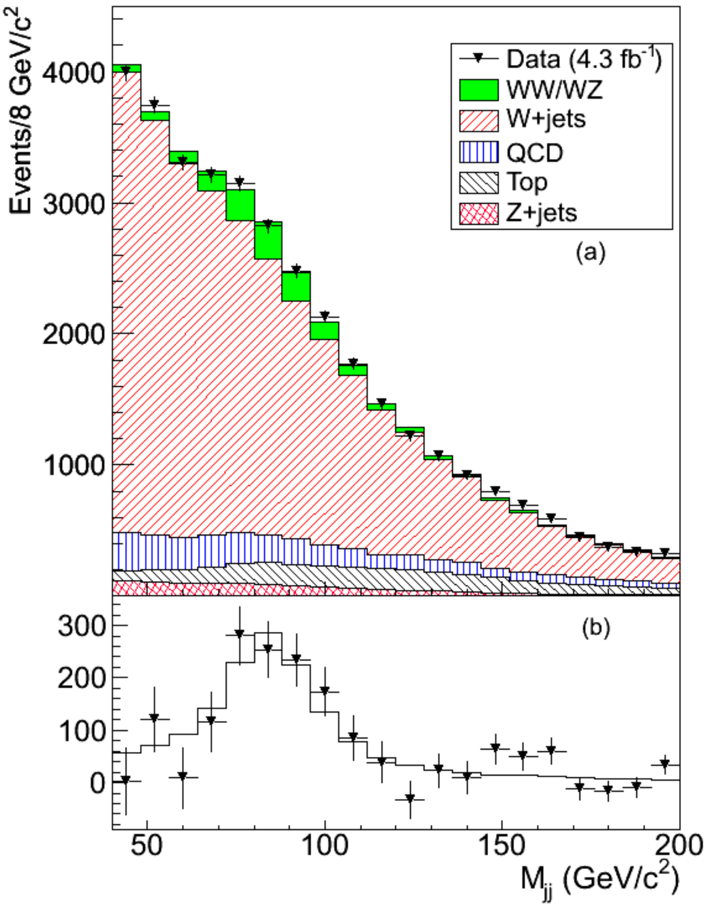

Figure 12: (color online). Sum of the electron and muon fit along with background subtracted plot.

Conferences 2009

1. F. Happacher, *Study of Multimuons Events at CDF*; Presented at Les Rencontres de Physique de la Vallée d'Aoste 2009, La Thuile, Aosta Valley (Italy) - 2009, March 1-7.

2. F. Happacher, *Study of Multimuons Events at CDF*; Presented at XVII International Workshop on Deep-Inelastic Scattering and Related Subjects DIS 2009, Madrid (Spain) - 2009, April 26-30.

3. F. Happacher, *Study of Multimuons Events at CDF*; Presented at The 2009 Europhysics Conference on High Energy Physics, Krakow (Poland) - 2009, July 16-22.

4. A. Annovi, *Diboson physics*; Presented at 17th International Conference on Supersymmetry and the Unification of Fundamental Interactions Boston, USA, 2009, June 5-10.

Publications

1. T. Aaltonen et al. (CDF Coll.), Phys. Rev. Lett. **104**, 101801 (2010). `arXiv:0911.4449`.

CMS

E. Basile (Dott.), L. Benussi, M. Bertani, S. Bianco (Resp.), M.A. Caponero (Ass.)
S. Colafranceschi (Dott.), F.L. Fabbri (Ass.)
F. Felli (Ass.), M. Ferrini (Tecn. Osp.), M. Giardoni (Ass.), T. Greci (Laur.)
B. Ortenzi (Tecn.), M. Pallotta(Ass.), A. Paolozzi (Ass.)
M. Parvis (Ass.), L. Passamonti (Tecn.), D. Piccolo
D. Pierluigi (Tecn.), C. Pucci (Dott.), A. Russo (Tecn.), G. Saviano (Ass.)

In collaboration with:
B. Dulach (SPECAS), D. Orecchini (SPECAS), B. Ortenzi (Tecn.), B. Ponzio (Tecn.)

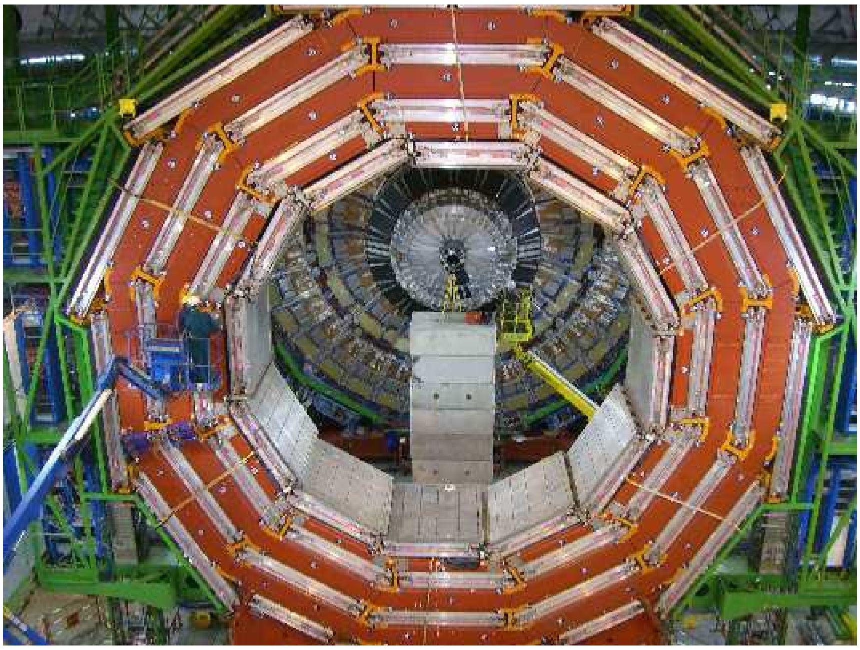

The Compact Muon Solenoid (CMS) experiment [1)] will search for the missing block of Nature - the Higgs boson - and for new exotic elementary particles that are predicted by theory and by cosmological observations. The CMS detector uses Resistive Plate Chambers (RPC) as muon detectors, coupled to Drift Tubes in the barrel region, and to Cathode Strip Chambers in the endcaps. Resistive Plate Chambers (RPC) detectors are widely used in HEP experiments for muon detection and triggering at high-energy, high-luminosity hadron colliders, in astroparticle physics experiments for the detection of extended air showers, as well as in medical and imaging applications. While gain and efficiency stability are always a must, in the case of RPC detectors in high-rate experiments which use freon-based gas mixtures, utmost care has to be paid also for the possible presence of gas contaminants. RPC counters [3)] are fast, efficient and economical charged particles detectors, well-suited for operation in high magnetic field. The elementary component is a gap, a gas volume enclosed between two resistive plates. Resistive plates are made of bakelite, coated with linseed oil for surface uniformity. Gas mix used is 95.2% $C_2H_2F_4$ / 4.5% Iso-C_4H_{10} / 0.3% SF_6, with a 45% relative humidity. Signal pulses are picked up by readout strips. In CMS, RPC counters are operated in avalanche mode to sustain high-rate operation, with the streamer suppressed by the addition of SF_6 gas in the mixture.

1 Status of the CMS experiment and the RPC muon detector

The RPC barrel system (5 wheels and 480 chambers) has been fully characterized during the 2009 participating at the CMS global runs. About 300 millions of cosmic ray events have been taken in 2009 and the RPC detector and trigger worked very well without any major problem. A large fraction of the cosmic data has been analyzed in real time using the DCS and the Data Quality Monitor in order to check online the quality of data. The two systems have been used to configure the detector and the trigger and to assure the quality of the data taken. At the same time, prompt analysis tools have been developed to have a more detailed and complete offline data analysis.

About 300 milions of cosmic muon events were collected and analyzed in 2009. They have been very useful to study in details the detector and trigger performances. The detector efficiency has been measured for each chamber with a resolution of about 100 cm^2, showing a very uniform distribution and an average value of about 95% in the barrel region. An anomalous behaviour has been found in the endcap chambers where the average distribution was around 50%. For this reasons we studied in details all the steps made to measure the efficiency founding few major errors in the geometrical description of the endcap chambers and realizing that the working point of most of the chambers was about 200 V lower than the plateau region.

The RPC system successfully participated to the November and December LHC data taking contributing in the detection and trigger of muon events. The beam splash events have been used to synchronize the endcap electronic channels and to check all the data taking procedures. The colliding beam muon events have been used to measure the overall detection and trigger efficiency showing results comparable to that obtained with cosmics. Data taken in December 2009 have been promptly analyzed and the first CMS paper was submitted to journal in March 2010. The stability of the RPC system, already shown in the 2008 and 2009 cosmic runs, has been confirmed at the initial low luminosity, showing a very low current and noise rate even in the endcap region. Instructions for the shifters and documentations have been developed and tested in this phase.

DCS (Detector Control System) is working since the 2007 and has been intensively used during the 2009 showing a stable behaviour and also an user friendly graphical interface. DCS data have been stored in the online database (OMDS) transferred to the offline database (ORCOFF) using the POPCON framework in order to analyze the data offline.

All the data taken by DCS and by XDAQ have been stored in OMDS and part (HV and Gas) of them has been transferred to the offline database (ORCOFF) after having been encapsulated in an object with an assigned interval of validity. When data are available in ORCOFF can be used in the event reconstruction, in the offline DQM and in any other data analysis. The RPC collaborators are using these data in the prompt analysis to correlate the detector performances with the environmental parameters and with the condition data.

The RPC DQM (data quality monitor) system has been extensively used during the 2009 data taking both by CMS central shifters and by RPC experts to study the detector and trigger performance. The central shifters have been used only the so called "summary plots" to understand the quality of the data taken by the RPC while the RPC experts have been used all the plots and histograms produced by the DQM to quantify the RPC performances and to make the run validation.

The monitoring of gas system, the gas gain monitoring system and purifier studies are responsibilities of the Frascati group. The CMS RPC muon detector uses a huge volume of expensive gas mixture. This has demanded the need for a gas recirculation system (Closed Loop) with filters for gas purification. The CL system has been in operation since years with performance meeting specifications. All modules of the gas system (primary supply, mixer, purifier module I e II, humidifier, pump, pre-distribution and distribution) have been operational in closed loop mode since mid 2008. The clean mix fraction is about 10%. The system is integrated in DCS PVSS. Both IR analyzer for isobutane and $O_2 + H_2O$ analyzer have been installed and are operational. The gas quality monitoring system (gas cromatograph and electrodes) are operational and routinely used to check the mix composition and presence of major pollutants. The gas system is stable and no currents increase have been observed due to closed loop mode. During year 2009 the activity at the scaled-down closed loop system in the ISR test area has continued for full characterization of purifiers. The CL system ran smoothly during the collision runs in December 2009.

2 Activity of the CMS group

The Frascati group has joined CMS in the RPC muon detectors at the end of year 2005. Frascati is responsible for the Gas Gain Monitoring system, RPC materials studies, and the test of the Closed Loop recirculation system for characterization of gas purifiers.

2.1 The CMS Closed Loop Gas System

Because of high costs and huge volumes of the freon-based gas mix used, CMS uses a recirculation (Closed Loop) gas system developed by the CERN gas group. The Closed Loop is a critical component of RPC. CMS has accumulated experience on its use and performances during the test at the Gamma Irradiation Facility at CERN in 2001 [4], and currently at the ISR where chambers are tested in CL prior to installation. At the GIF facility we observed substancial production of HF, linearly correlated with the signal current.

In the Closed Loop (CL) system, purifiers are the crucial component. Purifiers were determined after tests at the GIF in order to minimize the unknown contaminants which showed as spurious peaks besides the known gas mix components. Three filters were selected: 5A molecular sieve, Cu/Cu-Zn, Ni/Al_2O_3. A small scale CL system is currently in use with cosmic rays in the ISR test area.

A measurement campaign [5] on purifiers is in progress, using chemical, SEM/EDS (Scanning Electron Microscopy/Energy Dispersive Spectroscopy), XRD (x-ray Diffrattometry) analyses. During year 2009 the activity at the scaled-down closed loop system in the ISR test area has continued for full characterization of purifiers, with new sampling points for detection of gas pollutants produced in the system in correlation with RPC currents increase. The release of contaminants in gas was observed with correlation to the increase of currents.

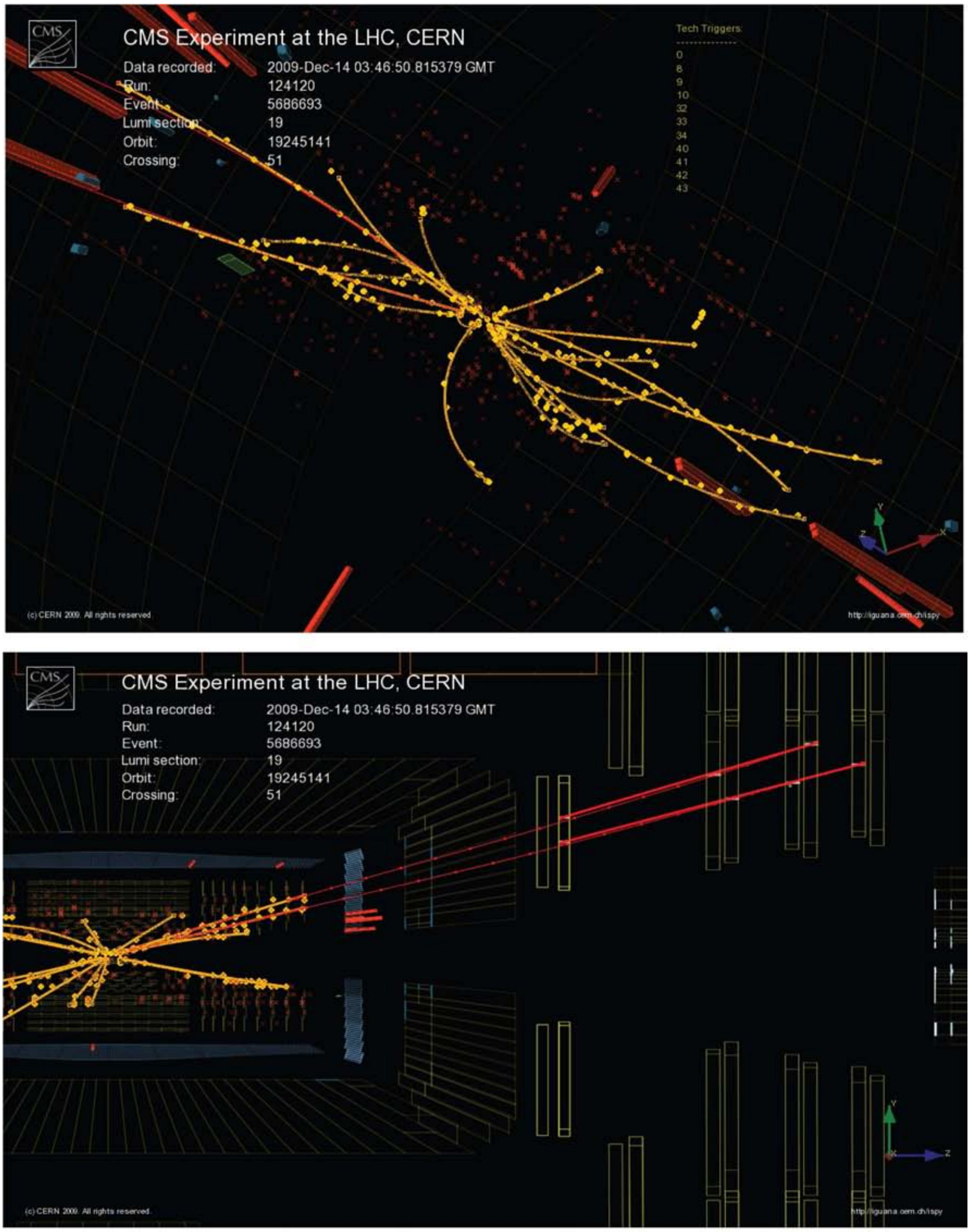

$p_T(\mu_1) = 3.6$ GeV, $p_T(\mu_2) = 2.6$ GeV, $m(\mu\mu) = 3.03$ GeV

Figure 1: A 2.36 TeV collision with a dimuon pair reconstructed.

2.2 Gas Gain Monitoring System

The Gas Gain Monitoring (GGM) system of RPC detectors in CMS monitors the changes in working point due to gas variations, by means of monitoring of anodic charge in small RPC gaps in a cosmic ray telescope. The system is composed of three subsystem of RPC single gaps, readout by 45cm x 45cm pads in a cosmic ray telescope located in the SGX5 gas building. Each subsystem is flushed with a different gas. The Reference subsystem is flushed with fresh open loop gas mixture. The MonitorOut subsystem is flushed with CL gas downstream of CMS RPCs. The MonitorIn subsystem is flushed with CL gas upstream of CMS RPCs. Each subsystem is composed of three gaps, whose high voltage is set to the standard working point voltage at the efficiency knee, and to 200 V above and below the knee respectively. Each cosmic ray track therefore provides completely correlated pulses in the three subsystems, allowing one to study the differential response of gaps and by disentangling any effect due to changes in the gas mixture. In case a working point change is detected, an alarm condition is released and the gas quality monitoring system will verify what the change of work point is due to.

The system was located in the SGX5 gas room of CMS in December 2008 and operated before the January 2009 shutdown. During 2008 the GGM was operated at the scaled down closed loop gas system in the ISR test area. The large experience allowed one to determine both sensitivity to working point changes and cancellation algorithms for changes due to environmental variables. Results have been presented at RPC07 and IEEE08. At the end of 2008 the integration of GGM with the CMS DCS-based monitoring has started, with data exchange with PVSS and data save to the OMDS online database. A beta-release control panel was released in December 2008. The system has been integrated during 2009 in the CMS DCS system. Data on operational experience in 2009 have been published. A novel model based on neural networks for the modellization of RPC response was developed on data from the GGM.

A proposal for PRIN was submitted and approved at the end of 2009. The PRIN will study optical fiber sensors for gas contaminants detection, in collaboration with Politecnico Torino and Sapienza Università di Roma.

3 Activity planned for 2010

The main activity in 2010 will be the participation to data taking shifts and operation of the RPC detector and the physics analysis. The test at the scaled down Closed Loop system will continue in at high-radiation environment at the GIF facility. At the GIF, optical sensors for contaminants detection will be developped in the framework of the PRIN project approved and funded.

The Frascati group is actively working in the CMS Electroweak Analysis group and is involved in the study of the measurement of inclusive $Z \rightarrow \mu^+\mu^-$ cross section. This process is characterized by a clear signature in an almost free background environment and will be studied very soon after the arrival of the first colliding beams.

The work has been focused on the development of methods to select events and measure reconstruction and trigger efficiencies directly from data. An original method has been proposed which consists in five different categories of Z candidates according to the way the muons have been reconstructed (tracker track, standalone muon detector system, combined track+standalone muon) and trigger topologies.

A fit of Z production yield, reconstruction and trigger efficiency is then performed simultaneously on the five categories, thus allowing to extract all the needed information in a single step. This method has been showed to be very robust in handling also a low statistical sample as could be expected in case of few pb^{-1} of integrated luminosity collected.

This work has been presented in several cms analysis meetings, it has been documented in an internal CMS Analysis note (CMS AN-2009/005) and has been reviewed and accepted by the CMS collaboration as a promising way to perform the analysis.

We expect to complete the analysis with a study of systematic effects and geometrical acceptance. Moreover an effort will be devoted in the next months to make the software tools ready for the arrival of data from the 3.5 TeV run of LHC. The analysis will be performed running the software through the GRID on the Tier2 where the data will be saved, and the development of the tools is essential in order to be able to run in a fast and efficient way as soon as the data will be ready. In 2010 the proposal for a CMS T3 in Frascati will also be finalized.

Studies for long-term upgrades of the RPC detector have been started in collaboration with the SPECAS service of Frascati. A simulation study was performed to verify the possibility of doubling the gaps in the inner layer of the barrel RPC, in order to add an orthogonal coordinate. Work on the option of installing a GEM detector in the forward region was started. Finally, the Frascati group will contribute to the construction and installation of a fifth endcap disk, so far missing (upscope), by installing FBG sensors for temperature humidity and gas contaminants, participation to design of and testing link boards trigger electronics, QA of gaps fabrication at General Tecnica, upscope of distributors in gas system.

4 Conference Talks

1. D. Piccolo for the CMS Coll., *Resistive Plate Chambers performance with Cosmic Rays in the CMS experiment*, 11th Pisa meeting on advanced detectors LaBiodola, Isola d'Elba, Italy, published on NIM.
2. S. Colafranceschi for the CMS Coll., *Operational Experience of the Gas Gain Monitoring System of the CMS RPC muon detectors*, 11th Pisa meeting on advanced detectors La Biodola, Isola d'Elba, Italy, published on NIM.
3. S. Colafranceschi for the CMS Coll., *Studio dei contaminanti al sistema di test del ricircolo Closed Loop del rivelatore per muoni RPC di CMS ad LHC*, XCV Congresso Nazionale Società Italiana Fisica - Bari, 2009.

5 Seminars

S. Bianco for the CMS Frascati group, *Primi risultati da CMS*, Frascati, February 2nd, 2009.

6 Preprints

1. S. Bianco et al., *Chemical Analyses of Materials Used in the CMS RPC Muon Detector*, Frascati preprint LNF-09-18(P). Submitted to JINST.

7 CMS Notes

1. D. Piccolo et al., CMS Analysis Note AN-2009/005.

8 Papers

1. L. Benussi et al., JINST **4** P08006 (2009). `arXiv:0812.1710`.
2. L. Benussi et al., Nucl. Instr. & Meth. A **602** 805 (2009), `arXiv:0812.1108`.
3. A. Colaleo et al., Nucl. Instr. & Meth. A **609** 114 (2009).
4. R. T. Rajan et al., Nucl. Instr. & Meth. A **602** 792, (2009).
5. G. Roselli et al., Nucl. Instr. & Meth. A **602** 696, (2009).
6. A. Colaleo et al., Nucl. Instr. & Meth. A **602** 67, (2009).
7. S. Chatrchyan et al. (CMS Coll.), *Precise Mapping of the Magnetic Field in the CMS Barrel Yoke using Cosmic Rays*, `arXiv:0910.5530`.

References

1. CMS Coll. home page is /cms.cern.ch/
2. R. Adolphi et al. (CMS Coll.), JINST **3** S08004, (2008).
3. M. Abbrescia et al., Nucl. Instr. & Meth. A **533** 102, (2004); M. Abbrescia et al., Nucl. Instr. & Meth. A **515** 342, (2003).
4. M.Abbrescia et al., *HF production in CMS Resistive Plate Chambers*, submitted to NIM, presented by R. Guida at the RPC Conference, Seoul (Korea) 2005.
5. M. Abbrescia et al., *Proposal for a systematic study of the CERN closed loop gas system used by the RPC muon detectors in CMS*, Frascati preprint LNF-06/26(IR).
6. M. Abbrescia et al., *Gas analysis and monitoring systems for the RPC detector of CMS at LHC*, presented by S. Bianco at the IEEE 2006, San Diego (USA), `arXiv:physics/0701014.`

KLOE / KLOE-2

The KLOE-LNF Collaboration

A. Antonelli, M. Antonelli, D. Babusci, M. Bazzi (AR), G. Bencivenni, S. Bertolucci, C. Bloise (Resp.), F. Bossi, P. Campana, G. Capon, T. Capussela (AR), P. Ciambrone, E. De Lucia, P. de Simone, D. Domenici (AR), M. Dreucci (Art. 2222), G. Felici, C. Gatti, S. Giovannella, F. Happacher, E. Iarocci (Ass.)*, M. Jacewicz (BS), J. Lee-Franzini (Ass), M. Martini (Ass)*, S. Miscetti, M. Moulson, S. Müller, F. Murtas, M. Palutan, V. Patera (Ass.)*, P. Santangelo, B. Sciascia, A. Sciubba (Ass.)*, T. Spadaro, O. Vasquez Doce, G. Venanzoni, R. Versaci (Ass)*

**Also Dipartimento di Energetica, "La Sapienza" University, Rome*

The KLOE-LNF Technical Staff
M. Anelli, G. Fortugno, M. Iannarelli, R. Rosellini, F. Sborzacchi, E. Turri

1 Outline

During 2009 the KLOE collaboration has finalized several analyses in the field of kaon physics, low-mass scalars and pseudoscalars, and precision measurements of hadronic cross section. The collaboration was also committed to the preparatory work for data–taking in year 2010 and to the R&D activities for the detector upgrades, to be installed during the third quarter (3Q) of 2011.

On the kaon sector, the analysis of the helicity–suppressed K_{e2} channel has been published. It has been presented to the international conferences over the year and to the CERN community with the seminar held in May. The ratio $R_{Kl2} = BR(K_{e2})/BR(K_{\mu 2})$ is sensitive to couplings beyond the Standard Model (SM) [1] which should enhance the BR(K_{e2}) well above SM prediction. The KLOE result [2], $R_{Kl2} = (2.493 \pm 0.025_{stat} \pm 0.019_{syst}) \times 10^{-5}$, is in agreement with SM expectation constraining lepton–flavor violating processes in minimal supersymmetric standard model (MSSM). Other published results in year 2009 include the upper limits on the BR($K_S \to e^+e^-$) and BR($\phi \to K_S K_S \gamma$), the measurement of the BR($\eta \to \pi^+\pi^-e^+e^-$) and the study of the $a_0(980)$ with the analysis of $\phi \to \eta\pi^0\gamma$. For the hadronic cross section, the results on $\pi\pi\gamma$ events with photons emitted at low polar angle ($|\cos(\theta)| > \cos(\pi/12)$) have been published [3]. The pion form factor in the $M_{\pi\pi}$ invariant mass range [0.592, 0.975] GeV has been determined and used in the evaluation of the hadronic contribution to the muon anomaly. The result confirms the 3–σ discrepancy between SM expectation and the measurement of the muon $(g-2)$ by the E821 experiment at the BNL. Independent and consistent results have been obtained with the study of the off-peak data, taken at $\sqrt{s} = 1$ GeV [4]. The summary on hadronic cross section measurements is presented in Sect. 4. For the kaon decays, the status of the analysis of the $K^+ \to \pi^+\pi^+\pi^-$ is described in Sect. 2. For the η decays, the first observation of the $e^+e^-e^+e^-$ mode and the study of the $\pi\pi\gamma$ channel are reported in Sect. 3.

Test and revision of the KLOE detector subsystems have been completed and the upgrade of obsolete components, including data storage and the software for data handling, has been worked on. The technical design report (TDR) of the tagger system for $\gamma\gamma$ physics at KLOE-2 has been finalized and the construction of the detector has started. A status report on the project is given in Sect.5. R&D activities on the calorimeters to detect photons at low polar angle (CCALT) and to instrument the zone of the DAΦNE quadrupoles in the new beam interaction region (QCALT) have progressed as described in Sect.6. The design of the cylindrical triple–GEM chamber has been finalized with the analysis of the detector response to test beam in magnetic field and the completion of the TDR as reported in Sect.7.

2 K_L lifetime and BR($K^+ \to \pi^+\pi^-\pi^+(\gamma)$)

The availability at KLOE of tagged kaons enables precision measurements of absolute branching ratios (BR). The detection of one K_L (K_S) guarantees the presence of the K_S (K_L) with opposite momentum and the same holds for charged kaons pairs [5]. The K_L beam is tagged by the reconstruction of $K_S \to \pi^+\pi^-$ decays. The selection of K^+ beam is done reconstructing the 2–body decays $K^- \to \pi^-\pi^0$ and $K^- \to \mu^-\nu$, which are identified from two clear peaks in the distribution of the momentum of charged secondary tracks in the kaon rest frame.

Two independent measurements of the K_L lifetime, τ_L, have already been published. The first one, $\tau_L = 50.92 \pm 0.17_{\rm stat} \pm 0.25_{\rm syst}$ ns [6], has been obtained from the fit to the proper–time distribution of $\sim 8.5{\times}10^6$ $K_L \to 3\pi^0$ decays tagged by K_S reconstruction, while the second one, $\tau_L = 50.72{\pm}0.11_{\rm stat}{\pm}0.35_{\rm syst}$ ns [7], from the measurement of the dominant K_L branching fractions imposing the constraint $\sum BR(K_L) = 1$ on a tagged sample of $\sim 13{\times}10^6$ K_L. Since the error on τ_L is the limiting factor on the accuracy of V_{us} from the K_L semileptonic decays [8], we are continuing the analysis of the KLOE data sample to improve both statistics and systematics on the τ_L measurement. Timing performance of the calorimeter (EMC) allows precision measurement of the flight path of the K_L neutral decay products from the arrival time of photons to the calorimeter and from shower position, while K_L momentum is obtained from drift chamber (DC) measurements of the charged pions from K_S decay. To obtain a high and uniform neutral vertex reconstruction efficiency, at least 3 photons are required to be reconstructed.

A control sample of $K_L \to \pi^+\pi^-\pi^0$ decays has been used to study efficiency and resolution of the neutral vertex reconstruction procedure. The proper–time distribution of residual background, $\sim$1.8%, shows two peaks at $t^* < 8$ ns due to regeneration on the the beam pipe and internal wall of the DC, and one peak at $t^* > 25$ ns due mainly to $K_L \to \pi^+\pi^-\pi^0$. The preliminary result is:

$$\tau_L = 50.56 \pm 0.14_{\rm stat} \pm 0.21_{\rm syst} \text{ ns } = 50.56 \pm 0.25 \text{ ns}$$

in agreement with previous KLOE [6, 7] measurements. The statistical error can be improved by increasing the sample by a factor of 1.5 and extending the fit region to lower values of the proper time, with a procedure to account for the K_L beam losses from regeneration process. A statistical error of ~ 0.1 ns is expected for the final result.

The measurement of the BR($K^+ \to \pi^+\pi^-\pi^+$) completes the KLOE program of precise and fully inclusive kaon dominant BR's measurements. The most recent result, BR($K^\pm \to \pi^\pm\pi^+\pi^-$) $= (5.56 \pm 0.20)\%$) [9], dates back to more than 30 years ago.

We use two normalization samples given by the two tagging modes, $K_{\mu 2}$ and $K_{\pi 2}$. The track of the tagging kaon is backward extrapolated to the interacion point and the kinematics of $\phi \to K^+K^-$ is exploited to obtain the momentum of the tagged kaon.

The three pions from kaon decay have momentum smaller than 200 MeV/c and curl up in the KLOE magnetic field increasing the probability to reconstruct broken tracks and fake vertices. If we select kaon decays outside the DC volume, the maximum number of tracks to be reconstructed is three instead of four, and the reconstruction quality improves. We require at least two reconstructed tracks in the DC (pion candidates) and, if their backward extrapolation crosses the path of the tagged kaon before the DC inner wall (geometrical acceptance is $\sim 26\%$), we evaluate the missing mass of the decay. Figure 1 shows the comparison between data and MC for the missing mass spectrum. The background contribution from MC simulation is also shown.

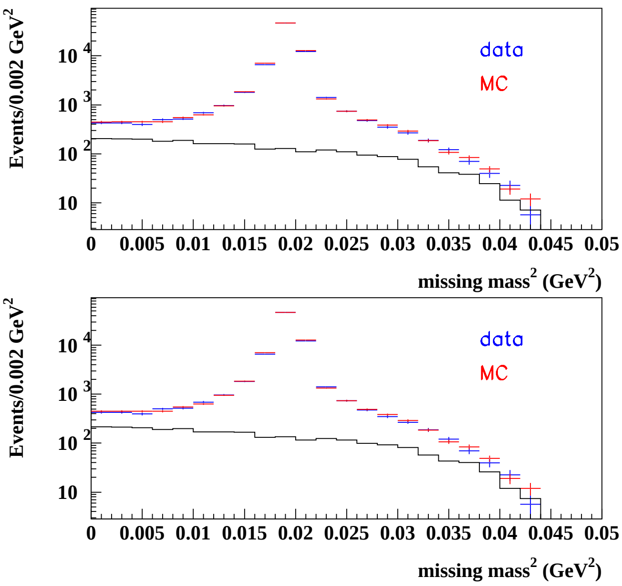

Figure 1: Squared missing mass distribution. Top: for $\mu\nu$ tag; bottom: for $\pi^+\pi^0$ tag. The background, from MC, is also shown.

The selection efficiency is being evaluated from MC, and corrections are applied to account for data-MC tracking differences. The measurement, still in progress, should reach a statistical relative error of a few per mil.

3 The study of η decays

In the $\eta \to \pi^+\pi^-\gamma$ decay, a significant contribution from chiral box anomaly is expected [10]. The box anomaly accounts for the direct (non–resonant) coupling of three pseudoscalar mesons with the photon. The invariant mass of the pions ($m_{\pi\pi}$) is a good observable to disentangle this contribution from other possible resonant ones, e.g. from the ρ-meson. However, the momentum dependence cannot be determined from chiral theory only because the kinematic range of the $\eta \to \pi^+\pi^-\gamma$ decay extends above the chiral limit, where the Weiss–Zumino–Witten term of the ChPT Lagrangian properly describes the direct coupling. Several theoretical approaches have been developed to treat the contributions of the anomalies to the decay [11, 12, 13].

The $\eta \to \pi^+\pi^-\gamma$ decay has been measured in 1970s [14, 15]. The analysis of the two data sets, 7,250 and 18,150 events respectively, shows some contradiction. Theoretical papers trying to

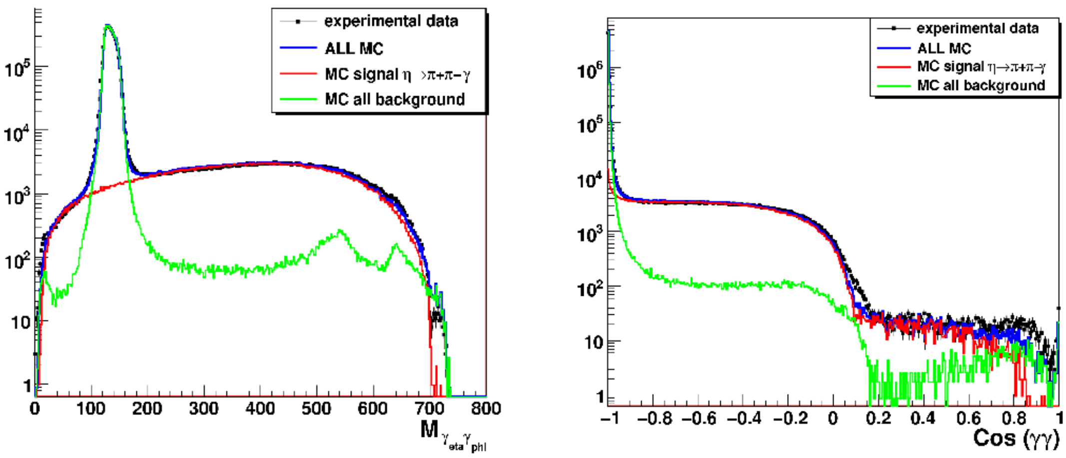

Figure 2: (color online). Invariant mass of two photons (left) and the cosine of the angle between γ_ϕ and γ_η calculated in the rest frame of π^0 (right). The experimental data (points) are fitted simultaneously in both plots with signal and dominant background contributions (the sum of all MC backgrounds is shown).

combine the two measurements have found discrepancies in data treatment and problems with obtaining consistent results [16]. Recently, the CLEO collaboration published the measurement of the ratio of branching ratios, $\Gamma(\eta \to \pi^+\pi^-\gamma)/\Gamma(\eta \to \pi^+\pi^-\pi^0) = 0.175 \pm 0.007 \pm 0.006$, which differs by more than 3–σ from old results. We aim at the solution of the inconsistency of experimental data with precision measurements of the branching ratio and $m_{\pi\pi}$ invariant mass distribution.

The analysis steps include selection of samples of $\eta \to \pi^+\pi^-\gamma$ and $\eta \to \pi^+\pi^-\pi^0$. The main background is the decay $\phi \to \pi^+\pi^-\pi^0$. In order to evaluate signal and background events, the two distributions in Fig.2 were simultaneously fitted with the two contributions. The preliminary measurement of the ratio of branching ratios, $\Gamma(\eta \to \pi^+\pi^-\gamma)/\Gamma(\eta \to \pi^+\pi^-\pi^0) = 0.2014 \pm 0.0004_{stat}$, is in agreement with the old results from Refs. [14, 15] while significantly differs from the recent CLEO results, as compared in Tab. 1.

Table 1: Comparison of the existing results for the ratio $\Gamma(\eta \to \pi^+\pi^-\gamma)/\Gamma(\eta \to \pi^+\pi^-\pi^0)$.

PDG08 Average		0.203 ± 0.008
LOPEZ (CLEO) 2007	859 events	$0.175 \pm 0.007 \pm 0.006$
THALER 1973	18k events	0.209 ± 0.004
GORMLEY 1970	7250 events	0.201 ± 0.006
KLOE Preliminary	611k events	0.2014 ± 0.0004

The finalization of the analysis with the control and the precise evaluation of the background sources is in progress.

Recently, KLOE has started studying the $\eta \to e^+e^-e^+e^-$ decay. This decay, together with the $\eta \to \mu^+\mu^-e^+e^-$, is interesting for the η meson form factor. Events with four electrons in the final state are selected using the time of flight to the calorimeter. Backgrounds from $\eta \to \gamma\gamma/e^+e^-\gamma$

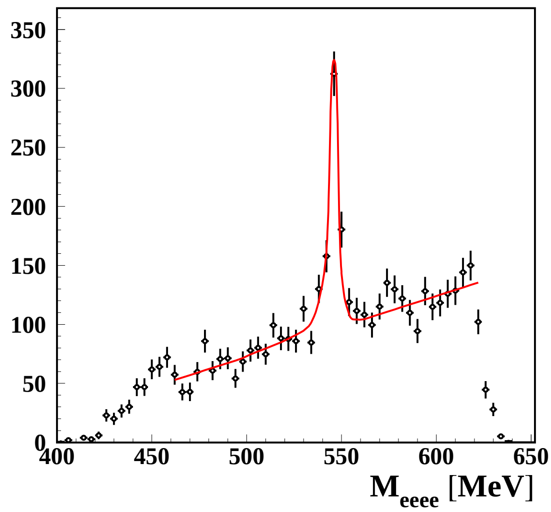

Figure 3: The $\eta \to e^+e^-e^+e^-$ analysis: fit of the four–electrons invariant mass.

with photon conversion are rejected by reconstructing the invariant mass and the distance of the candidate electron track from the beam pipe or drift chamber walls. Most of the background comes from events in the continuum, with a small contribution from ϕ decays. The latter is subtracted from data using the distributions from MonteCarlo (MC) simulation. The number of events is obtained fitting the data distribution of the four–electrons invariant mass, M_{eeee}, with signal and background shapes (Fig.3). From the fit we obtain 413 ± 31 events. This is the first observation of the decay.

4 The measurement of the hadronic cross section

The published KLOE measurements [17, 3] of the hadronic cross section for the process $e^+e^- \to \pi^+\pi^-$ were based on initial–state–radiation (ISR) events with photon emitted at small angle, resulting in kinematical suppression of events with $M^2_{\pi\pi} < 0.35$ GeV^2. To access the two–pion threshold, a new analysis is performed requiring events with photon at large polar angles ($50° < \theta_\gamma < 130°$), in the same angular region of the pions. The drawback of such acceptance cuts is a reduction in statistics of about a factor of five, as well as an increase of events with final–state–radiation (FSR) and from ϕ radiative decays. The uncertainty on the model dependence of the ϕ radiative decays to the scalars $f_0(980)$ and $f_0(600)$ together with $\phi \to \rho\pi \to (\pi\gamma)\pi$ has a strong impact on the measurement [18]. For this reason, the present analysis uses the data taken by the KLOE experiment in 2006 at a value of $\sqrt{s} = 1$ GeV, about 5 $\times\Gamma(\phi)$ outside the narrow peak of the ϕ resonance. This reduces the effect due to contributions from $f_0\gamma$ and $\varrho\pi$ decays of the ϕ-meson to a relative amount of 1%. Contaminations from the processes $\phi \to \pi^+\pi^-\pi^0$ and $e^+e^- \to \mu^+\mu^-\gamma$ are rejected using kinematical variables. A particle ID estimator based on calorimeter information and time–of–flight is used to efficiently suppress the high rate of radiative Bhabhas. The radiative differential cross section is then obtained subtracting the residual background events and dividing by the selection efficiencies and the integrated luminosity. The total cross section $\sigma_{\pi\pi}$ is obtained

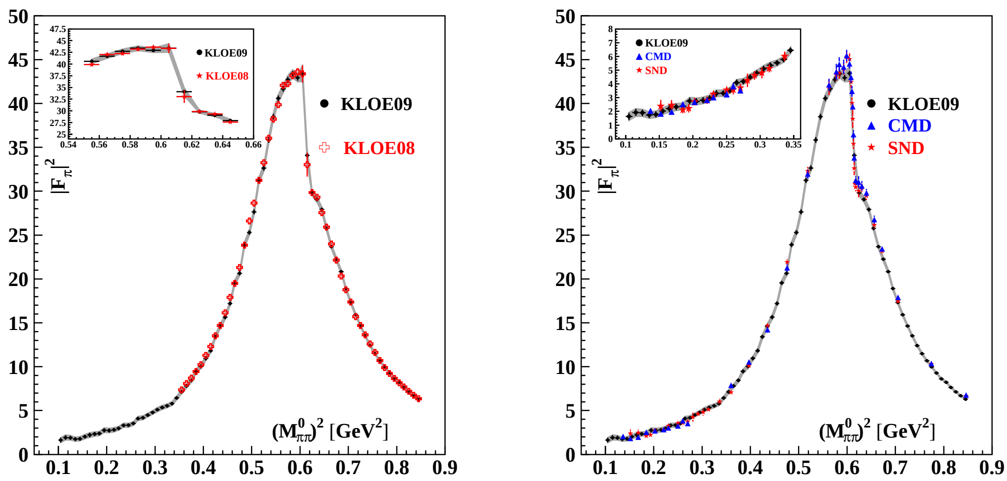

Figure 4: Pion form factor $|F_\pi|^2$ obtained in the present analysis (KLOE09) compared with the previous KLOE result (left) and results from the CMD and SND experiments (right). KLOE09 data points have statistical error attached, the superimposed band gives the statistical and systematic uncertainty (added in quadrature). Errors on KLOE08, CMD2 and SND points contain the combined statistical and systematic uncertainty.

using [19]:

$$s \cdot \frac{\mathrm{d}\sigma_{\pi\pi\gamma_{\mathrm{ISR}}}}{\mathrm{d}M^2_{\pi\pi}} = \sigma_{\pi\pi}(M^2_{\pi\pi})\ H(M^2_{\pi\pi}, s)\ , \tag{1}$$

where H is the radiator function describing the photon emission in the initial state. This formula neglects FSR terms, which are however properly taken into account in the analysis. From $\sigma_{\pi\pi}$, the squared modulus of the pion form factor $|F_\pi|^2$ can be derived. Fig. 4 shows $|F_\pi|^2$ as a function of $(M_{\pi\pi})^2$ for the new KLOE measurement (KLOE09) compared with the previous KLOE publication (KLOE08) and with results from CMD-2 [20, 21] and SND [22] experiments at the Novosibirsk collider. On the ρ–meson peak and above, the new analysis confirms KLOE08 data being lower than the Novosibirsk results, while below the ρ-peak the three experiments are in agreement.

The cross section, corrected for α_{em} running and inclusive of FSR, is used to determine the dipion contribution to the muon anomalous magnetic moment, $\Delta a_\mu^{\pi\pi}$:

$$\Delta a_\mu^{\pi\pi}((0.1-0.85)\ \mathrm{GeV}^2) = (478.5 \pm 2.0_{\mathrm{stat}} \pm 4.8_{\mathrm{exp}} \pm 2.9_{\mathrm{theo}}) \cdot 10^{-10}. \tag{2}$$

The evaluation of $\Delta a_\mu^{\pi\pi}$ in the range between 0.35 and 0.85 GeV^2 allows the comparison of the result obtained in this new analysis with the previously published result by KLOE [3], showing that these two independent analyses provide fully consistent contributions to the muon anomaly.

KLOE Analysis	$\Delta a_\mu^{\pi\pi}(0.35-0.85\ \mathrm{GeV}^2) \times 10^{-10}$
KLOE09	$376.6 \pm 0.9_{\mathrm{stat}} \pm 2.4_{\mathrm{exp}} \pm 2.1_{\mathrm{theo}}$
KLOE08	$379.6 \pm 0.4_{\mathrm{stat}} \pm 2.4_{\mathrm{exp}} \pm 2.2_{\mathrm{theo}}$

5 The tagger system for $\gamma\gamma$ physics

The term "$\gamma\gamma$ physics" (or "two–photon physics") stands for the study of the reaction $e^+e^- \rightarrow e^+e^- \gamma^*\gamma^* \rightarrow e^+e^- X$, where X is some arbitrary final state resulting by the fusion of two photons. Since the two (on-shell) photons are in a $C = +1$ state and the value $J = 1$ is excluded, the study of these processes at the e^+e^- colliders gives access to states with $J^{PC} = 0^{\pm+}$, $2^{\pm+}$, not directly coupled to one photon ($J^{PC} = 1^{--}$).

In the low-energy region covered by the KLOE detector at DAΦNE, existing measurements [23] are affected by large statistical and systematic uncertanties due to small detection efficiencies, large background contributions and particle identification ambiguities in the low-mass hadronic systems. KLOE-2 is the ideal place for precision measurements of low–mass hadronic systems with high statistics and well controlled systematic errors.

Many interesting channels can be investigated and both, the two-photon width of light pseudoscalar mesons, and the meson transition form factors [24], can be obtained. Search for σ meson, especially in the channel $\gamma\gamma \rightarrow \pi^0\pi^0$, is one of the interesting topics addressed by the $\gamma\gamma$ physics program. The precision of avalaible data does not allow any firm conclusion on the presence of a resonance in the region from (400-500) MeV. To improve on the measurement of the $\gamma\gamma \rightarrow \pi\pi$ cross section, high statistics has to be complemented by a careful control of the systematics which cannot be obtained without strong suppression of the background events. The main source of background comes from ϕ decays. Studies are underway on the KLOE data sample using the off-peak data in order to evaluate the experimental capability without the background from ϕ decays. At KLOE-2 we aim at the analysis of the on–peak data performing background suppression thanks to the information coming from the tagging system which is designed to efficiently detect scattered electrons. Scattered electrons from $\gamma\gamma$ reaction deviate from the main DAΦNE orbit while propagating on the machine lattice. For the design of the tagging system we performed MC studies of the trajectories of the scattered electrons whose initial kinematical distribution is given by $\gamma\gamma$ generators developed for these studies. The magnetic fields in DAΦNE have been fully simulated. The results show that the constraints coming from the DAΦNE structure do not prevent KLOE-2 from obtaining a good coverage of the kinematic region of interest.

Satisfactory results have been obtained using a tagging system composed by:

- A station to detect leptons at low energy (LET), located in the region between the two quadrupoles inside KLOE (QD0 and QF1), about 1 m from the interaction region (IP). Scattered leptons on the LET detector pass through the first quadrupole, QD0 and, being off-energy, are deflected with respect to the main orbit. The energy distribution of these leptons is very broad, with tails reaching 50 MeV on one side and 450 MeV on the other. The measurement of the lepton energy requires a calorimeter, being the position of the exit point weakly correlated with the lepton momentum.

- A station for leptons with high energy (HET), located at the exit of the first bending magnet (about 11 m from the IP). The leptons propagate through the magnetic fields of the machine and are separated by the B-fields according to their momenta. The energy of the scattered particles is in the range (425-475) MeV (for a minimum distance of 50 mm between the detector and the nominal orbit). In this case a position detector allows the measurement of the lepton momentum with good precision.

When both scattered leptons are detected by HET/LET taggers, the two–photons centre–of–mass energy $W_{\gamma\gamma}$ can be measured independently from the central KLOE detector. With the realistic assumption of a 3 mm pitch for the HET, and a LET resolution of $\sigma(E)/E = 5\%/\sqrt{E(\mathrm{GeV})}$, in the case of coincidence HET $\otimes$ LET, we obtain a resolution on $W_{\gamma\gamma}$ of $\sigma = 12.8$ MeV, while in the case of coincidence LET $\otimes$ LET the resolution becomes $\sigma = 33.4$ MeV.

5.1 The Low Energy Tagger detector

Several tests have been performed at the Frascati beam test facility (BTF), in order to study different technological options and geometrical design for the LET calorimeters.

We exposed different kinds of crystals and photosensors at the BTF with electron beams from 100 to 500 MeV in order to characterize all of the scintillators and photosensors, namely two PbWO and two LYSO crystals connected to either SiPM or APD.

For the measurement of the energy and time resolutions of the system made of several crystals and to test the assembly procedure, the calibration and the operational stability of the detectors, we built two full-size LET prototypes which have been studied with electrons from the test beam and with cosmic rays.

The first prototype had a transversal radius larger than 2 Moliere radius (R_M), and longitudinal dimension of 13 cm. This prototype was built on April 2009 and consisted of an inner matrix with LYSO crystals readout by SiPM and an external matrix of $PbWO_4$ crystals readout by standard photomultipliers of 1,1/8" diameter.

A second prototype was built in October 2009 using the first batch of LYSO crystals purchased for the construction of the LET detectors. It was simpler than the first one and of the same size and shape as one of the LET calorimeters to be built for data taking at KLOE-2. It consisted of 20 crystals, 15x15x120 mm^3 each, packed side-by-side to obtain a 5x4 crystal matrix structure. Each crystal was readout by one Hamamatsu MPPC, 3x3 mm^2 active area, 14,400 pixel each, coupled to custom front-end electronics realized by the LNF Electronics Service (SELF). An indirect coupling between SiPM and the front-end, i.e. via coaxial cable, was also tested with success. The front-end electronics has been custom–designed to satisfy the detector requirements in terms of power supply, stability, remote–control setting and sensing, low noise linear amplification, and to be compatible with the KLOE EMC readout chain [25)]. Both prototypes were tested at the BTF using a clone of the standard KLOE DAQ in order to acquire data with the same chain as in the experiment.

The first prototype was tested in May-June 2009, by exposing it to electrons of energy ranging from 150 to 500 MeV (cf. Sect.6). Linear response of LYSO+SiPM from 150 to 500 MeV was achieved. This implies that less than 10^3 photoelectrons were collected at the maximum energy which corresponds to about 2 photoelectrons/MeV. The stochastic term was $2.8\%/\sqrt{E(\mathrm{GeV})}$, consistent with the expected yield of ~ 2 photoelectrons/MeV. The noise term was evaluated from the pedestals of the electronic channels, and contributes with $0.7\%/E$ to the energy resolution. Some additional noise due to test beam setup brings the total noise contribution to $1.2\%/E$. The constant term in the energy resolution of $\sim 4\%$ is fully dominated by the leakage, according to the shape of the prototype.

The second prototype was exposed to electrons from 100 to 450 MeV and only 14 over 20 crystals were readout. The best energy resolution and linearity were obtained with the cable–coupling of SiPMs to front-end electronics as shown in Fig. 5.1. The contributions to the energy resolution from the beam energy spread, higher than expected, and from the lateral leakage on crystals which are not readout have been also observed. We moved the test beam across cracks among adjacent crystals, obtaining no dead-zone effect. The last test beam results validated the

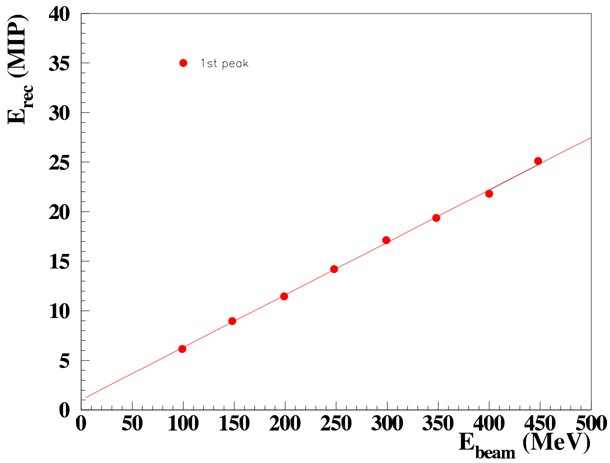

Figure 5: Energy response expressed in minimum-ionizing–particle unit (mip) with respect to beam energy for the LYSO crystals.

cable–coupling option, in agreement with previous laboratory test made with LED pulses.

In order to carefully study signals from the crystal and to extrapolate the results to the full matrix, we have simulated the first prototype with GEANT4, creating two different volumes for the inner matrix, one made of $PbWO_4$ and the other of LYSO. The external matrix was simulated with $PbWO_4$ crystals + PM. For each crystal we considered a dead space of 100 μm of mylar and activated the optical transport of photons inside the scintillating material. Photodetectors consist of a sensitive, 100% efficient area. The correct emission curve both in frequency and time has been considered for the different scintillators. An attenuation length of 100 cm has been also assumed.

The small available space for the LET makes it necessary to carefully choose the dimension of the active part of the detector in order to maximize the acceptance to e^+/e^- while minimizing the shower leakage. Extensive MC simulations, made with the GEANT4 simulation package, have been used to evaluate the expected energy and time resolution with different geometric options for the final design. Simulations of LYSO crystals energy response, based on test-beam data, have allowed us to optimize the LET design and positioning. A full simulation of the LET active volume and beam trajectories was used to determine the detector response to the off-momentum particles.

As the result, each detector will consist of 20 crystals, 1.5x1.5x12 cm^3 each, pointing to the average direction of the off-energy particles, i.e. 11° with respect to the beam axis, centered on the horizontal plane. The crystals will be readout by one SiPM each, the signals being taken out from the detector via coaxial cables to the front-end electronics. A LED pulsing system will also be installed to monitor the gain drift of the SiPMs. Figure 6 shows the integration of the LET in the interaction region of DAΦNE.

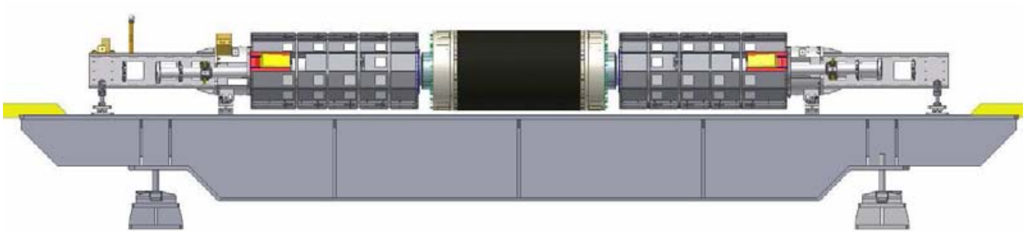

Figure 6: The DAΦNE interaction region with the LET detector.

5.2 The High Energy Tagger detector

The requirements for the HET detector are summarized as follows: good time resolution to disentangle each DAΦNE bunch coming with a period of ~ 2.7 ns; capability to acquire data at a frequency of 368 MHz in order to permit event reconstruction with the KLOE apparatus; radiation hardness in order to stand 50 mm from the beam (a closer position would interfere with the proper operation of DAΦNE) for long term data–taking; and tiny size to allow the installation by means of mechanical supports inside the vacuum chamber.

The tagger detector consists of a set of scintillators arranged in two “stairs” and is constituted of 30 EJ-228 scintillators $3 \times 6 \times 3$ mm^3, which provide a spatial resolution of 2 mm (corresponding to a momentum resolution of 500 keV). Two additional scintillators, $3 \times 6 \times 120$ mm^3, are used for the coincidence. The output light is collected by clear light guides coupled with Hamamatsu R9880U-110sel photomultipliers. To minimize the interference with the DAΦNE high–vacuum system, the detector will be installed inside a movable steel sleeve (cf. Fig.7).

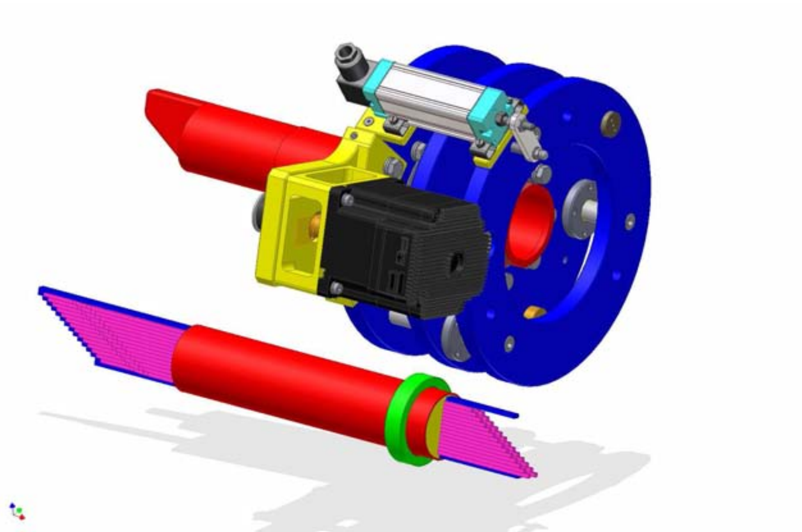

Figure 7: A rendering of the HET apparatus. Both the mechanical system (up) and the detector (down) are shown

During spring 2009, tests have been performed at the BTF in order to study the performance of the detector. The time of flight of electrons has been measured with a HET prototype composed by two modules only (scintillator and photomultiplier). A time resolution of ~300 ps has been obtained (cf. Fig. 8). Mechanics, flanges, box, and motors have been realized and the system will

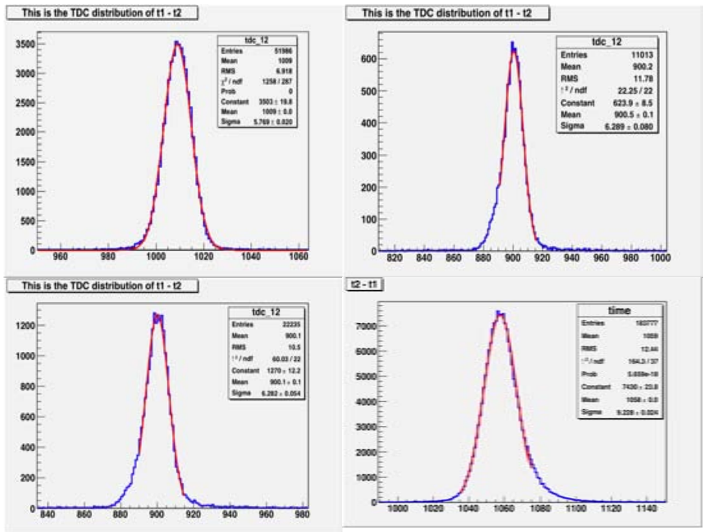

Figure 8: Time resolution measured for the HET prototype at the BTF.

be ready in April, 2010.

The PMT efficiency will be monitored and the ageing of the photocathode will be compensate (as much as possible) by increasing high voltage (HV) supply. An automatic system, controlled via Ethernet, is being developed. The system will be structured as follows:

- a pulsed LED controlled by a linear current generator (already successfully tested);
- 32 optical fibres to bring the same light to the each PMTs;
- 32–channels CAEN VME QDC to acquire the spectrum of every single PMT;
- a VME board with a PIC microcontroller to monitor the efficiency of the PMTs and change the HV supply.

In the case of serious damage of one PMT it can be easily replaced thanks to the design of the mechanical structure. The front-end electronic board (a fast buffer, an amplifier, two voltage regulators, and a thermometer) provides an analog signal to the Data Acquisition board with embedded discriminators. This part of the electronics has been successfully tested obtaining a signal with a rise time shorter than 0.5 ns. The signals come from the HET detector, DAΦNE (fiducial) and KLOE (Trigger and ACQ logic). The acquisition logic has been implemented inside the FPGA. A microcomputer, inside a Virtex5 FPGA, controls communication with KLOE DAQ via the VME bus. As the HET detector is placed far away from the IP, the number of beam bunches must be registered to reconstruct the related information in the KLOE-2 detector. Therefore, consecutive bunches must be separated in time and a resolution better than 1 ns is required. The time resolution can be reached with a 500 MHz clock which is under test. The complete acquisition system is planned to be ready in the 3Q of 2010.

6 The calorimeters for the detector upgrade

To improve the reconstruction of K_L decays in the DC with photons hitting the DAΦNE quadrupoles, a calorimeter with high efficiency to low energy photons, (20-300) MeV, time resolution better than 1 ns, and space resolution of a few cm, is needed. To match these requirements, we have designed a tile calorimeter, QCALT, where each single tile is readout by one SiPM, for a total of 2,400 channels.

A small angle calorimeter, CCALT, will extend the angular coverage of the KLOE-2 EMC, from polar angle of 20° down to 8°, increasing the photon detection capability of the experiment and enhancing the search reach for rare K_S, η and η' decays. The calorimeter extension consists of two small barrels of LYSO crystals readout with APD photosensors aiming at a time resolution of (300–500) ps for 20 MeV photons. The first test of a $(5.5 \times 6 \times 13)$ cm^3 prototype for such a detector was carried out in April 2009 at the BTF with an electron beam from 100 to 500 MeV. In the selected energy range, we measured a light yield of $500 \div 800$ p.e./MeV, an energy resolution which can be parametrized as $0.05 \oplus 0.01/(\mathrm{E/GeV}) \oplus 0.015/\sqrt{\mathrm{E/GeV}}$, a position resolution of 2.8 mm, and a time resolution of $200 \div 300$ ps.

6.1 The quadrupole instrumentation, QCALT

In the old IP scheme of DAΦNE, the inner focusing quadrupoles were surrounded by two calorimeters, QCAL [26], covering a polar angle down to 21°.

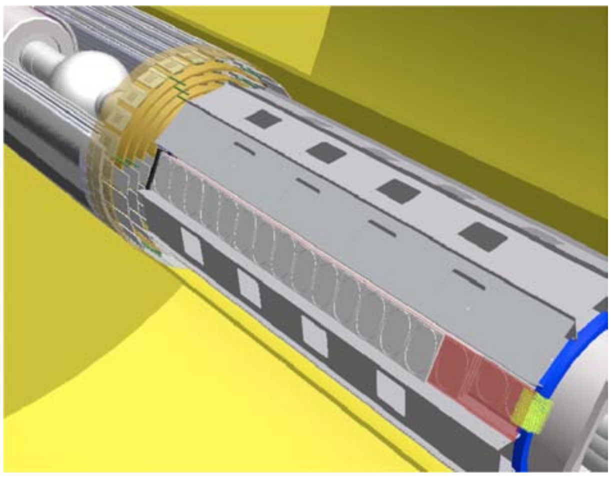

Figure 9: IP scheme of KLOE-2 with the QCALT calorimeter surrounding the DAΦNE quadrupoles.

The new QCALT design (Fig. 9) consists of a dodecagonal structure, 1 m long, covering the region of the new DAΦNE quadrupoles and composed by a sampling of 5 layers, 5 mm thick, of scintillator plates alternated with 3.5 mm thick tungsten plates, for a total depth of 4.75 cm (5.5 X_0). The active part of each plane is divided into twenty tiles of $\sim 5 \times 5$ cm^2 area, with 1 mm diameter WLS fibers embedded in circular grooves. Each fiber is then optically connected to a silicon photomultiplier of 1 mm^2 area, SiPM, for a total of 2,400 channels. R&D studies have been carried out on SiPM, fibers and tiles to select the components of the detector.

We compared the characteristics of two different SiPM produced by Hamamatsu (multi pixel photon counter, MPPC): 100–pixels MPPC (S10362-11-100U) and 400–pixels MPPC (S10362-11-050U), both with 1×1 mm^2 active area. We prepared a setup based on a blue light pulsed LED, a polaroid filter to modify the light intensity and a SiPM polarization/amplification circuit based on Minicircuits MAR8-A+ amplifier. We measured the gain and the dark rate variation as a function of both, the applied V_{bias}, and the temperature of the photodetector. The readout electronics was based on CAMAC, with a charge sensitivity of 0.25 pC/count and a time sensitivity of 125 ps/count.

Our tests confirm the performance declared by Hamamatsu and show a significative variation of the detector gain as a function of the temperature (3% for 400 pixels versus 6% for 100 pixels).

For the fibers, we studied the light response of two different, 1 mm^2, WLS from blue to green, optically connected to MPPC when hit by electrons produced by a ^{90}Sr source: Saint Gobain BCF92 single–cladding and Saint Gobain BCF92 multi–cladding fibers. The adopted solution is Saint Gobain BCF92 multi–cladding. For this fiber we find, as expected, larger light yield than the one with single–cladding fibers (×1.5), fast emission time (5 ns/pe) and long attenuation length.

Light response and time resolution of a complete tile have been measured using cosmic rays. The system was prepared connecting fiber to MPPC and using two external NE110 scintillators fingers to trigger the signal. We have prepared different tiles (3 and 5 mm thick) readout with 100– or 400–pixels MPPC. The adopted solution is 5 mm thick BC408 tile readout by 400–pixels MPPC which gives the best results in terms of light yield versus dark rate.

For this system we obtain 32 pe/mip with a time resolution of 750 ps after correcting for the time dependence on pulse height.

Controlling enviromental conditions and using LED light, we have also studied SiPM response when varying V_{bias}. By using the photon counting properties of the SiPM we observe an increase of the light yield when increasing V_{bias}. The device reach a plateau 600 mV above the operation voltage, which is consistent with a variation of the photon detection efficiency of the SiPM for the avalanche probability.

To manage the signals from many channels, the SELF has developed some custom electronics composed by a 1×2 cm^2 chip, containing the pre-amplifier and the voltage regulator, and a multifunction NIM board. The NIM board supplies the V_{bias} to the photodetector with a precision of 2 mV and a stability at the level of 0.03 per mil. A low threshold discriminator and a fanout are also present.

6.2 The Crystal Calorimeter, CCALT

In Fig. 10, we show a zoomed-view of the available region around the IP which can be used to extend the angular coverage of the main electromagnetic calorimeter, limited to a polar angle of $\geq 20°$, with the addition of a new dedicated calorimeter. Assuming to be able to lower the minimum

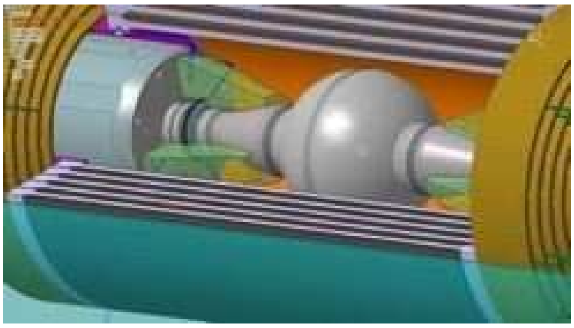

Figure 10: Zoomed-view of the IP region. The area available for the new calorimeter lies between the inner sphere and the closest quadrupoles.

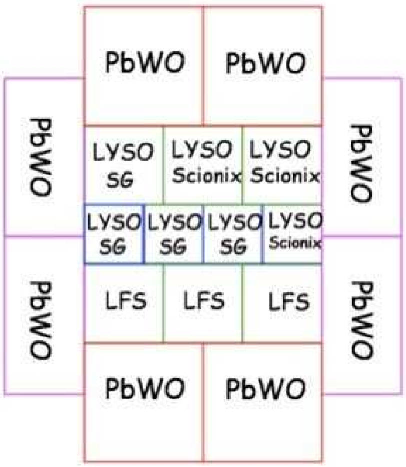

Figure 11: Composition of crystals used for the matrix prototype.

polar angle for photon detection down to 8°, this will enhance the multiphoton detection capability of the detector for the search of rare decays of K_S, η and η' mesons.

The only available area to place a calorimeter lies between the end of the spherical beam pipe, of 10 cm radius, and the first quadrupole, positioned at 30 cm from the IP.

This calorimeter has to be very dense, with a small value of both radiation length (X_0) and Moliere radius (R_M), not hygroscopic and with a large light output to improve photon detection efficiency at low energy (from 20 to 500 MeV). Moreover, the calorimeter has to be extremely fast in order to allow prompt photon reconstruction in an environment with a large background rate ($\sim 1 \div 5$ MHz) of secondary showers generated by off-axis e^+, e^- coming from intra–bunch scattering (*Touschek effect*). Preliminary simulation studies indicates the need to reach a time resolution of $300 \div 500$ ps for 20 MeV photons.

A suitable solution is offered by a crystal calorimeter with good timing performance, CCALT. A first detector layout consists of two concentrical barrels of 24 crystals each, with transversal dimension of 2×2 cm^2 and longitudinal length from 13 to 15 cm. The best crystal choice is provided by new generation of Cerium doped Lutetium Yttrium Orthosilicate, LYSO, which has

X_0 and R_M values (1.1 and 2 cm) comparable to the ones (0.9 and 2 cm) of the Lead Tungstanate, $PbWO_4$, with the advantage of a much larger light yield ($\times$ 300). On the negative side, LYSO shows a scintillation emission time (τ_{LYSO} = 40 ns) slower than $PbWO_4$ (τ_{PbWO} = 10 ns). However, from the basic scaling law of the time resolution, $\sigma_t = \tau/\sqrt{\mathrm{N_{pe}}}$, we expect LYSO to be a factor of four more performant than $PbWO_4$.

In the final location of the CCALT inside KLOE-2, the presence of an axial magnetic field of 0.52 kGauss forces the usage of silicon based photodetectors. Due to the large photon yield, the readout with APDs is a valid solution since, at the lowest photon energy of 20 MeV, the collected photoelectrons will be $\sim$ 10,000 which corresponds to $\sim$ 12 pC assuming an average gain of 300 and an amplification stage of $\times$25, well matching the ADC sensitivity of the KLOE calorimeter (100 fC/count). In the following, we specifically considered only the Hamamatsu S8664-55, which has an active area of 0.5 $\times$ 0.5 cm^2, fast timing characteristics and a quantum efficiency from 65 to 85 per cent in the wavelength range of interest, (390–500) nm for the LYSO emission spectra.

As reported in Sect. 5, we have built a medium–size crystal matrix prototype with transversal radius larger than 2 R_M, longitudinal dimension being constrained by budget limits from 13 to 15 cm. The prototype consists of an inner matrix of 10 LYSO crystals readout by APD and an outer matrix, for leakage recovery, composed by eight $PbWO_4$ crystals readout by standard Hamamatsu Bialcali photomultipliers of 1,1/8" diameter.s To test the quality of the crystals offered by different vendors, the inner matrix has been assembled in three rows (Fig. 11) composed (from bottom to top) as follows:

- 3 LFS crystals from Zecotek of 2 $\times$ 2 $\times$ 13 cm^3,
- 2 LYSO St. Gobain crystals of 1.5 $\times$ 1.5 $\times$ 15 cm^3, 1 LYSO St. Gobain + 1 LYSO Scionix crystals of 1.5 $\times$ 1.5 $\times$ 13 cm^3
- 1 LYSO St. Gobain crystal of 2 $\times$ 2 $\times$ 15 cm^3, 2 LYSO Scionix crystals of 2 $\times$ 2 $\times$ 13 cm^3.

The LFS from Zecotek is a Luthetium Fine Silicate crystal, with similar properties to LYSO. Each crystal is wrapped with 100 μm of tyvek on the lateral faces, leaving free both the front and end faces, thus allowing a fast change of the photosensors readout and the calibration light pulses to be brought through an external LED. Each APD is inserted in a PVC mask with the amplifier soldered on its anode and mechanically positioned inside a stainless steel box closed by a PVC cap with only the electronic pins coming out for connection to HV and readout cables. An external holder takes the PMs in position for the readout of the outer crystals while allowing to press the boxes containing the APDs. The optical connection of the photosensors with the crystals is done with optical grease. The amplifiers are based on the MAR8A+ chip from Minicircuits, with a gain factor of 25 and a bandwidth of 1 GHz.

The crystal matrix at the BTF was centered on the beam axis with an area delimited by the cross of two BC408 scintillators of 1 $\times$ 0.5 $\times$ 5 cm^3. In most of the tests, the fingers were aligned in such a way to define a beam spot of 1 $\times$ 1 cm^2. Moreover, a beam position monitor, BPM, consisting of sixteen horizontal and vertical scintillator strips readout by two Multi Anode PMs, was placed in front of the fingers. Each strip is built by three 1 mm diameter scintillating fibers thus providing an accuracy below 1 mm on the beam localization.

By using the UV LED, we have first equalized each channel at 10% level and then calibrated the calorimeter response of each channel with minimum ionizing particles, mip, crossing

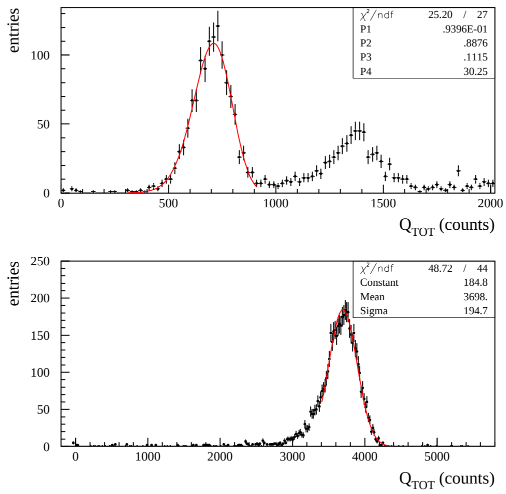

Figure 12: Distribution of Q_{TOT} for single electron events at 100 MeV (top) with a logG fit and (bottom) with a gaussian fit superimposed.

the calorimeter orthogonally to the crystal axis. We get σ_{ped} of 5 counts and a mip peak, M_i, of about 100 counts for the small–size crystals. The statistical precision on the peak determination is ∼1%. The total response of the detector is then defined as:

$$Q_{TOT} = \sum (Q_i - P_i) \times M_0/M_i, \tag{3}$$

where Q_i and P_i are the collected charge and the pedestal of the i-th channel, M_0 represents an average calibration of all channels in counts and the calibration for the larger crystals is corrected for the different size. In Fig. 12, we show the distribution of Q_{tot} for a beam of 100 and 500 MeV respectively after having selected single electron events with a cut on the finger scintillators. A surviving fraction of events with more than 1 electron is still observed in the matrix, especially at low energies. We have fit the distribution corresponding to one electron either with a simple gaussian, centered around the peak, or with a logarithmic gaussian, logG, as follows:

$$\mathrm{N} \cdot \exp(-\frac{1}{2\sigma_0^2} ln(1 - \frac{\eta}{\sigma_E}(E - E_{peak}))^2 - \frac{\sigma_0^2}{2}) \tag{4}$$

where N is a normalization factor, η represents the asymmetry, E_{peak} the most probable value of the distribution, $\sigma_0 = \frac{2}{2.36} \sinh^{-1}(2.36\,\eta/2)$ and $\sigma_E = \frac{\mathrm{FWHM}}{2.36}$ give the resolution.

In Fig. 13, we show the energy dependence of the energy resolution measured on data which has been fit with:

$$\sigma_E/E = a \oplus \mathrm{b/(E/GeV)} \oplus \mathrm{c}/\sqrt{\mathrm{E/GeV}}, \tag{5}$$

where, accordingly to MC, we have fixed the constant term to 5%. We found $b = 1.1\%$ and $c = 1.4\%$ when using the gaussian fit to the spectra, and $b = 0.8\%$ and $c = 2.4\%$ with the logG function.

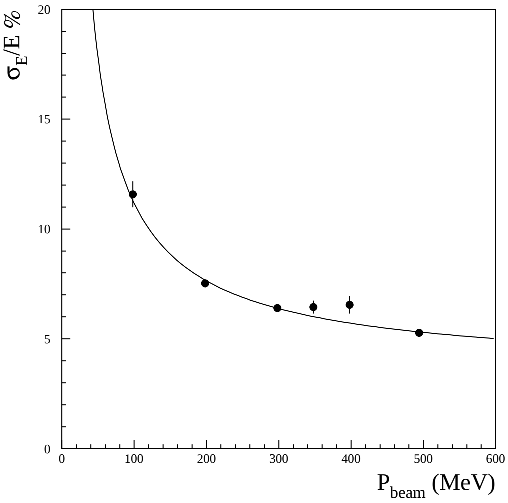

Figure 13: Dependence of the energy resolution of the LYSO crystals on beam momentum.

7 The KLOE-2 inner tracker

The innovative idea of the cylindrical triple–GEM chamber, CGEM, has been tested for the first time with a small prototype (7 cm radius and 24 cm length). The very positive results obtained opened the way for the project of a CGEM as the Inner Tracker (IT) for KLOE-2. Since then the R&D activities for the IT have been focused on [27]: i) the construction and complete characterization of a full-scale CGEM prototype, ii) the study of the XV strip readout configuration and its operation in magnetic field and iii) the construction and characterization of a large-area GEM realized with the new single–mask photolitografic technique.

The construction, safe operation and extensive test of an almost full-size Cylindrical-GEM prototype during 2007 has demonstrated the feasibility of such a novel low-mass and dead-zone-free vertex detector. Results show the expected spatial resolution from a digital readout of 650 μm pitch strips [28]. We have studied the XV readout configuration and operation in magnetic field. The results are reported in the following subsections, together with the progress on the large–area GEM. The simulation of the final detector by 3D Finite Element Code ANSYS has been also worked on thanks to the collaboration with L. Quintieri, to evaluate the structural response under tensile loads, i.e., strain, stress, and displacements [30]. The model has been validated by laboratory tests on prototypes and the simulation results used to settle the tensile load to be applied on the inner tracker.

The project has been approved and the construction of the CGEM will start by 2Q of 2010 in order to be ready for the installation by 3Q of 2011.

7.1 XV readout and operation in magnetic field

A typical orthogonal XY readout can not be used for the inner tracker, due to its cylindrical geometry. The final IT readout will be then performed with an XV pattern of strips and pads engraved on a polyimide foil substrate, 100 μm thick (Fig. 14). The X strips with 650 μm pitch

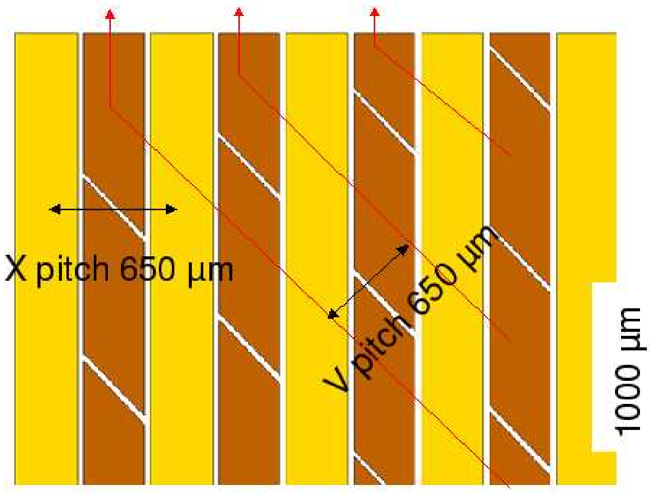

Figure 14: Scheme of the XV readout configuration.

will provide the r-ϕ coordinate while the pads, connected through internal vias to form V strips with 650μm pitch, will provide the z coordinate. This quite innovative readout solution was not implemented on the CGEM prototype, therefore its characteristics have been extensively studied with dedicated planar chambers. In addition, since the IT will operate inside the KLOE magnetic field, the effects on the cluster formation and electronics readout had to be studied. To address these issues a dedicated test has been done at the H4 permanent facility, setup at the CERN-SPS 150 GeV pion beam line within the RD51 collaboration. Five 10 $\times$ 10 cm^2 planar triple-GEM (PGEM) detectors with 650 μm pitch readout have been assembled and succesfully tested: four chambers with standard XY readout and the fifth with the XV readout. The setup was 1 m long with detectors placed equidistantly with the XV chamber placed in the center. For the operation in magnetic field, the GOLIATH magnet was used, providing a field adjustable up to 1.5 T, orthogonal to the horizontal beam–plane. The coincidence of 6 scintillators (3 $\times$ 3 cm^2) readout by silicon photomultipliers provided the trigger signal for the acquisition. The planar chambers were partially equipped with 22 digital readout GASTONE boards [29], 32 channels each, four on each XY chamber and six on the XV chamber. The working point was: Ar/CO2 (70/30) gas mixture and operating voltages $V_{\rm fields} = 1.5/3/3/5$ kV/cm and $V_{\rm GEM} = 390/380/370$ V ($\sum V_G =$ 1140V, Gain $= 2 \times 10^4$). The GASTONE threshold was set at 3.5 fC.

The effect of the magnetic field (B) is twofold: a displacement dx and a spread $\sigma_{\rm dx}$ of the charge over the readout plane. The expected values obtained from simulation studies of our chambers done with GARFIELD are dx=600 μm and $\sigma_{\rm dx} = 200$ μm at B = 0.5 T [27]. In the test beam configuration the magnetic field effect was mainly present on the X-view. The setup used to measure the displacement on the XV chamber due to the magnetic field is shown in Fig. 15. All four XY chambers are likewise oriented, with the same anode-cathode configuration, and provide the external tracking system for the XV chamber which is instead in a cathode-anode arrangement, reversed with respect to the other chambers. Since the XY chambers are subjected to the same Lorentz force, the reconstructed track will be shifted by the same offset dx with respect to the

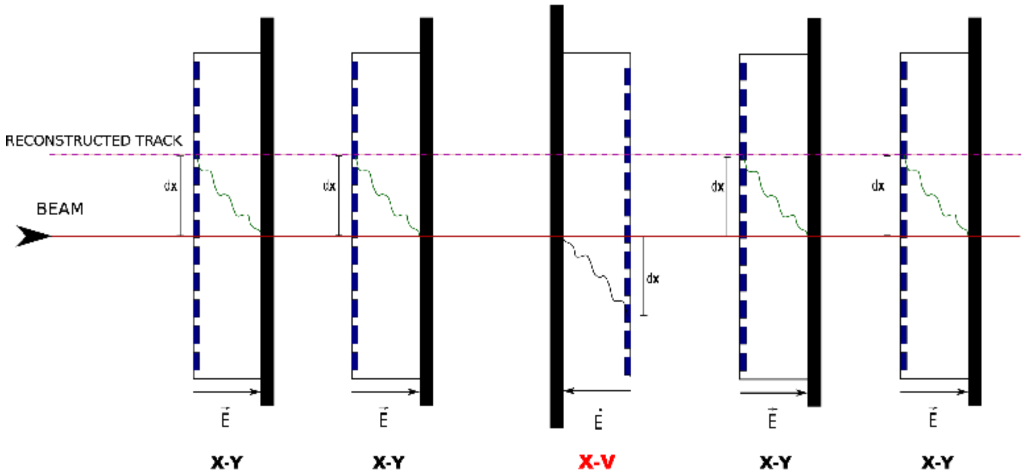

Figure 15: Test beam setup and definition of the measured quantity.

true track trajectory. The displacement in the XV chamber instead will be of the same magnitude dx but with opposite direction, due to the reversed cathode-anode arrangement. First, with zero magnetic field (B = 0 T), the setup was aligned to a few micrometer precision and then, with the magnetic field turned on, the total displacement (D) between the track reconstructed by the XY telescope and the point in the XV chamber was measured: D = 2 × dx (Fig. 15). The displacement dx was measured for 5 values of the magnetic field and found in good agreement with the value obtained from the GARFIELD simulation at B = 0.5 T (Fig. 16). Fig. 17 shows the resolution on

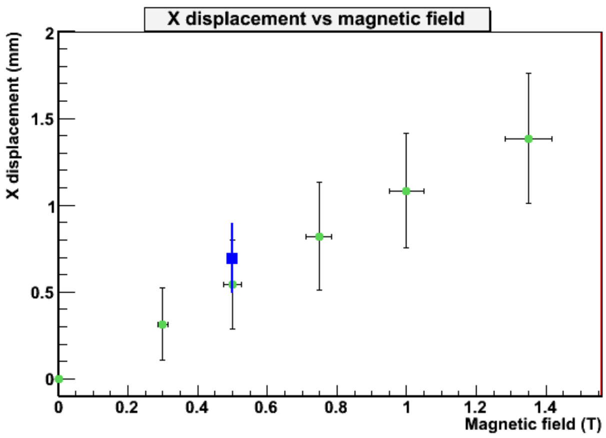

Figure 16: Displacement dx as a function of the magnetic field (points) with the result from GARFIELD simulation at B = 0.5 T (square).

the X coordinate as a function of the magnetic field, the values ranging from 200 μm at B = 0 T up to 380 μm at B = 1.35 T. The resolution on the Y coordinate, measured from the crossing of X and V strips readout, is $\sim$ 370 μm at B = 0 T, in agreement with what expected from the digital readout of the two X and V views (Fig. 18). The performance of the front-end chip GASTONE has been studied measuring the cluster size and reconstruction efficiency as a function of the magnetic field and operating the XV chamber with four different gain values.

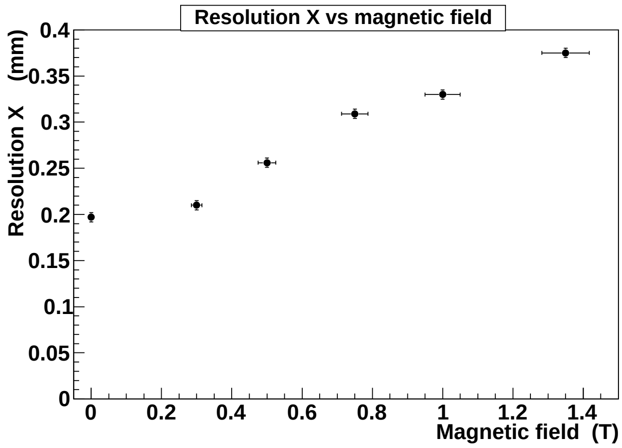

Figure 17: Resolution on the X coordinate as a function of the magnetic field.

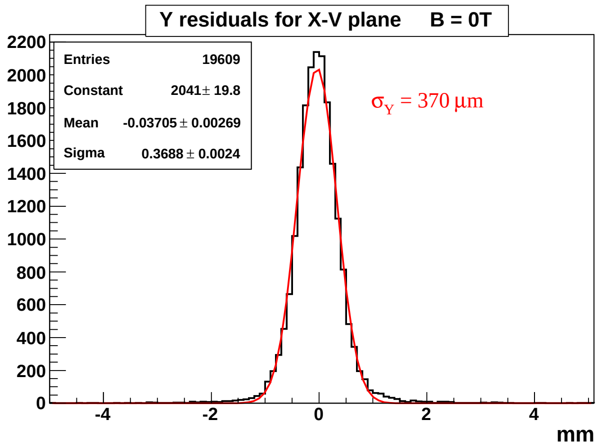

Figure 18: Resolution on the Y coordinate at B = 0 T.

The efficiency for the nominal KLOE magnetic field B = 0.52 T and voltage settings was measured to exceed 99%, slightly decreasing at higher B fields. The charge sharing, grounding and cross-talk between strips could have been in principle different for X and V views, due to the different readout geometry. Our measurements demonstrates the good behavior of both X and V readout views, which give equalized response.

7.2 Large Area GEM

To build the IT outermost layer, a GEM foil as large as 1440×700 mm^2 is needed. This foil can be obtained splicing 3 separate 480 x 700 mm^2 foils with a technique that we have developed, using an epoxy adhesive and a vacuum bag. The urge for larger GEM foils has driven a change of the production procedure by CERN TS-DEM-PMT laboratory, switching to a single-mask etching, more suitable for large surface. The procedure has been finalized: the new GEMs have quasi-cylindrical holes and a new characterization is necessary. The GEM foils produced with the new technique will be delivered in April 2010. Meanwhile dedicated tools for the stretching, handling and assembling of such large foils have been designed, realized and tested with a dummy chamber. A 700x300 mm^2 planar triple-GEM will be used to check the uniformity of the new single–mask GEMs over large area. The chamber, the largest GEM detector ever operated, will be equipped with the GASTONE 64-channels final release and readout by the Off Gastone Electronic (OGE) Board [27]. It will be studied with a test beam at CERN. The external tracking system will be provided by the four XY chambers used for the XV readout studies, replacing the XV chamber with the Large Area GEM.

8 Papers

1. F. Ambrosino et al. (KLOE), J. High Energy Phys. **0907**, 105 (2009).
2. F. Ambrosino et al. (KLOE), Phys. Lett. B **670**, 285 (2009).
3. F. Ambrosino et al. (KLOE), Phys. Lett. B **681**, 5 (2009).
4. F. Ambrosino et al. (KLOE), Phys. Lett. B **679**, 10 (2009).
5. F. Ambrosino et al. (KLOE), Eur. Phys. J. C **64**, 627 (2009).
6. F. Ambrosino et al. (KLOE), Phys. Lett. B **672**, 203 (2009).
7. F. Ambrosino et al. (KLOE), Phys. Lett. B **675**, 283 (2009).

9 Public notes

1. G. De Robertis et al. (KLOE-2), *Technical design report of the inner tracker for the KLOE-2 experiment*, KLOE-2 Note K2PD-3.

10 Contributions to Conferences and Seminars

1. S. Giovannella, *Hadronic physics with KLOE*, Les Rencontres de Physique de la Vallée d'Aoste, La Thuile, Italy, March 1-7, 2009.
2. T. Spadaro, *Precision measurements of the SM with K_{l2} and K_{l3} decays at KLOE*, Rencontres de Moriond on Electroweak Interactions and Unified Theories, La Thuile, Italy, March 7-14, 2009.
3. D. Domenici, *Activity at CERN and LNF on large area GEM detectors*, Frontier detectors for frontier physics, La Biodola, Italy, May 24-30, 2009.
4. M. Martini, *QCALT: a tile calorimeter for KLOE-2*, Frontier detectors for frontier physics, La Biodola, Italy, May 24-30, 2009.
5. S. Miscetti, *Energy and time response of LYSO and PbWO crystals to low–energy electron beams*, Frontier detectors for frontier physics, La Biodola, Italy, May 24-30, 2009.

6. S. Miscetti, *The calorimeter for KLOE-2 upgrade*, Frontier detectors for frontier physics, La Biodola, Italy, May 24-30, 2009.

7. G. Venanzoni, *A new KLOE precision measurement of* $|F_\pi|^2$ *with ISR events*, CIPANP 2009, San Diego, U.S.A., May 25-31, 2009.

8. M. Palutan, *Test of the SM with Ke2 decays at KLOE*, CERN EP Seminar, Geneva, Switzerland, May 25, 2009.

9. R. Versaci, *Hadronic physics at KLOE*, CIPANP 2009, San Diego, U.S.A., May 25-31, 2009.

10. B. Sciascia, *Test of lepton flavor violation with Ke2 decay at KLOE*, Kaon international conference, Tsukuba, Japan, June 9-12, 2009.

11. M. Moulson, *Recent KLOE results on radiative kaon decays*, Kaon international conference, Tsukuba, Japan, June 9-12, 2009.

12. M. Jacewicz, *The* η/η' *physics at KLOE*, Chiral Dynamics, Berne, Switzerland, July 6-10, 2009.

13. E. De Lucia, V_{us} *and lepton universality from kaon decays at KLOE*, EPS-HEP Cracow, Poland, July 16-22, 2009.

14. M. Dreucci, *Measurement of* K_S *lifetime and CPT symmetry tests in the neutral kaon system with kaon interferometry at KLOE*, EPS-HEP Cracow, Poland, July 16-22, 2009.

15. P. De Simone, *KLOE measurements of the* K_L *lifetime and absolute BR(*$K^+ \to \pi^+\pi^+\pi^-$*)*, EPS-HEP Cracow, Poland, July 16-22, 2009.

16. F. Bossi, *Search on the hidden sector with KLOE at DAFNE*, Dark forces workshop, SLAC, Menlo Park,, U.S.A., Sept. 24-26, 2009.

17. G. Venanzoni, *Status of KLOE-2*, International workshop on e^+e^- collisions from ϕ to ψ, Beijing, China, Oct. 13-17, 2009.

18. S. Müller, *KLOE measurements of the pion form factors*, International workshop on e^+e^- collisions from ϕ to ψ, Beijing, China, Oct. 13-17, 2009.

References

1. A. Masiero, P. Paradisi, and R. Petronzio, Phys. Rev. D **74**, 011701 (2006).

2. F. Ambrosino et al. (KLOE), Eur. Phys. J. C **64**, 627 (2009).

3. F. Ambrosino et al. (KLOE), Phys. Lett. B **670**, 285 (2009).

4. S. Müller et al. (KLOE), `arXiv:0912.2205`.

5. F. Bossi et al. (KLOE), La Rivista del Nuovo Cimento, Vol. 31, serie 5, N.10 (2008).

6. F. Ambrosino et al. (KLOE), Phys. Lett. B **626**, 15 (2005).

7. F. Ambrosino et al. (KLOE), Phys. Lett. B **632**, 43 (2006).

8. F. Ambrosino et al. (KLOE), JHEP **04**, 059 (2008).

9. I.H. Chiang et al., Phys. Rev. D **6**, 1254 (1972).

10. S.L. Adler, Phys. Rev. **177**, 2426 (1969).

11. B.R. Holstein, Phys. Scripta T **99**, 55 (2002).

12. M. Benayoun et al., Eur. Phys. J. C **31**, 525 (2003).

13. B. Borasoy and R. Nissler, Nucl. Phys. A **740**, 363 (2004).

14. P. Gormley, Phys. Rev. D **2**, 501 (1970).

15. J. Layter, Phys. Rev. D **7**, 2565 (1973).

16. B. Borasoy and R. Nissler, `arXiv:0705.0954`.

17. A. Aloisio et al. (KLOE), Phys. Lett. B **606**, 12 (2005).

18. D. Leone, PhD thesis at Karlsruhe University, KA-IEKP-2007-7 (2007).

19. S. Binner, J. H. Kühn and K. Melnikov, Phys. Lett. B **459**, 279 (1999).

20. R. R. Akhmetshin et al. (CMD-2), Phys. Lett. B **648**, 28 (2007).

21. R. R. Akhmetshin et al. (CMD-2), JETP Lett. **84**, 413 (2006).

22. M. N. Achasov et al. (SND), J. Exp. Theor. Phys. **103**, 380 (2006).

23. H. Marsiske et al. (Crystal Ball), Phys. Rev. D **41** 1990) 3324; T. Oest et al. (JADE), Z. Phys. C **47**, 343 (1990).

24. F. Ambrosino et al. (KLOE), Eur. Phys. J. C **50**, 729 (2007).

25. M. Adinolfi et al. (KLOE), Nucl. Instr. & Meth. A **482**, 364 (2002).

26. M. Adinolfi et al. (KLOE), Nucl. Instr. & Meth. A **483**, 649 (2002).

27. F. Archilli et al. (KLOE-2), *Technical Design Report of the Inner Tracker for the KLOE-2 experiment*, `arXiv:1002.2572` and LNF-10/3(P) INFN-LNF, Frascati, 2010.

28. G. Bencivenni et al., NSS Conference Record, 2008 IEEE, 19-25 October 2008, 1345.

29. A. Balla et al., Nucl. Inst. & Meth. A **604**, 23 (2009).

30. L. Quintieri et al., *Finite Element Model of the Cylindrical GEM Detector as New Inner Tracker of Kloe-2 and Mechanical Characterization of the Employed Materials*, Frascati Report LNF-09/12(IR), 2009.

LHCb

M. Anelli (Tecn.), G. Bencivenni, P. Campana, G. Capon, M. Carletti (Tecn.),
P. Ciambrone, E. Dané (Art. 23), P. de Simone, A. Di Virgilio (Tecn.),
G. Felici, S. Furcas (Bors.), G. Lanfranchi, G. Mannocchi, F. Murtas,
M. Palutan, M. Pistilli (Tecn., Art. 15), R. Rosellini (Tecn.),
G. Sabatino (Dott.), M. Santoni (Tecn.), A. Saputi, A. Sarti (Art. 23),
A. Sciubba (Resp., Ass.), S. Valeri (Tecn.), A. Zossi (Tecn., Art. 15)

In collaboration with:
G. Bisogni, U. Martini (LNF-SSCR); A. Battisti;
A. Balla, G. Corradi, M. Gatta, D. Tagnani (LNF-SEA)

1 Introduction

The activities of the LHCb-LNF group in the **Muon sub-detector** in year 2009 can be summarized as follows:

- the completion of the commissioning of the stations behind the calorimeters (M2-M5);

- the installation of the detectors (MWPC and GEM) on M1 and the commissioning of the station;

- the completion of the production of spare MWPC detectors in the LNF-LHCb clean room, as well as the recovery of old ones at CERN, so to prepare a reserve of detectors for the running of the experiment;

- the preparation of the *Roadmap for selected key measurements of LHCb* paper, and the activity of simulation and analysis of MonteCarlo samples, in particular for the muon-id, for the study of early physics with J/Ψ, and for the rare channel $B_s \to \mu\mu$;

- a first look to 2009 LHC data, in particular for the determination of the efficiency and timing of the Muon System and of the muon-id performances and calibration.

Futhermore, the whole group has participated to the cosmic rays and to the LHC collision runs and to their first analysis.

2 Installation of the M1 station

During 2009 a considerable effort has been spent to install and commit the M1 station, in order to cope with the start of the LHC run. This required a lot of qualified manpower from the Frascati group. The M1 station, being inserted between the RICH2 and the Preshower detectors, has very little room (some 40 cm) for the installation and deserves special attention to the mechanical issues. Moreover, the station has to comply with severe limitations to the material budget, being in front of the calorimeters, and to face the presence of approximately 40% of the total amount of electronic channels of the whole Muon detector, for a total of 276 chambers and 32256 physical channels. The high electronics density, which requires air-cooling and foresees a large amount of cables ($\sim 2\,350$), makes the whole project a real challenge.

The installation and testing of the services was completed in February 2009. This required exact routing and check of all the cables (low voltage, high voltage, signal and control cables) and gas piping. Moreover, a further task was to build the system for moving the cable chain and its suspension, which has been conceived to sustain the approximately 2 t of cables hanging from the walls. Last but not least, all of the mechanical supports needed to fix the chambers to the wall have been designed and machined between the end of 2008 and the beginning of 2009.

2.1 *M1 GEM detectors commissioning*

The central part of the first station of the LHCb Muon System, in the region closer to the beam pipe, is instrumented with Triple-GEM detectors with pad readout. In total, 24 Triple-GEM detectors, assembled in pairs to increase efficiency and redundancy, cover an area of about 0.6 m^2, for a total of 2304 digital readout channels. A special gas mixture with 40% CF4 is used to ensure that the Triple-GEM detectors have the required time resolution (better than 3 ns, rms). The Triple-GEM detectors, designed and assembled by INFN Cagliari and Laboratori Nazionali di Frascati, have been installed in the experimental cavern during Spring 2009 and after a commissioning phase they have started to be regularly in operation since the beginning of October when an intensive cosmic rays campaign took place. In November 2009, when the first proton-proton collisions occurred in LHCb, Triple-GEM detectors were operating at a gain of about 5000, a setting very close to nominal working point. The GEMs, together with the MWPC present in the rest of the muon system, allowed triggering on muons coming from the pp collisions. Since the end of November, the GEM detectors have been operated continuously and without any problem during the LHC operations. Many collision events have been recorded with proton beams both at 450 GeV and at 1.18 TeV, providing us with a muon sample in excess of 30k events. Approximately 20% of these muons have a hit in the GEM detectors.

In Fig. 1 the final M1 station installed can be seen, together with a detail of GEM detectors around the beam pipe.

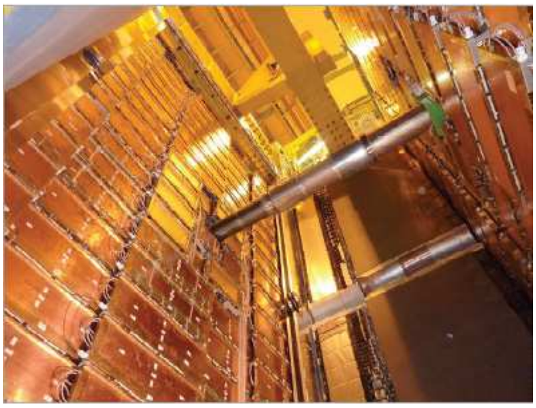

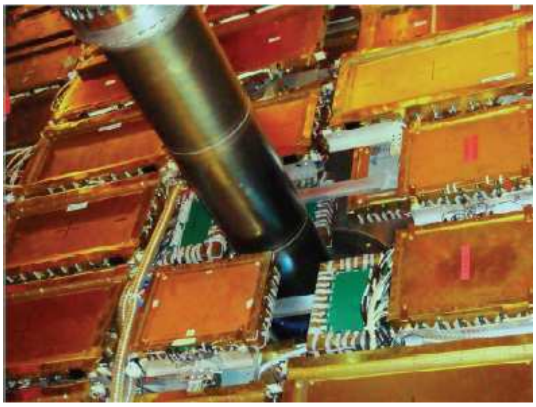

Figure 1: The M1 station installed (left) and a detail of the GEM detectors (right).

2.2 *M1 MWPC detectors commissioning and spare production*

Chamber installation started by the end of February, and was completed by the end of June. Operation on the apparatus required good coordination with the other subdetector teams (specifically calorimeter and RICH), for sharing the access to the same detector regions. Moreover, since two layers of chambers were mounted on each side of the support wall, chamber alignment and test of the detector basic functionality (noise and dead channels, gas connection) for the innermost layer were performed before starting the installation of the second layer. A second phase of chamber tests followed, asynchronous with the chamber installation. This consisted of testing the whole signal path, from chambers to the DAQ system, first with noise and pulse runs, and finally with cosmics. At the same time, the automated system for the wall movement was built. After a very carefully alignment of the wall, the final and crucial task was the closure of the M1 detector, which was achieved by the first week of July. Regular data taking campaigns with cosmics started early in September.

During 2009, the production and test of the spare MWPC for the experiment continued at the LNF site. A total of 37 new chambers have been built during 2009: 4 for region 2 of M4 and M5, 22 for region 3 of M1 to M5 and 11 for region 4 of M1 and M5. After construction, the detectors have been tested against gas leaks, checked and trained with HV, equipped and tested with FEE electronics, and sent to CERN.

3 Commissioning and calibration of the Muon System

The LHCb muon trigger architecture relies on 1248 Trigger Sectors (TS) originated by 122,112 front-end channels. These physical channels are merged to generate 25,920 logical channels both in the chamber front-end and in the Intermediate Boards (IB) system. Logical channels are grouped in Trigger Sector in the Off Detector Electronics (ODE) system. The last two items (IB and ODE systems) are under LNF responsibility and have been tested and installed on 2007; cabling was entrusted to LNF as well. The commissioning of stations M2 to M5 was succesfully completed during 2009, together with that of station M1. Commissioning procedure followed four phases which required a lot of qualified manpower, mainly provided by Cagliari and Frascati: connectivity test with noise, pulse time alignment, and optical link test to trigger and DAQ systems. As of mid December 2009, no trigger sectors were missing, and very few noisy spots appears in the readout channels.

During year 2009 data taking runs on cosmic rays have been regularly performed, to test the overall performances of the data acquisition and trigger systems after integration of of the various subdetectors. A typical pad map obtained with cosmic ray run is shown in Fig. 2.

Moreover, the analysis of cosmic ray data was crucial for time and space alignment of the muon detector, in view of the data acquisition with proton collisions. In Frascati the activity was focussed on the calibration of the time response of the muon chambers.

4 Time calibration and muon chamber efficiency with data from LHC collisions

In the first round of LHC collisions at a c.m. energy of 0.9 TeV, and at a maximum luminosity of few units of 10^{26} cm^{-2} s^{-1}, LHCb has collected approximately 500,000 triggers, part of them due to beam-gas interactions. A very short run has been performed also at 2.36 TeV, the highest energy ever reached in the world.

Since the muon system is used for triggering purposes, the time response of the stations has to be calibrated in order to give signals falling well within a 25 ns time coincidence window for a track generated at the interaction point. The average time of flight between two adjacent muon stations is 4 ns; on top of that one has also to account for obvious hardware delays which can vary

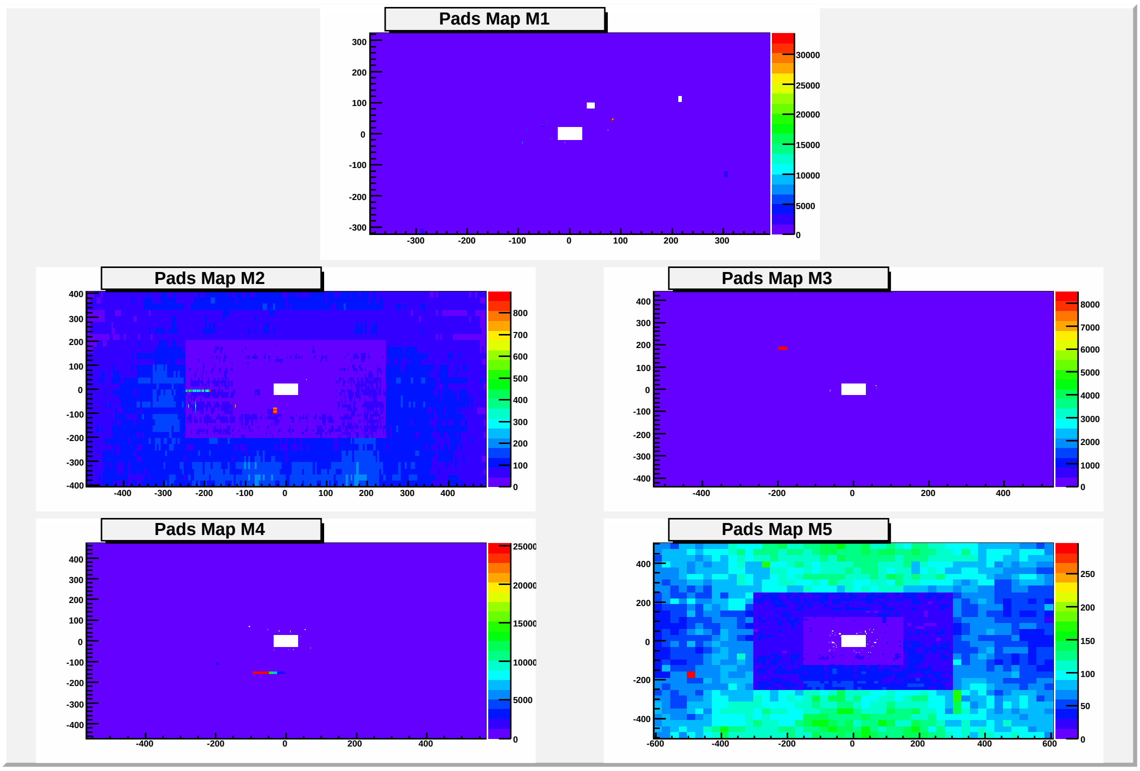

Figure 2: (color online). A map of Muon System pads obtained with cosmic ray runs. Different colors refer to the non uniform illumination of the detector.

on a channel by channel basis. For this reason, the trigger timing synchronization can only be fullfilled if a suitable set of delay constants are applied to each channel of the muon system. These constants have been first evaluated by pulsing the system. After that, cosmic ray data have been used to compute residual corrections to be applied to each channel of the apparatus.

The status of the time calibration was finally checked on real muons from collisions. Only data acquired with a calorimeter trigger have been used, not to bias the observed time spectra. The time spectrum of the muon hits from all of the stations is shown in Fig. 3. The core resolution from data is 3.6 ns, while the efficiency for having 5 muon hits within the same bunch crossing is $\sim 95\%$. The efficiency value drops to $\sim 44\%$ without using the calibration constants evaluated on cosmics. The previous results demonstrate the effectiveness of the time calibration procedure developed on cosmics.

Parallel to the calibration of timing, the Frascati group has developed a method for the monitoring of the muon chamber efficiency on real collision data. As a first step,a procedure to select a pure sample of muon candidates was defined. This procedure select tracks reconstructed by the tracking detectors of LHCb, with momentum above 3 GeV/c. Each track is extrapolated through the Muon Stations and is selected within the geometrical acceptance of the detector. For each Muon Station it is selected the closest hit to the impact point of the extrapolated tracks within a *search window* that takes into account of the extrapolation errors due to the multiple

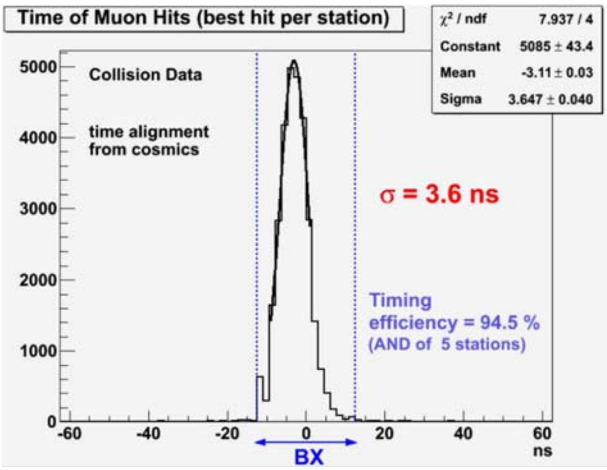

Figure 3: Muon hit time measured on stations M1-M5, collision data.

scattering. The tracks are selected as muon candidates if at least 3 hits over the 4 stations M2, M3, M4 and M5 are found.

Looking at the first data delivered by LHC in November 2009 (450 GeV/c protons beams), the efficiency values for M1 to M5 are shown in Fig. 4, for tracks with momentum above 8 GeV/c.

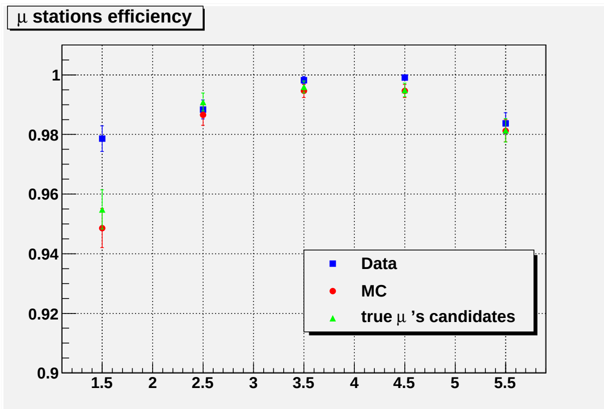

Figure 4: A comparison between collision data and Montecarlo for the efficiencies of muon reconstructed tracks in the five stations of the Muon System.

From the MC it is known that about 30% of the selected muons comes from decay in flight after the tracking detectors and before the first muon station: this entails that the collected sample has a contamination due to muons with a non tracked kink. The *search windows* have been therefore increased to minimize the inefficiency due to μ's with large kinks keeping the purity of the sample $\simeq 80\%$.

Furthermore, a preliminary analysis of muon candidates extracted from the muon-id algorithm, and originating from collisions at 0.9 TeV c.m. energy shows already a very good agreement of distributions between data and Montecarlo, as can be seen in Fig. 5.

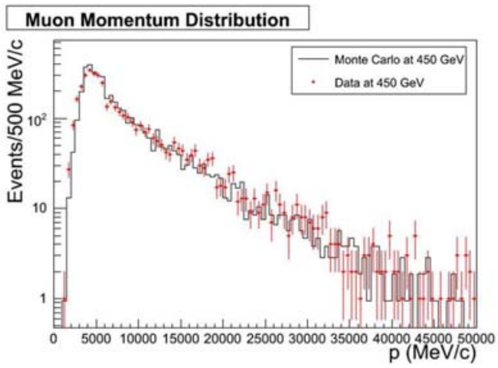

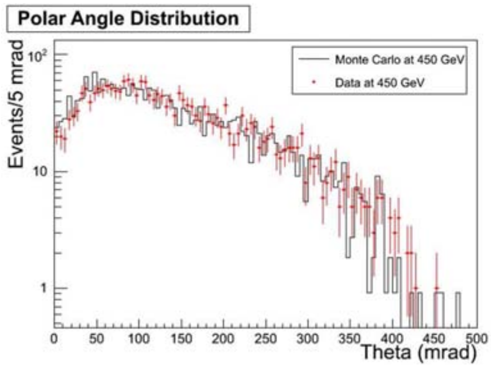

Figure 5: A comparison between data and Montecarlo for the muon momentum (left) and for the angular distribution (right).

5 Software activities

The software activities in 2009 of the LHCb-LNF group were mainly focused in finalizing the analysis using the full LHCb Monte Carlo production and starting to look to the performances of the Muon System with the first data. In particular, several members of the LNF group have participated actively in the preparation of the document (*Roadmap for selected key measurements of LHCb*) for the six main analysis that LHCb plans to perform with the first years of data taking.

5.1 *Preparation for data analysis*

In 2009 the LHCb-LNF group has been involved in the preparation of the following analysis:

1. the study of the muon-id and its calibration with real data;
2. the search for the $B_s \to \mu^+\mu^-$ rare decay;
3. the measurement of the ratio of the cross sections $\sigma_{(J/\Psi)}/\sigma_{(\Psi(2S))}$.

The study of the $B_s \to \mu^+\mu^-$ rare decay is considered top priority for the LHCb collaboration since it will be competitive with the Tevatron results already with 0.2 fb^{-1} of integrated luminosity (which is what LHCb expects to collect in the 2010 run). However, this measurement requires a deep understanding of the detector behaviour and rely on the calibration of many quantities (momentum scale, momentum resolution, particle ID, flavour tagging, proper time resolution).

Already with first data, a set of easiest measurements has been foreseen, such as the determination of $\sigma_{(J/\Psi)}/\sigma_{(\Psi(2S))}$, where both J/Ψ and $\Psi(2S)$ decays in muon pairs.

We underline the fact many of the six key LHCb measurements contains muons in the final state, making the Muon Detector one of the *main* LHCb detectors for the first years.

Due to its sensitivity to New Physics contributions, the Branching Ratio BR ($B_s \to \mu^+\mu^-$) is one of the most interesting measurements that the LHCb experiment can perform with the first data. The Standard Model predictions are $BR(B_s \to \mu^+\mu^-) = (3.35 \pm 0.32) \times 10^{-9}$ while the current upper limit given by Tevatron is $BR < 36 \times 10^{-9}$ @ 90% CL, with a statistics of 3.7 fb^{-1}, which is still one order of magnitude higher than predictions.

LHCb collecting data at 7 TeV c.m., has the potential to exclude at 90% CL any value of the BR down to the SM value with approximately 3-4 fb^{-1} of integrated luminosity, corresponding to 2 nominal years (10^7 sec) running at 2×10^{32} cm^{-2} s^{-1}.

The expected limit at the end of Tevatron, $\sim 2 \times 10^{-8}$, is overtaken by LHCb with less than 0.2 fb^{-1} even considering that LHC will run in 2010 and 2011 at reduced energy (3.5+3.5 TeV) (see Fig. 6).

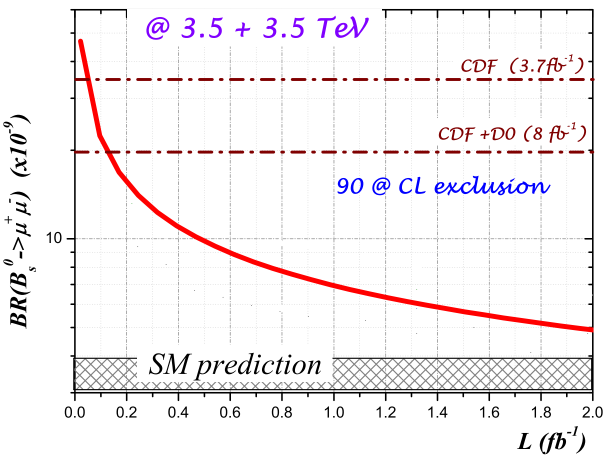

Figure 6: LHCb sensitivity limit for 90% CL for the rare decay $B_s \to \mu^+\mu^-$.

One of the crucial points of this analysis is the control of the background mainly coming from hadrons mistakenly identified as muons.

The responsibility of the LHCb-LNF group is to develop the muon-id algorithms and all the related tools for monitoring and calibrate the muon-id with data. The studies of the muon-id performance for muons belonging to the phase space interesting for the $B_s \to \mu\mu$ analysis continued in 2009.

In particular, the use of data samples coming from the modes $J/\Psi \to \mu^+\mu^-$ and $\Lambda \to \pi p$ have been implemented in the LHCb official software, to extract and to monitor the muon-id through all the data taking.

Moreover, it is worthwhile to mention that the interference between B_s^0 decays to $J/\Psi\ \phi$ with or without $B_s^0 - \overline{B}_s^0$ oscillation could give rise rise to a non-zero CP violating phase $\phi_{J/\Psi\ \phi}$. This mode is one of the strongest test of the Standard Model and a window for new physics, as possibly shown by Tevatron results, although affected by a large error.

As in the previous rare decay channel, LHCb is able already with 0.2 fb^{-1}, hopefully collected in 2010 run, to overcome present Tevatron measurement. A detailed comprehension of the performances of the Muon System is therefore crucial also for this kind of measurement. The statistical sensitivity expected at LHCb as a function of integrated luminosity is shown in Fig. 7.

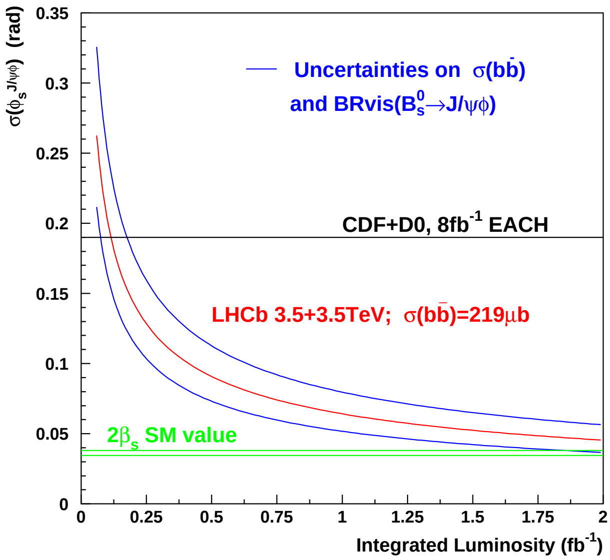

Figure 7: Sensitivity expected at LHCb for the CP phase of the $B_s^0 \to J/\Psi\ \phi$ decay.

5.3 *Measurement of the ratio of the* $\sigma_{J/\Psi}/\sigma_{\Psi(2S)}$

The measurement of this ratio even at a center-mass energy of 7 TeV is one of the parameters needed to theorists to understand the charmonium production mechanisms in the framework of the NRQCD theories.

The theoretical uncertainty on the production of charmonium at the LHC is dominated by arbitrary assumptions made on the $\Psi(2S)$ production mechanisms and even a measurement within an error of 20% will be a useful benchmark for Montecarlo tuning.

In first data at low luminosity the sample of J/Ψ and $\Psi(2S)$ will be already huge (a plot of the J/Ψ invariant mass is shown in Fig. 8).

The main experimental challenge of such a measurement is to keep under control the efficiencies and the angular acceptances in LHCb.

However, selecting only events with $\mu\mu$ in the final state we would expect a partial cancellation of the trigger, reconstruction and muon-id efficiencies, with a ratio constant or slowly dependent on the kinematics and on the geometrical variables. Preliminary results show that such a measurement is affected by a systematic error ranging up to 20%, allowing for un unknown value of the polarization.

A direct measurement of the polarization of the J/Ψ is under study.

5.4 *Control samples for the Muon Detector monitoring and muon-id calibration*

Since the assessment of the quality of the muon reconstruction, the evaluation of the muon-id and mis-id efficiencies and of its calibration play a fundamental role in several key first year physics measurements, the effort of the LHCb-LNF group has been focused on developing the strategy and tools for calibrating with data the muon-id procedure and to extract in-situ the performance.

Two main calibration samples have been chosen after a detailed study: the inclusive $J/\Psi \to \mu\mu$ decay, as a source of muons, and the $\Lambda(1115.6) \to \pi p$ decay as a source of hadrons decaying and non-decaying in flight. For each channel different luminosity scenarios, with corresponding selections, have been identified. The expected purity and the rates have been optimized against computing and performance requirements: the allowed rate cannot exceed 5 Hz per channel and the S/B needs to be maximized while keeping the sample unbiased for muon-id studies.

Results are shown in Fig. 8 for J/Ψ and Λ, corresponding to nearly 20 minutes of running in a starting low luminosity scenario at $\sim 10^{31}$ cm^{-2} s^{-1} with rate of the order of 10 Hz.

The J/Ψ are selected by requiring a well identified muon, paired with a long track of opposite charge: geometrical constraints are applied, leaving the non identified track unbiased for particle ID studies (tag and probe method). Lambdas are selected exploiting the golden kinematics in the $\Lambda \to \pi p$decay: since the production cross section is really large, strong geometrical (pointing) and kinematic (pT, IM) cuts can be placed on the proton and the pion, leading to a pure sample of pions and protons for particle id studies.

The Armenteros Podolansky distribution (momentum asymmetry vs transverse momentum of the two daughter tracks) is used to disentangle the $\Lambda - \overline{\Lambda}$ ambiguity, allowing a clear separation of pions and protons.

With those selected sample a monitoring of the muon-id performances is possible: an error of the order 1-2% is easily achievable, and distribution of ID and mis-ID (for protons) efficiencies vs P or P$_T$ can be made.

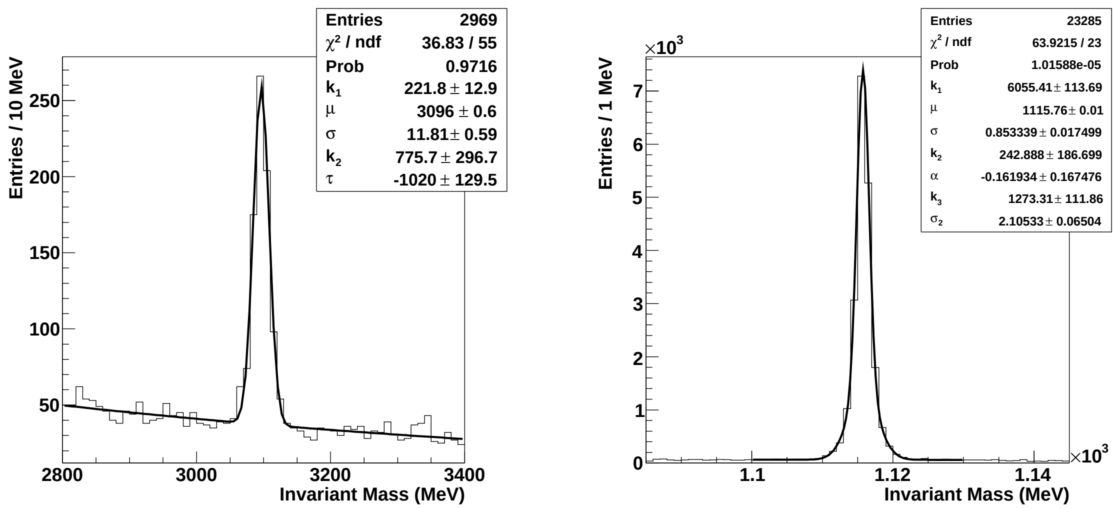

Figure 8: The J/Ψ and the Λ invariant mass peaks at LHCb.

6 Conference Talks

- P. Campana, *The LHCb Upgrade*, FPCP2009 Conference, Lake Placid (US), June 2009.
- A. Sarti, *Rare B decays at LHC*, Meeting IFAE2009, Bari, Aprile 2009.
- A. Sarti, *LHCb prospects for rare decays*, SPIN2009 Conference, Praga, July 2009.

7 Publications

- M.Calvi et al., *Calibration of the flavour tagging with $B^+ \to J/\Psi K^+$ and $B^0 \to J/\Psi K^*$ control channels at LHCb*, CERN-LHCb-2009-020.
- M.Calvi et al., *Lifetime unbiased selection of $B_s \to J/\Psi\ \phi$ and related control channels: $B^+ \to J/\Psi K^+$ and $B^0 \to J/\Psi K^*$*, CERN-LHCb-2009-025.
- G. Lanfranchi et al., *The Muon Identification Procedure of the LHCb experiment with first data*, CERN-LHCb-2009-013.
- A. Carbone et al., *Invariant Mass Line shape of $B \to hh$ decays at LHCb*, CERN-LHCb-2009-031.
- AA. VV., *Flavor Physics in the Quark Sector*, Proceedings of the CKM2008 conference, Rome, September 2008, arXiv:0907.5386.
- B. Adeva et al., *Roadmap for selected key measurements of LHCb*, `arXiv:0912.4179`.
- G. Sabatino, *Charmonium production at LHCb: measurement of the Ψ' to J/Ψ production ratio at LHCb with first data*, Tesi di Dottorato, Universita' di Tor Vergata, Roma, Dicembre 2009.

NA62

A. Antonelli (Resp.), G. Maccarrone, M. Moulson, M. Raggi (Art. 23), T. Spadaro

In collaboration with
E. Capitolo, R. Lenci, M. Santoni

the Servizio di Progettazione Apparati Sperimentali (SPAS):
C. Capoccia, A. Cecchetti, B. Dulach

the Servizio di Sviluppo e Costruzione Rivelatori (SSCR):
G. Bisogni, A. Franceschi

the Divisione Acceleratori, Servizio di Vuoto:
P. Chimenti, A. Clozza, V. Lollo

and the Servizio di Elettronica:
G. Corradi, C. Paglia, D. Tagnani

1 The NA62 Experiment

The branching ratio (BR) for the decay $K^+ \to \pi^+\nu\bar{\nu}$ can be related to the value of the CKM matrix element V_{td} with minimal theoretical uncertainty, providing a sensitive probe of the flavor sector of the Standard Model. The measured value of the BR is $1.73^{+1.15}_{-1.05} \times 10^{-10}$ on the basis of seven detected events [1]. NA62, an experiment at the CERN SPS, was originally proposed as P326 with the goal of detecting ~ 100 $K^+ \to \pi^+\nu\bar{\nu}$ decays with a S/B ratio of 10:1 [2]. The experimental layout is illustrated in Fig. 1.

The experiment will make use of a 75 GeV unseparated positive secondary beam. The total beam rate is 800 MHz, providing ~ 50 MHz of K^+'s. The decay volume begins 102 m downstream of the production target. 10 MHz of kaon decays are observed in the 120-m long vacuum decay region. Ring-shaped large-angle photon vetoes are placed at 12 stations along the decay region and provide full coverage for decay photons with 8.5 mrad $< \theta <$ 50 mrad. The last 35 m of the decay region hosts a dipole spectrometer with four straw-tracker stations operated in vacuum. The NA48 liquid krypton calorimeter [3] is used to veto high-energy photons at small angle. Additional detectors further downstream extend the coverage of the photon veto system (e.g. for particles traveling in the beam pipe).

The experiment must be able to reject background from, e.g., $K^+ \to \pi^+\pi^0$ decays at the level of 10^{12}. Kinematic cuts on the K^+ and π^+ tracks provide a factor of 10^4 and ensure 40 GeV of

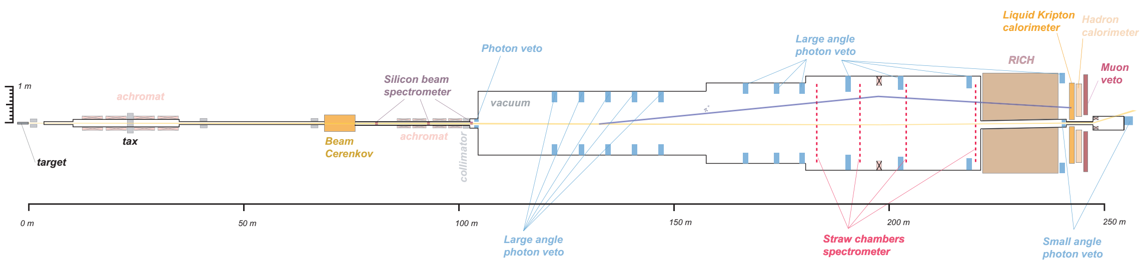

Figure 1: The NA62 experimental layout.

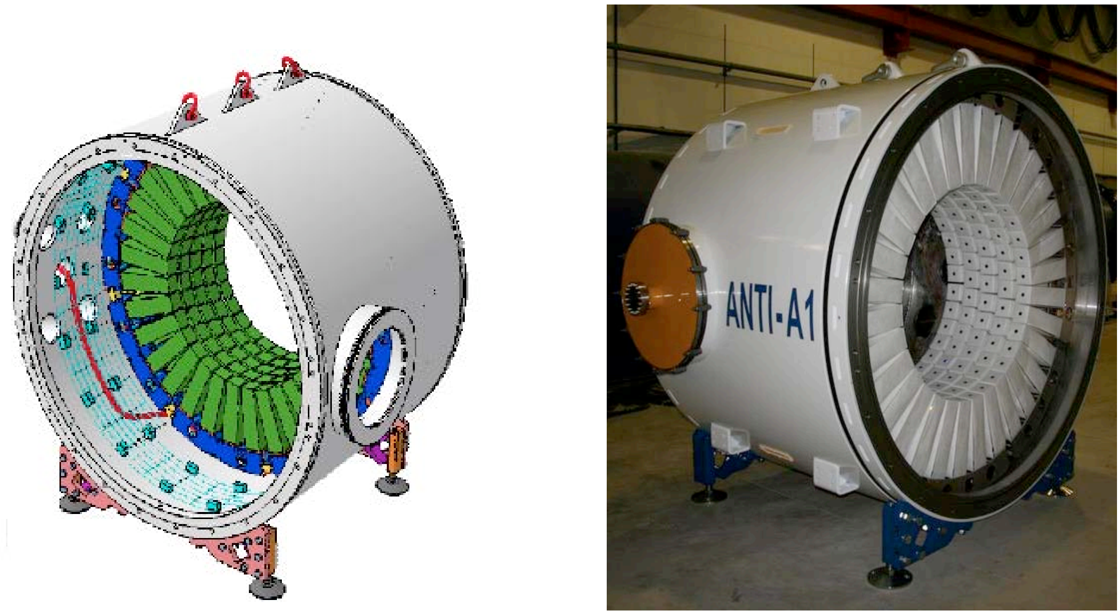

Figure 2: Left: Design study of the prototype veto station making use of the OPAL lead-glass calorimeter elements. Right: Photograph of the prototype ANTI-A1.

electromagnetic energy in the photon vetoes; this energy must then be detected with an inefficiency of $\leq 10^{-8}$. For the large-angle photon vetoes, the maximum tolerable detection inefficiency for photons with energies as low as 200 MeV is 10^{-4}. In addition, the large-angle vetoes (LAV) must have good energy and time resolution and must be compatible with operation in vacuum.

The principal involvement of the LNF NA62 group is in the design and construction of the LAV system. In 2009, the main responsibilities of the LNF NA62 group were:

- Development of tools and procedures for assembly of the ANTI-A1 station;
- Assembly of the ANTI-A1 prototype station;
- Vacuum testing and outgassing measurements for ANTI-A1;
- In-beam testing of the ANTI-A1 prototype;
- Development and testing of the front-end electronics for the large-angle veto system.

In addition the group continues to collaborate in the analysis of NA62 data on $R_K \equiv \Gamma(K_{e2})/\Gamma(K_{\mu 2})$.

2 Large-Angle Photon Veto

The 3800 modules from the central part of the OPAL electromagnetic calorimeter barrel [4] that became available for use in NA62 consist of blocks of SF57 lead glass with an asymmetric, truncated square-pyramid shape. The front and rear faces of the blocks measure about 10×10 cm^2 and 11×11 cm^2, respectively; the blocks are 37 cm long. The modules are read out at the back side by Hamamatsu R2238 76-mm PMTs, coupled via 4-cm cylindrical light guides of SF57. The current design of the LAV system calls for the construction of 12 cylindrical stations made of lead-glass blocks. The diameter of the stations increases with distance from the target, as does the number of blocks in each, from 160 to 256, for a total of about 2500 blocks. Each station consists of four or five rings of blocks, with the blocks staggered in azimuth in successive rings. The total depth of a five-layer station is 27 radiation lengths; this structure guarantees high efficiency, hermeticity, and uniformity of response. The overall design for the first prototype of such a station is illustrated in Fig. 2, left.

2.1 ANTI-A1 construction

The vessel is made of steel, is 192 cm in diameter, and includes five flanges for HV and signal feedthroughs and for vacuum pumping, a large flange for access, and a mesh for cable routing. The prototype vessel was constructed in early 2009 at Fantini SpA (Anagni (FR)), under the supervision of the LNF SPAS. The vessel was shipped to LNF in April 2009 for the installation of the lead-glass detectors.

The support brackets for the mounting of the lead-glass modules, also knowns as "bananas," were designed at Pisa. The ANTI-A1 consists of a 40-bracket setup in five rings for a total of 160 blocks.

ANTI-A1 was constructed in many different steps. The original gluing of the lead-glass block on the aluminum support by the OPAL experiment was considered too old to be reliable by the CERN safety authorities, so a new gluing procedure has been established. The original bond was reinforced by thin steel plates glued to the side of the block (see fig Fig. 3, top left).

The blocks were tested with a LED pulser and cosmic rays to measure light yield and PMT gain and to equalize the detector response. A common working point at 4.5 pC for MIP generated signals was selected. The test infrastructure, which was developed by INFN Naples, allows us to automatically test 12 block per day.

Four tested lead-glass modules are arranged on a support bracket ("banana") for installation in the vacuum vessel as shown in Fig. 3, left. During assembly, the fibers for the monitoring system and the signal and HV cables were also routed and fixed inside the bracket structure.

After the mounting of each single ring, composed of eight bananas as shown in Fig. 3, the cables were fastened to a stainless steel mesh, routed to the vacuum flanges, and connected to the feedthroughs. Each block was then tested for HV and signal connection integrity. A photo of the the fully assembled ANTI-A1 is shown in Fig. 2, right.

2.2 Vacuum tests and outgassing measurements

In the NA62 experiment, the interaction of the beam with residual gas in the decay region can produce a significant level of photon-free background to $K^+ \to \pi^+\nu\bar{\nu}$ if the vacuum in the decay region is worse than a few 10^{-6} mbar.

During 2008, a comprehensive series of measurements of outgassing rates of different components of the LAV system were made in close collaboration with the Servizio di Vuoto of the LNF Accelerator Division. Measurements were performed on components such as the wrapping materials for the lead-glass blocks, the PMT and mu-metal assemblies, fully wrapped blocks, and bare blocks. A complete vacuum test of the prototype vessel was also performed at the Fantini SpA facility. The measurement technique, the setup and the outgassing results are described in

Figure 3: LAV station construction phases (from top-left): gluing of steel plates, wrapping of crystals, assembly of four-block brackets, mounting of brackets inside the vessel, entire ring assembly and cable routing.

[6]. They have been summarized in Table 1. After the construction a measurement of the outgassing rate of the entire ANTI-A1 was also performed to verify the extrapolation in Table 1. The measured leak/outgassing rate after two weeks of pumping was $(0.9 \pm 0.15) \cdot 10^{-3}$ mbar $\cdot$ l $\cdot$ s^{-1}, which is in perfect agreement with the quoted extrapolation.

2.3 Front-end electronics

Monte Carlo simulations have shown that photons from $K^+ \rightarrow \pi^+\pi^0$ decay with a wide range of energies, from a few tens of MeV to several GeV, reach the veto stations. To be able to reject photons from $\pi^+\pi^0$ events with a maximum inefficiency of 10^{-4}, the detectors must simultaneously furnish time and energy measurements. The time resolution is dominated by the intrinsic contribution from the detectors. For the energy measurement, the biggest challenge in the design of the readout electronics is the need to accept signals over an extended dynamic range, from a few

Table 1: Outgassing measurement results Ref. 5.

	Q_S (mbar $\cdot$ l $\cdot$ s^{-1})	pumping time (days)
PbGl detectors (worst case)	$(2.9 \pm 2.0) \cdot 10^{-3}$	15
PbGl detectors (average)	$(1.5 \pm 1.0) \cdot 10^{-3}$	15
Monitoring system fibers	$(1.0 \pm 0.2) \cdot 10^{-5}$	15
Tyvek wrapping	$(3.1 \pm 0.6) \cdot 10^{-5}$	5
ANTI-A1 vessel	$(1.1 \pm 0.2) \cdot 10^{-5}$	4
Total ANTI-A1 (extrapolation)	$(1.5 \pm 1.0) \cdot 10^{-3}$	15

millivolts to tens of volts, and to provide charge measurements with a precision better than 10%. During 2009, the LNF group was responsible for the design and construction of prototypes of the

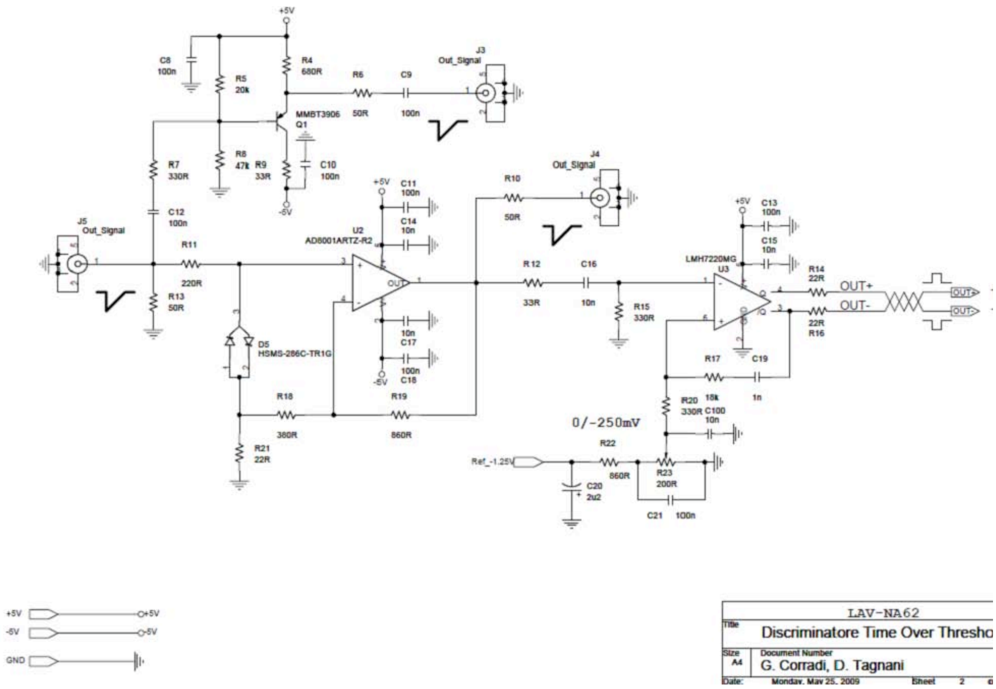

Figure 4: Layout of a single channel of prototype time-over-threshold board.

front-end electronics for the large-angle veto system. The basic idea is to exploit the time-over-threshold technique to measure the signal charge over a broad interval. A new board designed by the LNF Servizio di Elettronica converts the analog signals from the PMTs into an LVDS logic signal of the same width. The width will be measured by a TDC and its value used to reconstruct the charge. The energy can thus be measured via TDC time measurements only.

A first prototype of the front-end electronics was designed and tested during 2009. The system consists of three main stages, as shown in the single-channel layout of Fig. 4:

- **Clamping:** Protects the amplifier from PMT signals as high as 10V. The clamp stage preserves the time duration of the input analog signal to allow the measurement of time over threshold (ToT).
- **Amplifier:** Amplifies the input signal by a factor 5 to reduce the slewing in crossing the threshold at the comparator stage.
- **Comparator and LVDS driver:** Compares the amplified signals with an adjustable threshold (0-50 mV) and produces an LVDS output signal. The LVDS signal has a duration equal to the time the analog signal is greater than the threshold.

Six prototype boards for a total of 96 channels were produced and tested with cosmic rays at LNF and with muons and electrons during the ANTI-A1 beam test at CERN. In both cases a good correlation between ToT and charge was observed. Fig. 5 shows the correlation obtained with 2 GeV electrons during the ANTI-A1 beam test.

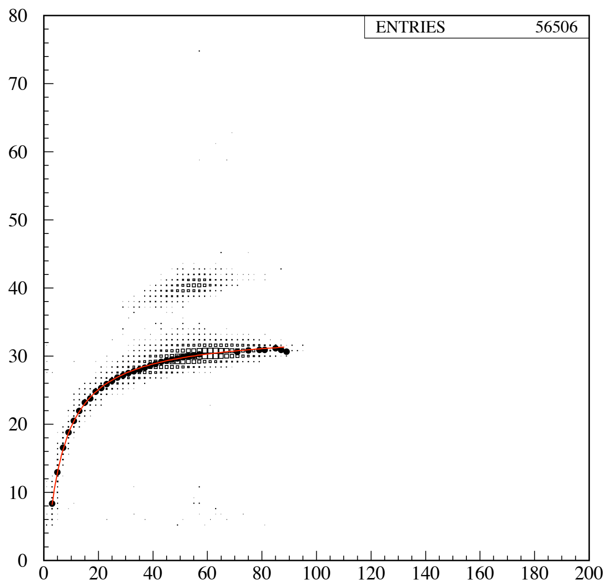

Figure 5: Charge vs time over theshold (ToT).

We expect to conduct a test of the final front-end electronics scheme and its integration with the data-acquisition system at CERN in 2010.

2.3.1 ANTI-A1 test beam

After the assembly of ANTI-A1 was completed at LNF in July 2009, the module was transported to CERN. It was installed in the existing NA48 vacuum vessel (the so-called "blue tube") in October 2009.

The five prototype front-end boards were also used to fully equip one half of the ring (80 crystals), so that we were able to perform extensive tests with muons and electrons using the SPS beam line.

The boards include an amplification stage with dual output: one copy of the signal is fed to the discriminator, which produces LVDS digital signals with time-over-threshold duration, while a second copy is available for routing to a different readout. The second copy was used for direct charge measurements for the purposes of comparison.

For the charge measurement, we used commercial 12-bit charge QDCs (CAEN V792), while for the time measurements we used commercial TDCs (CAEN V1190B). In order to provide a gate for QDC integration, a trigger signal was provided by the fast-OR of the 16 digital signals in the upstream ring of lead-glass detetctors. A stand-alone DAQ system was also prepared, capable of gating the acquisition with SPS status signals and sustaining a trigger rate of about 1 kHz.

We collected large samples of data both with a diffuse halo of muons, thus illuminating all the counters in the ring, and with electron beams of energy 2, 4, and 6 GeV.

The muon data were used first for checking the equalization of the PMT gains, which had been performed before installation with the cosmic-ray test stand at LNF. The average MIP response for all crystals is ~ 4 pC, as expected for a gain of about 10^6, with a RMS at the level of 10% using nominal HV settings.

Using muon data we also performed a calibration of the time-over-threshold discriminator threshold. We collected data at 7, 10, 15, and 25 mV/50Ω for the input signal, corresponding to a range from 0.3 to ~ 1 MIP.

Using electron data we were able to check the performance of the time-over-threshold technique, by comparing the time-width of the LVDS output of the discriminator measured by the TDC with the charge measured by the ADC (Fig. 5). The correlation is excellent, except for a fraction of events (in the top part of the figure) for which the time-over-threshold measurement is lengthened: this is due to the ringing of the analog signal, caused by a small dynode dispersive inductance in the PMTs, which has since been fixed in the HV divider circuit.

3 NA62 and the Measurement of R_K

Despite poor knowledge of the meson decay constants, ratios of leptonic decay rates of pseudoscalar mesons such as $R_K \equiv \Gamma(K_{e2})/\Gamma(K_{\mu 2})$ can be predicted with high accuracy within a given model, and have been considered to be stringent tests of the $V - A$ structure of the weak interaction and of lepton universality. By convention, the definition of R_K includes the contribution of inner bremsstrahlung (IB) to the radiative $K_{l2\gamma}$ width, while the structure-dependent (DE) processes are considered as background. The Standard-Model prediction is [6]:

$$R_K^{\rm SM} = \left(\frac{m_e}{m_\mu}\right)^2 \left(\frac{M_K^2 - m_e^2}{M_K^2 - m_\mu^2}\right)^2 (1 + \delta R_{\rm QED}) = (2.477 \pm 0.001) \cdot 10^{-5} \tag{1}$$

where $\delta R_{\rm QED} = -3.6\%$ is a correction due to the contributions to the $K_{l2\gamma}$ width from IB and virtual photon processes. Theoretical studies point out that lepton-flavor violating effects arising in supersymmetric extensions of the Standard Model can induce sizable violations of μ-e universality, shifting the value of R_K by as much as a few percent, without contradicting any other presently known experimental constraints [7]. The K_{e2} decay rate is particularly sensitive to new physics because the Standard Model contribution is helicity suppressed.

The 2006 world average [8] is determined by experiments performed in the 1970s; the relative error on this average is $\delta R_K/R_K = 4.5\%$. Inclusion in the average of the recent results from the

KLOE collaboration (final result [9]) and from NA48/2 (preliminary result) leads to a new value of $R_K^{2007} = (2.468 \pm 0.025) \cdot 10^{-5}$, with a precision of $\delta R_K/R_K = 1\%$.

During a dedicated run in 2007, NA62 collected more than 110 000 K_{e2} events, together with various smaller data samples to allow detailed systematic studies. The Frascati group contributed significantly to the success of this run. Group members participated in data taking for a significant fraction of the running period and provided on-call support for the hodoscope readout electronics. As run coordinators for five weeks of the 18-week run, LNF group members were directly responsible for the operational aspects of the experiment. The running period coordinated by LNF group members included K_{e2} data collection, the collection of samples for systematic studies, and the entire straw tracker beam test.

LNF group members are currently playing a central role in the analysis of the 2007 data. At the collaboration level, the analysis effort is being conducted by two independent groups to ensure redundancy and tighter systematic control. Frascati group members form the core of one of these two analysis groups. Some of the K_{e2} selection criteria have been first implemented by the LNF group and have been then accepted as standards. In particular, the treatment of radiative corrections has been completely revised. Since the DE component is not suppressed by helicity, it constitutes an order-unity background to IB. Therefore, the criteria for vetoing additional photons detected by the liquid krypton calorimeter have been defined, so as to retain as much as possible $K \to e\nu(\gamma)$ IB events, while rejecting radiative $K \to e\nu\gamma$ from the DE process, as well as other backgrounds. Moreover, $K \to e\nu(\gamma)$ events from IB are selected by kinematics by requiring the missing mass squared at the K decay vertex to be below ~ 0.001 GeV^2. The efficiency for this condition increases inversely with the energy of the emitted photon, so that the implementation of an accurate simulation of the $K \to e\nu\gamma$ IB component is crucial for an evaluation of the related acceptance with an accuracy better than the percent. The LNF group provided a new simulation of the IB signal, with an exponentiated photon energy spectrum and no photon energy cutoff. A preliminary result for R_K was released during the 2009 winter conferences, with a total error of about 0.6%.

References

1. E949 Collaboration, A. Artamonov et al., Phys. Rev. Lett. 101, 191802 (2008).
2. G. Anelli *et al.*, CERN, Geneva, Tech. Rep. CERN/SPSC 2005-013 (2005).
3. NA48 Collaboration, V. Fanti et al., Nucl. Instrum. & Meth. A **574**0, 433 (2007).
4. OPAL Collaboration, K. Ahmet et al., Nucl. Instrum.& Meth. A **305**, 275 (1991).
5. A. Antonelli et al., NA62-09-01, May 2009.
6. V. Cirigliano, I. Rosell, Phys. Rev. Lett. 99, 231801 (2007).
7. A. Masiero, P. Paradisi, R. Petronzio, Phys. Rev. D **74**, 011701 (2006).
8. Particle Data Group, W. M. Yao et al., J. Phys. G**33**, 1 (2006).
9. T. Spadaro et al. (KLOE Coll.), Eur. Phys. J. C **64**, 627 (2009).

P-Super$B$

A. Calcaterra, R. de Sangro, G. Felici, G. Finocchiaro (Resp.),
P. Patteri, I. Peruzzi, M. Piccolo, M. Rama

1 Introduction

A conceptual design report of a next generation asymmetric-energy e^+e^- collider (Super$B$) capable of delivering about 100 times the luminosity of the current B factories has recently been compiled [1]. This report discusses the physics motivation, detector, and accelerator designs for the next generation B factory at an e^+e^- collider. The LNF group is involved in the design of the Super$B$ Drift Chamber with important responsibilities. In particular, a member of the group is co-convening the general Super$B$ DCH group, which includes also several Canadian Institutions, and another member is co-convening the FastSim and the Detector Geometry working groups (see secs. 4 and 5).

The baseline of the Super$B$ tracking detector is the *BABAR* drift chamber, which was already optimized to perform measurements of B-physics events, and has been working quite well for the entire *BABAR* lifetime. The main differences, with respect to *BABAR*, concerning the tracking system to be designed for Super$B$ detector are:

- demise, in the machine design, of the support tube holding the final focus quads (as in PEP-II);
- higher occupancy due to radiative Bhabha events scattered in the tracking devices by bending/focussing elements of the machine optics;
- presence in the backward region of an electromagnetic calorimeter.

The three items mentioned before require a device possibly lighter in terms of radiation length with respect to *BABAR*, faster and with lighter endplates too. The lower boost, envisaged for the Super$B$, points also toward a detector more sensitive to multiple scattering.

2 DCH Mechanical Structure

The Drift Chamber mechanical structure must sustain the wire load – about 3 tons for 10 000 cells – with small deformations, while at the same time offer minimum material to the surrounding detectors. Carbon Fiber-resin composites have high elastic modulus and low density, thus offering performances superior to Aluminum-alloys based structures. Endplates with curved geometry can further reduce material thickness respect to flat endplates for a given deformation under load. For example, the KLOE Drift Chamber [2] features 8 mm thick Carbon Fiber spherical endplates of 4 m diameter. Preliminary design of Carbon Fiber endplates for Super$B$ indicate that adequate stiffness ($\simeq \mathcal{O}(1\,\mathrm{mm})$ maximum deformation) can be obtained with 5 mm thick spherical endplates, corresponding to $0.02\,X_0$ (compare $0.13\,X_0$ for the *BABAR* Aluminum DCH endplates).

Figure 1 and 2 show two possible endcap layouts, respectively with spherical or stepped endplates. We are also considering a convex spherical endplate, which provides a better match to

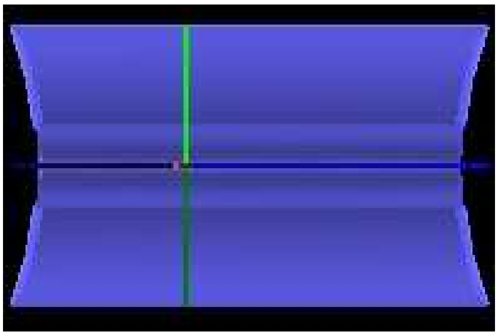

Figure 1: Possible Super$B$ Drift Chamber layouts with spherical endplate design.

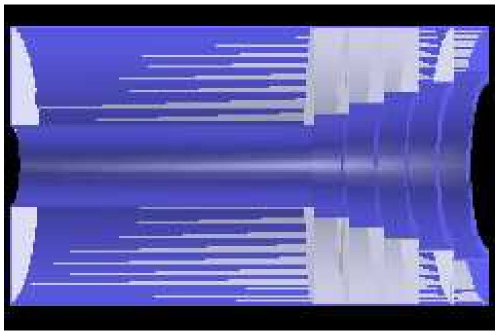

Figure 2: Possible Super$B$ Drift Chamber layouts with stepped endplate design.

the geometry of the forward PID and calorimeter, and would reduce the impact of the endplate material on the performance of these detectors, at the cost of greater sensitivity to the wide-angle Bhabha background.

3 R&D for the Super$B$ Drift Chamber

In order to design the tracking detector for Super$B$ R&D efforts have begun at LNF and Victoria University (Canada) to assess how to improve with respect to the *BABAR* DCH performances. At LNF a system including a high precision tracker with 52 Aluminum tubes of 3 cm diameter has been commissioned during 2009. The tubes operate in limited streamer mode and are arranged in two groups of 3 layers each. During the same period a small prototype with a cell structure

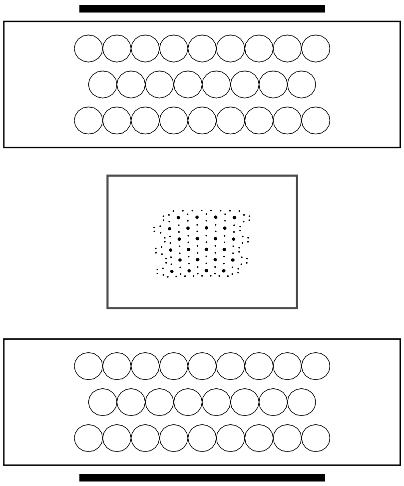

Figure 3: Scheme of the experimental setup. The drift chamber prototype is sandwiched between the tracking telescope assemblies. The scintillation counters used for trigger are shown in black.

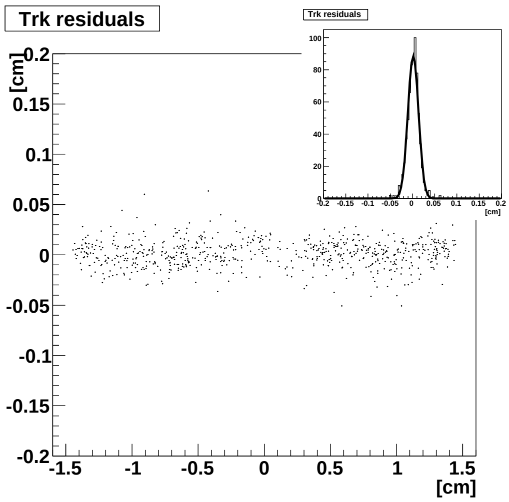

Figure 4: Track residuals as a function of the impact parameter for a tube of the tracking telescope. The inset shows the spatial resolution averaged over the entire tube.

resembling the one used in the *BaBar* DCH has been also built and commissioned. Tracker and prototype have been collecting cosmic ray data since October 2009. A schematic drawing of the setup arrangement is shown in Fig. 3.

The pointing accuracy of the external tracker is shown in Fig. 4, where the residuals of one tube with respect to the fitted tracks are shown as a function of impact parameter. A spatial resolution of around 100 μm on the single tube is observed, yielding a pointing accuracy better than 80 μm on the DCH prototype. Different gas mixtures have been tried in the prototype: starting with the original *BaBar* mixture ($80\%He - 20\%iC_4H_{10}$) used as a calibration point, both different quencher proportions and different quenchers (e.g methane) have been tested in order to explore the phase space leading to lighter and possibly faster operating gas. Fig. 5a shows the space-time correlation for one prototype cell: as mentioned before, the cell structure is such as to mimic the overall structure of the *BaBar* DCH. Preliminary analysis shows that space and energy loss resolutions are consistent with what has been obtained with the original *BaBar* DCH. As another example of the data collected in 2009, a space to time relation is depicted in Fig. 5b

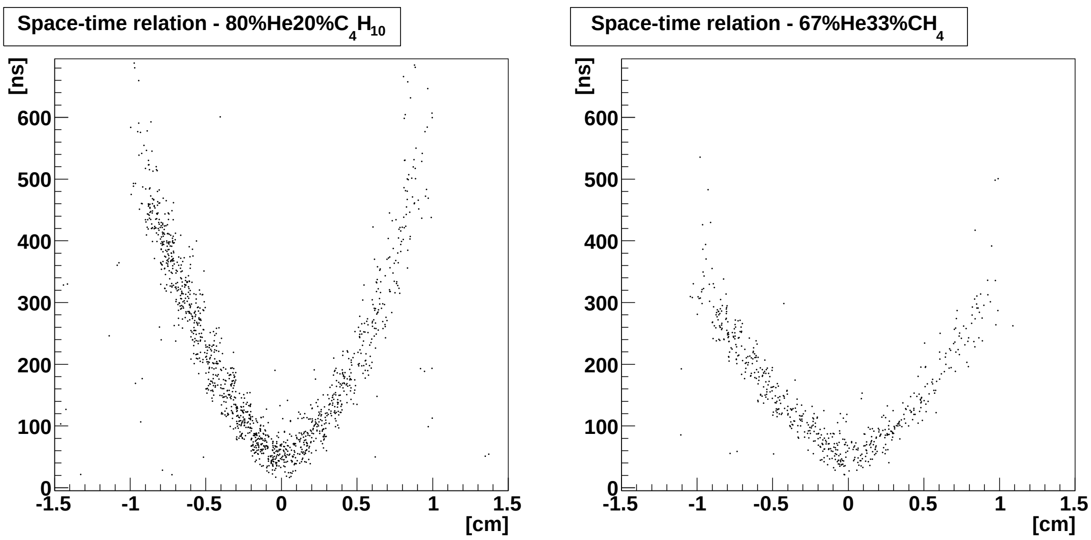

(a) 80%He-20%iC$_4H_{10}$ gas mixture.

(b) 67%He-33%iCH$_4$ gas mixture.

Figure 5: Examples of measured space-time relation in different He-based gas mixtures.

with a $67\%He - 33\%iCH_4$ gas mixture. This gas is roughly a factor two faster and 50% lighter than the original *BaBar* mix: preliminary analysis shows performances both in space and dE/dx resolution comparable to the original mix, however detailed studies of the Lorentz angle have to be carried out in order to consider this mixture as a viable alternative.

To improve performances of the gas tracker a possible road could be the use of the *cluster counting* method which in principle holds the promise of a better resolution both spatially and in the energy loss measurement. Detailed comparisons of the traditional methods to extract spatial position and energy losses and the *cluster counting* methods will be available in the near future.

4 Development of Simulation Tools for Detector Design and Physics Studies

The design of the Super$B$ detector and the study of the physics reach of the experiment require specific simulation tools. Depending on the nature of the study, a detailed simulation (Geant4) or a fast simulation are needed. The use of the latter is mandatory at the present stage to perform all those studies requiring the generation and complete reconstruction of the physics event. A member of our group is coordinating the development of the Super$B$ fast Monte Carlo (*FastSim*), which includes a simplified and flexible detector element description, a full modeling of particles interaction with the detector (energy loss, multiple scattering, showering, ...), the parameterization of the detector response (track hit resolution, cluster shape, Cherenkov ring resolution, dE/dx, ...) and particle reconstruction (tracks, clusters, photon rings, ...). It also allows to plug in the machine background simulated with Geant4. FastSim is designed in such a way that the output is compatible with an extensive set of analysis tools inherited from *BABAR* (composition, vertexing, tagging, etc.), allowing the user to perform even complex analyses. The LNF group has developed those aspects of FastSim concerning the drift chamber, including its geometry and material, the spatial resolution model and the measurement of dE/dx. Use of this tool include the optimization of the detector as described in the following section.

5 The Detector Geometry Working Group

There are several open questions concerning the Super$B$ detector design [1]. A Detector Geometry Working Group (DGWG) was setup at the end of 2008 to study the physics tradeoffs of the open detector options, such as a) a forward PID detector compared to a longer drift chamber (DCH), b) a backward EM calorimeter vs. no backward EM calorimeter, c) the internal geometry of the Silicon Vertex Tracker (SVT), d) the SVT-DCH transition radius and e) the distribution and amount of absorber in the muon system. The study of the design options has been performed by evaluating the physics reach of a set of benchmark decay channels or the general performance of tracks and neutrals reconstruction. A detailed simulation of the main sources of background has also been used to evaluate the rates at different subsystems. A member of our group is co-coordinating the DGWG.

Below is a selection of some preliminary conclusions from the DGWG studies.

- Performance of the SVT inner layer. The per-event-errors of the CP parameters measured through the time-dependent CP asymmetry of $B^0 \to \Phi K^0_S$ and $B^0 \to \pi^+\pi^-$ have been estimated as a function of the position of the innermost layer of the SVT and the technology used to build it (Hybrid Pixels or Striplets). These studies, together with the estimate of the background rate as a function of the distance from the interaction point, will be used to determine which is the most appropriate technology and position for the innermost tracker layer.

- *SVT-DCH transition radius.* Studies have shown that the best overall SVT+DCH tracking performance would be achieved when the outer radius of the SVT is kept small (14 cm as in BABAR or even less) and the inner wall of the DCH is as close to the SVT as possible. However, though in the Super$B$ detector there is not a fixed support tube as there was in BABAR, space between SVT and DCH must be left to allocate a removable support structure to be inserted when access to the inner part of the detector is needed. This constraint is expected to limit the minimum DCH inner radius to about 20-25 cm.

- *Impact of a backward EM calorimeter.* Preliminary studies of the benchmark channel $B \to \tau\nu$ indicate that when a backward calorimeter designed to be used in veto mode is introduced, the signal significance is enhanced by about 10%.

- *Impact of a forward PID.* The study of $B \to K^{(*)}\nu\bar{\nu}$ decays shows that moving from the BABAR detector to the Super*B* detector instrumented with a time-of-flight device, the signal significance increases by about 13%, of which 7-8% arises from the increase of the overall detector acceptance (reduced boost), and 5-6% is due to the improved pion/kaon separation in the forward region. The presence of a forward PID or backward EMC affects the maximum length of the DCH and therefore the tracking and the dE/dx performance in those regions. The impact of the TOF PID detector is negligible because it only takes a few centimeters from the DCH. On the other hand, the effect of a forward RICH device ($\sim$ 20 cm DCH length reduction) or the backward EMC ($\sim$ 30 cm) is somewhat larger. For example, it is found a $\sigma(p)/p$ increase of about 25% and 35% for tracks with polar angle of 23° and 150°, respectively. Even in this case, however, the overall impact is generally very limited because only a small fraction of tracks cross the extreme forward and backward regions.

- *Optimization of the IFR.* The current baseline design has an iron thickness of 92 cm segmented with 8 layers of scintillator. Preliminary results indicate an average muon efficiency of about 87% with a pion misidentification rate of 2% (the effects of background are not included).

6 List of Conference Talks in Year 2009

1. M. Rama, *Status of the SuperB project*, Congresso Nazionale SIF 2009, Bari, Italy
2. G. Finocchiaro, *The Scientific Case for SuperB Factories*, XXXVII International Meeting on Fundamental Physics, Benasque, Spain
3. M. Rama, *The SuperB project*, Les Rencontres de Physique de la Vallée d'Aoste 2009, La Thuile, Italy
4. R. de Sangro, *Status of the Super B Factory Projects*, XIII International Conference on Hadron Spectroscopy, Florida State University, Florida, USA.
5. R. de Sangro, Proceedings of Hadron09 Conference.
6. M. Rama, Proceedings of 23° Rencontres de Physique de La Vallee d'Aoste, `arXiv:0909.1239`.

References

1. *SuperB Conceptual Design Report*, `www.pi.infn.it/SuperB/CDR`, `arXiv:0709.0451v2`.
2. M. Adinolfi et al., (KLOE Coll.), Nucl. Instr. & Meth, A **488**, 51 (2002).

2 – Astroparticle Physics

BENE_DTZ

F. Ronga, F. Terranova (Resp.)

BENE-INFN is a study group closely related to the European initiative BENE (Beams for European Neutrino Experiments) and its follow-up in the 7th Framework Program of EU: EU-ROnu [1] and NEu2012 [2]. It is aimed at developing novel sources for high intensity neutrino beams and is focused on the conceptual design of Superbeams, Beta Beams and Neutrino factories. In 2009, the final outcome of the International Scoping Study for these future facilities has been published [3] and activities toward a Conceptual Design Report have started since 2008. LNF contributed particularly on future applications of OPERA-like detectors [3], i.e. hybrid emulsion cloud chambers with and without magnetic field, as a far detector to exploit the $\nu_e \rightarrow \nu_\tau$ transitions ("silver channel") at the Neutrino Factories. LNF is also involved in the search of more innovative source based on laser-accelerated protons to produce neutrinos in the GeV range. Further activities focused on the combination of accelerator data from Beta Beams with natural sources (atmospheric neutrinos) to improve the sensitivity to the neutrino mass hierarchy (sign of Δm^2_{32}), high-Q Beta Beams and the study of the upgrades of the CERN acceleration complex to host a European high intensity ν source [4].

Conference Talks

1. F. Terranova, *New neutrino facilities from the LHC injection complex and its upgrades*, Luxor, 15-19 November 2009.

References

1. EUROnu is a European Commission FP7 Design Study entitled: *A High Intensity Neutrino Oscillation Facility in Europe*. Info available at `http://www.euronu.org/`.

2. NEu2012 is a Networking Activity (WP3) in the Framework of the FP7 Integrating Activity EuCARD (European Coordinated Accelerator R&D). Info available at `http://bene.web.cern.ch/bene/NEU2012.htm`.

3. T. Abe et al. (ISS Detector Working Group), JINST **4** (2009) T05001.

4. R. Battiston, M. Mezzetto, P. Migliozzi and F. Terranova, *European facilities for accelerator neutrino physics: perspectives for the decade to come*, `arXiv:0912.3372`, to appear in Rivista del Nuovo Cimento.

NEMO

Marco Cordelli, Agnese Martini, Luciano Trasatti (Resp.), Roberto Habel (Ass.)

1 Activity

The NEMO collaboration aims at building a 1 km^3 Cerenkov neutrino detector in the Mediterranean Sea. During the year 2009 the collaboration has prepared, and deployed in february 2010, a tower made up of 16 floors, without photomultipliers, to demonstrate the mechanical pheasibility of the project.

The LNF group has developed a new addition to the project, PORFIDO, which is a method for acquiring oceanographic data from the optical modules without the use of connectors or penetrators, but using an RFID system that reads the data through the glass.

Moreover, we continued the development of NERONE, an instrument designed and built at the LNF to measure the attenuation length of light in water at 3500 m depth. We made a new test of the system in a cruise in may 2009.

We are also developing a new version of the instrument capable of staying underwater for a large amount of time.

The OPERA experiment

V. Chiarella, C. Di Troia (Ass.), B. Dulach, G. Felici, A. Franceschi,
F. Grianti (Ass.), A. Gambarara (Tecn.), N. Intaglietta (Tecn.)
A. Mengucci (Tecn.), T. Napolitano (Art.23), M. Paniccia (Ass. Ric.), A. Paoloni,
M. Spinetti, F. Terranova (Resp.), T. Tonto (Tecn.), M. Ventura (Tecn.), L. Votano

in collaboration with

LNF-SEA: A. Balla, G. Corradi, U. Denni, A. Frani, M. Gatta, G. Paoluzzi (Rm), G. Papalino
LNF-SPAS: A. Cecchetti, S. Cerioni, D. Orecchini
LNF-SSCR: G. Catitti, A. Ceccarelli, A. Tiburzi
LNF Divisione acceleratori: C. Fusco, F. Iungo, L. Pellegrino, C. Sanelli

1 The experiment

OPERA [1] has been designed to provide a very straightforward evidence for $\nu_\mu \rightarrow \nu_\tau$ oscillations in the parameter region indicated by Super-Kamiokande as the explanation of the zenith dependence of the atmospheric neutrino deficit. It is a long baseline experiment located at the Gran Sasso Laboratory (LNGS) and exploiting the CNGS neutrino beam from the CERN SPS. The detector is based on a massive lead/nuclear emulsion target. The target is made up of emulsion sheets interleaved with 1 mm lead plates and packed into removable "bricks" (56 plates per brick). Each brick is equipped with a detachable emulsion doublet ("Changeable Sheet", CS), which is scanned before the full development of the brick emulsions. The bricks are located in a vertical support structure making up a "wall". These bricks were produced in situ by a "brick assembly machine" (BAM) located near the OPERA experimental Hall; they are inserted into the wall support structure by a dedicated robot (BMS). Nuclear emulsions are used as high resolution tracking devices for the direct observation of the decay of the τ leptons produced in ν_τ charged current interactions. Electronic detectors positioned after each wall locate the events in the emulsions. They are made up of extruded plastic scintillator strips read out by wavelength-shifting fibers coupled with photodetectors at both ends. Magnetized iron spectrometers measure charge and momentum of muons. Each spectrometer consists of a dipolar magnet made of two iron walls interleaved with pairs of precision trackers. The particle trajectories are measured by these trackers, consisting of vertical drift tube planes. Resistive Plate Chambers (RPC) with inclined strips, called XPC, are combined with the precision trackers to provide unambiguous track reconstruction in space. Moreover, planes of RPC are inserted between the magnet iron plates. They allow for a coarse tracking inside the magnet to identify muons and ease track matching between the precision trackers. They also provide a measurement of the tail of the hadronic energy leaking from the target and of the range of muons which stop in the iron. A block of 31 walls+scintillator planes, followed by one magnetic spectrometer constitutes a "super-module". OPERA is made up of two supermodules (SM) located in the Hall C of LNGS (see Fig. 1). In 2008 all the bricks have been produced (except a small amount produced in January 2009): the OPERA target, therefore, is made of 150036 bricks corresponding to a target mass of 1.25 kton.
OPERA is able to observe the ν_τ signal with an impressively low background level. The direct and unambiguous observation of $\nu_\mu \rightarrow \nu_\tau$ appearance will constitute a milestone in the study

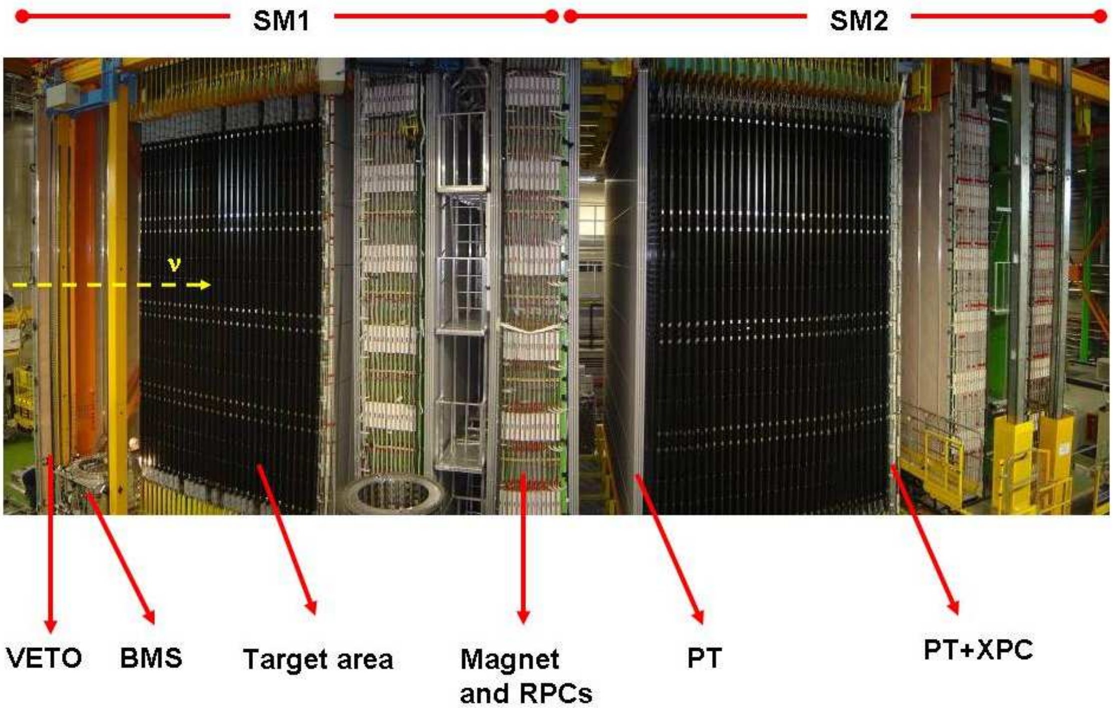

Figure 1: A fish-eye view of the OPERA experiment. The upper red horizontal lines indicate the position of the two identical supermodules (SM1 and SM2). The "target area" is made up of planes of walls filled with lead-emulsion bricks interleaved with planes of plastic scintillators (TT): the black covers visible in the photograph are the end-caps of the TT. Arrows show also the position of the VETO planes, the drift tubes (PT) followed by the XPC, the magnets and the RPC installed among the magnet slabs. The Brick Manipulator System (BMS) is also visible. The direction of incoming neutrinos from CERN is indicated by the yellow arrow.

of neutrino oscillations. Moreover, OPERA has some sensitivity to the sub-dominant $\nu_\mu \to \nu_e$ oscillations in the region indicated by the atmospheric neutrino experiments. It has been shown [2] that the CNGS beam optimized for ν_τ appearance, will improve significantly (about a factor of three) the current limit of CHOOZ. Further results, concerning sterile neutrinos and non-standard interactions have been considered in [3, 4].

Opera is an international collaboration (Belgium, Croatia, France, Germany, Israel, Italy, Japan, Russia, Switzerland, Tunis and Turkey) and the INFN groups involved are Bari, Bologna, LNF, LNGS (Gran Sasso), Naples, Padova, Rome and Salerno. The Technical Coordinator (M. Spinetti), the Coordinator for detector operation and maintenance (A. Paoloni) and the Deputy Spokesperson of the Collaboration (F. Terranova) are LNF researchers.

2 Overview of the OPERA activities in 2009

The 2009 run has been the most successful CNGS run since its startup in year 2006. In 2009, the CNGS facility accumulated 3.5×10^{19} proton-on-target, corresponding to about 3600 events in the bricks. In the meanwhile, all 2008 bricks have been extracted and scanned; the localization of the vertex was completed in January 2010, while the final decay search analysis is in progress. Before the startup of the run, the Collaboration had to face major difficulties due to the earthquake of April 6 in the region of L'Aquila. At that time OPERA was performing intense operations on the target aimed at replacing the first CS batch (13000 bricks), which was known to be defective since 2007. These operations were stopped on April 6 and resumed 5 weeks later, i.e. after the restart of the LNGS activities. The OPERA apparatus has not been damaged by the earthquake although the elastic structure of the target (walls) undergone a jitter of $\sim$ 1 cm. Careful re-alignment of the apparatus demonstrated that the net displacement experienced after the shock did not exceed 0 5mm, i.e. it is within the alignment tolerance of the bricks inside the walls. Another effect of the earthquake on OPERA was caused by the displacement of debris near the coils of the magnet. The latter generated anomalous dispersed currents at the beginning of the run (see below). In spite of the earthquake and thanks to the dedication of the LNGS personnel, the CNGS run started on June 1st - i.e. just two weeks later than the original schedule - with OPERA in nominal running conditions [5]. The defective CS replacement and the yearly maintenance of the Brick Manipulator system were completed in June 19 and the standard brick extraction procedure was restored on June 22. During 2009, several important results have been published. They include the results after the construction and commissioning of the detector [6], the analysis of cosmic ray data [7] and the publication of preliminary performance on fully reconstructed (emulsion+ electronic detector) events, together with the first charm candidates [8]. Fig. 2 shows a charm event (a dimuon event with a one prongs decay in flight of a charged meson) observed after emulsion scanning and occurred in the Opera target in summer 2009.

3 Activities in Frascati

The Frascati group has been responsible for the design and construction of the dipolar magnets and the general support structure for the subdetectors. It shares responsibility with INFN Padova and LNGS for the construction and running of the bakelite RPC planes. Frascati and Naples also designed and prototyped the wall support structures housing the lead/emulsion bricks and LNF was responsible for their production and installation. Moreover, the group contributes to software development and to analyses. LNF was highly involved in the construction and operation of the Brick Assembly Machine (BAM) and, since 2008, contributes to the emulsion scanning with two dedicated microscopes located in Frascati. Finally, since 2007 LNF follows the brick handling of OPERA, i.e. the operation chain that goes from the extraction of the brick after an interaction has occurred up to the emulsion development.

3.1 OPERA General layout

The OPERA general support structure is a project by LNF-SPAS and external firms and it has been mounted in parallel with the electronic subdetectors and the brick walls between 2003 and 2006 [9]. The project was completed in 2006 and, during 2007 and 2008, only auxiliary installations were added. The structure has been designed by LNF-SPAS; construction and mounting has been carried out by external firms under the supervision of LNF. LNF-SPAS has also been involved in the realignment and revision of the structure after the earthquake. The LNF technical support was actually the first group to inspect the apparatus a few days after the main quake of April 6.

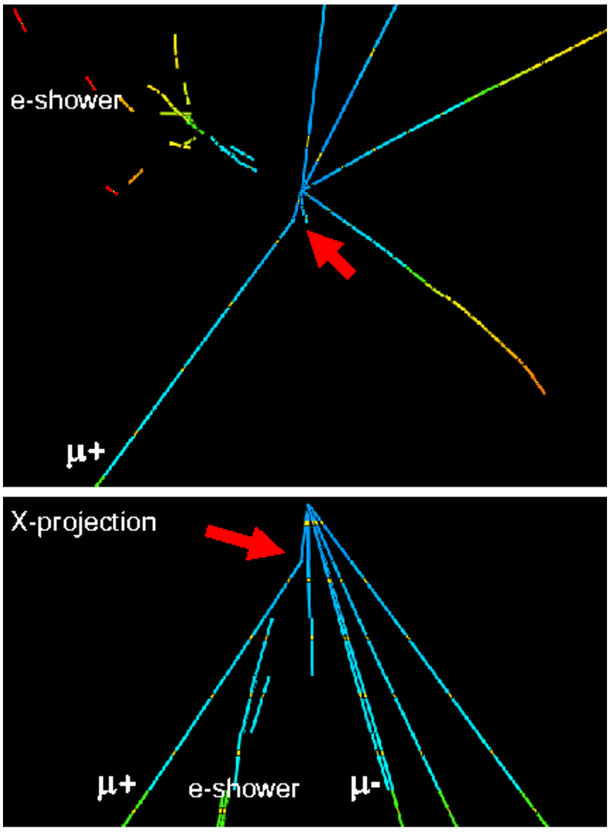

Figure 2: A dimuon charm candidate in OPERA.

3.2 Magnets

The OPERA magnets and their infrastructures have been commissioned in spring 2006 and were fully operative since the first CNGS run [10]. In winter 2008-2009, the standalone OPERA cooling system has been interfaced with the water circuits of LNGS through a dedicated heat exchanger; it will act as a backup system in case of failure of the chiller and it has been commissioned at the beginning of 2009.

During the 2009 physics runs the magnets were operated continuously and the performance were well in specs. On the other hand, at the beginning of the run, the first magnet experienced anomalous dispersed currents. The origin of these currents were traced back to debris produced at the time of the construction and moved toward the coils after the earthquake. It has been brought back in normal condition on June 11. Later on, only a few instabilities in the power supply of the first magnet were observed from time to time (about once per month) and are currently under investigation. The cooling system has improved its performance and live-time with respect to 2008 thanks to the automatic refill system for the demineralized water installed the year before.

3.3 Resistive Plate Chambers

After contributing to the construction, LNF is heavily involved in the running of the OPERA RPC system. One of the duties of the group is the monitoring of the performances of the RPC system. As mentioned before, Resistive Plate Chambers with bakelite electrodes are arranged into layers, 22 in each spectrometer, inserted into 2 cm gaps inside the magnetized iron. Two additional layers are placed in each Super-Module between the Target Tracker and the spectrometer. A complete description of the OPERA RPC system can be found on [6].

The detectors are operated in streamer mode at 5.7 kV with the gas mixture $Ar/C_2H_2F_4/i-C_4H_{10}/SF_6 = 75.4/20.0/4.0/0.6$ [11]. An automatic correction is applied for the pressure, according to [12]; the temperature is quite stable, between 15 and 18 °C, depending on the detectors position. Signals from the vertical strips, measuring the bending coordinate, are discriminated at 40 mV, while the threshold for the horizontal strips has been lowered at the beginning of 2009 run from 40 mV to 26 mV, in order to correct for the different impedance matching with the read-out twisted flat cables.

The XPC layers and 7 out of 22 RPC layers in each spectrometer are instrumented with dedicated Timing Boards (TBs) for triggering the drift tubes. The LNF OPERA group also is involved in the MonteCarlo simulation of the trigger.

The full RPC system ran smoothly during the 2009 run, with almost no dead-time and with performances similar to those observed in the previous years [9, 13, 14], matching the required specifications.

RPC layers showed typical efficiencies around 95%, mostly limited by their geometrical acceptance (dead areas between the chambers). Average cluster size values were about 2.76 strips in the bending projection and 1.74 strips in the other projection, with tracking resolutions $\sim$ 1 cm, shown in Fig. 3. Counting rates as low as 20 Hz/m^2 have been observed with operating currents around 500 nA for each RPC row (3 chambers, corresponding to a sensitive area of 9 m^2). The detector time resolution is $\sim$ 3 ns, ensuring 300 μm resolution of the drift tubes.

After four years of run, it is time for some considerations about the aging of the system. No major effect has been observed in terms of detector efficiency and performance, while $\sim$ 5% of the system is showing higher currents (up to 4 μA for single RPC rows) and rates (as high as 100 Hz/m^2). The effect is localized in the first spectrometer and it is probably due to the operation at low gas flux in presence of leakages during the previous years. This problem has now been fixed.

The high statistics of 2009 run, with $\sim$ 150000 muons crossing the spectrometers, has been used also for detector physics studies. In Fig. 4 the average value of the cluster sizes product (estimating the induced charge) is shown as a function of cos (Θ), where Θ is the angle between the particle direction and the normal to RPC layers (cos Θ =1 corresponds to perpendicular tracks, mostly in beam events). In order to fit the cluster size product in such a wide range (0.05 < cos Θ < 0.85) the function $(p0 - p1 * ln(cos\,\Theta)) * (1 + p2 * tg\,\Theta)$ is best suited, where the first term is the known dependence on the primary ionization and the second one accounts for geometric effects scaling with the projection of the particle trajectory on the RPC electrodes (production of more simultaneous streamers).

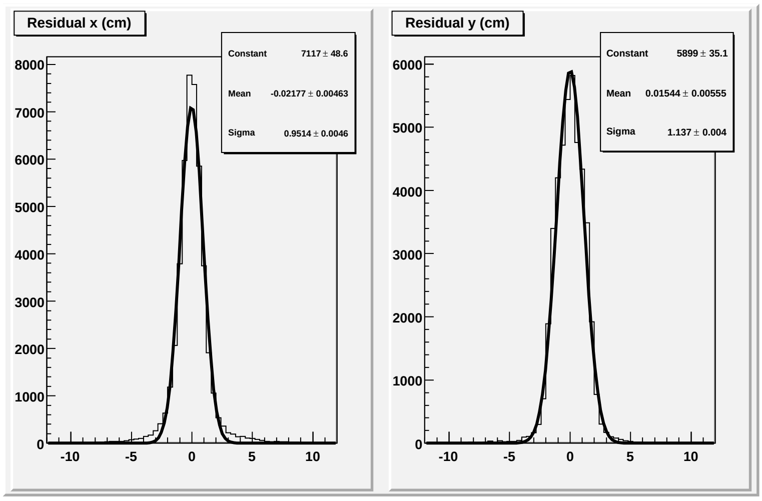

Figure 3: Tracking resolution for the bending (left plot) and for the orthogonal coordinates (right plot). Only tracks at angles lower than 40^o with respect to the beam direction have been considered in the plots.

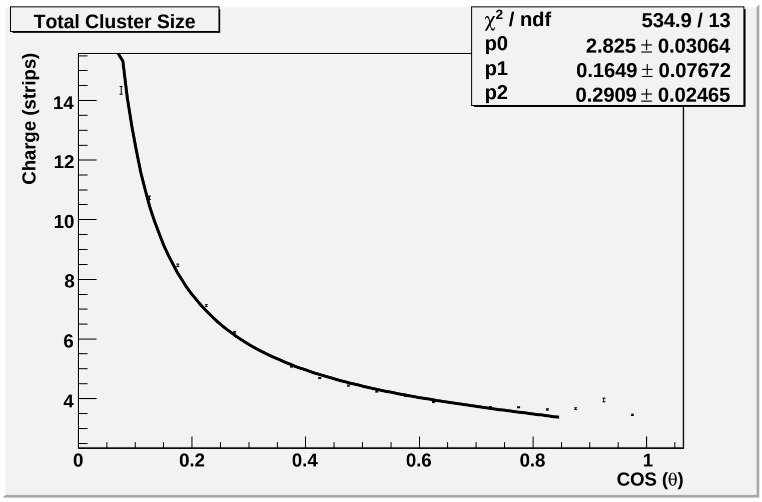

Figure 4: Cluster sizes product as a function of cos Θ. Average values on different events and RPC layers are considered.

3.4 Wall support structure

The wall support structure ("wall") is made of thin stainless steel vertical bands welded to light horizontal trays where the bricks are positioned with a precision of one millimeter. The structure is suspended through rods and joints from the general support structure and tensioned from the bottom through a spring system. The walls were installed in parallel with the plastic scintillators. This project has been under the responsibility of LNF-SSCR and was successfully completed in 2006 [9]. In 2009 only maintenance operations (see Sec. 3.7), fixing of damaged parts and alignment updates during the filling phase have been carried out. As already mentioned, the wall support structure properly reacted to the accelerations (3% of g) due to the earthquake and no permanent deformations or misalignment have been reported.

3.5 Brick Assembly Machine

After the production of the bulk of the target in 2007-2008, the Brick Assembly Machine (BAM) has been reactivated for a short time to build the last 3000 bricks of the target. In 2008, this small production was delayed by an accident occurred at the firm producing the lead for OPERA (JL Goslar, Germany). The residual target was produced in about two weeks in late January. The BAM project is, therefore, completed and the dismounting of the facility is scheduled in March 2010.

3.6 The LNF scanning station

The OPERA brick is composed by 57 emulsion films, 10 cm $\times$ 12 cm wide, interleaved with 56 lead plates 1 mm thick, plus two changeable emulsion films, the Changeable Sheets (CS) doublet, at the interface with the electronic detectors. Emulsion layers are made of gel with interspersed AgBr crystals; in the case of OPERA, two such layers, each 50 μm thick are poured on a 200 μm plastic base. A charged particle crossing an emulsion layer ionises the medium, leaving a sequence of "sensitized" sites. After emulsion film development, these sites are turned into silver grains, with a linear dimension of about 0.6 μm. About 30 grains every 100 μm are left by a minimum ionizing particle. The nuclear emulsion films are analysed with optical microscopes. The three-dimensional tracks of charged particles crossing the brick are reconstructed from the optical tomography of each field of view obtained adjusting the focal plane of the objective lens through the emulsion thickness. A detailed description of the automatic microscopes developed for OPERA can be found in Ref. [15].

The bricks selected by the electronic detectors as containing a neutrino interaction vertex are extracted from the OPERA target and equally shared between Japan and Europe for the scanning. For the events assigned to the European side the CS doublets are analysed at the LNGS scanning station. If the result from the CS scanning is positive, the brick is assigned to one of the European scanning laboratories dedicated to the neutrino vertex localization in Switzerland and Italy, one of which is at LNF. The scanning load at the LNGS scanning station is shared among the European members of the OPERA Collaboration. Since 2008 the LNF group contributes to the CS doublets scanning performing shifts at the LNGS station, in addition to the work load at the home scanning laboratory.

The LNF emulsion scanning station is equipped with two optical microscopes, one of them has been instrumented with a system for the emulsion plates loading on the microscope stage (Plate

Changer), which will allow to perform each set of emulsion scanning in fully automatic mode. The installation of the Plate Changer electronics and of its hardware interfaces to the microscope have been completed in spring 2009 while the installation of the software needed to remotely operate the machine from the scanning software framework as well as the commissioning of the fully automatic system is in progress.

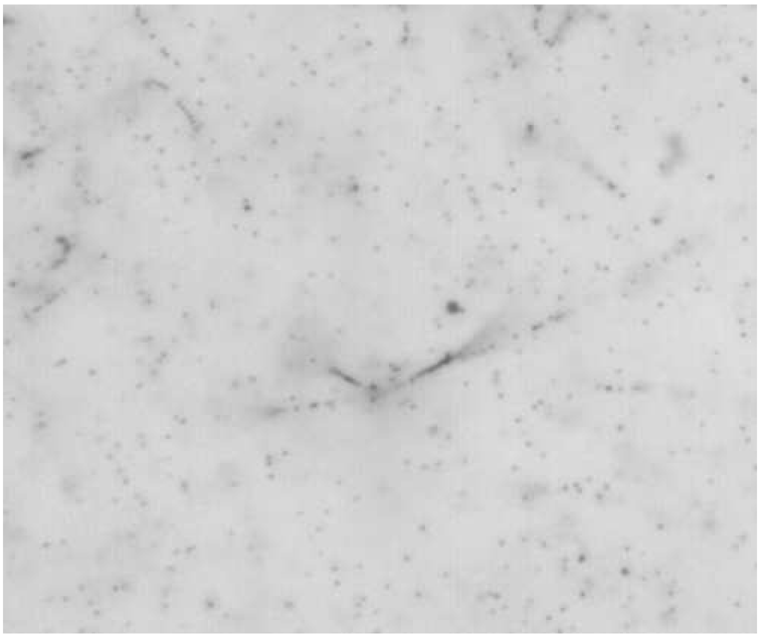

Figure 5: A vertex from a neutrino interaction occurred in lead nearby the emulsion film.

After a successful upgrade and commissioning of the scanning system architecture in semi-automatic mode (i.e. with manual load of the emulsion film on the microscope stage), at the end of 2008 the LNF scanning laboratory has been assigned its first OPERA event brick to analyse, actively entering the European scanning laboratories team.

The activity of the LNF scanning station in 2009 has been focused on the OPERA event scanning and analysis. Several neutrino interaction events were assigned to the Frascati Laboratories for the localization of the interaction vertex . The whole emulsion data production chain has been set-up and is now working smoothly: it starts with the emulsion scanning, proceeds with the vertex reconstruction and ends up with the data publication to the central database,

Once the brick is shipped from LNGS to the scanning laboratory the procedure for vertex localization begins. The tracks related to the neutrino event found in the CS doublet are followed up to their stopping point, which gives a first indication of the neutrino interaction vertex. Then a wide scanning of 1 cm^2 around the stopping point is performed for 15 consecutive emulsion films, corresponding to 6500 μm upstream and 11700 μm downstream the stopping point, such that all primary particle tracks and possible decay daughter particle tracks are reconstructed. Once the vertex is localized, a reconstruction procedure dedicated to the search of interesting decay topologies is applied. At the end of the whole procedure the scanning laboratory publishes a feedback of the vertex localization and of the decay search results, as well as the complete set of emulsions scanning data in the central OPERA database, where they are made available to the whole Collaboration for global analysis.

3.7 Brick handling

During nominal CNGS operation, about 20 neutrino interactions per day occur in the OPERA target and several candidate bricks are tagged as containing the corresponding primary vertex. These predictions are validated scanning preliminarily a pair of detachable emulsions ("changeable sheets", CS [16]). If confirmed, the corresponding brick is extracted, aligned using an X-ray machine and sent to the facilities located on surface for cosmic ray exposure (high precision alignment) and development. All the operations of CS and brick handling require dedicated tools and personnel running synchronously with the CNGS data taking. LNF is responsible of the coordination of these tasks and provides most of the tools for brick handling. In particular, in 2007 LNF-SPAS started the design of the unloading station and defined the procedure aimed at delivering the extracted bricks from the BMS to the X-ray marking area. The full operation chain started being operative by summer 2008. During the 2009 run, the brick handling system was able to keep pace with the record CNGS extraction rate from CS extraction to cosmic exposure and development. Moreover, in 2009, an automatic rotating system for the bricks in the cosmic ray pit designed by LNF-SPAS has been installed and commissioned and it is now in use during the run.

4 Conference Talks

1. A. Paoloni, *First results from the OPERA experiment*, NuHoRIzons09 Neutrinos in Physics, Astrophysics and Cosmology, Allahabad, India, 7 - 9 January 2009.
2. F. Terranova, *Neutrino Oscillations in the CNGS ν_μ Beam*, Talk at XIII International Workshop on Neutrino Telescopes, Venice, Italy, 10-13 March 2009.
3. M. Paniccia, Talk at the 95th Congresso Nazionale della Società italiana di Fisica, Bari, 28 September - 3 October 2009.

References

1. M. Guler et al., *OPERA proposal*, CERN/SPSC 2000-028, SPSC/P318, LNGS P25/2000.
2. M. Komatsu, P. Migliozzi, F. Terranova, J. Phys. G **29**, 443 (2003); P. Migliozzi, F. Terranova, Phys. Lett. B **563**, 73 (2003).
3. A. Donini, M. Maltoni, D. Meloni, P. Migliozzi, and F. Terranova, JHEP **0712**, 013 (2007).
4. M. Blennow, D. Meloni, T. Ohlsson, F. Terranova, and M. Westerberg, Eur. Phys. J. C **56**, 529 (2008).
5. F. Terranova, "CNGS1 - OPERA", 92th Meeting of the SPSC, CERN, 30 June 2009.
6. R. Acquafredda et al., JINST **4**, P04018 (2009).

7. M. Sioli et al., *Cosmic ray physics with the OPERA detector*, International Cosmic Ray Conference, Lodz, Poland, 7-15 July 2009.
8. N. Agafonova et al., JINST **4**, P06020 (2009).
9. See "LNF 2008 Annual Report", D. Babusci ed., LNF-09/04 (IR), p. 99, "LNF 2007 Annual Report", M. Antonelli ed., LNF-08/20 (IR), p.103; "LNF 2006 Annual Report", M. Antonelli ed., LNF-07/10 (IR), p. 87; "LNF 2005 Annual report", E. Nardi ed., LNF-06/10 (IR), p. 78; "LNF 2004 Annual Report", E. Nardi ed., LNF-05/5 (IR), p. 70; "LNF 2003 Annual Report", S. Dell'Agnello ed., LNF-04/08 (IR), p. 64.
10. A. Cazes et al., JINST **2**, T03001 (2007).
11. A. Mengucci, A. Paoloni, M. Spinetti, L. Votano, Nucl. Instr. & Meth., A **583**, 264 (2007); A. Paoloni et al., LNF Technical Note LNF-08/14(NT) (2008).
12. M. Abbrescia et al., Nucl. Instrum. Meth., A **359**, 603 (1995).
13. S. Dusini et al., Nucl. Instrum. Meth., A **602**, 631 (2009).
14. A. Paoloni et al., Nucl. Instrum. Meth., A **602**, 635 (2009).
15. N. Armenise et al., Nucl. Inst. Meth. A **551**, 261 (2005).
16. A. Anokhina et al., (OPERA Coll.), JINST **3**, P07005 (2008).

ROG

G. Giordano (Resp.), M. Iannarelli (Tecn.), R. Lenci (Tecn.),
A. Marini, G. Modestino, G.P. Murtas (Ass.), G. Pizzella (Ass.),
F. Ronga (Resp.), E. Turri (Tecn.)

Collaboration with:
University of Rome La Sapienza and INFN Roma 1,
University of Rome Tor Vergata and INFN Roma 2

1 Introduction

The ROG group is currently operating two cryogenic gravitational wave (GW) bar detectors: EXPLORER (at CERN) and NAUTILUS (in Frascati). The main goal of this search is the direct detection of the GW's that could be emitted by astrophysical sources (such as Supernovae or Coalescent Binaries). Such detection would be of enormous interest for general relativity and astrophysics.

Both detectors consist of an aluminum cylindrical bar having a mass of $\simeq 2.3$ tons, with a capacitive resonant transducer mounted on one of the bar faces. They are contained in a vacuum cryostat, cooled at cryogenic temperatures ($\simeq 3$ K) to reduce thermal noise, and are isolated from seismic and acoustic disturbances.

The capacitive transducer is coupled to a very low noise superconducting amplifier (d.c. SQUID) whose output is acquired by a VME ADC board, sampled at 5 kHz.

A GW signal would excite the mechanical resonant modes of the bar-transducer system. When searching for impulsive signals, the data are filtered with an adaptive filter matched to a delta-like signal. This search for bursts is suitable for any transient GW which shows a nearly flat Fourier spectrum at the two resonance frequencies of each detector.

Both EXPLORER and NAUTILUS have been kept in continuous observational mode since 2003, with a duty cycle between 80 and 90%, mainly limited by the necessary periodic cryogenic operations.

The LNF group has major responsibilities in the maintenance and running of NAUTILUS (including the production of liquid Helium), in the maintenance, upgrading and running of the cosmic ray detectors, in the development of a new nearly quantum limited signal read-out, in the data acquisition and in many items of data analysis.

2 NAUTILUS and EXPLORER

The ultra-cryogenic detector NAUTILUS is operating at the INFN Frascati National Laboratory since December 1995. It is equipped with a cosmic ray detector based on a streamer tube assembly.

The present data taking started in 2003, with a new bar tuned at 935 Hz, where a pulsar, remnant of the SN1987A, is supposed to emit GW's, with a more sensitive readout chain (the same as for EXPLORER), and a new suspension cable, to provide a more stable position setting. At present, the temperature of the bar is 3.5 K and the resulting strain noise (the minimum detectable spectral density) is $\tilde{\mathrm{h}} \simeq 1 \cdot 10^{-21}\ /\sqrt{\mathrm{Hz}}$ around 935 Hz, and $\tilde{h} \leq 10^{-20}\ /\sqrt{\mathrm{Hz}}$ over about 50 Hz. At

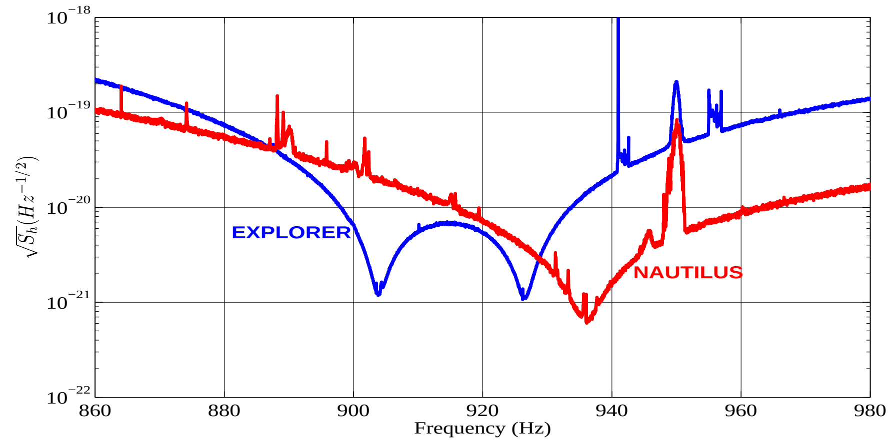

Figure 1: Explorer and Nautilus sensitivities in 2009.

the beginning of 2009, we discovered that some wide-band noise was due to a malfunctioning of the UPS system. After changing the UPS and some adjustments in the SQUID electronic chain, the noise temperature decreased down to less than 1 mK, corresponding to an adimensional amplitude of GW bursts $h \simeq 2.4 \times 10^{-19}$.

The EXPLORER antenna is located at CERN and is very similar to NAUTILUS. Also its duty cycle is very high (of the order of 90%), its noise temperature is about 2 mK, with a strain sensitivity $\tilde{h} \simeq (2 \div 3)\,10^{-21}\ /\sqrt{\mathrm{Hz}}$ around the two resonances at 904 Hz and 927 Hz, and $\tilde{h} \leq 10^{-20}\ /\sqrt{\mathrm{Hz}}$ over about 30 Hz. EXPLORER is equipped with a cosmic ray detector, based on a set of long plastic scintillators.

The read-out systems installed in 2001 on EXPLORER and in 2003 on NAUTILUS, obtained a larger bandwidth and consequently improved the time resolution (now less than 10 ms), as it is also been checked with the events due to cosmic ray showers.

In the last years a continuos effort has been paid in improving the data analysis system already present and in testing independent algorithms and new methods. As a result of these, still going, efforts we were able to improve the accuracy in the reconstruction of both the amplitude and time characteristic of the signals. At the same time, we performed detailed studies of the detectors response to other class of signals than the simple delta-like burst previously considered. All this was done also with a particular eye on the perspective of performing joint analyses with the interferometric type of GW detectors, which do have a much better sensitivity than the resonant bar detectors, but up to now have suffered from very long interruptions in their operation. This situation will persist in the next few years, when both the american interferometers (LIGO) and the french- italian one (VIRGO) will be down for major upgrades, leaving the INFN bar detectors (AURIGA, EXPLORER and NAUTILUS) the only operational GW detectors.

2.1 Analysis of EXPLORER-NAUTILUS data

We continued to study all possible wide-band noises that can result in a candidate event and also, through simulations and software injections of signals, to find the event characteristics (e.g. length vs. amplitude) that an event due to a real excitation must have. All this was used to reduce the number of candidate events by putting vetos on periods or single events with understood instrumental noise excess, in addition to the usual vetos on events triggered by cosmic rays showers. In 2009 we had a total overlap of $\simeq 250$ days of good data periods in the overlap between Explorer and Nautilus. We plan to analyze soon the amount of data (about 2.5 years) from the end of the period considered in the last IGEC analysis (April 2007) up to the end of 2009.

2.2 Other type of analyses

- Cosmic Rays - The study of the response of our detectors to cosmic ray showers continues to demonstrate experimentally the actual capability to detect very small mechanical excitations of the bars. While the study of the timing characteristics of the larger events produced by the rare very high density showers allows us a real measure of the accuracy in the time reconstruction, the study of the much more numerous cases of low density showers, performed with a cumulative-type analysis, constitutes an independent cross-check of the amplitude response calibration.
- RAP experiment - In 2009 new measurements have been done on the response of the superconductive Alluminium to ionizing particles, using the RAP (Rivelazione Acustica di Particelle) apparatus. The electron beam of the DAΦNE-BTF has been used for this purpose. A paper has been published on Physics Letters A on this argument.

References

1. F. Ronga (ROG & RAP Coll.) Nucl. Phys. (Proc. Suppl.) **190**, 44 (2009).
2. M. Barucci et al., Phys. Lett. A **373**, 1801 (2009). `arXiv:0901.1220`.

WIZARD

G. Basini, F. Bongiorno (Ass.), G. Mazzenga (Tecn.), M. Ricci (Resp.)

ITALY: INFN Bari, LNF, Firenze, Napoli, Roma 2-Tor Vergata, Trieste;
CNR Ist. Fisica Applicata "Nello Carrara" Firenze;
ASI (Italian Space agency);
Electronic Engineering Department, University of Roma 2 "Tor Vergata";
RUSSIA: MePhi Moscow;
FIAN Lebedev Moscow;
IOFFE St Petersburg;
TsSKB-Progress Samara;
SWEDEN: KTH Stockholm;
GERMANY: Siegen University;

1 Experimental Program and Scientific Objectives

The WIZARD experimental program is devoted to the extensive study of cosmic ray spectra (particles, antiparticles, isotopes, abundances and search for antimatter) in several energy ranges achievable through different instruments on board stratosferic balloons and long duration satellite missions. WIZARD is an International Collaboration between several Universities and Research Institutions from Russia, Sweden, Germany, USA togheter with the Space Agencies NASA, RSA (Russia), SNSB (Sweden), DLR (Germany) and ASI. The experimental activities have been and are carried out through three main programs:

- Stratospheric Balloon flights;
- Satellite missions NINA-1 and NINA-2;
- Satellite mission PAMELA.

We refer to previous editions of this report for the descrition of the activities related to the balloon flights and to the two NINA missions.

1.1 The satellite mission PAMELA

PAMELA is a cosmic ray space experiment installed on board a Russian satellite (Resurs-DK1) which has been successfully launched on June 15th, 2006 from the cosmodrome of Baikonur, Kazakhstan, by a Soyuz TM2 rocket.

The satellite is flying in a low altitude, elliptic orbit (350-610 km) with an inclination of 70.0 degrees. The PAMELA telescope consists of a magnetic spectrometer composed of a permanent magnet coupled to a silicon tracker, an electromagnetic silicon-tungsten calorimeter, a time-of-flight system, an anticoincidence system, a shower tail catcher scintillator and a neutron detector [1, 2]. A sketch of the PAMELA instrument is shown in Fig. 1 and a photo of the completed Flight Model is shown in Fig. 2.

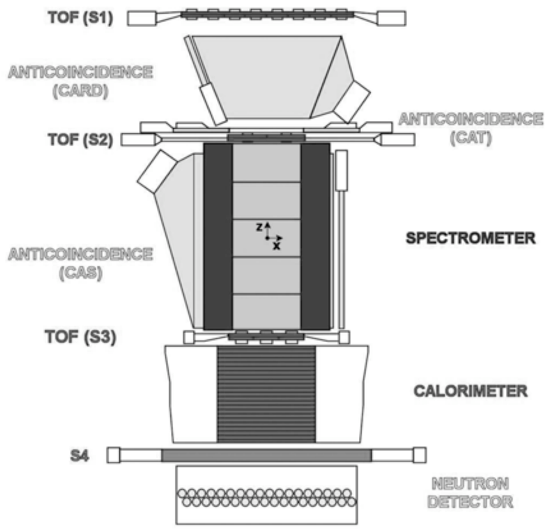

Figure 1: Schematic overview of the PAMELA detectors.

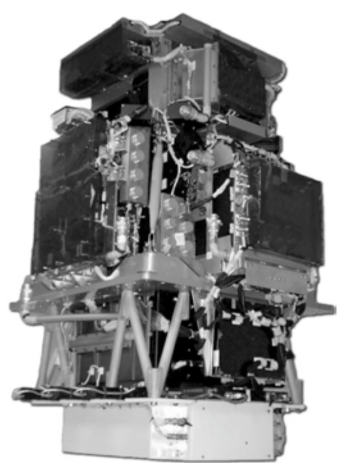

Figure 2: The PAMELA Flight Model.

The total height of PAMELA is ~ 130 cm, the mass is 470 kg and the power consumption is 355 W.

The observational objectives of the PAMELA experiment are to measure the spectra of antiprotons, positrons and nuclei over an extended range of energies, to search for antimatter and for indirect signatures of dark matter and to study cosmic ray fluxes over a portion of the Solar cycle.

The main scientific goals can be schematically listed as follows:
a) measurement of the antiproton spectrum in the energy range 80 MeV-190 GeV;
b) measurement of the positron spectrum in the energy range 50 MeV-300 GeV;
c) measurement of the electron spectrum up to 500 GeV;
d) measurement of the proton spectrumup to 700 GeV;
e) measurement of the electron+positron spectrum up to ~ 1 TeV;
f) measurement of light nuclei spectra (He/Be/C) up to 200 GeV/n;
g) search for antinuclei with a sensitivity of 3×10^{-8} in the $\overline{\mathrm{He}}/\mathrm{He}$ ratio.

Additional objectives are:
Long-term monitoring of the solar modulation of cosmic rays;
Measurements of Energetic Particles from the Sun;
High-energy Particles in the Earth magnetosphere and Jovian electrons.

After more than three and half years of operation, both the satellite and the PAMELA instrument have shown to be properly functioning and the overall performance of the detectors to be fairly good. Every day, an average of 14 GBytes of data are transmitted to the main Receiving Station NTsOMZ located in Moscow where quick-look and first control of the performances of the instrument are performed. Then, alla data are transferred through high-speed networks to CNAF, Bologna and to the participating institutions of the PAMELA International Collaboration for the full analysis of data. PAMELA, at present, has collected some 18 TBytes of data corresponding to about 2 billion events.

Due to the good performance of both the satellite and the instrument, the Russian Space Agengy, followed by INFN and ASI, have approved the decision to extend the mission (initially planned for three years) until the end of 2011.

Among the results so far obtained by the experiment, the most relevant are the anomalous spectrum of positrons and the antiproton to proton flux ratio studied up to the highest energies ever achieved so far (100 GeV) with the available statistics (see the list of publications for references). In particular, the positron result (Fig. 3) shows a significant distortion in the spectrum differently from what was expected according to the most credited models of propagation and acceleration of cosmic rays in the Galaxy. This effect could be an indication of production by dark matter particles or could be explained by the presence of an astrophysical source like, e.g., young nearby pulsars. Many articles (more than 400), showing several possible interpretations and new models, have appeared after the first presentations at Conferences and publication of the PAMELA results. Work is in progress to push - thanks to the increasing statistics - the spectrum to higher energies (beyond 100 GeV) and to study the electron spectrum which is of most interest also due to the recent results obtained by the South Polar balloon experiment ATIC and the space mission FERMI-GLAST.

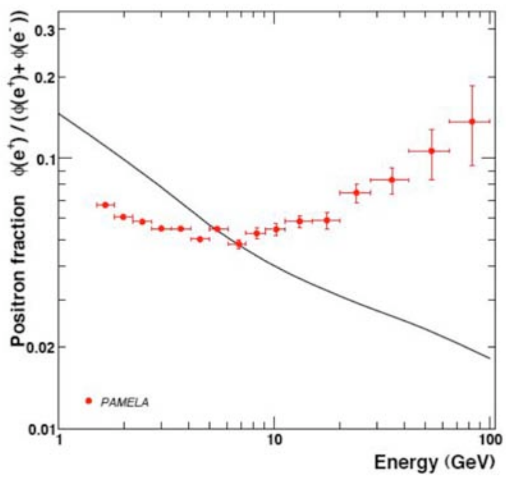

Figure 3: The PAMELA positron fraction compared with theoretical model. The solid line shows a calculation by Moskalenko and Strong [3] for pure secondary production of positrons during the propagation of cosmic-rays in the Galaxy. One standard deviation error bars are shown. If not visible, they lie inside the data points.

2 Activity of the LNF group during year 2009

The LNF WIZARD group has been fully involved in all the previous balloon and present satellite programs. During the year 2009 the LNF group has continued the activity in the analysis, quick-look and preparation and organization of next beam tests to be performed in 2010 at GSI Darmstadt for calibration with nuclei of the ground instruments of the Engineering Model.

3 A selection of most recent publications

1. O. Adriani et al., Phys. Rev. Lett. **102**, 051101-1 (2009).
2. O. Adriani et al., Nature **607**, (2009).
3. O. Adriani et al., J. Geophys. Res. **114**, A12218 (2009).
4. M. Boezio et al., New Journal of Physics **11**, 105023 (2009).

References

1. M. Casolino et al., Adv. Space Res. **42**, 455 (2008).
2. P. Papini et al., Nucl. Instr. & Meth. A **588**, 259 (2008).
3. I.V. Moskalenko, A.W. Strong, Astrophys. J. **493**, 694 (1998).

3 – Nuclear Physics

ALICE

N. Bianchi (Resp. Loc.), G.P. Capitani, A. Casanova (Ass.), G. Conesa (Ass.),
L. Cunqueiro (Ass.), P. Di Nezza, A. Fantoni, D. Hasch (Art. 23), A. Moregula (Ass.),
V. Muccifora, A. Orlandi (Tecn.), W. Pesci (Tecn.), F. Ronchetti (Ass.),
A.R. Reolon, R. Vieira (Stud.), A. Viticchié (Tecn.)

1 Introduction

ALICE is an experiment at CERN which involves about 1000 physicists from more than 100 Institutions from several Countries. Italy participates with 12 groups and more than 150 physicists. The Frascati group is participating to the electromagnetic calorimeter project (EMCal). The EMCal enables ALICE to explore the physics of jet quenching, i.e. the interaction of energetic partons with the QCD hot and dense medium, over the large kinematic range provided by the LHC. The EMCal provides fast triggers (level 0 and 1) for photons, electrons, and jets. The EMCal also measures the neutral energy component of jets, enabling full jet reconstruction in all collision systems, from proton-proton to Pb-Pb. The combination of the EMCal, the excellent ALICE charged tracking capabilities, and the modest ALICE magnetic field strength, is a preferred configuration for jet reconstruction in the high background environment of heavy ion collisions, allowing detailed optimization of background rejection while preserving the crucial jet quenching signals at moderate transverse momentum. The ALICE experiment was ready to take data at the start of LHC in November 2009 and with the first-day proton-proton collisions a first physic paper has been already produced and published. The data collected during the December 2009 run are currently under analysis.

2 The EMCal Calorimeter

The EMCal is a large Pb-scintillator sampling calorimeter with cylindrical geometry, located adjacent to the ALICE magnet coil at a radius of ~ 4.5 meters from the beam line. Its coverage in phase space is $-0.7 < \eta < 0.7$ and $\Delta\phi = 100°$. The EMCal is segmented into 11520 projective towers each with a front face dimensions of 6 x 6 cm^2 resulting in individual tower acceptance of $\Delta\eta x\Delta\phi \sim 0.014x0.014$. The chosen technology is a layered Pb-scintillator sampling calorimeter with a longitudinal pitch of 1.44 mm Pb and 1.76 mm scintillator. Wavelength shifting readout fibers are configured in a Shashlik geometry and are coupled to an Avalanche Photodiode (APD) sensor. The EMCal is composed by 10 SuperModules which represent the basic structural unit of the detector. Each full size super module is assembled from 12 x 24 = 288 modules arranged in 24 strip modules 12 x 1 modules each. Each module contains a 2 x 2 = 4 independent towers built up from 76 alternating layers of 1.44 mm Pb, white paper and 77 layers of 1.76 mm polystyrene base, injection molded scintillator with an intrinsic light output of 50% Anthracene.

3 Experimental activity at LNF

In 2009 the EMCal modules massive assembly, already started in 2008, continued at full speed using two production lines composed by two stacking fixtures and four kits of pressure sensors used to apply and measure the internal load of the modules. The modules have a trapezoidal shape (tapering of 1.5 deg in the η direction) to project the longitudinal module axis to the beam-beam interaction point. This, together with the complexity of the single unit structure, made by 831 single parts, requires careful metrological checks. In this respect, measurements are performed on random samples both on scintillator and lead tiles in order to keep all the geometrical parameters under control. In order to monitor the scintillator properties of the tiles, produced by the Russian company UNIPLAST in several bunches, at each bunch delivery the scintillator light emission of a random sample of tiles is measured by an acquisition test setup using a black box containing a ^{90}Sr radiative source and a PMT connected to the DAQ system. The light emission found for any of the sample acquired stays stable within 5% of accurancy.

The layers of the Shashlik calorimeter module are kept together by an internal load of 220 kgf guaranteed by stainless steel foils kept under tension by five sets of Belleville non-linear washers resident into the module itself. After a 24 hours of pre-load at 550 kgf able reduce the non flatness of the sandwich layers, the modules are stabilized in a temperature controlled container which reproduces the conditions of the ALICE cavern (21 °C). At the end of this long and accurate procedure the module, considered a self supporting unit, reaches a mechanical stability lifetime of more then 20 years.

A pre-assembled four bundles of 36 polished, aluminized and glued WLS fibers, produced in LNF, are inserted in each module. The bundles are optically isolated and run inside the module ending with a terminator for the coupling with the optoelectronic chain (light guide + APD + CSP package). Each module is also provided with a white paper diffuser placed at the center of the 4 towers to allow the diffusion of the light that pulsed by the LED driver for the gain monitoring of the APDs. In Frascati, a total of 120 modules have been produced in 2009 completing the second full European super-module unit.

The strip-module is a structure of 12 modules provided of all the read out cables for the APDs, preamplifier cards, light guide for the GMS control and temperature probes. The assembly of a strip unit is performed aligning and blocking the module units along the non tapered sides using a flat pinned iron plane. The mechanical stability of the unit is given by the insertion of an aluminum back cover (StrongBack) on the top. In 2009, a total of 10 strip modules have been produced at the LNF.

4 SuperModule Assembly and Cosmic Test

All stripmodules assembled in LNF have been delivered to Grenoble, with a safe and special aluminum structure, for testing the signals of APDs using a led system, and eventually adjusting the APD gain. Once tested, the strip-modules have been inserted in the SuperModule (SM) crate, the largest building block of the calorimeters. Its function is not only as a box of the individual modules, but rather as an integrated structure in which the 24 strip-modules contribute to the overall stiffness. The SM crate thus functions as a large I-beam in which the aluminum flanges of the beam are the longitudinal sides of the crate and the 24 transverse rows of strip-modules together form the 'core'. A calibration with cosmic muons was performed every 1/3 of SM, using scintillators at the top and at the bottom of the strip-modules. A picture of the muons cosmic test bench is reported in Fig. 1. Usually 200-500 muons per tower are required, leading to 16 h per pass and 3 passes are necessary to achieve a dispersion less than 3%, starting from 15%. Once tested with cosmic muons the SM were transported at CERN P2 for the installation. In 2009 four SM crates have been installed in ALICE, two from USA and two from Europe, in February and in July

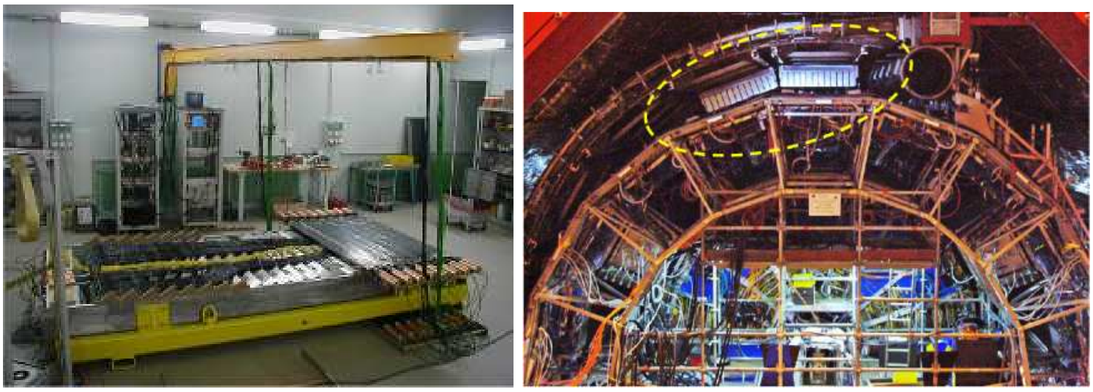

Figure 1: Left: Cosmic Test bench of the EMCal SuperModule. Right: SuperModule inserted in ALICE. Two SM are visible on one rapidity side, two other SM are installed on the other side.

2009. The interface between the SM crate and the EMCal support structure is achieved with a set of rails mounted on the inner surface of the EMCal support structure and rollers fitted to carriages mounted on SM crates. Each SM slides into its resting lace inside the ALICE L3 magnet on two U-shaped aluminum rails, allowing the installation of SM in ALICE during the LHC shutdown periods.

5 EMCal beam test at CERN

The performance of the first ALICE EMCal modules constructed according to final design was studied in CERN SPS and PS test beam lines. The test utilized a stacked 4×4 array of EMCal modules (8×8 towers). All towers were instrumented with the full electronics chain with shapers and APD gains operated as planned in ALICE. A LED calibration system was installed in order to monitor time-dependent gain changes. The readout of the front end electronics used the standard ALICE data acquisition system.

The performed studies demonstrate:

(i) an average light yield of (4.3 ± 0.3) photoelectrons/MeV;

(ii) an energy resolution as shown in Fig. 2 (left panel) compared with a GEANT3 simulation (dashed line). The increase of the stochastic term, representing a worse intrinsic resolution compared to the Monte Carlo simulations, is mainly due to light attenuation and light collection inefficiencies which were not modeled. The small increase of the constant term demonstrates a stable, high quality detector fabrication and a good tower-by-tower calibration;

(iii) a uniformity of the response within 1% and a good linearity of the response to electrons in the energy range 10-100 GeV;

(iv) a position resolution described by $1.5 \text{ mm} \oplus 5.3 \text{ mm}/\sqrt{E(\text{GeV})}$;

(v) a hadron rejection factor as shown in Fig. 2 (right panel). Results from a Monte Carlo simulation are also shown for an electron identification efficiencies of 90%. A rejection factor of 10^2 to 10^3 is obtained over the energy range of 40 GeV to 100 GeV. Hadron/electron rejection can be further improved by considering the characteristic shower shapes, as hadrons produce showers with wider spatial distributions than electrons.

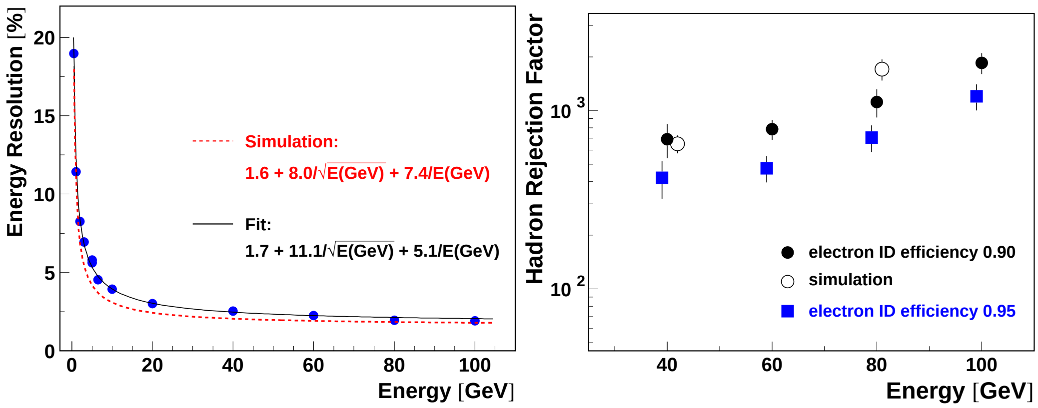

Figure 2: Left: Energy resolution for electrons as a function of the incident beam momentum. The beam energy spread was subtracted from the measured result. The dashed curve represents the resolution obtained from Monte Carlo simulations. Right: Hadron rejection as a function of the incident hadron beam energy for an electron identification efficiency of 90% (circles) and 95% (squares). Error bars represent the total uncertainty. The open circles show the result from a Monte Carlo simulation for 90% electron identification efficiency.

6 EMCal Commissioning at CERN

The four installed EMCAL modules have been commissioned from August up to December 09 using data from cosmic ray runs and data from the first pp collisions delivered from the LHC accelerator into the ALICE detector. Cosmic ray signals into the four super-modules triggered by the ALICE TOF paddles are shown in Fig. 3.

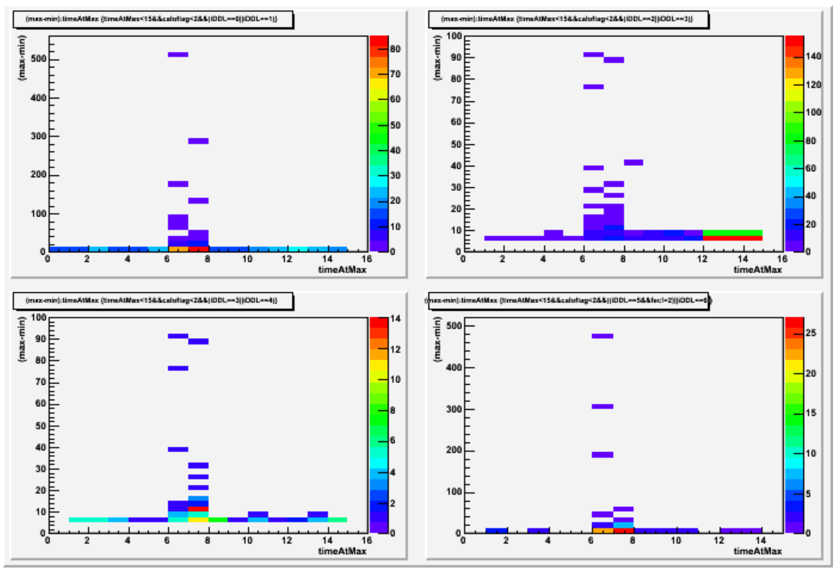

Figure 3: Cosmic signals in the four EMCal super-modules as a function of the time bin.

The different detector critical components, such as DCS (Detector Control System), the Front End Electronic readout (FEE cards), L0 local trigger generation (TRU, Trigger Region Unit cards), L1 (jet) triggering (STU, Summary Trigger Unit) board and the LED monitoring system have been extensively tested. In addition, software is being developed to include the EMCal into the ALICE High Level Trigger system. The calibration of the detector using the π^0 mass reconstruction is underway.

6.1 Detector Control System

The EMCal DCS (Detector Control System) setup was improved adding a new worker node to split the load between high voltage and low voltage controls. Control applications were developed to include the STU into the DCS system. Additional work was performed to include ACT (Alice Control Tool) into the EMCal DCS for automatically negotiation of interlocks.

6.2 Front End Electronics

Commissioning of the Front-end Electronics was initially performed by basic signal checking. Noisy/dead channels detector maps have been produced such the one shown in figure 4.

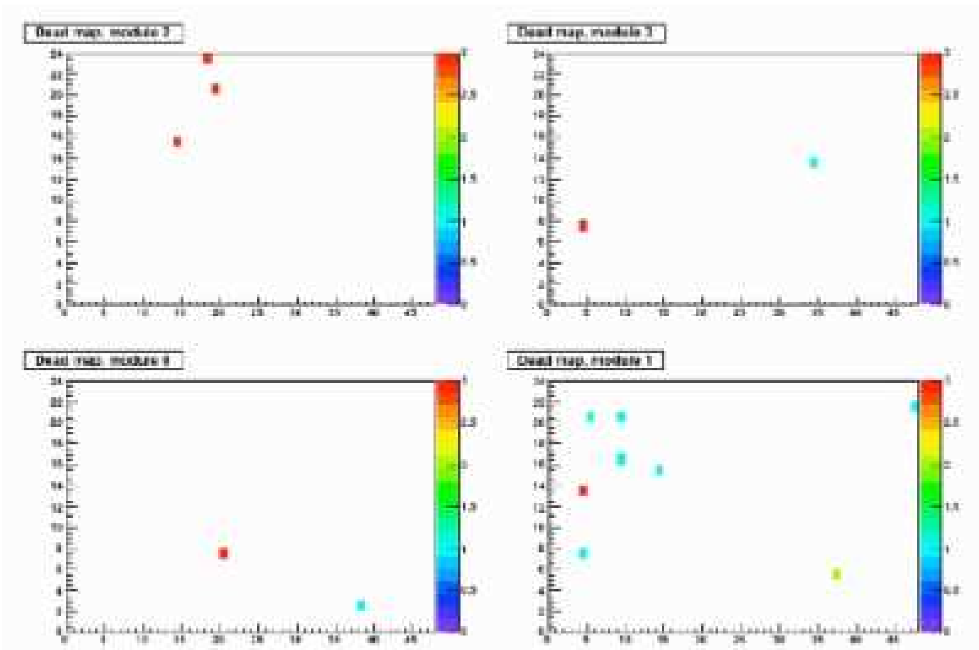

Figure 4: Noisy channels/towers in the 4 EMCal super-modules during the first run.

Investigations have been carried on to find out the causes of noise problems. It turned out that in most of the cases the noise could be eliminated or reduced by tightening loose connectors or with appropriate shielding such as in the case of pick up noise from temperature sensors.

Subsequently, the FEE card firmware has been rewritten to handle Zero-data Suppression (ZS), Sparse Data Scan (SDS) and multi event buffering in order to allow the EMCal detector to produce events with a data size size compatible with the ALICE bandwidth requirements.

6.3 Hardware Trigger and High Level Trigger

Trigger generation and timing studies have been performed to bring the L0 signal in time with the ALICE trigger scheme using cosmic data runs taken in coincidence with the TOF (as shown in figure 3). TRU Zero Suppression and Sparse Data Scan have been implemented to allow more compact trigger data size in the on-line stream. Software classes have been developed to recompute trigger primitives from raw data stream for on-line monitoring purposes. STU programming was performed to allow L1 trigger generation and communication debugging between TRUs and STU is underway.

The Alice High Level Trigger (HLT) system performs data reduction, trigger decisions based on on-line reconstruction and on-line detector calibration. Software development work for on-line monitoring and calibration was done to produce an histograming component able to produce the relevant histograms on-line. Low level monitoring information such as channel maps is presently implemented and work is underway to implement L1 (jet) trigger cross checks at the HLT level and on-line reconstruction of π^0 mass.

Raw data tower signal extraction was implemented using different methods (fitting, peak-finder, neutral-network) with the final goal to have a reliable and accurate algorithm performing fast enough to be used in the High Level trigger and offline reconstruction. Using the same algorithm will guarantee the absence of systematic errors between the two schemes.

Results from the comparison of different methods are shown in the figure 5 where a typical LED signal from a single tower is shown on the left panel and the distributions of the difference between the amplitude extracted with a 2-parameter standard Minuit fit and the candidate methods is visible on the right. Additional fine-tuning and benchmarking on the HLT cluster is required to make the final selection.

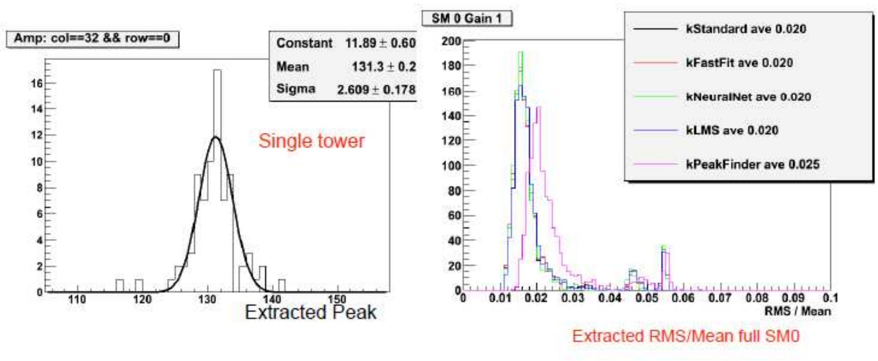

Figure 5: Comparison of different peak extraction algorithms. The LED delay scan run has been used to obtain overlapping peaks in order to test the extraction algorithms in the worst-case scenario.

6.4 Calibration

The π^0 mass was extracted using pp data collected during the first collisions delivered into ALICE during December 09. A lower mass shift was observed in this preliminary data. Investigations are underway to pin down the observed difference and resolve it. Non-linearity studies using Geant simulation have been done throwing single γ into the EMCal acceptance with a flat p_T distribution. However tower energies need to be smeared with the resolution effects (photo-electrons fluctuations), digitized with the presumed digitization factor (16 MeV/channel), and the ADC Zero Suppression applied (eliminate all towers with ADC=2 or less). In addition, imperfect track matching between clusters into the EMCal and ESD tracks contributes to the observed mass shift so studies are underway focusing on updating the EMCal geometry information and to debug the tracking code.

7 Offline

7.1 Photons and π^0 production

The LNF group has largely contributed to the EMCal Physics Performance Report (PPR), by editing of the photon section and preparing all the simulations needed for the other chapters related to jets and electron/b physics. PYTHIA predicts that it will be possible to measure up to about 150 GeV direct prompt photons (parton annihilation and Compton processes) in pp and Pb-Pb collisions, with good accuracy employing shower shape and isolation cut techniques. These predictions were in good agreement with NLO calculations regarding the direct photon yield (prompt plus fragmentation, not decay). The goodness of the PYTHIA predictions was studied with other particle generators, like HERWIG. The main conclusions were that the yield of direct prompt photons is similar but the direct fragmentation photons is half the one obtained with PYTHIA due to also the suppression of jets of a factor about 2.

Another topic in the PPR was the π^0 and η measurement, EMCal can measure π^0 in pp collisions via invariant mass from 1 to 10 GeV with good efficiency, for higher energy the efficiency drop due to the overlap of the photon showers at higher energies, and for lower energies the efficiency drops because of the energy thresholds of the calorimeter. It was shown that the width of the peak was about 10-12 MeV/c2. η can also be measured in pp collisions with invariant mass techniques from 2 GeV with a width of 30 MeV/c2. π^0 can also be measured in minimum bias PbPb collisions in the same energy range with a larger width of 16-18 MeV. For higher energies, shower shape techniques can be used to identify the π^0. It was obtained that this technique can be used from 10 to 50 GeV with average identification efficiency of 70% and purity of 60%. For energies higher than 50 GeV, the only way to separate direct photons and π^0 is with isolation cuts, which can also be used to improve the photon yield at lower energies. We showed that combining isolation cuts and shower shape we can have a signal (prompt direct photon) to background (clusters originated by jets) larger than 10 for energies larger than 20 GeV in pp and PbPb collisions.

The correlation between prompt photons and jets or just hadrons was also studied. In fact while the modification of the jet fragmentation function is due to the parton losing energy when traversing a QCD medium the QGP, on the opposite the photon does not feel the medium so it can provide directly the energy and direction of the original parton on the opposite side.

7.2 Jet quenching

Jet quenching is typically explained by a higher radiative energy loss in a dense medium, which, with respect to the vacuum case, which allows partons produced at large p_T to further emit gluons, to decrease the high-p_T multiplicity and enhance the low-p_T one.

For this purpose a Monte Carlo event generator was implemented with medium-modified splitting functions in the HERWIG parton shower algorithm, whose evolution satisfies the angular ordering prescription. Following the Q-PYTHIA implementation, we added to the Altarelli–Parisi splitting function a term depending on the medium properties, the virtuality and the energy of the radiating parton.

The measurement of a jet p_T can be approximated by the sum of three independent contributions:

$$< \delta p_T^2 > = < \delta p_T^H >^2 + < \delta p_T^P >^2 + < \delta p_T^{UE} >^2 \tag{1}$$

where H, P and UE stand for hadronization, perturbative radiation and underlying event contributions. Their dependences in a leading order approximation on resolution are:

$$< \delta p_T^P > \approx \log R + \mathcal{O}(1), < \delta p_T^{UE} > \approx R^2 + \mathcal{O}(R^4), < \delta p_T^H > \approx \frac{-1}{R} + \mathcal{O}(R) \tag{2}$$

from what is clear that an optimal choice of R is needed depending on which contributions should be minimized in a certain physics case.

The hadronization term in 1 accounts for the energy loss due to daughter hadrons ending up outside the jet cone coming from mother partons lying inside the cone. The effect grows inversely proportional to R and dominates over other contributions at very small R. In order to compare experimental data to parton level analytical calculations one has to take into account this energy shift due to hadronization. H and UE contributions go in opposite directions and they can partially cancel each other depending on the jet radius. For the large radius used at Tevatron, say $R = 0.7$, UE effects dominate and are responsible, for example, for the large uncertainties in the inclusive jet spectrum below $p_T = 100$ GeV.

Pileup and underlying event background contaminate the jet proportionally to its area. As a consequence, in the ALICE Heavy Ion Environment we will be forced to the use of small jet resolutions. This also means that we will need to have a neat proton proton reference for the different jet observables at small R. With this purpose we have performed a MC study of the hadronization corrections to the jet spectrum in proton-proton collisions at LHC energies for different jet resolutions R and for the two, in our view, key algorithms: k_T and antik_T. In Fig. 6 we see that at small R hadronization effects are large while at large R they are negligible. Hadronization effects are stronger at low-intermediate jet p_T. At larger values of p_T jets become more collimated: moving up in jet energy is qualitatively equivalent to increasing R and consequently hadronization effects decrease.

7.3 Code development

The approaching data taking, forced to develop software tools needed and still missing like the final calibration from cosmics, the π^0 calibration task the bad channel map awareness of the code, the first year geometry implementation (4 Super modules instead of 12), the QA tools to check the goodness of the simulated/real data reconstructed.

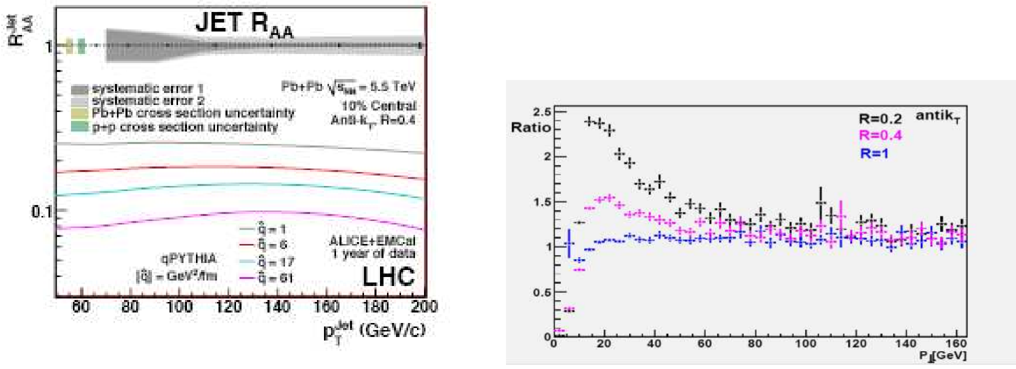

Figure 6: (color online). Left: Jet quenching (R_{AA}) for central Pb-Pb normalized to p-p for various densities ad calculated by Q-PYTHIA. Systematic error in the measurement with EMCal in ALICE is also shown. Right: Parton to hadron spectra for $R = 0.2$, 0.4, 1.

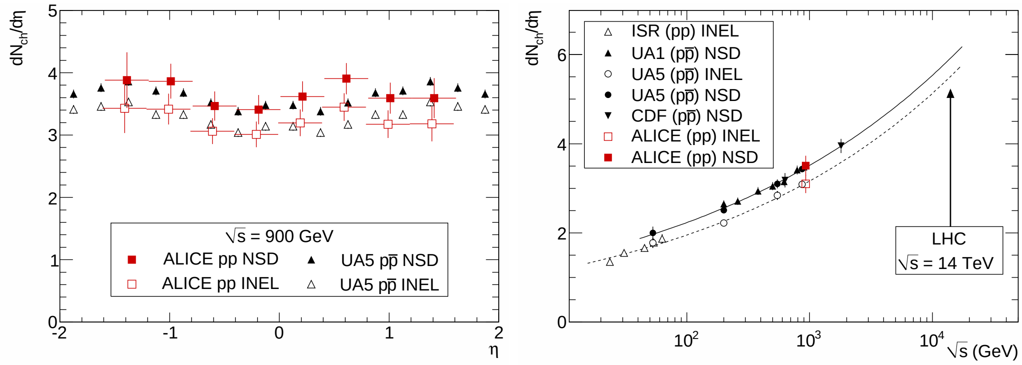

Figure 7: Left: Pseudo-rapidity dependence for Inelastic (INEL) and Non Single Diffractive (NSD) events. The errors shown are statistical only. The systematic error is about 7% Right: Charged-particle pseudo-rapidity density in the central rapidity regions function of the center-of-mass energy. The curves indicate the fit (for both INEL and NSD) using a power-law dependence on energy.

8 Data taking and first results

After the long period of shutdown, on 23$^{\rm rd}$ November 2009, during the early commissioning of LHC, two counter-rotating pilot proton bunches were circulated for the first time concurrently in the machine at the LHC injection energy pf 450 Gev per beam.In the ALICE experiment, the collision region was centered very well in both the longitudinal and the transverse directions and 284 events were recorded. The events were immediately reconstructed and analyzed both on-line and offline. We have used these events to measure the pseudo-rapidity density of charged primary particles in the central region as shown in Fig. 7. These results are consistent with previous measurements in proton-anti-proton interactions at the same center-of-mass energy. They also illustrate the excellent functioning and the rapid progress of the LHC accelerator, and both the hardware and software of the ALICE experiment, in this early start-up phase. Later on 6$^{\rm th}$ December, the luminosity run was declared and a more robust amount of data was collected for both physics and debugging the ALICE detector.

9 Plans for 2010

In 2010, the assembly of the remaining EMCal modules, strip-modules and SuperModules will be completed. The SuperModules will be inserted in ALICE if for any reason a suitable installation window will be available. Presently the schedule of LHC is not allowing for such a possibility since a long proton-proton run and 4 weeks of Pb-Pb run are foreseen. Therefore the long data taking will allow to complete the debugging of the EMCal detector and to analyze many different reactions in both proton and Lead collisions.

10 Conferences and Papers

10.1 Conferences

1. N. Bianchi, *Jet quenching at ALICE*, WONP 2009, Havana (Cuba), February 2009.
2. G. Conesa, *High pT direct photon measurement and correlation with jets in ALICE*, XXXII Workshop on Nuclear Physics in Brasil, Agua de Lindoia (Brasil), September 2009.
3. G. Conesa, *High pT direct photon measurement and correlations with jets at the LHC with ALICE*, Workshop on High-Density QCD at the LHC and Cosmic Rays, Santiago de Compostela (Spain), February 2009.
4. G. Conesa, *High pT photons and jets predictions with PYTHIA and HERWIG in pp collisions at s = 14 TeV at LHC*, Quark Matter 09, Knowxville (USA), March 2009.
5. L. Cunqueiro, *Monte Carlo for Jet Quenching*, Workshop on high-density QCD at the LHC and in cosmic rays, Santiago de Compostela (Spain), February 2009.
6. L. Cunqueiro, *QPythia Monte Carlo*, 4^{th} International workshop High p_T physics at LHC 09, Prague, March 2009
7. L. Cunqueiro, *Quenched jets and algorithms*, Workshop on Jet and Photon Physics and High Level Trigger, LNBL (USA), April 2009
8. L. Cunqueiro, *Tecniche Monte Carlo per la fisica dei jet*, Quark Matter Italia, Rome, April 2009
9. L. Cunqueiro, *R-dependence of p_T spectra in reconstructed jets*, Quark Matter 09, Knowxville (USA), March 2009.
10. P. Di Nezza, *Jet capabilities in the HI environment at LHC*, Workshop on high-density QCD at the LHC and in cosmic rays, Santiago de Compostela (Spain), February 2009.
11. P. Di Nezza, *Alice: l'esperimento e la fisica, LHC: la fisica, la macchina e gli esperimenti* Ischia, October 2009.

10.2 Publications

1. K. Aamodt et al., (ALICE Coll.), Eur. Phys. J. C **65**, 111, (2010), `arXiv:0911.5430` (2009).
2. J. Allen et al., (ALICE EMCAL group), arXiv:0912.2005v1 (2009), Nucl. Instr. and Meth. (2010).
3. A. Accardi, F. Arleo, W.K. Brooks, D.D' Enterria, V. Muccifora, La Rivista del Nuovo Cimento **032**, 439, (2009).
4. N. Armesto, L. Cunqueiro and C. A. Salgado, Eur. Phys. J. C **63**, 679, (2009).
5. N. Armesto, G. Corcella, L. Cunqueiro and C. A. Salgado, JHEP **0911**, 122, (2009).
6. F. Ronchetti, J. Phys. C **160**, 012012, (2009).
7. EMCal Coll., *ALICE Electromagnetic Calorimeter Physic Performance Report (2009)* .
8. A. Casanova and G. Conesa, *Prompt photon identification in the ALICE - EMCal calorimeter: The Isolation Cut Method at the generation level*, ALICE-INT-2009-02.

10.3 Seminars

1. N. Bianchi, CERN, July 2009 ; CERN, September 2009.
2. G. Conesa, USP, Sao Paulo, September 2009; IReS, Strasbourg, March 2009; Grenoble, March 2009; IPN, Lyon, February 2009.
3. L. Cunqueiro, CERN, February 2009; Frascati, June 2009.
4. A. Fantoni, Paris VI U., Paris, April 2009; CERN, December 2009.

FINUDA

L. Benussi (Art. 23, Resp), M. Bertani, S. Bianco, M. A. Caponero (Ass.), F. L. Fabbri (Ass.)
P. Gianotti, M. Giardoni, V. Lucherini (resp. naz.), E. Pace, M. Pallotta (Ass.), S. Tomassini,
L. Passamonti (Tecn.), D. Pierluigi (Tecn), F. Pompili (Art. 23), A. Russo (Tecn.)

1 Introduction

FINUDA (FIsica NUcleare a DAϕne) is an experiment devoted to hypernuclear physics studies at DAΦNE. Hypernuclei are nuclear systems in which one or more nucleons are replaced by hyperons. This feature adds explicit strangeness to the nuclear system allowing to study, in more general terms, the baryon-baryon interaction. FINUDA produces single-Λ hypernuclei via the reaction:

$$K^- + ^A Z \rightarrow^{A-1}_{\Lambda} Z + \pi^- \quad (1)$$

by stopping K^- from $\phi(1020)$ decay almost at rest into thin (~ 0.2 g cm^{-2}) nuclear targets. The spectroscopy of the produced hypernuclear levels is performed by measuring the momentum of the outgoing π^-. The products of the sub-sequent decay of the Λ bound to the nucleus can also be detected by FINUDA, allowing to investigate simultaneously the decay mechanisms of hypernuclei.

The hypernuclear program includes also the search for neutron-rich hypernuclei, systems with a large N/Z ratio, which could give information on nuclear matter under extreme conditions: this can have implications in nuclear astrophysics [1]. The unique combination of the clean K^- source (DAΦNE) and the very transparent and complete detector optimized for the study of the interactions of Kaons in thin nuclear targets (FINUDA) has allowed the study of new items, not foreseen in the original proposal, such as the ^{7}Li(K$^+$, K^0) reaction close to threshold [2] and topics related to the possible existence of Deeply Bound Kaonic States (DBKS). The interest in such an item was triggered by a theoretical suggestion by Akaishi and Yamazaki [3] about possible aggregates of few nucleons strongly bound by a K^-, with a narrow width and a density even ten times larger than the ordinar nuclear matter. The existence of such systems is however highly debated, and the high acceptance of the FINUDA spectrometr coupled to its ability to reconstruct final states with several charged particles turned out well suited to shed light on this item.

The FINUDA Collaboration consists of about 60 physicists coming from LNF, several INFN sections and Italian universities (Bari, Brescia, Pavia, Torino, Trieste) plus foreign researchers from Canada, the University of Victoria, Vancouver; from Japan, the KEK laboratory of Tsukuba, RIKEN and the University of Tokyo; from South Korea, the Seoul National University, from Russia, the Joint Institute for Nuclear Research of Dubna and from Iran, the S. Beheshty University of Teheran.

2 FINUDA Activity

The activity of the LNF FINUDA group in 2009 has been devoted to the analysis of the whole set of data corresponding to a total integrated luminosity of about 1.2 fb^{-1}.

In the first data taking (December 2003-March 2004), a total of 220 pb^{-1} (190 for physics) were collected with a set of eight targets: 2 ^{6}Li, ^{7}Li, 3 ^{12}C, ^{27}Al and ^{51}V. No measurements on medium A targets were performed before with stopped K^- and FINUDA showed that reaction (1) has a reasonable capture rate for p-shell nuclei only, and the analysis was focused mostly on light hypernuclei.

The targets installed for the 2006-2007 data taking were: 2 ^{6}Li, 2 ^{7}Li, 2 ^{9}Be, D_2O, ^{13}C, and 966 pb^{-1} were collected.

On the detector side the LNF group was on duty to follow the upgrade of the DAQ system in order to be ready for the third data taking period requested by the experiment for 2009-2010, that, however, was not approved.

2.1 Hypernuclear Spectroscopy Studies

The inclusive momentum distribution of π^- emerging from the targets in coincidence with a K$^-$ stop is shown in the insets of Fig. 1 for ^{7}Li, ^{13}C, D_2O and ^{9}Be: in the higher momentum region peaks or "bumps" can be clearly noticed, that indicate the production of hypernuclei. Considering the energy and the momentum conservation laws for the reaction (1), one can get the hypernucleus mass in the specific level i by the following equation $m_{Hyp,i} = \sqrt{(m_K + m_{^AZ} - E_{\pi^-,i})^2 - p^2_{\pi^-,i}}$ where m_K is the K mass, $m_{^AZ}$ is the target nucleus mass for the ground state, $m_{Hyp,i}$ the mass of the particular ^{A}Z hypernucleus formed in the ith energy level state, p_i is the pion momentum for the produced hypernucleus level and E the corresponding pion total energy. It is then possible to calculate the hypernuclear level binding energy $B_{\Lambda,i} = m_{^{A-1}Z} + m_\Lambda + m_{Hyp,i}$ where $m_{^{A-1}Z}$ indicates the mass of the hypernuclear core in its ground state and m_Λ the mass of the Λ particle. The experimental data have been fitted with histograms representing the backgrounds plus Gaussian curves for the signal peaks. The width of the Gaussians has been left free to vary and resulted in values between 1.65 and 1.95 MeV, depending on the target. The results of the fit are superimposed to the experimental data in Fig. 1 together with the Gaussian distributions corresponding to the hypernuclear peaks. The obtained values for the ground and excited levels of the formed hypenuclei agree very well with data in the literature. From the number of events in the Gaussians, corresponding to the number of formed hypernuclei, the capture rate can be evaluated, in other words the formation probability per stopped K$^-$: this has never be done before for such wide range of A. Preliminary analysis shows for the four elements under study a decreasing capture rate as a function of the atomic mass A. Taking into account all the bound states of each hypernucleus, an overall formation probability has been found ranging from about 0.15 % for $^{7}{}_\Lambda$Li to 0.03 % for $^{16}{}_\Lambda$O, with $^{9}{}_\Lambda$Be and $^{13}{}_\Lambda$C values around 0.06 %.

2.2 Study of the Hypernuclear Weak Decay

A Λ-hupernucleus in its ground state undergos a weak decay to an ordinary nucleus. The dominant weak decay modes of a bound Λ-hypernucleus are the following:

- Mesonic Weak Decay (MWD) in which the Λ decays as in free space:
  $\Lambda \to p + \pi^-$ or $\Lambda \to n + \pi^o$. Due to the empirical $\Delta I = 1/2$ rule in the strangeness-changing non-leptonic weak decay, in the free space the branching fraction of $\Lambda \to p + \pi^-$ decay is approximately twice larger than that of $\Lambda \to n + \pi^o$. But in the nuclear matter the decay of the Λ may not follow the same rule. Moreover, the final state nucleon produced in the MWD has a very low momentum ($<$ 100 MeV/c), therefore the process is Pauli-blocked (the Fermi momentum for a nucleon in nuclei is 270 MeV/c) and it is very suppressed in all but the lightest nuclei.

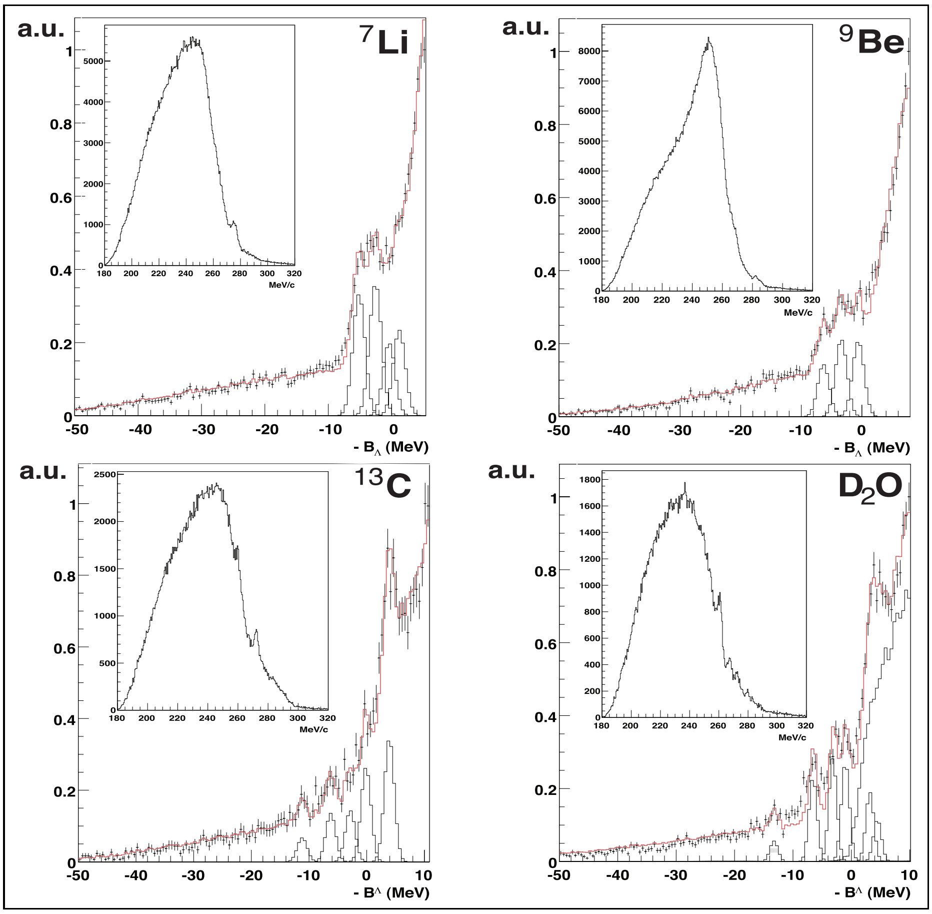

Figure 1: (color online). Binding energy (- B_Λ) distribution in the bound region for the ^{7}Li, ^{9}Be, ^{13}C and D_2O targets. The insets represent the corresponding π^- inclusive momentum distributions.

- Non-Mesonic Weak Decay(NMWD) which takes place through the weak interaction of the Λ with neighboring nucleons: $\Lambda + p \to n + p$ or $\Lambda + n \to n + n$. The momentum of the outgoing nucleons is 417 MeV/c and the decay has much larger phase space compared to the MWD and then is not Pauli-blocked.
- Another non-mesonic channel can be the so called "two-nucleon-induced-decay" $\Lambda NN \to NNN$ which has not been experimentally established yet.

The hypernuclear NMWD gives unique information on the four baryon weak process $\Lambda N \to NN$, with possible hints also on the ΛNN interaction.

FINUDA is optimized to perform high resolution spectroscopy of π^-s in the region 260-280 MeV/c, the interval for the production of the hypernculear states. It is also able to detect in coincidence the π^-'s from MWD, with momenta down to 80 MeV/c, and protons from NMWD with momenta down to 180 MeV/c. FINUDA succeded to measure the MWD and NMWD for p-shell Λ-hypernuclei formed in the ^{6}Li, ^{7}Li, ^{9}Be, ^{12}C, ^{13}C and D_2O targets.

2.2.1 Mesonic Weak Decays

MWD was studied [9] selecting events in which a low momentum π^- was detected in coincidence with a high momentum π^-, originating from the formation of ground or low lying excited hypernuclear states of ${}^7_\Lambda$Li, ${}^9{}_\Lambda$Be, ${}^{11}{}_\Lambda$B (from ^{12}C targets), and ${}^{15}{}_\Lambda$N (from ^{16}O nucleus).

The π^- momentum resolution is $\Delta p/p \simeq 1\%$ FWHM at 270 MeV/c and $\simeq 6\%$ FWHM at 110 MeV/c. The acceptance function for low momentum π^-'s was evaluated with simulated tracks. Background from quasi-free Λ production and decay was simulated and subtracted from the ${}^{11}_\Lambda$B and ${}^{15}_\Lambda$ N spectra. The decay π^- kinetic energy spectra were then extracted and compared with theoretical predictions of decay strength functions [5] and a good agreement was found. Decay rates and decay amplitudes were calculated, using, for each hypernucleus, known $\Gamma_{tot}/\Gamma_\Lambda$ or a linear fit to the measured value from the available A = 4-12 Λ-hypernuclei. FINUDA measured for the first time the π^- momentum spectra from MWD of ${}^7{}_\Lambda$Li, ${}^9{}_\Lambda$Be, ${}^{11}{}_\Lambda$B and ${}^{15}{}_\Lambda$N. MWD decay rates $\Gamma_{\pi^-}/\Gamma_\Lambda$ have also been evaluated and compared with previous measurements and theoretical calculations. The spin-parity assignments $J^\pi({}^7_\Lambda\mathrm{Li}_{g.s.}) = 3/2^+$ and $J^\pi({}^{11}_\Lambda\mathrm{B}_{g.s.}) = 5/2^+$ were confirmed and a new assignment, $J^\pi({}^{15}_\Lambda\mathrm{N}_{g.s.}) = 3/2^+$ was made based on the shape of the MWD spectra and the evaluated decay rates.

2.2.2 Non Mesonic Weak Decays

NMWD was studied [10] by selecting events with a π^- from the hypernucleus formation in coincidence with a proton from its decay. Kinetic energy spectra of the decaying protons were obtained featuring a detection threshold as low as 15 MeV, and a resolution $\Delta T/T \simeq 1.5\%$ FWHM at 80 MeV. The background due to the absorbtion of K^- on a (np) cluster of the target nucleus was simulated and subtracted, as described in [8]. Acceptance corrections were applied. All the spectra, show a similar shape, *i.e.* a peak around 80 MeV, corresponding to about half the Q-value for the free $\Lambda p \to np$ weak reaction, with a low energy rise due to the Final State Interactions (FSI) and an eventual contribution from two-nucleons induced NMWD. FINUDA was the first experiment to perform such a systematic study of the proton kinetic energy spectra following the NMWD of Λ-hypernuclei in a wide mass range (A=5-16), down to a kinetic energy of 15 MeV. Each proton spectrum was fitted, usign the data from 80 MeV onwards (shaded areas), with a gaussian function, whose width is due to the nucleon fermi motion: the obtained results are shown by the black solid line in Fig. 2 and reflect the contribution of the single-nucleon NMWD. To disentangle the two different contributions to the low energy tails, the following ansatz can be applyed: the FSI contribution should be linear with A, while the two-nucleon induced NMWD should be independent from A. Referring to Fig. 2, it is possible to calculate, for each spectrum, the value of the shaded area (A_{high}) and of the remaining lower energy part (A_{low}, in which are mainly concentrated the contribution of the FSI and of the two-nucleon induced NMWD. The ratio $A_{low}/(A_{low}+A_{high})$, plotted as a function of the hypenucleus mass number A, is shown in Fig. 3, nicely fitted by a linear function. The linear increase indicates the expected linear increase with A of the FSI contribution, while the intercept at A=0 of the line is realted to the constant contribution of the two-nucleon induced NMWD. Writing now the ratio as a function of Γ_2/Γ_p, were Γ_2 is the width of $\Lambda NN \to nNN$ while Γ_p correspond to $\Lambda p \to np$, it can be easily calculated $\Gamma_2/\Gamma_p = 0.43 \pm 0.25$. Assuming from theory that $\Gamma_2/\Gamma_p = (0.48 \pm 0.08)$ one can determine $\Gamma_2/\Gamma_{NMWD} = 0.24 \pm 0.10$, indicating the relevant role of the two-nucleon induced NMWD in hypernuclei.

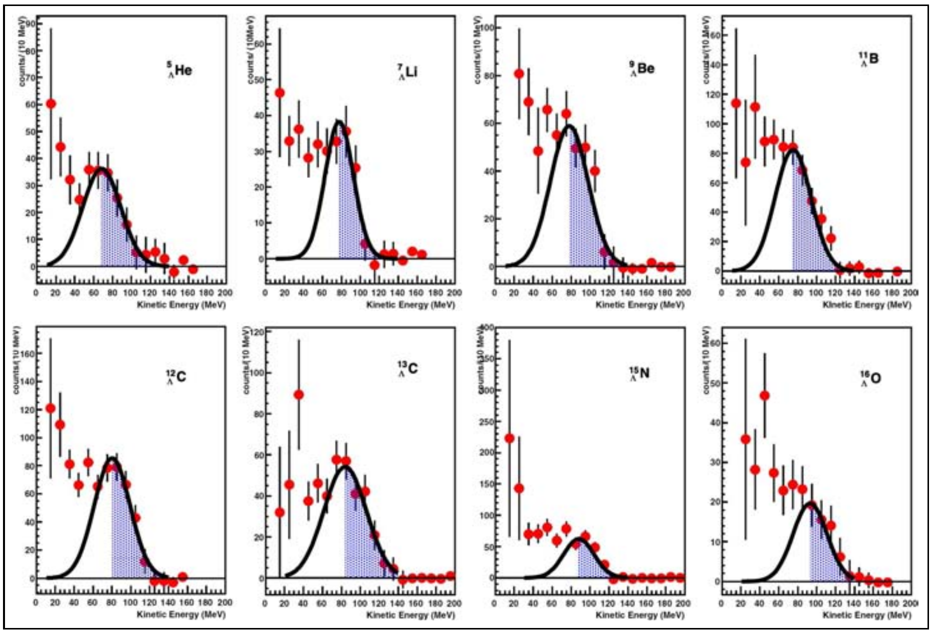

Figure 2: Proton kinetic energy spectra from the NMWD of (from left to right): ${}^{5}{}_{\Lambda}$He,${}^{7}{}_{\Lambda}$Li, ${}^{9}{}_{\Lambda}$Be,${}^{1}1_{\Lambda}$B, ${}^{12}{}_{\Lambda}$C, ${}^{13}{}_{\Lambda}$C,15$_{\Lambda}$N and ${}^{16}{}_{\Lambda}$O and . The blue filled area is the spectrum area in which the single-nucleon induced NMWD is prevalent.

2.3 Nuclear bound kaonic systems

The main features of $\bar{K}N$ and $\bar{K}A$ interactions don't foresee clearly detectable levels since the expected binding energies are around 10-30 MeV, and the widths of 80-100 MeV exclude the possibility of an experimental observation. Nevertheless, a different approach of recent theoretical works by Akaishi and Yamazaki [3] shows the possibility that $\bar{K}N$ interaction, under certain conditions, could became strongly attractive allowing the formation of kaon-multinucleon systems with a binding energy varying from 86 MeV to 113 MeV, depending on the target nucleus, and with widths of 20-40 MeV. These Authors also suggest that the presence of a K^- inside the nucleus should enhance the binding energy of the system increasing the density several times that of the ordinary nuclei. These aggregates should be formed with higher probabilities when the kaon interacts with light nuclei.

The first paper published by FINUDA on the evidence of a Deeply Bound K$^-$-Nuclear States observed in the (K^-pp) system [11] presented the first observations in agreement with Akaishi-Yamazaki model, but in the following years several criticisms raised [13]. In that it was claimed that the data could be simply explained by FSI effects. Due to the limited statistics at disposal, the results in [11] were obtained summing the data from several targets: 2 ^{6}Li, 1 ^{7}Li and 3 ^{12}C. A way to confirm the FINUDA interpretation would be the observation of the same signal in different targets, where the FSI effect should act differently, more sizably in heavier nuclear media: the larger statistics of the second FINUDA data taking is actually being analyzed to pursue this scope.

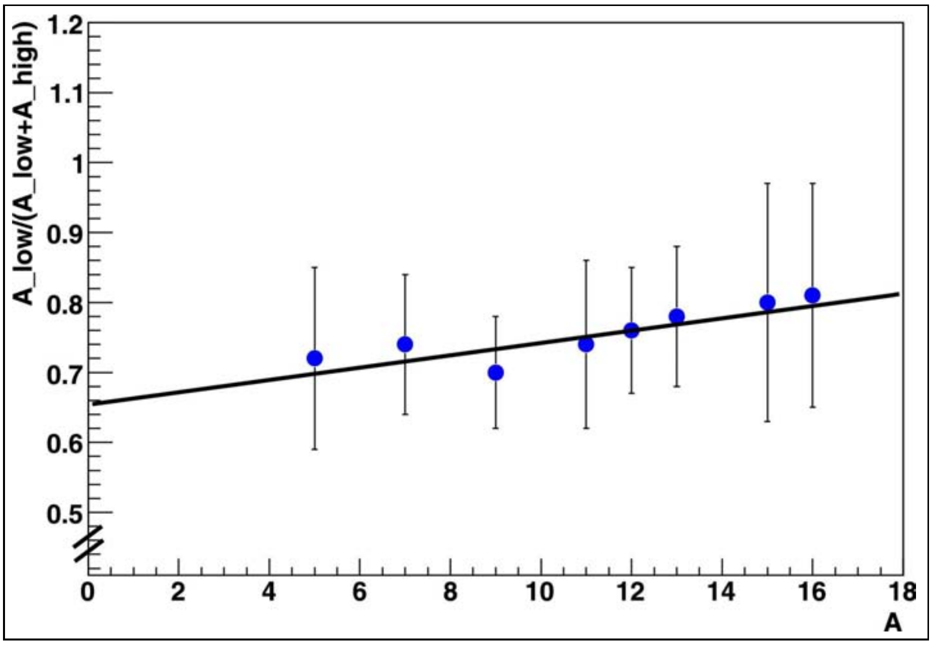

Figure 3: The ratio $A_{low}/(A_{low}+A_{high})$ as a function of the hypernuclear mass number.

2.3.1 K^--multinucleon absorption

In the FINUDA paper [15] the invariant mass spectrum of the (Λd) system following the capture of K^-_{stop} in ^{6}Li was shown. The presence of such a system produced in light nuclei would be a nice confirmation of a genuine bond, since in this case the FSI contribution should be largely reduced as compared to systems decaying in nucleons.

Thanks to the excellent (dE/dx) particle identification of FINUDA, it has been possible to clearly detect also tritons. Correlated Λt pairs [12] from K^-_{stop}A absorption reaction in light nuclei ^{6}Li,^{7}Li and ^{9}Be have been found. Regardless of A, the Λt pairs are preferentially emitted in opposite directions. Reaction modeling predominantly assigns to the $K^-_{stop}A \rightarrow \Lambda$t (N)A' direct reactions the emission of the Λt pairs whose yield is found to range from 10^{-3} to $10^{-4}/K^-_{stop}$.

3 Activity planned for 2010

The activity for the 2010 will be dedicated to the finalization of the undergoing analysis. The LNF has recently took the responsibility to finalize the analysis on Neutron Rich Hypernuclei on the whole statistic on ^{6}Li and ^{7}Li targets. The LNF group also started a new study on the Λ production mechanism on different nuclei. Since a further period of data taking for FINUDA was not approved, in 2010, it is planned the FINUDA decomissioning. In this respect, the LNF FINUDA group will coordinate the operations in the DAΦNE hall.

4 Publications

All the following papers are published after the publication of Activity Report 2008 and within December 2009.

1. M. Agnello et al. (FINUDA Coll.), Phys. Lett. B **681**, 139 (2009).
2. M. Agnello et al., Nucl. Phys. A **827**, 303C (2009).
3. B. Dalena et al., Nucl. Instr. & Meth. A **603**, 276 (2009).
4. P. Camerini, Int. J. of Mod. Phys. A **24**, 198 (2009).
5. A. Feliciello Rivista del Nuovo Cimento **32**, 147 (2009).
6. A. Filippi and S. Piano, Hyp. Int. **32**, 173 (2009).
7. E. Botta *et al.* (FINUDA Coll.), *Recent results on mesonic weak decay of Lambda-hypernuclei*, In Strangeness in nuclear and hadronic systems SENDAI08, World Sientific press, 2009, 274-280.
8. S. Bufalino *et al.* (FINUDA Coll.), *New results on nonmesonic weak decay of Lambda hypernuclei with FINUDA*, Strangeness in nuclear and hadronic systems SENDAI08, World scientific press, 2009, 281-286.
9. S. Piano *et al.* (FINUDA Coll.), *The search for antikaon nuclear bound states, recent results from FINUDA*, In Strangeness in nuclear and hadronic systems SENDAI08, World cientific press, 2009, 308-313.
10. V. Lucherini *et al.* (FINUDA Coll.), *The FINUDA experiment at DAΦNE*, In Strangeness in nuclear and hadronic systems SENDAI08, World scientific press, 2009, 222-230.

5 Conference Presentations

1. L. Benussi, *Search for neutron rich hypernuclei with FINUDA*, 10th International Conference on Hypernuclear and Strange Particle Physics, J-Park September 2009.
2. P. Gianotti, *Study of* Λ *production on different nuclei with FINUDA*. 10th International Conference on Hypernuclear and Strange Particle Physics, J-Park September 2009.
3. V. Lucherini, *The FINUDA experiment at DAΦNE*, Strangeness in Nuclear and Hadronic Systems, Sendai, December 2008.

References

1. Y. Yamamoto et al., Nucl. Phys. A **691**, 432c (2001).
2. M. Agnello et al., Phys. Lett. B **649**, 25 (2007); ibid *Study of the* (K^+,K^0) *reaction on medium light nuclei close to threshold*, Frascati Physics Series Vol. XLVI (2007).

3. Y. Akaishi, T. Yamazaki, Phys. Rev. C **65**, 044005 (2002); T. Yamazaki, Y. Akaishi, Nucl. Phys. B **535**, 70 (2002); Y. Akaishi et al., nucl-th/0501040.

4. FINUDA Coll., *Proposal for a new FINUDA Data taking*, February 2008;

5. T. Motoba, K. Itonaga, Progr. Theor. Phys. Suppl. **117**, 477 (1994).

6. S. Kameokada et al., Nucl. Phys. A **754**,173c (2005)

7. Y. Sato et al., Phys Rev. C **71**, 025203 (2005).

8. M. Agnello et al., Nucl. Phys. A **804**151 (2008).

9. M. Agnello et al., Phys. Lett. B **681**, 139 (2009).

10. M. Agnello et al., Phys. Lett. B **685**, 247 (2010).

11. M. Agnello et al., Nucl. Phys A **775**, 35 (2006).

12. M. Agnello et al., Phys. Lett. B **669**, 229 (2008).

13. V. Magas et al., Phys. Rev. C **7**4, 0205206. (2006).

14. M. Agnello et al., Phys. Lett. B **640**, 145 (2006).

15. M. Agnello et al. (FINUDA Coll.), Phys. Lett. B **654**, 80 (2007).

HERMES

E. Avetisyan (Ass.), N. Bianchi, E. De Sanctis, P. Di Nezza, A. Fantoni (Resp.),
D. Hasch (Art. 23), A. Orlandi (Tecn.), W. Pesci (Tecn.), E. Polli, A. Viticchié (Tecn.)

1 Brief description of the experiment and of the LNF activity in 2009

The HERMES (HERa MEasurement of Spin) experiment has been taking data at the HERA storage ring in Hamburg (Germany), from 1995 to 2007. HERMES scattered polarised electron and positron beams of 27.5 GeV from longitudinally or transversely polarised internal targets to the beam pipe, in order to study the spin structure of the nucleon. Featuring polarised beams and targets, and an open-geometry spectrometer with excellent particle identification, HERMES is well suited to study the spin-dependent inclusive and semi-inclusive Deep Inelastic Scattering (DIS) reactions. The Particle IDentification (PID) capabilities of the experiment were significantly enhanced in 1998 when the threshold Cerenkov detector was upgraded to a dual Ring Imaging system (RICH), providing a full separation between charged pions, kaons and protons over essentially the entire momentum range of the experiment. With the installation of a proton Recoil Detector in 2006, the identification of hard exclusive reactions has been greatly improved.

HERMES is still a large collaboration, of about 180 physicists from 31 Institutions from 12 Countries. Italy participates with 4 groups and more than 30 physicists from Bari, Ferrara, Frascati and Rome. The Frascati group had many responsibilities since the very beginning, holding the roles of Run Coordinators, Deputy Spokespersons and Analysis Coordinator for many years. Presently it is still involved in the HERMES planning (A. Fantoni), in the Editorial Board (P. Di Nezza and D. Hasch), in the analysis groups and in many Drafting Committees, covering nearly all topics of the broad HERMES physics program.

LNF members were main responsible for the Particle Identification (PID). In particular they worked on the maintenance and code development of the PID library function, on the PID calibration, on the new data productions of 2004, 2005, 2006, 2007, 2008 and 2009 on the flux corrections to PID for different physics analysis.

The LNF group acted also as HERMES Linux administrator and represented HERMES on DESY Linux user meeting, where user requirements and future strategy for Linux support were discussed.

All the analysis with LNF people involved, have been completed. In Fig.1 the latest results on the full set of data collected with transversely polarized target are shown. On the left panel the measurements of the Sivers amplitudes in semi-inclusive DIS for production of π^+, π^0, and $K^{\pm}$, as well as for the pion-difference asymmetry are reported. They can be explained by the non vanishing naive T-odd, transverse-momentum-dependent Sivers distribution function. On the right panel the Fourier amplitudes of the single-spin azimuthal asymmetry measured in exclusive electroproduction of π^+ mesons are shown. The observed amplitude of the $sin\phi_S$ modulation is large and positive, which implies the presence of a sizeable interference between contributions from longitudinal and transverse virtual photons.

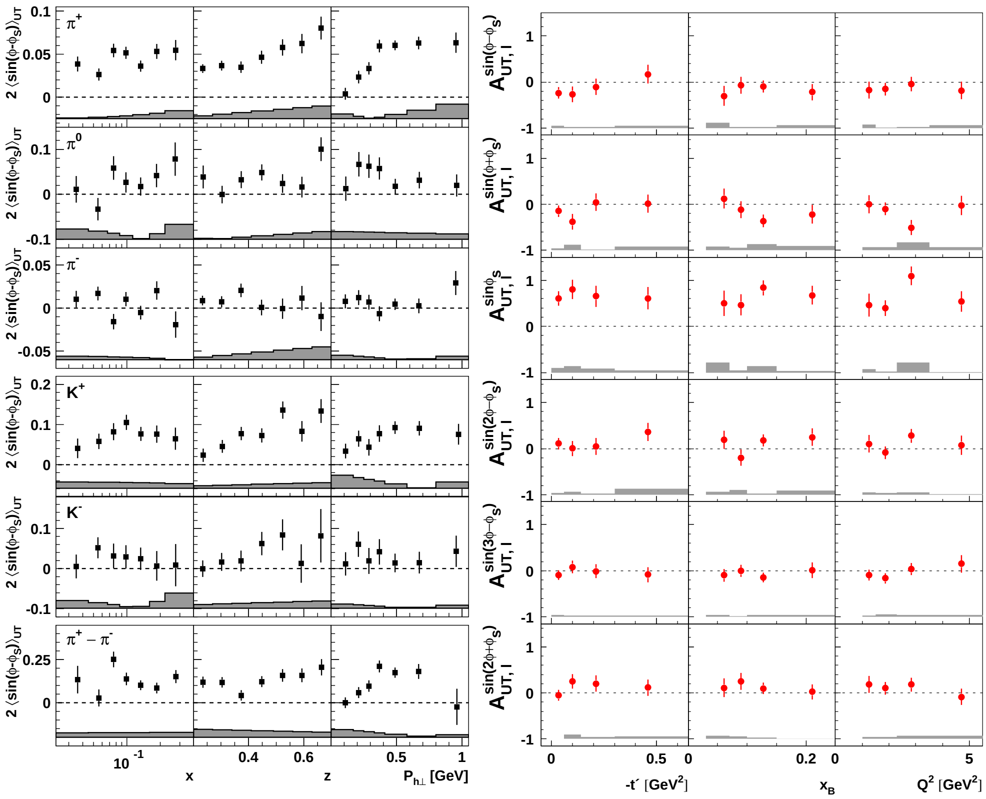

Figure 1: Left: Sivers amplitudes for pions, charged kaons, and the pion-difference asymmetry as functions of x, z, or $P_{h,\perp}$. The band is the systematic uncertainty. In addition there is a 7.3% scale uncertainty from the target-polarization measurement. Right: The set of six Fourier amplitudes ($A_{UT,l}$) describing the sine modulations of the single-spin azimuthal asymmetry for unpolarized (U) beam and transverse (T) target polarization, for the exclusive event sample. The error bars (bands) represent the statistical (systematic) uncertainties. The results receive an additional 8.2% scale uncertainty corresponding to the target uncertainty.

2 Conferences

2.1 Conference Talks

1. E. Avetisyan, *HERMES plans*, First Workshop on Data Preservation and Long Term Analysis in HEP, DESY, Hamburg, Germany, January 26-28 2009.

2. E. Avetisyan, *Recent results on exclusive meson production at HERMES*, 5th International Conference on Quarks and Nuclear Physics, Beijing, China, September 21-26, 2009.

3. A. Fantoni, *The status of the HERMES experiment*, National Scientific Committee of Nuclear Group, Rome, Italy, June 2009.

4. D. Hasch, *Spin structure of the proton*, XL Working Week of the German Nuclear Physics Society, Schleching, Germany, February-March 2009.

5. D. Hasch, *Detector integration at HERME*, Common ENC/EIC Workshop, GSI Darmstadt, Germany, May 2009.
6. D. Hasch, *GPDs: towards a 3D imaging of hadrons*, Workshop on the 'Transverse Partonic Structure of Hadrons', Yerevan, Armenia, June 21-26 2009.
7. D. Hasch, *Nucleon structure at low energy - the quest for the spin of the nucleon*, 24th International Symposium on Lepton-Photon Interaction at High-Energy, Hamburg, Germany, August 17-22 2009.
8. D. Hasch, *TMDs and friends from lepton scattering - experimental overview*, Workshop on "The Jefferson Laboratory Upgrade to 12 GeV", Seattle (USA), September 14-18 2009.
9. D. Hasch, *Experimental overview on TMD studies with lepton probes*, ECT* Workshop on Orbital Angular Momentum of Partons in Hadrons, Trento, Italy, November 9-13 2009.

2.2 Conference Organization and Advisory, Projects, Seminars, Lectures, Editors

1. N. Bianchi, Editor of The European Physical Journal A.
2. E. De Sanctis, Member of HERMES Nominating Committee.
3. P. Di Nezza, Member of HERMES Editorial Board.
4. A. Fantoni, Member of the Planning Committee.
5. D. Hasch, Member and Chair of HERMES Editorial Board.
6. D. Hasch, Organizer of the International Workshop on the 3D structure of the nucleon encoded in GPDs and TMDs within the series "The Jefferson Laboratory at 12 GeV", Sep.-Nov. 2009, Seattle (USA), September 2009.
7. D. Hasch, Discussion Leader at the XL Working Week of the German Nuclear Physics Society "Perturbative QCD and hadronic processes", Schleching (Germany), February-March 2009.
8. D. Hasch, Lecture Series on Deep Inelastic Scattering for the Physics School of SFB/TR16 "Subnuclear Structure of Matter", Bonn (Germany), August 2009.
9. D. Hasch, Transverse Spin Effects experiments at European Graduate School Basel-Tubingen (Germany), November 2009.

3 Publications of LNF Authors in Year 2009

1. A. Airapetian et al., Eur. Phys. J. C **62**, 659 (2009).
2. A. Airapetian et al., Phys. Lett. **B** 679, 100 (2009).
3. A. Airapetian et al., Phys. Rev. Lett. **103**, 152002 (2009).
4. A. Airapetian et al., JHEP **11**, 083 (2009).
5. E. Avetisyan, *Final HERMES Results on DVCS Transverse Target Spin Asymmetries*, Proc. of the 18th Particle and Nuclei International Conference (PANIC08), Elsevier Editor, 267 (2009).
6. D. Hasch, Nucl. Phys. B - Proce. Supp., Vol. **191**, 79 (2009).
7. D. Hasch, Nucl. Phys. A **827**, 101C (2009).

JLAB12

M. Aghasyan (Ass.), R. Baldini Ferroli, F. Coccetti, E. De Sanctis, L. Hovsepyan (Post-doc), M. Mirazita, J. de Oliveira Echeimberg (Bors. PD), A. Orlandi (Tecn.), S. A. Pereira (Art. 23), F. Ronchetti (Art. 23), W. Pesci (Tecn.), E. Polli, P. Rossi (Resp. Naz.), A. Viticchié (Tecn.)

1 Introduction

The JLAB12 group participates into the physics program carried on at the 6 GeV Continuous Electron Beam Accelerator Facility (CEBAF) at the Jefferson Laboratory (JLab). The program is focused on the precision study of the structure of the nucleon and the nature of the strong interaction. The JLAB12 collaboration is the result of the union, made in 2009, of two INFN collaborations already working at JLab for 18 years, AIACE and LEDA. At present it counts 41 physicists ($\sim$ 30 FTE) plus 20 technicians and it includes groups from the INFN units at: (1) the University of Bari, (2) the University of Catania, (3) the Frascati National Lab and the associated Fermi Center, (4) the University of Genova, (5) the Istituto Superiore di Sanità and Rome University "La Sapienza", and (6) the University of Rome Tor Vergata.

The Frascati JLAB12 group participates into the physics program carried on by the CLAS Coll. in Hall B which counts about 150 physicists from 36 Institutions from seven Countries.

CEBAF will increase its beam energy from currently 6 GeV to 12 GeV by 2014. This requires the upgrade of the CLAS detector, called CLAS12.

In the period covered by this report, the Frascati JLAB12 group has continued to work in the 6 GeV program and in the preparation of the 12 GeV one. In both cases it is focused on the study of the 3D-structure of the nucleon and its internal dynamics. This is achieved through the determination of new parton distribution functions which include information not only on the longitudinal but also on the transverse distributions of partons in a fast moving hadron. This information is encoded in the Generalized Parton Distribution functions (GPDs) and Transverse Momentum Distribution functions (TMDs). In addition to this physics program, in 2009 the group has completed the study of Σ^- photoproduction on neutron.

2 Transverse Momentum Dependent parton distribution functions (TMDs)

In the recent years it became clear that understanding of the orbital motion and the role of partonic initial and final state interactions of quarks is crucial in understanding the origin of the nucleon spin and in general in construction of a more complete picture of the nucleon in terms of elementary quarks and gluons. Orbital momentum of quarks can be accessed in semi-inclusive deep inelastic scattering (SIDIS) experiments ($lN \to e'hX$), when a hadron is detected in coincidence with the scattered lepton. Observables are spin azimuthal asymmetries, and in particular single spin azimuthal asymmetries (SSAs) which are due to correlations between the quark transverse momentum and the spin of the quark/nucleon.

Measurements of SSAs provide access to a list of novel distribution functions, namely Transverse Momentum Dependent distribution functions (TMDs) which contain information on the parton transverse momentum. TMDs are probability densities for finding a polarized/unpolarized parton with a longitudinal momentum fraction x and transverse momentum $\vec{k}_T$ in a polarized/unpolarized nucleon and they represents a generalization of the partonic momentum, longitudinal and transverse spin distribution functions, f_1, g_1, h_1. Two fundamental mechanisms have been identified leading to SSAs in hard processes: the Sivers mechanism [2, 3, 4, 5, 6], which generates an asymmetry in the distribution of quarks due to orbital motion of partons, and the Collins mechanism [5, 7], which generates an asymmetry during the hadronization of quarks. TMDs studies are one of the primary goal of experiments at JLab 12 GeV but their investigation has already started with the 6 GeV beam using unpolarized, longitudinally and transversely polarized target.

2.1 The 6 GeV program

Data with longitudinally polarized target and a 6 GeV electron beam have been collected in 2009 (experiment E05-133). For a longitudinally polarized target the only azimuthal asymmetry arising at leading order is the $\sin 2\phi$ moment [7, 8, 9], involving the Collins fragmentation function $H_1^\perp$ and the Ralston-Soper-Mulders-Tangerman (RSMT) distribution function $h_{1L}^\perp$ [7, 10], describing the transverse polarization of quarks in a longitudinally polarized proton [7, 8, 9, 11]. The statistic accumulated in 3.5 months of data taking of experiment E05-133, which is $\sim$ ten times that collected by the HERMES experiment in $\sim$ 10 years, will allow us for the first time a statistically significant measurement of the $\sin 2\phi$ moment. Along the line of this research program in 2009:

- a PRIN on the study of " Nucleon structure: transverse momentum, spin and orbital angular momentum" has been submitted to the Italian Ministry of Research.
- The workshop on "Transverse Partonic Structure of Hadrons" held in Yerevan (Armenia) in the period June 21-26 has been organized to address unsolved current issues of the physics of the transverse structure of the nucleon and also to identify directions for further development of this quickly developing field.
- The π^0 Beam Spin Asymmetries and Semi-Inclusive Λ polarization analyses have been completed/progressed.

2.1.1 *Beam Spin Asymmetries Measurement*

During 2009 the analysis note of the beam-spin asymmetries measurement in single neutral semi-inclusive pion electroproduction using a 5.77 GeV electron beam and the CLAS detector has been under the CLAS Coll. review. For this measurement scattering of longitudinally polarized electrons off a liquid-hydrogen target was studied over a wide kinematic region and the asymmetry, defined as the ratio of polarized and unpolarized cross-section

$$A_{LU}^{\sin(\phi_h)} = \frac{\sigma_{LU}}{\sigma_{UU}} \tag{1}$$

was extracted. In Eq. 1 the subscripts in σ_{LU} specify the beam and target polarizations, respectively (L stands for longitudinally polarized and U for unpolarized) and the azimuthal angle ϕ_h is the angle between leptonic and hadronic plane according to the Trento convention [12].

The beam-spin asymmetries in single-pion production off the unpolarized target are higher-twist by their nature [13, 14]. The higher twist observables are important for understanding the long-range quark-gluon dynamics. Different contributions to the beam SSAs, discussed so far, provide information on different leading and sub-leading parton distribution and fragmentation functions, related both to Collins and Sivers production mechanisms. At fixed and moderate values of the four momentum transfer Q^2 and at large values of x_B and z (where x_B is the fraction of the momentum of the nucleon carried by the struck quark and z is the fraction of the virtual photon energy carried by the detected π^0), the contribution of multiparton correlations or higher twist effects increases, eventually leading to a breakdown of the partonic description. Kinematical dependences of observables, thus, will provide tests of applicability of partonic description.

In CLAS we have measured the kinematic dependences of the π^0 beam-spin asymmetry on x_B, z and P_T (where P_T is the transverse momentum of the π^0). The asymmetry shows a strong enhancement at large values of z while no significant x_B-dependence is present within the measured range (see Fig. 1 right). There is also an indication that decrease of A_{LU} at large P_T, expected from perturbative QCD, starts already at $P_T \sim 0.6$ (see Fig. 1 left). Observed large beam spin asymmetry for π^0 indicates that major contribution in pion SSAs may be due to the Sivers mechanism. The obtained results provide very significant improvement in statistical errors compared with published HERMES data [15] (see Fig. 1 left), providing important input for studies of higher twist effects. For the comparison with HERMES data a kinematic factor has been applied to take into account the different kinematical range covered by the two experiments.

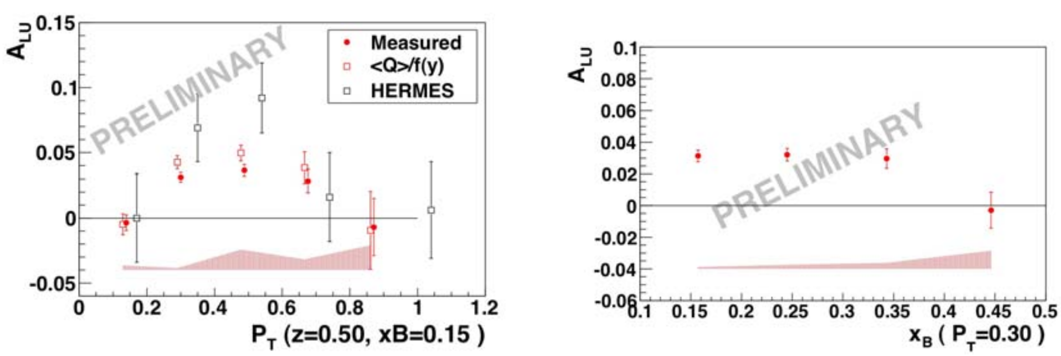

Figure 1: (color online). Beam spin asymmetry for the reaction $ep \to e'\pi^0 X$ versus P_T (left) and versus x_B (right). CLAS data (full circle) after kinematical correction (red empty square) are compared with the HERMES data [15] (black empty square).

2.1.2 Lambda Polarization in Semi-Inclusive Deep Inelastic Scattering

Measurements of Λ polarization in Semi-Inclusive Deep Inelastic Scattering (SIDIS) provide an important probe of the strange sea in the nucleon [16, 17] and may shed light on the proton spin puzzle. The advantage of detecting Λ in the final state lies in the fact that the Λ is self-analyzing and that it can be used as a s quark polarimeter since the polarization of Λ is almost completely determined by polarization of its s quark. Measurements of Λ polarization have been made in deep-inelastic scattering experiments at CERN with $\sim$ 44 GeV ν and $\bar{\nu}$ [18, 19, 20], Fermilab with 470 GeV muons [21] and HERMES with 27.5 GeV positrons [22]. Non-negligible *positive* longitudinal polarization of Λ, measured with respect to the direction of the momentum transfer from the beam, has been observed in the target fragmentation region, $x_F = 2P_\Lambda^{\parallel}/W < 0$ (being W the total CM energy and $P_\Lambda^{\parallel}$ is the CM Λ longitudinal momentum). All these early experiments, however, suffered from a lack of statistics, and the results could not be considered conclusive.

During the reporting period the Frascati group has started the analysis of the Λ polarizaxion transfer in the $ep \to e\Lambda X$ semi-inclusive reaction using data collected at CLAS with 5.5 GeV beam off an unpolarized hydrogen target 5 cm long. This data set corresponds to an integrated luminosity of $2.1 \times 10^{39} cm^{-2}$. The average beam polarization, frequently measured with a Møller polarimeter, was $P_B = 0.74 \pm 0.03$. Λ is identified by the invariant mass of the detected p and π^- (see Fig. 2 left). In Fig. 2(right) the missing mass of the $ep \to e'\Lambda X$ reaction is reported and the K^+ and K^{+*} peaks are clearly visible. A cut on the missing mass spectrum above 0.6 GeV has been applied in the analysis.

Preliminary results have showed that the beam spin asymmetry with the two helicities of the incoming electrons can provide a reliable way to extract the Λ polarization, relatively free of acceptance corrections and with small background contributions.

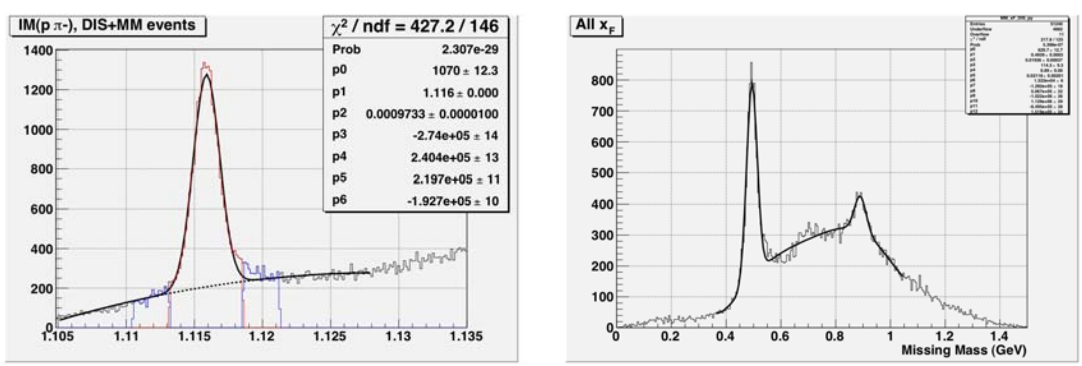

Figure 2: Invariant mass of the detected p and π^- (left); missing mass of the $ep \to e'\Lambda X$ (right). Clearly visible are the K^+ and K^{+*} peaks.

2.2 The 12 GeV program

To carry on the physics program at 12 GeV mainly focused on the study of TMDs and GPDs, the CLAS detector in Hall B be will be upgraded. The new detector, called CLAS12 optimized for studying exclusive and semi-inclusive reactions, consists of a two-part detector: a Forward Spectrometer and a Central Detector.

The LNF-JLAB12 group is deeply involved in the physics program of the Hall B: in January 2009 three proposals, having JLAB12 physicists as co-spokespersons, have been approved by the JLab Panel Advisory Committee for TMDs studies at 12 GeV [23, 24, 25] while for the hardware contribution the group has been working in the project of a RICH and a neutron detector.

In the forward spectrometer of CLAS12 the particle identification is made using low threshold gas Cerenkov counters (LTCC), high threshold gas Cerenkov counters (HTCC) and Time-of-Fligh scintillator counters. Neverthless, with this configuration in the $2.5-4$ GeV/c momentum region, the π/K separation relies only on the LTCC performance. Moreover, in the $4-8$ GeV/c momentum region it is not possible to separate protons from kaons. In general, this PID system is well matched to requirements of the main physics program at 12 GeV. However there are some physics measurements of high interest [23, 24, 25] which require a good kaon identification, that cannot be easily accessed without better PID. A RICH detector, to be installed in place of the low threshold Cherenkov counter, will significantly improve the CLAS12 particle identification overcoming the above limitations. A proximity focusing RICH similar to the one operating in Hall A at Jefferson Lab [30], may represent an adequate choice to fulfill our requirements. Several groups are working in this project both from INFN (Bari, Ferrara, Genova, Roma I/ISS) and from US (Argonne National Lab). The INFN has positively evaluated the project and in 2009 has started to fund it.

During the reporting period simulations have been started to determine different options for the radiator (C6F14, aerogel, C5F12), for the read-out of the Cherenkov photons (MWPC, SiPM, PMT) and to determine the best parameters and the main performances of the detector. Our preliminary results will be presented at the RICH2010 conference in may 2010.

Besides this, the group has also worked on the Neutron Detector. The physics motivation for having a neutron detector is to measure Deeply Virtual Compton Scattering (DVCS) on the neutron, with a deuterium target. The interest for this reaction is strong because it is the most sensitive to the Generalized Parton Distribution (GPD) E which allows, via the Ji's sum rule and with the knowledge of the GPDs H (accessible through DVCS on the proton) the extraction of the orbital angular momentum of the quarks. Following detailed Monte Carlo studies a scintillator barrel, 60 cm long and 10 cm thick, has been chosen for the realization of the neutron detector. During the year 2009 a laboratory set-up has been installed to test different scintillator types and different readout system for the signal (PMT, SiPM). The status of the project has been reported at the "CLAS12 Central Detector Meeting", held in Saclay (France) on December 2-3, 2009 (`http://irfu.cea.fr/Sphn/Clas/CLAS12CD2009/index_fichiers/slide0003.htm`).

3 Strangeness photoproduction

A major goal of hadron physics is to study the structure of the nucleon and its excited states (N and Δ resonances) . Concerning the latter, the situation is still unclear: many more states are predicted than observed and states with certain quantum numbers appear at energies much lower than predicted. This has been known for a long time as the missing resonance problem [26]. Because most of our present knowledge of baryon resonances comes from reactions involving pions in the initial and/or final states, a possible explanation could be that pionic coupling to the intermediate missing N^* or Δ^* states is weak. This suggests a search for these hadronic states in strangeness production reactions.

A recent measurement of the $\gamma p \to K^+\Lambda$ from CLAS Coll. [27] has shown, indeed, that a resonant type structure at energy ~ 1.9 GeV appears for kaon emitted at backward angles. To confirm and mostly to measure strangeness photoproduction on neutron, where data are almost inexistent, the Frascati group has analyzed the $\gamma n(p) \to K^+\Sigma^-(p)$ reaction in the invariant mass range from 1.54 to 2.76 GeV. These data are necessary to constrain phenomenological models which need the knowledge of the coupling constant NKY for proton and neutron, separately. In 2009 the analysis has been completed and the differential cross section has been measured for tagged photons in the energy range 1.0-3.6 GeV and at kaon center-of-mass angles between 10^o and 140^o in 10^o step. For energies up to $E_\gamma = 2.1$ GeV, the results are shown in Fig. 3 in linear scale, while for higher energies, logarithmic scale has been chosen in order to make more readable the behavior at the backward angles. The error bars represent the total (statistical plus systematic) uncertainties. This is the first high-precision determination of Σ^- photoproduction on the neutron covering a broad kaon-angle and photon-energy range. At a photon energy of ~ 1.8 GeV a clear forward peak starts to appear and becomes more prominent as the photon energy increases. This behavior, that is typically attributed to contributions from t-channel mechanisms, is not observed at lower energies, where the dominant contributions appear to be from s-channel mechanisms. Above ~ 2.1 GeV there are indications of a possible backward peak, which might suggest the presence of u-channel mechanisms. The few LEPS data [28] available for energies $1.5 - 2.4$ GeV and at forward angles are shown in Fig. 3. Also shown in Fig. 3 are the theoretical results of a Regge-based calculation [29]. The Regge-based model overestimates our results at forward and intermediate angles by about a factor of two. At backward angles the calculated cross section is too small by an order of magnitude, which is a reflection of the lack of resonances in the model.

These results will signicantly contribute to the improvement of the phenomenological analysis of meson photoproduction reactions at medium energies aiming to solve the missing resonance problem. The paper has been submitted to Physics Review Letters in December 2009 for publication.

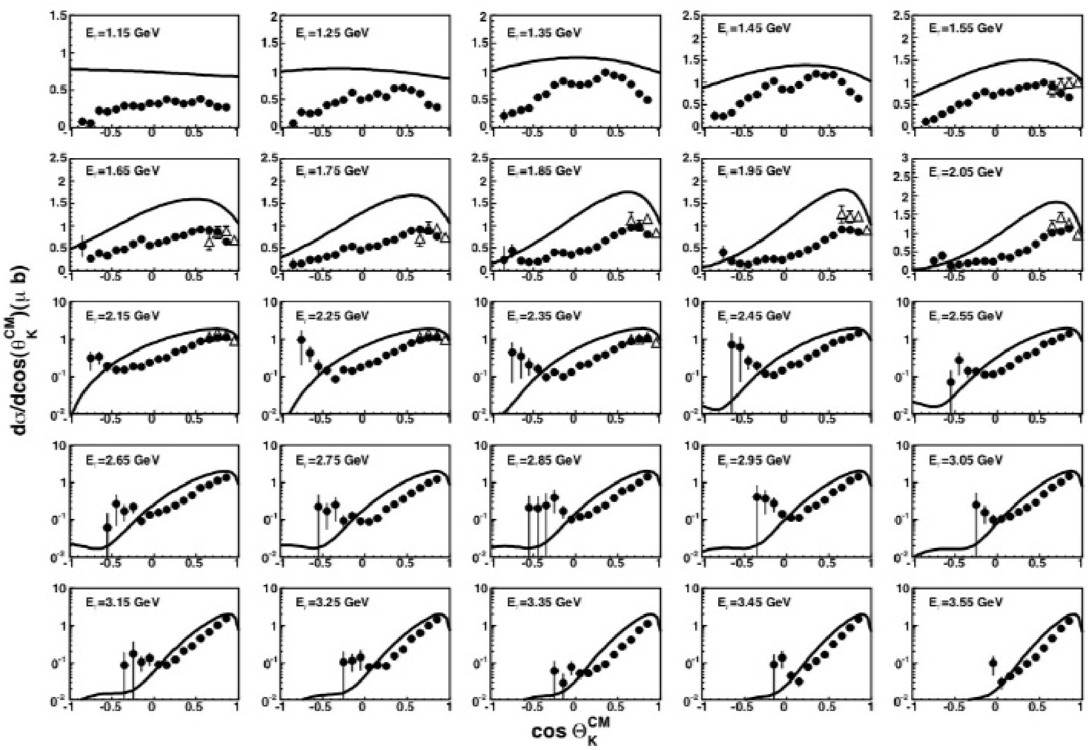

Figure 3: Differential cross sections of the reaction $\gamma d \rightarrow K^+\Sigma^-(p)$ obtained by CLAS (full circles). The error bars represent the total (statistical plus systematic) uncertainty. LEPS data [28] (empty triangles) and a Regge-3 model prediction [29] (solid curve) are also shown. Notice the logarithmic scale for energies above 2.1 GeV.

4 Publications

1. M. Nozar et al. and CLAS Coll., Phys. Rev. Lett. **102**, 102002 (2009).
2. S. Morrow et al. and CLAS Coll., Eur. Phys. Jour. A **39**, 5 (2009).
3. Y. Prok et al. and CLAS Coll., Phys. Lett. B **672**, 12 (2009).
4. M. Osipenko et al. and CLAS Coll., Phys. Rev. D **80**, 032004 (2009).
5. G.V. Fedotov et al. and CLAS Coll., Phys. Rev. C **79**, 015204 (2009).
6. J. Lachniet *et al. and CLAS Coll., Phys. Rev. Lett.* **102***, 192001 (2009).*
7. M. Battaglieri et al. and CLAS Coll., Phys. Rev. Lett. **102**, 102001 (2009).
8. M. Dugger et al. and CLAS Coll., Phys. Rev. C **79**, 065206 (2009).
9. W. Chen et al. and CLAS Coll., Phys. Rev. Lett. **103**, 012301 (2009).

10. D. Carman et al. and CLAS Coll., Phys. Rev. C **79**, 065205 (2009).
11. G. Gavalian et al. and CLAS Coll., Phys. Rev. C **80**, 035206 (2009).
12. R. Nasseripour et al. and CLAS Coll., Phys. Rev. C **80**, 044603 (2009).
13. X. Qian et al. and CLAS Coll., Phys. Lett. B **680**, 417 (2009).
14. M. Battaglieri et al. and CLAS Coll., Phys. Rev. D **80**, 072005 (2009).
15. M. Williams et al. and CLAS Coll., Phys. Rev. C80, 065209 (2009).
16. M. Williams et al. and CLAS Coll., Phys. Rev. C **80**, 065208 (2009).
17. M. Williams et al. and CLAS Coll., Phys. Rev. C **80** 045213 (2009).
18. I.G. Aznauryan et al. and CLAS Coll., Phys. Rev. C **80**, 055203 (2009).

5 Conferences, Workshops, Seminars

1. M. Mirazita, Σ^- *Photoproduction on the deuteron at CLAS,* Invited talk at WONP2009 Workshop on Nuclear Physics, Avana (Cuba), February 9-12, 2009.
2. P. Rossi, *The Jefferson Laboratory and its physics program: present and future,* Invited talk at WONP2009 Workshop on Nuclear Physics, Avana (Cuba), February 9-12, 2009.
3. M. Mirazita, *The physics at Jefferson Lab - Present and future,* Invited talk at Seminar at San Paulo University, San Paulo (Brazil), February 17, 2009.
4. P. Rossi, *A RICH detector for CLAS12,* Invited talk at CLAS12 European Workshop, Genova (Italy), February 25-28, 2009.
5. S. A. Pereira, *Measurement of the $\gamma n(p) \rightarrow K^+\Sigma^-(p)$ at Jefferson Lab.* Invited talk at European Nuclear Physics Conference (BOCHUM09), Bochum (Germany), March 16-20, 2009.
6. P. Rossi, *Future experiments DAΦNE.* Invited talk at MAMI and beyond Workshop, Mainz (Germany), March 30-April 3, 2009.
7. P. Rossi, *Transversity at CLAS.* Invited talk at XVII International Workshop on Deep-Inelastic Scattering and Related Subjects " - Madrid (Spain), April 26-30, 2009.
8. M. Aghasyan, *Beam Spin Asymmetries in Semi-Inclusive π^0 production at CLAS.* Invited talk at Transverse Parton Structure of Hadrons, Yerevan (Armenia), June 21-26, 2009.
9. M. Mirazita, *Semi-inclusive DIS and transverse momentum dependent distribution studies at CLAS.* Invited talk at XIII Workshop on High Energy Spin Physics, Dubna (Russia), September 1-5, 2009.
10. S. A. Pereira, *Measurement of the $\gamma n(p) \rightarrow K^+\Sigma^-(p)$ at Jefferson Lab.* Invited talk at XII International Seminar on Electromagnetic Interactions of Nuclei" - Moscow (Russia), September 17-20, 2009.

11. S. A. Pereira, *Hyperon Production and Polarization with CLAS and CLAS12 at Jefferson Lab*, Invited talk at International Conference on Nuclear Reactions on Nucleons and Nuclei, Messina (Italy), October 5-9, 2009.

12. P. Rossi, *JLAB experiment: results and future perspectives*, Invited talk at 39th LNF Scientific Committee, Frascati (Italy), October 26, 2009.

13. M. Aghasyan, *Latest Results from JLAB on TMDs* Invited talk at Orbital Angular Momentum of Partons in Hadron, Trento (Italy), November 9-13, 2009.

14. P. Rossi, *Partonic Transverse Momentum Distributions*, Invited talk at VIII Latin American Symposium on Nuclear Physics and Applications, Santiago (Chile), December 15-19, 2009.

References

1. PR-09-007, *Studies of partonic distributions using semi-inclusive production of kaons*, http://www.jlab.org/exp_prog/PACpage/PAC34/agenda.pdf.

2. D. W. Sivers, Phys. Rev. D **43**, 261 (1991).

3. M. Anselmino and F. Murgia, Phys. Lett. B **442**, 470 (1998).

4. S.J. Brodsky, D.S. Hwang and I. Schmidt, Phys. Lett. B **530**, 99 (2002).

5. J.C. Collins, Phys. Lett. B **536**, 43 (2002).

6. X.d. Ji and F. Yuan, Phys. Lett. B **543**, 66 (2002).

7. P.J. Mulders and R.D. Tangerman, Nucl. Phys. B **461**, 197 (1996)1.

8. A. Kotzinian, Nucl. Phys. B **441**, 234 (1995).

9. A. Kotzinian and P.J. Mulders, Phys. Rev. D **54**, 1229 (1996).

10. J.P. Ralston and D.E. Soper, Nucl. Phys. B **152**, 109 (1979).

11. E. Di Salvo, Int. J. Mod. Phys. A **22**, 2145 (2007).

12. A. Bacchetta et al., Phys. Rev. D **70**, 117504 (2004).

13. A. Afanasev and C.E. Carlson, (2003), hep-ph/0308163.

14. F. Yuan, Phys. Lett. B **589**, 28 (2004).

15. HERMES, A. Airapetian et al., (2006), hep-ex/0612059.

16. J. Ellis, D. E. Kharzeev and A. Kotzinian, Z. Phys C **69**, 467 (1996).

17. W. Melnitchouk and A. W. Thomas, Z. Phys. A **353**, 311 (1996).

18. P. Astier et al., (NOMAD Coll.), Nucl. Phys. B **588**, 3 (2000); D. V. Naumov (NOMAD Coll.), AIP Conf. Proc. **570**, 489 (2001).

19. S. Willocq et al., (WA59 Coll.), Z. Phys. C **53**, 207 (1992).

20. V. Ammosov et al., Nucl. Phys. B **162**, 208 (1980).

21. M. R. Adams et al. (E665 Coll.), Eur. Phys. J. C **17**, 263 (2000), hep-ex/9911004.

22. A. Airapetian et al. (HERMES Coll.), Phys. Rev. D **64**, 112005 (2001) hep-ex/9911017; S. Belostotski, *IXth Workshop on High-Energy Spin Physics*, Dubna, Russia, Aug 2 - 7, 2001.

23. PR-09-008, *Studies of the Boer-Mulders Asymmetry in Koan Electroproduction with Hydrogen and Deuterium Targets*, http://www.jlab.org/exp_prog/PACpage/PAC34/agenda.pdf.

24. PR-09-009, *Studies of Spin-Orbit Correlations in Kaon Electroproduction in DIS with polarized hydrogen and deuterium Targets*, http://www.jlab.org/exp_prog/PACpage/PAC34/agenda.pdf.

25. PR-09-007, *Studies of partonic distributions using semi-inclusive production of kaons*, http://www.jlab.org/exp_prog/PACpage/PAC34/agenda.pdf.

26. N. Isgur and G. Karl, Phys. Rev. D **18**, 4187(1978).

27. CLAS Coll., R. Bradfort et al, Phys. Rev. C **73**, 035202 (2006).

28. H. Kohri et al., Phys. Rev. Lett. **97**, 082003 (2006).

29. P. Vancraeyveld, L. DeCruz, J. RyckebuschandT. Van Cauteren, Phys. Lett. B **681**, 428 (2009).

30. F. Garibaldi et al., Nucl. Inst. & Meth. A **502**, 117 (2003); M. Iodice et al., Nucl. Inst. & Meth. A **553**, 231 (2005).

MAMBO

D. Babusci, P. Levi Sandri (Resp.), D. Pietreanu, G. Venanzoni.

1 Introduction

MAMBO groups together three complementary INFN activities in Germany: the experimental activity with the MAMI-C microtron in Mainz, approved until 2011, the development of MRPC counters and the preliminary measurements towards a full proposal to measure the electric dipole moments (EDM) of proton and deuteron, and the new BGO-OD experiment at Bonn-ELSA. LNF are involved in the last two activities.

2 BGO-OD experiment

The use of the electromagnetic probe and of it's polarisation, coupled to large acceptance detectors with cylindrical symmetry and high efficiency in the detection of all final state particles, is the technique chosen in many laboratories to perform the ambitious program of a full determination of the scattering amplitude of a given photonuclear reaction. Such determination requires, for each reaction channel, the measurement of the cross section, of the three single polarisation observables and of four appropriately chosen double polarisation observables.

The BGO-OD esperiment is performed in collaboration between INFN sections of Roma2, LNF, Messina, Pavia, ISS-Roma1 and Torino, the University of Bonn, Physikalisches Institut, ELSA department, the University of Bonn, Helmholtz Institut für Strahlen- und Kernphysik, the University of Edinburgh, the National Science Center Kharkov Institute of Physics and Technology, the University of Moscow, Russia, the Petersburg Nuclear Physics Institute (PNPI), Gatchina and the University of Basel. More that 70 physicists participate to this experimental program foreseen to last until 2017.

The INFN contribution consist in the *Rugby Ball* calorimeter and associated detectors previously used at GRAAL, the target system and the cylindrical tracking chambers.

The BGO *Rugby Ball* is made of crystals of pyramidal shape with trapezoidal basis which are 21 radiation lengths long (24 cm). This calorimeter has an excellent energy resolution for photons, a good response to protons, a high detection efficiency for neutrons and is very stable in time due to a continuous monitoring and to the calibration slow control system.

3 2009 activity

3.1 BGO-OD

At the end of 2008 and during the first months of 2009, the Graal experiment was completely dismounted. The BGO *Rugby Ball*, the scintillator barrel and the H2-D2 target system were transported to the Bonn ELSA accelerator and installed in the S-beamline. The support structure of the calorimeter was modified to allow for a larger opening of the two halves of the detector. All the crystals were checked after transportation and reinstalled with renewed light-tight coverage and reviewed voltage dividers.

3.2 EDM

In 2009, the EDm activity has been focused on the following main points:

- investigation of systematic polarimeter errors by a test beam at COSY (Jülich)
- development and test of a MRPC prototype

Concerning the first point, the investigation of systematic polarimeter errors at COSY-Jülich was undertaken to explore effects relevant to the search for an electric dipole moment on the deuteron [1)]. In that search, the signal would be a small change during the course of a beam store in the vertical component of the polarization, which starts with its components essentially in the horizontal, or ring, plane. Since the vertical component may not vanish initially, the polarization must be monitored as a function of time during the store. In particular the effects of geometric and rate-induced changes on the measured polarization observables, and in particular on the cross ratio was studied. The EDDA detector was used as a substitute for the EDM polarimeter, and its operating point was chosen to mimic as much as possible the EDM polarimeter operating point. Based on this study, it was possible to define a correction parameter for geometry and another for rate and to explain all observed systematic errors in terms of these two parameters [2)]. For observables such as the cross ratio, it appears that under the level of control expected in an EDM search, the corrections to the cross ratio and especially the precision with which they are known will be comfortably less than one part per million. Once calibrated, these corrections can be applied in real time to generate asymmetries that would be useful for feedback purposes in an EDM search.

About the second point, the MRPC technology has been proposed by us as a detector for the EDM experiment [3)]. Its performances in terms of efficiency, stability, time resolution, and rate capability seem to meet the experiment requirements. In 2009 we have started the tests on a prototype at Capannone Gran Sasso of LNF.

4 2010 activity

4.1 BGO-OD

During 2010, the apparatus will be fully installed and ready for debugging. The physics experimental program will start in 2011.

4.2 EDM

Test on MRPC will be continued and a second prototype built wit the goal of achieving 50 ps time resolution. When successful, the detector will be employed in the EDM polarimeter. A possible use for BGO-OD will also be investigated.

References

1. V. Anastassopoulos et al., *AGS Proposal: Search for a permanent electric dipole moment of the deuteron nucleus at the 10^{-29} e cm level*, submitted to the BNL PAC in April 2008.
2. E. J. Stephenson et al., *Correcting Systematic Errors in High Sensitivity Deuteron Polarization Measurements*, to be submitted to Nucl. Instr. and Meth.
3. D. Babusci et al., *Proposal for the dEDM Polarimeter based on MRPC technology*, dEDM internal note.

$\overline{\mathrm{P}}$ANDA - $\overline{\mathrm{p}}$ Annihilation at Darmstadt

B. Dulach (Ass.), P. Gianotti (Resp. Naz.), M. Giardoni, C. Guaraldo, M. Iliescu (Ass.),
V. Lucherini, D. Orecchini (Tecn.), E. Pace,L. Passamonti (Tecn.), D. Pierluigi, (Tecn.),
D. Pietreanu (Ass.), A. Russo (Tecn.), D. Sirghi (Art. 2222)

1 Introduction

$\overline{\mathrm{P}}$ANDA is one of the biggest future experiments in hadron and nuclear physics that will be carried out at the new Facility for Antiproton and Ion Research (FAIR) at Darmstadt, Germany. It is dedicated to the study of the annihilations of antiprotons on nucleons and nuclei up to a maximum center-of-mass energy in $\overline{\mathrm{p}}\mathrm{p}$ of 5.5 GeV.

Presently, the $\overline{\mathrm{P}}$ANDA collaboration consists of 400 physicists from 16 countries spread all over the world. The Italian groups involved are: Torino, University, Politecnico and INFN, Trieste, University and INFN, Genova INFN, Pavia, University and INFN, Ferrara, University and INFN, Frascati INFN laboratory, Catania, University and INFN. The LNF group is involved in the design and construction of the central tracker of the $\overline{\mathrm{P}}$ANDA detector.

2 $\overline{\mathrm{P}}$ANDA experiment

A new facility for hadronic physics is under construction in Germany. It consists of a major upgrade of the presently running GSI accelerator complex of Darmstadt [1]. An intense, high momentum

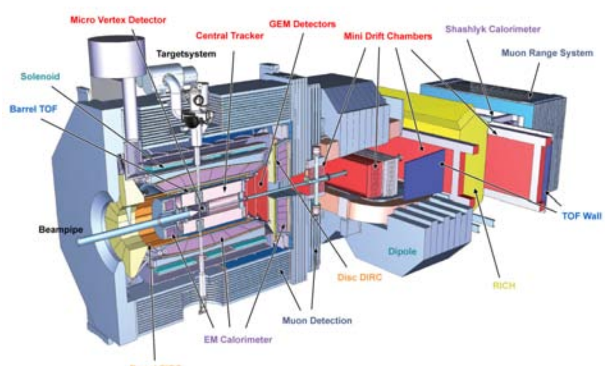

Figure 1: A schematic view of the $\overline{\mathrm{P}}$ANDA detector.

resolution antiproton beam, with momenta between 1.5 and 15 GeV/c, will be available at the High Energy Storage Ring (HESR), and the experimental activity will be carried out using a general purpose detector $\overline{\mathrm{P}}$ANDA that will be build surrounding an internal target station installed in one of the two straight sections of the storage ring. Figure 1 shows a schematic drawing of the $\overline{\mathrm{P}}$ANDA apparatus. It is designed as a large acceptance multi-purpose detector consisting of two distinct parts: a solenoidal spectrometer, surrounding the interaction target region, and a forward spectrometer to cover the solid angle between 5 and 22 degrees. It will allow the detection and the identification of either the neutral and the charged particles emitted following $\bar{p}p$ annihilation.

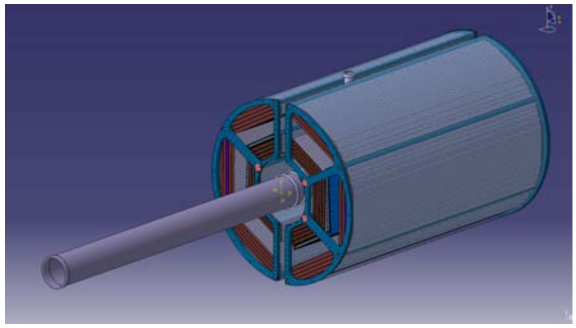

Figure 2: The layout of the STT. Details are in the text.

In March 2009, the $\overline{\text{P}}$ANDA collaboration has issued "The $\overline{\text{P}}$ANDA Physics Performance Report" [3]. This was one of the deliverables of the EU contract 515873 and it is a first attempt to evaluate the physics accessible with the designed detector. All the aspects of the $\overline{\text{P}}$ANDA scientific program have been deeply analyzed and checked. Benchmark channels, for each topic, have been identified and a complete set of Montecarlo simulations has been carried out.

3 The $\overline{\text{P}}$ANDA Central Tracker

The $\overline{\text{P}}$ANDA Central Tracker has to satisfy the following requirements:

- almost full solid angle coverage;
- momentum resolution $\delta p/p \sim 1.5\%$;
- low material budget $X/X_0 \sim$ few %;
- good spatial resolution $\sigma_{r,\phi} = 150$, μm, $\sigma_z =$ few mm.

This detector will be placed around the Micro Vertex Detector (MVD) at a radial distance from the interaction point between 15 and 42 cm. Along the beam axis the allowed space is 150 cm. Presently, for this detector, two options are under discussion: a Straw Tube Tracker (STT) and a Time Projection Chamber (TPC). The LNF $\overline{\text{P}}$ANDA group, having experience in straw tubes, is involved in the realization of the STT.

3.1 Straw tube detector layout

The overall $\overline{\text{P}}$ANDA tracking volume will be divided in two half by the target pipe, therefore the detector will consist of two identical semi-chambers. In the hypothesis of a straw tube tracker, each one will be made of aluminized mylar straw tubes, diameter 10 mm, length 1500 mm, thickness 30 μm, arranged in planar double layers (see figure 4). Inside a double layer the tubes are glued together and operated with an $Ar+CO_2$ (90+10) gas mixture with an over-pressure of 1 bar. This solution will help to avoid strong support structures and will keep the detector design modular and simple. To measure also particle z coordinate, some layers will be mounted with a skew angle $\pm 3^o$ with respect to the beam axis.

Figure 3: The STT mechanical structure prototype (see text for more details)

Figure 2 shows the layout for the STT. There are 4 internal double-layers parallel to the beam axis, then 4 double-layers mounted with opposite skew angles, and finally 2 other layers parallel to the beam axis. To fill up the cylindrical volume, the remaining region houses smaller tube layers.

In order to support the straw tube double-layers, and to precisely position them, an external mechanical structure is necessary.

4 Activity of the LNF $\overline{\mathrm{P}}$ANDA group

The activity of the LNF $\overline{\mathrm{P}}$ANDA group during 2009 has been devoted to the optimization of the STT components. A first prototype of the supporting mechanical frame has been designed and realized by and external company figure 3. This support structure is very light, and, in the hypothesis of using Aluminum for the final realization, we will have the following numbers:

- total weight 8.2 kg;
- Young modulus: 70 GPa;
- radiation Length (X_0): 9 cm;
- thermal expansion:24 ppm/^{o}C;

The two internal rods are needed only during the straw double-layers mounting phase and could be removed subsequently reducing furtherly the material budget. Next step will be to check the mounting procedure of straw tube double-layers with electronics and supplies. A complete description of the $\overline{\mathrm{P}}$ANDA STT and of the activities carried out during 2009 is given in ref. [4, 5]

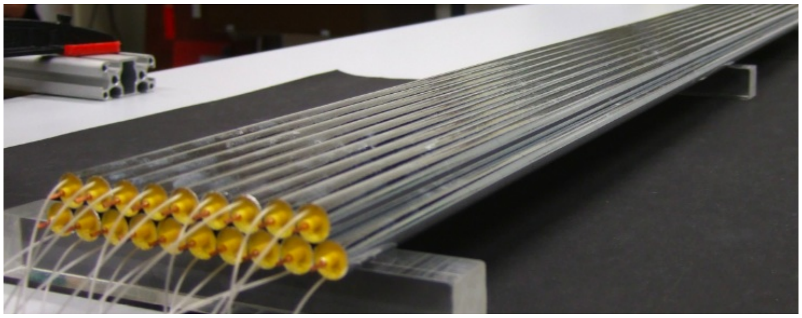

Figure 4: Layout of one straw tube double-layer prototype.

5 Conference Talks

1. P. Gianotti, *Search for exotics at $\overline{P}ANDA$*, invited talk at the International Conference on Excited QCD, Zakopane, Poland, 8-14 February 2009.
2. P. Gianotti, *$\overline{P}ANDA$ experiment at FAIR*, invited talk at the 10th International Conference on Hypernuclear and Strange Particle Physics "Hyp X, Tokai, Japan, 14-18 September 2009.

References

1. http://www.gsi.de/fair/.
2. http://www-panda.gsi.de/.
3. The $\overline{\mathrm{P}}$ANDA Coll., `arXiv:0903.3905v1`.
4. S. Costanza et al., in press on Nucl Inst. & Meth. A, doi:10.1016/j.nima.2009.06.105.
5. A. Braghieri et al., Nuclear Science Symposium and Medical Imaging Conference Record IEEE 2009.

SIDDHARTA

M. Bazzi (Ass. Ric.), M. Bragadireanu (Bors. UE), C. Curceanu Petrascu (Resp. Naz.),
A. D'Uffizi (Bors.), C. Guaraldo (Art. 2222), M. Iliescu (Ass.),
P. Levi Sandri, V. Lucherini, F. Lucibello (Tecn.), S. Okada (Bors. PD),
D. Pietreanu (Ass. Ric.), M. Poli Lener (Art. 23), A. Rizzo (Bors.),
A. Romero Vidal (Bors PD), A. Scordo (Bors. PD), D. Sirghi (Art. 2222), F. Sirghi (Bors. UE),
O. Vazquez Doce (Art. 23)

1 The SIDDHARTA scientific program

The objective of the SIDDHARTA (Silicon Drift Detector for Hadronic Atom Research by Timing Application) experiment is to continue, to deepen and enlarge the successful scientific line, initiated by the DEAR experiment in performing precision measurements of X-ray transitions in exotic (kaonic) atoms at DAΦNE.

The precise determination of the shift and width of the $1s$ level with respect to the purely electromagnetic calculated values, in kaonic hydrogen and kaonic deuterium, generated by the presence of the strong interaction, through the measurement of the X-ray transitions to this level, will allow the first precise experimental determination of the isospin dependent antikaon-nucleon scattering lengths, fundamental quantities in understanding low-energy QCD in strangeness sector.

The shift ϵ and the width Γ of the $1s$ state of kaonic hydrogen are related to the real and imaginary part of the complex s-wave scattering length, a_{K^-p}, through the Deser formula (in the isospin limit):

$$\epsilon + i\Gamma/2 = 2\alpha^3\mu^2 a_{K^-p} = (412 \text{ eV fm}^{-1}) \cdot \mathrm{a_{K^-p}} \tag{1}$$

where α is the fine structure constant and μ the reduced mass of the K^-p system. In the isospin limit, i.e. in the absence of the electromagnetic interaction and at $m_d = m_u$, a_{K^-p} can be expressed directly in terms of the scattering lengths for isospin I=0 and I=1:

$$a_{K^-p} = \frac{1}{2}(a_0 + a_1) \tag{2}$$

A similar relation applies to the case of kaonic deuterium and to the corresponding scattering length a_{K^-d}:

$$\epsilon + i\Gamma/2 = 2\alpha^3\mu^2 a_{K^-d} = (601 \text{ eV fm}^{-1}) \cdot \mathrm{a_{K^-d}} \tag{3}$$

An accurate determination of the $\mathrm{K^-N}$ isospin dependent scattering lengths will place strong constraints on the low-energy $\mathrm{K^-N}$ dynamics, which, in turn, constraints the SU(3) description of chiral symmetry breaking in systems containing the strange quark.

The DEAR measurement on kaonic hydrogen, performed in 2002 [1)]

$$\epsilon = -193 \pm 37(\text{stat.}) \pm 6\,(\text{syst.}) \text{ eV} \tag{4}$$

$$\Gamma = 249 \pm 111(\text{stat.}) \pm 39\,(\text{syst.}) \text{ eV}. \tag{5}$$

has already triggered an increased activity of the theoretical groups working in the low-energy kaon-nucleon interaction field, as well as in more general non-perturbative QCD.

The SIDDHARTA experiment aims to significatively improve the precision obtained by DEAR and to perform the first measurement ever of kaonic deuterium. SIDDHARTA performed as well accurately measurements on kaonic helium transitions to the 2p level (L-series). The kaonic helium 3 was measured for the first time (see below).

2 The SIDDHARTA setup

SIDDHARTA represents a new phase in the study of kaonic atoms at DAΦNE. The DEAR precision was limited by a signal/background ratio of about 1/70. To significantly improve this ratio, a breakthrough is necessary. An accurate study of the background sources present at DAΦNE was redone. The background includes two main sources:

- synchronous background: coming together with the kaons – related to K^- interactions in the setup materials and also to the ϕ-decay processes; it can be defined as hadronic background;
- asynchronous background: final products of electromagnetic showers in the machine pipe and in the setup materials originating from particles lost from primary circulating beams either due to the interaction of particles in the same bunch (Touschek effect) or due to the interaction with the residual gas.

Accurate studies performed by DEAR showed that the main background source in DAΦNE is of the second type, which shows the way to reduce it. A fast trigger correlated to a kaon entering into the target would cut the main part of the asynchronous background.

X rays were detected by DEAR using CCDs (Charge-Coupled Devices), which are excellent X-ray detectors, with very good energy resolution (about 140 eV FWHM at 6 keV), but having the drawback of being non-triggerable devices (since the read-out time per device is at the level of 10 s). A recently developed device, which preserves all good features of CCDs (energy resolution, stability and linearity), but additionally is triggerable - i.e. fast (at the level of 1μs), was implemented. This new detector is a large area Silicon Drift Detector (SDD), specially designed for spectroscopic application. The development of the new 1 cm^2 SDD device, together with readout electronics and very stable power supplies, was partially performed under the Joint Research Activity JRA10 of the I3 project "Study of strongly interacting matter (HadronPhysics)" within FP6 of the EU.

The trigger in SIDDHARTA was given by a system of scintillators which recognized a kaon entering the target making use of the back-to-back production mechanism of the charged kaons at DAΦNE from ϕ decay: of the type:

$$\phi \to K^+K^-. \tag{6}$$

The SIDDHARTA setup contains 144 SDD chips of 1 cm^2 each, placed around a cylindrical target, containing high density cryogenic gaseous hydrogen (deuterium). The SDDs are grouped in units of 3 detectors, read individually; bigger units of 18 SDDs are then realized, Fig. 1. The target is made of kapton, 75μm thick, reinforced with aluminium grid, see Fig. 2. 8 SDD 18 cm^2 units were placed all around the target cell, as shown in Fig. 3.

The SIDDHARTA setup was installed on DAΦNE in late summer 2008 (see Fig. 4) and the period till the end of 2008 was used to debug and optimize the setup performances (degrader optimization included). The kaonic atoms measurements were done in 2009, as described below.

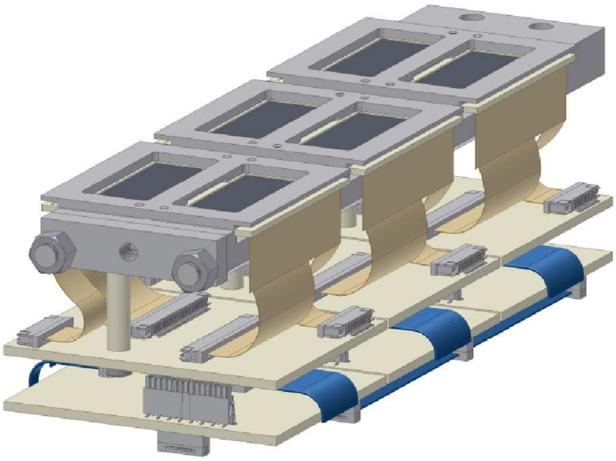

Figure 1: An 18 cm^2 SDD unit, containing 18 SDD individual chips.

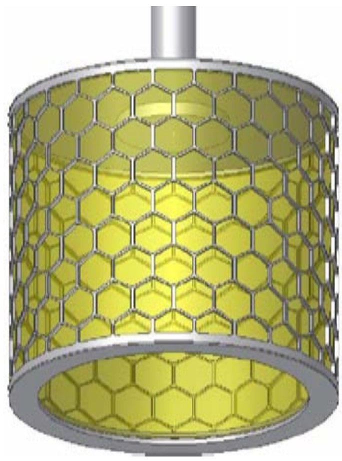

Figure 2: The SIDDHARTA target cell, done in kapton, reinforced with an aluminium grid. It will contain about 3 liters of cryogenic and high density hydrogen (deuterium) gas.

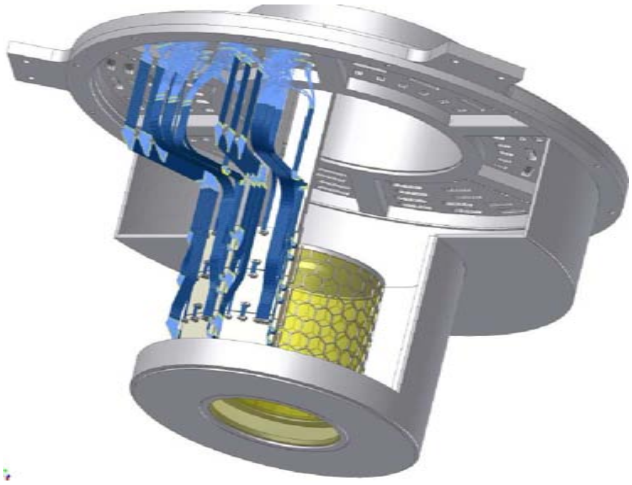

Figure 3: The SIDDHARTA target cell surrounded by SDD units (detail).

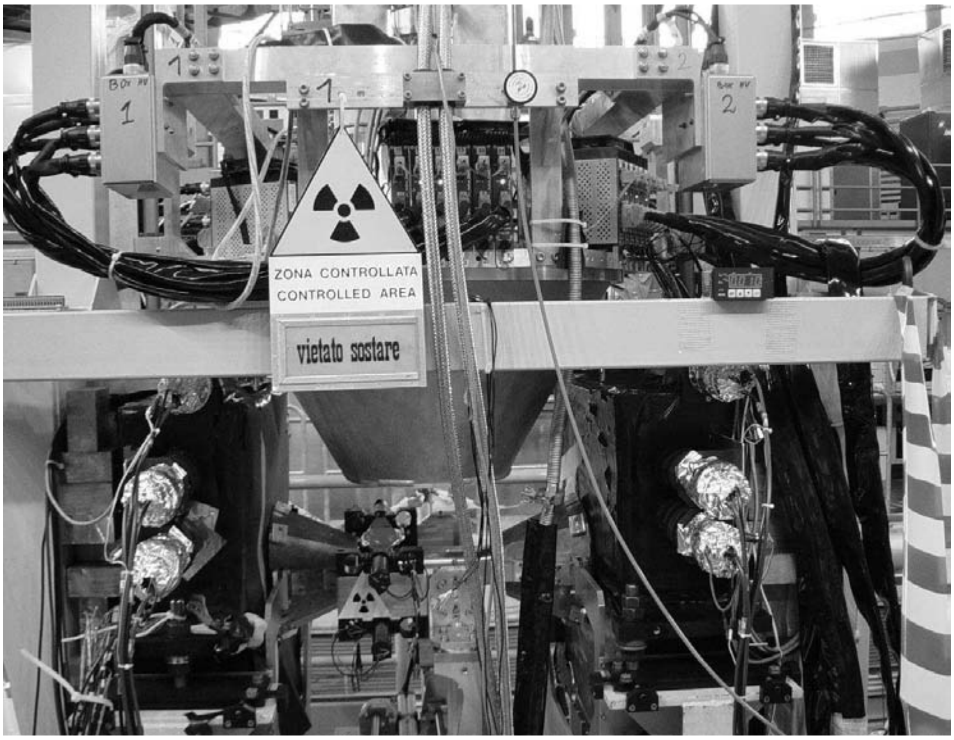

Figure 4: The SIDDHARTA full setup installed at DAΦNE.

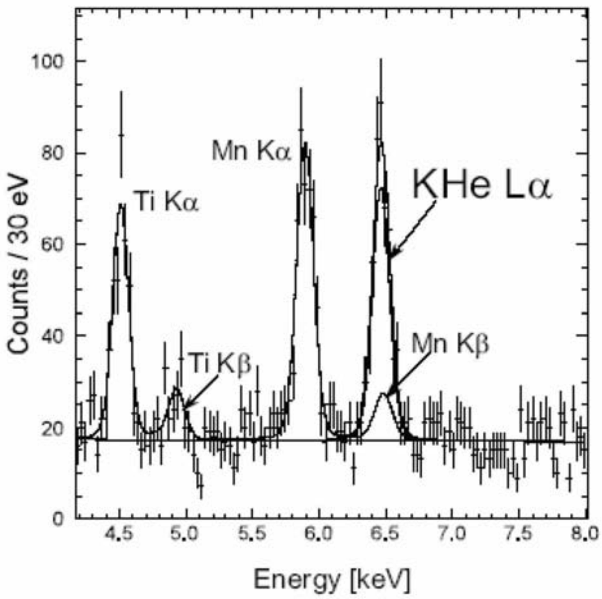

Figure 5: The Kaonic Helium triggered spectrum. The Mn and Ti lines are used for calibration. The kaonic helium4 transition at 6.4 keV is clearly seen.

3 Activities in 2009

SIDDHARTA was in data taking from late January 2009 until 9 November 2009, with a break during August month, used for the setup maintenance and some improvements. In what follows, we present the measurements SIDDHARTA performed in 2009.

3.1 Kaonic helium 4 measurement

After having installed the SIDDHARTA setup on DAΦNE, we optimized the performances of the setup, including degrader and callibration method, by using kaonic helium 4 transitions to the 2p level (L-series), due to the fact that the yield of these transitions is at least a factor 10 higher than the one of kaonic hydrogen transitions.

We have analyzed part of these data and published them in Ref. 2). It was the first measurement of kaonic helium in gas target - where the Compton scattering is neglijible (which is not the case of liquid targets, as those previously used). The obtained results (see Fig. 5 for the kaonic helium spectrum):

$$\Delta E = E_{exp} - E_{e.m.} = 0 \pm 6 \text{ (stat.)} \pm 2 \text{ (syst) eV} \tag{7}$$

definitely solves the so-called kaonic helium puzzle (see the paper for details).

We are presently analyzing all the data, with the aim to get a better precision and information on the yield for a second publication.

3.2 Kaonic hydrogen measurement

The kaonic hydrogen measurement was performed in the period 15 March - 31 July 2009 and during October 2009, for a total of about 400 pb^{-1} of integrated luminosity.

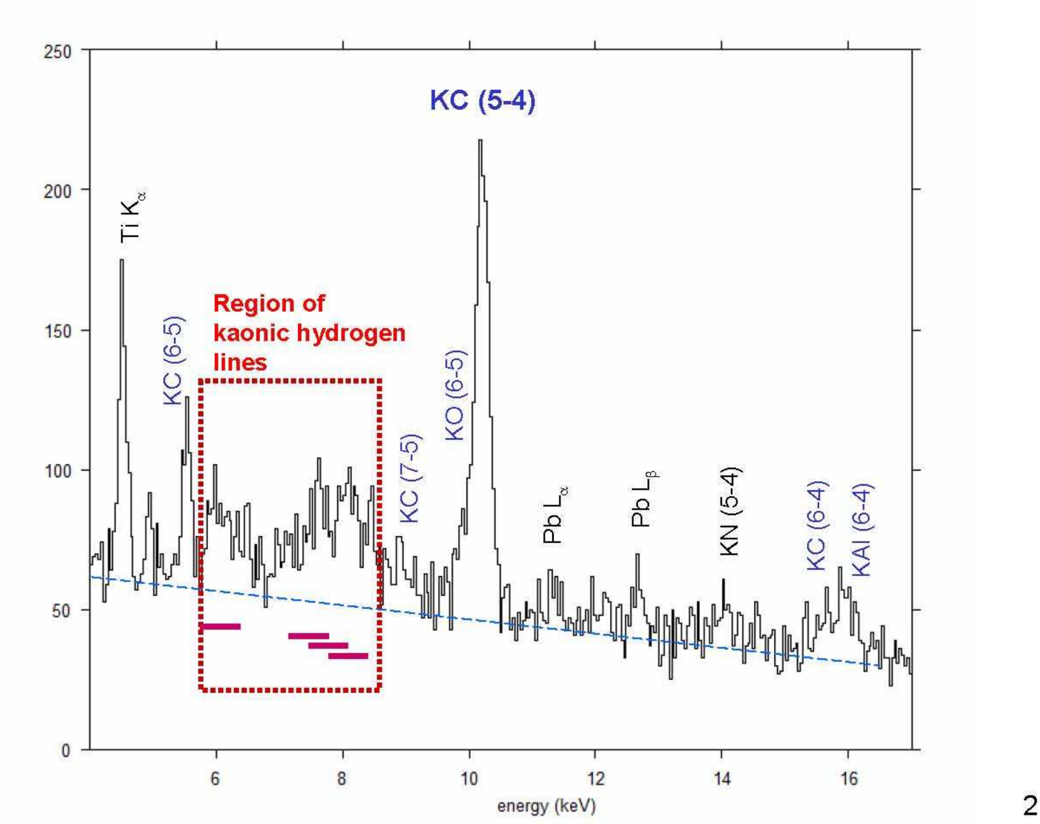

Figure 6: (color online). The Kaonic Hydrogen triggered spectrum. The kaonic Hydrogentransitions are clearly visible. In red the e.m. position of the lines.

In Fig. 6 we present a preliminary partial statistics triggered kaonic hydrogen spectrum, where kaonic hydrogen transitions to the 1s level (K-series) are clearly seen. Data analyses are undergoing

3.3 Kaonic deuterium measurement

We performed an exploratory measurement of kaonic deuterium transitions in September-October 2009, for a total integrated luminosity of about 100 pb^{-1}, to be confrounted with an original request of about 600 pb^{-1}. It is clear that the results of this exploratory measurement (analysis undergoing) cannot give a definitive result - however can be useful as an indication for a future measurement.

3.4 Kaonic helium 3 measurement

In the last days of data taking, early November 2009, we measured for the first time ever the kaonic helium3 L-transitions. The total integrated luminosity for this measurement was about 10 pb^{-1} and the preliminary spectrum is shown in Fig. 7. Data analysis is undergoing SIDDHARTA was dismounted from DAΦNE in early December 2009, (see Fig. 8) a picture taken the day after datataking was ended.

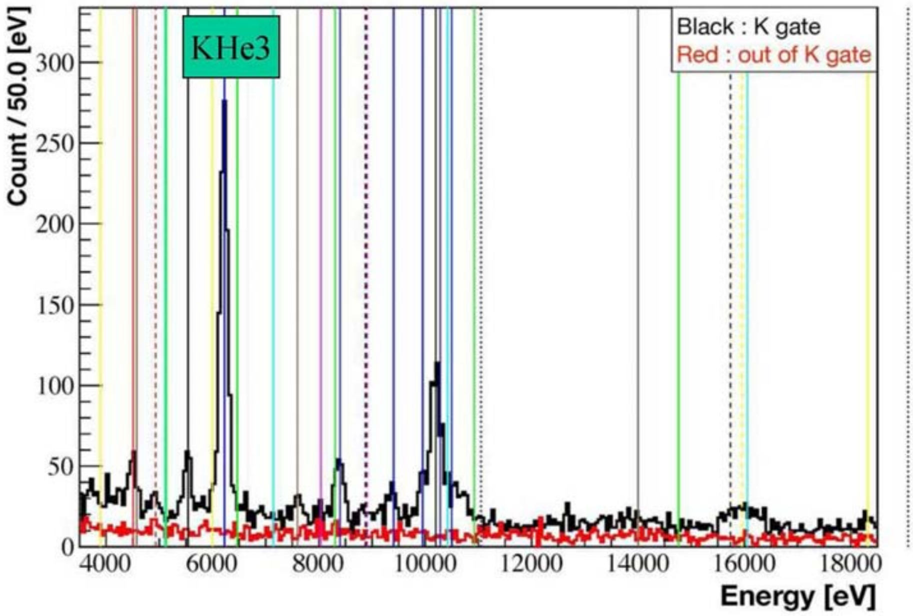

Figure 7: (color online). The Kaonic helium3 triggered spectrum (black line)where the 6.2 keV and 8.4 keV lines of kaonic helium transitions are clearly visible. The line at about 10 keV corresponds to kaonic carbon transition. The red line corresponds to the events out of kaon gate in the trigger system - representing background.

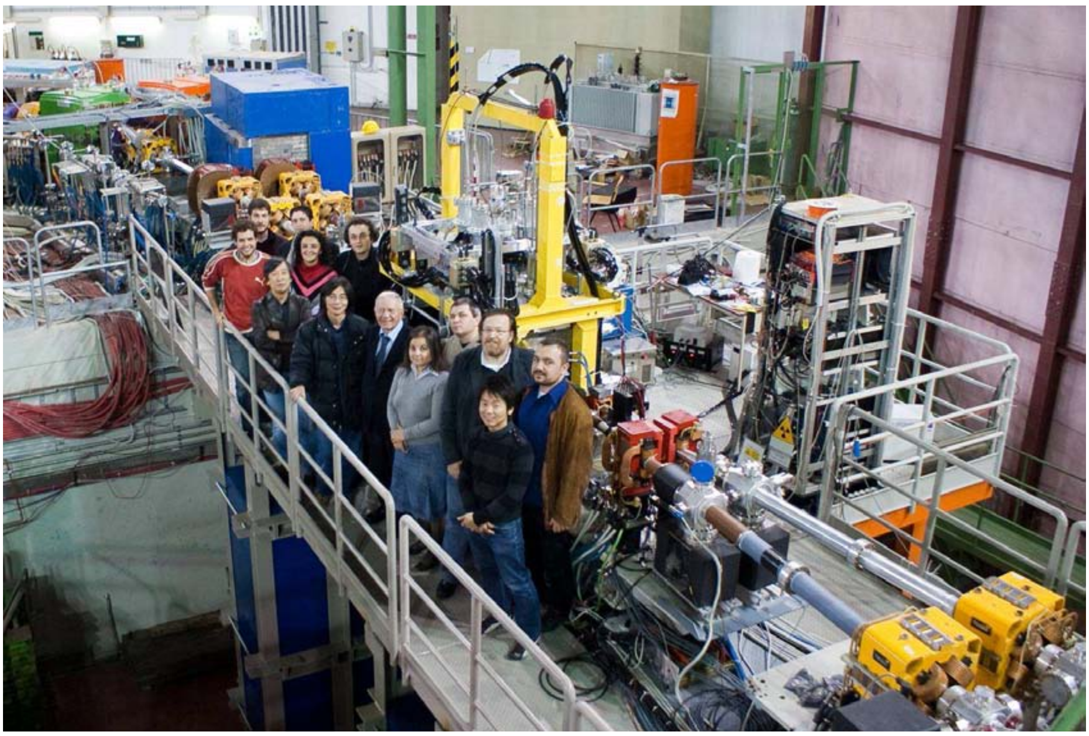

Figure 8: Part of the SIDDHARTA Collaboration in front of the SIDDHARTA setup in the day after the data taking ended (10 November 2009).

3.5 ECT* Workshop organization

In the period 12-16 October 2009 a Workshop entitled "Hadronic Atoms and Kaonic Nuclei - solved puzzles, open problems and future challenges in theory and experiments" was organized, having Catalina Curceanu as main Organizer, at the ECT* in Trento. The Workshop was very successful. For more details see CERN Courier, Volume 50, January/February 2010, page 28.

4 Activities in 2010

The LNF group main activities in SIDDHARTA for 2010 are the following ones:

- finalize analyses of kaonic helium 4 data and publish them;
- finalize analyses of kaonic hydrogen data and publish them;
- finalize analyses of kaonic deuterium data and publish them;
- finalize analyses of kaonic helium 3 data and publish them.

In parallel, the SIDDHARTA Collaboration is preparing a proposal for an upgraded setup - to perform the kaonic deuterium measurement in the near future. We are as well considering heavier kaonic atoms (a list is being discussed with theoreticians working in the field) measurements.

To be mentioned that the SIDDHARTA scientific program is important part of the Network LEANNIS (WP9) in the framework of the EU FP7 HadronPhysics2 program.

5 Publications

5.1 List of Conference Talks given by LNF Authors in Year 2009:

1. A. Scordo, *First kaon measurement with scintillating fibers read by MPPC at the DAΦNE e+e- collider*, talk at the XLVII International Winter Meeting on Nuclear Physics, Bormio, 26 - 30 january 2009, Italy.

2. A. Romero Vidal, *Measurements of kaonic atoms at DAΦNE: the SIDDHARTA experimen*, talk at the XLVII International Winter Meeting on Nuclear Physics, Bormio, 26 - 30 january 2009, Italy.

3. O. Vazquez Doce, *The AMADEUS experiment and the analyses of the K^-Ke in the KLOE data*, talk at the XLVII International Winter Meeting on Nuclear Physics, Bormio, 26 - 30 january 2009, Italy.

4. O. Vazquez Doce, *Deeply bound kaonic nuclear states at DAΦNE*, talk at the Excited QCD, 8 - 14 February 2009, Zakopane, Poland.

5. C. Curceanu, *SIDDHARTA and AMADEUS at LNF*, talk at the HadronPhysics2 FP7 LEANNIS kick-off meeting, 27 March 2009, Vienna, Austria.

6. S. Okada, *Kaonic atoms at DAΦN*, talk at the LNF Spring School in Nuclear, Subnuclear and Astroparticle Physics, 11-14 May 2009, Frascati, Italy.

7. M. Poli Lener, *Performances of a GEM-based TPC prototype for new high-rate particle experiment*, talk at the Fronteer detectors for fronteer physics, 24 - 30 May 2009, La Biodola, Italy.

8. O. Vazquez Doce, *Low energy kaon nuclei interaction studies at DAΦNE (AMADEUS experiment)*, talk at the 19th International IUPAP Conference on Few-Body Problems in Physics, 31 July - 5 September 2009, Bonn, Germany.
9. S. Okada, *The SIDDHARTA experiment*, talk at the 19th International IUPAP Conference on Few-Body Problems in Physics, 31 July - 5 September 2009, Bonn, Germany.
10. A. Scordo, *The trigger system for the AMADEUS experiment*, talk at the ECT* Workshop Hadronic Atoms and Kaonic Nuclei - solved puzzles, open problems and future challenges in theory and experiments, 12 - 16 October 2009, Trento, Italy.
11. A. Romero Vidal, *SIDDHARTA recent results*, talk at the ECT* Workshop Hadronic Atoms and Kaonic Nuclei - solved puzzles, open problems and future challenges in theory and experiments, 12 - 16 October 2009, Trento, Italy.
12. C. Curceanu, *AMADEUS: As a matter of fact it is a fact of matter*, talk at the ECT* Workshop Hadronic Atoms and Kaonic Nuclei - solved puzzles, open problems and future challenges in theory and experiments, 12 - 16 October 2009, Trento, Italy.
13. O. Vazquez Doce, *Analyses of the K^-He interaction in the KLOE Drift CHamber*, talk at the ECT* Workshop Hadronic Atoms and Kaonic Nuclei - solved puzzles, open problems and future challenges in theory and experiments, 12 - 16 October 2009, Trento, Italy.
14. O. Vazquez Doce, *The AMADEUS experiment: low energy kaon nuclei interaction studies at DAΦNE*, HADRON2009, 29 November - 4 December 2009, Tallahassee, USA.
15. C. Curceanu, *AMADEUS - an experiment to measure properties of strange and even stranger matter*, SMI - Colloquium, 14-15 December 2009, Vienna.

5.2 Papers and Proceedings

1. C. Curceanu and J. Marton, *The fascinating world of strangene exotic atoms*, CERN Courier, Volume 50, January/February 2010, page 28.
2. J. Zmeskal et al., Int. J. Mod. Phys. A **24**, 197 (2009).
3. M. Bazzi et al., Phys. Lett. B **681**, 310 (2009).
4. J. Marton et al., IEEE TRans. Nucl. Sci. **56**, 1400 (2009).
5. M. Poli Lener et al., Nucl. Instr. and Meth. A (2009) - to appear, doi:10.1016/j.nima.2009.06.074
6. O. Vazquez Doce et al., *The AMADEUS experiment and the analyses of K-He in the KLOE data*, Proceedings of the XLVII International Winter Meeting on Nuclear Physics, Bormio (Italy), 26-30 January 2009, p. 147.
7. A. Romero Vidal et al., *Measurements of kaonic atoms at DAΦNE: the SIDDHARTA experiment*, Proceedings of the XLVII International Winter Meeting on Nuclear Physics, Bormio (Italy), 26-30 January 2009, p. 165.
8. O. Vazquez Doce et al., Acta Phys. Polonica. Supp. **2**, 399 (2009).
9. C. Curceanu et al., Nucl. Phys. Proc. Suppl. **186**, 271 (2009).

References

1. G. Beer et al., Phys. Rev. Lett. **94**, 212302 (2005).
2. M. Bazzi et al., Phys. Lett. B **681**, 310 (2009).

VIP

S. Bartalucci, M. Bazzi (Ass. Ric.), C. Curceanu Petrascu (Resp. Naz.),
C. Guaraldo, M. Iliescu (Ass.), F. Lucibello (Tecn.), S. Okada (Bors. PD),
D. Pietreanu (Ass. Ric.), A. Romero Vidal (Bors. PD), D. Sirghi (Art. 2222),
F. Sirghi (Bors. UE), L. Sperandio (Ass.), O. Vazquez Doce (Art. 23)

1 The VIP scientific case and the experimental method

The Pauli exclusion principle (PEP), which plays a fundamental role in our understanding of many physical and chemical phenomena, from the periodic table of elements, to the electric conductivity in metals, to the degeneracy pressure (which makes white dwarfs and neutron stars stable), is a consequence of the spin-statistics connection. Although the principle has been spectacularly confirmed by the number and accuracy of its predictions, its foundation lies deep in the structure of quantum field theory and has defied all attempts to produce a simple proof. Given its basic standing in quantum theory, it seems appropriate to carry out precise tests of the PEP validity and, indeed, mainly in the last 15-20 years, several experiments have been performed to search for possible small violations. The indistinguishability and the symmetrization (or antisymmetrization) of the wave-function should be then checked independently for each particle, and accurate tests were and are being done.

The VIP (VIolation of the Pauli Exclusion Principle) experiment, an international Collaboration among 6 Institutions of 4 countries, has the goal to improve the limit on the probability of the violation of the PEP for electrons, (P $< 1.7 \times 10^{-26}$ established by E. Ramberg and G. A. Snow see Ref. [1]) by three-four orders of magnitude (P $< 10^{-(29\div30)}$), exploring a region where new theories might allow for a possible PEP violation.

The experimental method consists in the introduction of electrons into a copper strip, by circulating a current, and in the search for X-rays resulting from the forbidden radiative transition that occurs if one of the new electrons is captured by a copper atom and cascades down to the 1s state already filled by two electrons with opposite spins. The energy of this transition would differ from the normal K_α transition by about 300 eV (7.729 keV instead of 8.040 keV) providing an unambiguous signal of the PEP violation. The measurement alternates periods without current in the copper strip, in order to evaluate the X-ray background in conditions where no PEP violating transitions are expected to occur, with periods in which current flows in the conductor, thus providing "fresh" electrons, which might possibly violate PEP. The rather straightforward analysis consists on the evaluation of the statistical significance of the normalized subtraction of the two spectra in the region of interest.

The experiment is being performed at the LNGS underground Laboratories, where the X-ray background, generated by cosmic rays and natural radioactivity, is reduced.

2 The VIP experimental setup

The VIP setup was built in 2005, starting from the DEAR setup, reutilizing the CCD (Charge Coupled Devices) X-ray detectors, and consists of a copper cylinder, 4.5 cm in radius, 50 μm thick, 8.8 cm high, surrounded by 16 equally spaced CCDs of type 55.

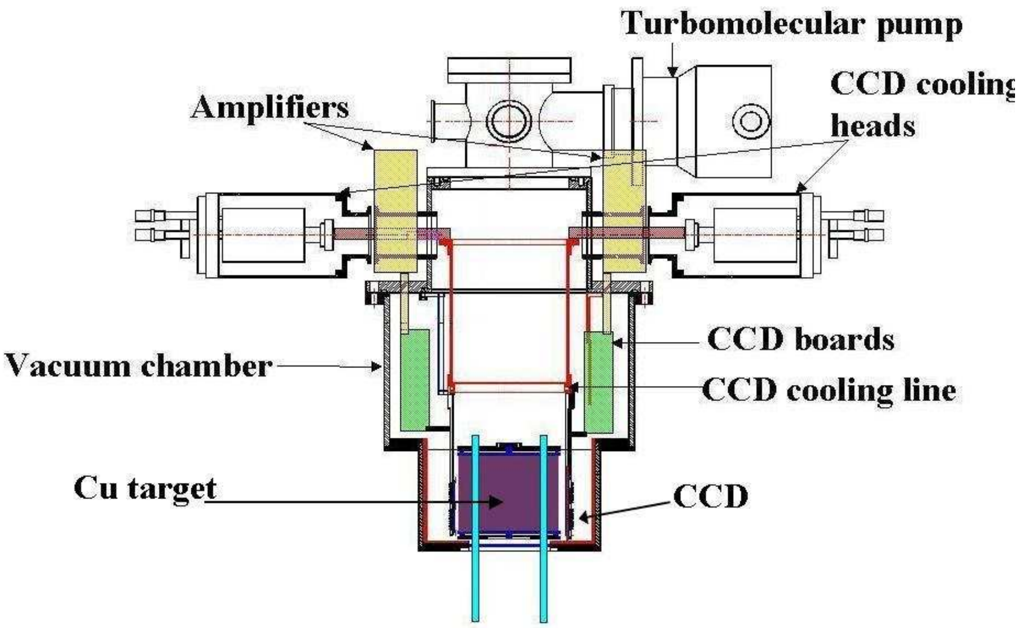

Figure 1: The VIP setup. All elements af the setup are identified in the Figure.

The CCDs are at a distance of 2.3 cm from the copper cylinder, grouped in units of two chips vertically positioned. The setup is enclosed in a vacuum chamber, and the CCDs are cooled to about 165 K by the use of a cryogenic system. A schematic drawing of the VIP setup is shown in Fig. 1.

The DAQ alternates periods in which a 40 A current is circulated inside the copper target with periods without current, referred as background.

VIP was installed and is taking data at the LNGS Laboratory since Spring 2006; see Fig. 2. The setup is surrounded by layers od copper and lead (as seen in the picture) to shield the setup against the residula background present inside the LNGS laboratory.

3 Activities in 2009

3.1 VIP data taking and analyses results

During 2009 the VIP experiment was in data taking, alternating periods of "signal" (I = 40 A) with periods without signal (I = 0 A). Data analyses were performed (energy calibration, sum of spectra, subtraction of background) and the probability of violation of PEP for electrons obtained (upper limit).

A new result, improving the previously published VIP result [2)] by more than an order of magnitude was obtained:

$$\frac{\beta^2}{2} < 4 \times 10^{-29} \tag{1}$$

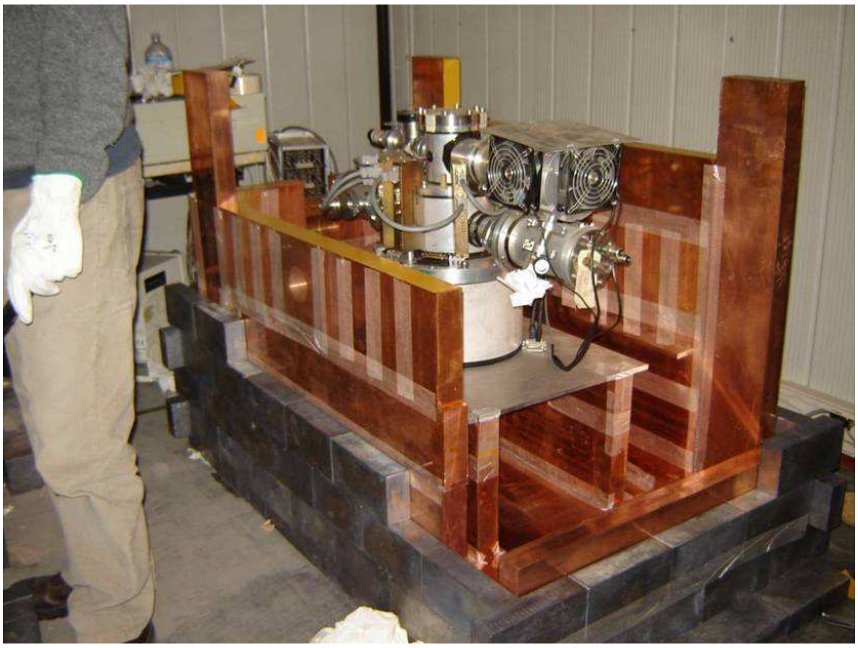

Figure 2: The VIP setup during the installation at LNGS.

3.2 The VIP upgrade

The present VIP setup uses CCD detectors which are excellent X-ray detectors (good energy resolution, background rejection based We plan to switch to a new type of detectors for precision X-rays measurements, the triggerable Silicon Drift Detectors (SSD) which have a fast readout time ($\simeq 1\mu$s) and large collection area (100 mm^2). These detectors, see Fig. 3, were successfully used in the SIDDHARTA experiment at LNF-INFN (see report on SIDDHARTA) for measurements of the kaonic atoms transitions at the DAΦNE accelerator of LNF-INFN; using a proper trigger system a background rejection factor of the order of 10^{-4} was achieved in SIDDARTHA.

With these new detectors is then possible to further reduce the background by using an external veto-system which should allow the elimination of all background produced by charged particles from the outside. A schematic layout of the new setup is shown in Fig. 4. Presently, experimental tests are under way to define the new experimental setup, which will be more compact than the present VIP setup and, as such, more manageable.

4 Activities in 2010

In 2010 the VIP setup will continue the data taking at LNGS, alternating periods of DAQ with current with periods of DAQ without current, at least until Spring. Periodical energy calibrations, using an X-ray tube which activates foils of Ti and Zr placed inside the setup, will be performed.

The data analyses will go on in parallel with the DAQ.

The feasibility of the upgrading of VIP by using a test setup containing 6 new X-ray triggerable detectors (Silicon Drift Detectors) and the veto system will proceed, with the aim to arrive at the (new) setup definition and to start its construction.

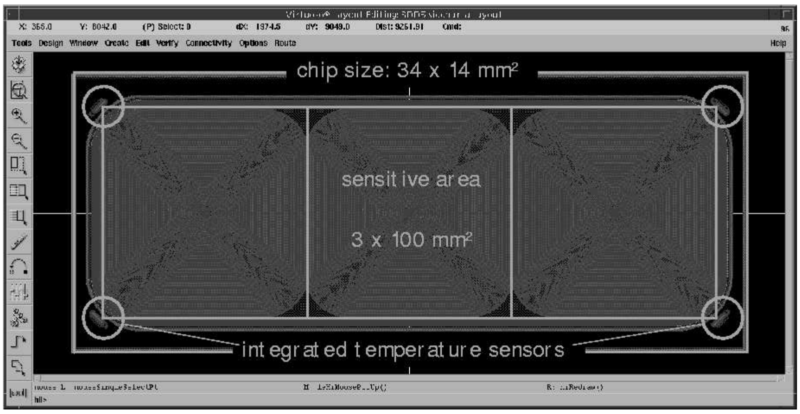

Figure 3: SDD layout on the readout side: 3 SDD cells, independently read, each with an area of 100 mm^2.

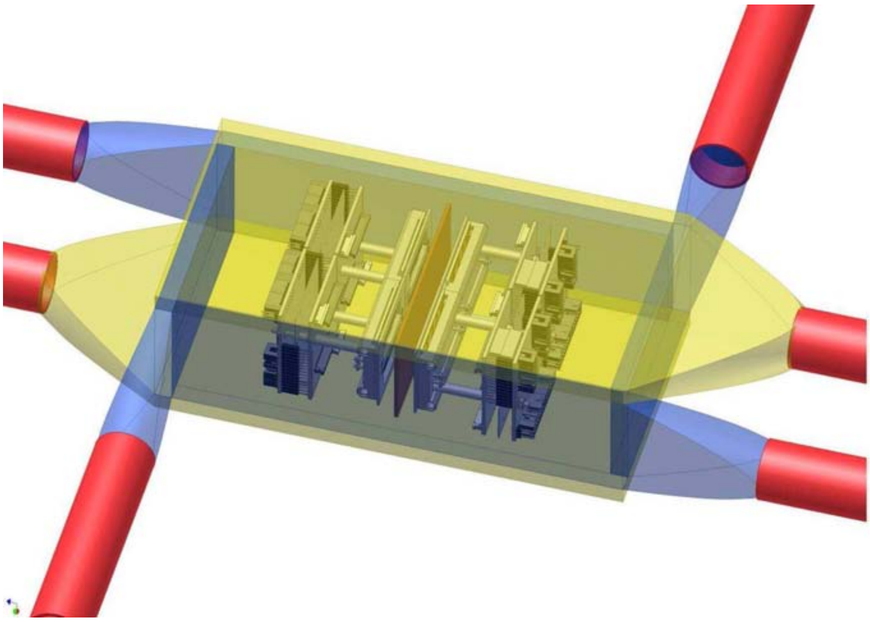

Figure 4: The possible implementation of the upgrade of the VIP experiment using SDD detectors and an external veto-system.

5 Publications

5.1 List of Conference Talks

1. C. Curceanu, *New experimental limit on the Pauli exclusion principle violation by electrons (the VIP experiment)*, Colloquium University of Vienna, 5 May 2009, Vienna, Austria.

2. C. Curceanu, *Is it always that electrons are unfriendly?*, Vienna Theory Lunch Club Seminar, 5 May 2009, Vienna, Austria.

3. C. Curceanu, *Experimental tests of quantum mechanics: Pauli Exclusion Principle and spontaneous collapse models*, talk at the Sestri Levante 2009, Convegno Informale di Fisica Teorica, Sestri Levante, Italy.

4. C. Curceanu, *New experimental limit on the Pauli Exclusion Principle violation by the VIP experiment*, talk at the QTRF5 - Quantum Theory: Reconsideration of Foundations 5, 14 - 18 June 2009, Vaxjo, Sweden.

5.2 Papers and Proceedings

1. D. Pietreanu et al., *VIP experiment: new experimental limit on Pauli Exclusion Principle violation by electrons*, Int. J. Mod. Phys. A **24**, 506 (2009).

2. C. Curceanu and E. Milotti, *The Pauli principle faces testing times*, CERN Courier January/February 2009, p. 25

3. S. Bartalucci et al., *The VIP experiment*, J. Phys. Conf. Ser. **174** 012065 (2009) .

4. C. Curceanu et al., *New experimental limits on the Pauli exclusion principle violatrion by electrons (the VIP experiment)*, J. Phys. Conf. Ser. **171**, 012031 (2009).

5. S. Bartalucci et al., *THe VIP experimental limit on the Pauli exclusion principle violatrion by electrons*, doi:10.1007/s10701-009-9346-1, to appear in Foundation of Physics.

6. E. Milotti, C. Curceanu, S. Adler and M. Berry, *Special issue on Spin STatistics*, doi:10.1007/s10701-010-9421-7, to appear in Foundation of Physics.

References

1. E. Ramberg and G. A. Snow, Phys. Lett. B **238**, 438 (1990).

2. S. Bartalucci et al., Phys. Lett. B **641**, 18 (2006).

4 – Theory and Phenomenology

FA51: Fisica Astroparticellare

D. Aristizabal Sierra (Bors.), E. Nardi (Resp.)

1 Description of the 2009 activity

During 2009 the research activities of the IS FA51-LNF focused on the following topics:

1. The relations between the seesaw parameters in the presence of a non-Abelian flavor symmetry were analyzed (independently) in pubs. [1] and [2]. Non-Abelian flavor symmetries in the neutrino sector are hinted by the closeness of the observed neutrino mixing pattern to tribimaximal mixing. We showed that in the limit of exact flavor symmetries all the CP asymmetries relevant for leptogenesis vanish exactly, and thus the Cosmological baryon asymmetry is directly related to the size of the flavor symmetry breaking. Due to the fact that symmetries generically imply a reduction in the number of free parameters, new relationships between parameters measurable at low energy, and high energy parameters not directly measurable, but relevant for leptogenesis, can arise. General results derived in [1] and [2] have been shown to hold in specific models and in particular in interesting realizations of the seesaw mechanism constrained by flavor symmetries involving A_4 as a non-Abelian factor.

2. Purely Flavored Leptogenesis is a scenario in which leptogenesis is basically seeded by flavor effects. The total CP asymmetry in the heavy seesaw neutrino decays, that is a lepton number violating quantity, vanishes exactly, and the relevant non-vanishing CP asymmetries only violate the lepton flavors. As a result, lepton number gets violated only in the washout processes. In pub. [3] we have studied in detail this scenario, showing that it has also the nice feature of allowing for leptogenesis at the TeV scale. Results obtained in pub. [3] have been reported also in pub. [4].

3. In pub. [5] we discuss a new effect, previously overlooked, that can have important consequences especially if leptogenesis occurs at low scales. In the presence of fast lepton-flavor violating interactions, that can often occur in models of new physics, all dynamical flavors effects become basically irrelevant. In this situation, no particularly large enhancement of the final baryon asymmetry can be obtained from special flavor configurations. Soft-leptogenesis (leptogenesis induced by SUSY breaking soft mass terms) is a good example of a framework in which lepton flavor equilibration must be taken into account, because of the generic presence of new sources of lepton flavor violation, as for example the off-diagonal sleptons soft breaking mass terms. The dynamics of soft leptogenesis with lepton flavor equilibration effects accounted for is presently under investigation.

4. In supersymmetric models extended with an anomalous $U(1)_H$ flavor symmetry the lepton and baryon number breaking operators (which induce proton decay) are either suppressed or forbidden. Accordingly, these models are phenomenologically viable without the need of R-parity. In these frameworks the horizontal charges H are fixed via a set of theoretical and phenomenological constraints, which generally also include neutrino physics data. Instead of using constraints from neutrino physics, in pub. [6] we replace them by other constraints arising from the requirement of having a stable LSP (at cosmological scales). By choosing the lightest neutralino to be the LSP we have shown that one can define different models characterized by different phenomenological properties. Interestingly, some of these models are able to explain the cosmic-ray anomalies on electron/positron fluxes reported by recent satellite experiments (PAMELA, FERMI).

5. In pub. [7] the $e^{\pm}$ cosmic rays excesses reported by PAMELA and ATIC where analyzed and interpreted in terms of decaying dark matter. It was found that this interpretation is compatible with all present constraints. ATIC data (now challenged by more recent FERMI measurements) were indicating a DM mass of about 2 TeV. We showed that this mass naturally implies the observed DM abundance relative to ordinary matter $\Omega_{\rm DM}/\Omega_{\rm matter} \sim 5$, if DM is a quasi-stable composite particle with a baryon-like matter asymmetry. In such a scenario the two apparently unrelated quantities $\Omega_{\rm DM}$ and $\Omega_{\rm matter}$ find nicely a common origin. Candidate particles of the type required in our scheme naturally occur in technicolor models.

Talks at Conferences

1. E. Nardi, *Some remarks on the fermion mass problem.* Invited talk at the International Conference: *Plank 09 - From the Planck Scale to the ElectroWeak Scale*, (parallel session A), 25-29 May, 2009; Centro Culturale Altinate (San Gaetano) Padova, Italy.
   `http://www.pd.infn.it/planck09/Talks/Nardi.pdf`
2. Enrico Nardi, *Leptogenesis".* Invited talk at the International Workshop: *NuFlavour - Flavour physics in the era of precision neutrino experiments*, 8-10 June 2009; The Cosener's House, Abingdon, UK.
   `http://conference.ippp.dur.ac.uk/conferenceDisplay.py?confId=267`
3. Enrico Nardi, *Recent developments in leptogenesis.* Invited talk at the: *Cosmo International Conference on Particle Physics and Cosmology – Cosmo09*, (parallel session: particle physics in the Early Universe) 7-11 September 2009, CERN, Geneva.
   `http://indico.cern.ch/conferenceDisplay.py?confId=46758`
4. Enrico Nardi, *Flavor issues in leptogenesis.* Invited talk at the II Prometeo Workshop: *CP violation and the baryon/lepton asymmetry* 9 -12 December 2009, Universidad de Valencia, Valencia, Spain.
   `http://ific.uv.es/ gabriela/workshop.html`

Editorial Work

1. *Physics Challenges In The LHC Era,*
   Proceedings, 1^{st} Young Researchers Workshop; 14^{th} Frascati Spring School 'Bruno Touschek', Frascati, Italy, May 11-14, 2009, 100p.
   E. Nardi, Editor.
   `http://www.lnf.infn.it/sis/frascatiseries/Volume48/volume48.pdf`

References

1. E. Bertuzzo, P. Di Bari, F. Feruglio, and E. Nardi, JHEP **0911**, 036 (2009). `arXiv:0908.0161`.
2. D. Aristizabal Sierra, F. Bazzocchi, I. de Medeiros Varzielas, L. Merlo, and S. Morisi, Nucl. Phys. B **827**, 34 (2010). `arXiv:0908.0907`.
3. D. Aristizabal Sierra, L. A. Munoz, and E. Nardi, Phys. Rev. D **80**, 016007 (2009). `arXiv:0904.3043`.
4. D. Aristizabal Sierra, L. A. Muñoz, and E. Nardi, J. Phys. Conf. Ser. **171**, 012078 (2009). `arXiv:0904.3052`.
5. D. Aristizabal Sierra, M. Losada, and E. Nardi, JCAP **0912**, 015 (2009). `arXiv:0905.0662`.
6. D. Aristizabal Sierra (INFN), J. Kubo, D. Restrepo, D. Suematsu, and O. Zapata, Phys. Rev. D **79**, 013011 (2009). `arXiv:0808.3340`.
7. D. Aristizabal Sierra, D. Restrepo, and O. Zapata, Phys. Rev. D **80**, 055010 (2009). `arXiv:0907.0682`.
8. Enrico Nardi, Francesco Sannino, Alessandro Strumia, JCAP 0901:043,2009. `arXiv:0811.4153`.

LF21: PHENOMENOLOGY OF ELEMENTARY PARTICLE INTERACTIONS AT COLLIDERS

O. Cata (Bors.), V. Del Duca, J. Kamenik (Bors.), G. Isidori (Resp.),
F. Mescia, S. Pacetti (Bors.), G. Pancheri (Senior Ass.), O. Shekhovtsova (Bors.)

1 Summary of the project

The research topics investigated by this project can be divided into the following three main areas:

- flavour physics, precision tests and physics beyond the Standard Model (O. Catà, G. Isidori, J. Kamenik, F. Mescia);
- theoretical and phenomenological aspects of QCD at colliders (V. Del Duca);
- hadronic cross-sections and form factors (S. Pacetti, G. Pancheri, O. Shekhovtsova).

The activity of the phenomenology group at Frascati can be seen in detail on our public web page [`www.lnf.infn.it/theory/pheno2.html`]. In the following we shall briefly describe some of most significant projects undertaken by the above participants in 2009.

2 Flavour physics, precision tests, and physics beyond the Standard Model

One of the strategies to obtain additional clues about the nature of New Physics (NP) is by means of precision tests of the Standard Model (SM) at low energies. These are particularly interesting in: i) electroweak processes calculable with high precision, where even tiny deviations from the SM can be detected; ii) processes which are not mediated by tree-level SM amplitudes, where the relative effect of NP contributions can be enhanced. Up to now there is no clear evidence for deviations from the SM in both type of processes, and this leads to significant constraints in building realistic extensions of the SM. For instance, realistic models must possesses a highly non-generic flavour structure. These constraints are particularlysevere for NP models with new degrees of freedom around the TeV scale, as required by a natural stabilisation the $SU(2)_L \times U(1)_Y \to U(1)_Q$ spontaneous symmetry breaking. The attempt to clarify this problem, both at the phenomenological level (with the help of precision data on rare decays) and at a more fundamental level (with the help of new symmetry principles), is one of the main activity of our group.

A closely related subject –which is also one of the primary research objectives of our group– is a better understanding of the SM itself, fixing his fundamental couplings (quark masses, CKM angles, non-perturbative condensates, ...) by means of precise calculations within the framework of effective field theories and Lattice QCD.

Within this general scenario, the highlights of the 2009 activity include:

Phenomenology of models with strong dynamics at the electroweak scale. [3, 7]

If the electroweak symmetry is broken by some unspecified strong dynamics, one or more heavy spin-1 fields may replace the Higgs boson in keeping perturbative unitarity up to a few TeV. We have analysed the Drell-Yan production of these heavy states at hadron colliders using a general description of spin-1 fields in the electroweak chiral Lagrangian. In

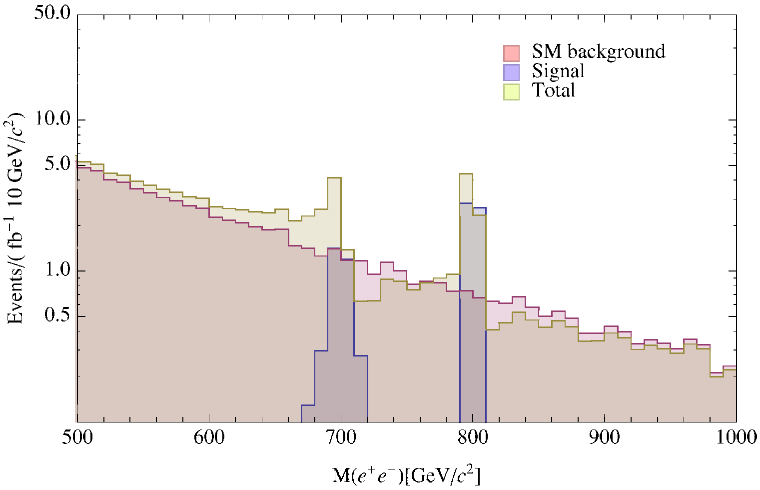

Figure 1: (color online). Possible signatures of heavy vectors in Higgsless models in $pp \to \ell^+\ell^-$ at $\sqrt{s} = 14$ TeV. [7)]

such models composite fermions may also exist with definite transformation properties under $SU(2)_L \times SU(2)_R/SU(2)_{L+R}$ and may play a role in giving masses by mixing to all the standard quarks and leptons. Assuming this to be the case, we have analyzed the role of Singlets, Doublets and Triplets in the ElectroWeak Precision Tests and in Flavour Physics. Doublets and Triplets are generically disfavoured. In the Singlet case, we have identified specific flavour-breaking patterns that allow to keep the success of the CKM picture of flavour physics. We have also discussed the effects of the mixing between composite and elementary fermions, which imply a rather peculiar LHC phenomenology of the composite fermion states.

Precision constraints in Supersymmetry extestions of the SM. [5)]
Motivated by recent progress in consistently and rigorously calculating electroweak precision observables and flavour related observables, we have updated our previous analyses of the Constrained Minimal Supersymmetric Standard Model (CMSSM), taking into account electroweak precision data, flavour physics observables and the abundance of Cold Dark Matter.

Lattice Simulation with light dynamical quark masses within the ETMC Collaboration. [4, 15)]
We have performed a systematic study of the pseudoscalar meson decay constants f_π, f_K, f_D and f_{Ds}, performed with $N_f = 2$ dynamical fermions using twisted-mass Lattice QCD. Our results for the light meson decay constants are $f_K = 158.1(2.4)$ MeV and $f_K/f_\pi = 1.210(18)$. From the latter ratio, by using the experimental determination of $\Gamma(K \to \mu\nu_\mu(\gamma))/\Gamma(\pi \to \mu\nu_\mu(\gamma))$ and the average value of $|V_{ud}|$ from nuclear beta decays, we obtain $|V_{us}| = 0.2222(34)$, in good agreement with the determination from semileptonic K_{l3} decays and the unitarity constraint. For the D and D_s meson decay constants we obtain f_D=197(9) MeV, $f_{Ds} = 244(8)$ MeV and $f_{Ds}/f_D = 1.24(3)$. Our result for f_D is in good agreement with the CLEO experimental measurement. For f_{Ds} our determination is smaller than the PDG

2008 experimental average but in agreement with a recent improved measurement by CLEO at the 1.4σ level.

Constraints from Kaon phyiscs on SM estensions with extra dimensions and warped geometry. [12]
The Randall-Sundrum (RS) framework has a built in protection against flavour violation, but still generically suffers from little CP problems. The most stringent bound on flavour violation is due to ϵ_K, which is inversely proportional to the fundamental Yukawa scale. Hence the RS ϵ_K problem can be ameliorated by effectively increasing the Yukawa scale with a bulk Higgs. However, as we have shown, ad additional independent constraint is provided by ϵ'/ϵ_K. The RS contribution ϵ'/ϵ_K has a different dependence on the Yukawa scale, which makes very difficult a combined fit to both ϵ_K and ϵ'/ϵ_K without a serious fine-tuning problem.

Lepton flavor violation in type I + III seesaw. [16]
In the presence of a low scale seesaw of type I + III, flavor violating effects in the leptonic sector are expected. Their presence in the charged sector is due to the mixing of the fermionic vector-like weak triplets with the chiral doublets, which cause non-universality of the tree-level Z coupling. We ihave nvestigated the bounds on the Yukawa couplings which are responsible for the mixing and present the results for two minimal cases, a fermionic triplet with a singlet or two fermionic triplets. Different channels for these processes have been considered and their current and future potential to probe these couplings has been analysed.

3 Hadronic cross-sections and form factors

Hadronic cross-sections were studied in two different type of processes and different energy ranges, namely at DAΦNE, and at high energy colliders in reactions of the type $A + B \to X$ where A, B could be a proton or an antiproton or a photon, with emphasis on the role played by soft gluons on the saturation of the Froissart bound.

Final State Radiation effects at DAPHNE. [18]
The problem of the final state radiation (FSR) is one of the main problems in the measurement of the the hadronic cross section at DAFNE. It is related with a fact that the FSR process is an irreducible background in radiative return measurements of the hadronic cross section and spoils the factorization of the cross section. In any experimental setup the process of FSR cannot be excluded from the analysis. The KLOE experiment has developed two different analysis strategies: the first one is with the photon emitted at small angle ($\theta_\gamma < 15°$) and the other one is for the photon reconstructed at large angle ($60° < \theta_\gamma < 120°$), being for both $50° < \theta_\pi < 130°$. In the case of the small angle kinematics the FSR contribution can be safely neglected, while for the large angle analysis it becomes relevant (upto 40% of ISR).

From another side the FSR process is interesting in itself. In fact, a detailed experimental study of FSR allow us to get information about pion-photon interaction at low energies. In the region below 2 GeV the pQCD is not applicable to describe FSR and calculation of the cross section relies on the low energy pion–photon interaction model. Thus the measured FSR cross section gives an unique possibility to get very interesting information on the dynamics of interacting mesons and photons, to test the pion–photon interaction models and extract their parameters.

We have developed the computer code FASTERD (FinAL STatE Radiation at DAΦNE): a Monte Carlo event generator written in FORTRAN that simulates both processes, where the hard photon can be emitted by the leptons. To test the accuracy of the program we compared the numerical results with the analytical prediction and with the results of the MC program PHOKHARA runnig the last one at the leading order approximation (only one photon is radiated). The results of the PHOKHARA program coincides with the FASTERD prediction better than 1%. An important feature of FASTERD is a possibility to estimate the double resonance contribution. At the first sight in the energy region about $s \approx m_\phi^2$ it is enough to include only the $\gamma^* \to \phi \to \rho\pi \to \pi\pi\gamma$ mechanism. However, at $s = m_\phi^2$ our simulation gives the $\sigma(\phi \to ((f_0 + \sigma)\gamma + \rho^0\pi^0) \to \pi^0\pi^0\gamma) = 0.451 \pm 0.001$ nb whereas $\sigma((\rho/\rho') \to \omega\pi^0 \to \pi^0\pi^0\gamma) = 0.529 \pm 0.012$ nb (in agreement with KLOE results).

Total cross-sections and the Froissart bound. [13, 14]

LHC will soon measure the total hadronic cross-section, adding one more point to a long quest in the understanding of hadronic collisions. As yet, there is no first principle calculation to predict the value of the total cross-section at any given energy, but it is possible to obtain QCD and QCD inspired descriptions, which, together with a certain degree of parameter fitting, can give some insight on the underlying dynamics. Since quite some time, a model was developed within this group, in which the rise with energy is driven by the increasing number of low x (fractional momenta) gluons. In such model high energy saturation is obtained through soft gluon emission, with integration of the soft gluon momenta extended down to zero, and with an appropriate ansatz for the behaviour of the strong coupling constant in this region. This model, inspired by the Bloch-Nordsieck (BN) theorem for soft photons and thus called the BN model, was applied to make predictions for the total proton-proton cross-section at LHC. Subsequently the model has been applied to photo-production. The predictions of the BN model were considered both in the present accelerator energy ranges as well as extended to very high energies, like the ones reachable though cosmic ray experiments.

A compilation of data from accelerator and cosmic ray experiments for both photon and proton processes is shown in Fig. 2.

Baryons form factors near the time-like threshold. [2]

A peculiar feature, observed in the *BABAR* data on $e^+e^- \to \mathcal{B}\overline{\mathcal{B}}$ cross sections ($\mathcal{B}$ stands for baryon), is the non-vanishing cross section at threshold for all these processes. This is the expectation due to the Coulomb enhancement factor acting on a charged fermion pair. Remarkably, in the case of $e^+e^- \to p\overline{p}$ it is found that Coulomb final state interactions largely dominate the cross section at threshold and it turns out a form factor $|G^p(4M_p^2)| \simeq 1$, as a pointlike fermion. A similar phenomena occurs in the $e^+e^- \to \Lambda_c\overline{\Lambda_c}$, recently measured by Belle In the case of neutral strange baryons the non-vanishing cross section at threshold is interpreted as a remnant of quark pair Coulomb interaction before the hadronization, taking into account the asymmetry between attractive and repulsive Coulomb factors. Besides strange baryon cross sections are successfully compared to U-spin invariance relationships.

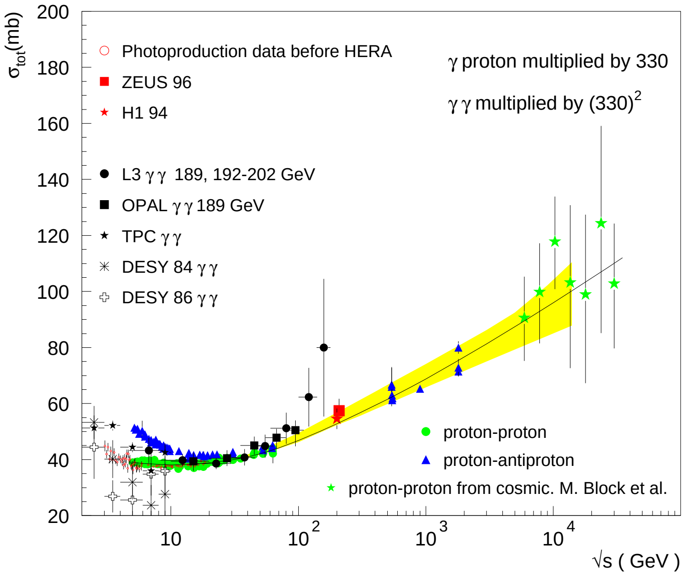

Figure 2: Photon and proton normalized total cross-sections with a typical curve expected from the Bloch Nordsieck (BN) model of G. Pancheri et al. [13], based on QCD mini-jets and soft k_t-resummation of infrared gluons.

4 Theoretical and phenomenological aspects of QCD at colliders

Higgs Boson Production in Hadronic Collisions. [1]

At the LHC, the Higgs boson will be produced mostly via gluon fusion, with the Higgs boson interacting with the gluons via a top-quark loop. This production mode is known at next-to-leading-order (NLO) accuracy in the strong coupling constant α_S for finite values of the top-quark mass m_t, and at next-to-next-to-leading-order (NNLO) accuracy in the limit $m_t \to \infty$. The latter, though, generates spurious logarithms $\ln(\hat{s}/m_H^2)$, which are not present when the full m_t dependence is taken into account. Higgs production via gluon fusion has been considered for finite values of m_t in the limit of high parton centre-of-mass energy $\hat{s}$, which allows us to improve upon the NNLO calculation mentioned above. Furthermore, multiple hard radiation emitted in the process can be resummed using a high-energy factorisation of the scattering amplitude.

Scattering amplitudes in the maximally supersymmetric $N = 4$ super-Yang-Mills theory. [8]

In the context of the maximally supersymmetric $N = 4$ super-Yang-Mills theory, we have analysed in the high-energy limit the question of the validity of a guess (the Bern-Dixon-Smirnov ansatz) on the exponentiation of a scattering amplitude at any number of loops and legs. The ansatz is believed to be valid for four-point and five-point amplitudes at any number of loops, but it is known to fail for two-loop amplitudes with six or more legs. However, the ansatz-violating contribution is known only numerically. This piece of information has proven insufficient, so far, to learn the correct form of the exponentiation, if any. In 2008 we have established that the simplest high-energy limit is not detailed enough to probe the ansatz-violating contribution. Accordingly, we have lain down the conditions for more sophisticated high-energy limits to probe the ansatz violation.

More recently we have considered the high-energy limit of the colour ordered one-loop five-gluon amplitude in the planar maximally supersymmetric $N = 4$ Yang-Mills theory in the multi-Regge kinematics where all of the gluons are strongly ordered in rapidity. We have applied the calculation of the one-loop pentagon in $D = 6 - 2\epsilon$ performed in a previous paper to compute the one-loop five-gluon amplitude through to $O(\epsilon^2)$. Using the factorisation properties of the amplitude in the high-energy limit, we have extracted the one-loop gluon-production vertex to the same accuracy, and, by exploiting the iterative structure of the gluon-production vertex implied by the BDS ansatz, we have performed the first computation of the two-loop gluon-production vertex up to and including finite terms.

5 Contributions to Conference Proccedings in 2009

1. A. Achilli, R. Godbole, A. Grau, G. Pancheri and Y. N. Srivastava, *QCD Mini-jet contribution to the total cross section,* presented at MPI08, Perugia, October 27-31, 2008, `arXiv:0907.0949` .

2. A. Achilli, Y. N. Srivastava, R. Godbole, A. Grau and G. Pancheri, *Relevance of ultra-soft gluons and kt resummation for total cross-sections,* presented at Low Energy Constraints on Extensions of the Standard Model, Kazimierz, Poland, 23-27 Jul 2009, `arXiv:0910.1867` .

3. F. Ambroglini *et al.*, Proceedings of the Workshop on Monte Carlo's, Physics and Simulations at the LHC PART I and PART II, `arXiv:0902.0293`, `arXiv:0902.0180` .

4. M. Antonelli *et al.*, *Flavor Physics in the Quark Sector,* proceedings of 5th International Workshop on the CKM Unitarity Triangle (CKM 2008), Rome, Italy, 9-13 Sep 2008, `arXiv:0907.5386` .

5. J. Bartels *et al.*, *Proceedings of the 38th International Symposium on Multiparticle Dynamics (ISMD08),* `arXiv:0902.0377` .

6. V. Bertone *et al.* (ETM Coll.), *Kaon oscillations in the Standard Model and Beyond using Nf=2 dynamical quarks,* to appear in the proceedings of 27th International Symposium on Lattice Field Theory (Lattice 2009), Beijing, China, 25-31 Jul 2009, PoS **LAT2009** (2009) 258 `arXiv:0910.4838`

7. O. Cata, M. Golterman and S. Peris, *Contribution from Duality Violations to the theoretical error on α_s,* presented at International Workshop on Effective Field Theories: From the Pion to the Upsilon (EFT09), Valencia, Spain, 2-6 Feb 2009, `arXiv:0904.4443` .

8. A. De Roeck *et al.*, *From the LHC to Future Colliders,* CERN Theory Institute Summary Report, `arXiv:0909.3240` .

9. S. Di Vita, *et al.*, (ETM Coll.), *Vector and scalar form factors for K- and D-meson semileptonic decays from twisted mass fermions with Nf = 2,* to appear in the proceedings of 27th International Symposium on Lattice Field Theory (Lattice 2009), Beijing, China, 25-31 Jul 2009, PoS **LAT2009** (2009) 257 `arXiv:0910.4845` .

10. S. Fajfer, I. Dorsner, J. F. Kamenik and N. Kosnik, *Search for new physics in charm processes,* presented at Low Energy Constraints on Extensions of the Standard Model, Kazimierz, Poland, 23-27 Jul 2009. `arXiv:0910.5407` .

11. R. M. Godbole, A. Grau, G. Pancheri and Y. N. Srivastava, *QCD and total cross-sections: Photons and hadrons,* AIP Conf. Proc. **1105** (2009) 291 `arXiv:0812.4705` .

12. A. Grau, R. M. Godbole, G. Pancheri and Y. N. Srivastava, *Infrared gluons, intrinsic transverse momentum and rising total cross-sections,* presented at 3rd International Conference on Hadron Structure '09 (HS09), Tatranska Strba , Slovakia, 30 Aug - 3 Sep 2009, `arXiv:0910.2267` .

13. G. Isidori, *Effective theories of electroweak symmetry breaking,* invited talk at the 6th International Workshop on Chiral Dynamics (CD09), July 6-10, 2009, Bern, Switzerland, `arXiv:0911.3219` .

14. G. Isidori, *Effective Theories for Flavour Physics beyond the Standard Model,* invited talk at International Workshop on Effective Field Theories: From the Pion to the Upsilon (EFT09), Valencia, Spain, 2-6 Feb 2009, `arXiv:0908.0404` .

15. J. F. Kamenik, *Theory of Semileptonic Charm Decays,* talk given at CHARM 2009 (International Workshop on Charm Physics), Leimen, Germany, 20-22 May 2009, `arXiv:0909.2755` .

16. Y. N. Srivastava, A. Achilli, R. M. Godbole, A. Grau and G. Pancheri, *Photoproduction total cross-sections at very high energies and the Froissart bound,* presented at 38th International Symposium on Multiparticle Dynamics ISMD08, Hamburg, Germany, 15-20 Sep 2008, `arXiv:0901.0109`.

References

1. J. R. Andersen, V. Del Duca, and C. D. White, JHEP **0902**,015 (2009).

2. R. Baldini, S. Pacetti, A. Zallo, and A. Zichichi, Eur. Phys. J. A **39**, 315 (2009).

3. R. Barbieri, G. Isidori, and D. Pappadopulo, JHEP **0902**, 029 (2009).

4. B. Blossier et al., JHEP **0907**, 043 (2009). `arXiv:0904.0954`.

5. O. Buchmueller et al., Eur. Phys. J. C **64**, 391 (2009).

6. O. Cata, M. Golterman, and S. Peris, Phys. Rev. D **79**, 053002 (2009).

7. O. Cata, G. Isidori, and J. F. Kamenik, Nucl. Phys. B **822**, 230 (2009).

8. V. Del Duca, C. Duhr, and E. W. Nigel Glover, JHEP **0912**, 023 (2009). `arXiv:0905.0100`.

9. J. Drobnak, S. Fajfer, and J. F. Kamenik, JHEP **0903**, 077 (2009).

10. I. Dorsner, S. Fajfer, J. F. Kamenik, and N. Kosnik, Phys. Lett. B **682** (2009) 67.

11. A. Filipuzzi and G. Isidori, Eur. Phys. J. C **64** (2009).

12. O. Gedalia, G. Isidori, and G. Perez, Phys. Lett. B **682**, 200 (2009).

13. R. M. Godbole, A. Grau, G. Pancheri, and Y. N. Srivastava, Eur. Phys. J. C **63**, 69 (2009).

14. A. Grau, R. M. Godbole, G. Pancheri, and Y. N. Srivastava, Phys. Lett. B **682**, 55 (2009).

15. V. Lubicz, F. Mescia, S. Simula, C. Tarantino, and F. T. E. Coll., Phys. Rev. D **80** (2009).

16. J. F. Kamenik, and M. Nemevsek, JHEP **0911**, 023 (2009).

17. J. F. Kamenik, and C. Smith, Phys. Lett. B **680**, 471 (2009).

18. O. Shekhovtsova, G. Venanzoni, and G. Pancheri, Comput. Phys. Commun. **180**, 1206 (2009).

LF61: Low-dimensional systems and spin-Hall effect

S. Bellucci (Resp. Naz.), M. Benfatto, M. Cini (Ass.), F. Corrente (Dott.), K. Hatada (Bors.), K. Hayakawa (Bors.), G. Iovane (Ass.), C. Natoli (Ass.), P. Onorato (Bors.), F. Palumbo (Ass.), R. Pastore (Ass.), E. Perfetto (Bors.), N. Pugno (Ass.), G. Stefanucci (Ass.)

1 External collaborating Institutions:

Univ. Roma La Sapienza, Univ. Roma Tor Vergata, IHEP-Protvino (Russia), Univ. Pune, India, Burnham Institute (La Jolla, CA, USA), ILL (Grenoble, France).

2 Research Activity

In collaboration with the Yerevan State University, Armenia, we studied Fermionic Casimir densities in toroidally compactified spacetimes with applications to nanotubes were considered, along with the Fermionic Casimir effect for parallel plates in the presence of compact dimensions with applications to nanotubes. An exactly solvable Ising-Heisenberg chain with triangular XXZ - Heisenberg plaquettes was also put forward.

Spintronic single-qubit gate based on a Pi-shaped lateral quantum dot with spin-orbit interaction was studied, in collaboration with the Seconda Universit di Napoli, Italy.

The use of a generalized waveguide approach to tight-binding wires allowed us to understand large vortex currents in quantum rings, in collaboration with the Universit di Roma Tor Vergata, Italy.

The atomic and electronic structure of single-walled BN nanotubes containing N vacancies as well as C and O substitutes of N atoms was investigated, in collaboration with the University of Latvia.

We have continued our work on a rigorous derivation of a real space full-potential multiple-scattering theory (FP-MST), valid both for continuum and bound states, for the calculation of core-level synchrotron radiation spectroscopy as applied to many interdisciplinary problems in condensed matter physics. We have been able to show that, contrary to the common belief in the literature, multiple scattering theory converges absolutely, so that the angular momentum truncation procedure is well founded. In this way we have solved a problem tha had been staying around for almost thirty years.

We have started the implementation of codes, based on our Full Potential MST, to calculate in real space properties of the ground state of molecules and in general clusters of atoms in a self-consistent way, in order to obtain self-consistent charge densities, the position of the Fermi level, the equilibrium atomic positions and other useful quantities both for ground state and continuum spectroscopies.

In collaboration with the ICMA Institute in Zaragoza (Spain), a resonant x-ray scattering study at the Mn K-edge and Tb L3-edge of TbMnO3 was performed to investigate the local distortions responsible for the ferroelectricity. TbMnO3 perovskite is indeed an interesting representative of those materials, of great technological importance, where antiferromagnetism (AFM) and ferroelectricity coexist at low temperatures.

In collaboration with the Univ. of Bourgogne-Dijon we have extended the multichannel MS program developed by P. Kruger in Dijon to complex algebra, in order to implement contour integration for the multichannel Green's Function and describe electronic correlation not only in the excited state but also in the ground states of molecules and clusters of atoms. It is hoped that this approach will cure the deficiences of the current Density Functional Theory (DFT) programs and go beyond the Dynamical Field Theory Approach (DMFT) in treating electronic correlations in solids.

We organized, so far, ten Schools and Workshops on nanoscale science and technology, aiming to assess the current state of the art and stimulate research networking, held under the patronage of INFN and other institutions from both the public and private sectors:

- 1. N&N2000, S. Margherita di Pula (Cagliari), Italy, September 24 - October 4, 2000, http://www.lnf.infn.it/conference/nn2000/default.html
- 2. N&N2001, Frascati (Roma), Italy, October 17 - 27, 2001, http://www.lnf.infn.it/conference/nn2001/Welcome.html
- 3. N&N2002, Frascati (Roma), Italy, September 23 - 28, 2002, http://www.lnf.infn.it/conference/nn2002/
- 4. N&N2003, Frascati (Roma), Italy, September 15 - 19, 2003, http://www.lnf.infn.it/conference/nn2003/
- 5. N&N2004, Frascati (Roma), Italy, October 14 - 20, 2004, http://www.lnf.infn.it/conference/nn2004/
- 6. N&N2005, Monteporzio Catone (Roma), Italy, November 14 - 16, 2005, http://www.lnf.infn.it/conference/nn2005/
- 7. N&N2006, Monteporzio Catone (Roma), Italy, November 6 - 9, 2006, http://www.lnf.infn.it/conference/nn2006/
- 8. N&N2007, Frascati (Roma), Italy, October 15 - 16, 2007, http://www.lnf.infn.it/conference/nn2007/
- 9. N&N2008 Frascati (Roma), Italy, October 20-23, 2008, http://www.lnf.infn.it/conference/nn2008/
- 10. N&N2009 Frascati (Roma), Italy, October 19-22, 2009, http://www.lnf.infn.it/conference/nn2009/

We published the Proceedings of the School and Workshop N&N2006, with the title: Nanoparticles and Nanodevices in Biological Applications. The INFN Lectures - Vol I, S. Bellucci (ed.), Lecture Notes in Nanoscale Science and Technology Vol. 4, Springer-Verlag Berlin Heidelberg, 2009, XII, 198 p., ISBN: 978-3-540-70943-5, <http://www.springer.com/series/7544.

3 Conference Talks

1. F. Micciulla, *Mechanical and electrical characterization of epoxy nanocomposites for electromagnetic screenin*, CANEUS Workshop, NASA Ames Research Center, California, USA, 1-6 March 2009.

2. S. Bellucci, *Nanotechnology*, ILO Turin, Italy, 18 March 2009.

4 Pubblications

1. S. Bellucci, A. A. Saharian, Phys. Rev. D **79:085019**, (2009).

2. K. Hatada, K. Hayakawa, M. Benfatto, and C. Natoli, J. Phys. Condens. Matter **21**, 104206 (2009).

3. S. Bellucci, P. Onorato, Phy. Rev. B **79**, 045314, (2009).

4. D. Antonosyan, S. Bellucci, V. Ohanyan, Phys. Rev. B **79**, 014432 (2009).

5. G. Stefanucci, E. Perfetto, S. Bellucci, and Michele Cini, Phys. Rev. B **79**, 073406 (2009).

6. Y.F. Zhukovskii, S. Bellucci, S. Piskunov, L. Trinkler, and B. Berzina, Eur. Phy. J. B **67**, 519 (2009).

7. S. Bellucci, and A. A. Saharian, Phys. Rev. D **80**, 105003 (2009).

8. S. Bellucci (ed.), *Nanoparticles and Nanodevices in Biological Applications*. The INFN Lectures Vol I, Berlin Heidelberg: Springer Verlag, vol. 4, p. 1-198, (2009).

9. B. Berzina et al., Nanophoton, **3**, 031950 (2009).

10. Y. F. Zhukovskii et al., Journal of Physics and Chemistry of Solids **70**, 796 (2009).

11. K. Hatada, K. Hayakawa, M. Benfatto, and C. Natoli, Journal of Physics: Condensed Matter, **21**, 104206 (2009).

12. C. Meneghini et al., J. Phys.: Condens. Matter **21**, 355401 (2009).

13. N.B. Perkins, S. Di Matteo, C.R. Natoli, Phys. Rev. B **80**, 165106 (2009).

14. D. Toledo et al., Photochemistry and Photobiology, **85**, 479 (2009).

15. S. Della Longa et al., Inorg. Chem. **48**, 3934 (2009).

16. E. Vorobeva, et al., Phys. Rev. B **80**, 134301 (2009).

17. S. Bellucci, P. Onorato, Phys. Rev. B **80**, 195115 (2009).

18. M. Cini, E. Perfetto, C. Ciccarelli, G. Stefanucci, and S. Bellucci, Phys. Rev. B **80**, 125427 (2009).

MI11

M.P. Lombardo

1 Collaborators

Kim Splittorff (Nordita), Jac Verbaarschot (Stonybrook), Elisabetta Pallante (Groningen), Albert Deuzeman (PhD student, Groningen), Owe Philipsen (Muenster), Lars Zeidlewicz (PhD student, Muenster), Michael Mueller Preussker (Humboldt Berlin), Edwin Laermann (Bielefeld)

2 Activity

The reasearch focus on theoretical and phenomenological aspects of strong interactions in the non perturbative regime. Main applications concern the physics of Quark Gluon Plasma and mechanisms of electroweak symmetry breaking based on strong dynamics to be explroed at the LHC.

1. We have completed our study of the phase diagram with twisted mass Wilson fermions at finite temperature, confirming the excellent qualities of the method, and we are now exploring the thermal transition at zero baryon density close to the physical pion mass. This is a large scale computing project of the Finite Temperature Twisted Mass Collaboration, promoted by Karl Jansen(Desy Zeuthen) and myself, and now comprising, besides myself, Owe Philipsen (Muenster), Michael Muller Preussker (Humboldt Berlin) and junior collaborators. Appeared as Phys. Rev. D **80**, 094502 (2009).

2. In collaboration with Kim Splittorff (Nordita) and Jac Verbaarschot (Stonybrook) we have continued our theoretical effort towards understanding and controlling the sign problem at nonzero baryon density by use of chiral perturbation theory and model studies. We have studied the mesoscopic dynamics of the system determining the fluctuactional properties of the order parameters and the number density, and indicated several implications on lattice simulations. Besides what reported in the database, arXiv:0910.5482 is accepted and in press as Phys. Rev. D.

3. In collaboration with Edwin Laermann (Bielefeld) and Postdoctoral Research Associate Rosella Falcone (Bielefeld) we are designing a hybrid method which should ameliorate on imaginary chemical potential and Taylor expansion by combining them, having in mind applications to the study of the strongly interactive Quark Gluon Plasma, the dynamics around the freezout line and the study of the endpoint of QCD. Preliminary results on the latter subject have been presented in collaboration with Claudia Ratti (Stonybrook/Wuppertal) at QuarkMatter08.

4. In collaboration with Elisabetta Pallante (Groningen) and phD student Albert Deuzeman (Groningen) we established a bound to the conformal region of QCD by using our own method based on the systematic exploration of the lattice phase diagram. The study is continuing in several directions aiming at further characterizations of the conformal dynamics and the properties of the infrared fixed point as well as at the study of the dynamical properties of the near-conformal phase. Besides what is available in the database, arXiv:0904.4662 is submitted to Phys. Rev. D

3 Planned Activity

Research will continue along the previous lines of 2009, in particular

1. We will start high statistics productions runs close to LHC conditions.

2. We will consider temperature effects and the role of baryons. Kim Splittorff will be visiting LNF for a few weeks to work on this project.

3. We will complete the study of the supercritical region. Rossella Falcone will be visiting LNF for a few weeks to this end.

4. We will analyze the transition as a function of Nf, we will study the conformal phase at large Nf as well as the subcritical dynamics relevant for technicolor modeling. Elisabetta Pallante will be visiting LNF to work on this project.

Postdoctoral associate Kohtaroh Miura, presently at Yukawa Institute, Kyoto, will join our group in Frascati.

4 Professional Service (partial list)

During 2009 I have served on the International Advisory Committee for Quark Matter 2009, The 21st International Conference on Ultra-Relativistic Nucleus-Nucleus Collisions; The XXVII International Symposium on Lattice Field Theory; Beijing, China, July 26 - 31, 2009;Extreme QCD 2009, the VII workshop on QCD in Extreme Conditions, Seoul , Corea del Sud, August 1–3 2009, Extreme QCD 2010, the VIII workshop on QCD in Extreme Conditions, Bad Honnef, Germany, 21-24 June 2010.

I am an appointed member of the LNF General Seminar Commettee, and I am coordinating the 2010 Theory Institute at the LNF, focussed on "Frontiers of Strong Interactions".

5 Talks (partial list)

I have been invited as a plenary speaker at
1. Lattice Gauge Theory for LHC Physics 6-7 November 2009, Boston MA(US)
2. FAIR Lattice QCD Days November 23-24, 2009, GSI Darmstadt (Germany).
3. Strong Coupling Gauge Theories in the LHC Era, Nagoya (Japan) December 2009.
4. Opening plenary speaker at the "Strong Interaction in the 21st Century", a celebration for the centenary of H.J. Bhabha, February 10-12, 2010, Mumbai, India.

References

1. M. P. Lombardo, K. Splittorff and J. J. M. Verbaarschot, `arXiv:0912.4410`.
2. M. P. Lombardo, K. Splittorff and J. J. M. Verbaarschot, PoS **LAT2009** (2009) 171 `arXiv:0912.3109`.
3. M. Muller-Preussker et al., `arXiv:0912.0919`.
4. A. Deuzeman, M. P. Lombardo and E. Pallante, `arXiv:0911.2207`.
5. M. P. Lombardo, K. Splittorff and J. J. M. Verbaarschot, `arXiv:0910.5482`.
6. L. Benussi et al., *Hadron Spectroscopy.* Proceedings, 12th International Conference, Hadron 07, Frascati, Italy, October 7-13, 2007.
7. E. M. Ilgenfritz et al., Phys. Rev. D **80**, 094502 (2009). `arXiv:0905.3112`.
8. A. Deuzeman, M. P. Lombardo and E. Pallante, `arXiv:0904.4662`.
9. M. P. Lombardo, K. Splittorff and J. J. M. Verbaarschot, Phys. Rev. D **80**, 054509 (2009). `arXiv:0904.2122`.

MI12: Gauge and String Theories

S. Bellucci (Resp.), S. Ferrara (Ass.), E. Latini (Dott.), S. Krivonos (Osp.),
A. Marrani (Bors. PD), V. Ohanyan (Osp.), A. Shcherbakov (Bors. PD),
A. Saharian (Osp.), A. Sutulin (Osp.), B.N. Tiwari (Bors. PD), A. Yeranyan (Bors. PD)

1 Research Activity

The topics covered are current issues in the theory of elementary particle interactions and of the theory of the gravitational force. The main research activity is on the following topics: 1) Study of BPS and non-BPS black hole attractors and their interpretation in the "fake supergravity"; 2) Study of the classes of perturbative quantum corrections to the N=2 Attractor Equations encompassed by modifications of the holomorphic prepotential; 3) Relation between the black brane potential and the entropy function for intersecting branes and their attractors; 4) Structure of N = 6 gauged supergravity at D = 4 and its dual theory with N = 2 supersymmetry; 5) Attractors and extremal black holes in 4-dimensional asymptotically non-flat backgrounds.

Active collaborations include: JINR-Dubna, Russia Tomsk Univ. Russia Univ. Hannover, Germany Turin Polytechnic, Italy CERN, Switzerland Annecy, LAPTH, France Valencia U., Spain

We also organized, so far, four Schools with the participation of fair amount of collaborators, both as lecturers and as students: 1) Winter School on Supersymmetric Mechanics Frascati (Italy), 7 - 12 March 2005; 2) Winter School on Attractor Mechanism Frascati (Italy), 20 - 24 March 2006; 3) School on Attractor Mechanism SAM2007, 18 - 22 June 2007 - INFN-Laboratori Nazionali di Frascati, Via E. Fermi 40, Frascati, Italy http://www.lnf.infn.it/conference/sam2007; 4) School on Attractor Mechanism SAM2009, 29 June - 3 July 2009 - INFN-Laboratori Nazionali di Frascati, Via E. Fermi 40, Frascati, Italy http://www.lnf.infn.it/conference/sam2009.

We published the Proceedings of the first School as Lecture Notes in Physics, Springer-Verlag Berlin Heidelberg 2006, two volumes, edited by S. Bellucci: as Lecture Notes in Physics Vol. 698, Supersymmetric Mechanics - Vol. 1: Supersymmetry, Noncommutativity and Matrix Models (ISBN: 3-540-33313-4), and Lecture Notes in Physics Vol. 701, Supersymmetric Mechanics - Vol. 2: The Attractor Mechanism and Space Time Singularities (ISBN: 3-540-34156-0). The third volume containing the lecture notes of the School SAM2006, was published with the title: Supersymmetric Mechanics - Vol. 3: Attractors and Black Holes in Supersymmetric Gravity, Stefano Bellucci Editor, Springer Lecture Notes in Physics 755, November 2008, ISBN: 3540795227, ISBN-13: 9783540795223, 373 pages. The fourth volume containing the lecture notes of the School SAM2007, will appear early in 2010 with the title: The Attractor Mechanism, Stefano Bellucci Editor, Springer Heidelberg, Germany.

We coordinate an INTAS project "Extended supersymmetry, strings and noncommutativity in field theory", involving a consortium of 12 international Institutions, with duration of 30 months starting Nov. 2006, until October 2009.

2 Conference Talks

1. S. Ferrara, *Supergravity and Black Holes*, lecture given at the School on Attractor Mechanism SAM2009, 29 June - 3 July 2009 - INFN-Laboratori Nazionali di Frascati, Italy .

3 Publications

1. S. Bellucci, S. Ferrara, A. Marrani, and A. Shcherbakov, Phy. Lett. Section B **672**, 77 (2009).
2. S. Bellucci, S. Krivonos, Phy. Rev. D **80**, 065022 (2009).
3. S. Bellucci, S. Ferrara, A. Shcherbakov, and A. Yeranyan, JHEP, **0910**, 024 (2009).
4. A. Ceresole, S. Ferrara, and A. Gnecchi, Phys. Rev. D **80**, 125033 (2009).
5. A. Ceresole, S. Ferrara, A. Gnecchi, and A. Marrani, Phys. Rev. D **80**, 045020 (2009).
6. B. L. Cerchiai, S. Ferrara, A. Marrani, and B. Zumino, Phys. Rev. D **79**, 125010 (2009).
7. S. Ferrara, A. Marrani, J. F. Morales, and H. Samtleben, Phys. Rev. D **79**, 065031 (2009).
8. L. Andrianopoli, R. D'Auria, S. Ferrara, P. A. Grassi, and M. Trigiante, JHEP **0904**, 074, (2009).
9. G. Iovane, Chaos Solitons Fractals **42**, 2338 (2009).
10. L. Marek-Crnjac, G. Iovane, S.I. Nada, and T. Zhong, Chaos Solitons Fractals **42**, 1974 (2009).
11. D. Cherney, E. Latini, A. Waldron, Phys. Lett. B **674**, 316 (2009).
12. S. Bellucci, S. Capozziello, M. De Laurentis, and V. Faraoni, Phys. Rev. **D 79**, 104004 (2009).

5 – Technological and Interdisciplinary Research

3+L (TIME RESOLVED e^+ LIGHT)

A. Bocci (Art.23), M. Cestelli Guidi (Art.23), A. Clozza, A. Drago (Resp. Naz.),
A. Grilli (Tec.), A. Marcelli, R. Sorchetti (Tech.), A. Raco (Tec.), G. Zangari (Ass.)

1 Introduction

At LNF, 3+L (Time Resolved e^+ Light), a beam diagnostics experiment funded for the years 2007-2009 by the National Scientific Committee V of the INFN, has been set-up on one of the bending magnet of the DAΦNE positron ring. The 3+L experiment has been designed to monitor in real time the e^+ bunch shape and to study the bunch dynamics in the DAΦNE Φ-Factory performing bunch-by-bunch and turn-by-turn longitudinal and transverse beam diagnostics by using compact uncooled IR detectors. 3+L operated during 2009 in the DAΦNE hall where a compact optical system has been installed and aligned. It collects the IR synchrotron radiation emission and focus the radiation on a small spot where a fast detector can be aligned to perform real-time bunch diagnostics. Several measurements have been carried out using different IR photodiodes. Moreover, efforts have been dedicated to test and characterize a prototype of an IR array detector that can be used to monitor the bunch-by-bunch transverse profile of the e^+ beam.

2 Experimental set-up

The 3+L experiment collects the IR light emitted by particles circulating in the DAΦNE positron ring and extracted from the first bending magnet after the Interaction Region 2. It consists of a compact front-end with an HV chamber that hosts a gold-coated silicon plane mirror. The mirror collects and deflects the light emission through a ZnSe window that transmits radiation in the range 0.6 to 12 μm (800-17000 cm^{-1}). Inside the storage ring hall, after the ZnSe window, five mirrors working in air focus the radiation in a spot of about 0.1 mm^2. This compact optical layout demagnifies the source of a factor ~ 5 and allows also the imaging of the source. Detectors placed behind the 4th mirror are mounted on a xyz micrometer stage to align them to the light spot. The installation is completed by a computer to remotely control the experiment. A PCI-COM bridge RS-232 board controls motors and the xyz stage and two webcams and a camera monitor the detector and the mirrors positions. A power supply connected to the PC by a USB-GPIB interface is used to supply amplifiers and detectors. Dedicated software packages have been developed under the LabVIEW platform for data acquisition, to control the power supplies and the xyz stage. An oscilloscope model Tektronics TDS 820 with 6 GHz of bandwidth connected to the PC by the same USB-GPIB interface is used for data acquisition.

3 Activity

During 2009 different measurements have been carried out with the 3+L optical system both to characterize the emitted light in the IR region and the detectors. In particular, measurements were carried out using fast PVMI 3-stages detectors from VIGO System S.A. These detectors are based on HgCdTe multilayer hetero-structures grown by the MOCVD technology on oriented GaAs (211) and (111) substrates. They have been optimized to work in the mid-IR at 10.6 μm and their best response time may reach 100 ps or lower when cooled at 205 K with the 3-stage Peltier cooler. Photodiodes were inverse polarized varying bias voltages in order to optimize performances, i.e., response times and the highest S/N ratio. The output of the device was connected to a broadband preamplifier to enhance the signal of the photodiode. The amplifier was characterized by ≈ 46 dB gain and 0.01- 2500 MHz of bandwidth. Detectors are very sensitive and during measurements we detected also noise associated to the two radio cavities of the DAΦNE rings. In order to shield the RF signal of the klystrons installed in the DAΦNE hall, the circuit used to polarize the photodetector, the photodiode and the amplifier were closed inside a metal box. Coaxial cables and SMA connectors were used to connect the output of the amplifier to two channels scope for data collection. For all IR devices, the measurements were carried out at room temperature.

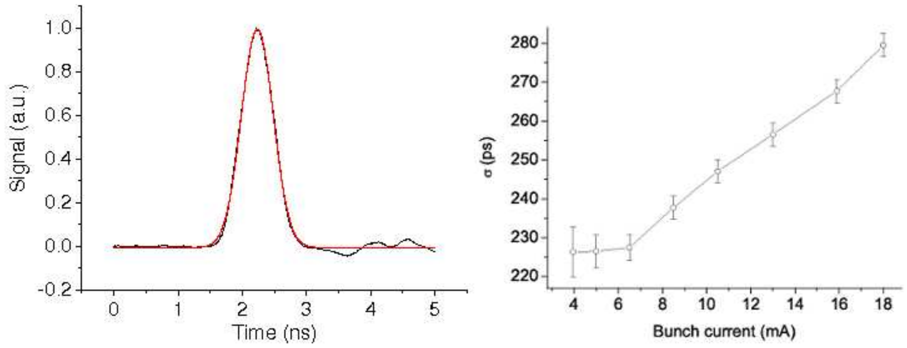

Figure 1: (color online). The shape of a typical positron bunch (black) measured at IR wavelengths and its Gaussian fit (red) (left panel). The behaviour of the rms bunch length vs. the bunch current measured with the IR uncooled photodiode (right panel).

Data in the left panel of Fig.1 show that with a bunch current of ≈ 5 mA the bunch profile is Gaussian with a length of $\sigma \approx 240$ ps while both the rise and fall time measured by this detector are ≈ 400 ps. Data have been collected vs. the positron current in order to characterize the bunch length behavior. In the right panel of Fig. 1 we show the rms bunch length of the Gaussian distribution used to fit data as a function of the bunch current. The σ of the Gaussian distribution increases as function of the bunch current, exhibiting a linear behavior for currents higher than $\approx$ 7 mA, while, at lower currents, the σ has a constant value of ≈ 225 ps. The observed behavior is probably due to the limited response time of the photodiode working at room temperature. In order to reduce the RF noise a new, better shielded device with a dedicated electronics was also used to amplify the photodiode. A photograph of the detector with its compact electronics, mounted at the focus of the 3+L experiment is showed in Fig. 2. The electronics allows to bias the device at a fixed voltage and cool down it at 205 K to optimize performances.

With the original set-up above described, because the RF power of klytrons increases with the beams currents we measured an increasing noise level as function of the e^- and of the e^+ currents. With the new experimental set-up we measured a peak-to-peak voltage associated to the RF noise at high beam currents in the range 10 to 30 mV that allows obtaining a S/N ratio ≥ 100, a factor 10 times better. The signal of the e^+ bunch pattern with a separation of 2.7 ns as measured by the PVI-3TE-10.6, SN 5986 device is showed in the right panel of Fig. 2. In these runs, in order to optimize the response time of the detector, we cut the power associated

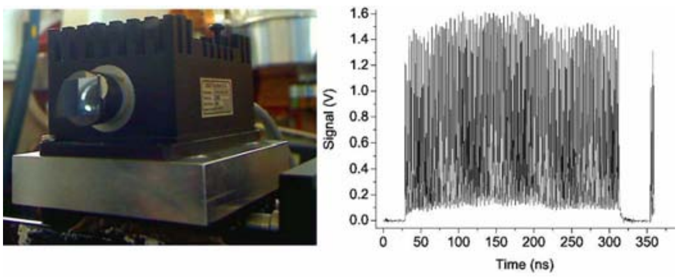

Figure 2: The amplifier, the IR photodiode with its mid-IR filter installed at the focus of the 3+L optical system inside the experimental hall (left panel). The typical bunch pattern with the 105 e^+ bunches and the gap measured with the shielded electronics of the cooled PVMI 3-stages VIGO detector (right panel).

to wavelengths lower than 10.6 μm for which the photodiode was optimized, using a mid-IR filter with a cut-off at 5 μm was in front of the device (Fig. 2). The electronics system was made by a transimpedance amplifier with a (high) bandwidth in the range 0.0001-1000 MHz and with a gain of 3900 V/A ($\approx$ 37 dB). Although an optimization of the voltage value was not possible, with the new electronics set-up, a reverse bias voltage was applied to the photodiode to obtain similar response times as those achieved with the previous electronics set-up. Actually the response time of this second device, that, in principle, may reach response time lower than 100 ps was $\approx$ 500 ps, a factor $\approx$ 2 slower than the best device previously measured. Nevertheless, the electronics set-up exhibited a much better shielding of the RF signal and a much lower noise level. In the future, this electronics should allow to achieve response times down to $\approx$ 100 ps really improving the longitudinal diagnostics of the 3+L experiment.
Finally during 2009 we carried out different tests of an infrared array prototype made by 32 x 2 pixels. For the preliminary measurements an interface board has been built and the pixels of the array have been connected by gold bonding wires to the board and finally to the input of an analog electronics board (see left panel in Fig. 3).

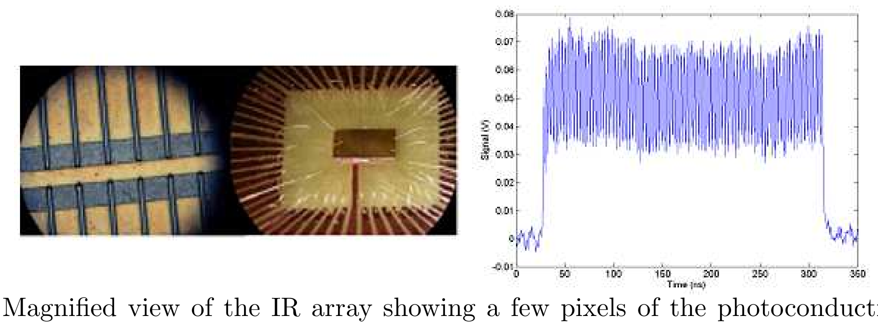

Figure 3: Magnified view of the IR array showing a few pixels of the photoconductive detector and the interface board of the device showing the connection between pixels and the gold bonding wires at the interface board (left panel). In the right panel the IR signals of the 105 e^- bunches collected by one of the pixels of the IR array.

The dedicated electronics of the array is composed by 64 channels with a bandwidth of 1 GHz for channel designed to amplify signals of the array with a gain of $\sim$ 40-50 dB depending by the power supply voltage. A four channels oscilloscope has been used to characterize each pixel of the device, to collect and analyze the signals. A dedicated digital electronics, based on powerful FPGA (Field Programmable Gate Array) chip, is under development to collect and store the signals from all the 64 channels. Up to now, during the preliminary measurements, only four pixels of the array have been connected to the data acquisition system. To perform tests we used the IR emission of the electron beam at the SINBAD beamline. The array has been placed at the focus spot of the optical system after the last toroidal mirror of the SINBAD optical system. It demagnifies the source image by a factor 2.3 with an estimated spot of about 2.0x1.5 mm at mid-IR wavelengths. The array has been placed in the vertical position in front to the IR spot. With a pixel size of 50x50 μm a large fraction of the spot can be monitored by the array with only 4 pixels connected to the electronics system. Measurements obtained from a single pixel of the array are shown in the right panel in Fig. 3 where the individual IR emission of the 105 bunches of the e^- beam and the gap are clearly resolved. Signals of four pixels have been also collected at the same time by an oscilloscope using four input channels and a bandwidth of 1 GHz with 4 Gsample/s. The analysis of the large amount of data collected by the array is still in progress but the first results are interesting. In Fig. 4 data acquired from the bunch pattern stored in the electron ring are shown in a 3D plot. Four pixels (of 64) are analyzed: they show clearly a change of intensity along the bunch train versus different transverse positions (correlated to pixel numbers).

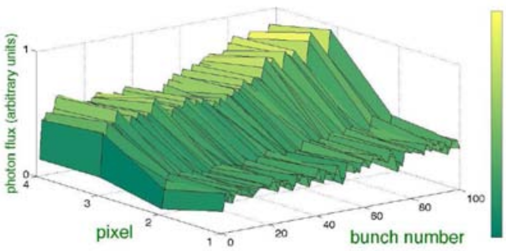

Figure 4: The image shows the multibunch pattern of the DAΦNE electron ring as reconstructed from the signals of the four pixels of the linear array. It is evident a change of the intensity along the bunch train.

4 2010 Activities

The activities foreseen in the year 2010, being finished both the beamline construction and the experimental program funded by the V$^{\text{th}}$ National Scientific Committee, shall consist mainly of the analysis of the large amount of data recorded in 2009 both by single-pixel and multi-pixels detectors. After the end of DAΦNE shutdown due to the installation of the KLOE detector, the 3+L vacuum chamber would be reinstalled on the exit port of the positron main ring. If this will happen, new and faster infrared detectors should be tested during next year. Moreover, data could be collected at the 3+L and/or at the SINBAD beam line using the new portable FPGA-based digital acquisition system.

5 Publications

1. A. Bocci et al., *Beam Diagnostics for positron beam at DAΦNE by 3+L experiment*, Proceedings PAC09, Vancouver, BC, Canada, MO4RAI01.

2. A. Bocci et al., *Beam Diagnostics at IR Wavelengths at NSRL*, Proceedings PAC09, Vancouver, BC, Canada, TH5RFP056

3. A. Bocci et al., Proceedings DIPAC09, Basel, Switzerland, May 25-27, 2009, 194.

4. A. Bocci et al., Frascati Report LNF - 09/15(R).

ALTCRISS

M.A. Franceschi, G. Mazzenga (Tecn.), T. Napolitano, M. Ricci (Resp.), B.Spataro

Participant Institutions:

Italy: INFN LNF, Roma 2-Tor Vergata; University of Genova
Germany: SIS (Darmstadt)
Russia: MePhi, IBMP, RKK "Energia" (Moscow)
Sweden: KTH (Stockholm)
ESA European Astronaut Center

1 Introduction

The ALTCRISS experiment (Alteino Long Term monitoring of Cosmic Rays on the International Space Station) - previously named SI-RAD - is a continuation of the activities carried out for the experiments SIEYE1 and SIEYE2 on board the Russian Space Station MIR in the years 1995-2002 and for the experiment SIEYE3/ALTEINO on board the International Space Station (ISS), still running [1) 2) 3)].

The experimental task of the ALTCRISS experiment (approved by ESA and ASI in Phase A) is to develop a detector to be placed on the external part of the ISS. The detector will be used to monitor cosmic rays and radiation environment in Low Earth Orbit. Long term (Solar modulation) and short term (coronal mass ejections, orbit dependence) effects on the particle flux will be monitored as well as the dose absorbed by the astronauts. In addition, data will be compared with measurements taken inside the ISS with ALTEA [4)], ALTEINO and LAZIO/SIRAD [5)] detectors to validate radiation transport and dose estimation codes. At the same time, the investigation, with a more sophisticated instrument, of the "Light Flashes" phenomenon [6)], will be conducted to improve and refine the results obtained with the previous SIEYE experiments.

The preparation of the next ALTCRISS extended mission is advancing towards the completion of the full flight instrument consisting of a 16-plane tower of double-sided silicon detectors (8x8 cm^2 area) equipped with trigger and anticoincidence counters. The total weight is about 15 kg and the total power consumption should not exceed 30 W. The hardware set-up is accomplished through three steps by the construction of a laboratory prototype model, an engineering model and the final flight, space qualified model.

The activity has been mainly focused on the development of the following systems of the engineering model:

- Trigger system.
- Development of Silicon Photomultiplier (SI-PM) technology for space applications and test of different SI-PM configurations.
- Completion and test of a highly integrated silicon board (16 cm x 16 cm).
- Production and test of a low-power, low-mass Digital Processing Unit (DPU).

For the year 2010, the planned activity includes the completion of the engineering ALTCRISS unit and the set-up of the flight configuration equipped with autotrigger capabilities for heavy nuclei and a trigger for crossing protons and nuclei. The interface with the ISS Space Station will be realized with an intermediate CPU to manage the telecommands from ground and the download of the data. Beam tests at the LNF-BTF, GSI/Darmstadt and other facilities are also planned together with the continuation of the R&D on the SI-PM technology.

2 Activity of the LNF group

The LNF group has taken the responsibility of the design, construction and test of the mechanical structures and interfaces of the three models of the detector also contributing to the integration of the mechanical support for the DAQ. This activity is carried out with the support and the participation of the LNF Service of Development and Costruction of Detectors (SSCR). The activity in 2009has been mainly devoted to the completion of the mechanical support of the engineering model and to the interfaces of the front-end and DAQ with the detector. These systems are being developed for the final space-qualified flight configuration in the year 2010. The LNF group participates as well in the beam test activities at the above mentioned facilities having the responsibility of the beam trigger counters and of the general arrangement and set-up.

3 Selection of recent publications

1. C. La Tessa et al., Nucl. Instr. & Meth., B **267**, 3383 (2009).
2. M. Casolino et al., Nuovo Cimento **31C**, 77 (2008).
3. V. Zaconte et al., Nucl. Instr. Meth. Phys. Res. B **266**, 2070 (2008).
4. M. Casolino et al., Adv. Space Res. **40**, 1746 (2007).

References

1. V. Bidoli et al., Journal of Physics G **27**, 2051(2001).
2. M. Casolino et al., Nucl. Phys. B **113**, 88(2002).
3. V.Bidoli et al., Nature **422**, 680 (2003).
4. L. Narici et al., Adv. Space Res. **31**, 141 (2003).
5. F. Altamura et al., *Preliminary results from the LAZIO-Sirad experiment on board the International Space Station*, Proc. XXIX ICRC, Pune (2005), SH35 p.101.
6. G. Horneck, Nucl. Tracks Radiat. Meas., **20**, 185 (1992).

CUP

S.B. Dabagov (Art. 23, Resp.), L. Quintieri (Art. 23), C. Natoli,
A. Babaev (Osp.), O. Bogdanov (Osp.), and B. Azadegan (Osp.)

Collaboration:	Italy	INFN - LNF, Frascati
	Russia	RAS P.N. Lebedev Physical Institute, Moscow
		Tomsk Polytechnic University, Tomsk
	Germany	MAMI, Mainz
	Denmark	Aarhus University, Aarhus
	Iran	Sabzevar University, Sabzevar

The CUP experiment is a first important step of a more ambitious project that investigates the feasibility to create new powerful sources of high-frequency monochromatic electromagnetic radiation: crystal undulator and γ-laser based on channeling of positrons in crystals. In this report the main goal of the CUP experiment and the results of theoretical studies on positron/electron both channeling and channeling radiation (CR) in mono and complex crystals performed in 2009 will be presented.

1 The CUP Experiment

The final objective of the CUP experiment (**C**rystal **U**ndulator for **P**ositrons) is to study the features of radiation emitted by positron channeling in a crystal. For our investigation the positron beam of the DAΦNE Beam Test Facility, the transfer line of which is presented by Fig. 1, will be used.

As known, the BTF facility provides electrons and positrons with energy ranging from 20 to 800 MeV (750 MeV for positrons). Working around the nominal DAΦNE energy of about 500 MeV, we expect to identify in a silicon monocrystal the radiation at (110) channeling of positrons having a peak at a photon energy of 1 MeV. The DAΦNE BTF is the unique European Facility that at present time is able to deliver positron beams in the energy range of interest for the CUP experiment. In fact, according to well accepted CR theories a strong photon peak with energy

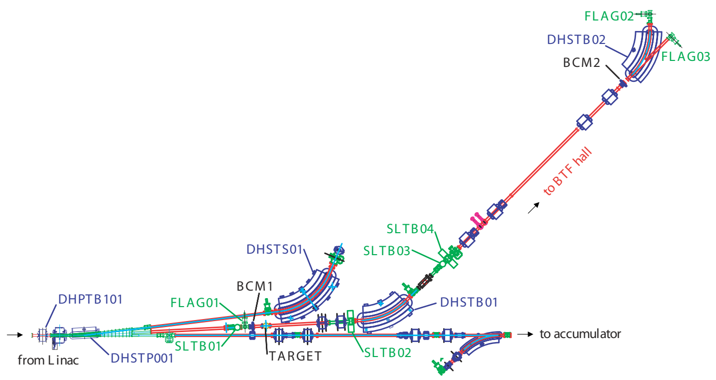

Figure 1: Transfer line of the DAΦNE Beam Test Facility.

from 20 KeV up to 1.5 MeV should appear for the (100) plane of a single crystal at a positron beam energy of about 600 MeV. At BTF this peak could be detected and its intensity should be investigated as a function of several parameters (crystal thickness, angle of incidence of impinging beam, etc). Unfortunately, the high background around the crystal in the experimental hall of the DAΦNE BTF has represented a strong limit to detectability of the signals we are looking for. Anyway important upgrade on the shielding structure along the BTF transfer line (part of which had been implemented soon after our measurement tests) and the use of suitable magnets to redirect the positrons at the transfer line exit could solve most of the problems we have met. These technical solutions are discussed in the following.

2 The DAΦNE BTF Facility

The DAΦNE Beam Test Facility is an electron/positron transfer line, by which the beam accelerated from the Linac, is transported to an experimental hall where the beam tests as well as the experiments can be performed. The facility can provide e-/e+ beam in a wide range of intensity: from single particle per bunch up to 10^{10} particles per pulse. The BTF is operating since 2002: during these years, tens of high energy physics experiments from all over Europe have been hosted. The main applications of the facility are: high energy detector calibration, low energy calorimetry, low energy electromagnetic interaction studies, detector efficiency and aging measurements, tests of beam diagnostic devices.

3 Experimental Setup

The aim of the first measurements at the DAΦNE BTF was to identify and investigate the intense radiation at (110) channeling of 500 MeV positrons in a plane silicon single crystal, for which a peak at photon energy of 1 MeV is expected.

In Fig. 2 the experimental-setup used for the BTF measurements campaign has been shown. The beam spot diameter at the target position was approximately 10 mm with a maximum angular divergence of 1 mrad according to the Linac parameters.

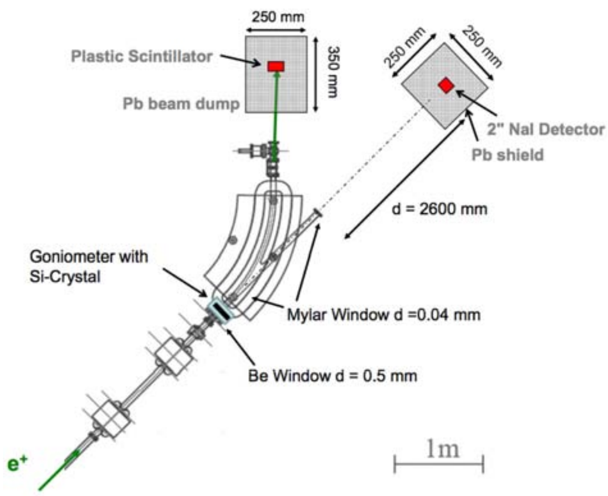

Figure 2: The end part of the DAΦNE BTF and the experimental setup for CUP.

As a conclusion, the most important thing we learnt from this measurement campaign was that it is mandatory to reduce the background level by at least one order of magnitude if we want to detect positron planar channeling. The latter requires upgrading of the BTF transfer line by multiple shielding. In addition, a possible solution could consists in installing a magnetic chicane in the straight line after the last 45^0 bending magnet as shown in Fig. 3.

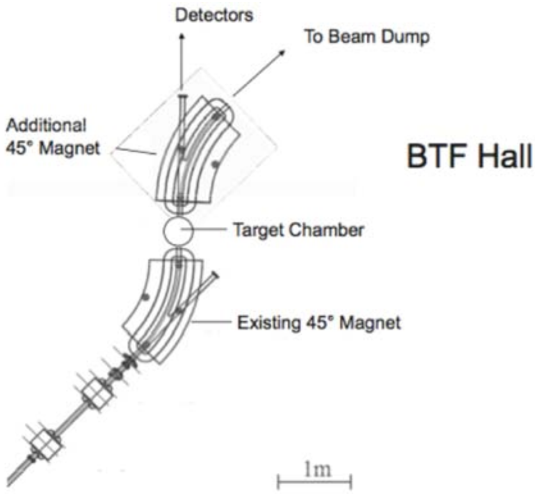

Figure 3: Proposed scheme of chicane solution for separation of positron beam and CR.

It should deflect the beam after the target into a dump. The detection device for recording the CR would be mounted after the last magnet in a straight line from the target chamber (as reference take in mind that we follow the particle motion). This setup offers several advantages:

- it is comparatively inexpensive;
- full advantage can be taken of the existing and optimized beamline to produce an adequate beam spot in the target chamber;
- with the slit systems the emittance can be reduced, the momentum spread of the linac positron beam be handled and, in turn, hopefully a high quality positron beam be generated with the required beam divergence of 0.2 mrad at a spot size of less than 10 mm diameter;
- the intensity can be adapted to make counter experiments feasible. Because the detector has in this geometry not anymore a direct line of sight into the region of the background producing slit systems, the background should be strongly reduced. Furthermore, it is also of great importance that the detectors could be shielded sufficiently well from the radiation produced in the beam dump.

The results of the first test we have done at BTF proved that we have high background, due to which it is difficult to resolve positron channeling and CR peaks. In 2009 we continued with upgrading our experimental layout and exploiting the advantages of the multiple shielding along the transfer line that is going to reduce of at least an order of magnitude the background level in the experimental hall. Multiple advantages can also be derived by a magnetic chicane that is going to be installed at the end of the BTF transfer line.

4 Theoretical Studies on Moderate Energy Electron/Positron Channeling

When electrons or positrons are planar channeled in a crystal, the spectrum of bound energy states forms and one can observe so-called CR. The intensity of CR depends on populations of bound energy levels. These populations change during projectiles motion through a crystal that, in turn, influences the CR intensity. During 2009 we have developed a theoretical model and computer codes to investigate the bound energy spectra of planar-channeled electrons and positrons and to obtain the initial populations of bound states. Solving the kinetic equations and using some approximations we explore the dynamics of bound state populations. The simple approximations used allow analytical solutions of kinetic equations to be obtained. Presented models have been applied to describe planar channeling of 80 MeV electrons and positrons along (220) planes in Si crystal.

Spectral distributions of CR by 20-800 MeV electrons in different planes of a thin 4H polytype silicon carbide crystal were obtained. We demonstrated that channeling in 4H SiC with hexagonal structure has some new features not available in other structures. Using Doyle-Turner approximation to the atomic scattering factor and taking into account thermal vibrations of atoms, the continuum potentials for different planes of 4H polytype SiC single crystal were calculated. In the frame of quantum mechanics, the theory of CR has been applied to calculate the transverse electron states in the continuum potential of the planes and to study transition energies, linewidths, depth dependence for population of quantum states and spectral radiation distributions. At electron energies higher than 100 MeV the spectral distributions of radiation are calculated by classical calculations and successfully compared with quantum mechanics solutions. Specific properties of planar CR in 4H polytype SiC were additionally revealed.

Fig. 4 shows the continuum potential along with eigenvalues and Bloch bands for 200 MeV electrons channeled along the $(11\underline{2}0)$ plane of SiC. At this energy 10 states are bound and it seems that channeling has classical character. In order to calculate the spectral angular distribution of CR for electrons of energies 200 MeV we have calculated the trajectories, velocities and acceleration of electrons obtained by numerical solution of the equation of motion in the $(11\underline{2}0)$ potential of SiC calculated within Doyle-Turner approxiamtion.

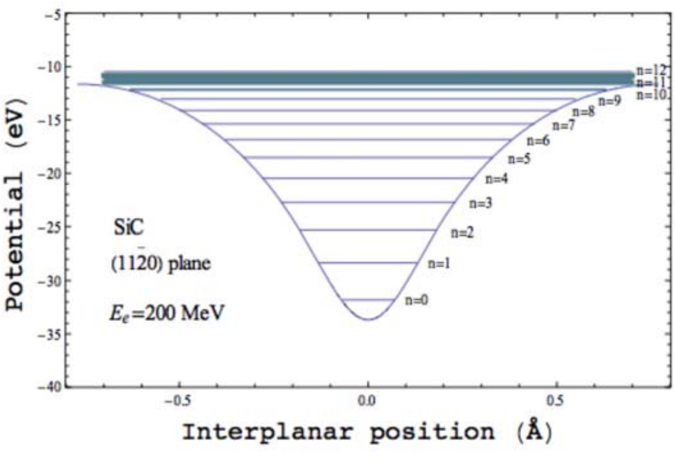

Figure 4: The channeling quantum states for 200 MeV electrons in SiC $(11\underline{2}0)$.

In practice, a beam of electrons hints a crystal surface forming different initial conditions for various electrons. Therefore, one has to find the spectral distribution of radiation for all points of incidence (possible trajectories). The total observed spectra obtains by averaging over partial spectral distributions. Fig. 5 shows the averaged spectral angular distribution of CR emitted in the forward direction by 200 MeV electrons in a 5 μm thick SiC crystal. In this intermediate energy region, however, for some specific cases CR is described with the same accuracy by both classical and quantum methods. In order to compare the classical calculations with quantum ones the spectral angular distribution of CR for 200 MeV energy electrons is simulated by a quantum method (Fig. 6). As seen, the energy distributions of both spectra (Figs. 5 and 6) are nearly the same but line structure is still seen for quantum approximation. In quantum mechanical model if one can assume that higher states have a shorter coherence lifetime and, therefore, bigger linewidth then classical and quantum methods give the same results.

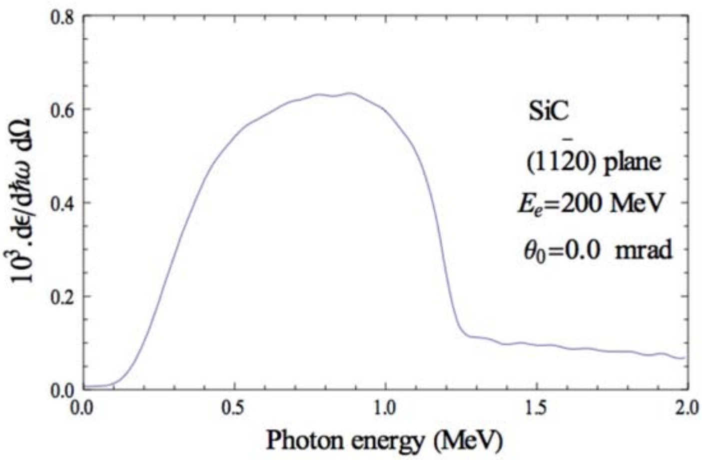

Figure 5: CR spectrum for 200 MeV electrons in SiC (11$\underline{2}$0) in classical approximation.

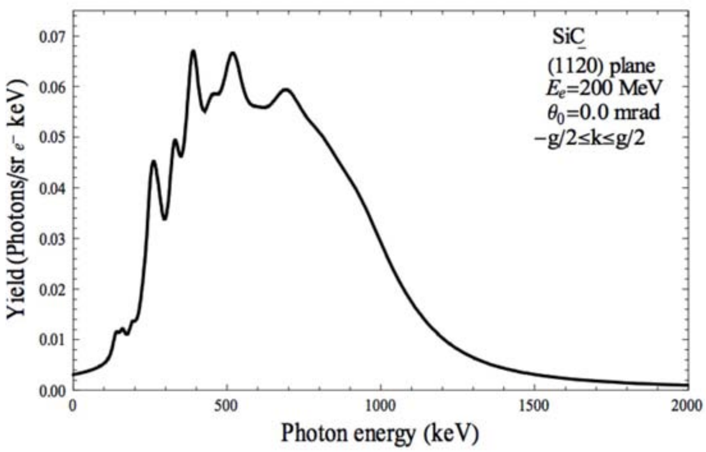

Figure 6: CR spectrum for 200 MeV electrons in SiC (11$\underline{2}$0) in quantum approximation.

In order to analyze the dechanneling processes for electrons and positrons of moderate energies we have developed special code for solving the Fokker-Planck equation for planar channeled particles. The algorithm allows studies on the diffusion coefficients for various scattering processes under the channeling conditions for relativistic light particles. First results have proved the correctness of the model used. Presently, it is under next step of development.

5 Conferences, Seminars

1. S. B. Dabagov, *Channeling of Radiations: From Crystal Undulators to Capillary Waveguides*, Invited lecture to the Ist Seminario Nazionale Rivelatori Innovativi, November 30 - December 4, 2009, Frascati, Italy.
2. S. B. Dabagov, *Channeling Studies at LNF*, Oral presentation at Crystal Collimation meeting at CERN, March 23 - 25, 2009, Geneva, Switzerland.
3. A. Babaev, and S. B. Dabagov, *Simulations of Electron and Positron Planar Channeling for BTF and SPARC Beams*, Poster presentation at Radiation of Relativistic Electrons in Periodic Structures, September 6 - 11, 2009, Zvenigorod-Moscow, Russia.
4. O. Bogdanov, and S. B. Dabagov, *On Planar Positron Channeling in Thick Si Crystals*, Poster presentation at Radiation of Relativistic Electrons in Periodic Structures, September 6 - 11, 2009, Zvenigorod-Moscow, Russia.
5. A. V. Dik, A.S. Podlesnaya, S. B. Dabagov, and M. Ferrario, *Electron Beam Forming by Laser Radiation Action inside the SPARC Photoinjector*, Oral presentation at Radiation of Relativistic Electrons in Periodic Structures, September 6 - 11, 2009, Zvenigorod-Moscow, Russia.

References

1. A. A. Babaev, and S. B. Dabagov, Nucl. Instr. & Meth. B (2010) (in press).
2. A.S. Podlesnaya, A.V. Dik, S.B. Dabagov, and M. Ferrario, *The motion of electron beam near the cathode of the SPARC photoinjector*, Nucl. Instr. & Meth. B (2010) (in press).
3. S.B. Dabagov, and L. Palumbo, (Eds.) *Channeling 2008: Charged and Neutral Particles Channeling Phenomena*, World Scientific Publishing, (2010) 823 p.
4. G. Barbiellini, G.P. Murtas, and S. B. Dabagov, *On the Discovery of Coherent Bremsstrahlung in a Single Crystal at the Frascati National Laboratories*, in book Channeling 2008: Charged and Neutral Particles Channeling Phenomena, S. B. Dabagov, and L. Palumbo, (Eds.), World Scientific Publishing (2010) 3-10.
5. L. Quintieri et al., *Positron Channeling at the DAΦNE BTF Facility: The Cup Experiment*, book Channeling 2008: Charged and Neutral Particles Channeling Phenomena, S.B. Dabagov, and L. Palumbo, Eds., World Scientific Publishing (2010) 319-330.
6. A. Babaev and S.B. Dabagov, Frascati Preprint LNF-09/07 (IR) (2009).
7. O. Bogdanov and S.B. Dabagov, *Solution of the Fokker-Planck equation for (110) planar channeling of 400 MeV positrons,* Report presented at RREPS'09 June 2009 (unpublished).
8. B. Azadegan and S. B. Dabagov, Frascati Preprint LNF-10/12 (IR), (2010).

ETRUSCO

S. Berardi (Bors.), A. Boni (Dott.), C. Cantone (Ass. Ric.), S. Dell'Agnello, G.O. Delle Monache, M. Garattini (Dott.), N. Intaglietta (Tecn.), C. Lops (Dott.), M. Maiello (Dott.), M. Martini (Bors.), L. Porcelli (Bors.)

In collaboration with
University of Tor Vergata

1 Introduction

The SCF-test, first developed under the ETRUSCO experiment has been later successfully used in 2009 to help us understand the behavior of Laser Retro-reflector Arrays (LRA) used by GNSS[1] constellations. We found the test to be important to help the design process of a 2nd generation Lunar Laser Ranging (LLR) array, which will help fundamental physics research done so far by LLR. The importance of the Laser Ranging technique was historically demonstrated with the LRAs deployed on the surface of the Moon by NASA's Apollo 11, 14 and 15 missions [1]. After four decades these arrays are still in operation, and are the only experiment on the Moon still producing scientific data. In the past 40 years, laser ranging to these arrays has provided most of the definitive tests of the many parameters describing General Relativity [2]. In addition, the analysis of the LLR data, has greatly enhanced our understanding of the interior structure of the Moon [3, 4, 5, 6]. However over the past four decades the ground station technology has greatly improved, enhancing LLR accuracy, such that the Apollo LRAs now contribute a significant portion of the ranging errors. This is due to the lunar librations, which move the Apollo arrays so that one corner of the array is more distant than the opposite corner by several centimeters. Thus even if a short pulse were sent to the Moon, the return pulse would be spread out in time, so that the accuracy achievable on the range estimate is no better than a few centimeters (for a single value of the libration angle). At present without hardware improvement, one can only progress by timing an extremely large number of single photoelectron returns to reduce the errors by the root mean square of the single photoelectron measurement error. The APOLLO LLR station at Apache Point has done such an improvement successfully [7]. The ultimate goal of 2nd generation LLR is to install new LRAs whose performance is unaffected not only by lunar librations, but also by regolith motion due to its very large thermal cycle, with a final LRA ranging accuracy below 10 μm. We present the status of the MoonLIGHT[2] payload design process and its possible application to GNSS constellations.

2 Science Objectives of LLRRA-21

The science objectives of the overall LLR program address a variety of goals, which primarily fall into three categories:

- *General relativity and beyond*

Almost all of the most accurate tests of General Relativity (GR) are currently derived from LLR

[1] Global Navigation Satellite Sytem
[2] Moon Laser Instrumentation for Genreral relativity High-accuracy Tests

to the Apollo arrays [8, 9, 10]. Over the long term, we expect to improve the current accuracy of these tests by factors as large as 100. This will address many tests concerning the validity of GR at a new level of accuracy. This is especially important as we confront two of the major issues in fundamental physics, astrophysics and cosmology, that is, 1) the conflict between the current formulations of GR and Quantum Mechanics and 2) the role and reason for the acceleration of distant galaxies (i.e. Dark Energy). At LNF we are also studying new gravitational theories beyond GR and how to look for their signature or constrain them with LLR and SLR data.

- *Lunar science*

Much of our knowledge of the interior of the Moon is the product of LLR [5, 6, 8, 9], often in collaboration with other modalities of observation. These physical attributes of the lunar interior include Love number of the crust, the existence of a liquid core, the Q of the Moon, the physical and free librations of the Moon and other aspects of lunar science.

- *Cosmology*

The improved accuracy of the LLRRA-21 would support the detection of the effects predicted by Dvali-Gabadadze-Porrati model [11] of Dark Energy and the acceleration of distant galaxies.

3 LLRRA-21 Array

As mentioned earlier Laser Ranging stations have improved the accuracy of their measurements with the advances in technology. Currently the APOLLO station at Apache point has reached a level of accuracy whose only limit is given by the LRAs themselves. With MoonLIGHT we want to overcome this limitation by replacing the array of CCRs with a series of single bigger CCRs deployed separately on the surface on the Moon. Instead of having a single pulse, spread by the array and the libration effect, we will have single pulses coming back with the same dimensions as the incoming one (see Fig. 1).

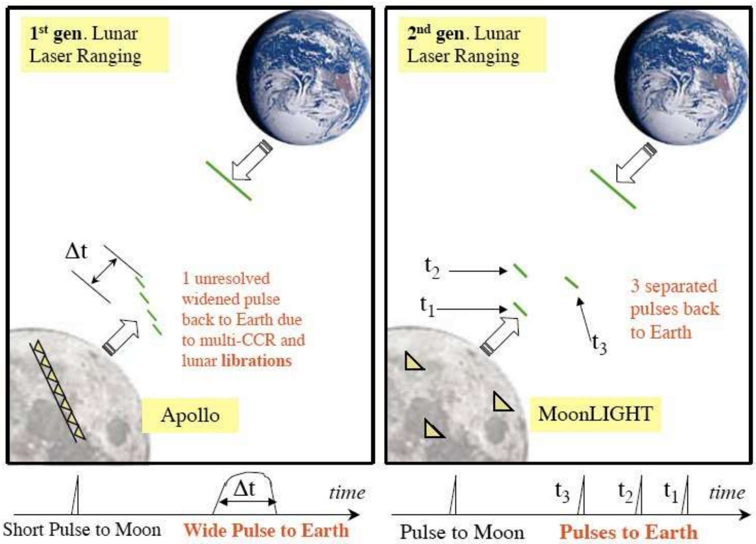

Figure 1: 2$^{\text{nd}}$ Generation Lunar Laser Ranging Concept.

Figure 2: Apollo and MoonLIGHT CCRs.

This new concept for the LLRRA-21 is being considered also for the NASA anchor nodes of the International Lunar Network (ILN) and for the proposed Italian Space Agency's MAGIA [12] lunar orbiter mission.

The CCR for LLRRA-21 has the same design style as the Apollo cubes (circular front face, with tabs on the non reflecting surfaces to help its emplacement inside the housing); however, it is much bigger than its predecessor, for the reasons explained above; the absolute intensity in return (optical cross section) would replace half of the Apollo 11 array intensity. Despite this loss in the intensity of the return, it should be noticed that with the APOLLO station, the efficiency of LLR is increased, and even with 50% reduction in the intensity of the return, a very good measurement is guaranteed.

The CCR has a diameter of the front face of 100 mm (Fig. 2 is a comparison with an Apollo CCR). The angles between the three back surfaces have a specification on the offsets of 0 arcsec, as Apollo CCRs, though with a more challenging tolerance of ± 0.2 arcsec. Fabrication, with certification of space qualification, has been commissioned to ITE Inc. of Beltsville, MD.

4 Technical challenges of LLRRA-21

The primary technical objectives of the LLRRA-21 are to provide adequate laser return to Earth ground stations and to be stable over long term, decades, with respect to the center of mass of the Moon. The major technical/engineering challenges that follow from the technical objective are then:

- Fabricate a large CCR with adequate homogeneity and that meet the required tolerances, mentioned in the previous section.
- Thermal control to reduce thermal gradients inside the CCR to acceptable levels. Thermal gradients produce index of refraction gradients, which cause beam spread and low return.
- Emplacement goal of long-term stability of $10\,\mu$m with respect to the Center of Mass of the Moon.

4.1 Fabrication challenge

The large diameter of the CCR introduces a great challenge in its fabrication, the availability of such material of the required homogeneity, the fabrication and polishing procedures and the measurement methods. The angle between the three back reflecting faces, which govern the shape of the pattern, have a more challenging tolerance of $\pm$ 0.2 arcsec; this is more restrictive by a factor of 2.5 than the current state of the art for SLR CCR fabrication. The material choice is primarily driven by three requirements:

- extremely uniform index of refraction (very good homogeneity)
- resistance to darkening by cosmic radiation
- low solar radiation absorption

To satisfy these requirements, this CCR has been fabricated with SupraSil 1. For the next generation of CCRs, LLRRA-21, we plan to use SupraSil 311 which has even better homogeneity.

4.2 Thermal/optical performance challenges

The optical performance of the CCR is determined by its Far Field Diffraction Pattern (FFDP), which represents the intensity of the laser beam reflected back to the ground by the CCR.

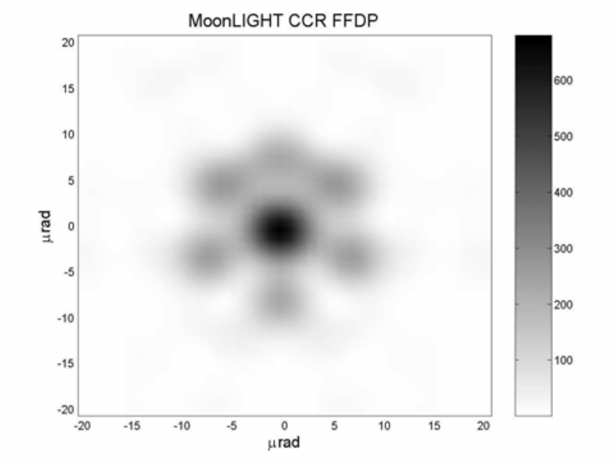

Figure 3: FFDP of LLRRA-21 under its design specification of offset angles (0.0" 0.0" 0.0"). Grid is in angular dimensions (μrad).

Fig. 3 is a simulation of the FFDP of the LLRRA-21 (performed with the software CodeV) according to its dimensions and angle specifications; at the correct velocity aberration the intensity (calculated in optical cross section) should have a value which guarantees that enough photons come back to the ground station. Optical cross section is an intrinsic characteristic of CCRs or LRAs, and its defined as follows:

$$\sigma_{CCR} = I_{CCR/MIRR}\left(\theta_x, \theta y\right) 4\pi \left(\frac{A_{CCR}}{\lambda}\right)^2 \tag{1}$$

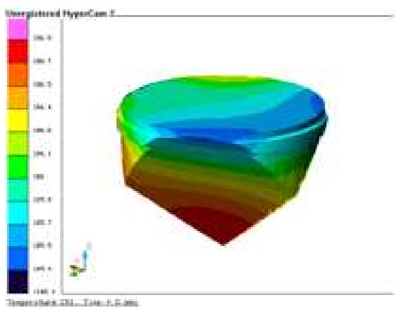

Figure 4: Typical distribution of temperature inside the CCR for a given set of conditions.

Where $I_{CCR/MIRR}$ is the intensity of the FFDP of the CCR, at a certain point of the (θx, θy) plane, referred to a perfect mirror of the same aperture as the CCR, λ is the laser wavelength. One of the most critical challenges of this new model is the issue of the thermal gradient. Since the index of refraction of the fused silica depends upon temperature, a thermal gradient inside the CCR will cause the index of refraction to vary within the CCR and thus modifying the FFDP. In Fig. 5, is represented the average intensity over the velocity

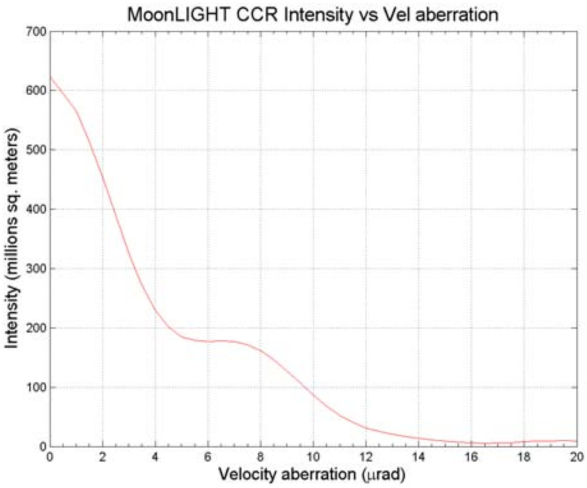

Figure 5: Average intensity over velocity aberration of an unperturbed MoonLIGHT CCR.

aberration for the LLRRA-21 at Standard Temperature and Pressure (STP). At the velocity aberration for the Moon, $\sim 4\mu$ rad, we will test thermal perturbations and, if needed, develop an optimized design to control the drop of FFDP intensity to an acceptable level. For this reason we need to understand in detail how the external factors heat the CCR and in what magnitude, either on the Moon or on a satellite. This is accomplished using dedicated programs developed in parallel at LNF and UMD.

To perform these simulations we use Thermal Desktop, a software package of C&R Technologies of Boulder CO. Then using IDL and CodeV we translate these thermal gradients into the effects on the FFDP of the CCR. There are three primary sources of heat that causes thermal gradients; here we briefly describe their effect:

- *Absorption of solar radiation within the CCR*: during a lunar day, the solar radiation enters the CCR and portions of this energy are absorbed by the fused silica. Since the different wavelengths in the solar radiation are absorbed with different intensity, according to fused silica absorptivity characteristic, the heat is deposited in different parts of the CCR.

- *Heat flux flowing through the mechanical mounting tabs*: if the CCR is at a temperature that is different than the housing temperature there will be a flux of heat passing into (or out of) the CCR through the holding tabs. Conductivity of the mounting rings should be reduced.

- *Radiation exchange between the CCR and the surrounding pocket*: in the case of the Apollo LRAs, the back surfaces of the CCRs view the aluminum that makes up the housing, machined with a relative high emissivity/absorptivity. If the temperatures of the CCR and the aluminum are different there is a radiation exchange of thermal energy, which in turn causes a flux in the CCR as the heat exits out of the front face to cold space. In the Apollo array this is not been a serious issue, but the bigger dimensions of the LLRRA-21 complicate things, and we need to reduce this effect. Thus we enclose the CCR into two thermal shields, with a very low emissivity (2%), that should prevent this radiative heat flow.

Thermal simulations performed on the current configuration show that currently the variation of the ΔT between the front face and the tip of the CCR is within 1 K. We are still proceeding to optimize this further, both with optical design procedures and with thermal stabilization of the overall housing.

4.3 Emplacement challenge

As mentioned earlier, to achieve the desired accuracy in the LLR, a long term stability is needed with respect the center of mass of the Moon; to attain this we must understand and simulate the temperature distribution in the regolith (and its motion), the effects of a thermal blanket that will be spread about the CCR and the effects of heat conduction in the INVAR supporting rod. A locking depth is chosen such that the thermal motion effects are small ($\sim$ 1m). The placement of the thermal blanket further reduces the thermal effects and also reduces the effects of conduction in the supporting rod. This simulation cycles through the lunation and annual cycles.

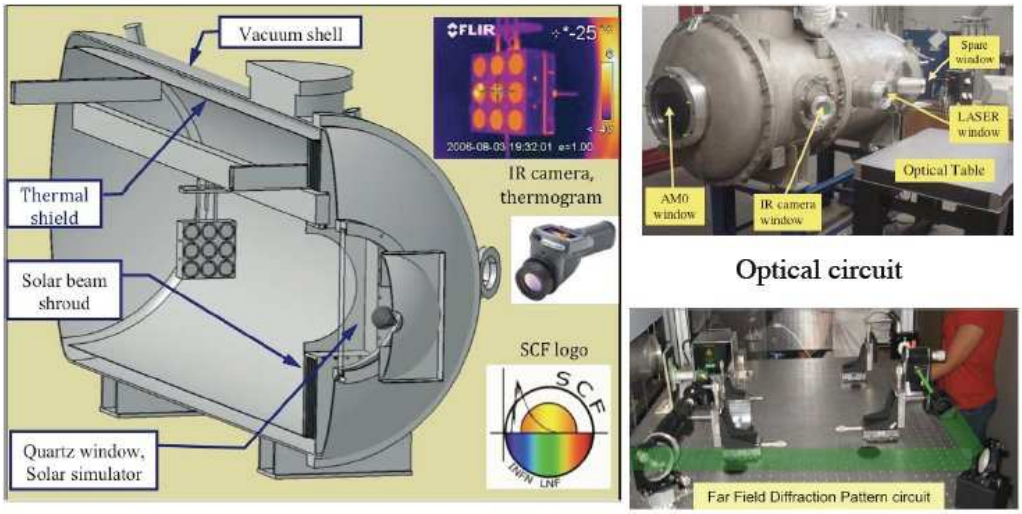

Figure 6: SCF sketch (left side), SCF cryostat and optical table (right side).

5 LNF/SCF thermal-optical testing

Up to this point the discussions have addressed concepts for the LLRRA-21 and thermal-optical computer simulations developed to validate the design concepts. We now address the thermal vacuum testing to further validate design issues. Thermal-optical tests are being performed at the Satellite/lunar laser ranging Characterization Facility (SCF), facility of the INFN-LNF (see Fig. 6). To validate design issues, we need to provide two classes of measurements. The first is the thermal behavior of the test configuration. A solar simulator that has a good representation of the AM0 solar spectrum (solar spectrum in space) is used to provide the solar input. To evaluate the thermal performance of the designs, we use both thermo-resistors and an infrared video camera. The former must be specially configured in order that the wires not conduct more heat than the test item, the latter yields temperatures over the entire test object at each instant. On the other hand, to address the relation between the thermal performance and the optical performance, we currently measure the far field diffraction pattern. This is the crucial test of a CCR package and is performed with the CCR inside the chamber. For the next run, we plan to implement a phase front measurement (which is optimal for diagnosing the details of the performance). Various configurations and designs of the CCR and the housing have been and are being tested in the SCF.

6 Current housing design

We are successively refining our design upon maximizing the overall performance by jointly optimizing the effects of the various different phenomena that affect the overall performance. This has been addressed using the computer simulations described in section 4 and using the data obtained with the SCF measurements. This addressed both the design for the manned emplacement and the use of the 100 mm solid CCR in the ILN anchor nodes. Thus we illustrate the current designs in Fig. 7. The left figure is the current design of the housing as used for the early tests, while the right one is the current design for the complete emplacement configuration; a mushroom shield is added for thermal control reasons.

Figure 7: MoonLIGHT CCR emplacement inside the housing (left) and the complete design for manned lunar missions (right)

7 Launch requirements

We are just beginning a study of the requirements of launch. This particularly addresses issues of the support of the CCR by the tabs in the vibration and acceleration environment of the launch phase. To this end, we have formulated a first example of a structural analysis with ANSYS [13, 14]. In particular we are addressing the contact between the CCR edge (i.e. the three tabs on the side of the CCR) and support plastic rings made of KEL-F. The role of the rings is particularly important since we have presumed a configuration with extremely low mount conductance. This will check the stability and strength of the tab support and the KEL-F line support for 10 g launch accelerations (e.g. in excess to the 6 g characteristic of the ATLAS V launch specifications). We are also performing a modal structural analysis of the inner gold plated thermal shield for an ATLAS V launch.

8 MoonLIGHT as a concept for future GNSS constellations

The study which UMD and INFN/LNF are carrying on for the LLR modernization could have an high impact for future GNSS constellations. Modern GNSS constellations require better and better positioning stability and precision, both provided in absolute terms, that is, with respect the International Terrestrial Reference Frame (ITRF). This can be achieved by tight integration of GNSS microwave tracking with SLR, as stated by the ILRS[3] [15] (the International organization responsible for data processing and publishing of SLR observations among a network of about 40 ground observatories all over the globe [16]). In recent years attention to SLR technique grew in the GNSS community to be used as an important improvement in the constellation performance. GPS constellation of the second generation has two satellites equipped with LRAs (GPS 35/GPS 36) and GLONASS has all of its satellites equipped with LRAs (both of them with coated retroreflectors). Measurements to both of them have demonstrated the great potential of SLR in increasing positioning accuracy of each satellite [17, 18]. This has been done also by combining the separate SLR and MW orbit products. The long-term goal is to combine SLR and MW data at observational level, both in space and at the ground station level, with a latency of the order of an hour. All modern growing GNSS (GALILEO, COMPASS, GPS-3) and regional geosynchronous (QZSS, IRNSS) constellations have designed all of their satellites with co-located MW antennas and SLR payloads (with uncoated retroreflectors); GPS planned a third constellation to might also be equipped with LRAs. All SLR systems deployed or designed on GNSS satellites are planar arrays of CCRs; they use the same principle used for LLR Apollo missions, to install on a plate a certain number of small CCRs to achieve the sufficient level of intensity (established by the ILRS as a fundamental requirement to perform good ranging measurements [19]), at the correct velocity aberration ($\sim 24\mu$ rad for GALILEO). For example on GIOVE-A (the first test satellite for GALILEO) there is an array of 76 28mm CCRs (same design as GPS and GLONASS ones). It is important to develop a design to minimize thermal problems on the arrays and to enable daylight ranging; these refinements will greatly help the possibility of doing SLR based orbits in quasi real-time, having more data through the entire orbit.

The array setup suffers though the same problems of the Apollo arrays: relative angular movement of the array with respect laser-CCR direction (of the same order of magnitude of the effect due to lunar librations on Apollo arrays). For GNSS satellites this effect has two different causes:

1. During a passage over the ground station, the array, always pointing to the nadir, will be hit by the laser beam at different inclinations (for example varying from $0°$ to $\sim 12°$ for GALILEO orbit), thus resulting in a significant pulse spread, especially for low elevations on the horizon (high laser inclination on the array).

2. Satellite attitude control.

To further increase the positioning precision, this uncertainty must be overcome. MoonLIGHT design could be feasible for such an improvement. Looking at the optical cross section formula (eq. 1), the intensity is proportional to A^2_{CCR}, hence R^4, so an increase, for example, of two times in the radius would produce a 16 times increase in the intensity; thus the passage from an array of small

[3]International Laser Ranging Service

CCRs to a single one. Comparing new LRAs equipped with uncoated CCRs with LLRRA-21, we can see that the solo CCR optical cross section, at the central peak, would be equal to the one of $\sim$ 80 CCRs (with no angle offsets, at the central peak). No pulse spread will result during the passage of the satellite and the location of a reference point for the distance calculation wont be uncertain. Moreover the reduction on the number of CCRs will reduce the area of the SLR system on the satellite and its weight. There are currently other configurations under design [20], always involving one big CCR, but the hollow CCR technology rather than solid fused-silica CCR is considered.

As described in the previous section, LLRRA-21 application for MoonLIGHT experiment needs a specific design which takes into account the environment around the CCR, to limit thermal gradients on the CCR and guarantee long-term stability with respect to the center of mass of the Moon; in the same way the proper design for GNSS applications would need simulations and tests of the characteristic heat and mechanical loads in the GNSS orbits. The single big CCR solution however has some disadvantages with respect to the array one. The passage to a single CCR will introduce a possible single-point failure; if the CCR didnt work (low intensity, strong thermal gradients or damage at launch) that satellite wouldnt have a functioning SLR payload (possible to be overcome using a second CCR as a backup). As mentioned in the previous sections, if the CCR were bigger, thermal gradients inside it would have greater effects than CCRs now under use; a design to reduce them will be necessary. Proper dimensions and dihedral angle offsets of the CCR will have to be studied to reach the proper absolute optical cross section required by ILRS, at the right velocity aberration ($\sim 24\mu$ rad for GALILEO). A specific design and lab testing such as the one described in this work would help to overcome the difficulties of this new approach to GNSS SLR and reach the desired capabilities.

9 Publications

1. A. Bosco et al., Inter. J. Mod. Phys. D **16**, No. 12A, 2007.
2. I. Ciufoloni et al., The Design of LARES: a satellite for testing General Relativity, IAC-07.
3. D. Arnold et al., *The INFN-LNF Space Climatic Facility*, 10th ICATPP, 8-12 October 2007.
4. S. Dell'Agnello et al., *Fundamental Physics and Absolute Positioning Metrology with the MAGIA Lunar Orbiter*, submitted to Experimental Astronomy, December 2009.
5. S. Dell'Agnello et al., *Creation of the new industry-standard Space Test of Laser Retroreflector for the GNSS, Fundamental Physics and Space Geodesy: the SCF-Test*, submitted to Advances in Space Research, December 2009.

10 Talks

1. M. Martini, *Design, Construction and SCF-Test of Laser-Ranged Test Masses to probe Gravity in Deep Space*, Sigrav School, Villa Olmo (Co), May 2009.
2. S. Dell'Agnello, *SCF-Test of Laser Retroreflector Arrays for Next GNSS Constellations*, ILRS technical workshop on SLR tracking of GNSS constellations, Metsovo (GR), Sept 2009.

3. S. Dell'Agnello, *Space Applications of Laser Retroreflectors*, SIF, Bari, Sept 2009, Space Applications of Laser Retroreflectors.

4. S. Dell'Agnello, *MoonLIGHT: a 2nd Generation Lunar Laser Ranging Payload for Precision Gravity and Geodesy Measurements and for the ILN*, ASI Workshop on Mobile robotics for unmanned lunar exploration, Rome, July 2009.

References

1. P. L. Bender, et al., Science, **182**, 229 (1973).

2. J. G. Williams, S. G. Turyshev, D. H. Boggs, and J. T. Ratcliff, *Lunar Laser Ranging Science: Gravitational Physics and Lunar Interior and Geodesy*, 35th COSPAR Scientific Assembly, July 18-24, 2004.

3. J. G. Williams, D. H. Boggs, and J. T. Ratcliff, *A larger lunar core?*, 40th Lunar and Planetary Science Conference, March 23-27, 2009.

4. Williams J. G., S. G. Turyshev, and D. H. Boggs, Inter. J. Mod Phys. D **18**, 1129, (2009).

5. N. Rambaux, J. G. Williams, and D. H. Boggs, *A Dynamically Active Moon-Lunar Free Librations and Excitation Mechanisms*, 39th Lunar and Planetary Science Conference, March 10-14, 2008.

6. J. G. Williams, D. H. Boggs, and J. T. Ratcliff, *Lunar Tides, Fluid Core and Core/Mantle Boundary*, 39th Lunar and Planetary Science Conference, March 10-14, 2008.

7. T. Murphy, J. Battat, et al., *The Apache Point Observatory Lunar Laser-Ranging Operation (APOLLO): two years of Millimeter-Precision Measurements of the Earth-Moon Range*, PASP 121, 29 (2009).

8. K. Nordtvedt, *Lunar Laser Ranging: a comprehensive probe of post-Newtonian gravity*, Gravitation: from the Hubble length to the Planck length, edited by I. Ciufolini, E. Coccia, V. Gorini, R. Peron, N. Vittorio, published by Institute of Physics Publishing, London, 2005, p. 97.

9. T. W. Murphy, E. G. Adelberger, J. D. Strasburg, C. W. Stubbs, and K. Nordtvedt, Nucl. Phys. B Proceedings Supplements, **134**, 155 (2004).

10. K. Nordtvedt, Adv. in Space Research, **32**, 1311 (2003).

11. G. Dvali, A. Gruzinov, M. Zaldarriaga, Phys. Rev. D **68**, 024012 (2003).

12. D. G. Currie, et al., *A Lunar Laser Ranging Retro-Reflector Array for NASA's Manned Landings, the International Lunar Network, and the Proposed ASI Lunar Mission MAGIA*, 16th International Workshop on Laser Ranging Instrumentation, October 13-17, 2008.

13. F. Prete, *Contact structural analysis of the MoonLIGHT Laser Retro-reflector Assembly with ANSYS*, Bachelor thesis (unpublished), Dipartimento di Meccanica e Aeronautica, University of Rome "La Sapienza".

14. Minghiglioni A., *Modal analysis of the MoonLIGHT Laser Retro-reflector Assembly with ANSYS*, Bachelor thesis (unpublished), Dipartimento di Meccanica e Aeronautica, University of Rome "La Sapienza".

15. `http://ilrs.nasa.gov/docs/retroreflectorspecification070416.pdf`

16. M. R. Pearlman, J. J. Degnan, and J. M. Bosworth, Adv. in Space Research, **30**, 135 (2002).

17. C. Urschl, G. Beutler, W. Gutner, U. Hugentobler, S. Schaer, Adv. in Space Research **39**, 1515 (2007).

18. C. Urschl, G. Beutler, W. Gutner, U. Hugentobler, M. Ploner, *Orbit determination for GIOVE-A using SLR tracking data*, ILRS Workshop, 2006.

19. `http://ilrs.nasa.gov/docs/ILRSRetroreflectorStandards200812.pdf`

20. R. Neubert, J. Neubert, J. Munder, L. Grunwaldt, *Proposed Single Open Reflector for the GALILEO Mission*, International Technical Laser Workshop on SLR Tracking of GNSS Constellations, 2009.

FAST

D. Alesini, M. Bellaveglia (Art. 23), A. Drago (Tecn.), L. Ficcadenti (Art. 23),
D. Filippetto (Art. 23), A. Gallo, G. Gatti (Art. 23), A. Ghigo, A. Mostacci (Ass.),
M. Serio, A. Stella, C. Vicario (Art. 23)

1 Introduction

The Femtosecond Active Timing and Synchronization (FAST) experiment supported by the INFN, V National Committee, is an R&D program to obtain general synchronization among laser pulses, RF fields and LINAC electron bunches in the femtosecond scale in the complex constituted by the SPARC FEL facility and the FLAME laser, both situated in the same experimental area of the LNF.
Timing and Synchronization in the femtosecond scale is becoming a crucial item for a large variety of applications:

- Laser seeding of FEL process;
- Pump and probe measurements with different sources (FEL, LASER, e-bunches);
- Wakefield Laser-plasma Acceleration of externally injected electron bunches;
- Thomson scattering of counter-propagating short laser pulses and electron bunches.

The high brightness beams required to drive the FEL process are characterized by minimum transverse emittance ($\epsilon \approx 1\mu$m) and short bunches ($\sigma_z \approx 1$mm).
One necessary condition to minimize the transverse emittance is to precisely synchronize the laser pulse on the photocathode with the accelerating RF field in the RF gun. The required synchronization is < 1 ps (SPARC working point).
A very efficient way to compress the bunch and reduce its length is to adopt the RF compression scheme. The bunch is injected into the 1st TW accelerating section of the linac at an optimal phase. Because of the velocity difference between the wave and the not fully relativistic bunch, there is a slippage between them, and the bunch shortens by rotating in the longitudinal phase space (the head is less accelerated than the tail). Optimization of the compression factor requires < 500 fs synchronization between bunch arrival time and RF field in the RF compressor (SPARC). These specifications have been already achieved by the SPARC synchronization system, which is based on a distribution of electrical reference signals through a coaxial cable network.
However, in the near future more severe synchronization specifications need to be achieved in order to cope with the requests of a family of new experiments where the SPARC beam will interact with the FLAME laser, which is presently under commissioning in a dedicated building close to the SPARC experimental area. In particular, the SPARC beam will be injected in a plasma wave generated by the FLAME laser colliding with a proper target to perform a wakefield laser-plasma acceleration experiment. This technique requires a synchronization between the SPARC electron bunch and the plasma wave (synchronous with the FLAME laser) at < 100 fs level.

2 Tasks and achieved results in the year 2009

The FAST collaboration is aimed at studying and implementing upgrades of the existing SPARC synchronization system to cope with the most demanding specifications of future experiments. During year 2009 the FAST work program for the LNF component of the collaboration consisted in the following points:

- Implementation of the laser-driven synchronization architecture at SPARC, to improve the relative phase jitter between the photocathode laser and the RF reference clock;
- Installation of the BAM (bunch arrival monitor) cavities at SPARC and first direct measurements of the bunch arrival time jitter;
- Test of the SPARC synchronization system in the RF bunch compression regime;
- Test of the SPARC synchronization system during first seeding FEL experiment.

2.1 Laser-driven architecture

The laser-driven is a particular synchronization architecture already tested with positive results at SPARC during year 2008. In this case the timing reference signal is extracted directly from the photocathode laser oscillator with a fast photodiode and reference sine-wave voltages for RF and diagnostic hardware are extracted from the pulse repetition by means of band-pass filters and/or PLLs. In this case the relative jitter between photocathode laser and the distributed RF reference can be reduced to $\approx$ 200 fs.
In preparation of the SPARC run dedicated to the RF bunch compression, requiring a $<$ 500 fs relative stability between the photocathode laser arrival time and the RF field in the first accelerating section, the SPARC synchronization system has been permanently migrated to the laser-driven architecture, according to the sketch of Fig. 1.

2.2 Bunch arrival monitors

The SPARC Bunch Arrival Monitors (BAMs) are precisely tuned cavities placed along the beam trajectory on the linac beam pipe. The electron bunch directly excite cavity field free oscillations that are sampled and carried outside by 2 antennas connected to vacuum coaxial feed-through. Two BAM cavities have been designed, built and characterized on the bench. The first one has been installed on the SPARC linac just beyond the 1st accelerating section. A picture of the 1st BAM installed on the linac is reported in Fig. 2, togheter with its characteristics. The BAM cavities are equipped with two tuning ports. The larger port accommodates a fixed tuning plunger to coarsely tune the cell, while the smaller port hosts a remotely controlled tuner plunger to finely correct the cavity natural resonant frequency of the fundamental mode to $<$ 10 kHz respect to the reference 3/4 RF to limit the detected phase slippage during the measurement time slot. The coupling of the antennas is designed to produce large detectable signals ($\approx$ 2 V for 1 nC bunches) which will eventually require no extra RF front-end amplification before being demodulated.
The use of the BAM cavity allows monitoring directly and routinely the electron bunch synchronization at SPARC. Thanks to the migration to the laser-driven synchronization architecture the

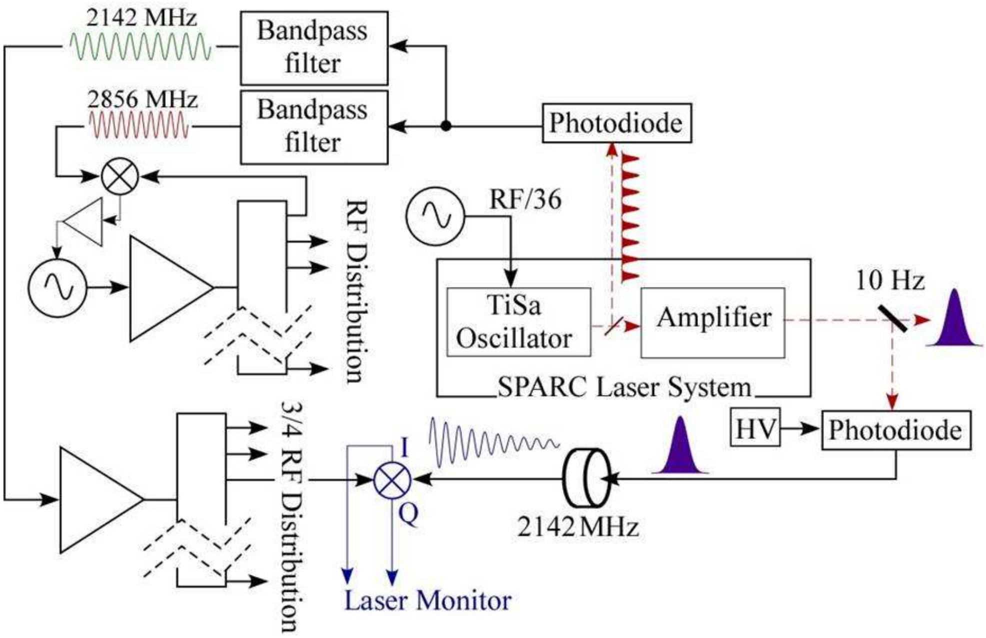

Figure 1: Sketch of a laser-driven synchronization architecture.

(a)

Operating mode	$TM010$
Frequency	$f_0 = 2142\,\mathrm{MHz}$
Unloaded Q factor	$Q_0 = 17000$ (simulations) $Q_0 = 17000$ (measurements)
R/Q factor	$R/Q = 40\,\Omega$
Antenna ext. Q fact.	$Q_{ext} = 30000$
Loaded Q factor	$Q_L = 7500$
Decay time	$\tau_d = 1\ \mu$s
Output peak voltage @1 nC bunch charge	$V_{pk} \approx 2$V
Tuning Accuracy	$\lvert\Delta f\rvert \leq 10$kHz

(b)

Figure 2: (a) a picture of the BAM cavity and (b) some of its useful parameters.

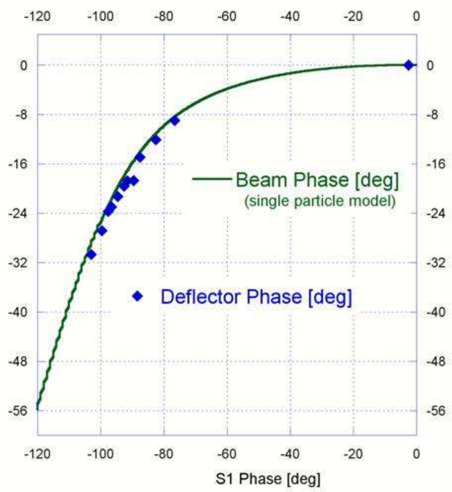

Figure 3: Bunch centroid arrival time at the RF deflector vs. beam injection phase in S1.

measured bunch arrival time jitter is typically ≈ 200 fs, a value which tends to decrease further in the RF bunch compression regime.

2.3 Longitudinal RF bunch compression

Starting from April 2009 some SPARC runs have been dedicated to the first extensive experimental test of joined bunch RF compression and emittance compensation. This is a very promising approach to obtain high brillance beams at low energies (≈ 100 MeV in the SPARC case) avoiding magnetic chicanes where the beam emittance can be degraded by interacting with the Coherent Synchrotron Radiation (CSR) emitted by the bunch itself while travelling in a bending magnet. A precise control of the bunch injection phase in the 1st accelerating section (S1) is crucial to control the bunch compression factor.

An RF deflector placed at the end of the linac is used to strike the bunch on a vertical target to measure the bunch longitudinal charge distribution for different injection phases into S1. A plot of the arrival phase of the bunch centroid as a function of the launching phase in S1 is reported in Fig. 3 and compared with the prediction of a single particle motion model. The agreement is very much acceptable, and demonstrate that RF phases and arrival times are stable and precisely measured at SPARC.

2.4 Seeding experiment

Recently, a first experiment of seeded FEL has been performed at SPARC. In the seeding process the bunch is pre-modulated by interacting with a high power laser pulse before entering the ondulator section. The FEL radiation growth is more regular and controlled in this case with respect to a pure SASE process, where the radiation grows from the schottky noise in a less deterministic way. To be effective, the seeding requires a very precise and stable spatial and temporal superpo-

sition of seed and bunch. The SPARC seeding laser systems shares the IR Ti:Sa oscillator with the photocathode laser, and basically consists in a separate laser amplification chain receiving the input laser pulse train through a remotely adjustable optical delay line. The laser seed temporal pre-alignment is obtained by superimposing the signals produced by a photodiode placed along the ondulator section and illuminated by both the seed and the spontaneous SASE radiation. Then the movable optical delay line is finely tuned to optimize the temporal superposition of seed and bunch by looking at the intensity of the seeded FEL radiation. By implementing this procedure a first test of seeded FEL at SPARC has been positively performed, demonstrating that the process is well reproducible and under control. This very important result can be considered another proof of the successful performances of the SPARC synchronization system.
In 2010 the optimization of synchronization at SPARC will continue, while tests in view of the implementation of an optical distribution of the synchronization reference for future experiments will be performed.

3 List of Conference Talks by LNF Authors in Year 2009

1. M. Bellaveglia, *SPARX Timing and Synchronization System*, Timing and Synchronization Workshop 2009, DESY, Hamburg.

References

1. M. Ferrario et al., Phys. Rev. Lett. **99**, 234801 (2007).
2. D. Alesini, M. Bellaveglia, A. Gallo, *Design, construction and characterization of a Bunch Arrival Monitor cavity for SPARC*, SPARC note RF-09/001.
3. M. Bellaveglia et al., *Measurement Devices for the SPARC Synchronization System*, Proceedings of DIPAC09, Basel, Switzerland.

FLUKA2

M. Carboni, M. Pelliccioni (Resp.), R. Villari (Ass.)

1 Report year 2009

The calculation of conversion coefficients for mono-energetic neutrons and protons of energy up to 10 GeV for various irradiation geometries has been completed. The work has been performed in collaboration with the ICRP. The results will be included in a new ICRP Publication on the subject.

A collaboration with the LNF Health Physics unit has been launched with the aim of providing the FLUKA code to solve some operative issues on radiation protection around high energy accelerators.

Finally the FLUKA code has been largely engaged to study the radiation problems of the CNAO (i.e. prediction of the activation of the chopper dump, design of PET exhaust system, etc.).

2 Publications

1. N.E. Hertel et al., *New ICRP reference phantoms and recommendations: How different are the dose conversion coefficients?*. Abstract NEUDOS11.

2. M. Pelliccioni (as Consultant to the Report Committee), *Reference doses from cosmic radiation exposure for air crew.* Report of ICRU/ICRP Task Group No. 50.

3. M. Pelliccioni (as Member of the Task Group on Dose Calculations of ICRP Committee 2), *Adult reference computational phantoms*, Annals of the ICRP , 2009. ICRP Publication 110.

4. R. Bedogni, M. Pelliccioni, A. Esposito, *A parametric model to describe neutron spectra around high energy electron accelerators and its application in neutron spectrometry with Bonner Spheres*, accepted for publication on Nucl. Instr. & Meth A.

HCPAF

S. Bini (Art. 2222), P. Chimenti (Art. 15), V. Chimenti (Ass.),
R. Di Raddo (Tecn.), V. Lollo (Tecn.), B. Spataro (Resp.)

1 Aim of the experiment

The HCPAF Group technological activity is dedicated to the construction of a 3 cells linear accelerating structures working at 11.424 GHz. Studies on the soft brazing bonding (or low temperature brazing) and sputtering Molybdenum material on the Copper have been carried out, too.

2 2009 Technological Activity

Soft brazing permits creating joints from similar or dissimilar base materials at temperatures below 450 °C and at any rate such as to permit the fusion of the brazing alloy while maintaining the base materials integral if they are temperature sensitive.

Soft brazing is utilized for creating joints on copper tubing in heating and sanitary fitting plants, and in general plants that operate at maximum working temperatures of 100 - 120 °C; higher temperatures require strong brazing.

The quality of the joint depends on various factors:

- joint design, normally spigot and socket joint;
- flow ability of alloy;
- appropriate activity of deoxidizer to be applied to joint surfaces;
- distance between the two surfaces to be brazed, recommended from 0.05 to 0.13 mm;
- stress studies, if necessary provide for expansion joints.

About the sputtering approach, the Molybdenum material deposition on the Copper one in order to improve the surfaces quality, some tests and checks using an Atomic force microscopy to understand the morphological aspect have been made.

2.1 Soft brazing bonding

In order to avoid mechanical stress and morphological one induced into the material during high temperature treatment (high temperature brazing) the soft brazing like is required. This method can be adopted when using metal for the RF accelerating structures construction which cannot be to sustain high temperature.

The alloy Sn/Ag 95/5 (melting point 230 °C) is under investigation. The procedure is the same we adopt for the high temperature brazing replacing Cusil alloy with the Sn/Ag one.

Preliminary tests on COPPER have given good vacuum tight results but also some problems due to the fact that Sn/Ag alloy doesnt act like Cusil regarding capillarity; in other words the Sn/Ag diffusion is not homogeneous on each contact surface so in some tests we found an unwanted alloy diffusion inside the cells. For this reason, we also studied the possibility of using Sn, as gasket, to joint the cells.

The procedure is quite simple, by plating a Sn layer on one of the surfaces we want to joint, making a temperature treatment close to the Sn melting point in order to make a vacuum tight boundary layer between the cells. The deposition is so called brush plating.

The electrolytic parameters can be used to estimate the thickness of the deposited material: in order to deposit 1 μm of Sn on 1 dm^2, we need 36 mAh and knowing the density of Sn, we can estimate the thickness.

By brazing bonding at temperature a little less than 230 °C we obtain a good mechanical structure stability. Some tests (Fig. 1) with copper OFHC remade with different shapes among the contact surfaces gave good results in term of helium vacuum leak.

Figure 1: Soft brazed 3 cells Cu prototype.

As a next step, the realization of the Cu-Zr three cells section, applying the above procedure, electrolytic plating plus temperature treatment, has been scheduled and is going to be completed in a couple of months.

If contact surfaces are machined at a very low roughness, in our case order of 70 nm, the thermal treatment after Sn deposition could be unnecessary. Vacuum tight of about 10^{-10}mbar*l/s has been obtained with a proper pressure applied to the structure with three bars (Fig. 2).

As a first prototype we use a soft brazing like with six bars, tight with a proper torque , in order to improve uniformly the pressure among cells. However we propose that standard model will be realized with the soft brazing bonding plus electroforming technique. In this case bolts will be replaced by electrolytic encapsulation.

Figure 2: Cu OFHC structure under vacuum leak test.

2.2 Molybdenum sputtering

It is known that the Molybdenum material could be an interesting choice for making RF linear accelerating structure since its melting point is higher than the copper giving higher performances under RF higher power.

Unfortunately it is very difficult to be machined with a good roughness (not less of 350 nm can be obtained) and could trap residual gas by limiting the sections performances in terms of breakdown effects, as it was observed at SLAC during the high power tests on dedicated and brazed three cells section.

For this reason we started the study to make the cavity resonators in copper with an excellent roughness and then to deposit Molybdenum by sputtering technique in order to reduce the breakdown phenomena.

To estimate the surfaces quality some tests under an Atomic force microscopy to understand the morphological aspects or the topic ones was used.

Studies on the molybdenum sputtering on the copper surfaces are in progress.

The Fig. 3 and 4 obtained with Atomic Force Microscopy show the surfaces of the machined copper with a very low roughness, of the 70 nm order, after and before the molybdenum sputtering.

In Fig. 4 one observes the undulations of the surface due to the step of lathe machine, about 700nm, with a lots of spikes overlapped, spikes that disappear when a layer of about 100 nm molybdenum is deposited on. It seems to be that molybdenum on the copper surface acts like a smooth layer, in other words the roughness improves. Further studies are in progress in order to verify this statement.

Since the materials have different thermal coefficients, the deposited molybdenum on the copper could be not stable rising temperature. One possible solution consists in depositing a film and make a thermal treatment, about 800 °C, in order to fix the film on the substrate (a similar

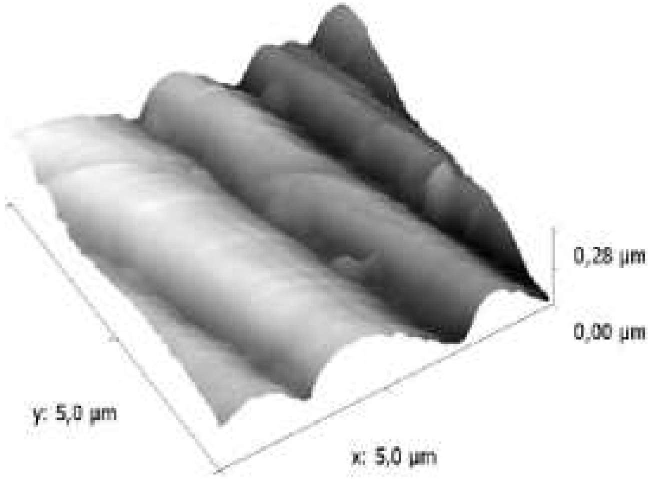

Figure 3: AFM image of deposited Molybdenum on copper cell by sputtering technique.

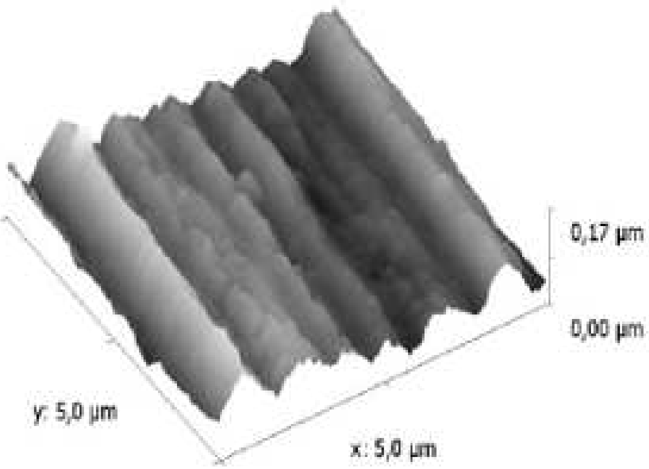

Figure 4: AFM shows surface of copper cell before molybdenum sputtering.

treatment has been adopted for other applications). We scheduled this activity and we believe to get these results in a couple of weeks.

2.3 Other materials

Presently some other materials, in addition to the Copper, are under study: essentially Molybdenum and alloy Copper Zirconium. Regarding Molybdenum some electroformed multicell structures with Mo irises have already been made with good results. These prototypes were made only to check the procedure. For these special materials the Electroforming technique could be used as a way to encapsulate the components of the multi-cell structures, making something like a cold brazing of the multi-cell elements, as well as the end flanges. The above procedure will have the advantage to avoid the high thermal stress of these metals during the brazing. In particular this is valid for the Cu/Zr because it loses its RF properties above a 300 ° treatment. Finally the way to obtain electroformed multi-cell structures with the presence of two tuners per cell will be considered as soon as a proper tuner structure designed for this procedure will be tested.

2.4 X-band sections working at 11.424 GHz

A Cu three cells electroformed section realized with no brazing procedure has been tested for the electromagnetic characterization at room temperature and helium vacuum leak checks (see Fig. 5).

Figure 5: Electroformed Cu three cells section.

X-band copper and molybdenum structures have been constructed at LNF using the brazing technique and have been tested at high power at SLAC. Results of the first high gradient test done at SLAC on brazed Cu and Mo LNF structures are discussed in another dedicated paper (see ref. 5).

3 Summary and activity 2010

A first method to make the soft brazing has been obtained. For practice opportunity reasons, a Cu/Zr three cells section using the soft brazing bonding and with six bars is under construction. Vacuum and electromagnetic tests at room temperature have been scheduled to be carried out within two weeks.

Another Cu/Zr three cells section realized with the soft brazing bonding and the electroforming procedure has been scheduled to be realized in a month. We believe this model will represent the standard solution for the construction of next accelerating sections.

Additional investigations about the sputtering technique are in progress, too.

In addition, it has been seen that the microscopic surface status plays an important role on the maximum gradient limiting for Cu X-Band RF accelerating structures (Sami Tantawi private communication), and not only from a point of view of surface roughness or cleanliness but also considering the metallurgical behavior of the material.

As known interaction of intense radiation with solids can change essentially its surface characteristics. We have discussed in ref. 6 the first results of our studies on irradiation of the Cu RF structures by dense X-ray beams. X-ray micro-beam shaped by means of poly-capillary semilens has been applied as a probe in a number of specified stripes on a surface. The indentation depth analysis has shown the change in surface hardness in correspondence to the applied radiation dose.

References

1. S. Bini et al., *Status Report on SALAF Technical Activity During the First Half of 2009*, RF-09/002, 30/04/2009.

2. S. Bini et al., *SALAF Group Technological Activity*, RF-09/003,30/06/2009.

3. D. Alesini et al., *High Power Test Results on X-Band Copper and Molybdenum Structures, Low Power RF Measurements of Copper Electroformed Structures and Technological Activity*, RF-09/004, 01/09/2009;

4. S. Bini et al., *Surface Modifications of Copper RF Structure Induced by Dense X-Ray Beam*, RF 09/005, 05/11/2009.

5. A. Bacci, L. Giannessi, M. Labat, and B. Spataro, *Self-seeding configuration at SPARC*, FEL Conference, August 23-28, 2009, Liverpool (UK).

IMAGEM

B. Buonomo, G. Corradi (Tecn.), G. Mazzitelli, F. Murtas (Resp.),
M. Pistilli (Tecn.), L.Quintieri, D. Tagnani (Tecn.)

1 Introduction

The main tasks of this R&D is the development of different detectors basted on GEM technologies essentially for beam diagnostics. The use of GEM foils for detector construction started in Frascati on 2002 with the R&D for LHCb muon chambers M1R1. Ever since, several triple GEM chambers have been built for different applications. The results obtained in several beam tests show high performances: high rate capability (> 50 MHz/cm^2), good time resolution (~ 4 ns), good space resolution O(200 μ m), and good aging resistance after 2 C/cm^2 of integrated charge. The IMAGEM R&D is devoted not only to the detectors but also to the readout electronics and power supply. The Scientific activity of IMAGEM this year can be resumed in these four main items:

- Construction and test of a Compact TPC for beam monitoring;
- Characterization and installation at FTU (ENEA) of a fast neutron flux monitor;
- GEM monitors for UA9 Experiment at CERN;
- Design and construction of Power Supplies and Readout Electronics for triple GEM Detectors;

2 Construction and test of a Compact TPC for beam monitoring

A compact Time Projection Chamber (TPC) has been designed, built and tested, for beam monitoring at the Dafne Beam Test Facility (BTF). The Facility provides electron and positron beams in a wide range of intensity, from single particle up to 10^{10} particles per pulse, and energy, from a few tens of MeV up to 500 MeV. The large range of operation of the facility requires the use of different detectors, for real-time beam monitoring. The main idea in developing this detector is to place a standard triple GEM detector parallel to the beam and to use it as a time projection chamber, by enlarging the drift gap. In this way the material crossed by the particle is particularly small (only two kapton windows) and the beam position measurement could be more precise, O(50 μ m), in the coordinate along the drift, by measuring the time of arrival of the electron clusters. Moreover, a very compact detector can be realized, using standard 10×10 cm^2 GEM foils and a drift gap of 4 cm. The 128 readout channels organized in a matrix of 8×16 pads allow to obtain a good resolution O(1 mm) also in the other two coordinates.

The TPC, working without a magnetic field, has been operated with a gas mixture $ArCO_2$ (70/30) or $ArCO_2$CF$_4$ (45/15/40) at a Gain 10^4: just opening a random time gate of 8 ms, clean cosmic tracks can be seen on the online event display, through a readout of 128 scalers, as shown in Fig. 1. The high rate capability of GEM technology allows the use of this monitor not only for single tracks events but also for multiparticle beam. The electron drift velocity measured at $2KV$/cm in the CF based gas mixture was 5.3 μm/ns. Thanks to a small material budget crossed by the particle (0.2% X$_0$) and the 3D reconstruction of the particles track, its use for ion beam

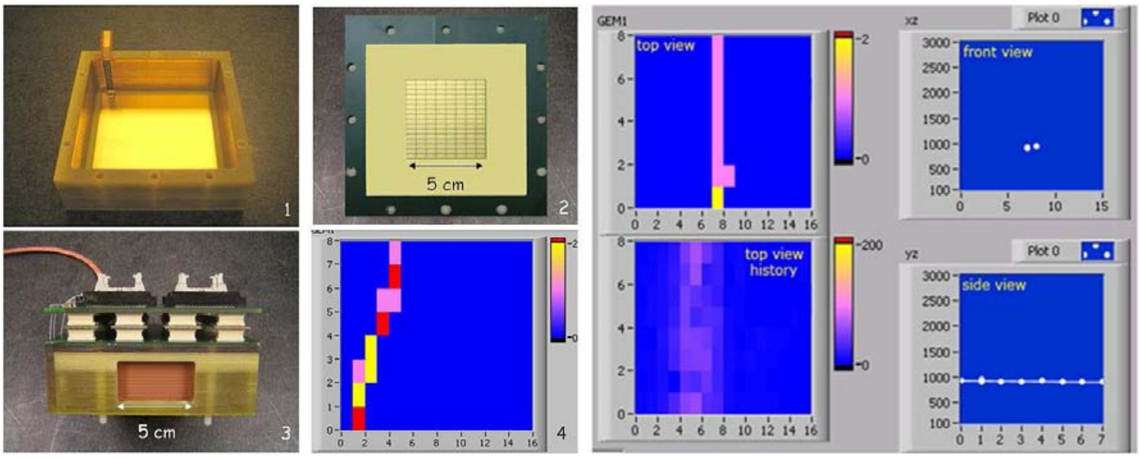

Figure 1: On the left the GEM TPC assembling and a 2D view of a cosmic ray; on the right the 3D view of an electron at BTF.

monitor in hadrotherapy is very promising and under study. This results have been shown by P. Valente (INFN-Roma1) at Vienna Conference 2010 talk.

3 Characterization and installation at FTU (ENEA) of a fast neutron flux monitor

In 2009 two tests have been done at FNG (Frascati Neutron Generator) at ENEA Frascati for the measurements of high neutron flux produced by strong nuclear reaction Deuterium-Deuterium e Deuterium-Tritium. Neutrons of 2.4 MeV e 14 MeV are produced by this two reactions. A prototype 10×10 cm^2 made of a triple GEM with a cathode of aluminum and polyethylene has been placed in front of the generator at few centimeter. The neutron, impinging on polyethylene, is converted in proton that releases its final energy inside the gas, producing electrons. The 128 readout pads, organized in a matrix 16×8, allow to create an intensity image of the neutron source. The total counting rate has been compared with the measurement done with a liquid scintillator NE213 detector, placed 10 meter far from the neutron source, showing a good linearity up to $12MHz/\mathrm{cm}^2$ (the maximum flux for FNG) as shown in Fig. 2. The detector efficiency is not high (4×10^{-4}), but enough for this type of measurements.

Thanks to the strength signal released by the proton inside the gas, the low gain settings of the chamber allow to have a good rejection to photons produced by the radio activation of material around the detector.

The active area of this monitor has been divided into two parts with the polyethylene converter optimized for the two energies (2.4 and 14 MeV): the efficiency measurements shows not only a zone at low gain with no photons contamination, but also a good discrimination between the two types of neutrons, as shown in Fig. 2. The chamber has been installed in September at Frascati Tokamac Upgrade (FTU) and the first measurements will start in April 2010.

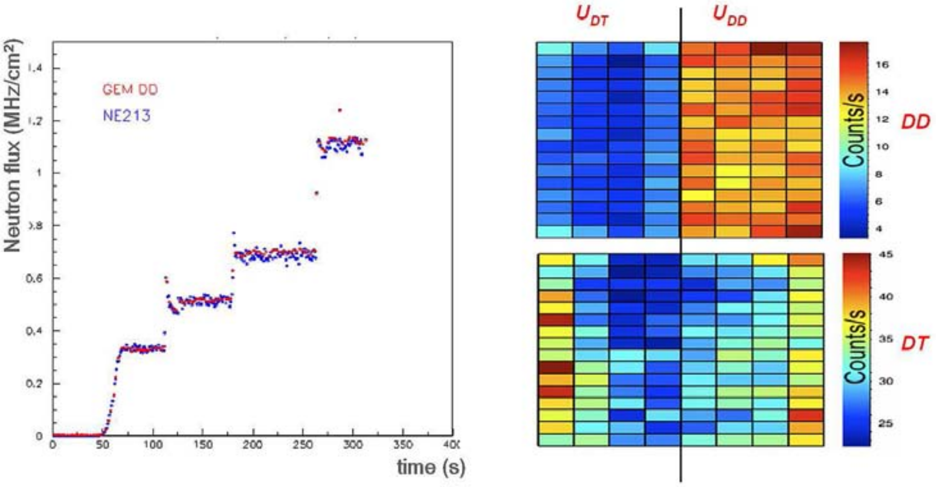

Figure 2: On the left the flux measurement with GEM compared with NE213 up to 1.2 MHz/cm^2; on the right the monitor online display whit two different neutron source : 2.4 MeV (up) and 14 MeV (down).

4 Monitor for UA9 experiment at CERN for Crystal beam collimation

In the mainframe of the proton beam collimation studies at CERN, the experiment UA9 has been setup in 2008. In a vacuum tank installed on the SPS machine, two goniometers with one crystals each, have been installed; the proton beam halo, impinging the bent crystal, could be channeled and deflected of about one mrad if correctly aligned with crystal planes. For the monitoring of the proton inelastic interactions with the crystal, two GEM detectors 10 $\times$ 10 cm^2 have been placed on the tank faces near the beam pipe as shown in Fig. 3 left. During the crystal angle scan, a drop in counting rate on GEM detectors, is a good indication thet the beam halo is channeled in the crystal. The channeled beam deflected is then monitored 40 m downstream with a medipix detector inside a beam pipe roman pot. Few Machine Developments periods were dedicated in 2009 for these measurements and for all of them the GEM detectors measured the beam background. In September 2009 the compact GEM TPC, described before, has been used for measurements on beam channeling on crystal, at CERN H8 proton beam test area. The two beams, the main one and the channeled one, have been observed in the same TPC volume with an on-line monitor, as shown in Fig. 3; the two beams were separated by 11 mm between each other.

Other measurements are foreseen in 2010 on crystal channeling with proton and ion beam, using this tracking device.

5 Development in electronics

5.1 Design and construction of a new version of HVGEM for triple GEM power supplying.

The HVGEM is a seven stage power supply specifically designed for this type of detector; it can be used also for thick GEM and other detectors. Two types of stage power supply have been designed in a modular way: - 1200 Volt and 100 μA - 500 Volt and 200 μA. A new version has been designed

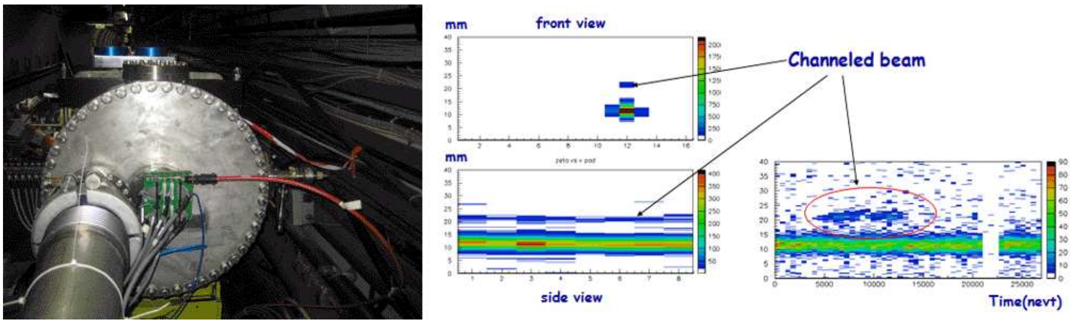

Figure 3: Left: The installation of a GEM monitor on one face of the Crystal Tank; Right: The main beam and the channeled beam seen by the GEM TPC.

in 2009, following the NIM standard (two units modue): each single HV stage can be plugged on the NIM mother board, making the HVGEM more flexible and adaptable to different detectors. The module can be controlled through CANbus and USB port.

5.2 Design and construction of LVGEM for Carioca Board LV Power Supplying and threshold settings.

The LVGEM is a NIM module for the LV power supplying of 8 Carioca Boards, specifically designed for the GEM detector. This module can power 128 channels (2.5 Volt) and set 8 thresholds (one for each group of 16 channels). The thresholds can be set manually with 8 screws in the front panel or driven by a VME DAC (rear connectors).

5.3 Design and construction of a Motherboard FPGA based.

In order to have a more flexible and portable system, a new mother board has been designed with an FPGA, that will be able to analyze the LVDS signals coming from the FEE board, both with scalers and multihit TDC with a resolution of 2 ns, sufficient to record the time drift of electrons along the 4 cm drift. The Board is under test (see Fig. 4).

6 Future

Other research groups inside INFN, ENEA, CEA and CERN are interested in use of these triple GEM detectors described above and the electronics made in Frascati. Recently also two monitors for X rays have been made for burning plasma diagnostic and will be installed in Frascati Tokamak and Tore Supra at Cadarache. A Memorandum of Understanding has been recently signed by INFN, ENEA and CEA for the R&D on these topics. The INFN part of this collaboration, will be done by GEMINI R&D, approved by CSN5 on September 2009.

Any other information can been found on the web site

`http://www.lnf.infn.it/esperimenti/imagem/`

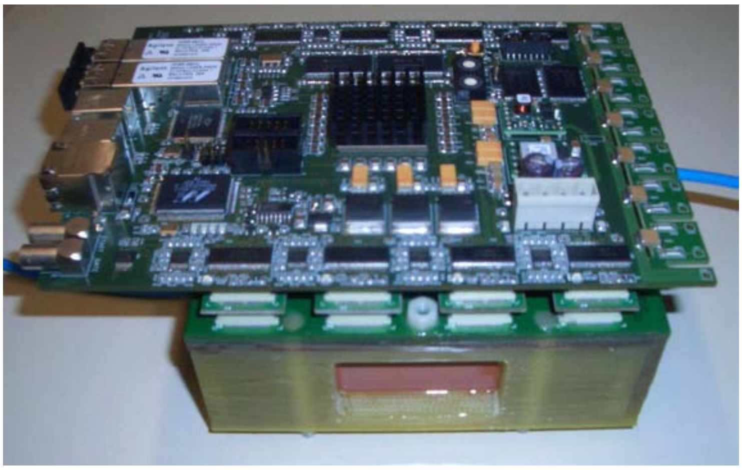

Figure 4: The mother board with FPGA monted on the compact TPC.

7 Conference Talks

1. F. Murtas, *Applications in beam diagnostics with triple GEM detectors*, 11th Pisa Meeting On Advanced Detectors: Frontier Detectors For Frontier Physics
   La Biodola, Isola d'Elba Italy

2. F. Murtas, *A GEM-Based Detectors for Beam Monitor and Neutron Fluxes Diagnostics*, 1st International Conference on Frontiers in Diagnostic Technologies, Frascati, Italy

8 List of Publication in Year 2009

1. R. Villari et al., IEEE Trans. Nucl. Sci., **56**, 1102 (2009).

9 Thesis

1. S. Puddu Universitá di Cagliari, Laurea Magistrale, *Sviluppo di sistemi diagnostici per plasmi nucleari accesi*, Rel. Prof. S. Serci, D.r F. Murtas, Dr. F. Bombarda.

References

1. F. Sauli, GEM: A new concept for electron amplification in gas detectors, Nucl. Instr. & Meth. A **386**, 531 (1997).

2. M. Alfonsi et al., *The Triple-GEM detector for the M1R1 muon station at LHCb*, N14-182, 2005 IEEE NSS Conference, Puerto Rico.

3. A. Corradi, F. Murtas, and D. Tagnani, Nucl. Instr. & Meth. A **572**, 96 (2007).

MicroX

S.B. Dabagov (Art. 23, Resp.), G. Cappuccio (Ass.), G. Cibin (Osp.), Yu. Dudchik (Osp.),
A. Esposito, V. Guglielmotti (Ass.), D. Hampai (Ass.), A. Marcelli, V. Sessa (Ass.)
L. Allocca (Osp.), L. Marchitto (Osp.), S. Alfuso (Osp.)

Participant Institutions:

Italy:	INFN Laboratori Nazionali di Frascati
	INFN Milano Bicocca
	Dipartimento di Energetica, Universitá di Roma “La Sapienza”, Roma
	CNR Istituto Studio Materiali Nanostrutturati, Roma
	Dip. Scienze e Tecnologie Chimiche, Universitá “Tor Vergata”, Roma
	CNR Istituto Motori, Napoli
Belarus:	Institute of Applied Physics Problems, Minsk
Russia:	P.N. Lebedev Physical Institute, Moscow
	Institute for Roentgen Optics, Moscow
EAU:	Unisantis FZE, Dubai

The aim of MicroX project is to study and, successfully, to realize a pototype of multifunctional X-ray microscopy unit based on polycapillary optics in combination with compound refractive lens. During the first two years of the project, a microscope prototype that can make μXRF mapping as well as X-ray imaging with high resolution simultaneously was realized on the base of various types of polycapillary optical structures. Moreover, we have developed a unified theory of X-ray propagation in ultra narrow guides (see MicroX 2007 annual report).

In 2009, we have combined our experimental setups to design a new compact and portable layout for simultaneous elemental and imaging analysis.

1 Introduction

During the year of 2009 apart of the main project activity, which was mostly to design a compact solution for new instrument design, we paid attention to the realization of novel ideas on the use of our technique for elemental analysis of low concentration samples in the TXRF geometry. This idea was originated from our ability to produce high X-ray flux of quasi parallel beam of a small cross section.

Another very important research attracted our attention is to clarify a feasibility of polycapillary X-ray technique application for fuel spray investigation. Due to the possibility of getting high contrast image of the samples studied at our polycapillary based station, we have realized several runs to investigate the fuel spray development in the engine.

Preliminary results of both research programs are presented below.

2 Activity in 2009

2.1 TXRF Prototype for low concentration samples

In the third year of the MicroX project, we continued to study and realize both a new X-ray microscopy based on the confocal geometry of two polycapillary optics and a new TXRF Spectrometer based on the use of one polycapillary lens. During the year of 2007, a first prototype of transmission imaging microscope was realized at LNF-INFN; it is composed by an X-ray source (Oxford, 50W, CuK_α), a semi-lens and two detectors, one of which is a scintillator while another one is a CCD. In 2008 we realized a new prototype version with a special confocal scheme for micro X-ray fluorescence measurements; that enables performing not only elemental mapping of a sample but additionally to that its own X-ray imaging.

To study and design X-ray optical systems a dedicated laboratory with experimental setup including a cabinet and an optical table was established at the Laboratori Nazionali di Frascati (LNF-INFN). For a TXRF prototype we have utilized, as a radiation source, an Oxford Apogee 5000 tube (Cu Kα), with a source spot of about 50×50 μm^2 and power of 50 W, an XGLab SDD with an active area of 5 mm^2 and a Photonic Science CCD (FDI 1:1.61) with a pixel resolution of 10.4×10.4 μm^2.

The used polycapillary semilens, previously tested according to a protocol developed at LNF [3], is characterized by the focal distance of 91 mm and the transmission of $\sim$ 60%. The intensity distribution behind the semilens is shown in Fig. 1 as a contour plot in horizontal cross-section plane where the maximum intensity has been registered. The X-axis is perpendicular to the optics longitudinal axis, along which the Z-axis is directed; thus, the Z value corresponds to the distance between the semilens and detector. In particular, the low value of residual divergence is about 1.4 mrad that reduced from the analysis of radiation peak distribution at 40 cm from the lens exit (the maximal value of the intensity behind the optics).

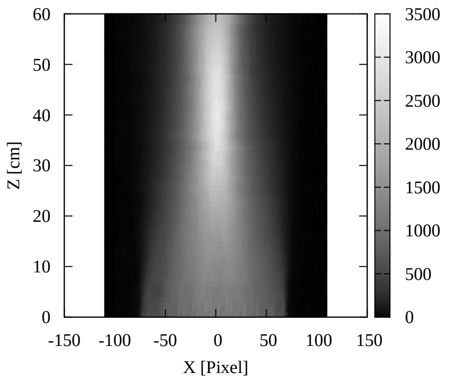

Figure 1: Contour plot of the intensity distribution obtained by the CCD sensor placed at different distances from the polycapillary optics exit. For the X-axis each pixel has 10.4 μm length, while the Z-axis has a range of 4 orders of magnitude greater. A small residual divergence of $\sim$ 1.4 mrad is evident.

Due to an optimized combination of X-ray tubes and polycapillary optical elements, that can provide intense radiation flux probes necessary to realize a layout for elemental analysis of low concentrated samples, specific design can result in a compact and portable X-ray instrument to be used for the research, even in situ. In this context, a prototype of X-ray spectrometer based on polycapillary semilens, Fig. 2, has been designed in our laboratory.

A preliminary comparison of synchrotron radiation (SR) (SSLR - beamline 10-2) and our prototype measurements on an Antarctic sample is presented in Fig. 3. The different spectra obtained with conventional X-ray source varies in dependence with the incident angle: in particular, a growth of the incidence angle results in the increase of Si line (the substrate is Si based). With the same acquisition time (10 minutes) and a simpler experimental vacuum chamber (in portability of the entire experimental setup), we found a partial agreement between our results with SR data shown in Fig. 3, especially at low energies (up to Fe). The problem with the discrepancy can be

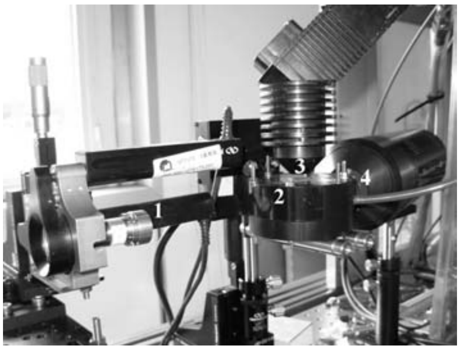

Figure 2: Prototype outline of X-ray fluorescence spectroscopy in total external reflection (TXRF): 1 - polycapillary semilens, 2 - sample holder chamber, 3 - SDD detector, 4 - CCD detector. The chamber could be in vacuum (10^{-6} mbar) in order to detect low Z elements (Mg).

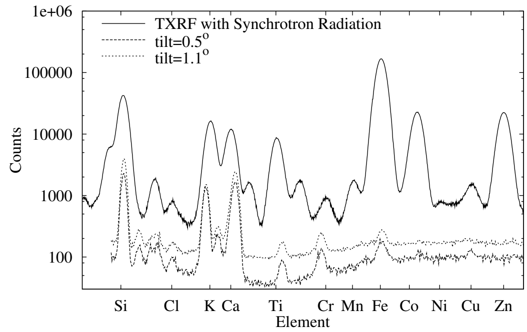

Figure 3: TXRF spectra: comparison of SR and our prototype (X-ray tube forced by polycapillary optics) results. For the prototype, four different spectra, one for each tilt angle, are given.

resolved by replacing a Cu anode with a Mo one for the current X-ray tube.

2.2 Fuel spray investigation by X-ray technique

Recently, internal combustion engine technology has undergone tremendous improvements in terms of efficiency, consumption and emissions due to increasingly stringent legislation. These improvements require deeper understanding of the engine systems combustion process whatever the thermodynamic cycle (Diesel, Otto, HCCI).

In this research activity, preliminary investigations on fuel sprays from a Gasoline Direct Injection (GDI) six-hole nozzle by polycapillary X-ray technique have been performed. A hydropneumatic pump, activated by pressured gas, enabled the injection of the fuel at pressures from 2.5 to 25 MPa. A 1.0 dm^3 reservoir pressure tank, located between the injection pump and the electroinjector, absorbed pressure oscillations caused by the fuel delivery. A Programmable Electronic Control Unit (PECU) has been used to control the injector according to the set strategies, (Fig. 4 shows a sketch of the apparatus).

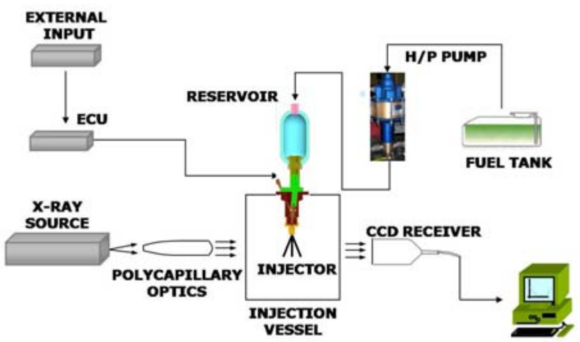

Figure 4: Experimental set-up.

Experiments have been performed at ambient temperature and atmospheric backpressure injecting the fuel in a chamber under quiescent conditions. The injector was positioned perpendicular to the X-ray beam. The focused X-rays met a spray area of 5 mm downstream from the nozzle. The detection acquisition mode was synchronized with the injection event. A detector exposure of 5 ms covered the entire injection duration. Outside this event the detection system is switched off to avoid background noise accumulation on an intrinsically weak signal. Due to the low absorption cross-section of the gasoline at 6 keV, doping oil containing Cerium (Eolys DPX9 Rhodia Terres Rares) is added to the fuel. An absorption increase of 50 % is expected for 4 weight % doping.

Two Cerium concentrations have been used to enhance the absorption signals: 4% for injection pressures of 5, 10 and 20 MPa and 6% for 5, 10, 15 and 20 MPa . The absorption of the incident X-ray through the spray is measured by the CCD detector at a repetition of 160 cycles for each condition with a total exposure time of 800 ms. The collected images have been smoothed and filtered by a low pass filter corrected with respect to the background level.

Due to the X-ray absorption features of the gasoline (typically rather weak at higher energies), it is much efficient to use soft X-rays. In our measurements a bremsstrahlung tail of the spectrum ($\sim$ 6 keV) has been used instead of characteristic line for Cu K_α ($\sim$ 8 keV). Moreover, measurements at both higher and lower energies were performed; these measurements had shown that the absorption signals for both cases were too weak; finally we proved that the energy of 6 keV was the optimal energy for our studies.

In Fig. 5 X-ray absorption, along a median line of the spray, is shown for different gasoline injection pressures and Cerium concentration of 6%. The absorption of the radiation through the gasoline is well defined as the region of highest absorption of about 400 pixels, corresponding to $\sim$ 40 mm. Till now it is to be clarified if the asymmetry in the shape reported in Fig. 5 is from the focusing setup or fuel density gradients inside the spray.

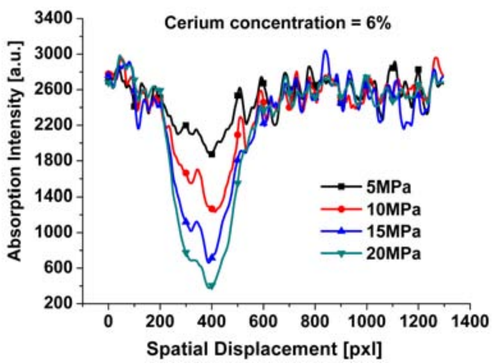

Figure 5: Absorption comparison profiles of X-ray beams for different fuel injection pressures at 6% Cerium additive.

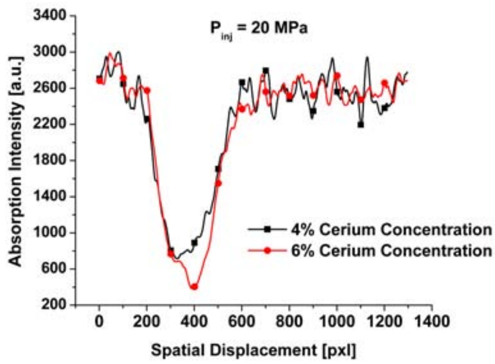

Figure 6: Absorption intensities for 4 and 6 % of Cerium additive.

The injection duration is constant at 3.0 ms, with a repetition rate of 3 Hz, while the pressure is set at 5, 10, 15 and 20 MPa, with total delivered fuel 29.1, 41.7, 51.7 and 57.7 mg/stroke, respectively. A coherent increase in radiation absorption versus the injection pressure is evident;

the higher the fuel pressure the stronger the absorption of the incident radiation. The intensity profiles have similar minima and are spaced regularly along the y-axis.

Higher injection pressures result in greater amount of fuel per volume unit and a fine atomization of the fuel bulk. This determines stronger radiation absorption according to the Beer's law. The effects of Cerium additive to the fuel sample are shown in Fig. 6 depicting increasing absorption properties. Equivalent values are found outside the spray location while, inside the jet, the absorption increases for highest additive values. The signals have been collected along the spot diameter.

Next work to be done is to correlate the absorption intensity and/or the small-angle X-ray scattering figures to the fuel physical and geometrical properties (refractive index, droplet diameter and shape factors). The advantage of the system is that it is based on a table-top setup with a conventional X-ray source, as opposed to being at a synchrotron facility. This reduces costs and optimizes access. Such studies open this methodological approach to new research opportunities.

3 Conferences, Seminars

1. S.B. Dabagov, *Advances in Capillary Optics Use for μXRF and X-Ray Imaging*, invited lecture to the JST International Symposium on Micro and Trace X-ray Spectrometry , February 12-14, 2009, Osaka-Tokyo, Japan.
2. S.B. Dabagov, *Advances in Polycapillary Optics*, Invited talk to SPIE 2009 - the Annual Meeting of SPIE, August 3-7, 2009, San Diego, USA.
3. D. Hampai et al., *Polycapillary Optics Based TXRF Analysis for Insoluble Dust Studie*, Oral report to ICXOM XX, September 14-18, 2009, Karlsruhe, Germany.
4. L. Allocca et al., *Gasoline Spray Imaging by Polycapillary X-ray Technique*, Poster report to ICXOM XX, September 14-18, 2009, Karlsruhe, Germany.
5. S.B. Dabagov, *Channeling of Radiations: From Crystal Undulators to Capillary Waveguides*, Invited lecture to the Ist Seminario Nazionale Rivelatori Innovativi, November 30 - December 4, 2009, Frascati, Italy.

References

1. D. Hampai et al., Optics Letters, **33**, 2743 (2008).
2. D. Hampai, S.B. Dabagov, G. Cappuccio, and G. Cibin, Nucl. Instr. Meth. B **244**, 481 (2006).
3. D. Hampai et al., *Capillary Optics Based X-Ray Micro-Imaging Elemental Analysis*, 3rd Intern. Conf. on Charged and Neutral Particles Channeling Phenomena - Channeling 2008, Proceedings of the 51st Workshop of the INFN Eloisatron Project, S. Dabagov and L. Palumbo (eds.), World Scientific (2010).
4. L. Allocca, S. Alfuso, L. Marchitto, and G. Valentino, *GDI Multi-Hole Injector: Particle Size and Velocity Distribution for Single and Jet-to-Jet Evolution Analysis*, ICLASS 2009, July 2009, Vail, CO, USA.

5. L. Allocca et al., *Gasoline Spray Imaging by Polycapillary X-ray Technique*, submitted to AIP for ICXOM XX Conference (2009).

6. D. Hampai et al., *Research and Development of X-Ray Spectroscopy Based on Polycapillary Optics at Laboratori Nazionali di Frascati*, submitted to AIP for ICXOM XX Conference (2009).

7. D. Hampai et al., *Polycapillary Optics Based TXRF for Low Concentration Elements*, submitted to Optics Letters (2009).

8. D. Hampai et al., Spectr. Acta B **64**, 1180 (2009).

9. S.B. Dabagov, Spectr. Acta B **64**, 747 (2009).

MUEXC

M. Cestelli Guidi (Art. 23), G. Della Ventura (Ass.), D. Di Gioacchino (Resp. Naz.), L. Gambicorti (Ass.), A. Marcelli, A. Mottana (Ass.), E. Pace (Ass.), P. Postorino (Ass.), A. Puri (Ass.), N. Saini (Ass.), F. Tabacchioni (Tecn.), R. Sorchetti (Tecn.)

1 *MUEXC* project

MUEXC is an experimental program based on the PRESS-MAG-O apparatus (one of the highlights of the INFN Vth Committee in 2005) and its first experiments on materials for technological applications of the interest of the Institute in extreme conditions of pressure, magnetic field in a wide temperature range. The project is based on a large collaboration between, the 'magneto-dynamic' group of the LNF, the SINBAD team, the LNF section of Florence, the High-pressure Raman group' and the 'Spectroscopy group' of the Department of Physics of the Sapienza University and the Department of Geological Science of the Roma Tre University. In 2009 the main activities of the MUEXC collaboration on the PRESS-MAG-O apparatus [1)] have been: a) continue the commissioning of the PRESS-MAG-O instruments and in particular the tests of the cryostat at cryogenic temperatures to fix the vacuum leak detected at low temperatures; b) a.c. magnetic response tests of the new *sapphire* sample holder of the PRESS-MAG-O insert; c) final design of the optical system necessary to focus the IR beam inside the diamond anvil cell (DAC) in the cryostat.

During the year we received important support to the MUEXC project from international teams interested to scientific researches with the PRESS-MAG-O device. The interest resulted in several letters of intent. In addition, a young Research Doctorate of the XXIV Material Science cycle of the University 'Sapienza' joined our project with the research program: *'Study of highly correlated materials under extreme conditions'*.

For the period of 2009 we also continued a.c. susceptibility experiments. In particular we investigated the superconducting non-linear magnetic behavior of the $NdAsFeO_{0.86}F_{0.14}$ compound [2,3] and explored the ordering/disordering behavior of oxygen atoms in the REO layers and FeAs slabs using the X-ray absorption near-edge structure (XANES) spectroscopy in oxypnictides materials [4].

Finally, we started the set up of the new LNF experimental area devoted to the MUEXC, called LAMP, acronym of Laboratory of Magnetism and High Pressure experiments. This laboratory will be dedicated to the electronic transport and magnetic measurements vs. magnetic field, pressure and temperature with PRESS-MAG-O other cryostats working with superconducting magnets.

2 *PRESS-MAG-O* cryostat

Many tests and improvements of the PRESS-MAG-O instrument have been performed in these months. Among the many, we proceeded to the upgrade of the cryostat in particular to fix the vacuum leak ($\sim 10^{-3}$ mbar) detected at low temperature (≤ 77 K) during the first cooling tests and that prevented the further commissioning at the LHe temperature. This leak is present only at low temperature. After several cooling cycles performed in 2008 and in the first six months of

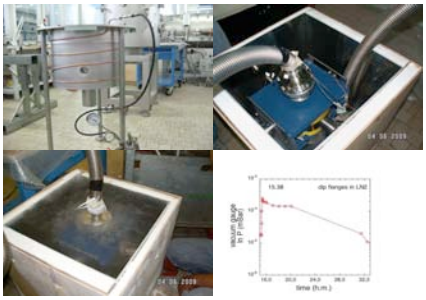

Figure 1: Photos of the PRESS-MAG-O cryostat during the tests in Parma. The internal tank with the copper cooling pipes (top left), the cooling test of the superconducting magnet (top right and bottom left) and the plot of the vacuum vs. time during the measurements.

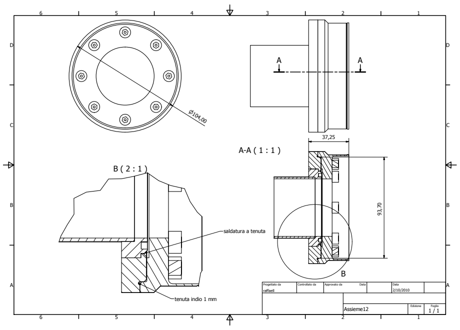

Figure 2: The construction drawings of the new flanges of the optical lines.

2009 and different attempts to fix this complex problem, the cryostat has been sent back to the factory in Parma (DG Tech nology). A further test at 77 K performed on the components of the cryostat (see Fig. 1), i.e., the tank of the cryostat and the split magnet with its optical lines and the cold finger, clarified that the leak is associated to the cryogenic aluminum rings used to seal the joints between the flanges of the optical lines connecting the superconducting magnet and the pipes of the cryostat. The problem will be solved using a new sealing configuration (Fig. 2) with indium based O-rings.

3 *DAC*-holder and Optical concentrators

After several technical evaluations and experiments performed with an a.c. magnetic field produced by the excitation coils of the PRESS-MAG-O insert, the original Cu-Be sample/ DAC-holder for the 'SQUID' micro-gradiometer pick-up coils have been redesigned and manufactured by a Swiss company in a unique block of *sapphire*, an electrical insulator but an excellent thermal conductor. The new DAC-holder (Fig. 3) improves the performances (Fig. 4) minimizing the losses due to the *Foucault currents* measured inside the bulk Cu-Be-holder, preserving about 80% of the applied magnetic signal. In addition we designed another DAC-holder manufactured in PEEK for Cu wire pick-up coils working in the *first derivative bridge configuration*, this holder made in thermoplastic material with excellent mechanical and chemical characteristics wide range of temperatures will be used for experiments that non required superconducting coils for experiments (Fig. 5).

In in these months we also finalized the design of the Cassegrain concentrator (Fig. 6) in agreement with the opto-mechanical constraints of the PRESS-MAG-O cryostat. This optical system has been customized in order to focus the IR synchrotron radiation within a small-size spot inside the diamond anvil cell and to fit the dimensions of the optical lines of the cryostat with the largest numerical aperture [5].The diameter of the Airy disk of this system is $\sim 200\ \mu$m at the shortest wavelength. The wavelength range of this optical system ranges from the visible to the far-IR domain, with an optimized behavior between 2 and 20 μm, and the possibility to work down

Figure 3: Different views of the *sapphire* sample/DAC-holder.

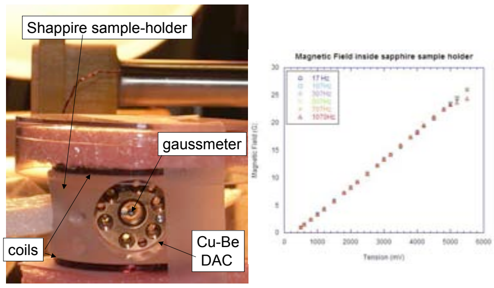

Figure 4: Experimental set-up (left) for the measurements of the magnetic field inside the *shappire*-holder vs. the applied voltage performed at different ac frequencies.

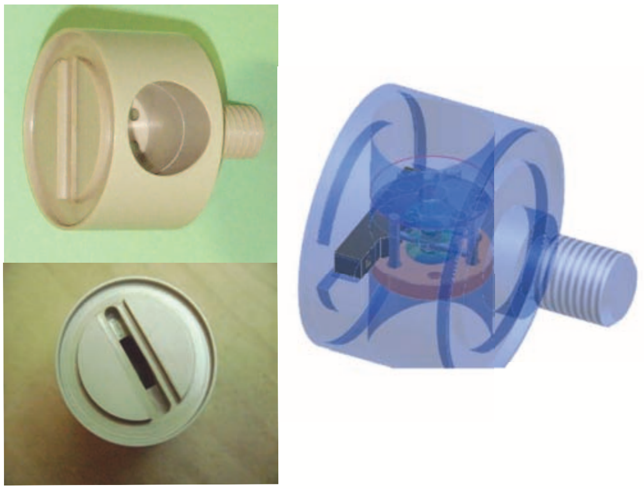

Figure 5: Photos of the DAC-holder made in PEEK (left); a 3D view of the pick-up bridge coils inside the DAC (right).

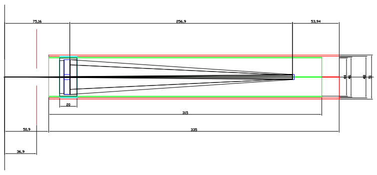

Figure 6: Schematical layout of the Cassegrain optics designed for the PRESS-MAG-O cryostat.

Figure 7: The PRESS-MAG-O optic steel pipe

to 50 μm. To match the tube diameter (Fig. 7) the maximum diameter of the entrance beam of the optical system is $\Phi \sim 30$ mm and the optical axis coincides with the axis of the tube splitted in two sections to allow installation of the optical system. The first is 225 mm long while the second including the temperature ceramic break is 325 mm. The optics will be delivered in the spring of 2010.

4 Experimental activity on highly correlated materials

In addition to the mechanical tests, within the framework of the future research of this experimental program, we continued the researches on new iron based high T_c superconductors. In these compounds a complex interplay among magnetism, layered structure and multiple surface Fermi sheets occur. In this case, a flux dynamic investigation as a function of the temperature and of the applied magnetic field to the sample has been performed to obtain superconductivity information on the thermal fluctuations of vortices and about the dimensionality of the pinning processes connected to the critical current behavior. These parameters are important for practical applications and the ac multi-harmonic susceptibility, in particular the third harmonic component is the best tool for this analysis. The results of the a.c. third harmonic study (χ_3') of the $NdFeAsO_{0.86}F_{0.14}$ 1, 2, 3) as a function of both temperature and frequencies in a low applied magnetic field, have been compared with ideal critical state models and with those of high T_c materials (HTSC) such as MgB_2, YBCO and BiSCOO2223. The frequency dependence of the third harmonic susceptibility components vs. temperature describes the change of the effective flux-diffusivity connected with the flux-pinning interaction. This variation can be associated to the change of the potential V induced by the frequency, as described in the superconducting I-V characteristic. As an example, to clarify the role of the χ_3' frequency dependence, we may analyze the polar plot (Cole-Cole) of χ_3' versus χ_3'' components. These lens shaped closed curves showed in Fig. 8, point out both a change of the initial χ phase and of the area of the closed curves as a function of the applied magnetic field frequency. This figure shows the presence of a pure critical state with a homogeneous 3D pinning bulk almost independent by the frequency with a lens shape (red curve) and a pure critical state with a 2D surface pinning barrier with a cardioid profile (violet curve). Data of the $NdFeAsO_{0.86}F_{0.14}$ with the lens shape closed curves indicate that a 3D flux bulk pinning occurs in the sample. Moreover, the change of the phase lag, Θ, with the frequency excitation identify a phase change with a clockwise rotation in the range $23° < \Theta < 64°$ at increasing frequency in the range 107-707 Hz. On the contrary, when the frequency increases in the range 707-1070 Hz, the polar plots are independent, however at $\Theta = 64°$ the value is different by the ideal one in the critical state ($\Theta_{Bulkpinning}$=90°) probably because of the finite thickness of the sample.

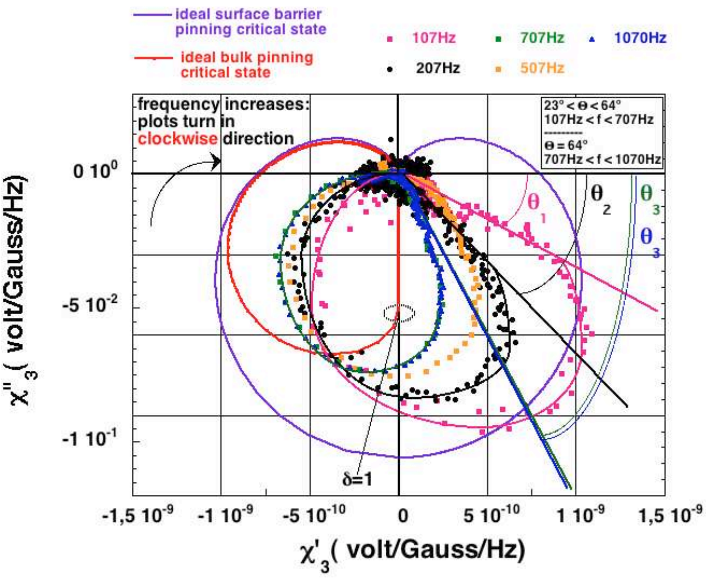

Figure 8: $NdFeAsO_{0.86}F_{0.14}$ polar plots (Cole-Cole), i.e., χ_3' vs. χ_3'' frequency. The ideal lens shape bulk pinning (red) and the cardioid shape surface barrier (violet) critical states are showed for comparison.

Oxypicnides have been investigated also by RE L_3 X-ray absorption near-edge structure (XANES) spectroscopy [4] to explore the structural contribution in these materials due to the REO spacers located between the electronically active FeAs slabs. XANES spectra have been also simulated by full multiple-scattering calculations to describe different experimental features and their evolution with the RE size. The near edge features just above the L_3 white line are highly sensitive to the order/disorder distribution of oxygen atoms in the REO layers. In addition, shape resonance peaks due to both As and O scatterings change systematically addressing not negligible local structural changes in the FeAs slabs and in the REO spacers correlated to the RE size. Results suggest that the interlayer coupling and the oxygen order/disorder in the REO spacers may have an important role in the superconductivity mechanisms these materials.

In November we started (Fig. 9) the set up of the new LAMP experimental area. The new laboratory will be located inside the LNF in the Building Capannone LEGNARO recently made available. The novel laboratory will host the PRESS-MAG-O apparatus and other cryostats for electronic transport and magnetic measurements with superconducting magnets up to 8 T. Work is in progress to start all experimental research programs in this new area within the first half of 2010.

Figure 9: Photograph of the internal area of the LAMP laboratory.

5 Acknowledgements

We thank the technical staff of the DAϕNE-Light laboratory for their continuous and invaluable technical support. We gratefully acknowledge also the support of the Italian Ministry Foreign Affairs in the framework of the 12$^{\mathrm{th}}$ Executive Programme of Scientific and Technological Cooperation between the Italian Republic and the Peoples Republic of China. A special thank is devoted to Haifeng Zhao for his contribution to the development of new software for data analysis.

6 Publications

L. Gambicorti et al., Frascati Preprint LNF-99/001 (P), (2009).

References

1. D. Di Gioacchino et al., *Flux dynamics in* $NdFeAsO_{0.6}F_{0.4}$, presented at the International Conference on FeAs High T_c Superconducting Multilayers and Related Phenomena (Roma, December 9-13 2008). Proceedings of Stripes 2008, J. Supercond. (2009) *in press*.

2. D. Di Gioacchino et al., J. Supercond. **22**, 549, (2009).

3. D. Di Gioacchino et al., *Status of PRESS-MAG-O: the experimental apparatus to probe material and phenomena under extreme conditions*, J. Phys. Chem. Solid (2010) in press.

4. D. Di Gioacchino, A. Marcelli, P. Puri, and A. Bianconi, *The a.c. susceptibility third harmonic component of NdO1-0.14F0.14FeAs*, J. Phys. Chem. Solid (2010) in press.

5. W. Xu et al., *Oxygen disorder and its effects on the local structure of REOFeAsO Experiments and multiple scattering calculations*, J. Phys. Cond. Matter (2010) in press.

N@BTF

R. Bedogni (Art. 23), B. Buonomo (Art. 23), A. Esposito, M. De Giorgi (Tecn.),
G. Mazzitelli (Resp.), L. Quintieri (Art. 23), P. Valente (Osp.)

1 Main objective of n@BTF

The main object of this project is to evaluate the feasibility of a neutron source at the DAΦNE Beam Test Facility. The experiment planned in spring 2010 will demonstrate whether the expected neutron fluxes are obtainable and thus it will enable us to evaluate the possibility of providing hadrons at the BTF, together with electrons, positrons and photons. Indeed, this additional possibility would make the DAΦNE BTF an unique facility in the world.

The basic idea of the "N@BTF" is to exploit the gamma shower coming from the interaction of electrons with matter, to produce neutrons by means of photo-absorption reactions. In fact, the impinging electrons, interacting with the target, produce bremsstrahlung photons that will have a continuos energy spectrum from low energy up to the end point corresponding to the electron beam energy. Photons excite the nuclei of the target with which they interact and these excited nuclei go back into the fundamental state by emitting one or more nucleons. The most probable reaction is (γ, n), in which only a neutron is boiled off the nucleus, but also $(\gamma, 2n)$ and (γ, p) reactions are possible even if less probable than the first one. Typically high Z materials have much higher cross section than the light nuclei.

The neutron photo-production is a threshold reaction since a neutron can be delivered from a nucleus only if the energy transferred by the photon overcomes the average binding energy of its nucleons. The threshold is lower in heavy nuclei (high atomic number) than in light nuclei: 5 to 7 MeV for the first case and 15 to 20 MeV in the second case.

2 Work done during 2009: MC simulations for target optimization

The rate of neutrons produced by photo-absorbtion depends on the following factors: beam power released in the target and atomic number, Z, of the target nuclei. The maximum beam power that can be released at present time on the target at the DAΦNE BTF is about 40 W, corresponding to bunches containing 10^{10} electrons of 510 MeV energy, that are injected at a repetition rate of 49 Hz[1]. The choice of the material, of which the optimized target has to be made, has been oriented toward high Z elements, since they have higher photo-neutron cross section and lower threshold with respect to light or middle Z elements. The possible candidates as suitable material taken into consideration have been: natural Tungsten (W), Lead (Pb) and Tantalum (Ta)[2]. The neutron

[1] The maximum injection rate from the Linac is 50 Hz, but there is always a bunch that is sent onto the spectrometer to reconstruct the energy spectrum of the beam at the end of the Linac, before entering in the BTF transfer line.

[2] Uranium is the element that in principle will give the best photo-neutron yield, but at present time it has been discarded as possible solution essentially due to the more severe safety rules for handling it.

yield [n/s] per unit power [kW] has been estimated for each of the selected materials by using the Monte Carlo code FLUKA [1].

2.1 Validation process of Monte Carlo estimations

Our simulations are based on the FLUKA code since, in addition to the fact that it implements the photo-nuclear physics on the whole energy range, it also offers a rich data base for the total photo-neutron cross sections, which, after the 2005 upgrade [3], has been derived from experimental data (or from existing evaluations) of 190 stable nuclides. For all the other nuclei, excitation functions are obtained from parametrisations or by interpolation.

The first important task we had to accomplish, as mandatory step, before proceeding in the computation of the optimum target with respect the BTF electron beam, consists in validating our Monte Carlo predictions, in order to become confident in having a reliable tool by which estimating the neutron source term. Semi-empirical correlations linking the neutron yield on target and the released beam power have been determined by Swanson [4] at SLAC for well known configurations and they have been used both for having an initial rough estimation of the maximum neutron yield and as a reference for our Monte Carlo model validations.

The comparison of the values derived by FLUKA simulations with those provided by Swanson have been reported in Table 1, showing a good agreement: even in the worst case the difference is less than 10% (with an average difference of only a few percent). The values reported in the

Table 1: Comparison between FLUKA predictions and Swanson's values.

Material	Swanson** [n/kWs] E+12	Fluka [n/kWs] E+12
Pb	1.98	2.0
Ta	2.13	2.37
W	2.42	2.67

** Values for enough thick targets ($\simeq$10 X_0) and for $E_e = 500\,\mathrm{MeV}$

last column of Table 1 have been derived from the neutron yield estimation per primary, obtained by Fluka code, according the following formula: $Rate[\mathrm{n/kW/s}] = \mathrm{C} \cdot \frac{\mathrm{Ne}}{\mathrm{Ne \cdot E[J]}}$, where: C is the conversion factor estimated by MC simulations (neutron produced per primary particle), *Ne* is the rate of primary particles (electrons/sec) and, finally, E[J] is the energy deposited in the target. In this estimation we have, implicitly, done the assumption that the whole primary electron energy is deposited in the target. This assumption is quite well realistic for thick targets as those we are considering here[3]

[3] We designed our optimized target in such a way that the deposited energy is only 3% less than the whole electron energy.

2.2 Choice of the material and definition of the dimensions of the optimized target

Among the materials taken into consideration for our target, W and Ta offer higher neutron yield per electron with respect to Pb case. The final choice between W and Ta has been done not on the base of nuclear considerations (the neutron yield is only few percent higher in the case of W with respect to Ta), but essentially on the base of thermo-physical properties. We have chosen W due to its better thermal conductivity, which means a more effective heat transfer by conduction: in the case of W it is almost 3 times larger than in Ta.

Once fixed the material, we passed to define the best geometrical configuration. The rate of neutrons escaping the target in which they are produced depends on the thickness of the target, so that an optimum value for which the neutron flux is maximum at a defined energy can be found. Monte Carlo calculations have been made in order to optimize the yield of neutrons produced per electron inside the target and the ratio of the neutron flux exiting from the target with respect to the photon one.

Figure 1: Optimized W target.

For our target we chose a cylindrical geometry and many cases have been simulated, changing both the length and the radius of the cylinder, in order to find the best solution. In particular, for each configuration we estimated the neutron flux coming out from the target and the ratio between the neutron and the photon flux, integrated, respectively, on all the energy spectrum and all solid angle. In addition, the neutrons to photons ratio has been also estimated along well defined directions respect to the incident primary beam (0, ± 30°, ± 45°, 90°, respectively). We identified the best solution as that for which, a further increase in the linear dimensions affects only marginally the photo-neutron yield (only few percent). The length has been chosen to be $\simeq 15X_0$[4] (about 60 mm): the increase of the cylinder length of 33% (from 15 to 20 X_0) induces an enhancement of the neutron yield of less than 3%. A fine tuning of the final radius has been also done and the optimum value for the radius has been determined to be $\simeq$ 10 X_0 (35 mm). At the end, the optimized cylinder for neutron photo-production at the DAΦNE BTF is a cylinder made of W with radius 35 mm and length 60 mm. It is shown in Fig. 1. The total energy deposited by each primary in the optimized target has been estimated to be about 493.1 MeV with low statistic error: this means that almost 97% of electron energy is left in the target.

[4]The radiation length for the W is 0.35 mm.

3 First measurement experimental set-up: calculation of neutron and photon energy spectra and spatial distribution

The first measurements have as main objective to show the photo-neutron source feasibility at the BTF. We have planned to use, during the initial measurement campaign, Bonner sphere detectors [5)].

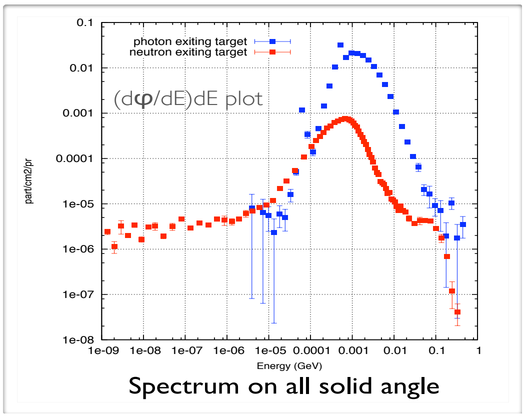

Figure 2: Energy spectrum of neutrons and photons leaving the target.

They are made of external spherical shell of polyethylene (density 0.95 g$\cdot$cm^{-3}), whose external radius spans from 2 up to 12 inches. Each polyethylene sphere can host in the middle a thermal detector: this can be active or passive, depending on the environment in which it has to work. In fact for high photon background, usually passive detectors as Gold or Dysprosium foils, that can be activated, are preferable. In addition ^{6}LiI(Eu) active scintillators or TLD detectors can be used. We will work in integration modality using the spheres in sequence, that means they will be exposed in turn, one after another, in the same position, 1 m apart from the upper surface of the shield, along one of the extraction line.

The main goal of the MC simulations is to provide estimation, as much accurate as possible, of the neutron rate as well as to study the neutron energy spectra and spatial distribution as function of the thickness of the chosen target and of all the materials that can be placed around the target in the experimental set-up. At the end, we calculated the neutron and photon fluxes we expect to have in the location where the Bonner Spheres are supposed to be placed during the measurements. In Fig. 2 the expected neutron spectrum [neutron/cm^2/pr] from the optimized target is shown[5] together with the photon one. As expected, up to 100 MeV the spectrum is described as a Maxwellian distribution with average energy around 1 MeV (0.7 MeV, for sake of precision). This contribution is due to the Giant Dipole Resonance (GD) mechanism, that is the predominant phenomenon for photon energy lower than 30 MeV. Approaching the higher energies, the Quasi-Deuteron (QD) effect adds a tail to the Giant resonance spectrum, whose slope becomes steeper as the incident electron energy is approached. In both mechanisms (GD or QD resonance) the information about the incident photon is lost in the interaction with nuclei and the neutron emission is quite well isotropic, as it is shown on the left side of Fig. 3. The neutron flux at

[5] This spectrum has been obtained in simulations of the whole assembly.

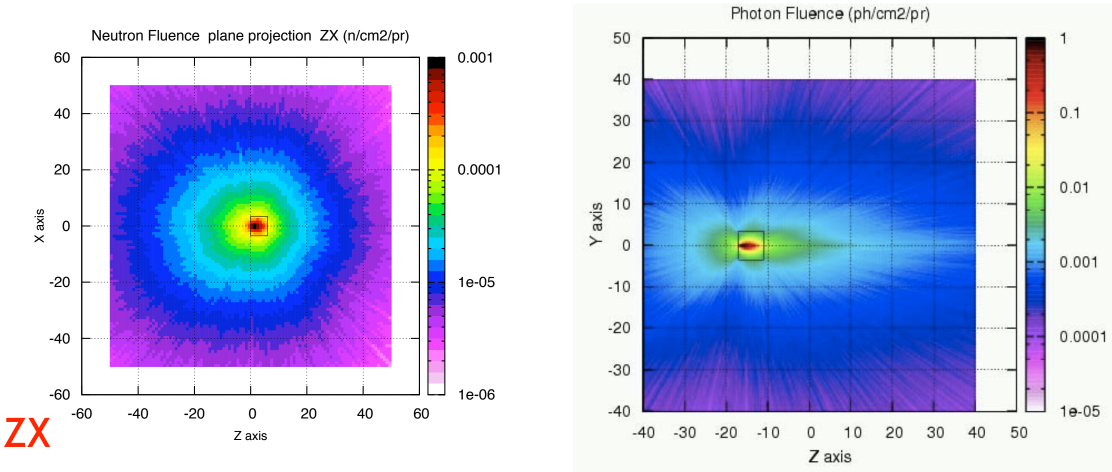

Figure 3: (color online). Neutron (on the left) and Photon (on the right) spatial distribution around the target: fluxes [n/cm^2/pr] projected on the ZX plane and averaged in the Y direction. Z is the beam incident direction.

the source has been estimated to be 1.8E-3 n/cm^2/primary, that in case of 4.9E+11 primary/s corresponds to a value of the neutron flux of about 9.E+8 n/cm^2/s.

One of the main limiting aspect of producing neutrons by photo-production is the high unavoidable background of gamma rays around the target. Nevertheless photons, and in particular those of higher energy, are essentially collimated forward around the beam direction (see right side of Fig. 3), so that we think to collect the neutron flux to use in experiment in the plane orthogonal with respect to the primary beam direction. Our simulations predict that the intensity of the photon flux decreases of more of two orders of magnitude passing from the primary beam direction to the orthogonal one, while the neutron flux intensity value remains almost unchanged in all the solid angle.

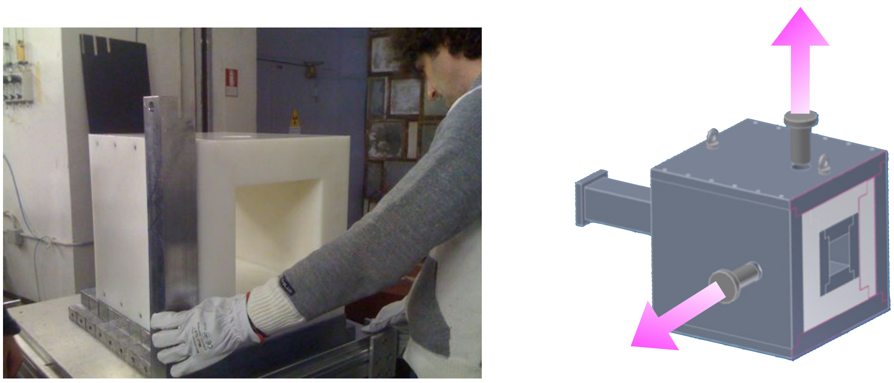

Figure 4: Shield: Mounting phase detail on the right, Cad on the left (Extraction Lines and Dumping system are put in evidence).

We expect to have a photon flux, integrated on all the solid angle and on all the energy spectrum, escaping the target of about 2E+10 photons/cm^2/s (to be compared with 9E+8 neutron/cm^2/s value for the integrated neutron flux). An accurate map of the neutron and photon

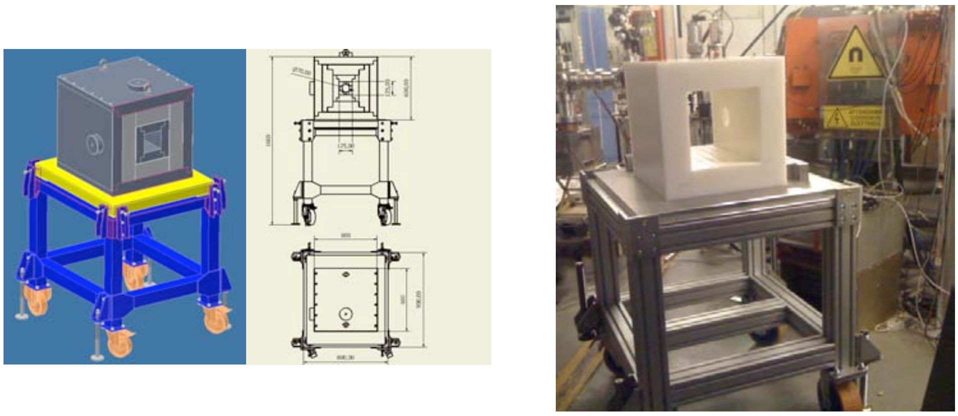

Figure 5: Shield and support structure: design (on the left), detail during mounting phase (on the right).

flux intensity expected around the target has been provided, allowing to design accurately the shield: it consists of 2 layers of lead (each one 7.5 cm thick in the XZ plane) and one of polyethylene (10 cm thick) in between. The shield has also an external lead layer with 20 cm thickness. This thicker layer is placed in front of the inlet square window, as final dump of the beam. The assembled shield has two holes of 70 mm diameter, whose axes are located in a plane perpendicular to the horizontal beam direction. These holes can be sealed by suitable plugs, as it is shown in Fig. 4. The overall structure (shield + support) is show in Fig. 5: the target is kept inside the shield by means two stainless-steel rings, in such a way that its center falls in the intersection of the axes of the extraction lines.

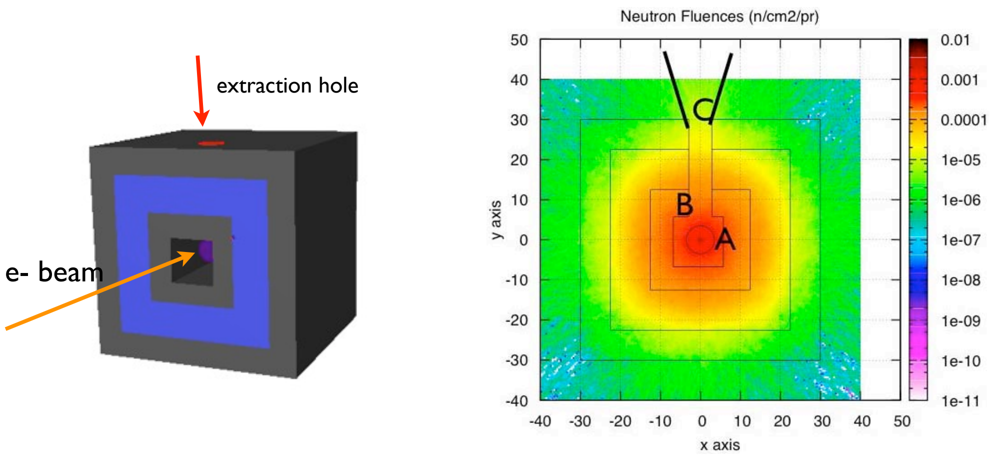

Figure 6: Projection of the neutron flux in the XY plane, being Z the primary beam direction.

3.1 Simulation results for the first measurement experimental set-up

Some results of the simulations, concerning the expected neutron fluxes in different locations, are reported in Table 2: the A, B and C points, cited in this table, are indicated in Fig. 6, that shows the projection of the neutron flux in the plane orthogonal to the direction of the impinging beam and passing by the center of the target[6].

Table 2: Neutron flux and Current values inside and outside the shield.

n@BTF Location	Neutron Flux [n/cm^2/s]	Neutron Current [n/s]*
Φ_1 exiting the target (A)	8.80E+08	1.10E+11
Φ_2 entering the shield (B)	2.30E+08	7.70E+09
Φ_3 leaving the shield (C)	2.50E+07	9.60E+08
Φ_4 at 1m from shield (D)	3.00E+05	8.00E+08

* Integrated over all the energy spectrum

The maximum available neutron flux that we expect to have along the extraction line, 1 m apart from the shield upper surface, is 3.E+5 n/cm^2/s that corresponds to an equivalent dose of about 43 mSv/h. The neutron current (integrated on all the spectrum) that we estimated to enter into the spherical detector of 60 cm diameter is equal to 8E + 8 n/s. We also calculated the neutron spectra along one of the extraction line: the shape of the spectrum remains essentially unmodified, whereas the intensity of the flux decreases according the inverse of the square distance from the neutron source.

The predicted photon rate arriving into the spherical detector is an order of magnitude greater than that foreseen for the neutron: 7.8 E + 9 photons/s.

Fig. 7 shows the energy spectra of the photons and neutrons that arrive onto the bigger Bonner sphere at 1m from the shield. Concerning the photon spectrum, we can observe that, as expected for, the higher and lower energy photons are cut away. In fact Bonner spheres are supposed to be placed at 90 degree respect to the primary beam direction while, as we have already seen, the harder component of the photon spectra is well collimated along the primary beam. Moreover, the lower energy photons are attenuated by absorption from the shield, whose attenuation factor has been estimated to be equal to 300 (we refer to the photon flux value integrated on all the energy spectrum).

We are still studying the possibility to optimize the design of the extraction lines in such a way to enhance the signal to noise ratio, where the signal is the neutron flux and the noise is the gamma background, respectively. This research consists not only in the identification of a suitable shape of the hole, but essentially the selection and use of special materials that are able to attenuate the photon without affecting too much the neutron flux. First attempts have done by testing caps for sealing the holes of various lead thickness and the results show that, using caps made of 10 cm of lead, the signal to noise ratio becomes equal to 1, while for 25 cm of lead, the SNR could reach a value of 6. These results show that there is an important possibility of improvement of the

[6] The values reported in the plot are averaged along the direction of projection.

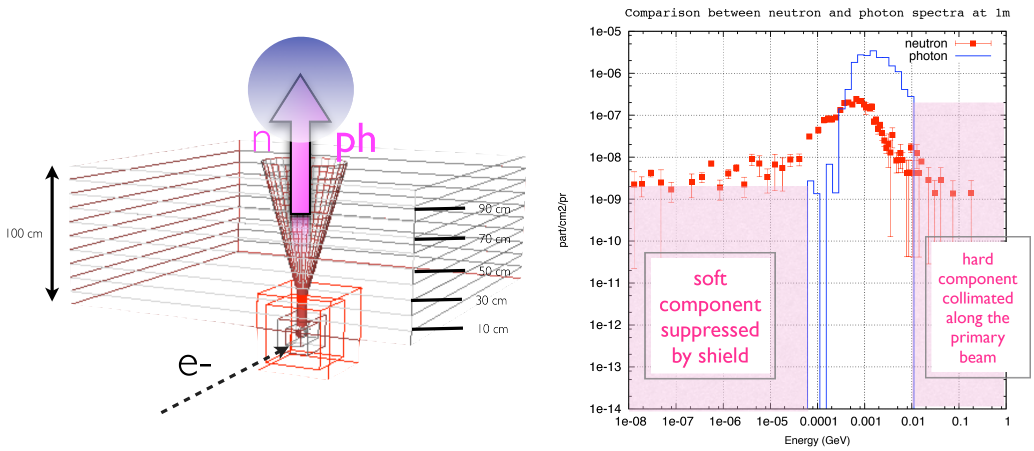

Figure 7: Comparison between photon and neutron spectra 1 m apart from the shield.

experimental set-up and that a finer work of definition of useful configurations could be planned, after the feasibility test, taking also into account the main possible user requirements.

4 Conference Talks

1. L. Quintieri et al., *N@BTF: Study and Design of an Experiment at the DAΦNE BTF for Neutron-Photoproduction*, Seminar at FLUKA meeting, CERN 14-15 December 2009.

2. G. Mazzitelli et al., *Sorgenti di Neutroni e loro applicazioni in ambito INFN*, Workshop 17-19 November 2009, Laboratori Nazionali Legnaro.

3. L. Quintieri et al., *Feasibility Study of a neutron source at the DAΦNE Beam test Facility, using Monte Carlo codes Orlando, Florida*, Oral presentation at NSS-MIC 2009, Orlando, 25-31 October 2009.

4. L. Quintieri et al., *Feasibility Study of a neutron source at the DAΦNE Beam test Facility*, Seminar at LNF, 7 October 2009.

5. L. Quintieri et al., *N@BTF: Study and Design of an Experiment at theDAΦNE BTF for Neutron-Photoproduction*, SIF-XCV National Congress, Bari 28-9 to 3-10 2009.

6. L. Quintieri et al., *N@BTF: Study and Design of an Experiment at theDAΦNE BTF for Neutron-Photoproduction*, CSN5, Rome 22 May 2009.

5 Publications in 2009

1. L. Quintieri *et al.*, *Feasibility Study of a Neutron Source at the DAΦNE Beam Test Facility Using Monte Carlo Codes*, Nuclear Science Symposium Record, 2009 IEEE 2:2081-2086, 25-31 Oct. 2009

References

1. A. Fassò et al., *A multi-particle transport code*, CERN-2005-10 (2005), INFN/TC-05/11

2. A. Fassò et al., Proc. 8th Int. Conf. on Radiation Shielding, Arlington (Texas) Apr. 24-28 1994, p. 643-649.

3. A. Fassò et al., *Photonuclear Reactions in FLUKA: Cross Sections and Interaction Models*, Presented at the International Conference on Nuclear Data for Science and Technology, Santa Fe, NM, USA, 26 Sep - 1 Oct 2004 In: AIP Conf. Proc. 769 (2005) pp.1303-1306.

4. W.P. Swanson, *Calculation of Neutron Yields Released by Electrons Incident on Selected Materials*, SLAC-PUB-2042, November 1977.

5. A. Esposito et al., *Measurement and unfolding of neutron spectra using Bonner Spheres*, Radiation Protection Dosimetry, **110**, 555 (2004).

NANO5

L. Quintieri (Art. 23)

1 NANO5: Description of main objectives

NANO5 is a Geant4-related R&D project. It was approved as part of INFN scientific program of Technology Research in September 2008, with start in January 2009. It gathers an international team of collaborating scientists at various institutes in Europe, Asia, Northern and Southern America.

Geant4 [1], [2] is an object oriented toolkit for the simulation of particle interactions with matter. It provides advanced functionalities for all the typical domains of detector simulation: geometry and material modeling, description of particle properties, physics processes, tracking, event and run management, user interface and visualization.

Nevertheless, new experimental requirements have emerged in the recent years, which challenge the conventional scope of major Monte Carlo transport codes like Geant4. Research fields as nano-dosimetry, nanotechnology-based detectors, radiation effects on components in space and at high luminosity colliders, nuclear power, plasma physics etc. have shown the need of new methodological approaches to radiation transport simulation along with new physics functionalities in Geant4.

The NANO5 project investigates conceptual and technological solutions to extend the current capabilities of the Geant4 toolkit to cope with the new experimental requirements and evaluates whether and how they can be supported by the Geant4 Kernel. In more detail, NANO5 investigates the possibility of introducing into Geant4 new physics functionality and implementing new methodological approach for radiation transport simulation in order to satisfy mainly the following requirements:

- To make possible to perform simulation at different scale in the same experimental environment (condensed-random-walk and discrete methods). In fact, in realistic cases, small-scale systems are often embedded in larger scale ones (i.e micro-component of an equipment inside an HEP experiment, cellular ans sub-cellular aggregate in biological system, etc).
- To exploit Monte Carlo and deterministic transport methods in the same simulation environment in case where performance issues are critical (nuclear reactor design).
- Developing of innovative design solutions in software architecture of Geant4 Kernel and consequent evaluation of their implications in terms of computational performances and quality assurance.

1.1 New Architectural Design Approach

The main feature of the new software architectural design, at the present under study with NANO5, is the minimalist approach based on the policy class design, whose potentialities have been explored in detail by Andrei Alexandrescu [3]. In brief, policy-based class design promotes to assemble a class with complex behavior out of many little classes (called policies), each of which takes care of only one behavioral or structural aspect. A policy class is a template parameter used to transmit behavior. As the name suggests, a policy establishes an interface pertaining to a specific issue: it is possible to implement policies in various ways as long as the policy interface is respected. Because it is possible to mix and match policies, we can achieve a combinatorial set of behaviors by using a small core of elementary components. Alexandrescu description of policy classes suggests that their power is derived essentially from granularity and orthogonality.

2 Main activities performed at Frascati

The work developed at Frascati has been essentially devoted to accomplish the following two tasks:

1. Application of the policy based design to implement the Photon Physics in Geant4 and study of the consequent effects it has on computational performance and quality assurance.
2. Set-up of an exhaustive data library as base of software developments to improve the PIXE (Particle Induced X-ray Emission) simulation in Geant4.

The details of the given contributions are better explained in the following paragraphs.

2.1 New Photon Interaction Models implementation

As start-up point, in order to test the implementation of the new architectural design, we focused on the electromagnetic physics package. In particular, a pilot project is currently in progress in the domain of photon interactions (Compton and Rayleigh scattering, photoelectric effect and photon conversion), with the aim of implementing the current Geant4 physics models in terms of the architectural design briefly described in §1.1. Performance measurements as well as first-hand evaluations of the capabilities and drawbacks of the policy-based design are, finally, studied.

We have redesigned the generic photon process in such a way that it acts as a host class, deprived of intrinsic physics fucnctionality. Physics behavior is acquired through policy classes, respectively responsible for cross section and final state generation (passed as concrete classes). In this new approach, cross section and final state policies are orthogonal (that means independently implemented and computed). The main advantages of this approach are:

- Flexible configuration of processes at granular level.
- Transparency of physics
- Performance optimization for computationally intensive use cases
- Effortless Verification & Validation

Figure 1 shows an example of the prototype design of photon interactions, applied to the Comptpn Scattering. Frascati has given a special contribution on the implementation (according the new architectural design) and consequent testing of the pair-production process in the Standard flavor[1]. Thanks to the new design, we could appreciate an improved transparency of physics models, that is, in fact, exposed at a fine-grained level.

[1]All photon interactions are implemented in Geant4 at least in 3 modeling variants, which are identified as Standard, Library-based and Penelope

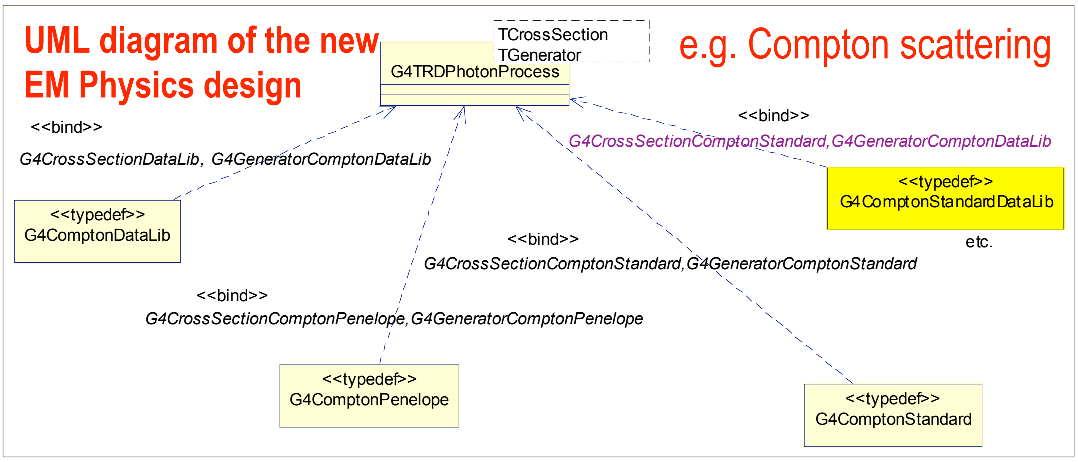

Figure 1: Main Feature of the Policy-Based prototype, illustrated for Compton Scattering.

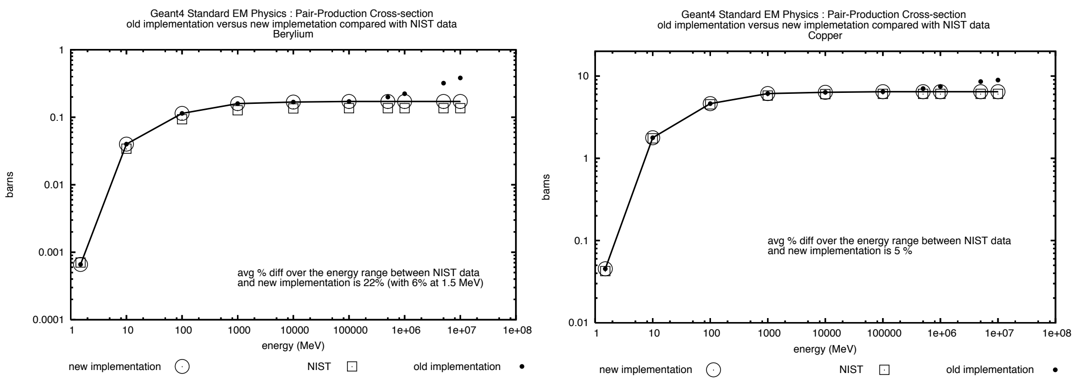

Figure 2: Photon conversion cross-section validation with respect to NIST reference data for Be and Cu.

2.1.1 Validation of the implemented models

The plots in Fig. 2 refer to the case of photon conversion cross-section comparison with respect to NIST reference data for two cases: Be and Cu. Discrepancies between the implementation in Geant4 9.1 standard electromagnetic package and the Official User Documentation of the cross-section model for photon conversion have been identified and reported to the maintainers of the original Geant4 implementations. The observed model behavior is shown in Fig. 3 (on the left). According to the Geant4 Physics Manual, above 100 GeV the cross-section for photon conversion, based on the Bethe-Heitler model, should be constant. The agility of NANO5 electromagnetic physics design allowed a quick re-implementation of the cross-section computation consistent with the specifications of Geant4 Physics Reference Manual. Other implementations of this cross section based on alternative models documented in literature are in progress; for instance, according to work reported in reference [4]the cross section above 1 TeV is expected to fall as a function of energy. Implementations by Geant4 standard electromagnetic group have been announced in Geant4 development plans.

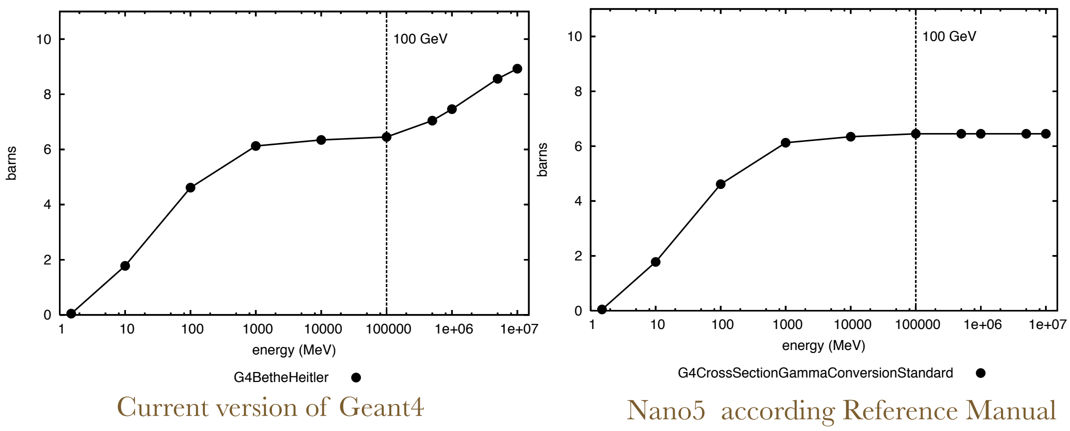

Figure 3: Differences between the implementation in Geant4.9.1 standard electromagnetic package and the User Documentation of the cross section calculation for photon conversion.

2.1.2 *Effects of the new architectural design on the computational performance and quality assurance*

The testing of basic physics components (like atomic cross sections or features of the final state models) is greatly facilitated wrt to the current Geant4 version: being associated with low level objects like policy classes, they can be verified and validated independently, while in the current design scheme a full-scale Geant4 based application is necessary to study even low-level physics entities. The gain in simplification of the physics testing code has been estimated as of approximately two orders of magnitude in terms of reduction of instruction lines to execute[2], while the computational resources needed for the test operation have been reduced dramatically. These achievements are relevant to the quality assurance of Geant4 physics.

Preliminary results of the electromagnetic physics pilot project indicate a performance improvement associated with the policy-based design. In table 1 we report the performance comparison (in terms of cpu time) between the Geant4.9.1 and NANO5 design for the estimation of the final status in a simple test for Compton scattering of photon with energy 40 keV on several atoms. Preliminary performance measurements in a few simple cases of photon interactions indicate a gain of the order of 30% in computational speed with respect to equivalent physics implementations in the current Geant4 design scheme. Other tests are in progress to check if the computational performance are affected also in all the other Photon Physics Models that have been reimplemented, up to now.

[2]The test for comparison of basic Geant4 electromagnetic physics features against NIST Physical Reference Data requires more than 4000 lines of code in a fully scale Geant4 based application. Equivalent tests for the physics parameters related to photons can be performed through simple tests, consisting of few tens of lines only and running very fast on a laptop computer.

Table 1: CPU time[s] for estimation of final status for Compton scattering of 40 keV Photons on several atoms (Penelope).

Atom	Policy-based design	Geant4 9.1	Gain
C	4.15	6.08	32%
Si	6.23	8.37	26%
Cu	7.64	10.78	29%
W	14.06	19.18	27%

40 keV, 10^6 events, Intel Core2 Duo Processor E6420, 2.13 GHz, 4GB RAM

2.2 Developments on PIXE Simulation with Geant4

At the present time Geant4 does not provide adequate capabilities for the simulation of PIXE in realistic case, as documented in [5]. For this reason, the capabilities of the Geant4 toolkit have been extended, in the frame of NANO5, by enabling the generation of PIXE associated with K, L and M shells for protons and α particles, providing a variety of cross section models.

In this context, an extensive ionisation cross section data library has been created as support of the development process. This extended data library represents essentially the main contribution given by Frascati for PIXE improvement in Geant4.

The adopted data-driven strategy and the software design improve the computational performance over previous Geant4 models. The validity of the implemented models has been quantitatively estimated with respect to experimental data, as shown in [5].

2.2.1 The PIXE data Library

The PIXE simulation in Geant4 identifies three main fields with associated responsibilities: the hadron ionization process, the creation of a vacancy in the shell occupancy resulting from ionisation, the deexcitation of the ionised atom with the associated generation of X-rays. The simulation of PIXE concerns a variety of experimental applications, that require the capability of calculating ionisation cross sections over an extended energy range: from a few MeV typical of material analysis applications to hundreds MeV or GeV range of astrophysical applications. Various theoretical and empirical models are available in literature to describe ionisation cross sections for different interacting particles, as well as compilations of experimental data.

The current software prototype, developed by the NANO5 collaboration, has adopted the strategy of providing an extensive collection of ionisation cross section models as a function of element, atomic (sub-)shell, and incident particle kinetic energy.

The cross sections for ionization of K, L and M shell by protons and α particles have been tabulated and assembled in an extensive data library (PAIX); the values at a given energy are calculated by interpolation. Cross sections have been derived from theoretical calculations based on the EPCSSR method, also including variants like Hartree-Slater, United Atom and high energy corrections, and from a variety of empirical models based on experimental data collections. The tabulations corresponding to theoretical calculations span the energy range between 10 keV and 10 GeV; empirical models are tabulated consistently with their energy range of validity. The adopted data-driven approach optimizes performance speed and offers flexibility for chosing a cross section model.

A collaboration with RSICC (Radiation Safety Information Computational Center) of Oak Ridge National Laboratories, is actually in progress, under the direct supervision of Frascati, in order to assemble and distribute to the whole scientific community the PAIX data libraries.

3 Conference Talks

1. L. Quintieri, *Inter-Comparison and Validation of Geant4 Photon Interaction Models*, Poster Session on Computing and Software for Experiments, (CHEP 2009) Orlando, Florida.
2. L. Quintieri, *Research in Geant4 electromagnetic physic design and its effects on computational performance and quality assurance*, (CHEP 2009), Orlando, Florida.

4 Publications in 2009

Journals

1. M. G. Pia et al., IEEE Trans. Nucl. Sci., **56**, 3614 (2009).

Conference Proceedings

1. M. Augelli et al., *Inter-Comparison and Validation of Geant4 Photon Interaction Models* Proceedings of the Nuclear Science Symposium and Medical Imaging Conference 2009, Orlando, Florida.
2. M. Augelli et al., *Geant4-related R&D for new particle transport methods*, Proceedings of the Nuclear Science Symposium and Medical Imaging Conference 2009, Orlando, Florida.
3. M. Augelli et al., *Research in Geant4 electromagnetic physics design, and its effects on computational performanc and quality assurance*, Proceedings of the Nuclear Science Symposium and Medical Imaging Conference 2009, Orlando, Florida.
4. M. G. Pia et al., *New models for PIXE simulation with Geant4*, Proceedings of CHEP (Computing in High Energy Physics) 2009.
5. M. G. Pia et al., *Design and performance evaluations of generic programming techniques in a R&D prototype of Geant4 physics*, Proceedings of CHEP (Computing in High Energy Physics) 2009.
6. M. G. Pia et al., *R&D on co-working transport schemes in Geant4*, Proceedings of CHEP (Computing in High Energy Physics) 2009.
7. M. G. Pia et al., *R&D for co-working condensed and discrete transport methods in Geant4 kernel*, Proc. Int. Conf. on Mathematics, Computational Methods & Reactor Physics (M&C 2009), New York, 2009.

References

1. S. Agostinelli et al., Nucl. Instr. and Meth. A **506**, 250 (2003).
2. J. Alliso, et al, IEEE Trans. Nucl. Sci. **53**, 270 (2006).
3. A. Alexandrescu, *Modern C++ Design: Generic Programming and Design Patterns Applied*, Addison-Wesley (E), February 2001.
4. S. R. Klein, Radiation Physics and Chemistry, **75**, 696 (2006).
5. M. G. Pia et al., IEEE Trans. Nucl. Sci. **56**, 3614 (2009).

NUVOLA

A. Balerna, R. Cimino (Resp.), M. Commisso, T. Demma (Art. 23), A. Drago, R. Larciprete, S. Guiducci, C. Milardi, F. Tombolini, C. Vaccarezza, M. Zobov

In collaboration with
INFN and Calabria University

In particle accelerators with intense and positively charged beams and/or vacuum chambers of small transverse dimensions, electrons can be produced by the interaction of beam synchrotron radiation with the walls, by stray beam particles striking chamber walls at grazing angles, or by ionization of residual gas. These primary electrons produce secondary electrons after impact with the vacuum walls, leading to a formation of an electron cloud (EC). EC cause detrimental effects to the performances of storage rings as vacuum degradation and beam instabilities [1, 2]. The scope of the Nuvola project, at its last year, aims to understand this phenomenon and clarify and reduce these effects in present and future accelerators.

In this year we continued experimental and theoretical studies started in previous activities. One of the main topic which was addressed in the Frascati laboratory, is the study of the so called scrubbing effect, i.e the reduction of SEY (Secondary Electron Yield) on industrial materials with electron bombardment. This phenomenon is at the base of LHC baseline design operation, but its not known in all its aspects and details. Up to now, in fact, experiments did investigate only SEY dependence with the dose (the number of impinging electrons per unit area on sample surfaces) of impinging electrons only by bombarding surfaces with 500 eV electrons. These various experiments showed that, in case of LHC Cu beam screen material, an impinging electron dose between 10^{-6} C$\cdot$ mm^2 and 10^{-2} C $\cdot$ mm^2 is sufficient to reduce the SEY of such as received surface from its initial value (about 2.1) to its final value (about 1.15). All those studies neglected the dependence of the "scrubbing effect" on the actual energy of the primary electrons, even if theoretical and experimental studies predict that the electrons in the e-cloud are of very low energy ($<$ 50 eV), and that such low energy electrons can be reflected from the walls without interacting, hence scrubbing, the surface [2]. Our studies proceded in this direction and some results are shown in Fig. 1 a) in which we report SEY measurements of a Cu prototype of the beam screen adopted for the Large Hadron Collider (LHC) bombarded with different doses of beams at the energy of 200 eV, 50 eV and 10 eV. This last energy was added o the experiment already performed in 2008 and confirmed the very important effect of the energy of the impinging electrons on the ability to reduce the SEY with a given dose.

After such evidences we launched two parallel and necessary activities: one theoretical and one experimental, both aimed to a deeper understanding of the electron energy in the cloud. Thanks to T. Demma effort and in collaboration with the CERN group who developed the ECLOUD code [4], we estimate the scrubbing efficiency in an accelerator environment, studying the the simulated energy components of the electron dose delivered to the chamber walls during the passage of a bunch train for different values of δ_{max}, bunch charge, and bunch spacing. An example is reported in Fig. 2, which indeed confirms that most of the electrons in the cloud are at low energy. A

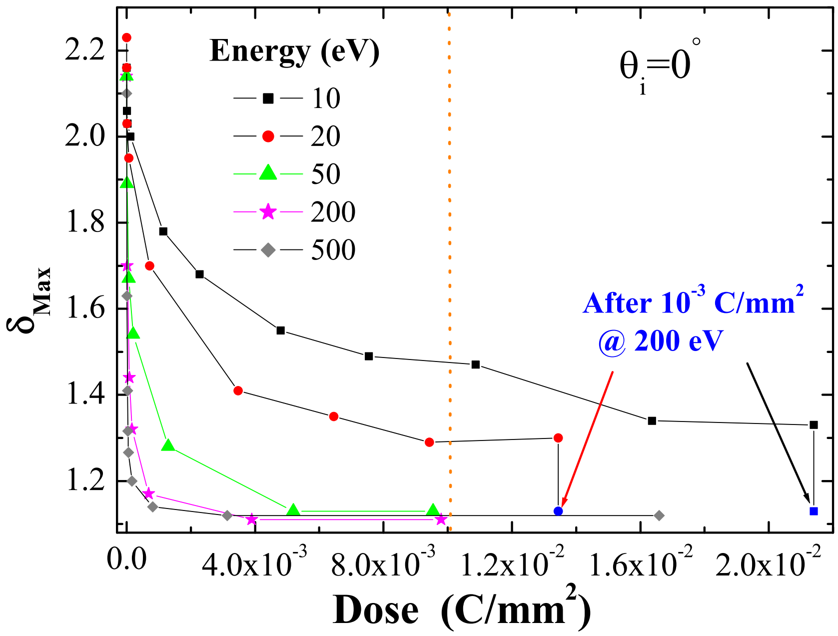

Figure 1: δ_{max} versus dose for different impinging electron energies at normal incidence.

preliminary study seems to indicate that one can individuate machine parameters which optimize the presence of high energy electrons in the cloud, hence increasing their scrubbing efficiency and reducing LHC scrubbing commissioning time.

This year and in collaboration with the Anka Undulator group we tested their standard retarding field analyser. We confirm that such 3 grids analysers (without etherodine acquisition technique as proposed in our detectors from last years), are not actually able to give a reliable measurement of the actual electron energy distribution, being hidden by the presence of secondaries mainly created within the detector itself. This forced us to continue the tests, in our laboratory, of our "home made" retarding field analyser [3] mentioned in the previous annual report. Despite some initial difficulties in running them with the necessary confidence, and some problems related to the gain of the channel-plates in use (much lower than specified by the Burle company) we are now obtaining encouraging results and we hope to be ready to mount two of such working detectors in the 2010 in the DAΦNE storage ring in order to measure in equivalent places in the positron and electron ring EDC curves.

Also, in close collaboration with Anka, we are partecipating in the development of a cold vacuum chamber for diagnostics, to be installed in various rings (as Anka and Diamond) in order to gain a deeper understanding on the heat load mechanisms to a cold vacuum chamber due to e-cloud processes [5].
Some experiments were also performed in the Surface Science laboratory of the University of Cosenza, where LHC samples were conditioned with incidend beams of 50 eV and 20 eV and

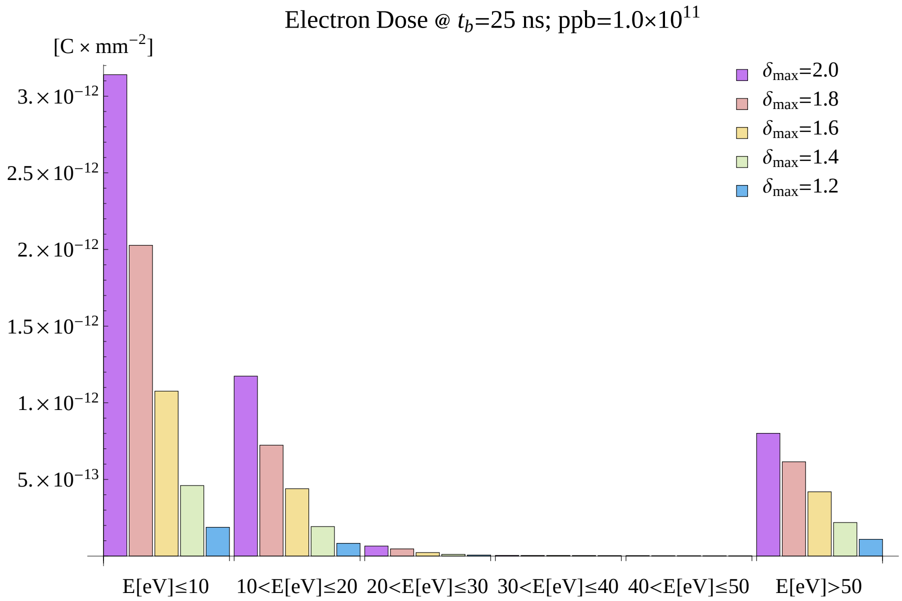

Figure 2: Simulated energy components of the electron dose delivered to the chamber walls during the passage of an LHC-like bunch train ($t_b = 25ns$, $ppb = 1 \times 10^{11}$) for different values of δ_{max}.

analyzed the contribution of Secondary and Elastic electrons to SEY. These measures confirmed results obtained in Frascati Laboratory, helping us to understand the different role played by reflected end secondary electrons in contributing to the total SEY as a function of scrubbing and obtained δ_{max}.

1 Conference Talks

1. D. Saez de Jauregui et al., *Spectrum of the Low Energy electrons Bombarding the Wall in the ANKA Storage Ring*, PAC 09, (2009).
2. T. Demma et al., *e-cloud studies at LNF*, TILC09 (2009).

References

1. R. Cimino et al., Nucl. Instr. & Meth. A **561**, 272275 (2006).
2. R. Cimino et al., Phys. Rev. Lett. **93**, 14801 (2004).
3. M. Commisso et al., *A Retarding Field Detector to Measure the Actual Energy of Electron Partecipating in e-Cloud Formation in Accelerators*, Proceedings of EPAC08, Genoa, Italy.
4. see for istance: T. Demma, R. Cimino, S. Guiducci, C. Vaccarezza, M. Zobov *Electron Cloud Simulations for DAΦNE*, Proceedings of EPAC08, Genoa, Italy. and references therein.
5. S. Casalbuoni et al., *Design of a vacuum chamber for diagnostics*, Proceedings of EPAC08, Genoa, Italy.

CATHERINE
(Carbon nAnotube Technology for
High-speed nExt-geneRation nano-InterconNEcts)

S. Bellucci (Resp. Naz.), R. Baldini (Tecn.), S. Bini (Art. 2222),
L. Coderoni (Laur.), G. De Bellis (Art. 2222), G. Giannini (Art. 2222),
M. Leone (Art. 2222), F. Micciulla (Art. 2222), P. Onorato (Art. 2222),
A. Petrucci (Art. 2222), I. Sacco (Bors.)

1 External collaborating Institutions:

Univ. Roma La Sapienza and Consorzio Sapienza Innovazione, Technische Universiteit Delft and Philips Electronics Nederland B.V. The Netherlands, Université Paul Sabatier Toulouse France, Univ. Salerno, IMT Bucharest Romania, Latvijas Universitates Cietvielu Fizikas Instituts, Swedish Defence Research Agency and Smoltek AB Sweden).

We participate as a partner (the INFN unit) to the EU FP7 Project CATHERINE, Carbon nAnotube Technology for High-speed nExt-geneRation nano-InterconNEcts, Grant Agreement number: 216215, Funding Scheme: Collaborative Project - Small or medium-scale focused research project (STREP). CATHERINE has a duration of 36 months and started its activities on 1st January 2008. The consortium binds together five Universities, three Research Organizations, one Large Industry, one SMEs and one Service Company. The partners are located in 6 EU Member States (Italy, The Netherlands, Sweden, France, Romania, Latvia).

2 Project objectives:

The final objectives of CATHERINE are: 1. Development of cost-effective and reliable technological process for the realization of high-performance next-generation interconnects; 2. Development of a multi-scale simulation tool for the prediction of the multifunctional performance of the interconnect and for the EMC analysis; 3. Development of electromagnetic and multifunctional test procedures and experimental characterization methods; 4. Manufacturing and testing of proof-of-concept samples of nano-interconnects at laboratory level.

3 Relevant results achieved:

Models of carbon nanotube (CNT) growth on nano-structured Ni catalyst and inside the nanopore of Al_2O_3 membrane were considered. Predictions were elaborated from ab initio calculations, in collaboration with Latvijas Universitates Cietvielu Fizikas Instituts.

Due to the unique properties, carbon nanotubes (CNTs) become an important constituent of future generation nanoelectronics. The progress in this field is still hindered by the inability to reproduce a growth of carbon CNTs with predetermined chirality indices (and thus the electronic properties) since contemporary methods of nanotube synthesis yield a mixture of metallic and semiconducting nanotubes with varying band gaps. The chemical vapor deposition (CVD) growth of CNTs above the particles of metallic catalyst positioned inside the alumina membrane (upon the bottoms of its semi-closed nanopores) is believed to be the most promising approach for gaining a control over the geometry and the electronic properties of nanotubes [1]. Moreover, the CVD growth of nanotubes can be achieved at low temperature, another important requirement for application of CNTs in nanoelectronics. The structure of interconnect between the nanoparticle of metallic catalyst and the CNT is important for understanding both the electronic transport through nanotube and the mechanism of its growth. Decomposition of gas-phase carbon-hydrogen precursors on the catalyst surface is the first step for the CVD growth of CNTs. This initial step is followed by two important processes: (i) the diffusion of carbon on the particle surface or across its interior (a rate-determining step) and (ii) the nucleation of the graphitic fragment [2]. as followed by further incorporation of carbon into the growing nanotube which determines a CNT chirality [3]. Depending on the size and the structure of such a metallic particle, either well-separated SW nanotubes and their bundles (containing up to several hundreds of the closely-packed nanotubes of different chiralities) or MW NTs, which shells also present various chiralities, could be synthesized. The microscopic images of CNTs growing from the catalytic nanoparticles [4] help to clarify how the atomistic models of interconnects can be drawn.

So far just a few theoretical (mainly, first principles) simulations were performed, only of a single SW CNT growth upon metal nanocluster (Me = Ag, Au, Co, Cu, Fe, Ni, Pd, Pt) where the most likely armchair- (m,m) and zigzag-type (n,0) chiralities were considered [5-8]. Another form of 1D-periodic nanostructure named by carbon nanoscroll (CNS) can be formed from a graphene sheet by its twisting, thus leading to a spiral configuration. CNSs were synthesized after sonication, to assist exfoliation and spiral wrapping of the graphite sheets [9]. Visually, CNSs are similar to MW CNTs showing similar interlayer distance of 3.4-3.6 . It is impossible to distinguish between the two structures based on the electron micrographs alone [10]. Unlike MW CNT, nanoscroll keeps the same chirality along the whole wrapped surface. However, the HRTEM study indicates the coexistence of NS and MW segments within the same C-tubular structure [11].

In our study, we have compared the results of ab initio simulations performed on 2D periodic models of C/Ni(111) and C/θ-Al_2O_3(010) nanostructures, which can describe peculiarities of the initial stage of growth for the SW CNT bundle upon the catalyst particle. We have used models of both nanostructured Ni(111) and θ-Al_2O_3 (010) surfaces, respectively, in order to perform simulations of adsorption processes. The nanostructured nickel surface has been modeled using the two-periodic slab model. The 5&$\times$5 supercell (SC) has been chosen to simulate the nanoparticle atop the Ni(111) substrate, while the single unit cell has been adopted to model the surface of monoclinic θ-Al_2O_3 (010). Our calculations have been performed using the gradient corrected (GGA) exchange-correlation functional of Perdew, Burke and Ernzerhof (PBE) [12] with spin-polarization as implemented into the CRYSTAL computer code [13].

Previously, we successfully applied a similar computational formalism for simulation of: (i) oxygen interaction with the Al(111), Al(001) and stepped Al(111) substrates [14], (ii) silver adhesion upon the α-Al_2O_3 (0001) surface [15] as well as (iii) SW nanotubes of AlN [16] and BN [17]. In the current study, the Ni all-electron basis set (BS) has been employed [18], with the innermost [4s3p1d] exponents being unchanged. In addition, Ni 2sp functions with exponents 0.63 and 0.13 a.u.-2 and d-function with the exponent 0.38 a.u.-2 have been used as optimized in bulk calculations, thus, Ni BS caould be described as [6s5p2d]. For both Al and O atoms, we have used the all-electron [4s3p1d] basis sets [13]. In order to provide a balanced summation in direct and reciprocal lattices, the reciprocal space integration has been performed by sampling the Brillouin zone with the 22 Pack-Monkhorst mesh [19], which for 55 supercell of Ni(111) substrate results in 2 k-points in total. (33 mesh with 5 k-points for θ-Al_2O_3 (010) have been used for the unit cell.) Calculations are considered as converged only when the total energy differs by less than 10-7 a.u. in two successive cycles of the self-consistency procedure. A smearing temperature of 0.001 a.u. has been applied to the Fermi function. This value for the temperature was chosen relatively low to ensure that the magnetic moment is not artificially modified by a too high value. The network of adsorbed carbon atoms, which transforms to the nanotube structures, arise after the dissociation of hydrocarbon molecules e.g., CH4, flowing towards the substrate when using the CVD method. We estimate the dissociation energies for CH4 molecules (Ediss) atop both substrates according to the total energy balance o the two-step dissociation mechanism: $(CH_4)_{ads} \rightarrow (CH)_{ads} + 3H_{ads}$, $(CH)_{ads} \rightarrow C_{ads} + H_{ads}$ (1b) The calculated energies of a complete dissociation (E_{diss}) have been found to be 2.33, 2.17, and 6.40 eV for perfect Ni(111), nanostructured Ni(111), and θ-Al_2O_3 (010) substrates, respectively.

The binding energies of the newly-formed C_{ads} atoms atop a perfect and nanostructured Ni(111) as well as θ-Al_2O_3 (010) surfaces have been calculated using the following equation: $E_{bind} = -(E_{complex} - E_{slab} - E_{ads})/N_C$. Here $E_{complex}$ is the calculated total energy of the slab with the attached adsorbate, E_{slab} is the total energy of the bare slab, E_{ads} is the energy of a single carbon atom in its ground state, and N_C is a number of carbon atoms. The corresponding results show that the most stable adsorption position with $E_{bind} \approx 8$ eV are (100) sites at nanostructured Ni(111), while θ-Al_2O_3 (010) gives adsorption sites with E_{bind} of maximum 2 eV. We have analyzed the electron charge distribution for both C/Ni(111) and C/θ-Al_2O_3 nanostructures sectioned by planes both parallel and perpendicular to the nanostructured substrates. In our study, we observe the transfer of electronic charge towards the carbon atoms from both nickel catalyst and nanopore of alumina membrane (about 1.0 and 0.5 e per adatom upon both Ni(111) and θ-Al_2O_3 substrates, respectively). As the result of our simulations, we predict an increase of catalytic activity of nanostructured Ni(111) surface due to nanofacet formation that potentially can play a role in a predictable growth of the CNT. The most unclear stage of carbon nanotube growth from catalyst is an initial swelling of an island formed from C_{ads} atoms atop the substrate up to creation of semi-fullerene. We clearly showed the energetic preference of CNT growth upon the nanostructured surface of nickel catalyst as compared with a smooth surface. In the former case nanotubes are connected with substrate much stronger which provides a higher stability of interconnects for nanocircuits.

Our results predict quite effective and reproducible growth of carbon nanotubes upon the nickel nanostructured substrate. In the absence of catalyst nanoparticles upon the bottom of the nanopores inside alumina membrane the carbon structures could grow from the walls towards the centers of nanopores: either carbon nanoscrolls or rather thick amorphous (soot-like) microtubes. At the bottom level of the multiscale modeling, ab initio methods can be used for determining the electronic structure of the assumed carbon-metal nanocomposites. Moreover, the obtained results can be employed in the construction of single-particle Hamiltonian used in the analytical tight-binding calculations of the conducting channels in the Me/MW-CNT interconnects, as well as in further MD and KMC simulations.

Also, calculations on resistance and conductance for junctions of SW and MW carbon nanotubes have been carried out for various metal substrates, within the framework of our collaboration with Latvijas Universitates Cietvielu Fizikas Instituts. In our study, simulations of conductivity and resistivity are performed using the multiple scattering theory and effective media cluster approach. The main problems at the current stage of researches on CNT interconnect resistance appear due to the influence of chirality effects in interconnects of SW and MW CNT with the fitting metals (Me = Ni, Cu, Ag, Pd, Pt, Au) for predefined CNT geometry. The main task of this study is the implementation of advanced *ab initio* simulation models for the construction of nanocircuits containing CNTs and their junctions with metallic contacts. Both the local and integral CNT properties have been simulated using prototype NT models such as a dispersion law, the electronic density of states (EDOS), the conductivity, resistivity, effective masses, etc. The scattering theory approach allows us to calculate both the electronic structure and elastic properties of condensed matter considered as the static phenomena simultaneously with the dynamical phenomena of the electron transport. A computational procedure developed for these calculations [21] is based on construction of the cluster potentials and evaluation of the S- and T-matrices for scattering and transfer, respectively. Certain approximations are necessary to obtain reliable results. For instance, the CPA (coherent-potential approach [22]) is considered as an effective-medium-approximation (EMA). The specific conductivity could be evaluated through the Kubo-Greenwood formalism [21,22] or, in simple cases, using the Drude-type formula. The specific resistivity could be described through participations of charge carriers in transport according to various mechanisms based on the scattering centers, namely, atoms of clusters, phonons, charge defects, structural defects, etc., including the pure elastic way, called as ballistic. The temperature and frequency properties can be also described and estimated using the formalism of scattering theory. The first step of CPA-EMA modeling is the construction of potentials, both atomic and crystalline which uses the special well-tested analytical procedures based the Gaspar-like potentials and X_α and X_{α_β} presentations for the electronic exchange and correlation in the form of electronic density expansions [21]. Then, to obtain the electronic structure, the calculations on scattering properties are necessary, generally, in the form of S- and T-matrices. The electronic structure calculations begin with the definition of the initial atomic structure to produce a medium for solution of the scattering problem for a trial electronic wave [21]. As the zero approach in the modeling procedure, one postulates the atomic structure on the level of short- and medium-range orders. Further calculations on the density of the corresponding electronic states (DOS) can be done using the variation principles. There exist a few algorithms both to estimate the conductivity in static and frequency regimes as well as to take into account the temperature effects. However, in the case of CNT we must consider not only the diffusive mechanism of conductivity, but also the so-called ballistic one. This is an evident complication for the interpretation of electrical properties of CNT and their systems.

The CPA-EMA model of the CNT-Ni nanointerconnect [23] has been developed in our earlier paper. Within the formalism of electronic transport it consists of two regions supporting two different electron transport mechanisms: ballistic (elastic) and collisional (non-elastic). In the mechanism of the ballistic conductivity, as a result of the multiple scattering (valid for CNT and metal substrate), We assume that the conducting nanotubes are not so long and the electrons are not scattered too much by any defect (imperfection) of this nanomaterial. The effect of the charge accumulation is neglected here as well. This situation is similar to an ideal billiard with moving elastic balls-electrons. According to the Landauer model [24], the conductance coefficients are given in terms of the transmission coefficients, while the current flows between two reservoirs with a difference between the chemical potentials (the transmission coefficient is found to be between 1 to 2 in the one-channel case), based on the concept of quantum conductance.

In considering the non-elastic electron transport mechanism, we consider, Using simulation models presented earlier [21,23], a resistance model for the metal interconnect with single- and multi-wall (SW and MW) CNTs based on the evaluation of the interface potential barriers and the implementation of Landauers formula. All resistance calculations have been performed taking into account that not all the electrons participate in a conduction process with the Fermi velocity. For this aim, we must take into account only thermally activated electrons. The reason for the determination of thermally activated electrons is caused by the scattering mechanism, which is changing in the space of CNT-Metal interconnect.

SW CNT simulations were considered first, also as a propedeutical calculation to the MW case. The effective bonds model means that the conductivity of CNT-metal interconnect is proportional to the number of direct chemical bonds between CNT and metal, which depends on the CNT chirality and metal substrate atomic configuration. Thus, we can evaluate the Landauers multiplier for conductance calculations We have also proposed a parameter ϕ (chirality angle) for the identification of the nanotube chirality. We showed the effects of nanotube diameter and chirality on CNT-Ni interconnect resistivity. It is clear that the larger is the CNT diameter, the larger the number of direct junction bonds and the total conductance (i.e., the resistance is smaller). A similar effect is observed for varying chirality: the number of direct bonds is higher for armchair and zigzag CNT chiralities. We also compared the resistance for the interconnects of the same SW CNT with various metal substrates (Ag, Au, Cu, Ni, Pd and Pt). Although nickel is a good catalyst for CNT growth, resistance of its interconnect with nanotube has been found to be noticeably higher as compared to that for silver, gold and platinum substrates.

MW NT simulations were also carried out using the simulation models presented earlier [21,23]. We have developed a model of multi-wall CNT-Me junction resistance based on the interface potential barriers evaluation and Landauers formalism described above. For these simulations, we have used a MW CNT model with a unit cell having 6.39 nm height and 19.89 nm external diameter. Using Landauers formula for the conductivity, we estimated the effective resistance of MW CNT-Me junctions, taking into account only thermally activated electrons, and established a comparison for the resistance of junctions between the considered MW CNT and the various metal substrates already considered in the SW CNT case above. We concluded that for the interconnects of metals with both SW and MW CNTs, the smallest resistance is once again observed for Ag, Au and Pt. Obviously, the resistance of the metal interconnect with MW CNT is several times smaller than that with SW CNT, since the number of direct junction bonds is substantially larger in the former case.

The evaluation of current losses between the adjacent shells in MW CNT was also carried out by us. In particular, using the model of the interwall potential in MW CNT we evaluated the coefficient of transparency which determines the possible radial current losses. For example, if the largest shell in the MW CNT possesses the zigzag chirality, whereas the chirality of the smallest one is armchair, while the distance between them is a = 13.54-12.88 = 0.66 nm, the radial current loss factor can be estimated as T = 3.469 10^{-6} per one C-C bond. In conclusion, using the model of effective bonds developed in our study, within the framework of the CPA-EMA formalism based on scattering theory and Landauers approach, we have been able to predict the resistivity properties for both SW and MW CNT-Me interconnects. The resistance of the latter for the same external nanotube diameter and metal substrate turns out to be substantially smaller, i.e., the effectiveness of the multiwall nanotubes for the CNT interconnects is noticeably higher. We have also developed the model of interwall interaction in MW CNT as well as estimated the transparency coefficient as indicator of possible radial current losses.

In our experimental activity we made progress in the thermal CVD deposition of carbon nanotubes on anodized alumina supported on silicon wafer. At LNF-INFN at Frascati we carried out carbon nanotube growth by the method of methane catalytic chemical vapor deposition (CVD) by performing several syntheses with different experimental conditions, including growth temperature, time, gas-flowing, and by analyzing using scanning electron microscopy the as-grown (i.e. without any purification treatment) samples produced. The main results obtained using a porous alumina template not completely anodized, i.e. with a residual aluminum layer, provided by the Université Paul Sabatier Toulouse France partner, in collaboration with IMT Bucharest Romania, are reported below.

The growth process involves heating a catalyst material to high temperatures in a tube furnace and flowing a hydrocarbon gas through the tube reactor for a period of time. Materials grown over the catalyst are collected upon cooling the system to room temperature. Key parameters in nanotube CVD growth are thus the hydrocarbons, catalysts and growth temperature. In our work methane has been used as a carbon source. The methane CVD approach is promising for enabling scale-up of defect-free nanotube materials to the kilogram or even ton level. By using methane as carbon feedstock, reaction temperatures in the range 800-850 Celsius degrees, suitable catalyst materials and flow conditions, one can grow high quality carbon nanotube materials by a simple CVD process. Among all hydrocarbon molecules, methane is the most stable at high temperatures against self-decomposition. Therefore catalytic decomposition of methane by the transition metal catalyst particles can be the dominant process in carbon nanotube growth. The choice of carbon feedstock is thus one of the key elements to the growth of high quality carbon nanotubes containing no defects and amorphous carbon over-coating.

The active catalytic species are typically transition-metal nanoparticles formed on a support material. The general nanotube growth mechanism in a CVD process reaction involves the absorption and decomposition of methane molecules on the surface of transition metal catalytic nanoparticles on the support surface; subsequently, carbon atoms dissolve and diffuse into the nanoparticle interior to form a metal-carbon solid state solution. Nanotube growth occurs when supersaturation leads to carbon precipitation into a crystalline tubular form. The size of the metal catalyst nanoparticle generally dictates the diameter of the synthesized nanotube.

In our work nickel-based material is used as a catalyst. Nanoparticles are formed during the first step of heating process in which H_2 flow supports reduction of unwanted species and formation of metal nanocluster. We have used gas (CH_4, H_2 and Ar used as inert carrier/cleaner) at low pressure (1bar) and varied temperature of various step in the range 800-850 Celsius degrees. The CVD apparatus used is basically composed of a quartz glass tube in a controlled oven, into which we introduce several samples and gas mixtures .

Every sample was produced by CVD method at Laboratori Nazionali di Frascati using the Alumina membranes realized at CIRIMAT U.P.S. All the syntheses were performed in the same furnace with the same conditions of gas flow. The difference is in the temperatures of deposition. In the case of samples SBW55-59 the temperature raised at about 7 Celsius /min, Hydrogen flow was 100sccm, the maximum temperature reached was 800 Celsius. At 800 Celsius degrees the gas flow was switched to Methane for about 45 min. In the case of SBW56-58 the temperature raised at about 7 Celsius degrees /min, Hydrogen flow was 100sccm, the maximum temperature reached was 850 Celsius degrees. At 850 Celsius degrees the gas flow was switched to Methane for about 45 min.

The S.E.M. analysis was carried out at IMT Bucarest: on sample SBW55; on sample SBW56; on sample SBW58; on sample SBW59. Thus, we observed that the thin film of niobium deposited by sputtering technique was useful in order to increase adhesion between the silicon wafer and the aluminium layer. Nickel electrodeposited nanoparticles were deposited, by our Toulouse collaborators, at the bottom of alumina pores produced by aluminium anodization. Obseving with the SEM the surface of the SBW55 sample at low magnification, it is possible to see that there are different zones (from the different grey tones). The difference of density of carbon nanotubes is evident. It drives the different grey tones. Where the carbon nanotube density is high the grey is dark, whereas where it is low the grey is white. At high magnification of the white grey zone it is easy to see the surface of the alumina membrane and, at the top, the presence of long and straight carbon nanotubes.

The length of carbon nanotubes we deposited is about 100 micron and the diameter around 40/50 nm, i.e. similar to the size of the template nanopores. In the dark zone it is not possible to see the surface of the membrane because the density of carbon nanotubes is very high. So it is not possible to know whether there are carbon nanotubes that are going out from the membrane pores. When the sample is tilted it is a possible to observe more easily the distribution of carbon nanotubes on the surface. Different zones of carbon nanotubes density are more evident.

At low magnification, the morphology of sample SBW56 seems to be close to that of the sample SBW55, but when the magnification increases it is possible to see differences with respect to the previous sample. The most important one is that there are not a lot of carbon nanotubes on the surface of the membrane but the presence of carbon nanotubes inside its pores is clear. The carbon nanotubes come out directly from the pores. The SEM images suggest the lack of carbon nanotubes bundles, and the show the presence of only isolated carbon nanotubes. The surface of membranes seems to be very clean, without any type of carbonaceous amorphous.

The analysis of sample on sample SBW58 shows how the sample is close to sample SBW56. There are no bundles of carbon nanotubes on the surface of the membrane, but the latter is clean and it is possible to see the pores. Carbon nanotubes are sticking out from the membrane. Once again, as in sample SBW56, carbon nanotubes are short, twisted and extremely rare.

In conclusion, the samples obtained using partially anodized alumina membranes in our CVD reactor yield results which are encouraging. The samples obtained can be divided into two classes, i.e. SBW55-59 on the one hand, and SBW56-58 on the other. The former, obtained at a lower temperature (800 Celsius), shows a higher density of nanotubes, indicating the effective action of the Ni catalyst. In contrast, the SBW56-58 class of samples whose growth required a temperature 50 degrees higher, display a very rare distribution of carbon nanotubes, indicating a much less effective action of the catalyst, which was probably hindered by the presence and activity of the melted aluminium originating from the residual layer left by the partial anodization of the membrane. However, it is precisely in the latter samples which is possible to see in a very clean way a feature probably common to all samples produced, namely the fact that each nanotube grows out of a pore in the membrane and there are no nantubes grown outside of it.

We are now attacking the new membranes just received from our partner at CIRIMAT, which are wholly anodized, and the interpretation of the future results will be unaffected by the presence of aluminium which made the present analysis more complex.

Within the conference Nanoscience and Nanotechnology - N&N2009, held in Frascati [25], we organised on 21st October 2009 a special session on the electonic prporties of nanotubes and carbon based nanostructures , open to all N&N2009 participants and devoted also to review some of the CATHERINE progresses. During the session, which was attended by 40 persons, the following presentations were given: 1) S. A. Maksimenko, Lab. of Electrodynamics of Nonhomogeneous Mediums Institute for Nuclear Problems, University, Minsk, Belarus "Theory of carbon nanotube-based electromagnetic devices: waveguide, antenna, traveling wave tube, etc."; 2) K. Ishibashi Advanced Device Laboratory, RIKEN, Japan "Quantum dots with carbon nanotubes"; 3) V. Kashcheyevs University of Latvia, Riga, Latvia "Decay cascade theory for dynamical quantum dot initialization and quantized charge transport"; 4) S. Piskunov University of Latvia, Riga, Latvia "Theoretical predictions for initial stage of CNT growth on nano-structured Ni catalyst and inside the nanopore of alumina membrane".

4 Conference

1. F. Micciulla, *Activity on carbon nanotube based interconnections at INFN-LNF, Warsaw Univ. Poland, 2009.*

5 References

1. F. Micciulla, *Activity on carbon nanotube based interconnections at INFN-LNF*, Warsaw Univ. Poland, 2 December 2009.

   [1] S. Bellucci, Nucl. Instr. & Meth. Phys. Res. B **234** 57 (2005).

2 A. Loiseau, J. Gavillet, F. Ducastelle, J. Thibault, O. Stephan, P. Bernier, C.R. Physique **4** 975 (2003).

3 H. Zhu, et al., Small **1**, 1180 (2005).

4 S. Hofmann et al., Nano Lett.**7** 602 (2007).

5 F. Ding et al., Nano Lett. **8** 463 (2008).

6 O.V. Yazyev, A. Pasquarello, Phys. Rev. Lett. **100**, 156102 (2008).

7 H. Amara, J.-M. Roussel, C. Bichara, J.-P. Gaspard, and F. Ducastelle, Phys. Rev. B **79,** 014109 (2009).

8 A. Bôrjesson, W. Zhu, H. Amara, C. Bichara, and K. Bolton, Nano Lett. **9**, 1117 (2009).

9 L.M. Viculis, J.J. Mack, and R.B. Kaner, Science **299**, 1361 (2003).

10 O. Zhou, R.M. Fleming, and D.W. Murphy, C.H. Chen, R.C. Haddon, A.P. Ramirez, S.H. Glarum, Science **263**, 1744 (1994).

11 S. Berber, D. Tomnek, Phys. Rev. B **69**, 233404 (2004).

12 J.P. Perdew, K. Burke, and M. Ernzerhof, Phys. Rev. Lett. **77**, 3865 (1996).

13 R. Dovesi et al., CRYSTAL06 Users Manual, University of Torino, Torino (2006), `http://www.crystal.unito.it/`

14 Yu.F. Zhukovskii, P.W.M. Jacobs, and M. Causá, J. Phys. Chem. Solids **64**, 1317 (2003).

15 Yu.F. Zhukovskii, E.A. Kotomin, B. Herschend, and K. Hermansson, P.W.M. Jacobs, Surf. Sci. **513**, 343 (2002).

16 Yu.F. Zhukovskii, N. Pugno, A.I. Popov, C. Balasubramanian, and S. Bellucci, J. Phys.: Cond. Matt. **19**, 395021 (2007).

17 Yu.F. Zhukovskii et al., J. Phys. Chem. Solids **70**, 796 (2009).

18 M.D. Towler et al., Phys. Rev. B **50**, 5041 (1994).

19 H.J. Monkhorst, J.D. Pack, Phys. Rev. B **13**, 5188 (1976).

20 G. Kalibaeva et al., J. Phys. Chem. B **110**, 3638 (2006).

21 Yu.N. Shunin, K.K. Schwartz, *Computer Modelling of Electronic and Atomic Processes in Solids (Eds. R.C. Tennyson, A.E. Kiv*, Kluwer Academic Publisher, Dodrecht, Boston, London, 1997) p. 241-257.

22 E.L. Economou, *Green's Functions in Quantum Physics (3rd Ed.)*, Solid State Ser. **7**, Springer Verlag, Berlin, Heidelberg, 2006.

23 Yu.N. Shunin, Yu.F. Zhukovskii, S. Bellucci, Computer Modelling and New Technologies **12**, 66 (2008).

24 D. Stone, A. Szafer, IBM Jour. of Res. and Development **32**, 384 (1988).

25 S. Bellucci (Guest Editorial), *Selected Papers from the INFN-LNF Conference on Nanoscience and Nanotechnology*, J. Nanophoton. **3**, 031999 (2009).

INNOVATIVE METHODOLOGIES FOR RISK ASSESSMENT IN THE OCCUPATIONAL EXPOSURE TO NANOMATERIALS

S. Bellucci (Resp. Naz.), R. Baldini (Tecn.), M. Chiaretti (Ass.),
L. Coderoni (Laur.), G. De Bellis (Art. 2222), G. Giannini (Art. 2222),
F. Micciulla (Art. 2222), P. Onorato (Art. 2222), I. Sacco (Bors.)

1 External collaborating Institutions

Universitá Roma La Sapienza, Policlinico Umberto I University Hospital Roma; ISPESL Monte Porzio Catone, Italy; Univ. Roma Tor Vergata, Italy; Univ. Parma, Italy; Fondazione Salvatore Maugeri Pavia, Italy; Agenzia Regionale Prevenzione e Ambiente Regione Puglia, Italy; CNR-Institute for Electromagnetic Sensing of Environment, Naples, Italy

We participate as a partner (the INFN unit) since 1 January 2008 to the project financed by the Italian Ministry of Health, "Innovative Methodologies for risk assessment in the occupational exposure to nanomaterials", coordinated by the Italian Institute for Occupational Health and Prevention (ISPESL). The project will run until 2011.

The mutagenic effect of multi-walled carbon nanotubes (MWCNTs) characterised by small surface/volume ratio, high diameter and less than 0.1 percentage of metal contaminants was evaluated by the bacterial reverse mutation assay (Ames test) on Salmonella typhimurium TA 98 and TA 100 strains, and on Escherichia coli WP2uvrA strain, in presence and in absence of the metabolic activation system S9. A preliminary cytotoxicity assay was carried out to ensure that cytotoxicity did not interfere with response. MWCNTs resulted devoid of mutagenic effect in the bacterial cellular systems tested in that they did not significantly increase the number of revertant colonies.

The mutagenic activity did not even appear in presence of the metabolic activator, sowe can exclude that MWCNTs metabolites, produced via cytochrome-based P450 metabolic oxidation system, may act as mutagens. Carbon nanomaterials seem to exhibit different biological activities and different toxicities in relation to their physico-chemical characteristics, size, shape, crystallinity and presence of metal traces, so it is difficult to establish their health risk. Due to the limited background of genotoxicity studies and the increased occupational and public exposure to nanomaterials, present results appear useful to extend the knowledge on the safety of carbon nanotubes in view of their possible applications.

Also, in a separate work, we evaluated the effect of buckypaper (BP) on cancer and primary cell lines in vitro and in vivo on laboratory rats. BP is an innovative material with interesting physical/chemical properties that has possible pharmacological and prosthetic employment. Given that precautions need to taken where carbon nanotubes are injected into human body for drug delivery or as contrast agent carrying entities for MRI or as the material of a new prosthesis generation, we assessed the toxicity of BP carbon nanotubes. BP has structural resemblance to asbestos whose toxicity has been linked to cancer. BP decreased proliferation of human colorectal, breast and leukemic cancer cell line in vitro. However, BP had no effect on the proliferation and viability of normal human arterial smooth muscle cells and human dermal fibroblasts, in vitro. In vivo, BP induced a moderate inflammatory reaction but had no mutagenic effects. The animals after the BP implantation showed an inflammatory reaction followed in the next two weeks by the cicatrisation reaction with the organization and the fibrosis of the scar. These results show a low toxicity of BP both in vitro and in vivo.

2 List of Conference Talks

1. S. Bellucci, *Nanotechnology for Biological and Medical Applications*, Postgraduate Course on Occupational Health and Safety in the Workplace, International Training Centre of the International Labour Organization (ILO), Torino (Italy), 18 March 2009.

2. S. Bellucci, *Toxicological and biological in vitro and in vivo effects of carbon nanotubes buckypaper*, Invited talk given at International Semiconductor Conference CAS 2009: 11-14 October 2009, Sinaia, Romania.

3. S. Bellucci, *Carbon nanotubes buckypaper toxicity*, Talk given at Nanoscience and Nanotechnology nn2009, LNF, Italy, 19-22 October 2009.

References

1. S. Bellucci, M. Chiaretti, A. Cucina, G.A. Carru, and A.I. Chiaretti, Nanomedicine, **4**, 531 (2009).

2. A. Di Sotto, M. Chiaretti, A. Carru, S. Bellucci, and G. Mazzanti, Toxicology Letters **184** 192 (2009).

3. S. Bellucci, *Nanoparticles and Nanodevices in Biological Applications. The INFN Lectures*, Vol. I Berlin Heidelberg: Springer Verlag, **14** 1, (2009).

6 – Accelerator Physics

DAΦNE

The DAΦNE Team

D. Alesini, M.E. Biagini, C. Biscari, R. Boni, M. Boscolo, F. Bossi, B. Buonomo, A. Clozza, G. Delle Monache, T. Demma (Art. 23), E. Di Pasquale, G. Di Pirro, A. Drago, A. Gallo, A Ghigo, S. Guiducci, C. Ligi, F. Marcellini, C. Marchetti, G. Mazzitelli, C. Milardi, F. Murtas, L. Pellegrino, M. Preger, L. Quintieri (Art. 23), P. Raimondi (Resp.), R. Ricci, U. Rotundo, C. Sanelli, M. Serio, F. Sgamma, B. Spataro, A. Stecchi, A. Stella, S. Tomassini, C. Vaccarezza, P. Valente, M. Zobov

The DAΦNE Technical Staff

G. Baldini, P. Baldini, A. Battisti, A. Beatrici, M. Belli, B. Bolli, L. Cacciotti, G. Ceccarelli, R. Ceccarelli, A. Cecchinelli, S. Ceravolo, R. Clementi, O. Coiro, P. Ciuffetti, S. De Biase, I. De Cesaris, M. De Giorgi, R. Di Raddo, M. Di Virgilio, A. Donkerlo, G. Ermini, M.R. Ferrazza, G. Fontana, U. Frasacco, C. Fusco, F. Galletti, E. Gaspari, M. Giabbai, O. Giacinti, E. Grossi, F. Iungo, V. Lollo, M. Marchetti, C. Marini, M. Martinelli, A. Mazzenga, C. Mencarelli, M. Monteduro, M. Paris, E. Passarelli, V. Pavan, S. Pella, D. Pellegrini, G. Piermarini, S. Quaglia, F. Ronci, M. Rondinelli, F. Rubeo, M. Sardone, M. Scampati, G. Sensolini, R. Sorchetti, A. Sorgi, M. Sperati, A. Sprecacenere, P. Tiseo, R. Tonus, T. Tranquilli, M. Troiani, V. Valtriani, R. Zarlenga, A. Zolla

DAΦNE is an electron-positron Φ-*meson factory* operating at Frascati since 1997. Factories are storage ring colliders designed to work at the energies of the meson resonances, where the production cross section peaks, to deliver a high rate of events to high resolution experiments.

The factory luminosity (the number of events per unit time produced by the reaction under investigation divided by its cross section weighted by the acceptance of the detector) is very high, about two orders of magnitude larger than that obtained at the same energy in colliders of the previous generation. One of the key-points to get a substantial luminosity increase is the use of separated vacuum chambers for the two beams merging only in the interaction regions (IRs). When sharing the same ring the two N-bunch trains cross in 2N points and the maximum luminosity is limited by the electromagnetic beam-beam interaction. The unwanted effects of this interaction can be reduced with a very strong focussing (called "low-β") at the interaction point (IP), obtained by means of quadrupole doublets or triplets. However these magnetic structures take up much space and excite chromatic aberrations which must be corrected elsewhere in the ring.

This limitation does not hold for the double ring option, consisting in two separate rings crossing at two low-β points. The number of bunches that can be stored in such a collider is limited only by the geometry of the IR's.

DAΦNE is an accelerator complex consisting of a double-ring collider, a linear accelerator (LINAC), an intermediate damping ring to make injection easier and faster and 180 m of transfer lines connecting these machines. The beam accelerated by the Linac can also be switched into a laboratory called "Beam Test Facility (BTF)", for dedicated experiments and calibration of detectors. Three synchrotron radiation lines, two from bending dipoles and the other from the wiggler are routinely operated by the DAΦNE-LIGHT group in a parasitic mode, providing photons from the infrared to soft x-rays.

1 Injection System

In a low energy electron-positron collider, such as DAΦNE, the lifetime of the stored current is mainly limited by the Touschek effect, namely the particle loss due to the scattering of the particles inside the bunches. In the present typical operating conditions the Touschek lifetime is below 1000 s. It is therefore necessary to have a powerful injection system, capable of refilling the beam without dumping the already stored one. In addition, flexibility of operation requires that any bunch pattern can be stored among the 120 available buckets. The injection system of DAΦNE is therefore designed to deliver a large rate of particles in a single bunch at the working energy of the collider.

It consists of a linear accelerator with a total accelerating voltage of 800 MV. In the positron mode, electrons are accelerated to ≈ 250 MeV before hitting a tungsten target (called positron converter) where positrons are generated by bremsstrahlung and pair production with an efficiency of $\approx$1%. The positrons exit from the target with an energy of few MeV and are then accelerated by the second section of the LINAC to their final energy of ≈ 0.51 GeV. The positrons are then driven along a transfer line and injected into a small storage ring, called Accumulator, at frequency of 50 Hz. Up to 15 positron pulses are stacked into a single bucket of the Accumulator, then injection stops and the bunch damps down to its equilibrium beam size and energy spread, which are much smaller than the LINAC ones. Damping takes ≈ 0.1 s and then the beam is extracted from the Accumulator and injected into the positron main ring at an overall repetition rate of 2 Hz. A powerful and flexible timing system allows the storage of any desired bunch pattern in the collider. In the electron mode, a magnetic chicane deviates the particle trajectory around the positron converter and electrons are directly accelerated to 0.51 GeV and injected into the Accumulator in the opposite direction with respect to positron operation. They are then extracted like in the positron case and injected into the electron main ring through the second transfer line.

The Accumulator ring has been introduced in the accelerator complex to increase the injection efficiency, especially for the positrons that are produced by the LINAC at 50 Hz rate in 10 ns pulses with a charge of ≈ 0.5 nC. Since the design charge of the main ring at the maximum luminosity is $\approx 1.5\ \mu$ C and the longitudinal acceptance of the main rings is only 2 ns, the number of 50 Hz pulses necessary to fill the ring is of the order of 10^4. In order to avoid saturation it is therefore necessary that at each injection pulse a fraction smaller than 10^{-4} of the already stored beam is lost, and this is not easy to achieve. The Accumulator instead works with a lower frequency RF cavity and therefore with a larger longitudinal acceptance. In this way the full charge coming from the LINAC can be stored in a single RF bucket. In a complete injection cycle, that has a duration of 500 ms, up to 15 LINAC pulse can be stored in a single Accumulator RF bucket, and after being damped to the ring equilibrium emittances and energy spread, the whole stacked charge can be stored into a single RF bucket of the main ring. In this way the nominal single bunch charge can be stored with only one pulse from the Accumulator, reducing to 120 the number of injection pulses (at 2 Hz) into each main ring. As an additional benefit, the transverse beam size and energy spread of the beam coming from the Accumulator are at least one order of magnitude smaller than those of the LINAC beam, and this strongly reduces the aperture requirements of the main ring and, as a consequence, the overall cost of the collider.

2 Main Rings

In the DAΦNE collider the two beam trajectories cross at the interaction point (IP) with an horizontal angle that has been recently increased from ≈ 25 mrad to ≈ 50 mrad. A positron bunch leaving the IP after crossing an electron one will reach the following electron bunch at a distance of half the longitudinal separation between bunches from the IP.

Due to the horizontal angle between the trajectories of the two beams, the distance in the horizontal direction between the two bunches is equal to the horizontal angle times half the longitudinal distance between the bunches in each beam. The beam-beam interaction can be harmful to the beam stability even if the distance in the horizontal direction between bunches of opposite charge is of the order of few bunch widths at points where the β function is high and this sets a lower limit on the bunch longitudinal separation and therefore on the number of bunches which can be stored in the collider. However, the so called *crab waist collision scheme* (CW) recently implemented in the machine alleviates this problem, as it will be exhaustively explained in the following of this report.

By design the minimum bunch separation at DAΦNE has been set to ≈ 80 cm, and the maximum number of bunches that can be stored in each ring is 120. This number determines the frequency of the radiofrequency cavity which restore at each turn the energy lost in synchrotron radiation, which must be 120 times the ring revolution frequency. The luminosity of the collider can therefore be up to 120 times larger than that obtainable in a single ring with the same size and optical functions. Crossing at an angle could in principle be a limitation to the maximum single bunch luminosity. In order to make the beam-beam interaction less sensitive to this parameter and similar to the case of single ring colliders where the bunches cross head-on, the shape of the bunches at the IP is made very flat (typical ranges of r.m.s. sizes are $15 \div 30$ mm in the longitudinal direction, $0.2 \div 1.5$ mm in the horizontal and $2.5 \div 10$ μm in the vertical one). The double ring scheme with many bunches has also some relevant challenges: the total current in the ring reaches extremely high values (5 A in the DAΦNE design, ≈ 1.4 A in the DAΦNE operation so far) and the high power emitted as synchrotron radiation needs to be absorbed by a complicated structure of vacuum chambers and pumping systems in order to reach the very low residual gas pressure levels necessary to avoid beam loss. In addition, the number of possible oscillation modes of the beam increases with the number of bunches, calling for sophisticated bunch-to-bunch feedback systems.

The double annular structure of the DAΦNE collider as it is now after the recent modifications to implement the crab waist scheme is shown schematically in Fig. 1. Both rings lay in the same horizontal plane and each one consists of a long external arc and a short internal one. Starting from the IP the two beams share the same vacuum chamber while traveling in a common permanent magnet defocusing quadrupole (QD) which, due to the beam off-axis trajectory increases the deflection of the two beam trajectories to ≈ 75 mrad. Shortly after the QD, at a distance of ≈ 82 cm from the IP, the common vacuum chamber splits in two separated ones connected to the vacuum chambers of the long and short arcs. Two individual permanent magnet quadrupoles (QFs) are placed just after the chamber separation. Together with the previous QD they constitute the low-β doublets focusing the beams in the IP. The long and short arcs consist of two "almost achromatic" sections (deflecting the beam by $\approx 85.4^o$ in the short arc and $\approx 94.6^o$ in the long one) similar to those frequently used in synchrotron radiation sources, with a long straight section in between. Each section includes two dipoles, three quadrupoles, two sextupoles and a wiggler. This structure is used for the first time in an electron-positron collider and it has been designed to let DAΦNE deal with high current beams.

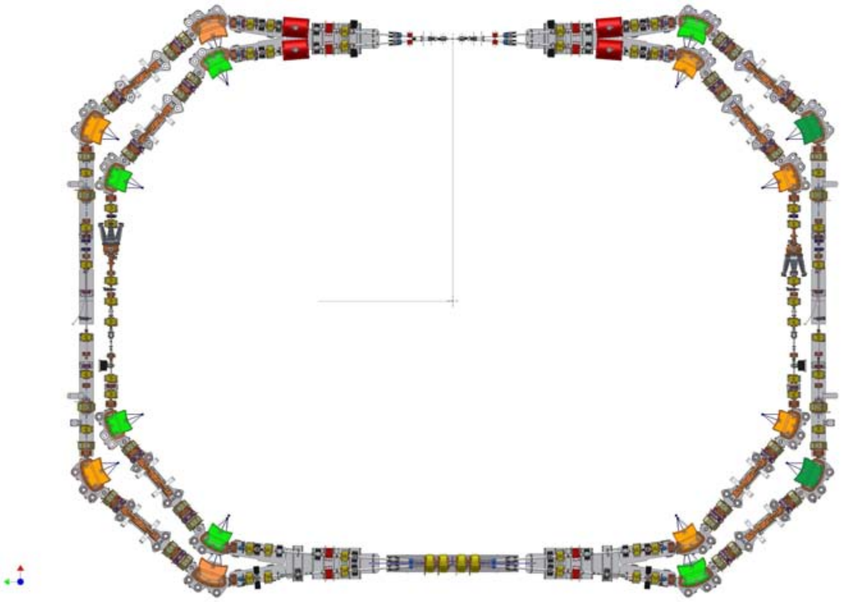

Figure 1: The DAΦNE Main Rings.

The amount of synchrotron radiation power emitted in the wigglers is the same as in the bending magnets and the wigglers can be used to change the transverse size of the beams. The increase of emitted power doubles the damping rates for betatron and synchrotron oscillations, thus making the beam dynamics more stable, while the possibility of changing the beam sizes makes the beam-beam interaction parameters more flexible.

The straight section in the long arc houses the kickers used to store into the rings the bunches coming from the injection system, while in the short straight arc there are the radiofrequency cavity and the equipment for the feedback systems which are used to damp longitudinal and transverse instabilities. The vacuum chambers of the arcs have been designed to stand the nominal level of radiation power emitted by the beams (up to 50 kW per ring). They consist of 10 m long aluminum structures built in a single piece: its cross section exhibits a central region around the beam and two external ones, called the antechambers, connected to the central one by means of a narrow slot. In this way the synchrotron radiation hits the vacuum chamber walls far from the beam and the desorbed gas particles can be easily pumped away. The chambers contain water cooled copper absorbers placed where the radiation flux is maximum: each absorber has a sputter ion pump below and a titanium sublimation pump above.

The Main Rings have undergone many readjustments during the years to optimize the collider performances while operating for different detectors.

In principle the rings could host two experiments in parallel, but only one at a time has been installed so far. Three detectors, KLOE, DEAR and FINUDA, have taken data until 2007 and logged a total integrated luminosity of ≈ 4.4 fb^{-1} with a peak luminosity of $\approx 1.6 \times 10^{32}$ cm^{-2}s^{-1} and a maximum daily integrated luminosity of ≈ 10 pb^{-1}.

KLOE has been in place on the first IP from 1999 to 2006, while DEAR and FINUDA have alternatively run on the second one. The detectors of KLOE and FINUDA are surrounded by large superconducting solenoid magnets for the momentum analysis of the decay particles and their magnetic fields represent a strong perturbation on the beam dynamics. This perturbation tends to induce an effect called "beam coupling", consisting in the transfer of the betatron oscillations from the horizontal plane to the vertical one. If the coupling is not properly corrected, it would give a significant increase of the vertical beam size and a corresponding reduction of luminosity.

For this reason two superconducting anti-solenoid magnets are placed on both sides of the detector with half its field integral and opposite sign, in this way the overall field integral in the IR vanishes.

The rotation of the beam transverse plane is compensated by rotating the quadrupoles in the low-β section. In the case of KLOE the low-β at the IP was originally designed with two quadrupole triplets built with permanent magnets, to provide high field quality and to left room to the detector.

The structure of the FINUDA IR is quite similar to the KLOE one. Since its superconducting solenoid magnet has half the length (but twice the field) of the KLOE one, the low-β focusing at the IP was obtained by means of two permanent magnet quadrupole doublets inside the detector and completed with two other conventional doublets outside.

The DEAR experiment, which was installed on the IR opposite to KLOE, took data during the years 2002-2003. It does not need magnetic field and therefore only conventional quadrupoles were used for the low-β. FINUDA rolled-in at DEAR's place in the second half of 2003 and took data until spring 2004. It was then removed from IP2 in order to run the KLOE experiment with only one low-β section at IP1, and rolled-in back in 2006 for a second data taking run ended in June 2007. After that the detector has been rolled-out again, and presently there are no detectors installed in IR2. The two chambers are vertically separated so that the two beams do not suffer from parasitic interactions in the whole IR2. A summary of the peak luminosity during these runs is shown in Fig. 2.

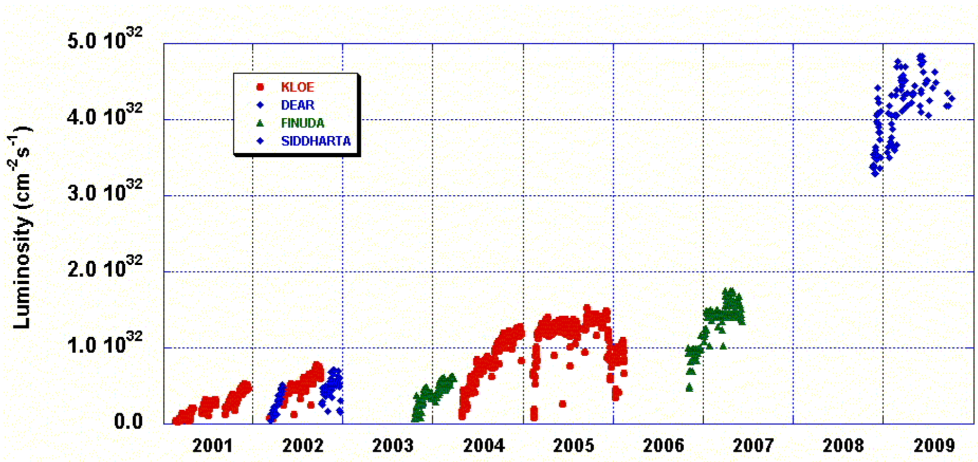

Figure 2: Peak luminosity at DAΦNE.

3 The large Piwinski angle and crab waist collision scheme at DAΦNE

In standard high luminosity colliders the key requirements to increase the luminosity are: very small vertical beta function β_y at the IP, high beam intensity I, the small vertical emittance ϵ_y and large horizontal beam size σ_x and horizontal emittance ϵ_x required to minimize beam-beam effects. The minimum value of β_y is set by the bunch length to avoid the detrimental effect on the luminosity caused by the hour-glass effect. It is very difficult to shorten the bunch in a high current ring without exciting instabilities. Moreover, high current implies high beam power losses, beam instabilities and a remarkable enhancement of the wall-plug power.

In the CW scheme of beam-beam collisions a substantial luminosity increase can be achieved without bunch length reduction and with moderate beam currents.

For collisions under a crossing angle θ the luminosity L and the horizontal ξ_x and vertical ξ_y tune shifts scale as:

$$L \propto \frac{N\xi_y}{\beta_y} \propto \frac{1}{\sqrt{\beta_y}}\,, \quad \xi_y \propto \frac{N\sqrt{\beta_y}}{\sigma_z\theta}\,, \quad \xi_x \propto \frac{N}{(\sigma_z\theta)^2} \tag{1}$$

The Piwinski angle ϕ is a collision parameter defined as:

$$\phi = \frac{\sigma_z}{\sigma_x}\tan\left(\frac{\theta}{2}\right) \approx \frac{\sigma_z}{\sigma_x}\frac{\theta}{2} \tag{2}$$

with N being the number of particles per bunch. Here we consider the case of flat beams, small horizontal crossing angle $\theta << 1$ and large Piwinski angle $\phi >> 1$.

In the large Piwinski angle and crab waist scheme described here, the Piwinski angle is increased by decreasing the horizontal beam size and increasing the crossing angle. In such a case, if it were possible to increase N proportionally to $\sigma_z\theta$, the vertical tune shift ξ_y would remain constant, while the luminosity would grow proportionally to $\sigma_z\theta$. Moreover, the horizontal tune shift ξ_x would drop like $1/\sigma_z\theta$. However, the most important effect is that the overlap area of the colliding bunches is reduced, as it is proportional to σ_x/θ (see Fig. 3). Then, the vertical beta function β_y can be made comparable to the overlap area size (i.e. much smaller than the bunch length):

$$\beta_y \approx \sigma_x/\theta << \sigma_z \tag{3}$$

We get several advantages in this case:

- Small spot size at the IP, i.e. higher luminosity L.
- Reduction of the vertical tune shift ξ_y with synchrotron oscillation amplitude.
- Suppression of synchrobetatron resonances.

There are also additional advantages in such a collision scheme: there is no need to decrease the bunch length to increase the luminosity as proposed in standard upgrade plans for B- and Φ-factories. This will certainly help solving the problems of HOM heating, coherent synchrotron radiation of short bunches, excessive power consumption etc. Moreover, parasitic collisions (PC) become negligible since with higher crossing angle and smaller horizontal beam size the beam separation at the PC is large in terms of σ_x.

However, large Piwinski angle itself introduces new beam-beam resonances which may strongly limit the maximum achievable tune shifts. At this point the crab waist transformation enters the game boosting the luminosity, mainly because of the suppression of betatron (and synchro-betatron) resonances arising (in collisions without CW) through the vertical motion modulation by the horizontal oscillations. The CW vertical beta function rotation is provided by sextupole magnets placed on both sides of the IP in phase with the IP in the horizontal plane and at $\pi/2$ in the vertical one (see Fig. 3).

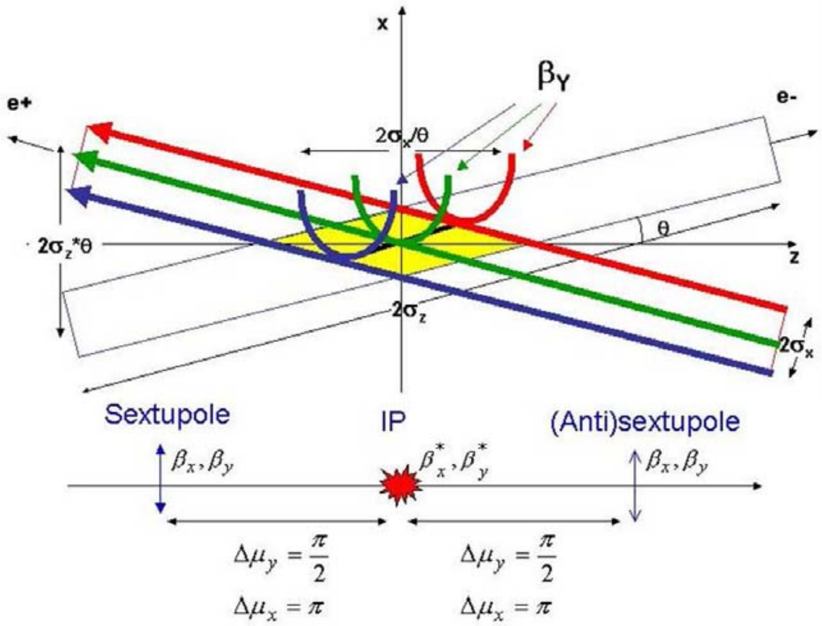

Figure 3: Crab waist scheme

For comparison, the parameters used during the last DAΦNE run with the KLOE detector (2005-2006) are shown in Table 1. As discussed above, in order to realize the CW scheme in

Table 1: DAΦNE Beam parameters for KLOE (2006) and SIDDHARTA (2008-2009)

PARAMETERS	KLOE Run	SIDDHARTA Run
L [cm^{-2}s^{-1}]	$1.5 \cdot 10^{32}$	$4.5 \cdot 10^{32}$
N_{part}/bunch	$2.65 \cdot 10^{10}$	$2.65 \cdot 10^{10}$
I_{bunch} [mA]	13	13
ϵ_x [10^{-9} m · rad]	340	260
ϵ_y [10^{-9} m · rad]	1.5	1
σ_x [μm]	760	200
σ_y [μm]	5.4	3.5
σ_z [mm]	25	17
β_x^* [m]	1.7	0.25
β_y^* [mm]	17	9
θ [mrad]	2×12.5	2×25

DAΦNE, the Piwinski angle ϕ should be increased and the beam collision area reduced: this is achieved by increasing the crossing angle θ by a factor 2 and reducing the horizontal beam size σ_x. In this scheme the horizontal emittance ϵ_x is reduced by a factor 1.5, and the horizontal beta function β_x lowered from 1.5 to 0.2 m. Since the beam collision length decreases proportionally to σ_x/θ, the vertical beta function β_y can be also reduced by a factor 3, from 1.8 cm to 0.6 cm. All other parameters are similar to those already achieved at DAΦNE.

4 Hardware upgrades for the Crab Waist test at DAΦNE

DAΦNE has been upgraded to allow the CW collision scheme test with the SIDDHARTA run during the summer shutdown of 2007.

The major upgrades on the machine are summarized as:

- new IR1 geometry for the CW test;
- new IR2 geometry with two completely separated vacuum chambers with half moon profile;
- new shielded bellows;
- the four e^+ e^- transverse feedbacks have been upgraded;
- solenoid windings in the two long IRs sections of the e^+ ring;
- new calorimeter for luminosity measurement and tuning;
- new longitudinal position of the two IRs horizontal collimators;
- new injection kickers.

The need of a new IR geometry is essentially due to have a very small β_y (9 mm) and a large crossing angle (25 mrad per beam). Splitter magnets installed in the original design have been removed thanks to the large crossing angle in the CW scheme. Defocusing and focusing quadrupoles (QD, QF) on both sides of the IP have been placed to obtain the required low-β structure. Further trajectory separation is provided by two small dipole correctors upstream and downstream the quadrupole doublets, while other three quadrupoles are used to match the betatron functions in the arcs.

The low-β section quadrupoles near the IP are of permanent magnet (PM) type. The QDs are located near the IP where the beams share a common vacuum chamber, while the QFs are positioned where the chambers are splitted and each one acts on a single beam. Therefore a total of two QDs and four QFs is required to get the two doublets around IP1. Four corrector dipoles provide a deflection of 9.5 mrad to match the inlet and outlet arc chamber flanges. CW sextupoles are placed at $\sim$ 9.3 m far from the IP1. Bending dipoles facing the IRs have been rotated and their field adjusted according to requirements. They have been powered with independent supplies to match these requirements.

For the SIDDHARTA experiment a new aluminium alloy (AL6082T6) chamber with two thin windows (0.3 mm 0.02 thickness) in the top and bottom sides has been designed and built.

Electromagnetic simulations have shown the presence of trapped modes which add resonant contributions to the beam coupling impedance in the Y-chamber junctions, the regions where the two separate ring pipes merge in the common vacuum chamber near the IP. In the worst possible scenario, that occurs when a beam spectrum line at a frequency equal to a multiple to the bunch repetition rate is in full coupling, the joule loss does not exceed 200 W. To keep this effect under control the Y-chambers have been equipped with cooling pipes.

This additional cooling circuit allows to remove the beam induced HOM heating and, if necessary, to reduce it by detuning the mode frequencies with respect to the dangerous beam spectrum lines.

A new design of the central IR2 beam pipe has been implemented, the two vacuum chambers are completely separated and their cross section has an half moon profile.

In order to ensure a fast, accurate and absolute measurement of the luminosity and to fully understand the background conditions, the new interaction region has been equipped with three different luminosity monitors (Fig. 4): a Bhabha calorimeter, a Bhabha GEM tracker and a gamma Bremsstrahlung proportional counter. Different processes are used to measure luminosity:

- the Bhabha elastic scattering $e^+e^- \to e^+e^-$: it has a very clean signature (two back-to-back tracks); the available angle is limited due to the presence of the low-β quadrupoles, however, in the actual polar angle range covered by our calorimeters, 18^o - 27^o, the expected rate ($\sim$ 440 Hz at a luminosity of 10^{32}cm^{-2}s^{-1} is high enough and the backgrounds low enough to allow an online clean measurement;
- the very high rate of the radiative Bhabha process $e^+e^- \to e^+e^-\gamma$: it has the advantage that 95% of the signal in contained in a cone of 1.7 mrad aperture, but it suffers heavily from beam losses due to interactions with the residual gas in the beam-pipe, Touschek effect, and particles at low angles generated close to IR;
- the resonant decay $e^+e^- \to \Phi \to K^+K^-$: a rate of about 25 Hz at 10^{32} is expected in the SIDDHARTA experiment monitor at $\approx 90^o$.

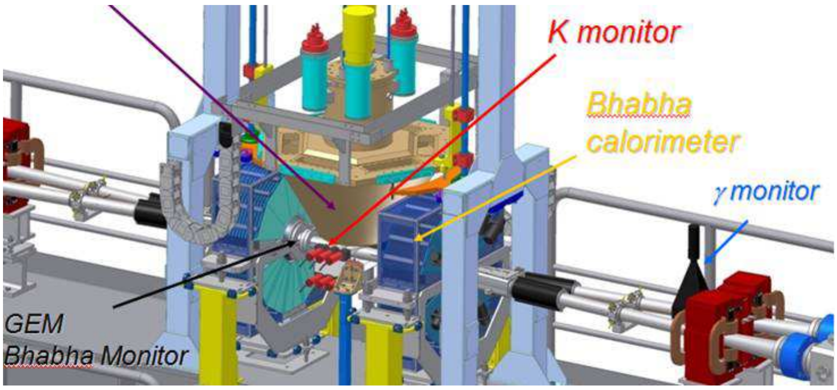

Figure 4: Overview of the upgraded DAΦNE IR1 showing the various luminosity detectors.

The main Bhabha monitor consists of a 4-modules sandwich calorimeter, made of lead and scintillator. Four modules of calorimeters surround the final permanent quadrupole magnets, located at a distance of 32.5 cm on both sides of the IR, as shown in Fig. 4. They cover an acceptance of 18^o - 27^o in polar angle, and are segmented in azimuthal angle in five sectors, 30^o wide.

Two gamma monitor detectors are located 170 cm away from the IR, collecting the photons radiated by electron or positron beam. The detectors are now made of four PbW04 crystals (squared section of 30×30 mm^2 and 110 mm high) assembled together along z, in order to have a 30 mm face towards the photon beam, and a total depth of 120 mm corresponding to about 13 X_0. Thanks to the high rate, those detectors are mainly used as a fast feedback for the optimization of machine luminosity versus background, since the relative contribution of background is changing with the machine conditions. A total systematic uncertainty on the luminosity measurement of 11% can be estimated.

5 Luminosity achievements during 2009

The commissioning of the upgraded machine started in November 2007. At the end of the year the ring vacuum was almost recovered, the beams were stored in the upgraded rings, all the sub-systems went quickly to regime operation.

The first collisions in the CW scheme have been obtained in February 2008, with the first experimental confirmation of the potentiality of the new configuration in terms of specific luminosity growth and reduction of the beam-beam detrimental effects.

Fig. 5 (top) reports integrated luminosity for each month during 2009 and Fig. 5 (bottom) shows the averaged daily integrated luminosity in the same year.

Fig. 6 summarizes daily integrated luminosity (top) and integrated luminosity (bottom) during the SIDDHARTA data taking, which ended at the beginning of November 09. The integrated

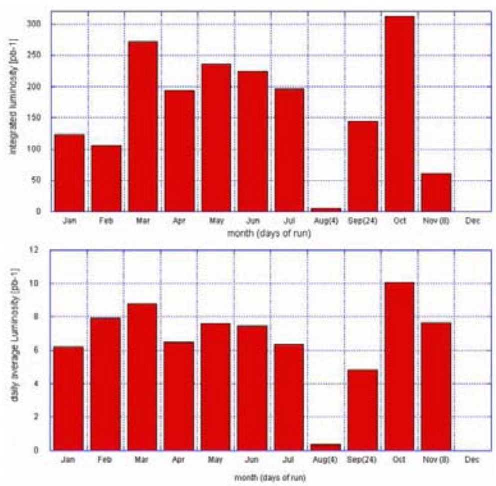

Figure 5: SIDDHARTA Integrated Luminosity (see text).

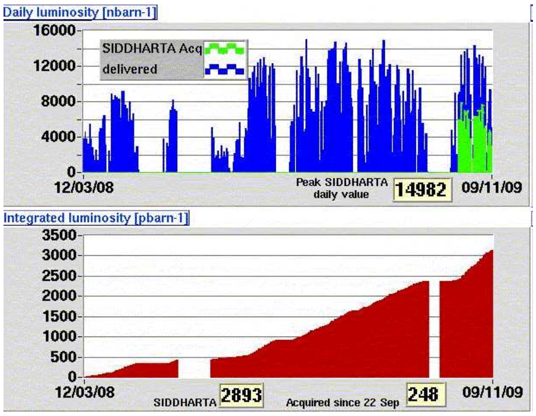

Figure 6: SIDDHARTA Integrated Luminosity (see text).

luminosity profited from implementing a new software procedure to switch the injection system from electrons to positrons and the other way round. The switch time has been reduced by a factor three and now it is less than one minute.

A continuos injection regime provides L $\approx$ 1 pb^{-1} hourly integrated luminosity, which is not compatible with the SIDDHARTA experiment data taking since the acquisition is vetoed during injection due the higher background level. However this result opens significant perspectives for the KLOE experiment, which is much less sensitive to background. The best integrated luminosity obtained in a moderate injection regime compatible with the SIDDHARTA operation with a $\approx$ 50% duty cycle is L $\approx$ .79 pb^{-1} hourly averaged over two hours.

DAΦNE luminosity as a function of the colliding bunches compared to past runs is reported in Fig. 7. Blue and red dots refer to the two KLOE runs, with the initial triplet low-β IR quadrupoles and with the new IR doublet, respectively. Yellow dots refer to the FINUDA run; in green is the luminosity with the CW scheme. The gain provided by the new IR gets higher with the products of the currents and the difference with respect to collisions with the crab sextupoles off can reach 50%.

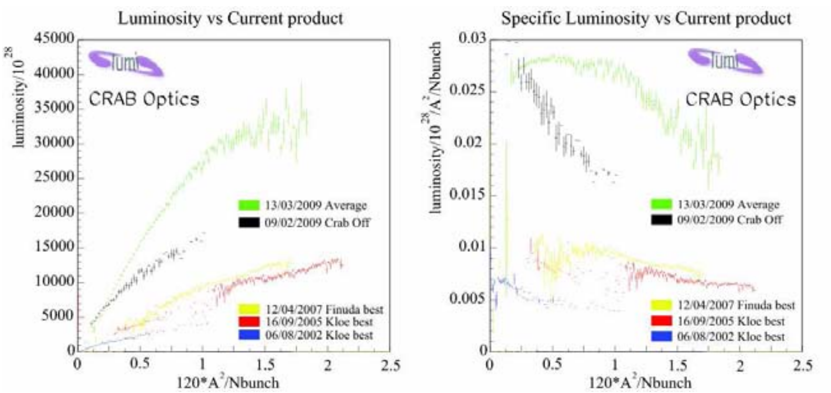

Figure 7: (color online). Comparison of the upgraded DAΦNE perfomance (green) with respect to the results during previuos KLOE (blue, red) and FINUDA runs (yellow).

Table 2: Present DAΦNE luminosity performances with the CW scheme and low-β parameters compared to the KLOE and FINUDA runs. SIDDHARTA data taking does not profit of the fast injection rate system, that would increase $L_{\int logged}$.

	SIDDHARTA March 08÷Nov 09	KLOE May 04÷Nov 05	FINUDA Nov 06÷Jun 07
L_{peak} [cm^{-2}s^{-1}]	4.5	1.5	1.6
$L^{MAX}_{\int day}$ [pb^{-1}]	15.24	9.8	9.4
$L^{MAX}_{\int hour}$ [pb^{-1}]	1.033	0.44	0.5
$I^{-\,MAX}_{coll}$ [A]	1.4	1.4	1.5
$I^{+\,MAX}_{coll}$ [A]	1	1.2	1.1
$n_{bunches}$	105	111	106
$L_{\int logged}$ [fb^{-1}]	2.9	2.0	0.966
β^*_x [m]	0.25	1.5	2.0
β^*_y [m]	0.009	0.018	0.019
ϵ_x [10^{-6} m $\cdot$ rad]	0.25	0.34	0.34
ξ_y	0.0443	0.025	0.029

During 2009 the peak luminosity has been progressively improved by tuning the collider and increasing the beam currents; the maximum value achieved is $\approx 4.5 \times 10^{32}$ cm^{-2}s^{-1} measured in several runs with good luminosity to background ratio. The present peak luminosity is close to the nominal one predicted by numerical simulations. The highest single bunch luminosity achieved is $\approx 5 \times 10^{30}$ cm^{-2}s^{-1} measured with 20 bunches in collisions instead of the usual 105. The single bunch specific luminosity, defined as the single bunch luminosity divided by the product of the single bunch currents, at low currents exceed by 4 times the best value measured during the past DAΦNE runs (present values are red and blue dots in Fig. 8). It gradually decreases with colliding beam currents, as can be seen in Fig. 8. This reduction can be only partially explained by the growing beam size blow up due to the beam-beam interaction. Another factor comes from the fact that in the large Piwinski angle regime the luminosity decreases with the bunch length, which in turn is affected by the ring coupling impedance.

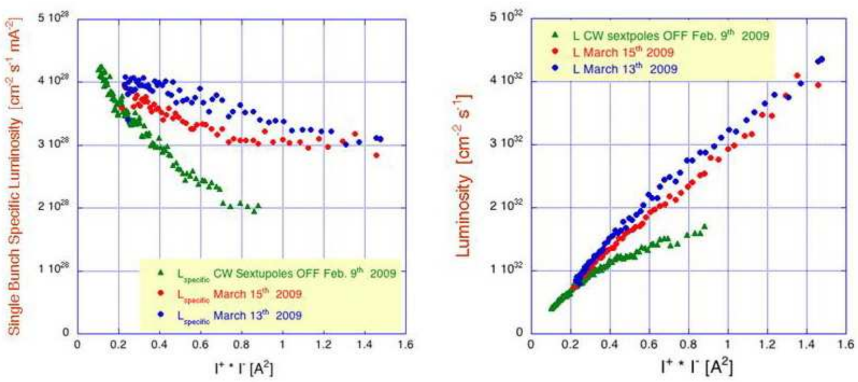

Figure 8: (color online). Single bunch specific luminosity (left) and luminosity (right) versus the product of the colliding currents for two of the best run and for the crab waist sextupoles off.

The impact of the Crab-Waist sextupoles can be recognized comparing runs taken with CW sextupoles on and off (Fig. 8). At low current the luminosity is the same in the two cases and higher than the one measured with the original collision scheme. As the product of the stored currents exceed 0.3 A, the luminosity with CW sextupoles off becomes lower and a corresponding transverse beam size blow up and beam lifetime reduction are observed as a consequence of the uncompensated beam-beam resonances.

The convolved vertical beam size at the IP in collision has been measured by means of a beam-beam scan technique. The measured Σ_y of 5.6 μm is compatible with the value obtained by using the coupling value (k=0.7%) as measured at the Synchrotron Light Monitor (SLM), being the single vertical beam size at the IP1 of the order of 4 μm.

Fig. 9 reports another proof of the crab sextupoles effectiveness, where the positrons transverse beam profile measured at the synchrotron light monitor with crab sextupoles OFF (left plot) and with crab sextupoles ON (right plot) is shown. The measurement refers to collision in a strong-weak regime (1 A electrons beam current against 0.1 A of positrons beam current): it is evident that the transverse beam size is smaller and its shape remains Gaussian during collision with the sextupoles ON.

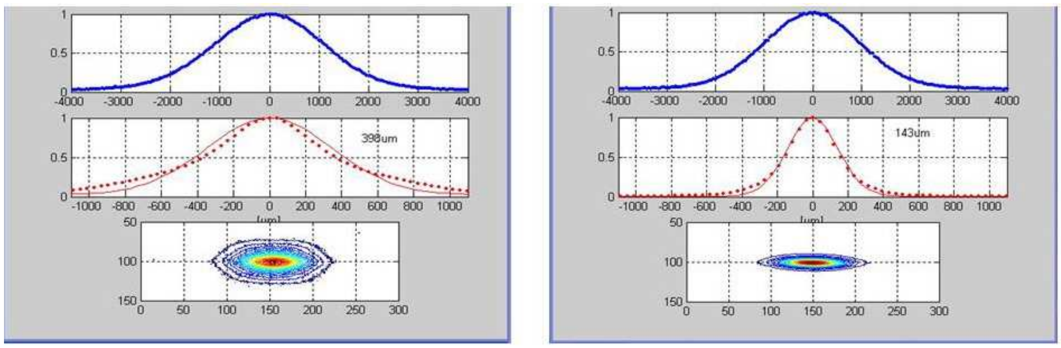

Figure 9: Transverse positron beam profile as measured at SLM with crab sextupoles off (left) and crab sextupoles on (right) for beams in collisions (103 bunches).

The crab waist sextupoles proved to be of great importance for the collider luminosity increase, since much lower luminosity is achieved with crab sextupoles off, with a larger blow up and a sharp lifetime reduction is observed for single bunch currents greater than 8-10 mA. This is in agreement with beam-beam simulations taking into account the DAΦNE nonlinear lattice. The results achieved at DAΦNE have pushed several accelerator teams to study and consider the implementation of this scheme on their machines. Besides, the physics and the accelerator communities are discussing a new project of a Super B-factory with luminosity as high as 10^{36} cm^{-2}s^{-1}, i.e. by about two orders of magnitude higher with respect to that achieved at the existing B-factories at SLAC and KEK.

6 Future Activities in view of the KLOE run

The new collision scheme based on large Piwinski angle and Crab Waist implemented on DAΦNE worked as predicted by the preliminary studies and numerical simulations. The present luminosity achievements opened new perspectives for the DAΦNE collider and a new run for the KLOE experiment has been planned for the year 2010. During 2009 the new interaction region design for KLOE has been completed and several components of the new hardware have been acquired. Main improvements with respect to the present optics and past KLOE run are:

- increased beam stay clear at the IR;
- better shielding;
- additional skew quadrupoles added across QF1;
- independent pair of anti-solenoids for each beam;

Due to the larger crossing angle, the vertical displacement of the beam in the IR is about an order of magnitude larger than the last KLOE run. A system of permanent magnet dipoles compatible with different fields of the KLOE detector has been designed and built to be installed after each QF1 to keep under control the vertical beam trajectory.

Hardware activities to allow the new KLOE run have been started immediately after the end of the SIDDHARTA run.

The LINAC gun cathode, almost exausted, will be replaced with a new one and a further accelerating section will be added at the end to improve stability during operation for positrons.

Stripline electrodes will be installed in all wigglers and dipole vacuum chamber for electron cloud clearing. The horizontal feedback power will be doubled and the horizontal feedback kicker will be modified to improve feedback effectiveness.

Wigglers magnet will be modified according to a novel technique that will improve the good field region. It will increase the manimum field for a given current and decrease the wall plug power. In the modified wiggler the beam trajectory passes always near the pole center, in this way the higher order terms in the magnetic field are significantly reduced.

Remaining old type bellow are being replaced with a modified one which have lower impedance and better mechanical performance. All remaining ions clearing electrodes in the electron ring will be removed. Fast kickers will be installed to dump the beams on a single turn basis in a clean way upon operator request or hardware failure, to reduce detector trips and radiation interlocks. A new low level RF feedback is under development to improve longitudinal stability reducing at the same time the wall plug power. The shutdown for the KLOE roll-in is foreseen to end on spring 2010, an overall improvement of the peak luminosity of the order of 20% with respect to the Siddharta one and an integrated luminosity of ≈ 0.5 fb^{-1} per month is expected after the initial commissioning.

7 Publications

1. M. Zobov et al., *Crab Waist Collision Scheme: Numerical Simulations versus Experimental Results*, Proc. of PAC09, Vancouver, (2009).
2. C. Milardi for the DAΦNE Collaboration Team: *Experience with DAΦNE Upgrade Including Crab Waist*, Proc. of PAC09, Vancouver, (2009).
3. T. Demma et al., *A Simulation Study of the Electron Cloud Instability at DAΦNE*, Proc. of PAC09, Vancouver, (2009).
4. A. Drago, *Fast Horizontal e+ Instability Measurements in DAΦNE*", Proc. of PAC09, Vancouver, (2009).
5. A. Drago, *DAΦNE Horizontal Feedback Upgrade*, Proc. of PAC09, Vancouver, 2009.
6. F. Marcellini et al., *Tests and Operational Experience with the DAΦNE Stripline Injection Kicker*, Proc. of PAC09, Vancouver (2009).
7. A. Stella et al., *Beam Tests with Libera in Single Pass Mode*, Proc. of DIPAC09, Basel(CH), (2009).
8. P. Valente et al., *Detectors for Absolute Luminosity Measurement at DAΦNE*, Proc. of DIPAC09, Basel (CH), (2009).
9. C. Milardi et al., *Results from the DAΦNE high luminosity test*, Nuovo Cimento C **32**, 379 (2009).
10. T. Demma et al., *Update of the electron cloud simulations for DAΦNE*, ICFA Beam Dyn. Newsletter **50**, 33 (2009).
11. M. Zobov et al., *Update Beam dynamics in crab waist collisions at DAΦNE*, ICFA Beam Dyn. Newsletter **48**, 34 (2009).
12. T. Demma et al., *Update Electron cloud simulations for DAΦNE*, ICFA Beam Dyn.Newsletter **48**, 64 (2009).
13. C. Milardi et al., *Crab waist collision at DAΦNE*, ICFA Beam Dyn. Newsletter **48**, 23 (2009).
14. M. Boscolo, *Touschek backgrounds experience at DAΦNE*, ICFA Beam Dyn. Newslett. **48**, 59 (2009).
15. C. Milardi et al., Int. J. Mod. Phys. A **24**, 360 (2009).
16. A. Drago, *Horizontal instability measurements and cure in DAΦNE*, ICFA Beam Dyn. Newsletter **48**, 50 (2009).
17. F. Marcellini et al., *The new DAΦNE kickers*, ICFA Beam Dyn. Newsletter **48**,45, (2009).

The DAΦNE Beam Test Facitily (BTF)

B. Buonomo (Art.23), G. Mazzitelli (Resp.), L. Quintieri (Art.23), P. Valente (Osp.)

The DAΦNE Operation Staff: G. Baldini, A. Beatrici, M. Belli, B. Bolli, G. Ceccarelli, R. Ceccarelli, A. Cecchinelli, S. Ceravolo, R. Clementi, O. Coiro, S. De Biase, M. De Giorgi, M. Di Virgilio, G. Ermini, G. Fontana, C. Fusco, O. Giacinti, E. Grossi, F. Iungo, C. Marini, M. Martinelli, C. Mencarelli, E. Passarelli, V. Pavan, D. Pellegrini, G. Piermarini, S. Quaglia, M. Sardone, M. Scampati, G. Sensolini, A. Sorgi, M. Sperati, A. Sprecacenere, R. Tonus, T. Tranquilli, M. Troiani, R. Zarlenga

The LNF Technical Staff:
M.R.Ferrazza, R. U. Frasacco, F. Galletti

BTF Committee
P. Di Nezza - INFN-LNF, F. Gatti -INFN, Genova, C. Matteuzzi (Chairperson) - INFN, Milano, G.Mazzitelli(Responsible) - INFN-LNF, A. Passeri - INFN, Roma III, P. Valente - INFN, Roma I

1 Description of the DAΦNE BTF 2009 Activities

The DAΦNE Beam Test Facility had a very intense activity during 2009, providing electron/positron and photon beams in the full range of energy (25-510 MeV), with intensity varying from single particle up to 10^7 particles per spill. Several experimental groups, coming from all over Europe, were hosted for a total of 256 allocated days.

In addition to access to external teams, during the last year we have continued and concluded the study for the feasibility of the neutron source at BTF. Details about this project are described in a specific report (N@BTF). The first tests of the new neutron beam are planned for Spring 2010, in order to characterize the neutron energy spectrum of the source.

The Beam Test facility staff also continued the job in optimizing the beam characteristics and diagnostic tools, as well as in the improvements of the DAQ, user devices, services, control and management software.

2 2009 User Experience

The experimental groups that have used the facility during 2009 are listed in reference [1]. Most of test-beam had mainly the objective of calibration, set-up and response characterization of high-energy detectors. In some of them, the BTF team has given a direct contribution, and we will describe the measurement performed during this run.

2.1 LWFA (laser-driven plasma accelerator)

The laser-driven accelerators, in which particles are accelerated by the electric field of a plasma wave (the wake-field) driven by an intense laser, have demonstrated accelerating electric fields of hundreds of GV/m. These fields are thousands of times greater than those achievable in conventional radio-frequency accelerators, spurring interest in laser accelerators, as compact next-generation sources of energetic electrons and radiation [2, 3].

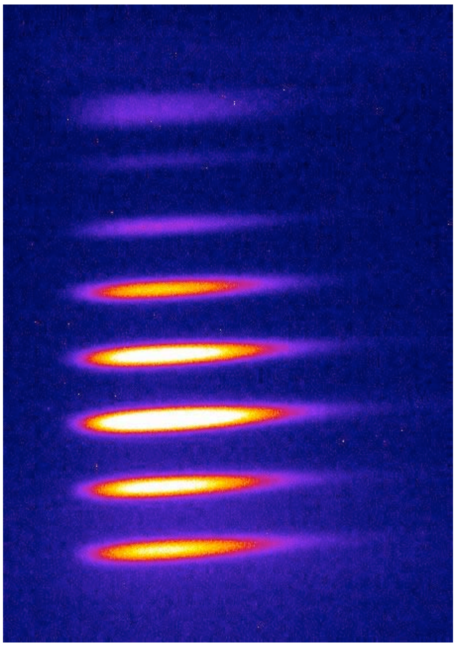

Figure 1: (color online). False color cropped pepper-pot image recorded on a Lanex screen. A single shot in this sample was of approximately 500 pC of 508 MeV beam electrons.

The need of new instrumentation to diagnose parameters of electron beam produced by laser-plasma accelerator is extremely important, and the potential depend in detail on the properties of the generated beams. Due to the high energy reached after the acceleration process, some of the diagnostics traditionally used in electron guns are not available and thus the characterization of the beam is a challenge in itself. In this test new single-shot diagnostics for the determination of the profile of the electron beam at different energies and intensities, have been investigated, in collaboration with John Adams Institute for Accelerator science (JAI) and Simon Hookers group in the Clarendon Laboratory. In particular, the following elements have been tested:

2.1.1 High-energy pepper-pot.

A modified pepper-pot design has been employed to measure, in a single shot, the emittance of electron beams with energy of 508 MeV. The set-up consists of several thin layers of tantalum with spacers in between to leave slits through which the electron beam can be sampled (see Fig. 1). A complete description of the set-up and the measurements, as well as the results obtained, have been presented at PAC09 conference [4).]

2.1.2 Charge calibration and linearity studies of scintillator screens.

Image plates are frequently used for charge measurement of electrons a low energy. For high energetic beams the calibration of image plates is not well known and simulations are used to

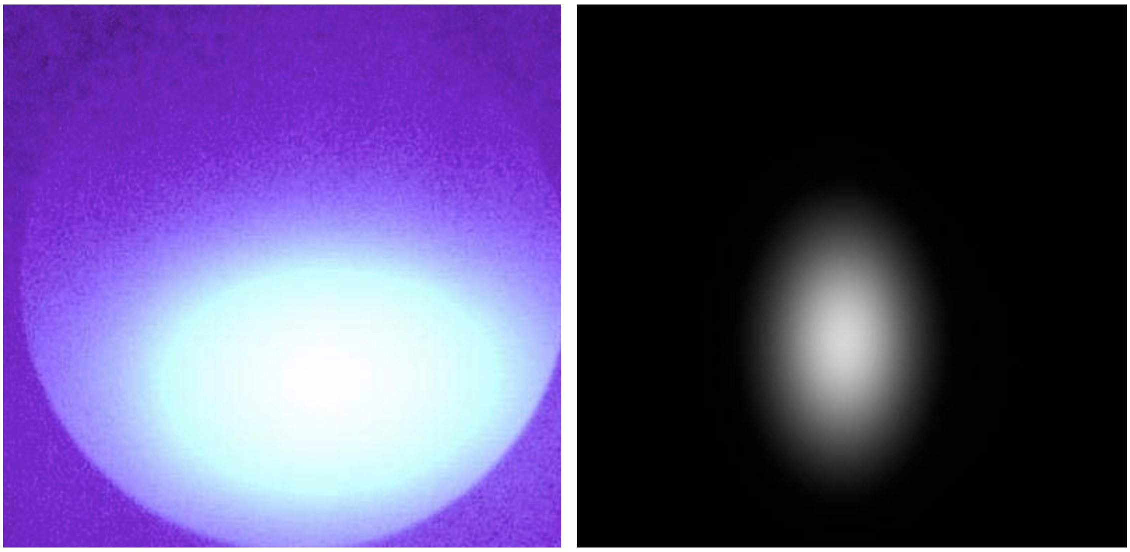

Figure 2: (color online). Left: Image plate data elaborate in false color. The figure shows the signal region (centre) and background (top). Right: CCD image of the Lanex screen.

predict the behaviour. This experiment is the first experimental calibration for image plates with electrons at high energy (500 MeV) which can be used in Laser Wake-Field Acceleration (LWFA) experiments.

Another method to measure charge is to use phosphor screens (Lanex). These inexpensive screens are already routinely used for LWFA experiments. In combination with an image plate calibration shot at low charge, one can deduce the charge of higher charge beams by assuming linearity of the Lanex screen (see Fig. 2). Further details on this scintillator screens and the results obtained during the beam-test can be found in Ref. [5, 6].

2.2 RAP

The aim of the experiment RAP is to measure the longitudinal vibrations of cylindrical test mass, when electrons provided by the BTF impinge on them, and to investigate if the mechanism of the particle energy loss conversion into mechanical energy depends on the conduction state of the bar [7].

During 2009 a shift of 4 weeks has been assigned and data at different temperatures, down to 344 mK, have been collected. This has been possible thanks to the 3He-4He dilution refrigerator installed inside the RAP cryostat.

The experimental results confirm that the first longitudinal mode of oscillation amplitude definitely depends on the conduction state of the material and the transition zone width between the normal-conducting and the pure super-conducting behavior depends on the material super-conductivity and its purity. The RAP (Al-5056 bar) measurements at the lowest T seem to be in agreement with the NAUTILUS data [8].

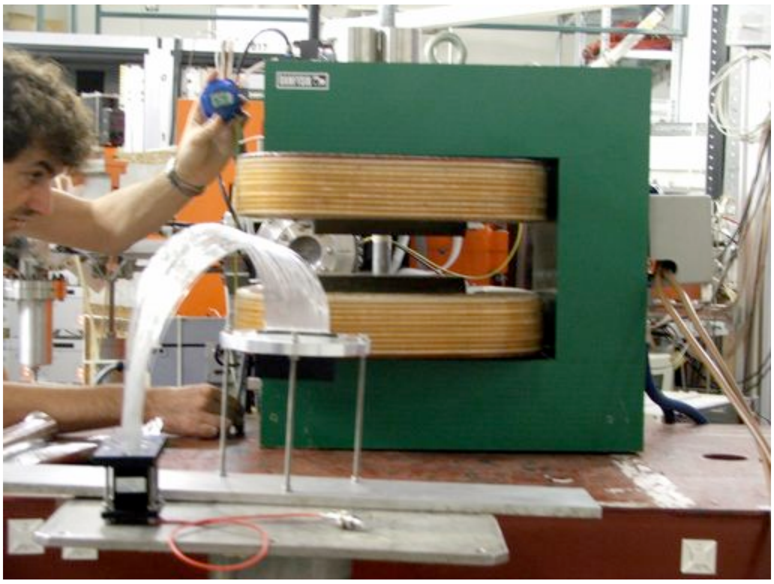

Figure 3: Dipole magnet and prototype scintillating fibers detector (before wrapping and cabling of read-out electronics).

2.3 PLASMAG

The advance in laser plasma acceleration techniques push the regime of the resulting accelerated particles to higher energies and intensities. In particular the upcoming experiments with the FLAME laser at LNF will enter the GeV regime with more than 10^7 electrons.

At the current status of understanding of the acceleration mechanism, relatively large angular and energy spreads are expected. There is therefore the need to develop a device capable to measure the energy of electrons over three orders of magnitude (few MeV to few GeV) under still unknown angular divergences.

Within the PlasmonX experiment at LNF, a spectrometer is being constructed to perform these measurements. It is made of an electro-magnet and a screen made of scintillating fibers for the measurement of the trajectories of the particles. The large range of operation, the huge number of particles and the need to focus the divergence present unprecedented challenges in the design and construction of such a device.

The tests at the BTF allowed testing the scintillating fibers device and above all verify the choice of the position of the detectors with the actual magnet in place (see Fig. 3). A prototype with 64 1 mm diameter fibers read by a multi-anode PMT and front-end electronics based on the MAROC-2 chip (developed at LAL, Orsay) has been tested, the main results are fully reported in [9], in terms of momentum resolution and optimization of focusing as a function of the distance from the magnetic axis (see Fig. 4).

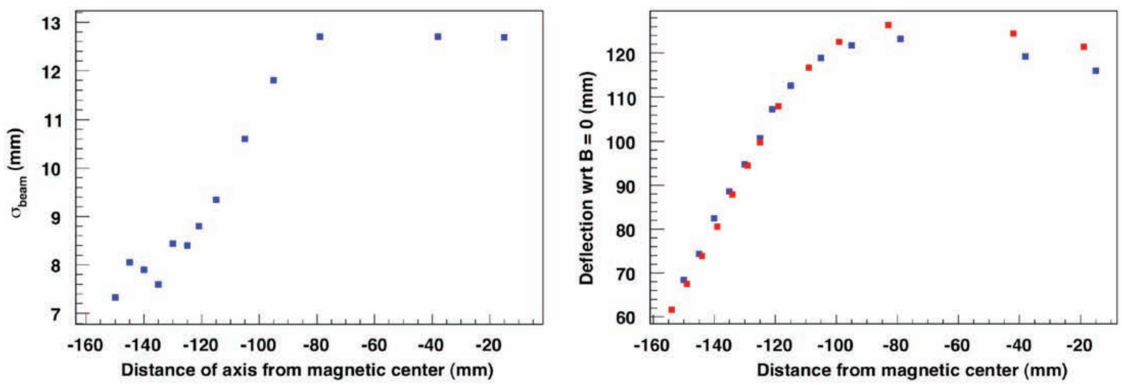

Figure 4: Optimization of beam focussing as a function of the distance from the magnetic axis: beam-spot dimension (left) and beam deviation (right).

3 Conclusion

The BTF is in operation since 2003, six years of tests performed in very different conditions of multiplicity, energy and beam characteristics. The facility operated with more than 60 experimental groups, 24 hours/day for an average of 250 days/year.

We are working to improve the efficiency of the facility in order to be able to host different user communities: from high-energy physics to accelerator physics. The complexity of operation of the facility requires a continuous integration and upgrade of the diagnostic system in order to improve the characterization of the beam quality (spot size, position, multiplicity).

In the next year, first tests will be done in order to check the feasibility of a photo-neutron source at the Beam Test Facility. The measurements of the neutron rate will be compared to the MC simulation results. Moreover suitable detectors (Bonner Spheres) will allow to characterize the energy spectrum of the neutron source.

4 Conference Talks

1. G. Mazzitelli et al., *LNF@BTF dalla singola particella fino a* 10^{10} *elettroni, positroni, fotoni e neutroni*, CSN1, Università La Sapienza, 28 January 2009.

2. P. Valente et al., *La Test Facility dei LNF*, CSN3, INFN Caprettari, 2 February 2009.

3. P. Valente et al., *Il Fascio di Test della BTF di Frascati*, CSN2, Università La Sapienza, 5 February 2009.

5 Publications

- Nicolas Delerue et al., *Single-shot emittance measurement of a 508 MeV electron beam using the pepper-pot method*, PAC 09 Proceeding, Vancouver 4-8 May 2009.

References

1. http://www.lnf.infn.it/acceleratori/btf/php/schedule.php?year=2009&acc=1

2. W. P. Leemans et al., Nature Physics **2**, 696 (2006).

3. W. P. Leemans et al., *GeV electron beams from a centimetre-scale accelerator*, Physics Today, March 2009.

4. N. Delerue et al., *Single-shot emittance measurement of a 508 MeV electron beam using the pepper-pot method*, PAC 09
   http://www-pnp.physics.ox.ac.uk/ delerue/lpwa/publications/TH5RFP065.pdf

5. P. A. Walker et al., *Charge Calibration of Image Plates and Lanex Screens for Electrons at 500 MeV*, Laser Plasma Accelerator Workshop, Kardamili, Greece, June 2009.

6. P. A. Walker et al., *Charge Calibration of Image Plates and Lanex Screens for Electrons at 500 MeV*, High Energy Density Physics UCLA Summer School, Los Angeles, CA, USA, July 2009.

7. M. Barucci et al., Phys. Lett. A **372**,1801 (2009).

8. F. Ronga et al., Nucl. Phys.Proc. Suppl. **190**, 44 (2009).

9. R. Faccini et al., *Multi-GeV electron spectrometer*, accepted by Nucl. Instr &. Meth. A, doi: 10.1016/j.nima.2010.02.095

DAΦNE-Light Laboratory and Activity

A. Balerna (Resp.), P. Calvani (Ass.), C. Castellano (Ass. Ric.), M. Cestelli Guidi (Art. 23),
R. Cimino, M. Commisso (Ass. Ric.), A. De Sio (Osp.), L. Gambicorti (Osp.), A. Grilli (Tecn.),
D. Hampai (Ass. Ric.), R. Larciprete (Ass.), S. Ning (Ass.), A. Nucara (Ass.), E. Pace (Ass.),
M. Pietropaoli (Tecn.), A. Raco (Tecn.), V. Sciarra (Tecn.), V. Tullio (Tecn.), G. Viviani (Art. 15)

1 Summary

During 2009 on the IR and soft X-ray beamlines, new experiments were performed by Italian, European and other users in parasitic mode, during the SIDDHARTA runs, but also using 12 dedicated days for some specific experiments from February 2009 up to the end of July and then from the middle of September up to the end of October 2009 when the DAΦNE shutdown started. In particular, 11 experimental teams were hosted including scientists who got access within FAI fundings and Italian teams coming from Universities and from other scientific institutions like ENEA and CNR, with the submission of their scientific proposals to the Synchrotron Radiation Scientific Committee got access to the synchrotron radiation facility. During this year no EU program was attended, since the DAΦNE- Light Synchrotron Radiation Facility now belongs to the new EU FP7-I3 initiative called E.LI.S.A. (European LIght Source Activities) for research cooperation involving the world largest network of synchrotron and FEL facilities throughout Europe and only at the beginning of November 2009, when the DAΦNE shutdown started, all related questions were solved.

Experimental activities, performed in 2009, were also related to the organization and improvement of the existing soft X-ray and IR beamlines, to the reorganization of the UV beamline but also to the construction of the two new XUV beamlines. Concerning the synchrotron infrared beamline (SINBAD), its instrumentation has been implemented in 2009 and now includes systems for the treatment of biological samples. Using Fourier transform IR microscopy with the FPA (focal plane array) detector, the high current and brilliance of DAΦNE IR synchrotron radiation source, that enhance the signal from small biological objects containing a reduced amount of organic matter, chemical imaging on individual cells and tissues in short times, going from tenths of seconds to a few minutes only was achieved. Many different samples have been investigated including skeletal muscle connective tissue and in this case it was possible to determine the presence of different types of collagens (Fig. 1).

In 2009 a new system to electronically control and set the pressure of the ionization chambers of the soft X-ray experimental chamber, including the a sensor, a control valve and a computer interface, has been installed and tested (Fig. 2) while concerning the X-ray beam alignment a relevant improvement was effectively given by the installed fluorescent target and the double wire beam monitor also if some improvements are still necessary and will be performed in 2010.

Concerning the UV branch-line, the optical design of the VIS-UV and VUV channels has been entirely revised during 2009 in order to reduce the number of mirrors and thus improving the photon flux at the focus. Measurements on diamond detectors in the UV-VIS spectral region have been performed in order to have information on their photoresponse, in terms of sensitivity and time response. Experiments on organic materials have been also performed to provide some clues on the processes that could be at the origin of life. Mixtures of formamide with two mineral

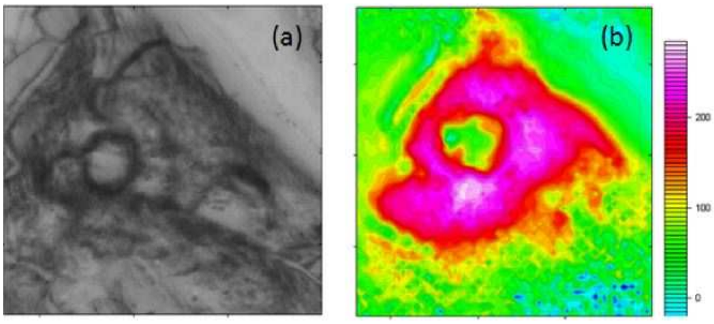

Figure 1: (a) Visible image of skeletal muscle connective tissue. The image size is 170x170 μm. (b) Infrared image of the tissue with 1.3 μm pixel resolution representing the protein (amide I) band distribution.

Figure 2: Part of the pressure control system including the sensor and the control valve.

forms of titanium dioxide, anatase and rutile were irradiated with UV light . Preliminary results are very positive, but still under analysis Concerning the new XUV laboratory its construction has been continued (Fig. 3) and the low energy beamline (LEB) is ready to be commissioned with synchrotron radiation at the restart of DAΦNE in 2010. Also the construction of the high energy beamline (HEB) is going on is foreseen to be completed by 2010.

2 Activity

2.1 SINBAD - IR beamline

SINBAD is the Synchrotron Infrared Beamline At DAΦNE, a facility that gives access to users for IR spectroscopy experiments since 2002. The beamline is equipped with two experimental stations which can be used both with synchrotron radiation and conventional sources. Biomedical, chemical and material science research activities are performed in different conditions of temperature and pressure, and high resolution ($\sim$1 μm) IR imaging of biological tissues and cells is taken with

Figure 3: The initial part of the new low and high energy beamlines entering the XUV laboratory.

an Infrared microscope equipped with a 64 x 64-element focal plane array (FPA) detector. In 2009 experiments with synchrotron radiation have been performed in parasitic mode during the SIDDHARTA runs and with 8 dedicated shifts for specific experiments. The scientific activity at SINBAD was associated to experiments performed by Italian teams that submitted scientific proposals approved by the LNF Synchrotron Radiation Scientific Committee and by European scientists who got access within the FAI funding. During this year no EU program was attended, since the DAΦNE -Light Synchrotron Radiation Facility now belongs to the new EU FP7-I3 initiative called E.LI.S.A., that will start at the end of 2009. In 2009, 8 experimental teams were hosted and 109 experimental days were assigned. Italian projects included the participation of graduates and PhD students who had access to the IR beamline performing experiments together with the SINBAD staff; almost all of t he teams re-applied to continue their researches in 2010. Measurements at SINBAD were performed also within the framework of the 5th INFN Committee with the experiment called 3+L to test high speed infrared detectors to be used for DAΦNE beams diagnostics. The SINBAD facility also participates in the TERASPARC project to install a Terahertz beamline on the SPARC FEL. A course on biological data analysis called PCA and multivariate analysiswas organized in collaboration with the IRS group of La Sapienza in November 2009. Some of the scientific highlights achieved within the experimental activity performed in 2009 are here summarized:

1. *Phase-separated states in high-pressure $LaMn_{1-x}Ga_x\ O_3$ manganites.*

   High-pressure Raman (0 < P < 12 GPa) and Infrared (0 < P < 24 GPa) spectra are collected on two samples of the $\mathrm{LaMn_{1-x}Ga_x\ O_3}$ series: x = 0.2 and 0.6 with cooperative Jahn-Teller distorted and regular $\mathrm{MnO_6}$ octahedra, respectively. Raman spectra are also collected at P = 0 on varying Ga-content (0 < x < 0.8). A remarkable octahedral symmetrization is observed on increasing P in the x = 0.2 sample, as well as x at P = 0. The x-driven symmetrization process is homogeneous whereas, compressing the lattice, a phase-separated regime (regular/distorted $\mathrm{MnO_6}$) is observed at intermediate P. The comparison between the spectra of the two samples (Fig. 4) in the high-pressure regime strongly suggests the presence of small residual distortion in the x = 0.2 even at the highest P. Infrared data show that P is effective only in the x = 0.2 sample P-driven band-gap filling, suggesting the relevance of orbital and magnetic order on the metallization process. The results achieved provide a unique experimental base to clarify the origin of the peculiar pressure behavior of the parent $LaMnO_3$.

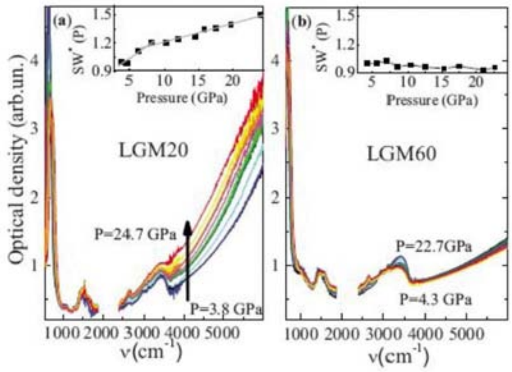

Figure 4: Optical densities of LGM20 ($LaMn_{0.8}Ga_{0.2}\ O_3$) and LGM60 ($LaMn_{0.4}Ga_{0.6}\ O_3$) at selected pressures. The black arrow indicates the increasing pressures. Insets: spectral weights as a function of pressure for the two samples.

2. *A bright future for synchrotron imaging*

   Among the analytical techniques able to yield molecular information about biological samples, a growing interest in Fourier transform infrared (FTIR) microscopy has emerged during the past decade. However, there are technical challenges and limitations when applying FTIR microscopy to biological issues, owing to the limited brightness of commercial infrared sources, and the poor sensitivity and resolution of detectors. We wish to draw attention to the fact that, thanks to the emergence of high-brightness synchrotron sources equipped with focal plane array (FPA) detectors, this situation now looks set to change. A synchrotron source has the capability of providing infrared light through a 10 μm pinhole that is 23 orders of magnitude brighter than a conventional Globar such as those available in commercial FTIR instrumentation. This superior signal-to- noise ratio (SNR) is expected to allow imaging with a spatial resolution down to the diffraction limit, or to allow analysis of thicker samples while maintaining good spatial resolution. The availability of the infrared FPA detector and its recent installation at ultrabright synchrotron radiation facilities around the world promise to reduce data acquisition time from hours to minutes, improving the spectral quality and overcoming possible contributions from synchrotron radiation instability. Alignment and optimization of these devices remains a challenge when noise or instabilities are present and because of optical layout limitations. A huge effort has already been made, with many ideas implemented and others under investigation at third-generation storage ring facilities, to improve stability and, as a consequence, spatial resolution, contrast and acquisition time of an image. There is thus a brilliant future for infrared synchrotron microscopy and imaging, and important results in biological and biomedical applications are expected in the coming years.

3. *Temperature Dependence Discontinuity of the Phonon Mode Frequencies Caused by a Zero-Gap State in HgCdTe Alloys*

In the HgCdTe (MCT) alloys, a zero-gap state $Eg = \Gamma_6 - \Gamma_8 = 0$ may occur as the composition varies from HgTe to CdTe. This singular mechanism of the Eg variation may be triggered by an external pressure or by a temperature. In this Letter, the experimental data of the optical reflectivity in the far-infrared (FIR) domain in a wide interval of temperature (from 10 to 290 K) of the $Hg_{1-x}Cd_x$ Te (x = 0.115) samples were presented. Since the intensity of classical IR sources drops abruptly in this spectral region, a brilliant synchrotron radiation FIR source has been used. The results (Fig. 5) clearly show that frequencies of the optical phonon modes exhibit discontinuity in their temperature dependence in the zero-gap state.

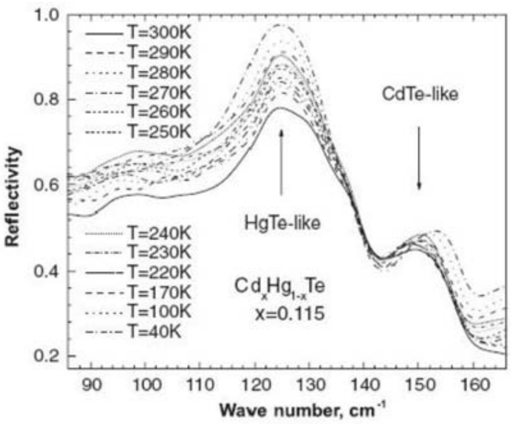

Figure 5: Reflectivity spectra for $Hg_{1-x}Cd_x$ Te (x=0.115) in the 80-180 cm^{-1} frequency range, in the temperature region 40-300K.

2.2 DXR1 - Soft X-ray Beamline

The DAΦNE soft X-ray beamline, DXR-1, is mainly dedicated to soft X-ray absorption spectroscopy. The X-ray source of this beamline is one of the 6-poles equivalent planar wiggler devices installed on the DAΦNE electron ring (0.51 GeV) for the vertical beam compaction. The 6 wiggler poles and the high storage ring current (higher then 1 Ampere) give a useful X-ray flux for measurements well beyond ten times the critical energy. The useful soft X-ray energy range is 900 eV - 3000 eV where the lower limit is given by the Beryl crystals used in the double-crystal monochromator and the higher limit is given by the wiggler working conditions.

During 2009 tests were performed on many of the important elements installed in 2008 like the fluorescent target and the double wire beam monitor but small changes including an horizontal slit are now under study. A new system to control, set and include in the experimental files the values of the pressures of the ionization chambers has been installed and tested and only small changes in the acquisition program are now necessary. The possibility to remotely control the allignments of the input and output slits and of the new support of the experimental chamber was quite important to find and center the X-ray beam once the DAΦNE new working conditions were setted.

The scientific activity at the soft X-ray beamline included the use of 4 dedicated beam time days (4 weeks) starting from February, after making some tests in January to check the beam stability and availabe flux, distributed between 2 experiments performed by Italian teams and one by an Indian scientists. Other Italian scientists used the beamline during parasitic beamtime for about 4 weeks. The LNF staff performed some tests using the SDD detector and the cryostat (4 IR dedicated days).

Some of the 2009 scientific experimental activities performed are here summarized:

1. *Mirror exposure in the DAΦNE-Light facility for exploring the effect of soft X-ray on the performance of mirrors coated with protective dielectric coatings or carbon films*

   In the forthcoming International Thermonuclear Experimental Reactor (ITER) the diagnostic of burning plasma will be of fundamental importance. A large number of the foreseen diagnostics (about 25%) will use a mirror as the first optical element, refractive optics being ruled out by its large degradation under the expected neutron and gamma ray fluxes. These mirrors have to preserve their optical characteristics throughout the whole lifetime of ITER because they will influence the general performance of the respective diagnostic systems. In most cases these first mirrors will be metal mirrors fabricated with bulk metals. One mirror in each arrangement must face the plasma. These first mirrors will be subject to all types of radiation emanating from hot plasmas (neutrons, gammas, photons and energetic particles), and the strongest modification of the surface of mirror will come from charge exchange atoms (CXA). The scope of the present project was the investigation of the morphological and chemical changes occurring in a carbon layer deposited on the mirrors under high soft X-ray dose as well as the characterization of optical properties modifications of mirrors coated with dielectrics. Mirror samples (Fig. 6), 22x22x4 mm, with one half coated with Al_2O_3 of about 250 nm in thickness as well as mirror samples of 29 mm in diameter (5mm thick) with Sisubstrate and $Ag+Al_2O_3$ and/or $Cu+SiO_2$ coatings were studied.

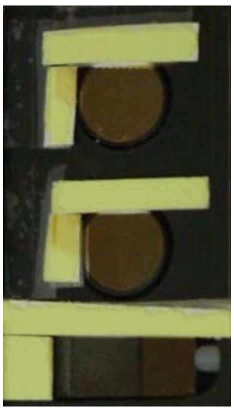

Figure 6: Some of the mirrors prepared for the high dose soft X-ray exposure.

2. *Electronic structure of magnesium sulphate with and without amino-acid doping studied by X-ray absorption spectroscopy at the Mg K-edge.*

   Epsomite or heptahydrite or $MgSO_4$ - $7H_2O$, hydrated magnesium sulfate, is one of only a few water soluble sulfate minerals. Among numerous magnesium salts, $MgSO_4$ is the most commonly used in the field of medicine and agriculture. $MgSO_4$ is often used in clinics and sometimes used as a tocolytic medication. These salts are very important both in basic than in applied science, so the aim of the proposal was to understand the how their electronic structure changes as a function of the water content with and without amino-acids doping. This study is quite important because amino-acids are the building blocks of proteins. The interesting results of the investigations performed at the DAΦNE-Light soft X-ray beam line using X-ray absorption near-edge structure (XANES) at the magnesium K-edge were likely to provide a selective investigation of the local atomic environment about the Mg atoms in the different systems studied. The amino acids included in the study at different percentages were: serine, L-alanine, L-glutamic and glycine.

2.3 DXR2 -UV branch Line

The synchrotron radiation (SR) photon beam from a wiggler installed on the DAFNE storage ring is split by a grazing incidence Au-coated mirror ($\theta_i = 40$ mrad, cut-off energy about 800 eV), in order to provide the X-ray and UV beamlines. The reflected UV radiation travels through the UV beamline and ends in a 38 mm diameter sapphire window. The experimental apparatus installed at the exit window of the beamline is partially refurbishing and partially under construction.

The layout of the whole apparatus, that is shown in (Fig. 7), has been designed in collaboration with the Istituto Nazionale di Ottica Applicata at Firenze and it will allow measurements in a very wide spectral range from 120 nm up to 650 nm (2-10 eV).

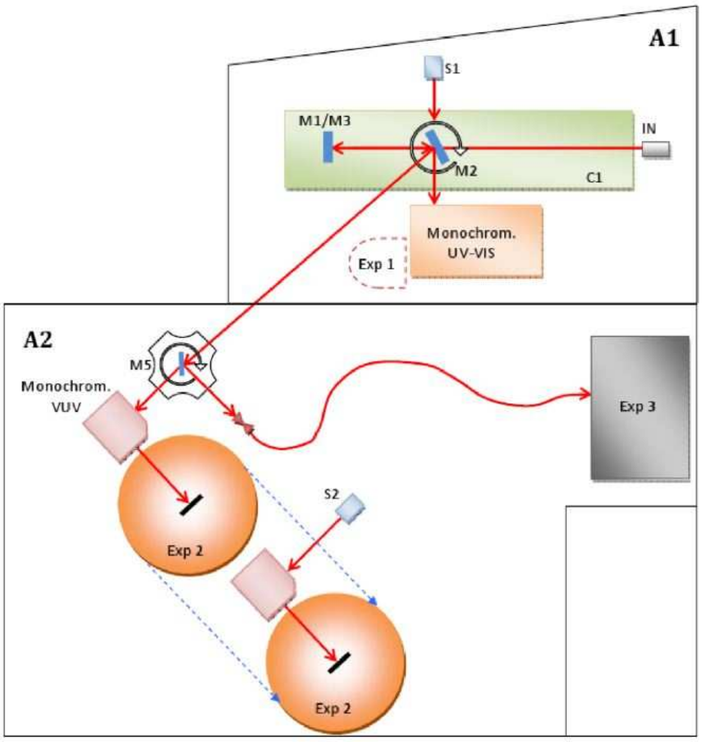

Figure 7: New schematic layout of the experimental apparatus at the exit of the VIS-UV beamline.

The first experimental area (EXP1) is irradiated by monochromatic VIS-UV SR in the wavelength range 180-650 nm after exiting the beamline and being collected by two focusing mirrors

(M1 and M3) and dispersed by a Czerny-Turner monochromator. This instrumentation was already available in a small hutch (A1) and has been refurbished and aligned. This light channel has been also provided by a 500 Watt Hg/Xe VIS-UV radiation source in order to perform experiments even when SR is off. This source is optically coupled to the entrance slit of the monochromator (the M2 flat mirror can be pulled up opening the optical path between the lamp and the monochromator) through a double-mirror system that has been fully developed and tested during 2009. The optical path in the area A1 has been enclosed in a vacuum chamber C1 that has been designed and produced during the last year. C1 includes the mirrors M1, M2 and M3, which are moved and aligned by vacuum feedthroughs, allowing x-y-z-θ movements and it is optically coupled to SR, the Hg-Xe lamp and the VIS-UV monochromator. The arrangement of the spherical mirror M2 can be substituted for another optical setup supporting the toroidal mirror M3, which is used to feed the VUV channel in the experimental area Exp.2 The optical design of the VIS-UV and VUV channels has been entirely revised during 2009 in order to educe the number of mirrors and thus improving the photon flux at the focus. The current arrangement is based on a spherical mirror (M1) and a flat mirror (M2) to send radiation at the entrance slit of the VIS-UV monochromator, while a toroidal mirror (M3) substitutes M1 to send radiation directly at the entrance slit of the VUV monochromator. This optical solution avoids a third mirror that previously was introduced to focus radiation. After impinging on M3 and M2, VUV SR beam is sent to the experimental areas EXP2 and EXP3 that are located in a clean room (A2, class 1000). The new layout of this arrangement is clearly visible in Fig. 7. The EXP2 HV chamber has been designed in order to perform any kind of optical experiments: r eflectivity, absorption, scattering, detector calibration, etc. A rotational stage, moving also along the z-axis can put any sample in the center of the chamber and in front of the focused SR beam. Another rotational stage, entering from the bottom, moves a C-shaped arm that can support a photon detector in order to measure the incident SR beam intensity or the reflected, diffused or scattered radiation at any angle from the incident beam direction.

A folding mirror, M5, can be introduced along the optical path to focus SR on a UV-grade optical fiber that brings SR to an optical bench (EXP3) where the beam can be used filtered or not for testing and calibration measurements of optical components and detectors or to irradiate any kind of material sample.

A 150 Watt D2 VUV radiation source can also be put in line when SR is off, thus allowing a full-time use of the facility. This can be achieved by replacing the VUV lamp for the SR channel at the entrance slit of the monochromator, because the optical aperture of the lamp is very similar to the aperture angle of the monochromator (F= 4.5). This system allows a much greater photon flux from the lamp to the focus after the monochromator. The instrumentation of this apparatus will be fully remotely controlled by software routines that have been specifically designed and developed in house by U. Denni and A. Frani. I/O peripherals and interfaces as well as data acquisition instrumentation have been installed in order to have a remote control of any experimental step and to facilitate the users. The just described experimental apparatus has been partially redesigned and mostly setup during 2009. All the nstrumentation has been already acquired. In the meantime, testing of vacuum components, testing of the remotely controlled movements, testing of the optical components, such as the mirrors and the MgF_2 and sapphire windows have been carried out. Wavelength calibration of the two monochromators has been performed and the remote control and data acquisition has been completed, solving also some major problems occurred to the VUV monochromator. Besides testing measurements, several experiments have been performed during the last year. Experiments on diamond detectors in the UV-VIS spectral region have been performed in order to have information on their photoresponse, in terms of sensitivity and time response. These measurements where related to the characterization of the same detectors in the X-ray range that has been performed at the NSRL and SSRF facilities in China and at GILDA-ESRF. These experiments provide the currently wider spectral response for diamond detectors, i.e. from 2 eV up to 50 keV. Experiments on organic materials have been also performed to provide some clues on the processes that could bring to the origin of life. The DXR-2 UV channel provides a high photon flux that opens new and unexplored opportunities for studying the impact of UV irradiation on biotic and organic materials. Laboratory experiments have shown that different chemical and physical mechanisms might be responsible for the richness of molecules observed in space. However, to describe the presence of more complex molecules, or radicals and even organic refractory material, irradiation processes due to ions and UV photons are required. Formamide is confirmed to be a promising route to understand the first chemical steps that brought simple C-bearing molecules towards largely complex mixtures of bio-macro-molecules. The experiment proposed was aimed at investigating the reactivity of the formamide in the presence of titanium dioxide. TiO_2 is an important photo-catalytic material, thus an experimental protocol must be developed to investigate the role of UV irradiation on bio-molecules formation. Mixtures of formamide with two mineral forms of titanium dioxide,anatase and rutile were irradiated with UV light . Preliminary results are very positive, but still under analysis. Once completed, that will be during 2010, the three light channels will be used for experiments in materials science as nano-carbons, wide bandgap materials, coatings, characterization and calibration of optical instrumentation for ground-based or space experiments, photobiology, astrobiology and search for the origin of life, medicine and mutations of organic and genetic materials, analysis of extraterrestrial materials, ecc.

2.4 New XUV beamlines

In 2009, the new XUV laboratory has continued its construction, based both on the detailed plans approved by the SRL Committee and on available resources. Aim of this laboratory is to host two bending Magnet beamlines covering the photon energy range from 30 eV to 1000 eV. One beamline will cover the low energy part of this interval (30-200 eV) and is called LEB (Low Energy Beamline), the other will cover from 60 eV to 1000 eV and is called HEB (High Energy Beamline).

All the optical and vacuum components of the LEB beamline did become available during 2008-2009, and the entire DAΦNE-L team worked to mount them in the foreseen position. Now the HEB optical system is ready to be commissioned with light at the restart of DAΦNE in 2010. The safety protocol and control systems havebeen completed (with the aid of the Control Service of Research Division) and tested. The 2009 has been also devoted to the optimization of a ″state of the art″ spectroscopic chamber, in order to be able to do angle resolved photoemission experiments, also at low temperature. This system has been tested at length during this year and a fast load lock system has been implemented in order to be able to change samples to be studied with LdS without breaking vacuum. A partial picture of this system is shown in Fig. 8. In parallel the optical elements and UHV vacuum chambers needed for the construction of the HEB, have been bought. Some have been delivered in our Laboratory during 2009, some (like the PGM monochromator) are still under construction and will be delivered in the first half of 2010. The final construction of this second beamline will follow the delivery of all the mechanical parts and is forseen to be

Figure 8: Picture of experimental chamber with: an angle resolving energy analyzer; a LT (10-300 K) close cycle manipulator; LEED; SEY measurement station; Farady cup; fast load lock system.

completed by 2010. Than we will be ready to commission it and deliver photons to users. Also for this beamline we are designing and assembling an experimental set-up to be able to perform SR photoemission and absorbtion spectroscopy in UHV condition. The setup will be ready within next year thanks to the active collaboration with R. Larciprete (C.N.R.) both for uman resources and goods.

References

1. M. Pociask et al., Phys. Status Solidi C **6**, 2016 (2009).
2. J. Polit et al., Phys. Status Solidi C **6**, 2012 (2009).
3. A. Marcelli et al., Phys. Status Solidi C **6**, 1999 (2009).
4. M. Baldini et al., Phys. Rev. B **80**, 045123 (2009).
5. C. Petibois et al., Nature Photonics **3**, April (2009).
6. E. M. Sheregii et al., Phys. Rev. Lett. **102**, 045504 (2009).
7. A. Voloshyovskii et al., P. Savchyn, I. Comm. **149**, 593 (2009).
8. P. Innocenzi et al., Analytical Chemistry **81**, 551 (2009).
9. A. Nucara et al., J. Supercond. Nov. Magn. **22**, 13 (2009).

GILDA

A. Balerna, A. Grilli (Tecn.), S. Mobilio (Resp.), A. Raco (Tecn.),
V. Sciarra (Tecn.), V. Tullio (Tecn.)

1 Introduction

GILDA (General Purpose Italian beamLine for Diffraction and Absorption), is the Italian CRG beamline, built to provide the Italian scientific community with an easy access to the European Synchrotron Radiation Facility to perform experiments with a high energy and brilliance X-ray photon beam. GILDA was proposed, designed, constructed and commissioned by a collaboration between LNF and a large number of University groups; it is operative since autumn 1994. Today GILDA is funded by the Italian public research Institutes: Consiglio Nazionale delle Ricerche (CNR) and Istituto Nazionale di Fisica Nucleare (INFN). Experimental stations for X-ray Absorption Spectroscopy, Anomalous X-ray Scattering and X-ray Diffraction (XRD) are present on the GILDA beamline.
The LNF group is involved in the technical maintenance and update of the beamline, with particular emphasis to the electronic and software controls of all the instrumentation and to the apparatus for X-ray diffraction.

2 Summary of the Activity on the GILDA beamline during 2008

During 2008 the main technical works performed on the instrumentation were the test of a Laue diffracting crystal for fluorescence detection, the design, realization and commissioning of the new motorized sample holder for measurements at grazing incidence with high accuracy, a software programme for a complete quantitative data analysis of the ReflEXAFS spectra.
During 2008 about 4000 hours of the 5300 delivered by the ESRF were used for user's experiments, the remaining for in-house research, beamline improvements, maintenance and alignment. Totally 37 experiments were performed, 25 of Italian users and 12 of European users.
Among the relevant studies performed, we mention the study of the exchange bias effect in Ni/NiO nano-granular alloys; the local structure of Mn-rich nanocolumns; the temperature dependence of the structural parameters of gold nanoparticles and the photoresponse of diamond based solid state ionization chambers.

3 Activity on the GILDA beamline during 2009

During 2009 some implementations on the instrumentation were performed both to increase the reliability of the beamline and its compatibility with the ESRF standard instrumentation. Namely:

1. the vacuum control system of the beamline was upgraded in a new version fully compatible with the ESRF standard one;

2. a new software developed by the ESRF, which control all the items of the front end of the beamline through a single interface, was installed and commissioned;

3. the cooling system of the first mirror was modified to increase the mirror stability;
4. the motor control system in the absorption hutch was upgraded to the ESRF standard icepap based one.

4 Beamtime use during 2009 and scientific outcomes

During 2009 ESRF delivered beam for about 5300 hours; about 4000 hours were used for user's experiments, the remaining for in-house research, beamline improvements, maintenance and alignment. Totally 34 experiments were performed, 16 of Italian users and 18 of European users.
Studies and results to be mentioned are the followings:

1. *The nature of disorder in ordered double perovskite, Sr_2FeMoO_6 oxides*
   C. Meneghini, Sugata Ray, F. Liscio, F. Bardelli, S. Mobilio, D. D.Sarma , Phys. Rev. Lett. **103**, 046403 (2009).
   The degree of B/B' alternate cation order is known to heavily influence the magnetic properties of $A_2BB'O_6$ double perovskites although the nature of such disorder has never been critically studied. Our detailed x-ray absorption fine structure studies in conjunction with synchrotron radiation x-ray diffraction experiments on polycrystalline Sr_2FeMoO_6 samples with various degrees of disorder reveal that a very high degree of short range order is preserved even in samples with highly reduced long range chemical order. Based on these experimental results and with the help of detailed structural simulations, we are able to model the nature of the disorder in this important class of materials and discuss the consequent implications on its physical properties.

2. *Proton dynamics in In:BaZrO3: insights on atomic and electronic structure from X-ray absorption spectroscopy*
   F. Giannici, A. Longo, A. Balerna, K.-D. Kreuer and A. Martorana, . Chem. Mat. **21**, 2641 (2009).
   The local structure of Ba^{2+}, Zr^{4+} and In^{3+} in $In : BaZrO_3$ is investigated with EXAFS for samples having 0 to 75% In^{3+} content. It is found that indium can be inserted in any ratio in the host matrix oxide and that the oxygen coordination shell displays an in-O distance very similar to the Zr-O length. In the Zr-rich compositions, there is a preferred dopant-vacancy association that, however, does not give rise to dopant-proton interaction in the hydrated samples. The tendency of Ba^{2+} to be attracted toward the dopant site is attributed to the electrostatic interaction with the dopant and to the structural rearrangement around the In^{3+} site. Third cumulant analysis at high temperatures (up to 673 K) allows to conclude that the anharmonicity of In-O thermal motion is about 1 order of magnitude lower than in other perovskites with higher proton conductivity. It is argued that the lower proton diffusivity displayed by $In : BaZrO_3$ depends on (a) proton trapping at the dopant site due to the formation of a stable O-H3 3 3O hydrogen bond; (b) reduced anharmonicity of the M-O vibrations; (c) different strength of O-H bonds originated by electronic density rearrangement

3. *Ag site in Ag-for-Na ion-exchanged borosilicate and germanate glass waveguides*
   C. Maurizio, A. Quaranta, E. Ghibaudo, F. D'Acapito, J.-E. Broquin, J. Phys. Chem. C

113, 8930-8937 (2009).
The Ag site in Ag-for-Na ion-exchanged borosilicate and germanate waveguides has been investigated by EXAFS spectroscopy. In contrast with the results generally reported in literature, it is shown that, for both silicate and germanate waveguides, the Ag site is strongly dependent on the Ag content and the Ag-O distance is longer for higher doping levels. It is demonstrated that this trend is related to a structural rearrangement of the Ag site in the whole doped layer; the EXAFS results on the samples that underwent the ion exchange at higher temperatures and the comparison with literature data suggest that the sites with shorter distances are more stable. The correlation between local structure around Ag and the photoluminescence properties of the borosilicate waveguides is established. In particular, the red shift of the blue band observed in the absorption and excitation spectra by increasing the Ag concentration has been univocally related to the increase of the Ag-O bond length.

4. *Local structure of (Ga,Fe)N and (Ga,Fe)N:Si investigated by x-ray absorption fine structure spectroscopy'*
M. Rovezzi, F. D'Acapito, A. Navarro-Quezada, B. Faina, T. Li, A. Bonanni, F. Filippone, A. Amore Bonapasta, T. Dietl, Phys. Rev. B. **79**, 195209 (2009).
X-ray absorption fine-structure (XAFS) measurements supported by ab initio computations within the density functional theory (DFT) are employed to systematically characterize Fe-doped as well as Fe- and Si-codoped films grown by metalorganic vapor-phase epitaxy. The analysis of extended-XAFS data shows that depending on the growth conditions, Fe atoms either occupy Ga substitutional sites in GaN or precipitate in the form of Fe_3N nanocrystals, which are ferromagnetic and metallic according to the DFT results. Precipitation can be hampered by reducing the Fe content, by increasing the growth rate, or by codoping with Si. The near-edge region of the XAFS spectra provides information on the Fe charge state and shows its partial reduction from Fe^{+3} to Fe^{+2} upon Si codoping, in agreement with the Fe electronic configurations expected within various implementations of DFT.

5 Beamline Review Panel and future plans

At the end of 2009 the memorandum of understanding between the ESRF and the Italian Institutions INFN and CNR which regulates the beamline activity expired; in view of a renewal of the memorandum in spring 2009 ESRF organized a Review Panel made of internationally well known scientists experts in the field, which reviewed the GILDA scientific activity of the last five years. The Panel judged the activity of excellent quality and suggested ESRF to renew the memorandum and continue the activity for the next five years. This possibility is under consideration of the CNR and INFN.
Moreover since ESRF is doing an extensive refurbishment of the storage ring and of the beamlines, the Panel recommended also a renewal of the beamline instrumentation. At this purpose in December 2009 a two days User Meeting was organized at the University of Palermo for discussing the beamline refurbishment to be implemented during the ESRF shutdown in 2012, to review the scientific activity of the last years and to define a scientific case for the next years. A complete report on the meeting and on the conclusions achieved will be available in the next weeks and will be submitted to the INFN and CNR.

6 2010 - GILDA Forseen Activity

During the 2010 the activity foresees:

1. the beamline running by approved experiments for at least 4000 hours of user activity;
2. to complete the proposal of beamline refurbishment;
3. to complete the standardization of the beamline motor control

7 Publications

1. C. Meneghini et al., Phys. Rev. Lett. **103**, 046403 (2009).
2. F. Bardelli et al., J. Phys.: Condens. Matter **21**, 195502 (2009).
3. T. Comaschi et al., J.Phys.: Condens. Matter **21**, 325404 (2009).
4. F. Giannici et al., Chem. Mat. **21**, 597 (2009).
5. F. Giannici et al., Chem. Mat. **21**, 2641 (2009).
6. C Meneghini et al., J. Phys.: Condens. Matter **21**, 355401, (2009).
7. T. Comaschi et al., J. Phys.: Conf. Ser. **190**, 012122 (2009).
8. M. A. Soldatov et al., J. Phys.: Conf. Ser. 1**90**, 012210 (2009).

NTA CLIC

D. Alesini, C. Biscari, B. Buonomo, M. Castellano, A. Ghigo (Resp.),
F. Marcellini, M.A. Preger, M. Serio, A. Stella, C. Vicario (Art. 23)

1 Introduction

The Compact LInear Collider (CLIC) is an electron-positron collider with a c.m. energy up to 3 TeV based on two-beam acceleration scheme. The construction and commissioning of the CLIC Test Facility CTF3 are almost completed at CERN; the aim of the facility is the feasibility demonstration of the acceleration gradient of 100MeV/m, provided by high power 12 GHz radiofrequency. The 12 GHz RF power is generated decelerating a powerful electron drive beam in power extraction structures: the power is transferred to the 12 GHz structures in which the main beam is accelerated.

The INFN Frascati Laboratory (LNF) designed the two rings of the drive beam recombination system in the framework of CTF3-CLIC international collaboration. The first ring, named Delay Loop, was realized under LNF fully responsibility, installed in 2005 in the existing building at CERN and commissioned in 2006. INFN was in charge of the construction of the RF deflectors, the vacuum chambers, the wiggler and diagnostics of the second ring (Combiner Ring), installed in 2006 and completed in 2007.

In 2008 the commissioning of the ring continued sharing the machine time with the installation of the CLIC experimental area. In 2009, after the change of the two RF deflectors with new one, the recombination at full current was proven with the multiplication of factor 8 of the linac current, achieving the project value of 28 A.

2 LNF group contribution in the year 2009

During the Combiner Ring commissioning a strong vertical instability had been observed at high current and long pulse. After dedicated measurements, the source of this instability has been detected in the two RF deflectors that provide the injection in the ring.

The LNF group studied, realized and installed and commissioned the two new RF deflectors in which the high order modes, responsible of the vertical instability, have been absorbed by antennas introduced in the cavities. The instability disappeared and after a short commissioning period the high current foreseen in the project was achieved. The linac pulse train, 1.4 μsec long with bunch frequency of 1.5 GHz and current 3.5 A, was injected in the Delay Loop. At the Delay Loop exit a series of 4 pulses 140 nsec long, 3 GHz and 7A have been produced. These four pulses have been injected in the Combiner Ring, interleaving the bunch trains, producing a current of 28A on 140 nsec pulse duration at 12 GHz frequency (see Fig. 1).

The extraction line from the ring has been also commissioned and the high current beam sent to the CLIC experimental area through the transfer line. The high RF power has been produced in the 12 GHz power extraction structure and used to test the 12 GHz accelerating structures. The

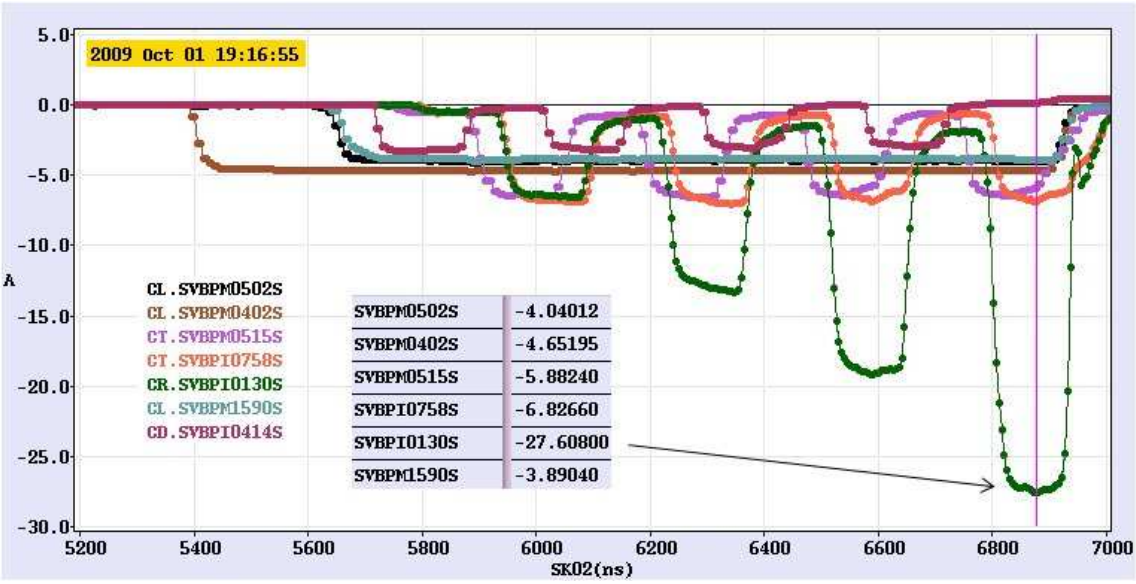

Figure 1: (color online). Measured currents at: Gun exit (brown); Delay loop entrance (grey); Delay loop exit (orange); Combiner Ring (green).

following characteristics of the Delay Loop and Combiner Ring have been measured: the tune, the dispersion, the orbit and path length, the isochronicity. The check of the optical function respect to the lattice model has been also performed.

3 Foreseen activity of the LNF group during year 2010

In 2010 the foreseen activities include:

- The participation to the commissioning of the two-beams test stand and of the power extraction and transfer structure.
- The measurements of the bunch length and bunch spacing with the streak camera now installed on a synchrotron radiation line of the Combiner Ring.
- The study and realization of the phase monitor that permits the test of the synchronization of the CLIC drive beam with the main beam.
- The participation to the CLIC Conceptual Design and to the entire CLIC Test Facility scientific program.

4 References

1 D.Alesini et al., *The new RF deflectors for the CTF3 Combiner Ring*, Proc. of PAC09, Vancouver, BC, Canada, WE1PBC04.

2 C.Biscari et al., *CLIC drive beam frequency multiplication system design*, Proc. of PAC09, Vancouver, BC, Canada, WE6PFP076.

NTA DISCORAP

G. Celentano (Ass.), A. Della Corte (Ass.), U. Gambardella (Resp.)

1 General program

The DISCORAP (DIpoli Super COnduttori RApidamente Pulsati) program comes from the need of fast ramped superconducting dipoles for the SIS 300 of the FAIR accelerator complex at GSI, Darmstadt, Germany. The four years program includes the development of a fully working, bent (66.6 m bending radius) dipole 3.8 m long in its horizontal cryostat. The dipole peak field is 4.5 tesla with a ramping rate of 1 tesla/sec [1)]. Among other requirements it has to keep dissipations at reasonable levels as well as to generate low harmonic contents [2)]. Three INFN sections are involved: Genova (group leader), Milano LASA, and LNF, in cooperation with Ansaldo Superconduttori Genova, Italy, and LUVATA Pori, Finland. The LNF group in 2009 took care of the wire characterizations, analyzing NbTi superconducting wires for low losses applications developed within the framework of our program as well as of the design and manufacture of the horizontal cryostat.

2 Resume of the 2009 LNF group activities

The activity on NbTi wire characterization has been devoted either to refine further techniques to increase the capability of measuring the transverse resistivity ρ_{et}, or to test the first wire prototypes specifically developed for the DISCORAP magnet. The coupling (*ac*) losses among the superconducting filaments, are one of the relevant losses for the dipole, being $\approx 25\%$ of the total losses. These losses are due to the closing current loops through normal conducting part of the wire: the less these currents the lower the dissipation. A way to decrease these induced currents is to increase the resistivity around the superconducting filaments. Using the *ac* magnetic susceptibility option in the VSM magnetometer, we analyzed the in phase susceptibility signal χ" coming from the voltage picked up around the sample, as a function of the frequency excitation in the primary coil. This signal is related to the *ac* losses in the NbTi wire [3)]. The losses, after a normalization, show a peak in the frequency dependence, which corresponds to the characteristic frequency of the NbTi wire. This frequency is also reported as the wire characteristic time $\tau = 1/(2\pi f)$. For sample length larger than the twist pitch L_p we have $\rho_{et} = (\mu_0/2\tau)(L_p/2\pi)^2$. In Figure 1 is shown the transverse resistivity ρ_{et} in a NbTi wire with a 2.5 μm filament size computed from the measured characteristic frequencies at different magnetic field strengths.

The Frascati group is also in charge of the design and procurement of the horizontal cryostat for the bent DISCORAP dipole. Our design was based on the latest dipole design (LHC, RICH, etc.) including plastic supports for the cold mass. However, the bending of our dipole made the design difficult. In fact, in spite of the straight geometry of the outer shell, the mechanical analyses revealed new problems on the mechanical stability of the dipole, which have to be supported by the cryostat pillars and structure. In 2009 we made the bid for the executive design and manufacture of the cryostat. The five plastic POSTs were commissioned from CERN in the framework of a

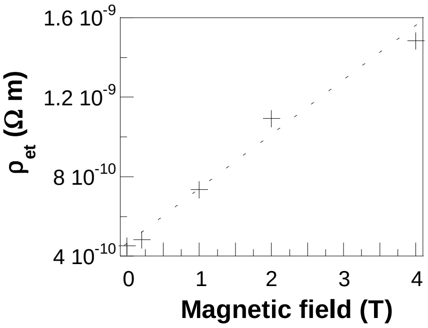

Figure 1: ρ_{et} extracted from the measurement of the characteristic frequency in a multifilament NbTi wire at different applied magnetic field.

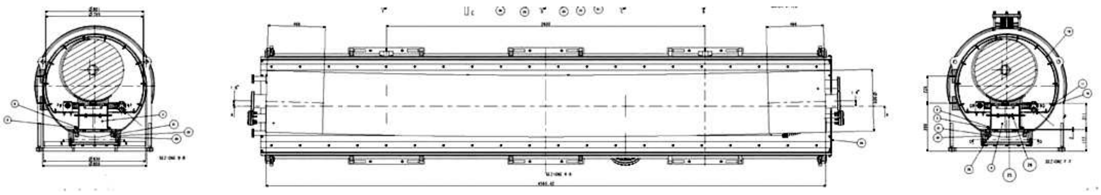

Figure 2: Vertical and horizontal cross sections of the cryostat with the cold mass. The bending of the magnet follows the central beam tube.

wider POSTs manufacture to replace CERN stock. SIMIC S.p.A., Camerana (CN), Italy won the bid and it is now processing our design to set a complete executive design. Soon after will start procurement of materials, and manufacture. The delivery of the cryostat is foreseen by July 2010. In this year also the cold mass will be completed by AS-G SUperconductors, and it will be tested at Milano LASA in a vertical cryostat. After these tests we will integrate the cold mass into the horizontal cryostat and will ship everything to GSI, Darmstadt by the end of 2010. At GSI in 2011 will be carried out the final tests with supercritical He.

References

1. S. Farinon et al., IEEE Appl. Supercon. **19**, 1141 (2009).

2. M. Sorbi et al., IEEE Appl. Supercon. **19**, 1131 (2009).

3. P. Fabbricatore et al., J. of Appl. Phys. **106**, 083905 (2009).

NTA ILC

D. Alesini, M. E. Biagini, R. Boni, R. Cimino, A. Ghigo, S. Guiducci (Resp.),
F. Marcellini, P. Raimondi, A. Stecchi

1 Introduction

The INFN has contributed to the GDE (Global Design Effort) for the International Linear Collider (ILC) since the beginning in 2005 with a qualified participation to the project design and R&D. The LNF activity is focused on damping rings and consists of studies and simulations and on the realization of prototypes of some critical elements. The possibility of making experimental observations at DAΦNE offers a great opportunity to test simulation studies and prototypes. This activity is fully integrated at the international level: within the GDE LNF has the responsibility of the Damping Rings (DR) area system.

2 Year 2009 Activities

The crucial R&D issues for the Damping Rings are simulation and mitigation of the e-cloud instability, fast kickers and low emittance tuning. The first two issues are the objective of R&D at DAΦNE, which is considered as a test facility for the DR, together with CesrTA and KEK-ATF. In 2009 LNF have coordinated the R&D activity on damping rings with a significant contribution in the preparation of the SB2009 Proposal a new configuration of the accelerator to be used as a base for the next phase of Technical Design. This proposal includes the lattice design for a DR with half the circumference with respect to the present reference design (3.2 km instead of 6.4 km), an evaluation of the critical aspects and the work needed to define the operating performances. LNF made the lattice design, based on periodic cell similar to that of the SuperB collider and has participated to the simulation work for the evaluation of the effects of the electron cloud in positron ring.

The electron cloud instability could produce limitations of the storable current or deterioration of the vertical emittance in the positron DR. Studies performed at DAΦNE have shown a good agreement between simulations and experimental data showing that the instability is mainly due to the high density of the electron cloud in the dipole and wiggler magnets. Therefore clearing electrodes have been designed and realized in order to reduce by more than one order of magnitude the e-cloud density in the dipole and wigglers vacuum chambers.

The realization of fast kickers with pulse rise/fall times shorter than 3 ns is one of the very high priority issues in the GDE R&D plan. In 2009 fast kickers with pulse rise/fall times of less than 6 ns and maximum voltage of 24 kV have been operated on the DAΦNE electron ring for about two months, demonstrating the design performance and a high temporal stability. A new ultra fast kicker, with pulse duration suitable for the 3 ns bunch distance, has been realized. This kicker, designed to get a low beam impedance, will be tested at KEK-ATF2, the beam delivery international test facility.

3 Plans for Year 2010

The LNF activity will continue to focus on damping rings and in particular on fast kickers and e-cloud studies. The comparison between simulations and experimental observations at DAΦNE will continue in order to improve the comprehension and mitigate the electron cloud instability. Electron clearing electrodes have been installed in DAΦNE and the effects on the beam, including e-clooud density and beam impedance, will be tested at the machine start-up after the KLOE detector installation. Continuing the research on e-cloud mitigation techniques It is also foreseen to realize a sputtering system for thin film deposition on vacuum chamber samples.

The new fast kickers will be tested for continuous operation at DAΦNE. The new ultra fast kicker, with pulse duration suitable for the 3 ns bunch distance, will be tested at KEK-ATF2. The optimization of the optical structure and dynamic aperture for a half circumference DR, proposed for the new reference configuration, will continue in 2010. LNF keeps the responsibility of the damping rings for the definition of the new reference configuration to be adopted for the Technical Design.

4 Publications and Talks

1. F. Marcellini et al., *Tests and Operational Experience with the DAΦNE Stripline Injection Kicker*, Proc. of PAC09, Vancouver, Canada, (2009).

2. F. Marcellini, D. Alesini, *Strip line kicker design*, presented at TILC09 - joint ACFA Physics and detector workshop and GDE meeting on the International Linear Collider, Tsukuba, Japan, April 17-21, 2009.

3. S. Guiducci, *Damping Rings*, presented at TILC09 - joint ACFA physics and detector workshop and GDE meeting on the International Linear Collider, Tsukuba, Japan, April 17-21, 2009

4. S. Guiducci, *Update on ILC Accelerator Design and Linear Colliders R&D", Pres. at LC09 e+e- Physics at the TeV Scale and the Dark Matter Connection*, Perugia, 21-24 September 2009.

5. S. Guiducci, M.E. Biagini, *SB2009 lattice update*, presented at LCWAS Linear Collider Workshop of the Americas, September 29-October 3 2009, Albuquerque, New Mexico.

6. S. Guiducci, *ILC damping rings and common design issues with CLIC*, Pres. at CLIC09 Workshop, CERN, 12-16 October 2009.

7. D. Alesini, *ILC kicker design*, Pres. at CLIC09 Workshop, CERN, 12-16 October 2009.

8. F. Marcellini, D. Alesini, ICFA Beam Dyn. News Lett. **50**, 64 (2009).

NTA PLASMONX

S. Bellucci, S. Bini, M. Castellano, A. Clozza, L. Cultrera, G. Di Pirro, A. Drago, M. Esposito, M. Ferrario, D. Filippetto, A. Gallo, G. Gatti, P. Gaudio, A. Ghigo, G. Giannini, A. La Monaca, T. Levato, F. Micciulla, M. Migliorati, D. Nanni, E. Pace, L. Palumbo, A. Petrucci, M. Richetta, C. Sanelli, A. Tenore, F. Terra, S. Tomassini, C. Vaccarezza, C. Vicario
Laboratori Nazionali di Frascati

C. Benedetti, G. Turchetti
Sezione INFN Bologna

A. L. Bacci, F. Broggi, M.M. Cola, A. Flacco, C. Maroli, M. Passoni, V. Petrillo, N. Piovella, R. Pozzoli, M. Romé, A. R. Rossi, L. Serafini
Sezione INFN Milano

D. Batani, R. Benocci
Sezione INFN Milano Bicocca

C.A.Cecchetti, A.Gamucci, D.Giulietti, L.A.Gizzi,
L.Labate, N.Pathak, F. Piastra
Intense Laser Irradiation Laboratory, INO-CNR and Sezione INFN, Pisa

N. Drenska, R. Faccini, P. Valente
Dip. Fisica Univ. La Sapienza, Roma

1 Introduction

In the 2009 the NTA-PLASMONX project [1] has seen the completion of the FLAME-laboratory and the installation start of the laser system previously tested at the Amplitude Technologies Laboratories. The main subsystem have been installed: the clean room, the laser, the cooling and the conditioning systems.
A self-injection test experiment (SITE) has been planned to establish the performance of the FLAME laser system and to assess the degree of control of critical laser parameters. The experimental setup has been realized and the study of a suitable MultiGev spectrometer has been performed to provide a device able to characterize the momentum of the GeV-class self-injected electrons of the SITE experiment. First measurement on a prototype have been carried on at the BTF facility at LNF.
The Interaction Region layout has been completed for the Thomson source experiment driving the procurement of the magnetic elements for the electron beam focusing system and of the multi-way vacuum chamber for the interaction point. The magnetic elements and the power supplies for the electron beam transfer lines have been committed together with the main components of the radiation transportation in vacuum. The description of this activity is given in the following.

2 FLAME

The FLAME laser (Amplitude Tech.) is based upon a Ti:Sa, chirped pulse amplification (CPA) system that will deliver 20 fs, 800 nm, up to 300TW, laser pulses with a 10Hz repetition rate at a fundamental wavelength of 800 nm. The system features a high, sub-ns contrast ratio ($> 10^{10}$) and has a fully remotely controlled operation mode. In the experiment, the main laser pulse is focused onto a gas-jet target using an F/10 off-axis parabola at a maximum intensity above $5 \times 10^{19} W/cm^2$.

Several optical and high-energy diagnostics including Thomson scattering, optical interferometry , scintillators coupled to photomultipliers, a phosphor screen (LANEX) and custom dose sensitive, radiochromic film stacks are under implementation to investigate laser-target interaction and the accelerated electrons. The 2009 has seen mostly the progress of the laser system installation and the fundamental steps can be summarized as follows:

- Jan-Mar: Laser system delivery at LNF completed
- May: Clean Room installation started
- Jun: "Cold" FLAME installation started: components in place
- Aug: Clean room fully operational
- Sep: FLAME laser start up: oscillator start-up and YAGs connections
- Oct: Compression test below 100 mJ level, YAGs pre-alignment and training
- Nov: Main amplifier pumps alignment, cryo amplifier installation (see figure 1)
- Dec: Main compressor optics aligned (see figure 2)

Figure 1: Main amplifier pumps alignment, cryo amplifier installation.

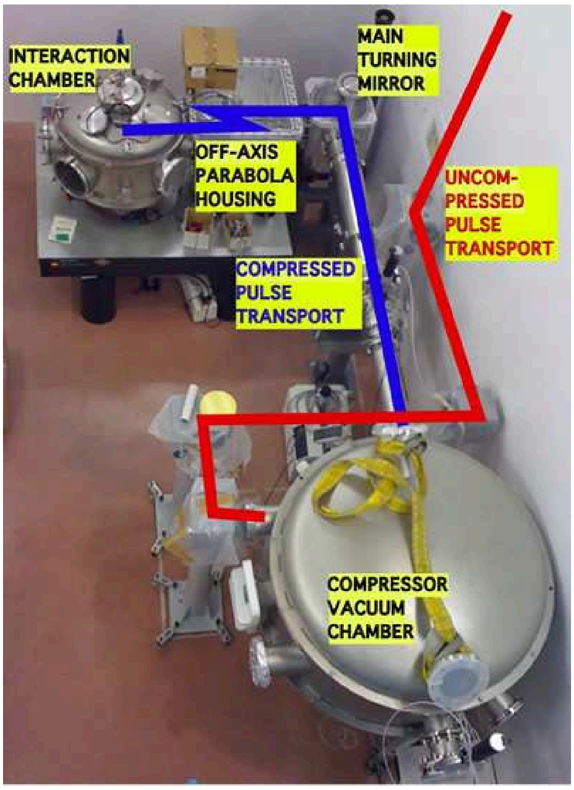

Figure 2: The SITE experiment setup with the main compressor optics aligned.

3 The SITE experiment

The self-injection test experiment at FLAME [2] aims at generating GeV-class electron bunches from laser-plasma interaction using a gas-jet of a few millimeters, working in the so-called bubble regime [3–5]. In the bubble regime a short ($c\tau < \lambda_p/2$) and intense ($a_0 > 2$) laser pulse expels the plasma electrons outward creating a bare ion column. The blown-out electrons form a narrow sheath outside the ion channel and the space charge generated by the charge separation pulls the electrons back creating a bubble-like wake. For sufficiently high laser intensities ($a_0 > 4$) electrons at the back of the bubble can be injected in the cavity and where the longitudinal accelerating field is of the order of $100\sqrt{n(cm^3)}V/m$ [7] . The FLAME laser meets both the two conditions of short pulse length and high intensity. As a consequence when the laser pulse impinges onto the gas-jet it promptly excites (without significant pulse evolution) a bubble wake where electrons are readily injected and so the entire gas-jet length can be utilized for the acceleration process. In order to have a controlled acceleration mechanism, which ensures a better final bunch quality, the plasma and laser parameters must be chosen according to the phenomenological theory described in [6]. A possible working point for the SITE is described in table 1.

In this case, following [6], a quasi-monochromatic (few % momentum spread) bunch is expected with a charge of 0.6 nC and an energy of approximately 1.0 GeV after 4mm (dephasing length). The acceleration process has been investigated also through 3D PIC simulations performed

Table 1: A possible working point of the test experiment on laser-acceleration at FLAME.

$L\_gasjet(mm)$	$n_p(e/cm^3)$	$\tau(fs)$	$I_0(W/cm^2)$	$w_0(\mu m)$
4	3×10^{18}	30	5.2×10^{19}	16

with the fully self-consistent, relativistic, electromagnetic PIC code ALaDyn [8, 9]. At the end of the simulation we obtained a bunch with an energy of 0.9 GeV and a momentum spread (rms) of 3.3 %, the charge is 0.6 nC, the bunch length is 1.8μm (the average current is 50 kA) and the beam divergence (rms) is 2.8 mrad. In Fig. 3 the resulting electron density at the end of the simulation is shown together with the. corresponding energy spectrum that shows two components, a peak with total charge $\approx 700pC$ at high energy (around 900 MeV) and a $\approx 3nC$ low energy tail.

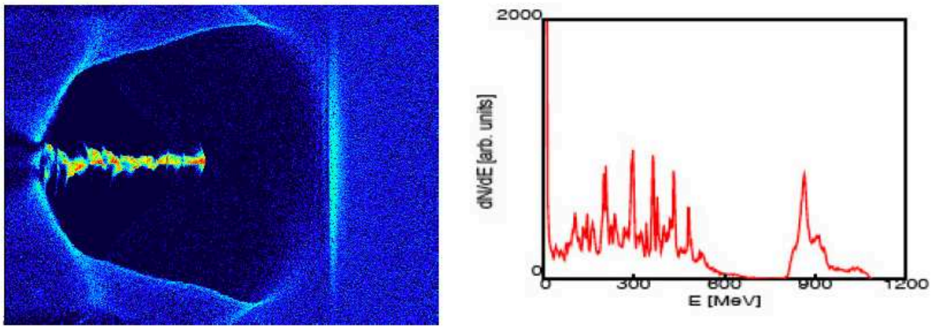

Figure 3: Results of the 3D PIC simulation: (left) electron density distribution shortly before the end of the acceleration and (right) out coming energy spectrum.

4 The Multi-GeV Electron Spectrometer

As shown in these simulations, experiments at FLAME will enter the GeV regime with almost 1nC of electrons. A spectrometer is being constructed to perform these measurements and it is made of an electro-magnet and a screen made of scintillating fibers for the measurement of the trajectories of the particles. From the high-energy point of view, this detector represents a challenge because it must measure the momentum spectrum of tens of millions of particles arriving simultaneously spread over three order of magnitudes in momentum (10 MeV to 10 GeV), and with a large (2mrad) divergence. Since the goal of the experiment is to find the optimal configuration to reduce the low energy tail and shrink the distribution of the high energy portion of the spectrum, the whole spectrum needs to be retained for all bunches. It is therefore not foreseen any form of focusing before the spectrometer (e.g. quadrupoles) since this would select only portions of the momentum spectrum. The transport of the electron bunches from the exit of the plasma to the spectrometer has been simulated with a 3D parallel tracking code for the beam dynamics of charged particles [10] in order to test possible collective effects in such high charge bunches. The position of the electrons when impacting on the optimized detector of the spectrometer as described later is shown in Fig.

4 with and without considering the electromagnetic interactions among the electrons. The effect is negligible, the resolution being dominated by the angular divergence of the beam at origin.

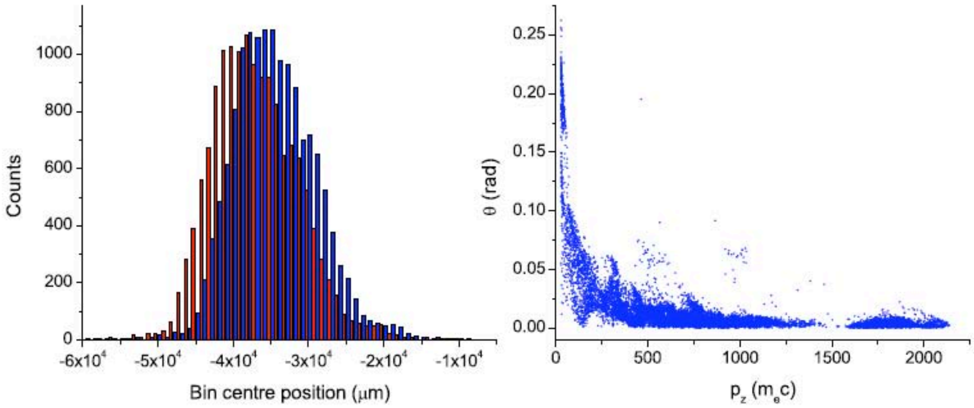

Figure 4: Left: generated (red) and reconstructed (black) momentum distributions overlayed. Right: resolution on momentum (blue squares) and the contribution from the position measurement only (red dots). The difference between the two is an estimate of the angular divergence.

For the purpose of designing the spectrometer, which is insensitive to the vertical position of the particles and to their direction of flight when impacting the detector, it is therefore sufficient to consider the motion of the particles on the horizontal plane (i.e. the one perpendicular to the magnetic field). This justifies why in the following the bunch is treated as a beam of independent particles coming from a point-like source located at the end of the gas-jet and with an angular divergence estimated with the simulation. Fig. 4 shows that the high energy particles are contained within 2 mrad, while the low energy tail can have a significantly larger divergence. To shorten the spectrometer set up schedule a spare magnet from the SPARC experiment will be employed, therefore the results shown below refer to an available but non-optimal magnetic setup. In Fig. 5 the experimental set-up is shown where the position detectors are located in such a way to intercept the low energy electrons (up to 150 MeV) at the focii of their trajectories and to collect as far as possible the higher energy ones in order to maximize the resolution of the energy measurement with the dispersive element.

A scintillating fiber detector has been chosen that could operate in vacuum, tolerate a large number of impacting particles and be of limited cost. The scintillating fibers Ku- raray SCSF-81-SJ with diameter $1.00 \pm 0.05mm$ have $50 \pm \mu m$ thickness of cladding and emission wavelength 437 nm. Fibers are connected to fvie multi- channel photo-tubes Hamamatsu H7545 (R7600-00) for a total of five PMT and 320 electronic channels. In order to read a larger number of fibers, since the overall resolution is not affected, the fibers coming from the low momentum detector are merged in groups of three. The choice of the front end card was studied in collaboration with INFN BA, GE and ISS-Roma1 [11].

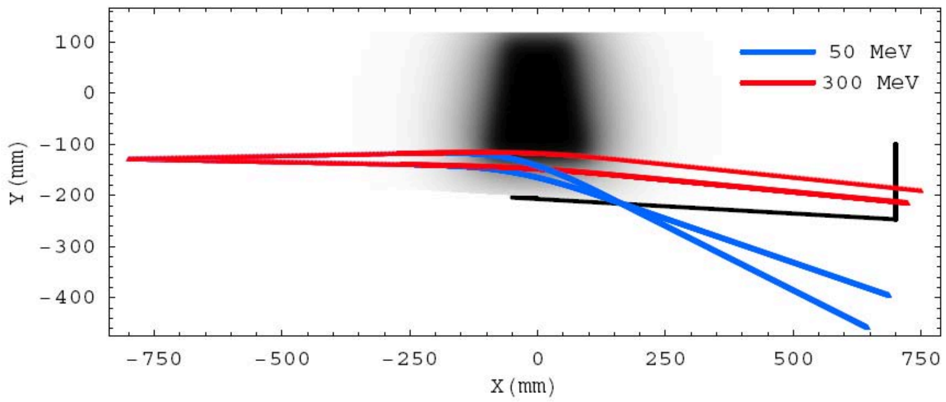

Figure 5: Trajectories in the available magnetic setup of particles with fixed momenta and divergence angle = ± 2 mrad. The position detectors are located along the black lines.

4.1 Estimated detector performance

Fig. 6 shows the effect of resolution from a fast simulation of almost mono- energetic beams. The worsening of the reconstruction with increasing momentum is clear. We also estimate the resolution of the detector, separating the intrinsic detector resolution caused by the physical dimension of the fibers (1mm of diameter) and the angular divergence. Fig. 6 shows the total resolution as a function of the momentum and the component due to the detector granularity. Performances between low and high detector will be different mainly because of the angular effect for the high energies. The pointing instability of the laser was also studied and our results show that the situation shown above is not significantly different even if these effects are of the order of degree. We can conclude that with the Prototype it is possible to measure energies up to 200 MeV with a very good resolution less then 1% and the resolution remains less then 5% up to about 500 Mev.

4.2 Tests with a prototype

A prototype with 64 fibers read by one PMT has been built and tested with electrons at the Frascati Beam Test Facility (BTF [12]) and in laboratory with LEDs. At the BTF test the electron beams was passing through the magnet that will be part of the detector, so that we could test the existence of the focii and the understanding of the fringe field region. The fact that the trajectories lie in the fringe area is in fact one the major concerns for this device. Fig. 7 shows that moving the beam from the center of the magnet to the fringe, the resolution, due to multiple scattering in air, improves and that the deviation of the beam as a function of the beam position is well reproduced by the numerical calculation.

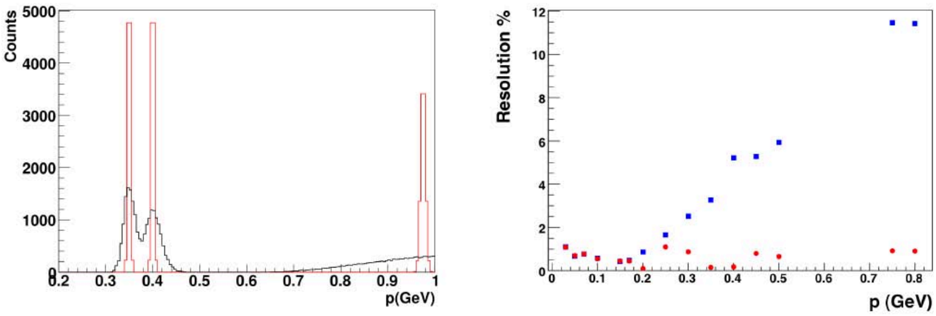

Figure 6: Left: generated (red) and reconstructed (black) momentum distributions overlayed. Right: resolution on momentum (blue squares) and the contribution from the position measurement only (red dots). The difference between the two is an estimate of the angular divergence.

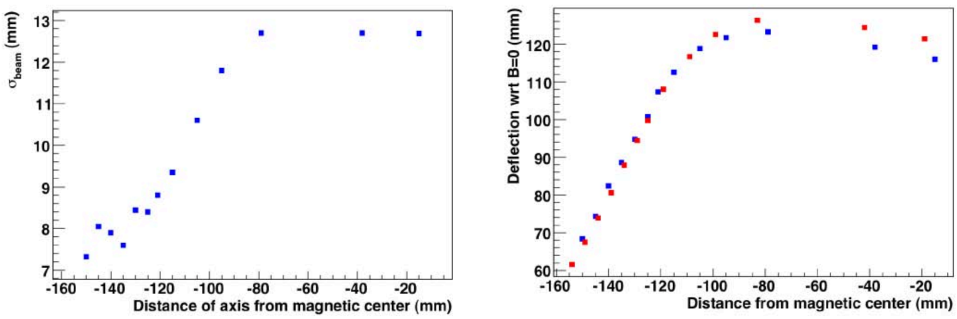

Figure 7: BTF test beam: (left) measured resolution as a function of the distance from the magnetic center and (right) comparison between prediction (red) and measurement (blue) for the beam deflection as a function of the position of the beam wrt the magnetic center.

5 The Thomson Source

Several experiments are foreseen within this facility, among the others: high gradient plasma acceleration as much as the production of monochromatic ultra-fast X-ray pulses by Thomson back-scattering(TS), which is hereafter pointed out [13]. TS X-ray source is attracting strong attention because of its flexibility and potential compactness with respect to conventional synchrotron sources. A TS source driven by high-quality electron beams can work in different operating modes, e.g.: the high-flux- moderate-monochromaticity-mode(HFM2) suitable for medical imaging when high-flux sources are needed; the moderate-flux- monochromatic-mode(MFM) suitable to improve the detection/ dose performance [14]; short-and-monochromatic-mode(SM) useful for pump-and-probe experiments e.g. in physical-chemistry when tens of femtosecond long monochromatic pulses are needed.

Table 2: Electron beam parameters at the interaction point.

Parameter	value
Bunch charge(nC)	$1 \div 2$
Energy (MeV)	$28 \div 150$
Length (ps)	$15 \div 20$
$\epsilon_{nx,y}$ (mm-mrad)	$1 \div 5$
Energy spread(%)	$0.05^1 \div 0.2$
Spot size at interaction point rms (mm)	$5 \div 10$

Table 3: X-ray beam characteristics (numerically computed).

Parameter	Value
Photon energy (KeV)	$20 \div 500$
Photon per pulse (at 1nC for 6 mrad collected angle)	$1.5 \div 2.0 \times 10^9$

5.1 Electron beam and Thomson Interaction region

The electron beamlines design has been completed, with the capability to transport electron beams with energies ranging from 28 MeV up to150 MeV. The key point in electron beam transport is preserving the high brightness coming from the linac, hence ensuring a very tight focusing for the whole energy span.The final features that the electron beam will show at the interaction point, are reported in Table 2, while a nover all view of the PLASMONX beam lines within the SPARC hall is showed in Fig. 8.

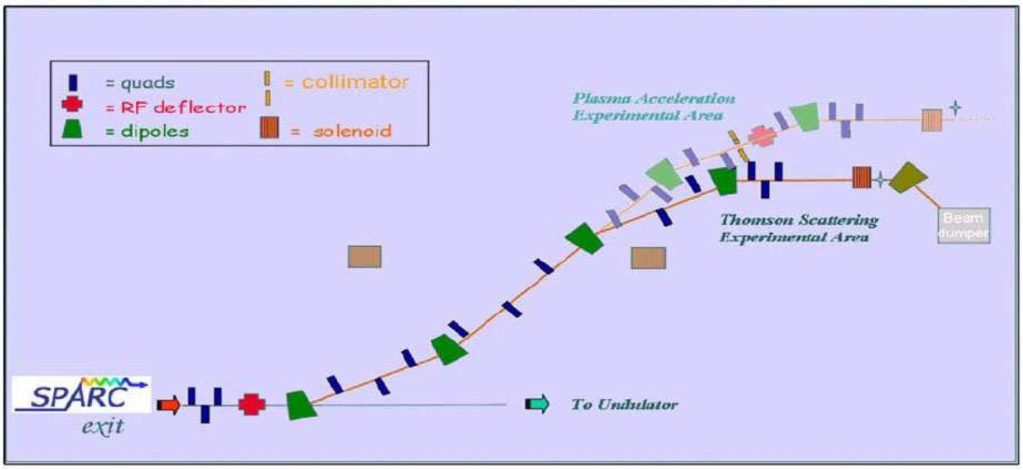

Figure 8: Lay-out of the dog-leg like electron beamline for the TS experimental area.

These properties of the electron beam are strictly necessary in order to reach the high X-ray beam flux as reported in Table 3 (10^9 photons/s with a rep.rate of 10 Hz are required to perform the experiment of mammography at SPARC).

The main challenge regarding the electron beam generation is related to the capability to focus down a high-charge beam (1-2 nC) to focal spot sizes in the order of $10\mu m$ in the collision point, which in turns implies to accurately take under control emittance and energy spread of the beam itself [15]. The emittance growth is controlled by the emittance compensation method, which is one of the main challenges addressed to the SPARC project. The low energy spread values will be obtained by a proper setting of the injection phases into the accelerating structures, which compensates the linear correlation of the longitudinal phase-space, while, in a second step,the use of an X-band short length RF structure [16] will allow to reach an rms energy spread smaller than 5×10^{-4}. The electron beamline consists in a 30 m double dogleg starting downstream the SPARC photoinjector; it ends in a two branch beam delivery line that provides two separate Interaction Regions with the possibility to host two different experiments at the same time. The total beam deflection is about six meters from the SPARC photoinjector and undulator axes. A total of six 25 degrees dipoles and 20 quadrupoles are needed to drive the electron beam up to the two IRs, their procurement has been finalized in July 2009 and the complete delivery is expected by the end of 2010, together with the related Power Supplies for a total of 26 units.

A normal conducting large solenoid has been chosen as the final focusing element.This will ensure a high field on axis (0.9T), in spite of the wide aperture in the magnet, necessary for the FLAME laser beam to pass through it avoiding interactions with the internal surface of the vacuum chamber. The technical specifications of the solenoid have been finalized in 2009, and the delivery is expected by the end of 2010. In Fig. 9 the a sketch of the final engineered model are shown.

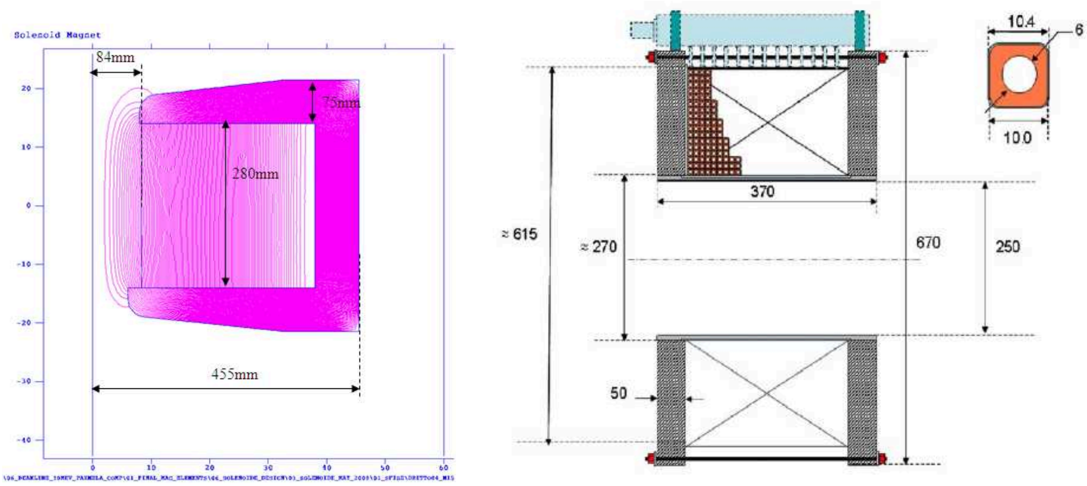

Figure 9: IR solenoid two dimensional profile (left) and enginered model (right).

Also the final dipole meant to dump the electron beam downstream the interaction has been defined; the presence of a high permeability metal shield will prevent the presence of the bipolar field in the interaction point to perturb electrons trajectories. Fig. 10 points out the dipole field profile as modified by the shield, standing to 3D FEM simulations.

The interaction chamber layout has been designed in this year in order to fit all the necessary devices (magnetic elements, optical elements, vacuum vessels, diagnostics, etc.) in agreement with the beams transport constraints. the procurement will be completed in 2010. In this setup the electron beam alignment will be monitored using BPMs and high resolution imaging systems.Time

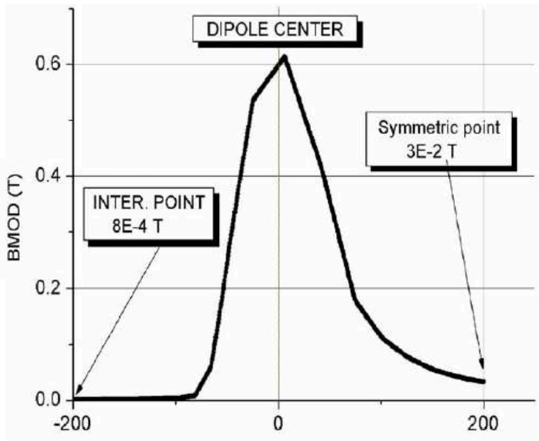

Figure 10: Last dipole field profile.

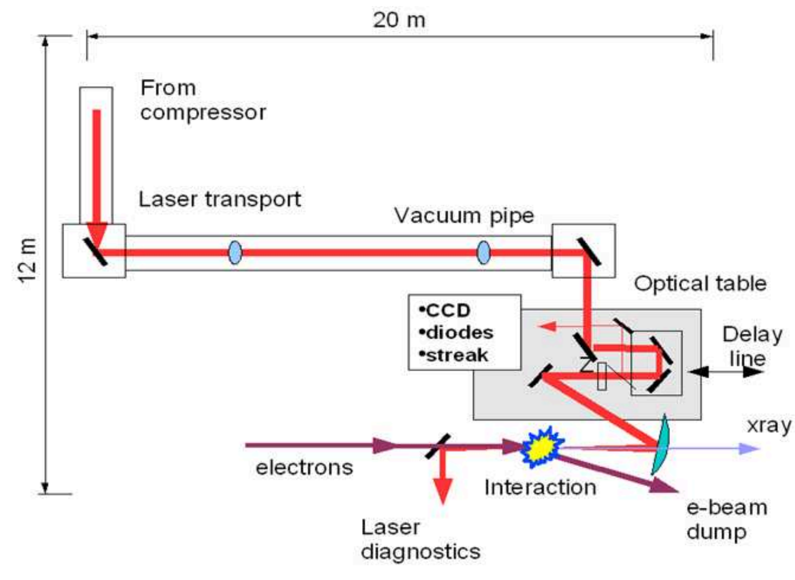

Figure 11: Schematic drawing of the radiation beamline for the Thomson Source.

Table 4: List of expected laser beam parameters.

Parameter	Value
Wavelength(nm)	800
Compressed pulse energy(J)	5
Pulse duration/bandwidth (ps/nm)	$3 \div 12(80)$
Rep.Rate(Hz)	10
Prepulses contrast	$> 10^6$
Contrast ratio at 1 ns before (ASE)	$> 10^8$
Contrast ratioat 1100 ps before	$> 10^6$
Contrast ratio of replica	$> 10^5$
Beam quality M^2	≤ 1.5
Energy stability	10%
Pointing stability (μm)	< 2
Synchronization with SPARC clock	< 1 ps

overlapping between laser pulse and electron beam (in the interaction chamber) will be adjusted using an optical delay line, while jitter/delay readout will be made through a picosecond streak-camera, by monitoring laser and some kind of electron beam induced radiation (e.g.Cherenkov, transition radiation).

5.2 The laser beam transferline

After the compressor, the laser beam will be transported to the experimental chambers through 30 m in vacuum pipe.The beam will be then focused to the interaction point using an off-axis parabola (focal length 75 cm and aperture15 cm). A series of diagnostics, controls and motorized optical elements will be useful tools to optimize the overlapping between the laser and the electron beam. In Fig. 11 a schematic drawing of the radiation beamline is shown, while in table 4 the laser parameters for the Thomson experiment are given.

References

1. L.A. Gizzi et al., Europ. Phys. Journal Special Topics, 175, 3-10 (2009)

2. F. Anelli, A. Bacci, D. Batani, M. Bellaveglia, C. Benedetti, R. Benocci, L. Cacciotti, C.A Cecchetti, O. Ciricosta, A. Clozza, L. Cultrera, G.Di Pirro, N. Drenska, R. Faccini, M. Ferrario, D. Filippetto, S.Fioravanti, A. Gallo, A. Gamucci, G. Gatti, A. Ghigo, A. Giulietti, D. Giulietti, L. A. Gizzi, P. Koester, L. Labate, T. Levato, V. Lollo, E. Pace, N. Pathack, A.R. Rossi, L. Serafini, G. Turchetti, C. Vaccarezza, P. Valente, C. Vicario, *Design of the Test Experiment for the Sub-Pw Flame Laser System at LNF-Frascati: Electron Acceleration with Self-Injection (SITE)*, Unpublished, October 2009.

3. L. A. Gizzi et al., Il Nuovo Cimento C, 32, 433 (2009).

4. A. Pukhov and ter Vehn J., Appl. Phys. B, **74**, 355 (2002).

5. Gordienko S. and Pukhov A., Phys. Plasmas, **12**, 043109 (2005).

6. Lu W. et al., Phys. Rev. Special Topics - Accelerators and Beams, **10**, 061301 (2007).

7. L. A. Gizzi et al., Phys. Rev. E 79, 056405 (2009).
8. C. Benedetti, A. Sgattoni, G. Turchetti and P. Londrillo, IEEE Trans. Plasma Sci., **36**, 1790 (2008).
9. C. Benedetti et al., Nucl. Instr. & Meth. A, **608**, 594 (2009).
10. A.R. Rossi et al., Phys. Rev. S.T.A.B. **12**, 104202 (2009).
11. A.G. Argentieri et al., Nucl. Instr. & Meth. A (2009).
12. G. Mazzitelli et al., Nucl. Instr. & Meth. A **515**, 524 (2003).
13. A. Bacci et al., Nucl. Instr. & Meth., doi:10.1016/j.nima.2009.05.041 (2009).
14. U. Bottigli et al., Il Nuovo Cimento, **29C**, N.2 , Marzo Aprile 2006.
15. W.J. Brown et al., Phys. Rev. STAB **7**, 060702 (2004).
16. D. Alesini et al., Nucl. Instr. & Meth. A **586**, (2008).

NTA SUPERB

M.E. Biagini (Resp.), R. Boni, M. Boscolo, T. Demma (Art. 23), A. Drago, M. Esposito (Art. 23), S. Guiducci, G. Mazzitelli, M. Preger, P. Raimondi, C. Sanelli, M. Serio, A. Stella, S. Tomassini, M. Zobov

1 Introduction

SuperB is an asymmetric (7 GeV HER, 4 GeV LER) e^+e^- collider at the center of mass B pairs production energy (10.58 GeV), to be built in the Rome (Italy) area, with a design peak luminosity of 10^{36} cm^2 s^{-1}. A collider like SuperB will open a unique window on this physics allowing for high statistics study of the current hints of new aggregations of quarks and gluons. Besides the physics one can study in running at the Υ(4S) resonance, the following alternative energies are of interest: Υ(3S) (at least 0.3 ab^{-1}) and a high luminosity scan between 4-5 GeV (5 MeV steps of 0.2 fb^{-1} each would require a total of 40 fb^{-1}). While this is not huge statistics, this scan is only feasible with SuperB. The only possible competitor, BES-III, is not planning to scan above 4 GeV, since their data sample would, in any case, be lower than that of the B Factories alone. Finally, the search for exotic particles among the decay products of the "bottomonia" can probe regions of the parameters space of non-minimal supersymmetric models that cannot be otherwise explored directly, for instance at LHC.

The superiority of SuperB with respect to the planned upgrade of KEKB lies both in the higher statistics, which broadens the range of cross sections the experiment is sensitive to, but also in the flexibility to change center of mass energy, and the possibility to collide with a polarized electron beam.

A Technical Design Report (TDR) is due to be issued in Spring 2011 to present the accelerator design and R&D activities before to proceed with construction.

In the following section the work performed at LNF on the design of the accelerator will be briefly described. LNF contribution is essential for the design and construction of SuperB. This activity at LNF has been funded by the INFN NTA commission, and has received by INFN a special funding in Fall 2009.

2 Design strategy

The construction and operation of modern multi-bunch e^+e^- colliders have brought about many advances in accelerator physics in the area of high currents, complex interaction regions, high beam-beam tune shifts, high power RF systems, controlled beam instabilities, rapid injection rates, and reliable uptimes (90%). The SuperB design is based on a novel collision scheme, the so called “large Piwinski angle and crab waist” [1, 2], which will allow to reach unprecedented luminosity with low beam currents and reduced background at affordable operating costs. A polarized electron beam will allow for producing polarized leptons, opening an entirely new realm of exploration in lepton flavor physics. The principle of operation of this scheme has been tested in 2008-2009 at the upgraded DAΦNE Φ-Factory in Frascati with very successful results [3] (see also the DAΦNE section in this report).

A Conceptual Design Report (CDR) [4] was issued in May 2007, with about 200 pages dedicated to the accelerator design. This report discusses site requirements, crab waist compensation scheme, parameters optimization in order to save power, IP quadrupole design, ring lattice design, Touschek backgrounds, spin rotator scheme, injection and other hardware systems, as well as project costs. The ring lattices have been designed to produce very small horizontal (a few nm-rad) and vertical emittances (a few pm-rad). The crab waist scheme, with a couple of sextupoles per ring in a dispersive section near the Interaction Region (IR), and appropriate betatron phase with respect to the IP, will create a longitudinal waist shift over the width of the beam, so allowing for a vertical beta function which is much smaller than the bunch lengths and providing suppression of betatron and synchro-betatron resonances arising from the crossing angle geometry.

SuperB consists of two rings of different energy (positrons in HER, 6.7 GeV, electrons in LER, 4.2 GeV) colliding in one IR at a large (66 mrad total) horizontal angle. Spin rotator sections in the LER will provide helicity of a polarized electron beam. With respect to the past years design an important change is to have polarized electrons in the LER instead of the HER. This was chosen for easier insertion of Spin Rotator (SR) sections in LER lattice. Also the beam energies have been changed in order to avoid spin resonances, with a consequent small reduction of the center-of-mass boost.

The two rings lay in the horizontal plane, each has two arcs and two long straight sections. The Final Focus (FF) in one straight is combined with the two ARCs in two half-rings (one inner, one outer) and a straight section on the opposite side. The straight section comes naturally to close the ring and readily accommodate the RF system and other necessities (e.g. injection). In this utility region crossing without collisions for the two rings will be provided.

Two sites have been considered for the construction of SuperB: the University of Tor Vergata campus and the Frascati National Laboratories. The latter presents advantages from the point of view of the infrastructures, with the drawback of less available space to allocate the wholes complex inside the laboratory. A possible solution is to build SuperB underground both the ENEA and LNF laboratories, and for this reason a shorter machine design has been carried out. A possible layout at LNF is shown in Fig. 1.

The injection system for SuperB will be capable of injecting electrons and positrons into their respective rings at full energies. At full luminosity and beam currents, up to 4 A, the HER and LER have expected beam lifetimes as low as 5 minutes. Thus, the injection process must be continuous, called top-up injection, to keep nearly constant beam current and luminosity. Multiple bunches will be injected on each linac pulse into one or the other of the two rings. Positron bunches are generated by striking a high charge electron bunch onto a positron converter target and collecting the emergent positrons. The transverse and longitudinal emittances of the electron bunches and, especially, of the generated positron bunches are larger than the LER and HER acceptances and must be pre-damped. A specially designed Damping Ring at 1 GeV, shared between the two particle types to reduce costs, will be used to reduce the injected beam emittances. Electrons from the gun source are longitudinally polarized. The particle spins are rotated to the vertical plane in a special transport section downstream of the gun. The spins remain vertical for the rest of the injection system and injected in this vertical state into the LER. A bunch compressor system between the DR and the accelerating sections has been also designed.

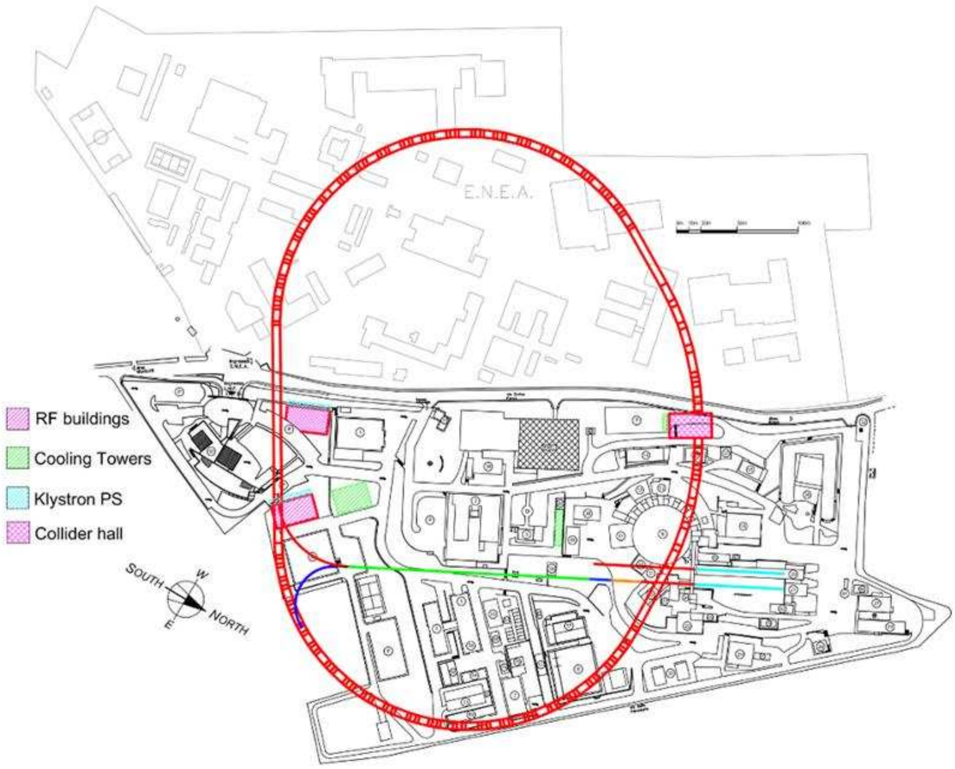

Figure 1: Possible SuperB location at Frascati National Laboratories, with a ring circumference of 1260 m.

A sketch of the injection system is shown in Fig. 2.

3 Year 2009 activity

During 2009 the activity has been focused to address the most crucial aspects of the project, such as lattice design, beam dynamics studies, parameters choice, site issues. The results will be summarized in a new edition of the Conceptual Design Report, to be published in Spring 2010.

The lattice has been optimized to fit the smaller LNF site, the IR re-designed to get better performances in terms of IP quadrupoles gradients, betas and aperture, and the overall optics design has been improved in terms of nonlinear behaviour. Work on the compensation scheme of the detector solenoidal field has also started.

The IP and ring parameters have been optimized based on several constraints. The most significant are:

- to maintain wall plug power, beam currents, bunch lengths, and RF requirements comparable to present B-Factories;
- to plan for the reuse as much as possible of the PEP-II hardware;
- to require ring parameters as close as possible to those already achieved in the BFactories, or under study for the ILC Damping Ring or achieved at the ATF ILC-DR test facility;

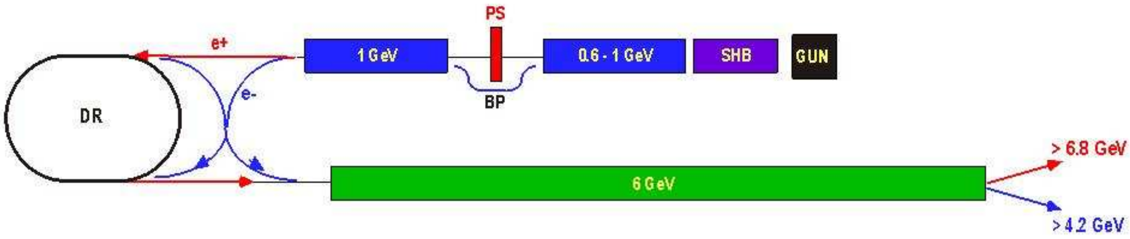

Figure 2: Schematic of the SuperB injector.

- to simplify the IR design as much as possible. In particular, reduce the synchrotron radiation in the IR, reduce the HOM power and increase the beam stay-clear;
- to eliminate the effects of the parasitic beam crossing;
- to relax as much as possible the requirements on the beam demagnification at the IP;
- to design the Final Focus system to follow as closely as possible already tested systems, and integrating the system as much as possible into the ring design.

Simulations of intensity related effects, such as beam-beam, electron cloud and fast ion instabilities, Intra Beam Scattering (IBS), have been updated for the new parameters and design. For example, the design beam emittances have been decreased in order to take into account the emittance growth due to the IBS.

Work on the RF and feedbacks systems (to damp multibunch instabilities) have continued, showing that good performances and design luminosity can be achieved, if needed, even in a "high" beam current (4 A) regime. High Order Modes in all vacuum chamber components have been simulated.

Ground motion measurements at different locations on the LNF site have been performed by the Annecy-LAPP group who has worked for the Virgo facility. All the results clearly show that the noise coming from various vibrations sources (such as traffic, air cooling, railway track...) is well attenuated in depth.

The Machine Advisory Committe (MAC) for the accelerator, chaired by J. Dorfan (SLAC) with 10 international accelerator experts from US and EU, has met for the second time in April 2009, to perform an initial assessment of the current design, review its viability to achieve the design operating parameters and provide clear guidance regarding perceived weaknesses in the design and would further identify those areas in need of more detailed design work and focused R&D. MAC recognized important progresses in crab waist studies, beam-beam simulations and new IR design: *"MAC now feels secure in enthusiastically encouraging the SuperB design team to proceed to the TDR phase, with confidence that the design parameters are achievable".*

Four General SuperB Project Meetings have been organized on in 2009, respectively in LAL-Orsay (France) in February, Perugia (Italy) in June, SLAC (US) in October, LNF (Italy) in December. A complete description of the work done is available from the meetings slides at: http://agenda.infn.it/categoryDisplay.py?categId=109.

3.1 Lattice studies

The SuperB HER and LER ring lattices need to comply with several constraints. First of all, extremely low emittances and IP beam sizes, needed for the high luminosity, damping times,

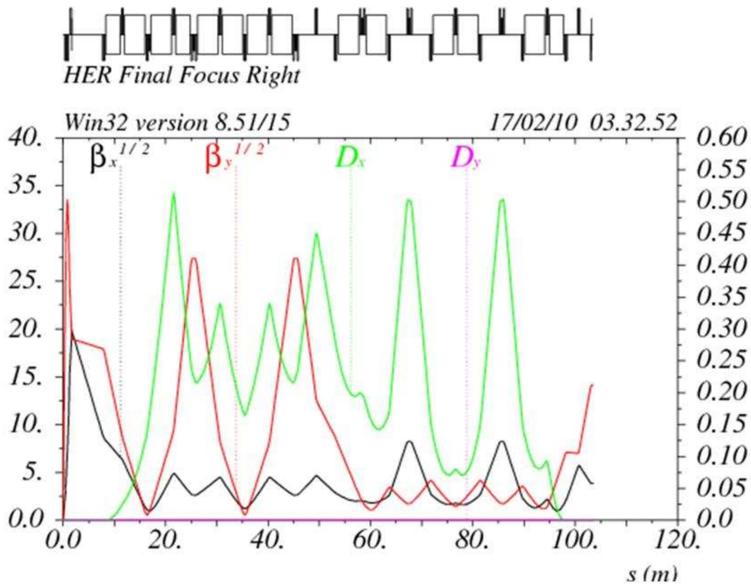

Figure 3: Optical functions for half Final Focus.

lifetimes and polarization for the electron beam. The rings can be basically considered as two Damping Rings (similar to ILC and CLIC ones) with the constraint to include a Final Focus section for collisions. So, the challenge is not only how to achieve low emittance beams but how to choose the other beam parameters to be able to reach a very high luminosity with reasonable lifetimes and small beams degradation. Inspirations from the design of the linear collider DRs, as well as from lattices of the last generation synchrotron light sources, are being very useful to define SuperB lattice characteristics. Nevertheless a new "Arc cell" design has been adopted for SuperB and is now under study for the ILC-DR. All the SuperB lattice studies so far are quasi parameters free. After an intense optimization work, the parameters corresponding to both asymmetric emittances and beam currents for the two rings seem to be more consistent with other requirements.

The lattice design has evolved in order to:

- improve the transverse dynamic aperture;
- improve the energy acceptance;
- improve the flexibility in modifying its parameters (emittance etc) during the run;
- decrease its intrinsic chromaticity;
- increase the momentum compaction for a given emittance;
- increase all the instability thresholds;
- increase its tunability in order to achieve the target parameters;
- relax the tolerances;
- decrease its complexity.

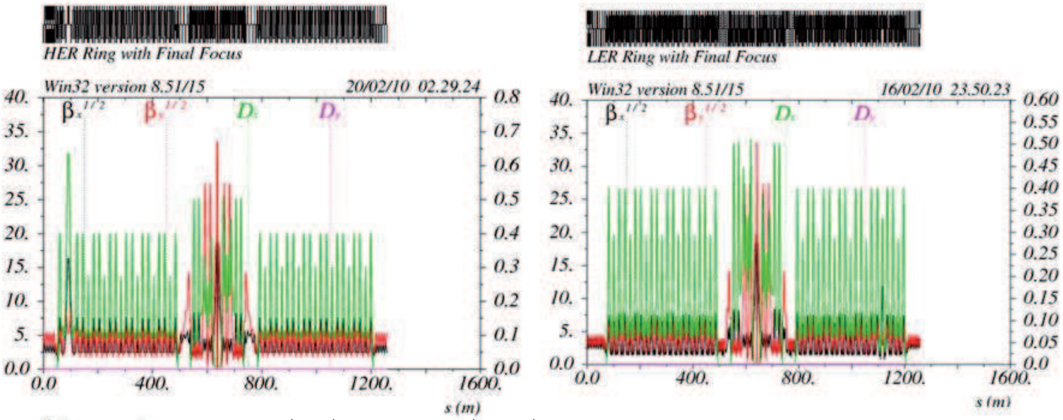

Figure 4: HER (left) and LER (right) optical functions. IP is in the middle.

The LER and HER lattices are very similar, and based on the reuse of most PEP-II (SLAC) hardware. Their main difference is that the LER arc dipoles are shorter (bend radius about 3 times smaller) than in the HER in order to match the ring emittances at asymmetric beam energies. The two horizontal crossings (main and parasitic) result in each ring having one inner and one outer arc. Both the inner and outer arcs provide the same bending angle but the outer arc is made longer by increasing the drift space around the dipole magnets in order to provide the same azimuth location with the inner arc. The FF is the most crucial system in order to achieve the SuperB performances. The luminosity goal is based on the capability of the FF to de-magnify the vertical beam size at the IP down to 35 nm and beyond. In addition, it has to ensure the full functionality of the Crab Waist optics that has been proven fundamental to minimize the beam-beam unwanted nonlinearities. The present design is based on the optics developed for the "Next Linear Collider" (NLC) that has been successfully tested on a dedicated single pass beam line, the "Final Focus Test Beam" (FFTB) build at SLAC, where beam sizes down to 50 nm have been measured. The total FF length is about 100 m, much shorter than in the previous design. A plot of the optical functions in the incoming half of the FF region is presented in Fig. 3, and the HER and LER rings optical functions are shown in Fig. 4.

3.2 Polarization scheme

At SuperB energies, Sokolov-Ternov polarization takes too long and so polarized electrons will be injected. The injector will have the necessary spin handling, and polarized sources with the required intensity exist (e.g. the SLC gun). At the IP, the desired polarization is longitudinal; this can be provided in principle either by 90 deg Spin Rotators (SR) up and downstream of the IP or by a Siberian Snake (180 deg rotator) diametrically opposite in the ring, thus avoiding the need for spin rotators (SR) matched to the critical IR optics. The rotators or Snake(s) can be designed either using solenoids or vertical dipoles together with horizontal dipoles. The overall spin matching in SuperB will be less critical than in facilities like HERA or LEP because of the short beam lifetime. This causes frequent injection of freshly polarized beam, thus reducing the effect of depolarization in the ring, so that maintaining above 90% of the injecting polarization is an achievable goal, provided rotators are spin-matched across the whole energy spread of the beam. It is still important to avoid integer spin tunes (and their synchrotron sidebands) as the spin orientation will move away from longitudinal at the IP for such values.

Several schemes have been studied in order to provide a longitudinal polarization at the IP. All the polarization schemes do require physical constraints and quantized conditions that are intrinsic to the spin dynamics, since the rotation of the spin in a given plane is directly related to the beam energy, the bend angle in a given section and the integrated field of a solenoid (if any). In the LER case the impact is minimal since it is possible to get SR conditions by just a re-optimization of the dipoles in the FF. Two SR insertions, on each side of the IP, are inserted between the FF and the Arcs. Each insertions contains 4 solenoids and 5 quadrupoles needed for the coupling correction. Studies of spin dynamics and beam-beam depolarization effects are in progress.

4 Year 2010 activity

In Spring 2010 we will publish an updated Conceptual Design Report, summarizing the main changes in the design since 2007. We will also start R&D activities for the Technical Design Report, due 2011, as well as continue the theoretical work to optimize SuperB performances.

Four general SuperB meetings are planned in 2010: in March at LAPP (France), in June at Elba (Italy), in September at LNF (Italy) and in December at Caltech (US).

In the following is a list of the publications the Accelerator Division SuperB group has issued in the framework of the SuperB collaboration in 2009.

5 List of Publications

1. M.E. Biagini et al., *The SuperB accelerator project*, ICFA Beam Dyn. Newslett.**48**, 243 (2009).

2. M Sullivan et al., *Further Progress on a Design for a SuperB Interaction Regio*, SLAC-PUB-13636, and Proc. of Particle Accelerator Conference (PAC09), Vancouver, BC, Canada, 4-8 May 2009.

3. W. Wittmer et al., *Polarized beams in the SuperB high energy ring*, Proc. of Particle Accelerator Conference (PAC09), Vancouver, BC, Canada, 4-8 May 2009.

4. K. Bertsche et al., *A Proposed Fast Luminosity Feedback for the SuperB Accelerator*, SLAC-PUB-13616, and Proc. of Particle Accelerator Conference (PAC09), Vancouver, BC, Canada, 4-8 May 2009.

5. K. Bertsche et al., *Longitudinal Bunch Position Control for the SuperB Accelerator*, SLAC-PUB-13615, and Proc. of Particle Accelerator Conference (PAC09), Vancouver, BC, Canada, 4-8 May 2009.

6. S. Tomassini et al., *The SuperB project site layout*, Proc. of Particle Accelerator Conference (PAC09), Vancouver, BC, Canada, 4-8 May 2009.

7. M. E. Biagini et al., *SuperB project overview*, Proc. of Particle Accelerator Conference (PAC09), Vancouver, BC, Canada, 4-8 May 2009.

8. E. Paoloni et al., *Advances in the studies of the magnetic design for the Final Focus quadrupoles of the SuperB*, Proc. of Particle Accelerator Conference (PAC09), Vancouver, BC, Canada, 4-8 May 2009.
9. Alessandro Drago, *SuperB fast feedback systems*, Proc. of Particle Accelerator Conference (PAC09), Vancouver, BC, Canada, 4-8 May 2009.
10. M. Boscolo et al., *Touschek background and lifetime studies for the SuperB factor*, Proc. of Particle Accelerator Conference (PAC09), Vancouver, BC, Canada, 4-8 May 2009.
11. P. Piminov et al., *SuperB ler dynamic aperture study and optimization*, Proc. of Particle Accelerator Conference (PAC09), Vancouver, BC, Canada, 4-8 May 2009.
12. M. Boscolo et al., *Status of SuperB projec*, Nuovo Cim. C **32** 401, (2009).

6 References

1 P. Raimondi, *SuperB design directions*, Proc. of Particle Accelerators Conference, Albuquerque, June 2007.

2 P. Raimondi, D. Shatilov, M. Zobov, LNF-07/003 (IR), January 2007.

3 P. Raimondi et al., *DAΦNE crab waist beam tests*, Proc. of 11th European Particle Accelerator Conference (EPAC 08), Genova, Italy, June 2008.

4 *SuperB Conceptual Design Report*, INFN/AE-07/2, SLACR-856, LAL 07-15, arXiv:0709.0451 [hep-ex] March 2007.

THE SPARC FEL EXPERIMENTS

M. Ferrario (Resp), D. Alesini, F. Anelli (Art.15), A. Battisti (Tecn.), M. Bellaveglia (Art.23), M. Benfatto, R. Boni, M. Boscolo, L. Cacciotti (Tecn.), M. Castellano, E.Chiadroni (Art. 23), P. Chimenti (Art. 15), A. Clozza, L. Cultrera (Art. 23), G. Di Pirro, A. Drago, A. Esposito, M. Esposito (Art. 23), L. Ficcadenti (Art. 23), D. Filippetto (Art. 23), S. Fioravanti (Art. 15), A. Gallo, G. Gatti (Art. 23), A. Ghigo, V. Lollo (Tecn.), A. Marinelli, A. Marcelli, C. Marrelli (Dott.), M. Migliorati (Ass), A.Mostacci (Ass.), E. Pace, L. Palumbo (Resp. Naz), L. Pellegrino, R. Ricci, L.A. Rossi (Art. 15), U. Rotundo, R. Sorchetti (Tecn.), F. Sgamma, B.Spataro, S. Straboioli (Ar. 15), S. Tomassini, C. Vaccarezza, M. Vescovi, C. Vicario (Art. 23),

1 Abstract

The SPARC is a collaboration between different institution, the main is ENEA, INFN, University Tor Vergata and CNR; the project foresees the realization of a free electron laser operating at 500 nm driven by a high brightness photo-injector at a beam energy of 150-200 MeV. The SPARC photoinjector is also the test and training facility for the recently approved VUV/soft X-ray FEL project named SPARX [1]. The second stage of the commissioning, that is currently underway, foresees the demonstration of the 'velocity bunching' technique in the linac and the characterisation of the spontaneous and stimulated radiation in the SPARC undulators, this part was developed in close collaboration with ENEA. In this paper we report the experimental results obtained so far with the self amplified spontaneous emission (SASE) FEL [2-6] and the near future plan.

2 Introduction

Commissioning of the SPARC FEL initiated in autumn 2008 with the following main goals:

1. transport the beam through the vacuum chamber up to the beam dump consistently with the matching condition in the undulators
2. characterisation of the spontaneous and stimulated radiation in the undulators
3. demonstration of 'velocity bunching' technique in the linac with emittance compensation.

All these steps were carried out during winter 2009, with the first SASE FEL spectra obtained on February 17th and beam compression via velocity bunching with emittance compensation demonstrated in April 2009 [7]. In July 2009 a substantial increase of the extracted radiation from the FEL source was obtained with a longitudinally flat top e-beam by increasing the bunch charge and by anticipating the phase in the gun to reduce the debunching in the first stage of acceleration. The present layout of the injector is shown in Fig. 1. The first two accelerating structures are surrounded by two long solenoids providing the additional focusing (with a maximum field of 0.18 T) required to match the beam envelope to the linac, according to the invariant envelope conditions. In Fig. 2 a picture of SPARC taken from the undulator end is shown. The undulator, projected by ENEA and realized by ACCEL Gmbh, is made of six permanent magnet sections with 2.8 cm period, 25 to 6 mm variable gap with maximum undulator parameter Kmax $\sim$ 2.2. In the next sections we will discuss the injector performances, the first observation of the Self Amplified

Figure 1: Picture of the SPARC photoinjector showing the 3 accelerating structures with 2 long solenoids.

Figure 2: Picture of the SPARC undulator sequence.

Spontaneous Emission (SASE) at 500 nm in the SPARC FEL and the preliminary results obtained applying the Velocity Bunching technique to the first linac section.

3 SPARC injector commissioning

An unsatisfactory emission uniformity, probably due to RF break downs in the gun that irreversibly damaged the cathode surface or to a damage of the in vacuum mirror delivering the laser light to the cathode itself, limits the brightness of the SPARC photoinjector. In order to reduce to a minimum the radiofrequency (RF) discharge rate, the gun is operated at a gradient of about 105 MV/m.

The beam has been transported up to the undulator entrance and the longitudinal phase space is measured with an rf-deflector introducing a linear correlation between the arrival time and the vertical position on the screen monitor. The analysed phase space image provided the information on the local current, energy and energy spread. In this stage of commissioning we have been operating with a laser pulse with flat-top longitudinal profile, 6-8 ps FWHM long. The bunch charge was in the range of 200 - 450 pC resulting in a peak current between 30 and 55 A. The beam has been accelerated up to 150 MeV with an energy spread of 0.2% and an energy stability better than 0.1%. At the linac exit the rms emittance has been measured by quadrupole scan and the bunch length, slice emittance and slice energy spread have been measured downstream of the high resolution RF deflector. In Fig. 3 the beam energy (blue) and the beam energy spread (red) as a function of the position along the microbunch is shown. In Fig. 4 the 'slice' beam current is

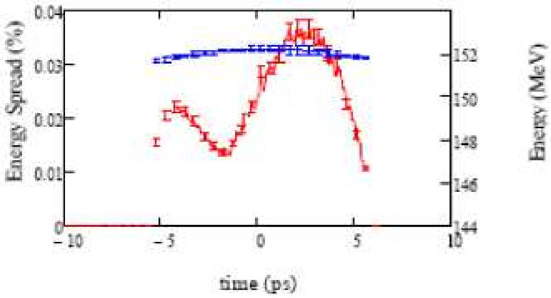

Figure 3: (color online). Beam energy (blue) and the beam energy spread (red) as a function of the position along the microbunch.

shown. In this condition the maximum current is about 53A and the rms bunch length is 2.65ps.

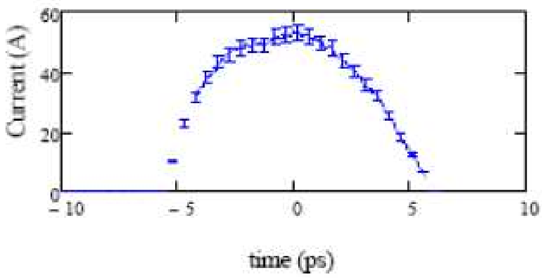

Figure 4: Beam current as a function of the position along the microbunch.

The transverse emittance measured with the quadrupole scan is 2.9 (2.5) mm-mrad in the vertical (horizontal) plane. As reported in the next section in these conditions the beam has been injected in the undulator for FEL amplification.

4 SASE experiments

A layout of the SPARC undulator is shown in Fig. 5. The undulator is composed by six independent modules. The gap between the modules host quadrupoles for horizontal focusing and radiation diagnostic stations.

Each station is equipped with actuators allowing the insertion of alumina screens and aluminum mirrors to extract the radiation. Two CCD cameras per diagnostic chamber are available to monitor the electron beam orbit and the radiation. At the end of the undulator sequence, an in-vacuum spectrometer built by the LUXOR Laboratory (Padova) is installed. The instrument is a 1 m long normal incidence spectrometer with a Princeton UV grade CCD camera allowing the

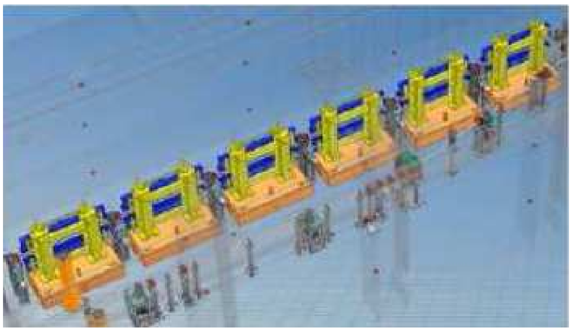

Figure 5: Layout of the SPARC undulator.

detection of spectra both in single shot and in the integrated mode in the spectral range 40 - 570 nm. The CCD camera is calibrated and the signal permits the reconstruction of the total energy per pulse at the end of the FEL.

The first clear signature of coherent radiation was observed at 500 nm on February 17th, 2009. In July 2009 the higher accelerated charge and the higher peak current available at the undulator allowed to increase the radiation intensity by about two orders of magnitude.

A typical image of the spectrum at the end of the six undulator sections is shown in Fig. 6. The vertical axis indicates the position on the vertical entrance slit of the spectrometer. The

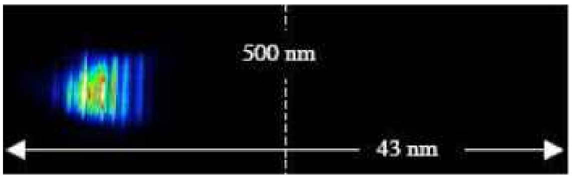

Figure 6: SPARC spectrum with 6 sections closed. The window is centred at 500 nm and the window full width is 43 nm.

horizontal axis corresponds to wavelengths in a window of 43 nm of width and centred at 500 nm. The FEL spectrum is centred at about 492 nm. The instrument resolves the spiky nature of the SASE radiation.

The evolution of the pulse energy as a function of the position in the undulator sequence is obtained by turning off the FEL interaction by progressively opening the gap of the undulators. The measured pulse energy is shown in Fig. 7. Each of the data points corresponds to a single shot spectrum. The error bars are related to the uncertainty in the spectrometer calibration and transmission through the spectrometer slit and vacuum chamber. We have observed an amplification factor of about 107 and the observed gain length was ~ 0.7 m. Saturation is expected in these conditions at a pulse energy $\sim$ 0.2-0.3 mJ. The maximum energy in Fig. 7 was about 0.01 mJ. With all the undulators set at resonance spectra at the third harmonic wavelength have been acquired. The sequences 2009.07.24 1H (blue) and 2009.07.24 3H (purple) represent the measured data on the fundamental and third harmonic respectively. The sequence 2009.07.24 1H o. represents the

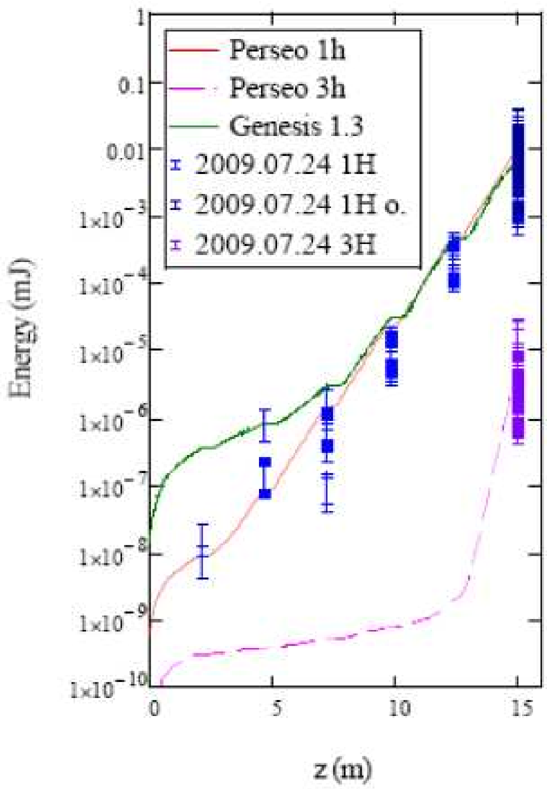

Figure 7: (color online). Pulse energy vs. longitudinal position in the undulator. The sequences 2009.07.24 1H and 2009.07.24 1H o. (blue) and 2009.07.24 3H (purple) represent the measured data on the fundamental and third harmonic respectively. The continuous lines represent simulations with Perseo (1st harmonic, red and 3rd harmonic, purple) and Genesis 1.3 (green).

result of an optimization of the delivered energy varying the rf injection phase of the gun and of the three linac sections. The continuous lines represent simulations with Perseo [8] and Genesis 1.3 [9]. The third harmonic simulation is obtained with Perseo. Simulations have been obtained assuming a beam with the longitudinal phase space corresponding to the measured data in figures 3 and 4, and with transverse emittances given by the quadrupole scan measurement (2.5/2.9 mm-mrad). Even though not included in the figure, similar results are provided by different numerical and analytical tools, like Prometeo [10] and Parsifel [11].

In Fig. 8 we have shown the behaviour of the radiation linewidth as a function of the longitudinal position in the undulator. The continuous lines represent simulation data obtained with Perseo (black) and Genesis 1.3 (blue). The agreement with the simulations is fairly good. Perseo (as Prometeo) is a one dimensional code assuming a single mode matched to the e-beam, and provides a slightly underestimated linewidth. Genesis 1.3, which is a three dimensional code, calculates the spectrum as it is given by the field at the coordinate z, propagated in the far field. This operation is affected by the Rayleigh range oscillations induced by the gain variations at the undulator gaps and is spatially filtered by the transverse mesh where the field is represented. The

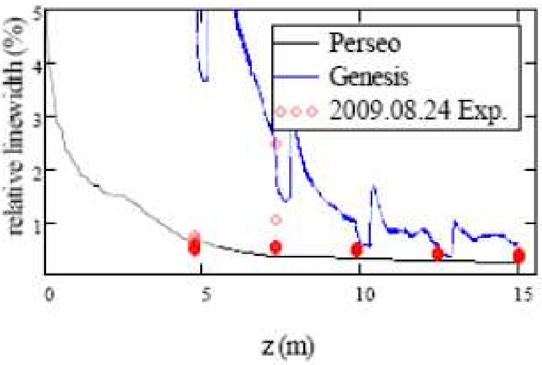

Figure 8: Linewidh of the FEL radiation as a function of the longitudinal position in the undulator. The continuous lines represent simulation data obtained with Perseo (black) and Genesis 1.3 (blue).

measured spectra are acquired at the end of the undulator line, about two meters after the last undulator. The geometry of the vacuum chamber and the transport line to the spectrometer selects the low divergence part of the radiation field affecting both the measured energy and linewidth.

5 Experimental programme for the near future

The SPARC FEL can be operated in both SASE and seeded modes. One of the future experiments at SPARC, is to study and test the amplification and the FEL harmonic generation process of an input seed signal obtained as higher order harmonics generated in gases [12] and compare it with the single spike operation described in [13] and [14]. The main components of the seed source consist in a second laser amplification chain operating in parallel to the photo-injector laser system, in a chamber devoted to the generation of high harmonics in gas, which has been realized at CEA [15], and finally in the hardware required for injecting the radiation generated in the chamber, in the electron transfer line connecting the SPARC linac with the SPARC undulator. A chicane deflecting the e-beam from the linac axis and a periscope allowing the injection of the harmonic beam have been realized for this purpose. The experiment setup for seeded FEL experiments is ready, the reader is addressed to refs. [16-17] for more details. A number of beam experiments will be also performed taking advantage of the velocity bunching technique developed at SPARC, as reported in the following. Additional SASE investigations are foreseen by injecting a progressively shorter bunch in the undulator chain. A transition of the radiation spectrum from the multi-spike to the single spike regime is expected [5-17] when a sub-picosecond long bunch corresponding to a few SASE cooperation lengths[5] is injected in the undulators. The measurement of the properties of the electron beam, the determination of shape and spectrum of the radiation pulse and the validation of the single spike scaling laws will be analysed in order to foresee future operations at shorter wavelength with SPARX. In collaboration with UCLA a dedicated FROG system [18] will be soon installed at the undulators exit in order to measure the temporal profile of the emitted radiation. A dedicated beamline for a THz radiation source driven by sub-picosecond long bunch produced with the velocity bunching is also under commissioning at SPARC. The form factor of the recently measured compressed beam (charge of 200 pC) is shown in the upper plot of Fig. 9, together with the one obtained from a simulation. A more advanced experiment is foreseen with

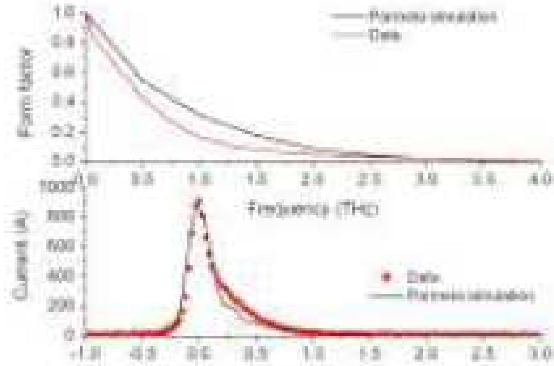

Figure 9: Form factor of the measured compressed beam compared to the simulated one (upper) and corresponding longitudinal beam distribution (lower).

a comb beam (a train of few sub-picosecond electron pulses at THz repetition rate) leading to a narrower spectrum of the THz radiation [19].

Careful attention has been devoted in the last years to the effects of high frequency modulation of the bunch current, leading to enhanced COTR radiation [20] or even to a seed for microbunching in a SASE FEL [21]. HOMDYN simulations of the electron emission process including the electron beam-laser interaction near the cathode [22] show that a longitudinal charge modulation occurs on the scale of the laser wavelength, in case of laser oblique incidence on the cathode, driven by the longitudinal component of the laser field. Preliminary simulations up to the photoinjector exit show that charge modulation is partially conserved which may produce enhanced microbunching at shorter modulation wavelength when the beam is further compressed. In Figs. 10 and 11 the charge modulation is shown right after the electron emission and at the gun exit. A dedicated experiment will be soon performed at SPARC with a minor modification of the cathode driving laser system: the laser IR light will be transported up to the cathode with oblique incidence (working as a modulator) and superimposed to the normally incident UV light. The induced energy spread of the extracted electron beam and the OTR radiation signals will be compared with the IR light on and off.

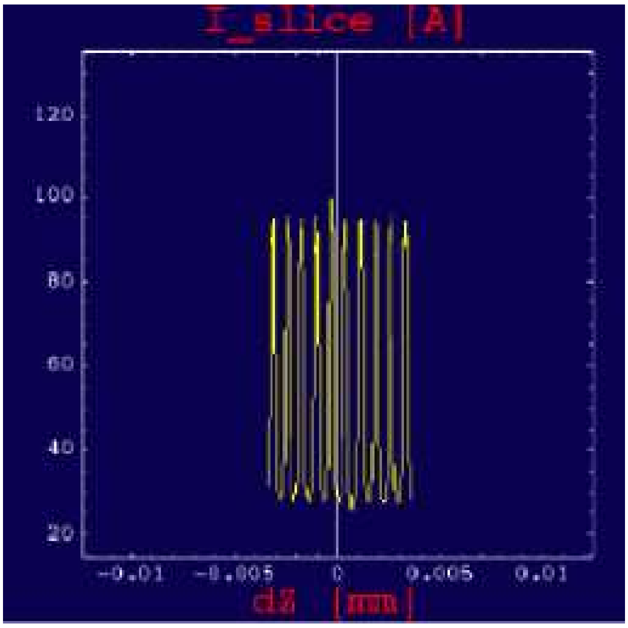

Figure 10: Modulation induced on a 100 pC 1 ps long bunch right after the interaction with a IR laser pulse with grazing incidence (75^o) on the cathode, superimposed to the UV pulse. Only central part of the bunch is shown.

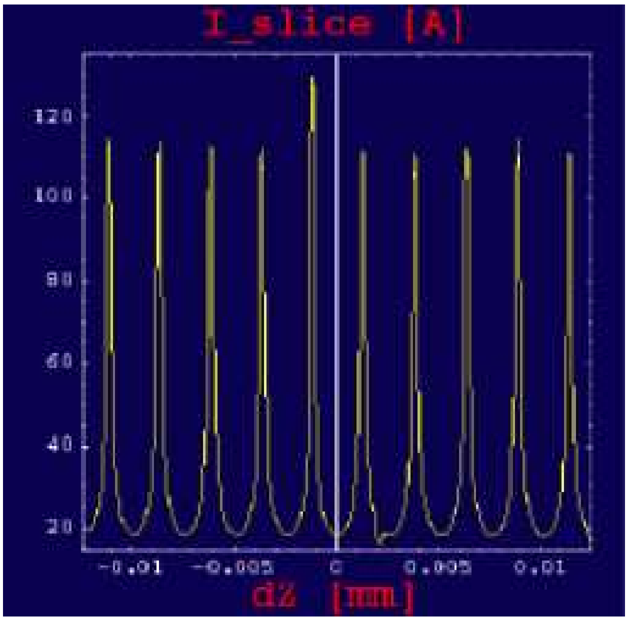

Figure 11: Modulation remaining at the gun exit. Same bunch of Fig. 10.

6 Conferences

1. E. Chiadroni et. al., *High energy emittance measurement at SPARC*, Proc. of 9th European Workshop on Beam Diagnostics and Instrumentation for Particle Accelerators, Basel (Switzerland), 25-27 May 2009, p. 402.
2. L. Cultrera et al., *Charge and laser beam energy monitor for SPARC LINAC*, Proc. of 9th European Workshop on Beam Diagnostics and Instrumentation for Particle Accelerators, Basel (Switzerland), 25-27 May 2009, p. 140.
3. M. Bellaveglia et al., *Measurement devices for the SPARC synchronization system*, Proc. of 9th European Workshop on Beam Diagnostics and Instrumentation for Particle Accelerators, Basel (Switzerland), 25-27 May 2009, p. 363.
4. D. Alesini et al., *Sliced beam parameter measurements*, Proc. of 9th European Workshop on Beam Diagnostics and Instrumentation for Particle Accelerators, Basel (Switzerland), 25-27 May 2009, p. 146.
5. M. Ferrario et al., *Recent results of the SPARC FEL experiments*, Proc. of Free Electron Laser Conference 2009, Liverpool (Great Britain), 23-28 August 2009, p. 734.
6. M. Esposito et al., *The alignment of the SPARC facility experiments*, Proc. of Free Electron Laser Conference 2009, Liverpool (Great Britain), 23-28 August 2009, p. 262.
7. L. Giannessi et al., *Self seeding configuration at SPARC experiments*, Proc. of Free Electron Laser Conference 2009, Liverpool (Great Britain), 23-28 August 2009, p. 43.
8. M. Labat et al., *Seeding experiments at Sparc experiments*, Proc. of Free Electron Laser Conference 2009, Liverpool (Great Britain), 23-28 August 2009, p. 639.
9. D. Filippetto et al., *Velocity bunching experiment at SPARC*, Proc. of Free Electron Laser Conference 2009, Liverpool (Great Britain), 23-28 August 2009, p. 734.
10. V. Petrillo et.al., *SINGLE Spike radiation production at SPARC*, Proc. of Free Electron Laser Conference 2009, Liverpool (Great Britain), 23-28 August 2009, p. 47.
11. D. Di Giovenale et.al., *On-line beam loss position monitors for SPARC*, Proc. of Free Electron Laser Conference 2009, Liverpool (Great Britain), 23-28 August 2009, p. 517.
12. M. Ferrario et al., *Recent Results of the SPARC FEL Experiments*, Proc. of Particle Accelerator Conference 2009, Vancouver (Canada), 4-8 May 2009.
13. M. Ferrario et al., *Velocity Bunching Experiments at SPARC*, Proc. of Particle Accelerator Conference 2009, Vancouver (Canada), 4-8 May 2009.
14. D. Filippetto et al., *Status of the SPARC Photocathode Drive Laser*, Proc. of Particle Accelerator Conference 2009, Vancouver (Canada), 4-8 May 2009.
15. A. Cianchi et al., *Beam Slice Characterization at SPARC High Brightness Photoinjector*, Proc. of Particle Accelerator Conference 2009, Vancouver (Canada), 4-8 May 2009.

16. M. Boscolo et.al., *Design Study of a Dedicated Beamline for THz Radiation Generation at the SPARC Linac*, Proc. of Particle Accelerator Conference 2009, Vancouver (Canada), 4-8 May 2009.

17. V. Petrillo et al., *Single Spike Radiation Production and Diagnostic at SPARC*, Proc. of Particle Accelerator Conference 2009, Vancouver (Canada), 4-8 May 2009.

18. G. Di Pirro et al., *The SPARC Control System*, Proc. of 12th International Conference on Accelerator and Large Experimental Physics Control Systems 2009, Kobe (Japan), 12-16 October 2009.

19. G. Di Pirro et al., *The Camera Acquisition System in the SPARC Control System*, Proc. of 12th International Conference on Accelerator and Large Experimental Physics Control Systems 2009, Kobe (Japan), 12-16 October 2009.

20. E. Pace et al., *PostgreSQL Usage within the SPARC Control System*, Proc. of 12th International Conference on Accelerator and Large Experimental Physics Control Systems 2009, Kobe (Japan), 12-16 October 2009.

21. E. Pace et al., *The SPARC Vacuum System*, Proc. of 12th International Conference on Accelerator and Large Experimental Physics Control Systems 2009, Kobe (Japan), 12-16 October 2009.

References

1. SPARX TDR http://www.sparx-fel.it/

2. H.A. Haus, IEEE J. Quantum Electron. **QE-17**, 1427 (1981).

3. G. Dattoli, A. Marino, A. Renieri, F. Romanelli, IEEE J. Quantum Electron. QE-17 (1981) 1371.

4. R. Bonifacio, et al., Phys. Rev. Lett. **73**, 70 (1994).

5. E.L. Saldin, et al., Opt. Commun. **148**, 383 (1998).

6. S. Reiche, Nucl. Inst. & Meth. A **429**, 243 (1999).

7. D. Filippetto, et al., Velocity bunching experiment at SPARC, Proc. of FEL09, Liverpool (Great Britain), 23-28 August 2009, p. 734.

8. L. Giannessi, *Overview of Perseo, A System For Simulating Fel Dynamics In Mathcad*, Proc. of the 2006 FEL Conference, www.jacow.org (2006) 91.

9. G. Dattoli, M. Galli, and P.L. Ottaviani, *1-dimensional simulation of FEL including high gain regime saturation, Prebunching, and Harmonic Generation*, ENEA Internal Report RT/INN/93/09 (1993).

10. G. Dattoli, P. L. Ottaviani and S. Pagnutti, *Booklet for FEL design: A collection of practical formulae*, ENEA Internal Report.

11. D. Garzella et al., Nucl. Inst. & Meth. A **528**, 502 (2004).

12. J. Rosenzweig et al. Nucl. Inst. & Meth. A **593**, 137 (2008).

13. I. Boscolo et al. *Single Spike experiments with the SPARC SASE FEL*, in Proc. of the 2008 Int. FEL Conf. Gyeongju, Korea, www.jacow.org, 258 (2008).

14. O. Tcherbakoff, *Seeding the SPARC FEL facility with harmonic generation in gases: preliminary tests of the harmonic generation chamber*, Proc. of the 2006 FEL Conference, www.jacow.org (2006) 142.

15. M. Labat, et al., *Seeding Experiments at SPARC*, Proc. of FEL09, Liverpool (Great Britain), 23-28 August 2009, p. 639.

16. L. Giannessi et al., Nucl. Inst. & Meth. A **593**, 132 (2008).

17. G. Marcus et al., *Longitudinal Diagnostic For Single- Spike Sase Fel Operationin*, Proc. of the 2008 Int. FEL Conf. Gyeongju, Korea, www.jacow.org, 274 (2008).

18. M. Boscolo et al., *Design Study of a dedicated beamline for THz radiation generation at the SPARC Linac*, Proc. of PAC 2009, Vancouver, CA.

19. R. Akre et al., Phys. Rev. ST Accel. Beams **11**, 030703 (2008).

20. G. Stupakov, Phys. Rev. Lett. **102**, 074801 (2009).

21. M. Ferrario et al., *Electron Beam-Laser interaction near the cathode in a High Brightness Photoinjector*, Proc. of EPAC 2006, Edinburgh, Scotland.

General Information

COMMUNICATION AND OUTREACH

R. Centioni (Resp.), V. Ferretti (art.15), L. Sabatini,
S. Vannucci (Resp.)
Scientific Information and Documentation Service

The “Laboratori Nazionali di Frascati dell’INFN” (INFN-LNF) provide basic education in Physics for the general public, students and teachers. The LNF Educational and Outreach programmes are made possible by the enthusiastic involvement of the laboratory graduate students, postdocs, researchers, engineers and technicians.

1 Visiting LNF

`http://www.lnf.infn.it/edu/`

- *LNF Guided Tours.* A well established tradition: for general public, students and teachers: about 3300 people. 75 volounteers have received 149 groups. A typical visit consists of: a brief historical presentation of the laboratory; a presentation of the activities on site and abroad; a visit to the ”en plein air museum” and the experimental areas.
- *LNF Scientific Week and Open day: 570 visitors.* Most of LNF employees are in action to present their research center, answer questions and care for their guests. The standard format of the event provides for guided tours; conferences and public lectures; scientific videos.

2 Scientific Itineraries

The aim is to offer a more complete view of the scientific institutions operating in the area and improve the communication with the general public. In collaboration with: ASI, CNR, ENEA Frascati, ESA-ESRIN Frascati, INAF, INGV, Frascati Scienza, Associazione Eta Carinae, Associazione Tuscolana Astronomia, Frascati and Castelli Romani Municipalities, Regione Lazio, Provincia di Roma, International non-government organizations.

3 Students’ programme

- *LNF Stages for high school students.* Scientific Coordinators: F. Bossi, P. Gianotti.

`http://www.lnf.infn.it/edu/stagelnf/`

The aim is to enable students to acquire the knowledge and understanding of INFN research activities. 2009 programme consisted of:

- Winter stages, 9 days: 36 students with 20 tutors;
- EU Project Masterclasses 2009, 4 days: 38 students with 5 tutors;
- Summer stages, 2 weeks: 104 students with 49 tutors;
- Lectures at school by LNF researchers, 2-3 days: 260 students with 4 tutors. In occasion of the 10th edition of Summer Stages, the event has been recorded. The video can be requested to SIDS Comunication and Scientific Education Office.
- Special Programme for Primary School: *QUASAR*. Care of F. Murtas and B. Sciascia.

  `http://www.lnf.infn.it/edu/quasar/`

  Age: 10 - 14. First meeting with the children at their school to introduce the world of research and some concepts of modern physics. Then, visit to the Frascati National Laboratories by small groups. Total of children and teachers in visit: 220.

4 High school teachers' programme

- *Incontri di Fisica*, Organizing Committee: P. Di Nezza (chair), M. Calvetti, P. Campana, R. Centioni, C.O. Curceanu, M. Dreucci, V. Ferretti, S. Miozzi, L. Sabatini, S. Vannucci, G. Venanzoni.

  `http://www.lnf.infn.it/edu/incontri/`

  The event consists in lectures for high-school science teachers and people involved in scientific

Figure 1: High school teachers programme: Incontri di Fisica. (INFN-LNF Photo).

research dissemination. The aim is to stimulate teachers' professional traning and provide an occasion for interactive and hands-on contact with the latest developments in physics. 9th edition (October 7-9, 2009): 147 participants and 56 LNF Tutors (researchers, engineers and technicians).

In the framework of Incontri di Fisica 2009 a special event has been organized in INFN - Firenze Section: LABEC Laboratorio di Tecniche Nucleari per i Beni Culturali (March 23, 2009): 30 participants and 11 Tutors.

- Online resources for teachers and students:*Lezioni di Fisica, live lectures by scientists*

  `http : //www.lnf.infn.it/media/`

  Care of M. Calvetti, O. Ciaffoni, G. Di Giovanni and SIDS - Comunication and Outreach.

5 General public programme

- *Seminars*

  `http : //www.lnf.infn.it/edu/seminaridivulgativi/`

  Upon request, LNF researchers gave seminars to high school students and the general public. The following is the list of the seminars 2009 (about 680 students):

  - *From Galilei to modern physics, a journey beyond the common sense*, January 20, 2009, Lic. Cl. P. Albertelli, Roma - C. Curceanu.
  - *Special Relativity*, February 23, 2009, Lic. Sc. F. D'Assisi, Roma - S. Miozzi.
  - *Nuclear Physics and Elementary Particle Physics*, February, 24 2009, Lic. Sc. F. D'Assisi, Roma - F. Bossi.
  - *Women in Science*, March 10, 2009, Salone delle Bandiere di Palazzo Rospigliosi, Zagarolo (RM) - G. Pancheri.
  - *Energy from nuclei*, April 22-23, 2009, Lic. Sc. T. Calzecchi Onesti, Fermo (AP) - M. Calvetti.
  - *April 6. 2009 L'Aquila Eartquake: a multidisciplinary analisys*, April 30, 2009, LNF Aula Bruno Touschek - W. Plastino.
  - *Cultural Heritage and Arheometry*, May 6, 2009, LNF Aula Bruno Touschek - A. Esposito.
  - *The CNAO Centro Nazionale di Adroterapia Oncologica*, 21 May 2009, LNF Aula Bruno Touschek - S. Rossi, C. Sanelli.

- *Incontri con l'Autore*

  `http : //www.lnf.infn.it/edu/ica/`

  - *La città restituita - Il Vulcano laziale: Ambiente, Storia, Archeologia*, April 21, 2009, LNF Aula Bruno Touschek - R. Del Nero.

6 Events

- *European Researchers' Night 2009*

  `http://www.lnf.infn.it/nottedellaricerca/`

  The event has been organized within the European Researchers' Night on September 25, 2009. About 350 visitors at LNF.

  An important feedback of the success of the event comes from the questionnaire (available on the web site http://www.infn.it/nottedellaricerca) addressed to investigate the achievement of the main purpose of the project and of the quality of the activities.

Figure 2: Christmas Concert December 15, 2009 (INFN-LNF Photo).

- *Christmas Concert.* Since 2002, in the week preceding Christmas, the LNF organize a Concert in the Bruno Touschek Auditorium, located in the High Energy Building. An evening in solidarity with a voluntary association operating in the neighborhood. In 2009 the concert has been held by Coro Eufonia della Scuola dei Canti di Frascati (RM), LNF December 15, 2009.

7 Conferences

For the list of International Conferences, Workshops and Meeting hosted and/or organized by the LNF see next chapter.

8 Conferences, Workshops and Meetings

International conferences, workshops and schools hosted and/or organized by LNF:

1. *HIPER Executive Board & Participants Meeting*, LNF March 5-6, 2009;
2. *II Timing & Synchronization Workshop*, Trieste March 9, 2009;
3. *Working Group on Radiative Corrections and Generators for Low Energy Hadronic Cross Section and Luminosity*, LNF April 6-7, 2009;
4. *Quark Matter Italia*, Roma April 22-24, 2009;
5. *The XIV Frascati Spring School Bruno Touschek*, LNF May 11-15, 2009
6. *La fisica nella società italiana*, LNF May 21, 2009;
7. *2nd International Conference on Ultra-Intense Laser Interaction Science*, LNF May 24-29, 2009;
8. *Nuclear Physics in Astrophysics IV*, LNF June 8-12, 2009;
9. *School on Attractor Mechanism*, LNF July 29 - July 3, 2009;
10. *Local distortions and Physics of Functional materials*, LNF, July 22-24, 2009;
11. *14th International Conference on X-ray Absorption Fine Structure*, Camerino (MC) July 25-31, 2009;
12. *Low X Meeting 2009*, Ischia (NA) September 8-13, 2009;
13. *Lecture on Monte Carlo methods for high energy physics*, LNF September 21-25, 2009;
14. *Nanoscience & Nanotechnology*, LNF October 19-22, 2009;
15. *3rd EuCARD Steering Committee Meeting*, LNF November 4-5, 2009.
16. *Lectures on The Physics of Vacuum Polarization: from GeV to TeV scale*, LNF November 13, 2009;
17. *1st International Conference on Frontier in Diagnostic Technologies*, LNF November 25-27, 2009;
18. *Comunicazione e Divulgazione della Fisica*, Marino (RM) November 30 December 3, 2009;
19. *XI SuperB Workshop*, LNF December 1- 4, 2009;
20. *1 Seminario Nazionale Rivelatori Innovativi*, LNF November 30 December 4, 2009;
21. *Bruno Touschek Memorial Lectures*, LNF December 9, 2009.

YEAR 2009 FRASCATI PUBLICATIONS

Available at www.lnf.infn.it

LNF Frascati Reports

LNF - 09 / 1(P)
F. Celani, P. Marini, V. Di Stefano, A. Spallone, M. Nakamura, E. Purchi, O. M. Calamai, V. Andreassi, E. Righi, G. Trenta, A. Marmigi, G. Cappuccio, D. Hampai, F. Todarello, U. Mastromatteo, A. Mancini, F. Falcioni, M. Marchesini, P. Di Biagio, U. Martini, P. G. Sona, F. Fontana, L. Gamberale, D. Garbelli
Deuteron Electromigration in Thin PdWires CoatedWith Nano-Particles: Evidence for Ultra-Fast Deuterium Loading and Anomalous, Large Thermal Effects
Invited talk at ICCF14, Washington DC, USA, 9-15 August 2008
Publishing by World Scientific, Condensed Matter Nuclear Science Series

LNF - 09 / 3(IR)
L. Quintieri, D. Babusci, F. Archili, D. Moricciani, R. Messi
Simulations of off-momentum particle trajectories along DAΦNE optics
Presented at the 51st Workshop of the INFN ELOISATRON Project 3rd International Conference on Charged and Neutral Particles Channeling Phenomena - Channeling 2008, Erice, October 25-November 1, 2008

LNF - 09 / 4(IR)
AA.VV
2008 ANNUAL REPORT

LNF - 09 / 5(P)
Accelerator Division
Papers presented at EPAC 2008

LNF - 09 / 6(IR)
S. Bartalucci, Vl. Angelov, K. Drozdowicz, D. Dworak, G. Tracz
A Photo-Neutron Facility for Time-of-Flight Measurements

LNF - 09 / 7(IR)
A. Babaev, S.B. Dabagov
Dynamics of Bound State Populations for Channeled Electrons/Positrons

LNF - 09 / 8(P)
E. N. Tsyganov
Thermal Equilibrium of Light Contaminant Atoms in a Crystal

Presented at the 51st Workshop of the INFN ELOISATRON Project 3rd International Conference on Charged and Neutral Particles Channeling Phenomena Channeling 2008 Erice, Oct. 25-Nov.1, 2008

LNF - 09 / 9(P)
M. Boscolo, F. Bossi, B. Buonomo, G. Mazzitelli, F. Murtas, P. Raimondi, G. Sensolini, M. Schioppa, F. Iacoangeli, P. Valente, N. Arnaud, D. Breton, L. Burmistrov, A. Stocchi, A. Variola, B. Viaud, P. Branchin
Measurement of the Luminosity at the DAΦNE Collider Upgraded with the Crab Waist Scheme
arXiv:0909.1913v1 [hep-ex]

LNF - 09 / 10(P)
E. N. Tsyganov
Concept of DD Fusion In Crystals
Presented at the Channeling 2008, Proc. of Conference, World Scientific Publ. 2009

LNF - 09 / 11(P)
C. Biscari
Accelerators R&D
Presented at the: European Physical Society Europhysics Conference on High Energy Physics
EPS-HEP 2009, Krakow, Poland - July 16-22, 2009

LNF - 09 / 12(IR)
L. Quintieri, G. Bencivenni, A. Ceccarelli, S. Cerioni, S. Lauciani, D. Domenici, M. Pistilli
Finite Element Model of the Cylindrical GEM Detector as New Inner Tracker of Kloe2 and Mechanical Characterization of the Employed Materials

LNF - 09 / 13(P)
B. Bolzon, L. Brunetti, M. Esposito, A. Jeremie, U. Rotundo, S. Tomassini
Ground Motion Measurements at LNF
Submitted to the IPAC10 Conference, Kyoto, Japan, 23-28 May 2010

LNF - 09 / 14(P)
S. Actis, A. Arbuzov, G. Balossini, P. Beltrame, C. Bignamini, R. Bonciani, C. M. Carloni Calame, V. Cherepanov, M. Czakon, H. Czyz, A. Denig, S. Eidelman, G. V. Fedotovich, A. Ferroglia, J. Gluza, A. Grzelinska, M. Gunia, A. Hafner, F. Ignatov, S. Jadach, F. Jegerlehner, A. Kalinowski, W. Kluge, A. Korchin, J. H. Kuhn, P. Lukin, P. Mastrolia, G. Montagna, S. E. Muller, F. Nguyen, O. Nicrosini, D. Nomura, G. Pakhlova, G. Pancheri, M. Passera, A. Penin, F. Piccinini, W. Placzek, T. Przedzinski, E. Remiddi, T. Riemann, G. Rodrigo, P. Roig, O. Shekhovtsova, C. P. Shen, A. L. Sibidanov, T. Teubner, L. Trentadue, G. Venanzoni, J. J. van der Bij, P. Wang, B. F. L. Ward, Z. Was, M. Worek, and C. Z. Yuan
Quest for precision in Hadronic Cross Sections at Low Energy: Monte Carlo tools vs. Experimental data. (Working Group on Radiative Corrections and Monte Carlo Generators for Low Energies)
Eur. Phys. J. C **66**, 585-686 (2010)

LNF - 09 / 15(R)
A. Bocci, M. Cestelli Guidi, A. Clozza, A. Drago, A. Grilli, A. Marcelli, A. Raco and R. Sorchetti, L. Gambicorti, A. De Sio, E. Pace
The Time Resolved Positron Light Emission (3+L) Experiment: A Novel Diagnostics Tool for the DAΦNE Positron Ring

LNF - 09 / 16(NT)
C. Bisegni
JAVA REF Framework

LNF - 09 / 17(IR)
L. Gambicorti, F. Simonetti, A. Marcelli, D. Di Gioacchino, E. Pace, A. De Sio
Optical Study of IR PRESSMAGO Collector

LNF - 09 / 18(P)
S. Bianco, S. Colafranceschi, D. Colonna, M. Giardoni, F. Felli, T. Greci, A. Paolozzi, L. Passamonti, D. Pierluigi, C. Pucci, A. Russo, G. Saviano, M. Abbrescia, R. Guida
Chemical Analyses of Materials Used in the CMS RPC Muon Detector
Submitted to the IPAC10 Conference, Kyoto, Japan, 23-28 May 2010

INFN Reports

INFN / AE–09 / 1
Elvio Di Salvo
Deep Inelastic Processes and the Equations of Motion

INFN / FM–09 / 1
H. Laqua, M. Otte, Y. Podoba, D. Mascali, S. Gammino, L. Celona, F. Maimone, G. Ciavola, R. Miracoli, N. Gambino
Study of the Bernstein Waves Heating in the WEGA Stellarator Plasma and Possible Applications to ECRIS - ECR Ion Sources

INFN / TC–09 / 1
V. Pettinacci, S. Morganti, A. Zullo
Cuore Experiment: Towers' Construction System

INFN / TC–09 / 2 M. Battaglieri, G. Firpo, M. Ivaldi, F. Pratolongo
Splitter Box per l'Esperimento CORMORAD

INFN / TC–09 / 3
C. Aiftimiei, P. Andreetto, S. Bertocco, S.e Dalla Fina, A. Dorigo, E. Frizziero, A. Gianelle, M. Marzolla, M. Mazzucato, M. Sgaravatto, S.o Traldi, L. Zangrando
Design and Implementation of the gLite CREAM Job Management Service

INFN / TC–09 / 4
F. Alessandria, S. Angius, G. Bellomo, P. Fabbricatore, S. Farinon, U. Gambardella, R. Marabotto, R. Musenich, R. Repetto, M. Sorbi and G. Volpini
Technical Design Report of a Superconducting Model Dipole for FAIR SIS300

INFN / TC–09 / 5
A. Codino
Il Ginocchio Nudo del Ferro, sua Necessit ed Evidenza Empirica

INFN / TC–09 / 6
A. Codino
Flussi Misurati di Protoni ed Elio e l'Origine del Ginocchio nello Spettro della Radiazione Cosmica

INFN / TC–09 / 7
A. Badal, P. La Rocca, G.S. Pappalardo, C. Petta, A. Pulvirenti, F. Riggi
Investigation of the Temperature Dependence of Avalanche Photo Diodes for the Alice Electromagnetic Calorimeter

INFN / TC–09 / 8
I. Boscolo
A Twin-Laser System Driving a Powerful Inverse Compton X-ray Source

INFN / TC–09 / 9
A. D'Ambrosio
Manuale di Installazione di un Servizio di Posta Elettronica Completo di Filtri Anti-Virus e Anti-Spam con Politica di Implementazione OPT-OUT

INFN / TC–09 / 10
F. Noto, A. Palmeri
Load Test on the EMCAL Module Frame

INFN / CCR–09 / 1
M. Corosu, F. Costa, O. Pinazza, A. Spanu, R. Veraldi, G. Vita Finzi
Centralizzazione del Servizio di Posta Elettronica per l'INFN

INFN / CCR–09 / 2
S. Arezzini, A. Ciampa, T. Boccali, E. Mazzoni
Il "GRID Data Center" dell'INFN di Pisa

INFN / CCR–09 / 3
S. Arezzini, T. Boccali, F. Calzolari, A. Ciampa, S. Marini, E. Mazzoni, S. Sarkar, S. Taneja, G. Terreni
INFN-Pisa Network and Storage Scenario for LHC TIER 2 and GRID Data Center

INFN / CCR–09 / 4
Ruggero Ricci
Criteri di Progettazione degli Impianti Elettrici per l'Alimentazione dei Centri di Calcolo TIER2

INFN / CCR–09 / 5
Alberto Ciampa
Riflessioni sulla Virtualizzazione

INFN / CCR–09 / 6
A. Ciampa, E. Mazzoni
Calcolo Scientifico: Prime Metodologie Quantitative per un Ambiente di Produzione

SEMINARS in 2009

Oleg Krokhin	Lebedev Physical Institute - Russian Academy of Sciences
22-01-2009	*Modulating Wave Holography*
Zavestovskaya	Lebedev Physical Institute - Russian Academy of Sciences
22-01-2009	*Ultrashort Laser Pulses Induced Material Surface*
Starodub	Lebedev Physical Institute - Russian Academy of Sciences
22-01-2009	*Studies on Interaction of Partially Coherent Laser Radiation*
Alexey Lyashenko	Weizmann Israel Science
26-01-2009	*New developments in visible-sensitive gas avalanche photomultipliers*
Norbert Holtkamp	ITER - France
24-02-2009	*Overview and Challenges of the ITER Project*
R. Chidambaram	Bhabha Atomic Research Centre Mumbai-India
16-03-2009	*Nuclear Energy and Climate Changes*
Simona Bettoni	CERN - European Organizatin for Nuclear Research
02-04-2009	*Commissioning of CTF3 Test Facility at CERN*
Arnon Bernstein	Massachussets Institute of Technology
08-04-2009	*Chiral Dynamics: New Experimental Tests*
Leonardo de Giorgi	Swiss Federal Institute of Technology - Zurich
20-04-2009	*Infrared and Raman study of the charge-density-wave ground state*
Raimondo del Nero	Letterato
21-04-2009	*Presentazione del libro "La citta' restituita"*
Wolfango Plastino	Univ. Roma Tre
30-04-2009	*Il terremoto a L'Aquila del 6 Aprile 2009: analisi multidisciplinari*
Alain Blondel	Univ. Genova
05-05-2009	*MICE, the International Muon Ionization Cooling Experiment*
Adolfo Esposito	Laboratori Nazionali di Frascati - INFN
06-05-2009	*Archeometria, Fisica dei Beni Culturali*
Peter Lukin	Budker Institute of Nuclear Physics of Russian Academy of Science
07-05-2009	*Improving on hadronic contributions to (g-2)/2 of muon with CMD-3 detector at VEPP-2000*
Sandro Rossi e Claudio Sanelli	Centro Nazionale di Adroterapia Oncologica
21-05-2009	*Il Centro nazionale di adroterapia oncologica*
Sara Casalbuoni	ANKA - Institute of Technologyr Karlsruhe
09-06-2009	*COLDDIAG: a COLD vacuum chamber for DIAGnostics*

Jean-Louis Chartie 18-06-2009	European Radiation Dosimetry Group *Simulation of radionuclide neutron sources with Monte Carlo codes*
Pei Guoxi 29-06-2009	Institute of High Energy Physics - Chinese Academy of Sciences *BEPCII Linac Upgrades*
San Vinko 08-07-2009	Atomic & Laser Physics-Clarendon Laboratory-of Oxford *Saturable absorption with XUV FEL radiation*
Saxena Surendre 08-07-2009	Florida International University *What is in the Earth's core? An experimental and thermodynamic study*
Alex Chao 13-07-2009	SLAC - National Accelerator Laboratory *A Computational Tool for luminosity Optimization*
Shiqiang Wei 23-07-2009	University of Science and Technology of China, Hefei *Structures and ferromagnetic properties of dilute magnetic semiconductors studied by x-ray absorption fine structure and first principles*
Francisco Fernandez 23-07-2009	Consejo de Secutitad Nuclear - Spain *The LNT Model in Radiation Protection System*
H. Tomizawa 04-09-2009	Japan Synchrotron Radiation Research Institute *Novel Single Shot EO based 3D Bunch Charge Distribution Monitor with Femto-second Bunch Resolution*
V.A. Dolgashev 15-09-2009	SLAC - National Accelerator Laboratory *Progress on High Gradient Research*
Cyril Petibois 22-09-2009	Bordeaux University *Multimodal imaging of single cells with high performance analytical techniques: recent results with infrared synchrotron radiation*
John Byrd 02-10-2009	Lawrence Berkeley National Laboratory *Timing and Synchronization for Ultrafast Light Sources*
Michael Peskin 08-10-2009	SLAC - National Accelerator Laboratory *A Top top ten list*
Ricardo Sussman 12-10-2009	Kings College London *CVD diamond applications in high-tecnology*
Massimo Ferrario 15-10-2009	Laboratori Nazionali di Frascati - INFN *Free electron lasers and the SPARC project*
Teresa Montaruli 16-10-2009	Wisconsin University *Searching Extraterrestrial High Energy Neutrinos*
Bruno Carli 12-11-2009	Istituto di Fisica Applicata - CNR Firenze *I Cambiamenti Climatici*
Peter Lukin 19-11-2009	Budker Institute of Nuclear Physics of Russian Academy of Science *Status of Hadronic cross sections measurements*

Fabio Bossi	Laboratori Nazionali di Frascati - INFN
23-11-2009	*Signals from a low energy dark world*
Qin Qing	Institute of High Energy Physics - Chinese Academy of Science
10-12-2009	*Design, commissioning and luminosity upgrade of the BEPC-II storage rings*

Glossary

These are the acronyms used in each status report to describe personnel qualifications other than Staff Physicist:

Art 15	Term Contract (Technician)
Art. 2222	Collaboration Contract
Art. 23	Term Contract (Scientist)
Ass.	Associated Scientist
Ass. Ric.	Research Associate
Bors.	Fellowship holder
Bors. PD	PostDoc Fellow
Bors. UE	European Community Fellow
Dott.	Graduate Student
Laur.	Undergraduate Student
Loc. Coor.	Local Coordinator
Osp.	Guest Scientist
Perfez.	PostLaurea Student
Resp.	Local Spokesperson
Resp. Naz.	National Spokesperson
Specializ.	PostLaurea Student
Tecn.	Technician